Quantum Computational Particle Physics: Algorithms, Resource Estimation, and Model-Building

by

Angus Kan

A thesis
presented to the University of Waterloo
in fulfillment of the
thesis requirement for the degree of
Doctor of Philosophy
in
Physics (Quantum Information)

Waterloo, Ontario, Canada, 2022

Examining Committee Membership

The following served on the Examining Committee for this thesis. The decision of the Examining Committee is by majority vote.

External Examiner:	Zohreh Davoudi Assistant Professor, Department of Physics, University of Maryland
Supervisor:	Christine Muschik Assistant Professor, Department of Physics and Astronomy, University of Waterloo
Internal Member:	Raymond Laflamme Professor, Department of Physics and Astronomy, University of Waterloo
Internal-External Member:	David Gosset Associate Professor, Department of Combinatorics and Optimization, University of Waterloo
Other Member:	Kazi Rajibul Islam Assistant Professor, Department of Physics and Astronomy, University of Waterloo

Author's Declaration

This thesis consists of material all of which I authored or co-authored: see Statement of Contributions included in the thesis. This is a true copy of the thesis, including any required final revisions, as accepted by my examiners.

I understand that my thesis may be made electronically available to the public.

Statement of contributions

The content of Chapter 3 was previously published in [1]:
D. Paulson, L. Dellantonio, J. F. Haase, A. Celi, A. Kan, A. Jena, C. Kokail, R. van Bijnen, K. Jansen, P. Zoller, C. A. Muschik. Simulating 2D effects in Lattice Gauge Theories on a Quantum Computer. *PRX Quantum*, 2:030334, 2021.
Author contributions:
P. Zoller, and C. A. Muschik proposed and supervised the project.
D. Paulson, L. Dellantonio, A. Celi, and A. Kan produced the theoretical and analytical results.
J. F. Haase, C. Kokail, and R. van Bijnen performed the numerical simulations.
A. Jena produced the measurement circuits.
D. Paulson, L. Dellantonio, and J. F. Haase wrote the paper with inputs from all other authors.

The content of section 2.1 and chapter 4 were previously published in [2]:
A. Kan, Y. Nam. Lattice Quantum Chromodynamics and Electrodynamics on a Universal Quantum Computer. *arXiv preprint arXiv:2107.12769*, 2021.
Author contributions:
A. Kan and Y. Nam designed the project.
A. Kan and Y. Nam designed the circuits.
A. Kan performed the analytical resource estimation with input from Y. Nam.
A. Kan and Y. Nam wrote the paper.

The content of Chapter 5 was previously published in [3]:
J. F. Haase, L. Dellantonio, A. Celi, D. Paulson, A. Kan, K. Jansen, C. A. Muschik. A resource efficient approach for quantum and classical simulations of gauge theories in particle physics. *Quantum*, 5:393, 2021.
Author contributions:
A. Celi, K. Jansen, and C. A. Muschik designed and supervised the project.
J. F. Haase, L. Dellantonio, and A. Kan performed the numerical simulations.
J. F. Haase, L. Dellantonio, and A. Celi produced the theoretical and analytical results, with input from D. Paulson and A. Kan.
J. F. Haase, L. Dellantonio, and A. Celi wrote the paper with inputs from all other authors.

The content of Chapter 6 was previously published in [4] and [5]:
A. Kan, L. Funcke, S. Kühn, L. Dellantonio, J. Zhang, J. F Haase, C. A. Muschik, K. Jansen. Investigating a (3+1)D Topological θ-Term in the Hamiltonian Formulation of Lattice Gauge Theories for Quantum and Classical Simulations. *Phys. Rev. D*, 104:034504, 2021.
A. Kan, L. Funcke, S. Kühn, L. Dellantonio, J. Zhang, J. F Haase, C. A. Muschik, K. Jansen. 3+1D θ-Term on the Lattice from the Hamiltonian Perspective. *Contribution to the proceedings of the 38th International Symposium on Lattice Field Theory; arXiv preprint arXiv:2111.02238*,

2021.

Author contributions:

C. A. Muschik and K. Jansen proposed and supervised the project.

A. Kan and L. Funcke derived the analytical and theoretical results.

A. Kan performed the numerical simulations.

A. Kan, L. Funcke, and S. Kühn wrote [4], and A. Kan wrote [5], with input from all other authors.

Abstract

Quantum simulation is one of the most promising applications of quantum computers. It is anticipated that quantum simulation will accelerate scientific discovery, and advance our understanding of nature. One area that stands to benefit from quantum simulation is particle physics. This thesis contains my contributions to quantum simulation of lattice gauge theories–a well-known first-principle computational method in particle physics.

The limitations of current and near-term quantum processors, such as high error rates and small number of qubits, severely restrict the size and depth of quantum circuits that can be executed with high fidelity. Tailored to these hardware constraints, short-depth variational quantum algorithms are proposed to solve small lattice quantum electrodynamics models in two spatial dimensions. The proposal is based on, and made possible by a novel lattice quantum electrodynamics model designed to lower the simulation memory overhead.

There is no better time than now to understand and minimize fault-tolerant computational resource requirements of quantum simulations of lattice gauge theories so that they can be implemented sooner than later. To this end, complete gate-by-gate quantum algorithms with concrete fault-tolerant resource estimates are constructed to simulate lattice quantum electrodynamics and chromodynamics.

Finally, a topological θ-term, directly relevant to the strong CP problem in particle physics, in the Hamiltonian formulation of lattice gauge theories is derived for future quantum simulations. Classical numerical results suggest a phase transition due to this term in a three-dimensional U(1) lattice gauge theory. Verification of this transition, and large-scale simulations of quantum chromodynamics with a θ-term will likely require a quantum computer.

Acknowledgements

I would like to thank my supervisor Christine Muschik, for her guidance and introducing me to the topic of quantum simulations of lattice gauge theory. I would also like to thank other members of my thesis committee, Zohreh Davoudi, David Gosset, Rajibul Islam, and Raymond Laflamme for reading my thesis and providing feedback.

Many thanks to all my collaborators for their contributions to the projects that constitute this thesis. In particular, I thank my particle physics theory collaborators, Lena Funcke, Stefan Kühn, and Karl Jansen for patiently answering my many naive questions about lattice gauge theories and particle physics. A special thanks to my friend, Yunseong Nam, from whom I have learnt plenty about circuit implementation of quantum simulation.

My time at Waterloo would not be the same without my fellow research group members: Danny Paulson, Luca Dellantonio, Jan Haase, Jinglei Zhang, Ryan Ferguson, Yasar Atas, and Amin Jahanpour. Finally, a special shout-out to Erica Boland for keeping the group in order, and helping out whenever and in whatever ways she can.

Table of Contents

List of Figures

List of Tables

Chapter 1

Introduction

1.1 Quantum Simulation for Particle Physics

Simulating quantum physics is one of the most promising applications of a quantum computer. Forty years ago, Feynman argued that simulating quantum dynamics on a conventional computer was exponentially difficult [10]. This catalyzed the idea of quantum computation. In contrast, it has been shown since then that quantum computers can efficiently simulate physical systems from a wide range of fields including quantum chemistry, condensed matter physics, and high-energy physics. As such, it is anticipated that quantum simulation will accelerate scientific discovery [11, 12] in both applied research areas, such as chemicals and materials design, and more fundamental disciplines, such as particle and nuclear physics. This thesis aims to connect two fields at the frontier of science, namely, quantum computation and particle physics, and contributes to the development of quantum simulation for particle physics.

Particle physics is best described by the Standard Model (SM) because it captures the most fundamental building blocks, including electroweak and strong forces, of the known universe, while producing accurate phenomenological predictions. The SM is a quantum field theory (QFT), in which particles are described as excitations of the underlying fields. For instance, photons are excitations of the electromagnetic field. Furthermore, the underlying fields can undergo certain local transformations, called gauge transformations, without affecting measurable observables, a property known as local gauge invariance or symmetry. A quantum field theory equipped with a local gauge symmetry, such as the SM, is a gauge theory.

In order to fully utilize the SM to predict nature's behaviors, it is necessary to explore non-perturbative methods, as analytical calculations, which typically employ perturbative methods, have failed to answer important questions that are even within the description of the SM, such as the quantum chromodynamics (QCD) phase diagram [13]. One of the best-known first-principle

non-perturbative computational methods for QCD is lattice gauge theories (LGTs) [14]. Indeed, LGTs have been employed to successfully compute classically multifarious non-perturbative aspects of particle and nuclear physics, such as the low-lying baryon spectrum [15], various fundamental parameters of the SM [16], and the reactions of nucleons [17]. In classical simulations of LGTs, usually performed in the Euclidean-time path integral formulation, sampling from an exponentially large configuration space with Markov chain Monte Carlo (MCMC) methods often suffices to extract static properties [18]. However, MCMC simulations, due to the infamous sign problem [19], suffer from computational inefficiency for example in simulating fermions, topological terms, and non-equilibrium real-time dynamics.

Quantum simulation circumvents the sign problem, and does not suffer the curse of exponentiality. In 1996, the first explicit algorithm for quantum simulation was provided by Lloyd [20]. Twenty years later, using this algorithm, the first simulation of the real-time dynamics of the Schwinger model–a LGT that describes quantum electrodynamics (QED) in one spatial dimension was successfully implemented on a four-qubit trapped-ion quantum computer [21]. Lloyd's algorithm is based on the first-order product-formula approximation of the Hamiltonian time-evolution operator. Higher-order variants [22] have subsequently been studied in the context of quantum simulation [23]. Algorithms with better asymptotic dependence on evolution time and desired precision, such as, Taylor-series algorithm [24] and quantum signal processing [25], have been considered in more recent studies. While these algorithms are efficient in their asymptotic gate complexities, in practice, their estimated quantum computational resource requirements, i.e., the number of required qubits and quantum gates, even for simple physical systems, far exceed the capabilities of existing hardware [26].

Currently, we are in the age of the so-called "noisy intermediate-scale quantum" (NISQ) devices [27]. In general, NISQ devices have a small number of qubits and noisy gates. Therefore, they can only run quantum circuits that are very limited in their size and depth. Constrained by these limitations, the study of a class of heuristic algorithms call variational quantum algorithms (VQAs) [28, 29] has emerged in recent years. While the limitations of VQAs are still under active research [30, 31, 32], their proposed applications span many fields including chemistry, physics, optimization, and machine learning. An advantage of VQAs is that they often can be executed by running a short-depth circuit on a NISQ device. A type of VQAs called variational quantum eigensolver (VQE) [33] is particularly relevant to physics and chemistry, due to its objective of solving for ground states, and extracting static expectation values of physical observables. The first VQE applied to a LGT, once again the Schwinger model, was implemented on a 20-qubit device [34] in 2019. The hope is that more complex problems in LGTs can be solved using VQEs.

1.2 This Thesis

This thesis addresses three important aspects of quantum simulation of LGTs: algorithms, resource estimation, and model-building. In chapter 2, we begin by providing a brief introduction to the Hamiltonian formulation of LGTs, VQE and product-formula simulation algorithms, and finally, a short overview of fault-tolerant resource estimation. In chapter 3, we design VQE protocols for simulating QED in two dimensions, and demonstrate the potential of near-term quantum computers in simulating LGTs beyond one dimension. We provide in chapter 4 scalable quantum algorithms down to a gate-by-gate level, along with concrete estimates of the quantum computational resources required, to simulate lattice QED and QCD in arbitrary spatial dimensions on a fault-tolerant quantum computer. In chapter 5, we formulate a novel basis for lattice QED, which reduces the memory requirements for both quantum and classical simulations, and is crucial for the algorithmic design in 3. Finally in chapter 6, we derive a topological θ-term, which is directly relevant to the famous strong CP problem [35], in the Hamiltonian formulation, and provide numerical evidences for a phase transition.

This collection of works represents our efforts in the development for near-term and longer-term quantum simulation of LGTs. Designing near-term algorithms not only pushes the capabilities of current hardware, but also provides insights into the type of particle-physics models that near-term devices can solve despite their limitations. These insights are particularly useful for designing models that are suitable to near-term hardware and capture the wanted physics at the same time. This co-design process was crucial in the fruition of the work in chapters 3 and 5. With the anticipated arrival of the first-generation fault-tolerant error-corrected quantum computers from scores of companies, including Google, Honeywell, IBM, and IonQ, by the end of this decade [36, 37, 38, 39, 40], it is important to address the question of how powerful of a fault-tolerant quantum computer is needed for a large-scale LGT simulation. The resource estimates in chapter 4 aim to not only address this question, but also serve as a concrete benchmark for future software improvements. While large-scale simulations are the ultimate goal, rich physical behaviors also appear in smaller systems. The models we derived in chapter 6 are good examples. In certain system sizes, these models are amenable to both classical and quantum simulations, where the phase diagrams obtained classically can act as a benchmark for the quantum results.

1.3 Related Works

In recent years, there have been significant advances in quantum simulation of various QFTs, including but not limited to LGTs, such as scalar field theory, nuclear effective field theory, etc. They are all important to the overarching goal of simulating different aspects of particle physics. For a review, we refer readers to [41] and [42]. Here, we try to include a comprehensive list of references in this area. On the experimental front, a plethora of proof-of-concept simulations of

QFTs have been implemented on currently available quantum devices, using approaches including analog quantum simulation [43, 44, 45, 46], variational quantum simulation [47, 48, 34, 49, 50, 51, 52, 53, 54, 55], quantum frequency processing [56], quantum annealing [57], and digital quantum simulation [21, 58, 59, 60, 61, 62]. On the theoretical front, there exists a host of methods to realize QFTs on various types of quantum hardware [6, 63, 64, 65, 66, 67, 68, 69, 70, 71, 72, 73, 74, 75, 76, 77, 78, 79, 80, 81, 82, 83, 84, 85, 86, 87, 88, 89, 90, 91, 92, 93, 94, 95, 96, 97, 41, 98, 99, 7, 1, 100, 101, 102, 103, 104].

Chapter 2

Background

This chapter contains background information on key topics that are useful to understand the upcoming chapters, namely, lattice gauge theories (LGTs), variational quantum eigensolver (VQE), product-formula (PF) algorithms, and resource estimation, each of which is introduced in a self-contained section. We note that while LGTs are pertinent to chapters 3-6, VQE is relevant to only chapter 3, and PF and resource estimation are relevant to only chapter 4. To guide the readers, we make references to the related chapters in each section whenever necessary.

2.1 Lattice Gauge Theories

We consider a universe, coarse-grained to form a lattice, capable of hosting fermions and bosons at lattice sites and links, respectively. LGTs then capture the excitation of both the fermions and gauge bosons. Fermionic excitation can readily be encoded in the usual occupation number basis. The basis for bosonic excitation is however carefully chosen based on the considered symmetry group. For instance, in a U(1) LGT, each bosonic link is described by the angular momentum basis of a quantum particle constrained to move along a circle, also known as a planar rotor, with an integer-valued quantum number. The quantum number represents the angular momentum where its sign denotes the two directions of rotation. In a SU(2) LGT, each gauge boson can be interpreted as a rigid rotator, which can be represented by an angular momentum basis with three quantum numbers: total angular momentum, the angular momenta in the space-fixed and body-fixed frames of reference [105]. The SU(N) ($N > 2$) generalization of this angular momentum basis is labelled by $N^2 - 1$ (the dimension of SU(N)) quantum numbers [6, 106]. Note that the quantum number(s) are unbounded. In order to encode them using a finite number of qubits on a quantum computer, each quantum number must be truncated. In our algorithms, we apply a cutoff Λ such that each quantum number takes on $\sim \Lambda$ values. In chapter 4, we consider Λ as a

parameter in the Hamiltonian. In [107], it was shown that Λ can be determined as a function of the precision at which the truncated theory simulates the original theory with infinite-dimensional gauge bosons.

In the following, we provide an overview of the Kogut-Susskind Hamiltonian [105]–the standard Hamiltonian formulation of lattice gauge theories. Note that the notation used here is adopted in chapter 4. The notations used in other chapters differ slightly and will be introduced appropriately. The Kogut-Susskind Hamiltonian is defined as

$$\hat{H} = \hat{H}_{gauge} + \hat{H}_{matter}, \tag{2.1}$$

where $\hat{H}_{gauge}$ describes the dynamics of the bosonic electric and magnetic gauge fields, and $\hat{H}_{matter}$ describes the dynamics that involve the fermionic matter. The Hamiltonian is defined on a d-dimensional spatial lattice, and the temporal direction is continuous. A site on the lattice is denoted by a vector $\vec{n} = \sum_{i=1}^{d} n_i \hat{i}$, where $\hat{i}$ is a unit lattice vector pointing in one of the orthogonal directions. A site is labelled even or odd, depending on whether $(-1)^{\vec{n}} = (-1)^{\sum_i n_i}$ evaluates to 0 or 1, respectively. A link between neighboring sites is denoted by a tuple $(\vec{n}, l)$ of the starting site $\vec{n}$ and its direction $\hat{l}$. On the lattice, the fermions and anti-fermions reside on the sites, while the gauge fields, which mediate the interaction between them, occupy the links.

The matter Hamiltonian consists of two terms, mass $\hat{H}_M$ and kinetic $\hat{H}_K$ Hamiltonians defined by [105]

$$\begin{aligned}
\hat{H}_{matter} &= \hat{H}_M + \hat{H}_K, \text{ where} \\
\hat{H}_M &= m \sum_{\vec{n}} \sum_{\alpha} (-1)^{\vec{n}} \hat{\psi}^{\dagger}_{\alpha}(\vec{n}) \hat{\psi}_{\alpha}(\vec{n}), \\
\hat{H}_K &= \frac{1}{2a} \sum_{\vec{n}} \sum_{l=i,j,k} \sum_{\alpha,\beta} (\hat{\psi}_{\alpha}(\vec{n})^{\dagger} \hat{U}_{\alpha\beta}(\vec{n}, l) \hat{\psi}_{\beta}(\vec{n} + \hat{l}) + \hat{\psi}_{\alpha}(\vec{n}) \hat{U}^{\dagger}_{\alpha\beta}(\vec{n}, l) \hat{\psi}^{\dagger}_{\beta}(\vec{n} + \hat{l})),
\end{aligned} \tag{2.2}$$

where m is the bare mass, a is the lattice spacing, $\hat{\psi}_{\alpha}(\vec{n}), \hat{\psi}^{\dagger}_{\alpha}(\vec{n})$ are vectors of the fermionic annihilation and creation operators, respectively, at site $\vec{n}$ with α labelling different fermionic species, and $\hat{U}_{\alpha\beta}(\vec{n}, l), \hat{U}^{\dagger}_{\alpha\beta}(\vec{n}, l)$ are matrices known as parallel transporters [108], of which the elements are gauge field operators that couple fermion-anti-fermion pairs, for instance, a fermion and an anti-fermion of species α and β that occupy sites $\vec{n}$ and $\vec{n} + \hat{l}$. The alternating sign $(-1)^{\vec{n}}$ reflects the use of the staggered fermions [105]. Physically, we can interpret creating (destroying) a particle at an even (odd) site as creating a fermion (anti-fermion). $\hat{H}_M$ computes the mass of all fermionic matter by multiplying the number of fermions and anti-fermions in the lattice by m. As such, $\hat{H}_M$ governs the dynamics of free fermions and anti-fermions in the absence of gauge fields. $\hat{H}_K$ describes the dynamics of fermion-anti-fermion pair creation and annihilation, and the corresponding changes in the mediating gauge fields.

As an explicit example, consider the Abelian U(1) LGT. This theory describes QED on a lattice, each site can either be occupied by an electron or a positron due to the Pauli exclusion

principle. As such, there is only one component each in the vectors $\hat{\psi}_\alpha, \hat{\psi}^\dagger_\alpha$, and hence, one component each in the parallel transporter matrices. In electrodynamics, Gauss' law implies that point charges emanate electric fluxes. In order to satisfy Gauss' law on a lattice, creating or destroying an electron-positron pair will necessarily generate or remove an electric flux between them. The electric fluxes are raised and lowered by the parallel transporters.

In SU(N) LGTs, the gauge fields are non-Abelian, and the vectors of fermionic operators have N components and the parallel transporters are $N \times N$ matrices. As opposed to only one type of electric charge in QED, there are N different species of fermions carrying N types of charges known as colors. On a lattice, the N species are represented by N-component vectors $\hat{\psi}_\alpha, \hat{\psi}^\dagger_\alpha$. Similar to QED, SU($N$) LGTs allow for pair creation and annihilation. However, there are N^2 different types of fermion-anti-fermion pair creation or annihilation, to account for all possible combinations of colors. As a consequence of the non-Abelian Gauss' law, there are N^2 different types of electric fluxes that can be generated in or removed from the non-Abelian chromoelectric field. Those changes in the chromoelectric field are induced by the N^2 elements of the parallel transporters.

In the absence of matter, the Kogut-Susskind Hamiltonian is reduced to a pure gauge Hamiltonian, which consists of an electric $\hat{H}_E$ and magnetic $\hat{H}_B$ Hamiltonian given by [105]

$$\begin{aligned} \hat{H}_{gauge} &= \hat{H}_E + \hat{H}_B, \text{ where} \\ \hat{H}_E &= \frac{g^2}{2a^{d-2}} \sum_{\vec{n},l} \sum_a [\hat{E}^a(\vec{n},l)]^2, \\ \hat{H}_B &= -\frac{1}{2a^{4-d}g^2} \sum_\square \mathrm{Tr}[\hat{P}_\square + \hat{P}^\dagger_\square], \end{aligned} \tag{2.3}$$

where g denotes the bare coupling strength, Tr denotes a trace operator, and $\square$ represents the elementary square cells, called plaquettes, of a lattice. The magnetic Hamiltonian $\hat{H}_B$ is formed from products of the parallel transporters around each plaquette, called plaquette operators

$$\mathrm{Tr}[\hat{P}_\square] = \sum_{\alpha,\beta,\gamma,\delta} \hat{U}_{\alpha\beta}(\vec{n},i)\hat{U}_{\beta\gamma}(\vec{n}+\hat{i},j)\hat{U}^\dagger_{\gamma\delta}(\vec{n}+\hat{j},i)\hat{U}^\dagger_{\delta\alpha}(\vec{n},j), \tag{2.4}$$

traced over the matrix elements. In particular, the plaquette operators create loops of electric fluxes surrounding the plaquettes, and generate magnetic fluxes. The electric flux at each link is measured by a vector of electric field operators $\hat{E}^a$, where the number of components a is the same as the number of generators of the considered gauge group. Moreover, depending on the gauge group, the electric field operators and parallel transporters satisfy a specific set of commutation relations.

Once again, considering U(1) LGT as an instance, the gauge fields are the usual Maxwell electric and magnetic fields. In the case of SU(N) LGTs, the gauge fields are non-Abelian

chromoelectric and chromomagnetic fields, which are considerably more complicated. Let us use SU(3) LGT, which describes QCD, the theory of strong interaction, on a lattice as an example. Here, the non-Abelian electric fluxes are excitations of the underlying gauge field, known as the gluon field, which is eponymously named after the gauge boson for the strong force. Gluons are analogous to photons in QED. However, an important distinction between them is that gluons can self-interact, due to their non-Abelian nature, and may form composite particles, called glueballs, among themselves. This self-interacting nature makes QCD significantly more difficult to analyze than QED. We note that, SU(3) LGT is perhaps the most interesting one in the context of particle physics, due to its relation to QCD. In this thesis, the results in chapters 3 and 5 apply to U(1) LGT, those in chapter 4 apply to U(1), SU(2), and SU(3) LGTs, and the analytical results in chapter 6 apply to both Abelian, e.g., U(1), and non-Abelian, e.g., SU(N) for $N > 1$, LGTs, while the numerical results applies to U(1) LGT.

2.2 Variational Quantum Eigensolver

The VQE [33, 28] belongs to a class of heuristic algorithms called variational quantum algorithms (VQAs) [29], where a problem is encoded in a parameterized cost function to be evaluated on a quantum computer, and an optimizer on a conventional computer trains the parameters, thereby forming a closed feedback loop between the quantum and classical computer. The main objective of a VQE is to prepare the ground state and compute the ground state energy of a given Hamiltonian $\hat{H}$. Naturally, the cost function is chosen to be the expectation value of the Hamiltonian, i.e., $\mathcal{C}(\boldsymbol{\theta}) = \langle \hat{H}(\boldsymbol{\theta}) \rangle$, since it is an upper bound of the ground state energy. The expectation value is estimated by measuring $\hat{H}$ with respect to a parametrized variational state $|\Psi(\boldsymbol{\theta})\rangle = \hat{U}(\boldsymbol{\theta}) |\Psi_{in}\rangle$. Here, $|\Psi_{in}\rangle$ is the input state to a quantum computer, and $\hat{U}(\boldsymbol{\theta})$ is the quantum circuit applied to it, where $\boldsymbol{\theta}$ are the parameters of the quantum gates in the circuit. Once estimated, the expectation value is then fed into a classical computer, where an optimization algorithm attempts to minimize $\mathcal{C}(\boldsymbol{\theta})$, and provides an updated set of variational parameters $\boldsymbol{\theta}'$ to be used for the next round of cost function evaluation on the quantum computer. The VQE is deemed suitable for NISQ devices, since $\hat{U}(\boldsymbol{\theta})$ is typically a short-depth circuit. It is a heuristic algorithm because its output is not guaranteed to be the ground state. Obtaining a close approximation of the ground state often relies on an educated guess of an ansatz, i.e., $|\Psi_{in}\rangle$ and $\hat{U}(\boldsymbol{\theta})$. The fact that VQEs and more generally, VQAs are heuristic algorithms is a concern, as they often do not have scalable performance guarantees. However, heuristic algorithms can be useful, with neural networks being an example. In fact, VQAs' resemblances to neural networks has led to the creation of an entire research area in their abilities to perform machine learning tasks (see [29] and references therein), but this is beyond the scope of this thesis. In chapter 3 of this thesis, we provide constructions of VQEs to solve certain U(1) LGTs in two dimensions.

2.3 Product Formulas

The first step for any product-formula (PF) algorithms is to divide up a total simulation time T into r segments. Then, the evolution generated by a Hamiltonian $\hat{H}$ can be expressed as $e^{-i\hat{H}T} = (e^{-i\hat{H}T/r})^r \equiv (e^{-i\hat{H}t})^r$. Further, the Hamiltonian $\hat{H}$ is decomposed into a sum of simpler Hamiltonians, $\hat{H} = \sum_{j=1}^{l} \hat{H}_j$, where each $e^{-i\hat{H}_j t}$ can be simulated with an efficient quantum circuit. The first-order PF, or Lie-Trotter formula, which underlies the first explicit quantum simulation algorithm [20], is given by

$$\hat{U}_1(t) = \prod_{j=1}^{l} e^{-i\hat{H}_j t}. \tag{2.5}$$

Its error is bounded by [23]

$$||e^{-i\hat{H}T} - \hat{U}_1^r(t)|| \leq \frac{1}{2} \sum_j |||[\sum_{i>j} \hat{H}_i, \hat{H}_j]||| \frac{T^2}{r}. \tag{2.6}$$

Therefore, for a given spectral-norm error ϵ, the value of r grows as $O(T^2/\epsilon)$. This scaling can be improved by using a higher-order PF. For instance, consider the second-order PF, defined as

$$\hat{U}_2(t) = \prod_{j=1}^{l} e^{-i\hat{H}_j t/2} \prod_{j=l}^{1} e^{-i\hat{H}_j t/2}. \tag{2.7}$$

In this case, the error bound is [23]

$$||e^{-i\hat{H}t} - \hat{U}_2(t)|| \leq \frac{1}{12} \sum_i |||[[\hat{H}_i, \sum_{j>i} \hat{H}_j], \hat{H}_i]||t^3 + \frac{1}{24} \sum_i |||[[\hat{H}_i, \sum_{j>i} \hat{H}_j], \sum_{k>i} \hat{H}_k]||t^3, \tag{2.8}$$

which leads to a Trotter-step r scaling of $O(T^{3/2}/\epsilon^{1/2})$. Further improvements can be achieved with high-order PF, which can be constructed recursively [22]. However, it is reported in [7] the higher-order PFs are rarely preferred for quantum simulations due to the fact that (i) the second-order formula can actually cost fewer computational resources and outperform asymptotically more efficient methods such as LCU and QSP [26], and (ii) compared to the error bounds for the first- and second-order PF, those for higher-order PF are unlikely to be tight and are more difficult to compute [23]. In chapter 4 of this thesis, we construct explicit second-order PF algorithms down to a gate-by-gate level for U(1), SU(2), and SU(3) LGTs in arbitrary dimensions.

2.4 Resource Estimation

The goal of resource estimation is to estimate the amount of quantum computational resources needed to run a given quantum algorithm to solve a particular problem. These resources can be divided into two types: space and time costs.

In chapter 4, we focus on the fault-tolerant setting, as we expect that fault-tolerance is necessary to run large-scale quantum simulations. In the fault-tolerant setting, the space and time costs can be quantified by the required number of logical qubits and quantum gates, respectively. However, not all quantum gates cost the same. We consider a standard gate set for fault-tolerant quantum computations, namely, the Clifford+T gate set, where the Clifford gates include the Hadamard (H), phase (S), and controlled-NOT (CNOT) gates that are defined by

$$\mathrm{H} = \frac{1}{\sqrt{2}}\begin{pmatrix} 1 & 1 \\ 1 & -1 \end{pmatrix}, \ \mathrm{S} = \begin{pmatrix} 1 & 0 \\ 0 & i \end{pmatrix}, \ \mathrm{CNOT} = \begin{pmatrix} 1 & 0 & 0 & 0 \\ 0 & 1 & 0 & 0 \\ 0 & 0 & 0 & 1 \\ 0 & 0 & 1 & 0 \end{pmatrix}, \tag{2.9}$$

and the non-Clifford T gate is defined by

$$\mathrm{T} = \begin{pmatrix} 1 & 0 \\ 0 & e^{i\frac{\pi}{4}} \end{pmatrix}. \tag{2.10}$$

Generally, applying a T gate incurs significantly more overhead than applying any Clifford gate [109, 110]. Therefore, the number of T gates is commonly considered as a good metric to approximate the time cost.

We now sketch out the resource estimation pipeline for a PF quantum simulation. When one implements a PF algorithm, there are two kinds of errors: Trotter and synthesis errors, the sum of which is bounded by a chosen total error budget ϵ_{total}. The Trotter error $\epsilon_{\text{Trotter}}$, evaluated using commutator bounds [23], can be used to determine the number of Trotter steps r, as shown in Sec. 2.3. For each Trotter step, we approximate $e^{i\hat{H}t}$ by a product of sub-evolutions $e^{i\hat{H}_j t}$, which are synthesized using Clifford and T gates as $\hat{U}_j$ such that $||\hat{U}_j - e^{i\hat{H}_j t}|| < \delta_j$, for a chosen synthesis error δ_j. Typically, the smaller the error tolerance δ_j is, the larger the number of gates in the circuit $\hat{U}_j$ will be. Then, the total synthesis error of the product of sub-evolutions is bounded by $\sum_j \delta_j$, using the fact that $||\hat{U}_1\hat{U}_2 - \hat{V}_1\hat{V}_2|| \leq ||\hat{U}_1 - \hat{V}_1|| + ||\hat{U}_2 - \hat{V}_2||$ for unitaries $\hat{U}_i$ and $\hat{V}_i$. Finally, one can compute the total gate count from ϵ_{total}, and the total qubit count via careful bookkeeping of the qubit count for each $e^{i\hat{H}_j t}$.

Chapter 3

Variational Quantum Eigensolver for (2+1)D U(1) Lattice Gauge Theory

In this chapter, we use a variational approach to simulate ground state properties of U(1) lattice gauge theories (LGTs). In contrast to previous schemes, our protocols provide the novel opportunity to use existing quantum hardware to simulate 2D [1] effects in LGTs, including dynamical matter and non-minimal gauge field truncations, with a perspective to go to the continuum limit, i.e., when the lattice spacing approaches zero. We consider quantum electrodynamics (QED), the gauge theory describing charged particles interacting through electromagnetic fields. In contrast to 1D QED, where the gauge fields can be fully eliminated [21, 81, 111, 112] and magnetic fields do not exist, in higher dimensions, non-trivial magnetic field effects and the Fermi statistics of the matter fields become important. Many-body terms due to these non-trivial effects appear in the Hamiltonian, and thus, implementations on currently available quantum hardware become challenging. In this work, we outline novel approaches to overcome these difficulties and to render near-term demonstrations possible.

Specifically, we provide effective simulation techniques for simulating quasi-2D and 2D lattice-QED systems with open and periodic boundary conditions. To address the problem of finding the ground state of these models on NISQ hardware, we develop variational quantum eigensolver (VQE) algorithms [28] for current qubit-based quantum computers. In the quest of simulating LGT with these VQE algorithms, we address the crucial points of

1. developing a formulation of the problem within the resources of NISQ devices,

2. implementing the model efficiently on the quantum hardware,

[1] In the remainder of this chapter, we use '1D' and '2D' to denote one and two spatial dimensions, respectively. The temporal dimension, denoted by '+1' in the title, is neglected.

3. having a clear procedure to scale up to larger, more complex systems, and

4. verifying the results in known parameter regimes.

For the first step, we cast the model into an effective Hamiltonian, as done in [3] (see chapter 5). The total Hilbert space is then reduced to a smaller gauge-invariant subspace by eliminating redundant gauge degrees of freedom, at the cost of introducing non-local interactions. Secondly, in order to measure this effective Hamiltonian on the quantum hardware, we find an encoding for translating fermionic and gauge operators into qubit operators. The quantum circuits for the VQEs are subsequently determined, respecting the symmetries of both the encoding and the Hamiltonian. On the one hand, this allows for an optimal exploration of the subsector of the Hilbert space in which gauge-invariant states lie. On the other side, our circuits are Hamiltonian-inspired, and can be scaled up to bigger systems and to less severe truncations. The fourth and last step in the list above is taken care by comparing the outcomes of the VQE algorithms with analytical results, in parameter regimes that are accessible to both. We resort to perturbation theory (see Sec. V in [1] for the perturbative analysis) and exact diagonalization, but more sophisticated classical analytical and numerical tools [113, 114, 115] can be in principle used.

In Sec. 3.1, we introduce lattice QED Hamiltonian, and present an effective Hamiltonian description. In Sec. 3.2, we provide a short description of the available quantum hardware on which our VQEs may be implemented, along with the classical optimizer used in our VQEs. In Sec. 3.3, we provide the qubit-encoding of the Hamiltonian, circuits for our VQEs, and a classical simulation of the proposed VQEs. Conclusions and outlooks are presented in Sec. 3.4.

3.1 Simulated models

In this section, we present the models to be simulated in our proposal. In Sec. 3.1.1, we review the Hamiltonian formulation of lattice QED in 2D and the truncation applied to gauge degrees of freedom. Note that the notation used here is slightly different from that in Sec. 2.1. The specific systems considered in the rest of this chapter are then described in Sec. 3.1.2 [open boundary conditions (OBC)] and Sec. 3.1.3 [periodic boundary conditions (PBC)].

3.1.1 Lattice QED in 2 dimensions

In this chapter, we consider two-dimensional lattices, with matter and gauge fields defined on the sites and on the links, respectively. Using staggered fermions [105], electrons and positrons are represented by single component fermionic field operators $\hat{\phi}_i$ for each site i. As shown in Figs. 3.1(b) and 3.1(c), odd (even)-numbered lattice sites hold particles (antiparticles), that carry a $+1$ (-1) charge q_i.

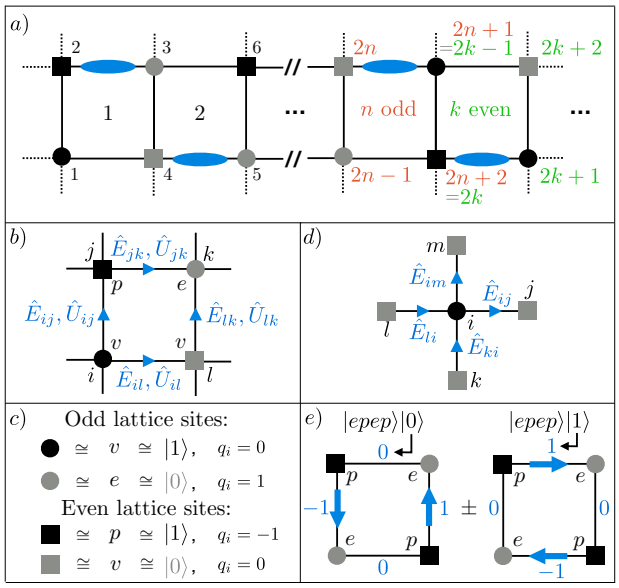

Figure 3.1: Conventions for lattice QED in 2D. **(a)** Ladder system with open boundary conditions. Using Gauss' law, the number of gauge degrees of freedom can be reduced to one per plaquette (blue ellipses). **(b)** A single plaquette with matter sites at the vertices and gauge fields on the links. Circles (squares) represent odd (even) sites, and black (grey) corresponds to unoccupied (occupied) fermionic fields. Positive field direction is to the right and up. **(c)** Table showing the mapping between fermionic sites, particles (e) and antiparticles (p), and spins. **(d)** Conventions for Gauss' law. **(e)** The two gauge-field configurations that minimize the electric field energy for a single plaquette with two particle-antiparticle pairs. As explained in the main text, these configurations are relevant for the 2D effects discussed in Sec. V.A in [1].

Gauge fields on the links between sites i and j are described by the operators $\hat{E}_{ij}$ (electric fields) and $\hat{U}_{ij}$. Electric field operators take integer eigenvalues $e_{ij} \in \{0, \pm 1, \pm 2, \dots\}$ with $\hat{E}_{ij} |e_{ij}\rangle = e_{ij} |e_{ij}\rangle$, while $\hat{U}_{ij}$ acts as a lowering operator on electric field eigenstates, i.e., $\hat{U}_{ij} |e_{ij}\rangle = |e_{ij} - 1\rangle$, with $[\hat{U}_{ij}, \hat{U}^\dagger_{kl}] = 0$ and $[\hat{E}_{ij}, \hat{U}_{kl}] = -\delta_{i,k}\delta_{j,l}\hat{U}_{ij}$. Using the Kogut-Susskind formulation [105] (see Sec. 2.1), the Hamiltonian consists of an electric, magnetic, mass, and kinetic term

such that $\hat{H} = \hat{H}_{\rm E} + \hat{H}_{\rm B} + \hat{H}_{\rm m} + \hat{H}_{\rm kin}$, where

$$\hat{H}_{\rm E} = \frac{g^2}{2} \sum_{\substack{i, \\ i \xrightarrow{+} j}} \hat{E}_{ij}^2, \tag{3.1a}$$

$$\hat{H}_{\rm B} = -\frac{1}{2g^2a^2} \sum_{n=1}^{N} \left(\hat{P}_n + \hat{P}_n^\dagger \right), \tag{3.1b}$$

$$\hat{H}_{\rm m} = m \sum_{i \in \text{sites}} (-1)^{i+1} \hat{\phi}_i^\dagger \hat{\phi}_i, \tag{3.1c}$$

$$\hat{H}_{\rm kin} = \Omega \Big(\sum_{\substack{i \text{ odd}, \\ i \xrightarrow{+} j}} \hat{\phi}_i^\dagger \hat{U}_{ij} \hat{\phi}_j + \sum_{\substack{i \text{ even}, \\ i \xrightarrow{+} j}} \hat{\phi}_i \hat{U}_{ij}^\dagger \hat{\phi}_j^\dagger \Big) + \text{h.c.}. \tag{3.1d}$$

In the summations, we use $i \xrightarrow{+} j$ to denote the link between lattice sites i and j with a positive orientation [see Fig. 3.1(a) and (b)]. We denote the bare coupling, fermionic mass, lattice spacing, and kinetic strength by g, m, a, and Ω, respectively. We use natural units $\hbar = c = 1$ and all operators in (3.1) are dimensionless [3]. In the Hamiltonian above, we introduced the operator $\hat{P}_n = \hat{U}_{ij}^\dagger \hat{U}_{jk}^\dagger \hat{U}_{il} \hat{U}_{lk}$, where sites (i, j, k, l) form a closed loop clockwise around the plaquette n as in Fig. 3.1(b) [14]. This allows us to define the plaquette operator

$$\square = \frac{1}{2N} \sum_{n=1}^{N} \left(\hat{P}_n + \hat{P}_n^\dagger \right), \tag{3.2}$$

with N being the number of plaquettes. At each vertex i, gauge invariance is imposed by the symmetry generators, known as Gauss' law operators [105, 106], $\hat{G}_i = \hat{E}_{li} - \hat{E}_{ij} + \hat{E}_{ki} - \hat{E}_{im} - \hat{q}_i$ [see Fig. 3.1(d) for the definition of l, j, k, m], where $\hat{q}_i = \hat{\phi}_i^\dagger \hat{\phi}_i - \frac{1}{2}\left[1 + (-1)^i\right]$ is the charge operator. Gauge-invariant quantum states are defined by Gauss' law $\hat{G}_i \left|\Psi_{\rm phys}\right\rangle = \epsilon_i \left|\Psi_{\rm phys}\right\rangle$ for each lattice site, where the eigenvalue ϵ_i corresponds to the static background charge at site i. We consider the case $\epsilon_i = 0 \ \forall i$.

3.1.2 Effective Hamiltonian for open boundary conditions

In this section, we consider a one-dimensional ladder of plaquettes with OBC [see Fig. 3.1(a)]. Although this system does not encapsulate the full 2D physics of QED, it allows us to study important aspects of gauge theories that are not present in one spatial dimension, such as magnetic phenomena. The OBC for a ladder of N plaquettes appear as dashed lines in Fig. 3.1(a). There are $2N + 2$ Gauss' law operators on the ladder, forming a set of $2N + 1$ linearly independent constraints over the electric field operators. Therefore, the $3N + 1$ gauge fields on the ladder

can be reduced to N independent gauge fields. Given the freedom in choosing the independent gauge fields, we select the $(2n, 2n+1)$ links for each plaquette n, as shown by the blue ellipses in Fig. 3.1(a). On each link that does not hold an independent gauge field, the corresponding unitary operator $\hat{U}$ is set to the identity. As a result, the plaquette operator becomes $\hat{P}_n = \hat{U}_{2n,2n+1}$ and both the kinetic and magnetic terms are simplified. The effective Hamiltonian for the full ladder is shown in App. A in [1].

We now focus on the basic building block of the 2D ladder system, the plaquette [see Fig. 3.1(b)]. The effective Hamiltonian for a single plaquette with OBC becomes

$$\begin{aligned}
\hat{H}_{\mathrm{E}} =& \frac{g^2}{2}\Big[\Big(\hat{E}_{23}\Big)^2 + \Big(\hat{E}_{23} + \hat{q}_2\Big)^2 \\
&+ \Big(\hat{E}_{23} - \hat{q}_3\Big)^2 + \Big(\hat{E}_{23} + \hat{q}_1 + \hat{q}_2\Big)^2\Big], && \text{(3.3a)}\\
\hat{H}_{\mathrm{B}} =& -\frac{1}{2g^2}\Big(\hat{U}_{23} + \hat{U}_{23}^\dagger\Big), && \text{(3.3b)}\\
\hat{H}_{\mathrm{m}} =& m\sum_{i=1}^{4}(-1)^{i+1}\hat{\phi}_i^\dagger\hat{\phi}_i, && \text{(3.3c)}\\
\hat{H}_{\mathrm{kin}} =& \Omega\Big(\hat{\phi}_1^\dagger\hat{\phi}_2 + \hat{\phi}_1^\dagger\hat{\phi}_4 + \hat{\phi}_2\hat{U}_{23}^\dagger\hat{\phi}_3^\dagger + \hat{\phi}_4\hat{\phi}_3^\dagger\Big) + \text{h.c.}. && \text{(3.3d)}
\end{aligned}$$

The notation for describing the state of the plaquette with OBC is a tensor product of two kets, with the first ket representing the matter sites $1-4$ (v, e, and p are the vacuum, particle, and antiparticle, respectively) and the second ket the state of the gauge field on the $(2,3)$ link [see Fig. 3.1(e) for examples]. We remark that in 1D QED, all gauge fields can be eliminated for systems with OBC. As a result, the Hamiltonian becomes fully fermionic, and contains only two-body terms [111, 112, 21, 81]. However, many-body terms are unavoidable on a plaquette since gauge degrees of freedom survive. This represents one of the main challenges in simulating LGTs in more than one spatial dimensions on a near-term hardware.

3.1.3 Effective Hamiltonian for periodic boundary conditions

For the second model, we consider a square lattice with PBC and without fermionic matter. This system has been considered in [3] and is discussed in chapter 5, but for the benefit of the reader we summarize the main results that are required for the VQE simulation. As explained in Sec. 3.1.1, Gauss' law can be used to eliminate redundant gauge fields, resulting in an unconstrained effective Hamiltonian. The basic building block, a single plaquette with PBC, includes eight gauge fields [see Fig. 3.2(a)], and is equivalent to an infinite 2D lattice of four distinct plaquettes [see Fig. 3.2(b)]. Due to the absence of matter, we consider the pure gauge Hamiltonian $\hat{H}_{\mathrm{gauge}} = \hat{H}_{\mathrm{E}} + \hat{H}_{\mathrm{B}}$, given by (3.1a) and (3.1b). Since we are interested in studying ground state

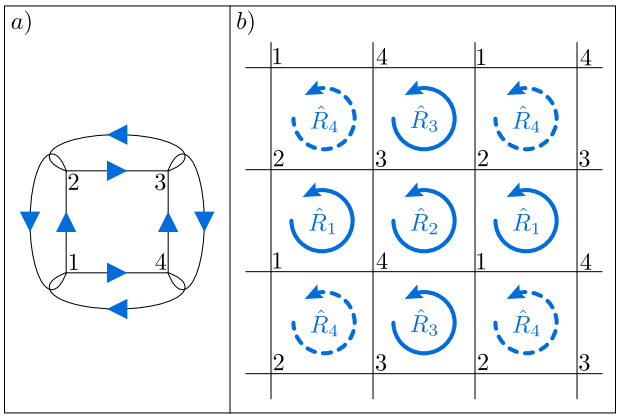

Figure 3.2: Single periodic boundary plaquette for a pure gauge theory. **(a)** Representation in terms of the eight gauge fields (blue arrows), that are associated with the links of the lattice. **(b)** Representation in terms of independent gauge-invariant (i.e., physical) operators called "rotators". As explained in [3], the plaquette can be seen as an infinite lattice of plaquettes. Moreover, to explore ground state properties, only three independent rotators $\hat{R}_1$, $\hat{R}_2$, and $\hat{R}_3$ (shown in solid blue) are sufficient for describing the system.

properties, it is sufficient to consider three independent gauge degrees of freedom (see [3] and chapter 5), called "rotators" $\hat{R}_i$, $i \in \{1, 2, 3\}$ shown in Fig. 3.2(b). Each rotator corresponds to the electric field circulating around a specific plaquette. The operators $\hat{P}_n$ ($\hat{P}_n^\dagger$) in (3.1b) and (3.2) are their ladder operators. Indeed, the commutation relations between a rotator $\hat{R}$ and its conjugate operator $\hat{P}$ are the same as the ones of an electric field $\hat{E}$ and its lowering operator $\hat{U}$, presented in Sec. 3.1.1. The notation for describing the state of the plaquette with PBC is thus a tensor product of three kets, each corresponding to one of the three rotators represented by full lines in Fig. 3.2(b).

Usually, LGT Hamiltonians are formulated in the so-called electric basis, in which $\hat{H}_\mathrm{E}$ is diagonal. For large values of the bare coupling g, the term $\hat{H}_\mathrm{E}$ is dominant, and this representation is efficient. For small g, however, the off-diagonal magnetic term $\hat{H}_\mathrm{B}$ is dominant, and the eigenstates of $\hat{H}_\mathrm{gauge}$ can be superpositions of all electric field basis states. Since the Hilbert space of these operators is infinite-dimensional, this necessarily leads to truncation errors when the Hamiltonian is mapped to any quantum device. To mitigate the truncation errors, we apply the novel techniques introduced in [3], and resort to two different formulations of the Hamiltonian. The electric formulation in (3.1) is applied in the region $g^{-2} \lesssim 1$, while for $g^{-2} \gtrsim 1$ a so-called magnetic basis is used, for which $\hat{H}_\mathrm{B}$ is diagonal. For more details on the magnetic basis, please consult [3] or chapter 5. Here, we simply provide the Hamiltonian $\hat{H}^{(\gamma)}_\mathrm{gauge} = \hat{H}^{(\gamma)}_\mathrm{E} + \hat{H}^{(\gamma)}_\mathrm{B}$, where

$\gamma = e$ indicates the electric representation, i.e.,

$$\hat{H}_{\mathrm{E}}^{(e)} = 2g^2\Big[(\hat{R}_1)^2 + (\hat{R}_2)^2 + (\hat{R}_3)^2 - \hat{R}_2(\hat{R}_1 + \hat{R}_3)\Big], \tag{3.4a}$$

$$\hat{H}_{\mathrm{B}}^{(e)} = -\frac{1}{2g^2}\Big(\hat{P}_1 + \hat{P}_2 + \hat{P}_3 + \hat{P}_1\hat{P}_2\hat{P}_3 + \mathrm{h.c.}\Big), \tag{3.4b}$$

and $\gamma = b$ indicates the magnetic representation, i.e.,

$$\hat{H}_{\mathrm{E}}^{(b)} = g^2\sum_{\nu=1}^{2L}\Big\{f_\nu^c\sum_{i=1}^{3}(\hat{P}_i)^\nu + \frac{f_\nu^s}{2}\big[(\hat{P}_2)^\nu - (\hat{P}_2^\dagger)^\nu\big]\sum_{\mu=1}^{2L} f_\mu^s\big[(\hat{P}_1)^\mu + (\hat{P}_3)^\mu\big]\Big\} + \mathrm{h.c.}, \tag{3.5a}$$

$$\hat{H}_{\mathrm{B}}^{(b)} = -\frac{1}{g^2}\Big[\sum_{i=1}^{3}\cos\Big(\frac{2\pi\hat{R}_i}{2L+1}\Big) + \cos\Big(\frac{2\pi(\hat{R}_1+\hat{R}_2+\hat{R}_3)}{2L+1}\Big)\Big], \tag{3.5b}$$

where the coefficients f_k^c and f_k^s are

$$f_\nu^s = \frac{(-1)^{\nu+1}}{2\pi}\Big[\psi_0\Big(\frac{2L+1+\nu}{2(2L+1)}\Big) - \psi_0\Big(\frac{\nu}{2(2L+1)}\Big)\Big], \tag{3.6}$$

$$f_\nu^c = \frac{(-1)^{\nu}}{4\pi^2}\Big[\psi_1\Big(\frac{\nu}{2(2L+1)}\Big) - \psi_1\Big(\frac{2L+1+\nu}{2(2L+1)}\Big)\Big], \tag{3.7}$$

with $\psi_k(\cdot)$ being the k-th polygamma function [3].

3.2 Practical considerations for variational quantum simulations

We refer readers to Sec. 2.2 for an overview of the VQE protocal. In the following, we discuss the feasibility on currently available quantum platforms (Sec. 3.2.1). Then, we describe our optimization algorithm, which is run on the classical device to find the desired state (Sec. 3.2.2).

3.2.1 Quantum hardware considerations

In this work, we consider qubit-based platforms for the realization of a proof-of-principle experiment with present-day technology. In particular, we compare two leading hardware, namely, superconducting and trapped-ion devices. On a superconducting processor, entangling gates are of nearest-neighbour type, which implies that entangling non-neighbouring qubits requires applying a number of swap gates. This hardware constraint translates to a large gate overhead when implementing the long-range interactions, which result from the elimination of redundant gauge fields in our models. In contrast, ion-based processors have all-to-all connectivity, which allows for entangling gates between arbitrary qubits. This aligns well with our target models,

motivating their use for this proposal. Despite their measurement budget being limited by slow readout, we mitigate this issue with both an efficient measurement strategy (see App. B in [1]) and a suitable classical optimizer (see Sec. 3.2.2). A realistic budget for currently available ion-based quantum computers is roughly 10^7 measurement shots per experiment.

3.2.2 Classical Optimization Routine

The classical optimization routine employed for the VQE needs to be chosen depending on the requirements from both the hardware and the cost function $\mathcal{C}(\boldsymbol{\theta})$. Indeed, the stochastic nature of the latter has to be taken into account, and the experimental repetition rate poses limitations on the number of data points that the classical machine can use for minimization.

A limitation of the available quantum hardware is the small number of experimental shots, particularly true for trapped-ion platforms due to their slow gate operations and measurements. This drawback is especially limiting to optimization algorithms that requires many function evaluations, e.g., gradient based optimization [116, 117]. Here, we employ an optimization algorithm similar to the one used in [34], which is a modified version of the Dividing Rectangles algorithm [118, 119, 120, 121, 122]. This algorithm divides the search space into so-called hypercells. Each hypercell is labelled by a single sample point representative of the cost function value. The algorithm selects promising hypercells, to be divided into smaller cells, based on the cost function value as well as the cell size. Larger cells contain more unexplored territory, and thus, are statistically more likely to harbour the global minimum. During the optimization, the algorithm maintains a regression model as used in Bayesian optimization. This metamodel is used for a function value estimation that aids in selecting the hypercells to be divided. Furthermore, at regular intervals, one or more direct Bayesian optimization steps are carried out [123]. We observe that this algorithm performs well with a small number of measurement shots, and the limited number of variational parameters required in our VQEs.

3.3 Quantum simulation of 2D LGTs

In this section, we present the VQE protocols for simulating the two models introduced in Sec. 3.1. We give numerical results from a classical simulation, which includes projection noise errors. Both proposed experiments prepare the ground state of the theory and measure the ground state expectation value of the plaquette operator $\langle \square \rangle \sim \left\langle \hat{H}_{\mathrm{B}} \right\rangle$, as defined in Sec. 3.1.1. For OBC, this allows one to study the dynamical generation of gauge fields by pair creation processes, while in the case of PBC it is related to the renormalization of the coupling at different energy scales (see Sec. V in [1] for a more in-depth discussion).

3.3.1 Encoding for quantum hardware

To run a VQE, we first require an encoding of the models outlined in Sec. 3.1 for qubit-based quantum hardware. We use the Jordan-Wigner transformation [124] for mapping the fermionic operators. The gauge-field encoding is chosen to reduce the complexity of the quantum circuits and to respect symmetries that both suit the simulated models and the quantum platform.

Gauge field operators are defined on infinite dimensional Hilbert spaces and the electric field takes the values $0, \pm1, \pm2, \ldots$ (see Sec. 3.1.1). To simulate them using finite-dimensional quantum systems, a truncation scheme is required. Let us take $2l+1$ basis states into account, i.e. the gauge field can take at most the values $\pm l$. Consequently, we substitute the electric field operator $\hat{E}$ with the z-th component of a spin $\hat{\vec{S}} = (\hat{S}^x, \hat{S}^y, \hat{S}^z)$ of length $|l| = \sqrt{l(l+1)}$,

$$\hat{E} \longmapsto \hat{S}^z = \sum_{i=-l}^{l} i|i\rangle\langle i|. \tag{3.8}$$

The lowering operator $\hat{U}$ is mapped to

$$\hat{U} \longmapsto \begin{bmatrix} 0 & \ldots & \ldots & 0 \\ 1 & \ldots & \ldots & 0 \\ 0 & \ddots & \vdots & 0 \\ 0 & \ldots & 1 & 0 \end{bmatrix}. \tag{3.9}$$

For $|l| \to \infty$, the above mapping ensures that $\hat{U}^\dagger\hat{U} = 1$ and the correct commutation relations between $\hat{E}$ and $\hat{U}$ is preserved. The errors introduced by finite $|l|$ have been studied in Refs. [125, 3], where they were shown to be negligible in most scenarios.

For a given l, each gauge degree of freedom is then described by the $2l+1$ states $|e\rangle$, $e = -l$, $-l+1, \ldots, 0, \ldots, l-1, l$. We map [2] this vector space onto $2l+1$ qubits using

$$|-l+j\rangle = \left|\overbrace{0\ldots0}^{j} 1 \overbrace{0\ldots0}^{2l-j}\right\rangle, \tag{3.10}$$

where $0 \leq j \leq 2l$. With this unary encoding, the gauge field operators can be expressed as

$$\hat{E} \mapsto \hat{S}^z = \frac{1}{2}\sum_{i=1}^{2l}\prod_{j=1}^{i}\hat{\sigma}_j^z, \tag{3.11a}$$

$$\hat{U} \mapsto \sum_{i=1}^{2l}\hat{\sigma}_i^-\hat{\sigma}_{i+1}^+, \tag{3.11b}$$

[2] After the publication of this work, we learned that the same mapping had first been proposed in [6].

where $\hat{\sigma}_i^{\pm} = \frac{1}{2}(\hat{\sigma}_i^x \pm i\hat{\sigma}_i^y)$, and $\hat{\sigma}_i^{\mathrm{x}}$, $\hat{\sigma}_i^y$, $\hat{\sigma}_i^z$ are the Pauli operators associated with the i^{th} qubit. From these mapping we directly recover the relations $\hat{E}\,|e\rangle = e\,|e\rangle$ and $\hat{U}\,|e\rangle = (1-\delta_{e,-l})\,|e-1\rangle$ for all $-l \leq e \leq l$. As an example, for $l = 1$ the states in the gauge field basis become

$$|1\rangle = |001\rangle\,, \tag{3.12a}$$
$$|0\rangle = |010\rangle\,, \tag{3.12b}$$
$$|-1\rangle = |100\rangle\,. \tag{3.12c}$$

For our protocol, the required resources scale linearly in terms of both the parameter l and the number of gauge and matter fields. The encoding presented in Eq. (3.10) requires $2l+1$ qubits for storing $2l+1$ states. In principle, the same information can be stored in $\log(2l+1)$ qubits [7, 2]. The reasons for which we choose the qubit encoding in Eq. (3.10) are the following. First, the operator $\hat{U}$ in Eq. (3.11b) consists if only two-body terms, which are easily implementable on different hardware platforms including trapped-ion systems. Second, the states in Eq. (3.10) form a subspace of fixed magnetization, which is decoherence-free under the action of correlated noise (e.g. a globally fluctuating magnetic field) and allows for detection of single qubit bit-flip errors. Importantly, the latter is separately true for each individual gauge field and for the fermionic state. Since all the utilized quantum states are in the single excitation subspace, a measurement resulting in states outside of this subspace can only be due to errors, as long as the applied gates conserve the excitations. Hence, erroneous outcomes can be discriminated from faithful ones.

In the following, we will use the term "physical states" to refer to the computationally relevant qubit states. For the gauge fields, this means that the qubit states lie in the computational space spanned by the states in (3.12). For the matter fields whose computational states are obtained via the Jordan-Wigner transformation, we operate in the zero-charge subsector (see Sec. 3.1.1), which translates into matter states of zero magnetization. As a final remark, we highlight that our encoding for the electric field operators $\hat{E}$ and $\hat{U}$ applies equally well to the rotator $\hat{R}$ and plaquette $\hat{P}$ operator used for the plaquette with PBC (see Sec. 3.1.3).

3.3.2 Open boundary conditions: dynamically generated magnetic fields

In the case of a plaquette with OBC, the simulation involves four qubits for the matter fields and $2l+1$ qubits for the gauge field. Here, we consider $l = 1$ and thus the system consists of seven qubits. According to Fig. 3.3(c), we number the matter qubits as 1, 2, 3, and 4, and the gauge qubits 5, 6, and 7. Plugging the encoding presented in Sec. 3.3.1 into the Hamiltonian in

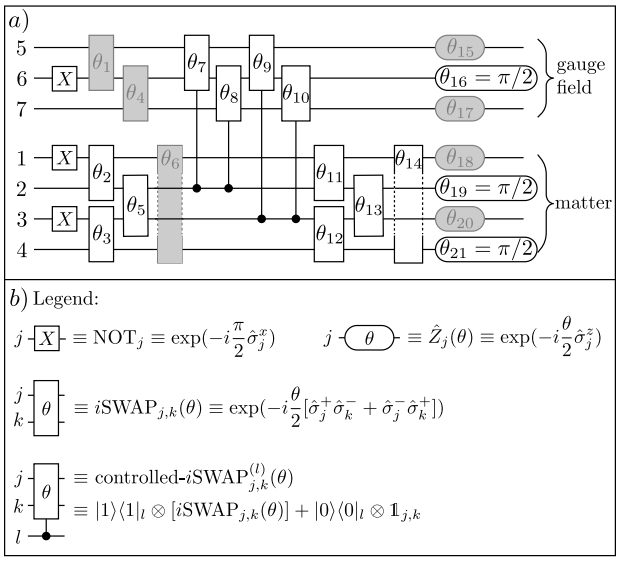

Figure 3.3: VQE circuit for preparing the ground state of a plaquette with open boundary conditions. **(a)** Quantum circuit with variational parameters θ_l shown for each gate. By identifying symmetries and redundancies via classical simulation, gates shaded in grey can be eliminated, and we set $\theta_{16} = \theta_{19} = \theta_{21} = \pi/2$, leaving eleven variational parameters. **(b)** Definitions of the gates used.

Eq. (3.3), we get

$$\hat{H}_\mathrm{E} = \frac{g^2}{4}\Big\{\hat{\sigma}^z_5\left[\hat{\sigma}^z_1 - \hat{\sigma}^z_3 + \hat{\sigma}^z_6(\hat{\sigma}^z_1 - \hat{\sigma}^z_3 - 2) - 1\right] + \hat{\sigma}^z_2\left[\hat{\sigma}^z_1 + 2\hat{\sigma}^z_5\left(\hat{\sigma}^z_6 + 1\right) - 1\right] + 4\hat{\sigma}^z_6\Big\}, \tag{3.13a}$$

$$\hat{H}_\mathrm{B} = -\frac{1}{2g^2}\left[\hat{\sigma}^+_6\left(\hat{\sigma}^-_5 + \hat{\sigma}^-_7\right) + \hat{\sigma}^-_6\left(\hat{\sigma}^+_5 + \hat{\sigma}^+_7\right)\right], \tag{3.13b}$$

$$\hat{H}_\mathrm{m} = \frac{m}{2}\Big(\hat{\sigma}^z_1 - \hat{\sigma}^z_2 + \hat{\sigma}^z_3 - \hat{\sigma}^z_4\Big), \tag{3.13c}$$

$$\hat{H}_\mathrm{kin} = -i\Omega\Big[\hat{\sigma}^+_1\hat{\sigma}^-_2 + \hat{\sigma}^+_1\hat{\sigma}^-_4 + \hat{\sigma}^-_4\hat{\sigma}^+_3 - \hat{\sigma}^-_2\left(\hat{\sigma}^+_5\hat{\sigma}^-_6 + \hat{\sigma}^+_6\hat{\sigma}^-_7\right)\hat{\sigma}^+_3\Big] + \mathrm{h.c.}. \tag{3.13d}$$

The matter qubit states are also given in Fig. 3.1(c). Recall that we chose the encoding such that physical states have total magnetization $\left\langle \hat{S}^z_\mathrm{tot} \right\rangle = 1$. The VQE quantum circuit shown in Fig. 3.3(a) preserves not only the total magnetization of the system, but also the magnetization of each of the gauge and matter subsystems. Hence, as mentioned in Sec. 3.3.1, our magnetization-preserving quantum circuit used in combination with physical input states confines the VQE to the space of physical states. The VQE circuit in its unreduced form [i.e., including the grey-shaded gates in Fig. 3.3(a)] is motivated by the form of the Hamiltonian in (3.3). All qubits are initialized

to $|0\rangle$, to which we apply NOT gates to prepare the bare vacuum $|vvvv\rangle\,|0\rangle$ [see Fig. 3.1(c)] as the initial state for the VQE. For the gauge field subsystem, the application of the parameterized iSWAP gates allows for accessing all three gauge field states $|1\rangle$, $|0\rangle$, and $|-1\rangle$, ensuring that the free ground state for $\Omega = 0$ could be produced. Similarly, the parameterized iSWAP gates on the qubits 1 to 4 are used to allow for accessing all physical basis states within the matter subsystem, and resemble the hopping terms of the kinetic Hamiltonian in Eq. (3.13d). These gates correspond to particle-antiparticle pair creation/annihilation in the model, and as a consequence, all matter basis states in the zero-charge subsector are made available by this part of the circuit. The kinetic Hamiltonian is likewise responsible for the entanglement between the gauge and matter fields, as the pair creation/annihilation processes are combined with a correction of the gauge field. The layer of parameterized controlled-iSWAP gates hence takes the role of the annihilation operator $\hat{U}$ and entangles the matter and gauge subsystems. In the effective Hamiltonian of (3.3), the gauge degree of freedom lies on the $(2, 3)$ link and is directly coupled to matter sites 2 and 3. Accordingly, the circuit couples the gauge field with only these two fermions, which act as controls in the layer of controlled-iSWAP gates. Finally, parameterized iSWAP gates are applied on the matter qubits again to adjust the state after entangling the two subsystems, and a layer of single-qubit z-rotations is to correct for relative phases. Other single-qubit operations are avoided as they are generally not magnetization preserving. We highlight that this circuit (as well as the ones in Fig. 3.5), being Hamiltonian-inspired, from the one hand, ensures the capability of exploring the subsector of physical states in the Hilbert space. From the other hand, it avoids redundant gates and has a short circuit depth, and thus, prevents barren plateaus in the energy landscape, which increases the difficulty of the optimization task [30, 126, 31]. The quantum circuit described above involves a total of 21 variational parameters. By classically simulating the circuit in Fig. 3.3, we find that the solution space is still accessible by fixing $\theta_{16} = \theta_{19} = \theta_{21} = \pi/2$, and removing the gates shaded in grey in Fig. 3.3(a), leaving a total of eleven parameters. Furthermore, θ_{11}, θ_{12} and θ_{13} can be set to zero outside the transition region $2 \lesssim g^{-2} \lesssim 5$.

Since the circuit design is based on the structure of the Hamiltonian, the same design principles can be applied to larger scale systems. When adding more plaquettes, additional parametric iSWAP gates are used to populate all basis states within the matter and gauge subsystems. Then, the gauge degrees of freedom are coupled to their respective neighbouring matter sites using additional controlled-iSWAP gates. Finally, z-rotations adjust the relative phases of all qubits. When increasing the truncation l, additional iSWAP gates are inserted for populating the newly introduced gauge field states, and controlled-iSWAP gates are added for entangling them with the respective matter sites. As such, we anticipate that in both cases – adding more plaquettes and increasing the truncation cut-off – a linear increase in the number of qubits and iSWAP gates and a quadratic increase in the number of controlled-iSWAP operations. A classical simulation of the proposed experiment, including statistical noise on the cost function $\mathcal{C}(\boldsymbol{\theta})$, is shown in Fig. 3.4. The data points (blue and black dots) correspond to the lowest

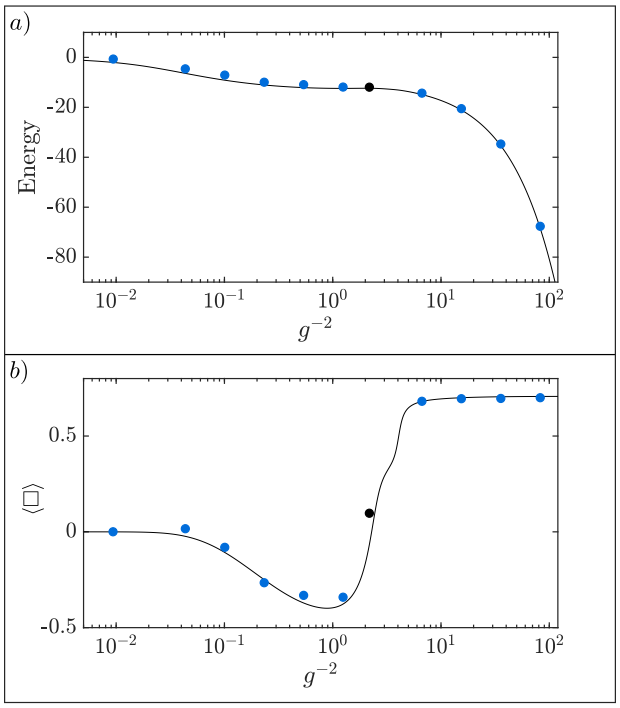

Figure 3.4: Classical simulation of the proposed experiment for observing the dynamical generation of magnetic fields where $\Omega = 5$ and $m = 0.1$ using the circuits given in Fig. 3.3. The blue and black dots represent data points obtained by variational minimization with a total finite measurement budget of 10^7 measurements for the entire plot. Half of this budget is spent for the black dot alone. The black solid lines are determined via exact diagonalization of the Hamiltonians in (3.13). **(a)** Energy of the variational ground state. **(b)** Plaquette expectation value $\langle\square\rangle$ as a function of g^{-2}. All dots are calculated using the exact state corresponding to the optimal variational parameters found by the VQE.

energies found by the VQE. The energies and the plaquette expectation values are calculated using the exact state corresponding to the optimal variational parameters found for each value of g^{-2}. We verified that the VQE resorts to statistical errors affecting $\mathcal{C}(\boldsymbol{\theta})$ that are always lower than the ground and first excited states' energy gap. The black solid lines are obtained via exact diagonalization of the Hamiltonian in (3.13). Using the measurement procedure based on the methods in [127] and taking statistical error into account, the entire plot corresponds to approximately 10^7 measurements to be performed on the quantum device. In VQEs, measuring the expectation value of a Hamiltonian involves three steps: (i) express it as a linear combination of Pauli operators, i.e., tensor products of Pauli matrices; (ii) group the Pauli operators into commuting sets; (iii) measure each set of operators in a basis that diagonalizes them. Using

our strategy, we first minimize the number of commuting sets, and then, measure each set in an entangled basis. This allows us to estimate the Hamiltonian expectation value to a higher accuracy within a fixed measurement budget, at the cost of additional measurement circuits that produce the entangled bases. We refer readers to App. B in [1] for more technical details. Half of this budget is used for the point at $g^{-2} \simeq 2.18$, where the energy difference between the ground and first excited states is much smaller if compared to other values of g^{-2} (see above). The ground state energy found by the VQE approximates well the energy of the exact ground state, as shown in Fig. 3.4(a). We find that the plaquette expectation value is sensitive to small changes in the variational state, which leads to relatively large deviations with respect to the results obtained via exact diagonalization in Fig. 3.4(b), even for states whose energy is very close to the exact energy. Yet, the variational optimization is able to accurately resolve transitions in the order parameter. The fidelity of the variational ground state with respect to the exact ground state is particularly high in the extremal regions, exceeding 98%. All points achieve a fidelity greater than 90%.

3.3.3 Periodic boundary conditions: running coupling

In this section, we provide a VQE protocol for simulating the running coupling in LGTs. The running coupling is a 2D effect that can be studied experimentally in a proof-of-concept demonstration by first preparing the ground state of a plaquette with PBC and subsequently measuring the expectation value $\langle \square \rangle$ (see Sec. V.B in [1]). Noting that the definitions in Sec. 3.3.1 presented for the electric gauge field and their lowering operators are trivially extended to rotators and plaquette operators, we encode the plaquette with PBC into nine qubits. Rotator 1 is represented by qubits 1 through 3, rotator 2 by qubits 4 through 6, and rotator 3 by qubits 7 through 9 (see Fig. 3.5). Thus, the Hamiltonian in the electric representation becomes

$$\hat{H}_{\mathrm{E}}^{(e)} = -\frac{g^2}{2}\Big\{\hat{\sigma}_4^z\left(\hat{\sigma}_5^z+1\right)\left(\hat{\sigma}_1^z+\hat{\sigma}_7^z+\hat{\sigma}_7^z\hat{\sigma}_8^z\right)+\hat{\sigma}_2^z\left[\hat{\sigma}_1^z\hat{\sigma}_4^z\left(\hat{\sigma}_5^z+1\right)-2\right]-2\left(\hat{\sigma}_5^z+\hat{\sigma}_8^z+3\right)\Big\}, \tag{3.14a}$$

$$\begin{aligned}\hat{H}_{\mathrm{B}}^{(e)} = -\frac{1}{2g^2}\Big[&\hat{\sigma}_1^-\hat{\sigma}_2^+ + \hat{\sigma}_2^-\hat{\sigma}_3^+ + \hat{\sigma}_4^-\hat{\sigma}_5^+ + \hat{\sigma}_5^-\hat{\sigma}_6^+ + \hat{\sigma}_7^-\hat{\sigma}_8^+ + \hat{\sigma}_8^-\hat{\sigma}_9^+ + \left(\hat{\sigma}_1^-\hat{\sigma}_2^+ + \hat{\sigma}_2^-\hat{\sigma}_3^+\right)\\ &\times\left(\hat{\sigma}_4^-\hat{\sigma}_5^+ + \hat{\sigma}_5^-\hat{\sigma}_6^+\right)\left(\hat{\sigma}_7^-\hat{\sigma}_8^+ + \hat{\sigma}_8^-\hat{\sigma}_9^+\right)\Big] + \mathrm{h.c.},\end{aligned} \tag{3.14b}$$

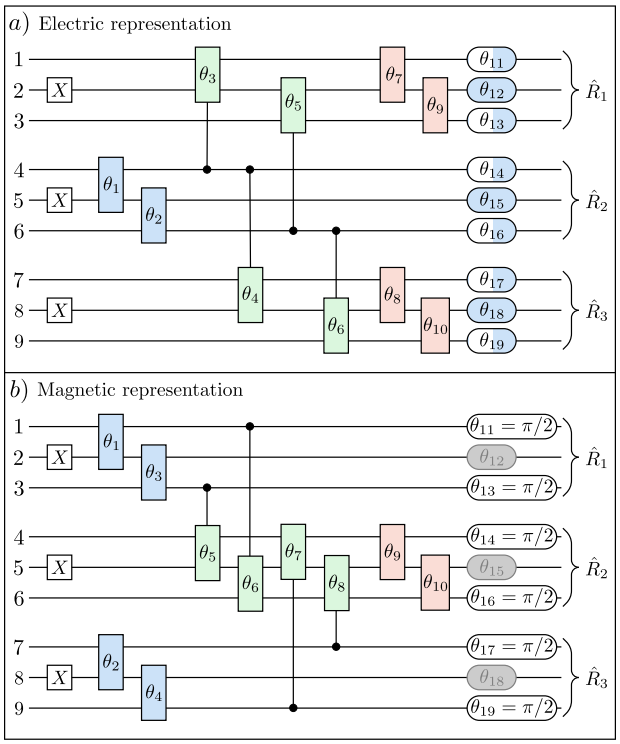

Figure 3.5: VQE circuits for preparing the ground state of a plaquette with periodic boundary conditions. Gate definitions are given in Fig. 3.3. Gates of the same color in each circuit share a variational parameter after eliminating redundant parameters. The half-shaded gates include an offset of $+\pi/2$ added to the shared parameter, while the grey-shaded gates can be eliminated entirely. **(a)** Circuit for the electric representation of the Hamiltonian, and **(b)** for the magnetic representation.

used in case $g^{-2} \lesssim 1$, and the Hamiltonian in the magnetic representation is

$$\hat{H}_{\mathrm{E}}^{(b)} = g^2 \sum_{\nu=1}^{2L} \Bigg\{ f_\nu^c \sum_{i=1}^{3} \left(\hat{\sigma}_{3i-2}^- \hat{\sigma}_{3i-1}^+ + \hat{\sigma}_{3i-1}^- \hat{\sigma}_{3i}^+\right)^\nu + \frac{f_\nu^s}{2} \left[\left(\hat{\sigma}_4^- \hat{\sigma}_5^+ + \hat{\sigma}_5^- \hat{\sigma}_6^+\right)^\nu - \left(\hat{\sigma}_4^+ \hat{\sigma}_5^- + \hat{\sigma}_5^+ \hat{\sigma}_6^-\right)^\nu\right] \times \sum_{\mu=1}^{2L} f_\mu^s \Big[\left(\hat{\sigma}_1^- \hat{\sigma}_2^+ + \hat{\sigma}_2^- \hat{\sigma}_3^+\right)^\mu + \left(\hat{\sigma}_7^- \hat{\sigma}_8^+ + \hat{\sigma}_8^- \hat{\sigma}_9^+\right)^\mu \Big] \Bigg\} + \mathrm{h.c.}, \tag{3.15a}$$

$$\hat{H}_{\mathrm{B}}^{(b)} = -\frac{1}{g^2} \left[\sum_{i=1}^{3} \cos\left(\frac{\pi \left(\hat{\sigma}_{3i-2}^z + \hat{\sigma}_{3i-2}^z \hat{\sigma}_{3i-1}^z\right)}{2L+1} \right) + \cos\left(\frac{\pi \sum_{i=1}^{3} \left(\hat{\sigma}_{3i-2}^z + \hat{\sigma}_{3i-2}^z \hat{\sigma}_{3i-1}^z\right)}{2L+1} \right) \right], \tag{3.15b}$$

used when $g^{-2} \gtrsim 1$. As for the case of OBC, the circuit design for a plaquette with PBC is motivated by the structure of the Hamiltonian and employs the same gate set. Due to the differences between the electric and magnetic representations, we use two different VQE circuits which are shown in Fig. 3.5. Contrary to the plaquette with OBC, the controlled iSWAP gate are not used to entangle the matter with the gauge subsystems. Instead, they are motivated by the coupling of the rotators and plaquette operators in the last terms of (3.4a) and (3.4b), respectively, and the corresponding ones in the magnetic representation. Both circuits have 19 variational parameters and allow us to thoroughly explore the associated Hilbert spaces. The number of variational parameters can be reduced by exploiting the symmetries between rotators 1 and 3 [which are apparent from the Hamiltonians in (3.4) and (3.5)] and by identifying additional redundant parameters through classical simulation of the VQE. As a result, in Fig. 3.5(a), each of the sets, $\{\theta_1, \theta_2, \theta_{11}, \ldots, \theta_{19}\}$, $\{\theta_3, \ldots \theta_6\}$, and $\{\theta_7, \ldots, \theta_{10}\}$, can be constrained to a single parameter, as indicated by the color coding. Parameters θ_{11}, θ_{13}, θ_{14}, θ_{16}, θ_{17}, and θ_{19} include an offset of $+\pi/2$ added to the shared variational parameter, which is indicated by the half-shaded gates. For the circuit in Fig. 3.5(b), we identify the groupings $\{\theta_1, \theta_2, \theta_3, \theta_4\}$, $\{\theta_5, \ldots, \theta_8\}$, and $\{\theta_9, \theta_{10}\}$, while θ_{12}, θ_{15}, and θ_{18} can be eliminated, and θ_{11}, θ_{13}, θ_{14}, θ_{16}, θ_{17}, and θ_{19} are fixed at $\pi/2$. This leaves just three variational parameters for each circuit.

The circuit for the electric representation of (3.14) is shown in Fig. 3.5(a). All qubits are initialized in the input state $|0\rangle$, and NOT gates prepare the vacuum state $|0\rangle = |010\rangle$ for each of the three rotators as the intial state for the VQE. The layer of controlled-iSWAP gates reflects the coupling between the rotators in the electric Hamiltonian $\hat{H}_{\mathrm{E}}^{(e)}$ [see Eq. (3.4a)], which takes the form $-\hat{S}_2^z(\hat{S}_1^z + \hat{S}_3^z)$. This term results from the elimination of rotator 4 as a redundant degree of freedom, and introduces an asymmetry between rotator 2 and rotators 1 and 3. When increasing g^{-2}, the ground state spreads from $|0\rangle\,|0\rangle\,|0\rangle$ to all other electric levels, and states in which all three rotators have the same sign ($|1\rangle\,|1\rangle\,|1\rangle$ and $|-1\rangle\,|-1\rangle\,|-1\rangle$) receive the strongest negative contribution. To encourage the VQE to prepare the correct superposition of states, the parameterized controlled-iSWAP gates are connected to control the spread of population within rotators 1 and 3 based on the population of rotator 2.

The circuit for the magnetic representation of (3.15) is shown in Fig. 3.5(b). Its construction is similar to the circuit for the electric representation described above, but rather encourages the flip-flop interactions between rotators described by $\hat{H}_{\mathrm{E}}^{(b)}$ [see Eq. (3.5a)]. Both the electric and magnetic circuits maintain constant magnetization of each gauge field, which prevents access to unphysical states. Designing the VQE circuit based on the form of the Hamiltonian allows for a scalable architecture. For systems with additional plaquettes, the coupling between rotators remains pairwise, which translates into the addition of controlled-iSWAP gates between all pairs of coupled gauge fields, as was described above for OBC. When considering larger truncations l, additional iSWAP gates are introduced to allow for all gauge field basis states. Additional controlled-iSWAP gates are then added to share entanglement in a similar fashion as for the case $l = 1$ considered here. In both cases, the scaling is the same as for the OBC circuit, i.e., the

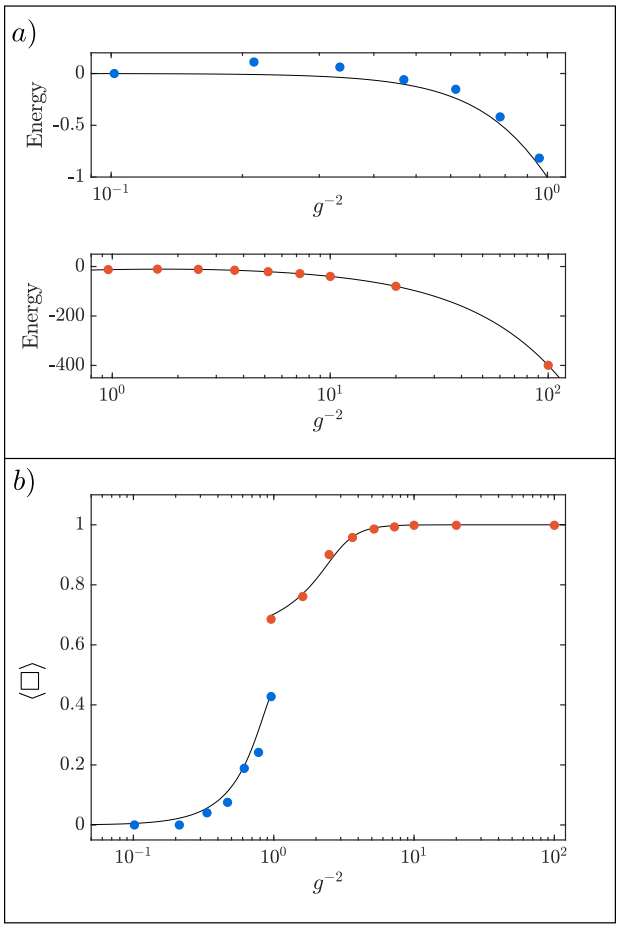

Figure 3.6: Classical simulation of the proposed experiment for observing the running of the coupling using the circuits given in Fig. 3.5. The red and blue data points are obtained from variational minimization with a total finite measurement budget of 6×10^5 measurements for the entire plot. The electric (magnetic) representation is shown in blue (red), and the black solid lines are determined via exact diagonalization of the Hamiltonians in (3.4) and (3.5). **(a)** Energy of the variational ground state using the electric representation in the region $g^{-2} < 1$ and using the magnetic representation in the region $g^{-2} > 1$. **(b)** Plaquette expectation value $\langle\square\rangle$ as a function of g^{-2}. All dots are calculated using the exact state corresponding to the optimal variational parameters found by the VQE.

number of qubits and the number of iSWAPs scale linearly, while the number of controlled-iSWAP gates scales quadratically in the worst-case scenario.

We simulate the proposed experiment classically, including statistical noise on the cost function $\mathcal{C}(\boldsymbol{\theta})$. Our results are shown in Fig. 3.6. Points obtained with the electric and the magnetic representation of the Hamiltonian are shown in blue and red, respectively, while the black solid lines come from exact diagonalization of the Hamiltonians. As for the OBC, the energy and the plaquette expectation value $\langle \square \rangle$ are calculated using the exact state obtained with the optimal variational parameters found by the VQE. Using the measurement procedure described in App. B in [1] and taking statistical errors into account, the entire plot corresponds to 6×10^5 measurements to be performed on the quantum device. The VQE protocol reaches the correct ground state energy [see Fig. 3.6(a)], and the expectation value of the plaquette operator is accurate if compared to the exact truncated results [Fig. 3.6(b)]. The fidelity of the variational ground state with respect to the exact ground state exceeds 96% for all points, and for the majority of points it exceeds 99%.

3.4 Conclusion

In this chapter, we proposed a protocol to observe 2D effects in LGTs on currently available quantum computers. By using the methods in [3], we provided a practical VQE-based framework to simulate two toy models using NISQ devices. Importantly, we include the numerics for observing 2D phenomena in a basic building block of 2D QED with present-day quantum resources. The effective models studied here include both dynamical matter and a non-minimal gauge field truncation, providing the novel opportunity to study several 2D effects in LGTs. More specifically, we showed how to observe dynamical generation of magnetic fields as a result of particle-antiparticle pair creation, and paved the way for an important first step towards simulating short distance quantities such as the running coupling of QED. While the protocols presented in Sec. 3.2 are designed for trapped ion systems, our approach can be easily adapted to suit different types of quantum hardware. An interesting extensions of our work include simulations that involves more plaquettes both in two and three spatial dimensions.

Chapter 4

Lattice Quantum Chomodynamics and Electrodynamics on a Fault-Tolerant Quantum Computer

In this chapter [1], we provide a complete layout of computational instructions at a gate-by-gate level to be run on a quantum computer, to efficiently simulate quantum electrodynamics (QED) and quantum chromodynamics (QCD). Here, we consider U(1), SU(2) and SU(3) lattice gauge theories (LGTs) based on the fact that (i) the Standard Model (SM) of particle physics is a gauge theory with the symmetry group U(1)× SU(2)×SU(3) and (ii) LGTs [14] are one of the best-known non-perturbative first-principle computational methods for QED and QCD. In the SM, the U(1)×SU(2) symmetry and SU(3) symmetry correspond to the electroweak theory [128, 129, 130] and QCD [131, 132, 133], respectively. We remark that how to simulate chiral gauge theories such as the electroweak theory on a lattice is a longstanding open problem [108, 12]. Regardless, U(1) and SU(2) LGTs are simulated separately to model QED [108] and provide valuable insights to QCD [134]. For the above reasons, we choose to consider quantum simulation of U(1), SU(2), and SU(3) LGTs.

To this end, our main contributions are

- Explicit, gate-by-gate level construction of quantum circuits that simulate real-time dynamics of U(1), SU(2), and SU(3) LGTs, fully incorporating both fermions and gauge bosons, in an arbitrary spatial dimension d.
- Rigorous upperbounds on the quantum computational resources (quantum gate counts), including quantum-simulation algorithmic errors (second-order Trotter) [23], circuit-synthesis

[1] This chapter presents research carried out independently of the thesis supervisor, resulting in [2].

errors [135], and quantum arithmetic errors [136], relevant for the fault-tolerant regime.

- Efficient use of quantum computational space and time: Specifically,
  - Exponential reductions in the space requirement (qubit counts), determined by the largest bosonic quantum numbers simulated, for the SU(2) and SU(3) LGTs, by use of a binary encoding of the bosonic quantum numbers, (see table 4.2)
  - Superpolynomial savings in the gate counts per time step in quantum simulation by an efficient use of quantum fixed-point arithmetic operations. (see table 4.3)

This chapter is structured as follows. In Sec. 4.1, we provide a technical summary of the results, which contain our findings on the quantum resource requirements for simulating U(1), SU(2), and SU(3) LGTs on a fault-tolerant quantum computer, and a careful comparison to prior art. In Sec. 4.2, we discuss our findings and future work. We leave the details of the circuit construction and resource analyses, which include the Trotter error and synthesis error analyses, as well as the in-depth analyses of prior art, in Secs. 4.3- 4.6.

4.1 Results

4.1.1 Gate complexity

We employ the second-order Suzuki-Trotter formula [22] to implement the evolution operator $e^{i\hat{H}T}$, where $\hat{H}$ is the Kogut-Susskind Hamiltonian in (2.1) and T is the total evolution time. In particular, according to the formula, we approximate

$$e^{i\hat{H}T} = (e^{i\hat{H}T/r})^r \approx \left\{ \left[\prod_{s=1}^{N_s} e^{i\hat{H}_s T/(2r)} \right] \left[\prod_{s=N_s}^{1} e^{\hat{H}_s T/(2r)} \right] \right\}^r , \tag{4.1}$$

where $\hat{H} = \sum_s \hat{H}_s$, N_s is the number of Hamiltonian subterms $\hat{H}_s$ used for Trotter formula, and the number of Trotter steps r is chosen so that T/r is small. The ordering of all individual $\hat{H}_s$ we used follows the ordering of mass, electric, kinetic, and magnetic Hamiltonians, up to subdivisions of each Hamiltonian into multiple subterms if applicable. This choice is used for all the different symmetries, U(1), SU(2), and SU(3) LGTs, we considered. We chose the second-order formula based on [7], wherein it has been shown that the second-order formula achieves a quadratically better gate complexity in the truncation parameter Λ, when compared to other algorithms, such as quantum signal processing [25].

We next describe the way qubits are used in our simulations. For SU(N) LGTs, we use N qubits per lattice site to encode the occupation by the N different fermions or anti-fermions,

each with a distinct color charge. For each lattice link, where we encode the quantum numbers of the gauge-field bosons, we use approximately $(N^2-1)\log_2(\Lambda)$ qubits, with the logarithmic dependence arising from the binary encoding of the quantum numbers, i.e., a binary number b is used to denote the quantum number b in our quantum computer. This may be contrasted to an unary encoding, where $\sim \Lambda$ many qubits would be used to encode the quantum number, with b'th qubit in the state of $|1\rangle$ and the rest in the state of $|0\rangle$ corresponding to the number b.

With the particular encoding chosen above, each Trotter term $\exp\left[i\hat{H}_s T/(2r)\right]$ can be implemented as follows. The mass term is implemented by an application of R_z rotations applied to the lattice-site qubit registers, since it induces phases based on the occupation of the fermions or anti-fermions. In the angular momentum bases described above, the electric term is diagonal and thus, is implemented in a similar fashion for the link qubit registers, except we precompute, using quantum integer arithmetic operations, the eigenvalue expression of the electric Hamiltonian operator. This way, for the eigenvalue expression computed, one can use R_z rotations to induce and accumulate appropriate phases implied by the electric term. In some parameter regimes, we provide an alternative method that can more efficiently induce the phases using an adder circuit instead of R_z rotations [137]. For the kinetic term, we simultaneously operate over a neighboring fermion-anti-fermion pair and the bosonic link that connects the pair. Further, we observe that the distance between the bosonic quantum numbers that interact is limited by the fermion-boson interactions. As such, the kinetic term can always be written as a multiply-banded matrix, where the bandwidth of the matrix scales as $\sim 2^{N^2-1}$ in SU(N) LGTs. We then decompose the matrix into a sum of a number, constant with respect to the truncation parameter Λ, of matrices that individually encode interactions within a selected subspace. The decomposition is chosen carefully such that each constituent matrix appears identical to one another in the non-zero element locations, but differs by some constant shifts in the quantum numbers, accessing different parts of the bands. For a decomposed, constituent matrix, we use a CNOT-and-Hadamard network to efficiently diagonalize the evolution implied by it. This makes the simulation problem into a diagonal phase oracle construction problem. We implement each phase oracle by first computing the state-dependent phases with quantum fixed-point arithmetics [136] and then inducing the appropriate phases with a layer of R_z gates, similar to the electric term. As for the magnetic term, essentially the same approach is used as in the kinetic case, except, here, we drop the fermion-anti-fermion parts and consider four links that form a plaquette at the same time. The bandwidth is $\sim 2^{4(N^2-1)}$.

Contrasted to SU(N) LGTs, U(1) LGTs can be more easily simulated because the U(1) kinetic and magnetic terms impart phases that depend trivially on the input state. As a result, the phase oracles can be executed with only R_z rotations and without the use of fixed-point arithmetics. This is reflected in the separation between the gate-complexities of U(1), and SU(2) and SU(3) LGT simulations, as shown in Eqs. 4.2 and 4.3 down below. We in fact propose an alternative approach for the U(1) LGTs, where we use the quantum Fourier transform to diagonalize (the bosonic part of) the U(1) kinetic term and magnetic term. The phase oracles needed to induce

the evolution implied by the two terms can be efficiently implemented using quantum signal processing techniques [25].

We direct the readers to various upcoming sections for the exact division of $\hat{H}$ into the sum of $\hat{H}_s$ for any d-dimensional U(1), SU(2), and SU(3) LGTs. In particular, we provide the details of the chosen bases for the U(1), SU(2), and SU(3) bosonic gauge fields, and their relations to the corresponding gauge field operators in Secs. 4.3.1, 4.4.1, and 4.5.1, respectively. Furthermore, we describe the circuit implementations of the U(1) mass, electric, kinetic, and magnetic subevolutions in Secs. 4.3.2, 4.3.2, 4.3.2, and 4.3.2, respectively. In Secs. 4.4.2, 4.4.2, 4.4.2, and 4.4.2, we lay out the circuit implementations of the SU(2) mass, electric, kinetic, and magnetic subevolutions, respectively. Finally, the circuit implementations of the SU(3) mass, electric, kinetic, and magnetic subevolutions are discussed in Secs. 4.5.2, 4.5.2, 4.5.2, and 4.5.2, respectively.

As to the simulation errors, we allocate a total error budget of ϵ for the entire simulation. In our circuit synthesis, we evenly split this budget into two halves for the U(1) LGT case, spending each on the algorithmic (Trotter) error and the R_z gate synthesis error (incurred for the approximation using single-qubit Clifford and T gates). For SU(2) and SU(3) LGTs, we split the budget three ways, two of which are used on the algorithmic and R_z synthesis errors as in U(1) case. The third is used on fixed-point quantum arithmetic operations.

Whenever possible, we carefully choose the subdivision of the Trotter term implementations over the lattice topology to maximize parallelism. This includes considering different spatial dimensions and choosing different lattice sites, links to include in one time step. A careful consideration here comes with two benefits, in addition to the obvious circuit depth or execution time reduction. One is the applicability of efficient quantum circuit constructions. More specifically, we employ the weight-sum trick, reported in [137, 138], to synthesize a layer of same-angle R_z gates in parallel. This leads to an exponential reduction in R_z-gate count at the cost of a modest increase in T-gate and ancilla-qubit counts. Therefore, we take a full advantage of this trick by arranging as many same-angle R_z gates as possible into layers across the entire lattice. This optimization is performed for the mass and electric terms, as well as the kinetic and magnetic terms in the U(1) case. The other is the ability to enable streamlined Trotter error analysis. For instance, terms applied in parallel commute with one another, and thus, the commutators to be evaluated for the Trotter error can be more tightly bounded by considering Trotter term collisions at the lattice topology level.

Note the system to be simulated on a quantum computer is a d-dimensional lattice with periodic boundary condition, with L lattice points along each dimension. We therefore study the gate complexity in the electric (bosonic) truncation Λ, the total error budget ϵ, and L, assuming the dimension d and the Hamiltonian parameters g, a, and m [see Eqs. 2.2 and 2.3] are fixed. We use a standard library of controlled-NOT, single-qubit Clifford, and T gates as our basis gate set and consider T gates as our metric of resource requirement as they are the

most expensive operations in a fault-tolerant quantum computer and thus are widely used to be a good proxy for the quantum computational resource requirement in the fault-tolerant regime. The gate complexities for the three different LGTs are (see Secs. 4.3.3, 4.4.3 and 4.5.3 for detailed derivations)

$$\text{U(1) complexity: } O\left(\frac{T^{3/2}d\Lambda L^{d/2}}{\epsilon^{1/2}}\left[d(\log(\Lambda))^2 L^d + \log(\Lambda)\log\left(dL^d\right)\mathcal{C}\right]\right),$$
$$\text{where } \mathcal{C} = \log\left(\frac{T^{3/2}d\Lambda L^{d/2}\log(\Lambda)\log\left(dL^d\right)}{\epsilon^{3/2}}\right) \tag{4.2}$$

and

$$\text{SU(2) or SU(3) complexity: } O\left(\frac{T^{3/2}d\Lambda L^{d/2}}{\epsilon^{1/2}}\left[d^2 L^d \mathcal{K}^2\log(\mathcal{K}) + \log(\Lambda)\log\left(dL^d\right)\mathcal{C}\right]\right),$$
$$\text{where } \mathcal{K} = \log\left(\frac{T^{3/2}d^3\Lambda L^{3d/2}}{\epsilon^{3/2}}\right) + \log\log\left(\frac{T^{3/2}d^3\Lambda L^{3d/2}}{\epsilon^{3/2}}\right)$$
$$\text{and } \mathcal{C} = \log\left(\frac{T^{3/2}d^3\Lambda L^{3d/2}\mathcal{K}}{\epsilon^{3/2}}\right). \tag{4.3}$$

We now apply our complexity results to obtain the upper bounds on T-gate and logical qubit count for simulations of various parameters. In particular, we fix $d = 3$, $a = 0.1$ and $\epsilon = 10^{-8}$, and consider $m, g \in \{0.1, 1, 10\}$. The results are summarized in Table 4.1.

4.1.2 Comparison to prior art

Table 4.2 shows the comparison between our work and the state of the art reported in the literature. In particular we compare our work with Refs. [6] and [7], since they both simulate LGTs over unitary groups on a gate-based, universal quantum computer. Briefly, our work is of the most general and complete kind to date in that, we (a) explore U(1) and SU(N) groups with $N = 2, 3$ being explicitly worked out, (b) consider a lattice in an arbitrary dimension d, (c) include the complete Kogut-Susskind Hamiltonian, i.e., both fermionic (mass, kinetic) and bosonic (electric, magnetic) terms, (d) use an efficient, binary gauge field encoding, and (e) work out the quantum-gate-by-quantum-gate construction of the entire simulation with a full visibility into the gate complexity.

In [6], methods to simulate U(1), SU(2) and SU(3) LGTs without fermions on a universal quantum computer were proposed. The work reported therein also lacks a rigorous analysis of

			U(1)		SU(2)		SU(3)	
L	T	Λ	# T gates	# qubits	# T gates	# qubits	# T gates	# qubits
10	1	5	5.37×10^{17}	6.1×10^{4}	2.67×10^{34}	2.1×10^{5}	2.46×10^{49}	4.8×10^{5}
10	1	10	7.35×10^{17}	7.3×10^{4}	2.83×10^{34}	2.2×10^{5}	3.01×10^{49}	5.5×10^{5}
10	10	5	1.70×10^{19}	6.1×10^{4}	9.10×10^{35}	2.2×10^{5}	7.94×10^{50}	4.9×10^{5}
10	10	10	2.33×10^{19}	7.3×10^{4}	9.60×10^{35}	2.3×10^{5}	9.68×10^{50}	5.6×10^{5}
20	10	10	5.16×10^{20}	5.8×10^{5}	2.31×10^{37}	8.3×10^{5}	2.22×10^{52}	2.0×10^{6}
20	10	20	6.86×10^{20}	6.8×10^{5}	2.43×10^{37}	9.8×10^{5}	2.66×10^{52}	2.4×10^{6}
20	20	10	1.46×10^{21}	5.8×10^{5}	6.68×10^{37}	8.3×10^{5}	6.32×10^{52}	2.0×10^{6}
20	20	20	1.94×10^{21}	6.8×10^{5}	7.02×10^{37}	9.8×10^{5}	7.56×10^{52}	2.4×10^{6}
50	10	10	3.18×10^{22}	9.1×10^{6}	1.55×10^{39}	1.3×10^{7}	1.40×10^{54}	3.2×10^{7}
50	10	50	5.46×10^{22}	1.21×10^{7}	1.70×10^{39}	1.8×10^{7}	1.97×10^{54}	4.4×10^{7}
50	50	10	3.55×10^{23}	9.1×10^{6}	1.81×10^{40}	1.3×10^{7}	1.58×10^{55}	3.2×10^{7}
50	50	50	6.10×10^{23}	1.21×10^{7}	1.99×10^{40}	1.8×10^{7}	2.23×10^{55}	4.4×10^{7}
100	10	10	7.19×10^{23}	7.3×10^{7}	3.71×10^{40}	1.0×10^{8}	3.22×10^{55}	2.6×10^{8}
100	10	100	1.55×10^{24}	1.1×10^{8}	4.27×10^{40}	1.6×10^{8}	5.26×10^{55}	4.0×10^{8}
100	100	10	2.27×10^{25}	7.3×10^{7}	1.25×10^{42}	1.0×10^{8}	1.03×10^{57}	2.6×10^{8}
100	100	100	4.91×10^{25}	1.1×10^{8}	1.43×10^{42}	1.6×10^{8}	1.69×10^{57}	4.0×10^{8}

Table 4.1: **The upper-bounds of the T-gate and logical qubit counts for simulating the time-evolution of U(1), SU(2), and SU(3) lattice gauge theories.** We fix $d = 3$, $a = 0.1$ and $\epsilon = 10^{-8}$. Further, we consider $m, g \in \{0.1, 1, 10\}$, while only the highest estimates are reported in this table. More detailed analyses of the resource requirements can be found in Secs. 4.3.3, 4.4.3 and 4.5.3.

the required gate or qubit counts. Therefore, we analyze the T-gate complexities according to the methods proposed, adapting them to the fault-tolerant setting (see Sec. 4.6 for details). A comparison between the gate complexities of our work and [6] is summarized in Table 4.3. We briefly describe the main methods of [6] for completeness. First, the bosonic quantum numbers are represented in unary encoding, which requires exponentially more logical qubits than our binary encoding. Then, both the electric and magnetic Hamiltonian operators are first expanded element-wise into linear combinations of Pauli operators [2]. As such, for every simulation time (Trotter) step, using well-known circuit templates for Pauli-evolution operators $e^{it\otimes_k \hat{\sigma}^z_k}$ and $e^{it\otimes_i \hat{\sigma}^{\pm}_i + h.c.}$, our analysis shows that the electric evolution requires $\tilde{O}(\Lambda)$ T gates for U(1) and SU(2) LGTs,

[2]Each element in a diagonal operator, i.e., $e_{j,j} |j\rangle\langle j|$, and each pair of elements in the off-diagonal magnetic operator, i.e., $e_{j,k} |j\rangle\langle k| + h.c.$ can be expanded bit-wise into $e_{j,j} \otimes_i |j_i\rangle\langle j_i|$ and $e_{j,k} \otimes_i |j_i\rangle\langle k_i| + h.c.$, respectively, where j_i, k_i are the ith bits of j, k. Using the relations $|0\rangle\langle 0| = (\hat{I} + \hat{\sigma^z})/2$, $|1\rangle\langle 1| = (\hat{I} - \hat{\sigma^z})/2$, $|0\rangle\langle 1| = \hat{\sigma}^-$ and $|1\rangle\langle 0| = \hat{\sigma}^+$, $e_{j,j} \otimes_i |j_i\rangle\langle j_i|$ and $e_{j,k} \otimes_i |j_i\rangle\langle k_i| + h.c.$ can be expressed as a linear combination of the identity and Pauli-z operators, and that of the identity and Pauli ladder operators, respectively.

and $\tilde{O}(\Lambda^2)$ T gates for SU(3) LGTs, whereas the magnetic evolution requires $\tilde{O}(\Lambda^4)$, $\tilde{O}(\Lambda^{12})$, and $\tilde{O}(\Lambda^{32})$ T gates for U(1), SU(2), and SU(3) LGTs, respectively. While the polynomial T-gate complexities are technically efficient, quantum simulations, particularly of SU(2) and SU(3) LGTs, will likely be prohibited in practice by the large degrees of the polynomials. In comparison, our implementation requires at most $\tilde{O}(\log^2(\Lambda))$ T gates per time step for both electric and magnetic term. This superpolynomial improvement can be attributed to an efficient use of integer and fixed-point arithmetic circuits for the electric and magnetic terms, respectively. Furthermore, for the magnetic term, in contrast to the element-wise approach here, our approach requires only a constant number of queries, with respect to Λ, to the state-dependent phase oracles.

To compare with [7], we apply our methods to the one-dimensional U(1) LGT, and demonstrate that we achieve a better gate complexity for all terms (see Sec. 4.6.1 for details), which can be attributed to the R_z gate optimization discussed in section 4.1.1.

	[6]	[7]	Ours
Groups	U(1),SU(2),SU(3) Extensible to SU(N)	U(1)	U(1),SU(2),SU(3) Extensible to SU(N)
Lattice dimension	d	1	d
Hamiltonian	Electric, Magnetic (fermion free)	Mass, Kinetic, Electric	Mass, Kinetic, Electric, Magnetic
Gauge-field encoding	Unary	Binary	Binary
Gate complexity	Unavailable	$\tilde{O}\left(\frac{L^{3/2}T^{3/2}\Lambda}{\epsilon^{1/2}}\right)$	See equations 4.2 and 4.3.

Table 4.2: **Comparison to prior art.** This table displays the lattice gauge theories considered in [6, 7] and our work, specified by their unitary symmetry groups, spatial dimension, and the Hamiltonian terms included, as well as the type of gauge-field encoding employed and the resulting gate complexity. Our work is the most general and complete to date, as we include the complete Kogut-Susskind Hamiltonian with both fermionic and bosonic term in arbitrary spatial dimensions for the Abelian U(1) and non-Abelian SU(N) groups. Compared to [6], our algorithms require exponentially fewer qubits by using an efficient binary gauge-field encoding, and include much more detailed circuit constructions down to a quantum-gate-by-quantum-gate level, along with the gate complexity.

4.2 Discussion

LGT simulations, to be performed on a quantum computer, has massive potential to advance fundamental particle physics. They open up the possibilities to investigate exotic matter at extreme

	[6]			Ours	
	U(1)	SU(2)	SU(3)	U(1)	SU(2), SU(3)
Electric	$\tilde{O}(\Lambda)$	$\tilde{O}(\Lambda)$	$\tilde{O}(\Lambda^2)$	$O(\log^2(\Lambda))$	$\tilde{O}(\log^2(\Lambda))$
Magnetic	$\tilde{O}(\Lambda^4)$	$\tilde{O}(\Lambda^{12})$	$\tilde{O}(\Lambda^{32})$	$\tilde{O}(\log^2(\Lambda))$	$\tilde{O}(\log^2(\Lambda))$

Table 4.3: **Superpolynomial reduction in the gate complexity per simulation time step.** We work out the fault-tolerant circuit construction of the methods proposed in [6], and analyze their gate complexity per simulation time step in Sec. 4.6. Λ is the bosonic truncation parameter discussed in Sec. 2.1. The results summarized in this table show that our circuits, by making use of efficient quantum fixed-point arithmetic circuits, achieve superpolynomial improvements over [6].

conditions [13, 139] such as the core of a neutron star, probe physics related to the matter-anti-matter asymmetry [140, 4] essential to our very existence, and guide experimental particle physics beyond our current theoretical understanding [12]. Furthermore, efficient lattice QCD quantum simulations may one day help us explore complex nuclear dynamics on a quantum computer, via ab-initio simulations. Simulating nuclear dynamics could, for instance, help elucidate fusion processes.

In this chapter, we provided a concrete starting point for future quantum simulations – efficient quantum algorithms to simulate U(1), SU(2) and SU(3) LGTs including mass, kinetic, electric, and magnetic terms. Our work included explicit gate-by-gate circuit constructions, and rigorous upper-bounds on the fault-tolerant quantum computational resource required via analyses of Trotter error, synthesis error and quantum arithmetic error. However, our algorithms, while asymptotically efficient, incur astronomically large T-gate overhead. Moreover, we only investigated the time-evolution part of an LGT simulation, but have left state preparation and observable measurement for future work. We expect that continuous software improvements, such as algorithms with lower constants and gate complexity, and invention of efficient algorithms for state preparation and observable measurement, built upon our work are necessary to eventually bring quantum simulations of LGTs to reality.

4.3 Methodology for Simulating U(1) Lattice Gauge Theory

In this section, we detail the methodology to implement the Abelian U(1) lattice gauge theory, of which the continuum describes quantum electrodynamics (QED), on a quantum computer. Due to its Abelian nature, the theory is more straightforward than non-Abelian theories, such as SU(2) or SU(3) that we investigate in detail in the subsequent sections. We therefore take advantage of the simplicity to lay out the ground work useful for SU(2) and SU(3) discussion.

4.3.1 Preliminaries

As discussed in the main text, there are four Hamiltonian terms of interest: The electric Hamiltonian $\hat{H}_E$, magnetic Hamiltonian $\hat{H}_B$, mass Hamiltonian H_M, and kinetic Hamiltonian $\hat{H}_K$. Inspecting these terms, the first two operate on the links that connect two sites, the mass Hamiltonian operates on the sites themselves, and the kinetic Hamiltonian acts on nearest pairs of sites and the links that connect the pairs. Thus, it is natural to consider two different types of qubit registers, one for the gauge fields ($\hat{H}_E$, $\hat{H}_B$, $\hat{H}_K$) and the other for the fermionic fields ($\hat{H}_M$, $\hat{H}_K$).

To simulate this system, we need to first choose a good basis for each register. For the fermionic register, we consider an occupation basis. The use of an occupation basis of fermionic particles to simulate on a quantum computer is well studied in the literature [141]. For concreteness and simplicity, we use the Jordan-Wigner (JW) transformation [142] for the rest of the chapter.

As for the gauge-field register, extra care needs to be taken. In particular, we need to ensure the U(1) gauge invariance is satisfied. Gauge invariance is generated by a local constraint, known as Gauss' law, i.e.,

$$\hat{G}(\vec{n}) = \sum_k (\hat{E}(\vec{n}, k) - \hat{E}(\vec{n} - \hat{k}, k)) - \hat{Q}(\vec{n}),\ \forall \vec{n}, \tag{4.4}$$

where $\hat{G}(\vec{n})$ is the Gauss operator, $\hat{E}(\vec{n}, k)$ is the electric field of the link that starts from site $\vec{n}$ in direction k, and $\hat{Q}(\vec{n})$ is the charge operator defined according to

$$\hat{Q}(\vec{n}) = \hat{\psi}(\vec{n})^\dagger \hat{\psi}(\vec{n}) - \frac{\hat{I}}{2}[1 - (-1)^{\vec{n}}], \tag{4.5}$$

where $\hat{\psi}(\vec{n})^\dagger$ and $\hat{\psi}(\vec{n})$ are the fermion creation and annihilation operators and $\hat{I}$ denotes an identity operator. On a d-dimensional lattice, $\vec{n} = (n_1, n_2, ..., n_d)$ is a vector with d coordinates. Further, we define the parity of each site,

$$(-1)^{\vec{n}} \equiv (-1)^{\sum_{i=1}^{d} n_i}. \tag{4.6}$$

The Gauss operator generates local gauge transformation and must commute with the Hamiltonian. The physical, gauge-invariant Hilbert space $\mathcal{H}_G$ is defined through the eigenstates of the Gauss operator:

$$\mathcal{H}_G = \{|\Psi\rangle \in \mathcal{H}_G \,|\, \hat{G}_{\vec{n}} \,|\Psi\rangle = 0\,, \forall\, \vec{n}\}. \tag{4.7}$$

In the current case of U(1) lattice gauge theory, the eigenstates of the electric field operator qualify for the link-space basis, as the electric field operator and the Gauss operator commute. More specifically, the electric field operator forms a complete set of commuting observables on the link space. Therefore, the eigenbasis of the complete set of commuting observables, i.e., the eigenbasis of the electric field operator, is a good basis or a good quantum number.

As the last step of preliminaries to a quantum simulation of U(1) lattice gauge theory, we note that

$$[\hat{E}(\vec{n},k),\hat{U}(\vec{n}',k')] = \delta_{\vec{n}',\vec{n}}\delta_{k,k'}\hat{U}(\vec{n},k),$$
$$[\hat{E}(\vec{n},k),\hat{U}(\vec{n}',k')^\dagger] = -\delta_{\vec{n}',\vec{n}}\delta_{k,k'}\hat{U}(\vec{n},k)^\dagger, \tag{4.8}$$

where $\hat{U}(\vec{n},k)$ is the parallel transporter operator. In the electric field basis $|E\rangle$, defined according to

$$\hat{E} = \sum_{E\in\mathbb{Z}} E\,|E\rangle\langle E|\,, \tag{4.9}$$

we have

$$\hat{U} = \sum_{E\in\mathbb{Z}} |E+1\rangle\langle E|\,,\ \ \hat{U}^\dagger = \sum_{E\in\mathbb{Z}} |E-1\rangle\langle E|\,. \tag{4.10}$$

Note that we dropped site and direction indices for notational convenience.

4.3.2 Simulation circuit synthesis

In order to represent the infinite-dimensional gauge-field operator on each link on a finite-size quantum computer, its Hilbert space must be truncated at a cutoff, Λ. The electric field operator then becomes

$$\hat{E} = \sum_{E=-\Lambda}^{\Lambda-1} E\,|E\rangle\langle E|\,. \tag{4.11}$$

A non-negative integer $0 \le j < 2^\eta$ is represented on the binary η-qubit register as

$$|j\rangle = \left|\sum_{n=0}^{\eta-1} j_n 2^n\right\rangle = \bigotimes_{n=0}^{\eta-1} |j_n\rangle\,. \tag{4.12}$$

Using this binary computational basis, the eigenbasis $|E\rangle$ is encoded via $E = j - \Lambda$. Then, the number of qubits on the link register for each link is given by $\eta = \log(2\Lambda)$, where Λ is assumed to be a non-negative power of two, and we have and will continue to assume all logarithms are base two, unless otherwise specified.

In [7], the authors periodically wrapped the electric fields at Λ such that

$$\hat{U}\,|\Lambda-1\rangle = |-\Lambda\rangle\,,\ \hat{U}^\dagger\,|-\Lambda\rangle = |\Lambda-1\rangle\,. \tag{4.13}$$

This spoils the on-link commutator at the cutoff to give

$$[\hat{E},\hat{U}] = \hat{U} - 2\Lambda\,|-\Lambda\rangle\langle\Lambda-1|\,, \tag{4.14}$$
$$[\hat{E},\hat{U}^\dagger] = -\hat{U}^\dagger + 2\Lambda\,|\Lambda-1\rangle\langle-\Lambda|\,. \tag{4.15}$$

However, as is also explicitly discussed in [7], for a truncation with a large cutoff value, the states $|-\Lambda\rangle$ and $|\Lambda-1\rangle$ are energetically unfavorable, and hence, will hardly be populated at all. Therefore, the spoiled commutator will likely not be a problem.

Equipped with all the necessary tools, we now write the Hamiltonian in the qubit space as

$$\hat{H} = \sum_{\vec{n}} \left[\hat{D}^{(M)}_{\vec{n}} + \hat{D}^{(E)}_{\vec{n}} + \hat{T}^{(K)}_{\vec{n}} + \hat{L}^{(B)}_{\vec{n}} \right], \tag{4.16}$$

where

$$\hat{D}^{(M)}_{\vec{n}} = -\frac{m}{2}(-1)^{\vec{n}}\hat{Z}(\vec{n}), \tag{4.17}$$

$$\hat{D}^{(E)}_{\vec{n}} = \frac{g^2}{2a^{d-2}} \sum_{l=1}^{d} \hat{E}^2(\vec{n}, l), \tag{4.18}$$

are diagonal operators, where $(-1)^{\vec{n}}$ is either $+1$ or -1 depending on whether $\vec{n}$ is a fermion or anti-fermion site, respectively, reflective of the use of staggered-fermions [105], and

$$\begin{aligned}\hat{T}^{(K)}_{\vec{n}} = \sum_{l=1}^{d} \frac{1}{8a} [&(\hat{U}(\vec{n}, l) + \hat{U}^\dagger(\vec{n}, l))(\hat{X}(\vec{n})\hat{X}(\vec{n}+\hat{l}) + \hat{Y}(\vec{n})\hat{Y}(\vec{n}+\hat{l}))\hat{\zeta}_{\vec{n},l} \\ &+ i(\hat{U}(\vec{n}, l) - \hat{U}^\dagger(\vec{n}, l))(\hat{X}(\vec{n})\hat{Y}(\vec{n}+\hat{l}) - \hat{Y}(\vec{n})\hat{X}(\vec{n}+\hat{l}))\hat{\zeta}_{\vec{n},l}]\end{aligned} \tag{4.19}$$

is an off-diagonal operator. We use $\hat{X}$, $\hat{Y}$, and $\hat{Z}$ as the Pauli x, y, and z matrices, respectively. We abuse the notation $\hat{l}$ to denote a unit vector in direction l. The operators $\hat{\zeta}_{\vec{n},l}$ are tensor products of $\hat{Z}$, which arise from the JW transformation. We consider a d-dimensional L^d-site lattice, where there are L sites in each direction. The length of each $\hat{\zeta}_{\vec{n},l}$ is $O(L^{d-1})$. For brevity, we suppress the $\hat{\zeta}_{\vec{n},l}$ operators in the remaining part of the section. The second off-diagonal operator due to the magnetic contribution is given by

$$\hat{L}^{(B)}_{\vec{n}} = \frac{-1}{2a^{4-d}g^2} \sum_{j\neq i; j,i=1}^{d} [\hat{U}(\vec{n}, i)\hat{U}(\vec{n}+\hat{i}, j)\hat{U}^\dagger(\vec{n}+\hat{j}, i)\hat{U}^\dagger(\vec{n}, j) + h.c.], \tag{4.20}$$

where $h.c.$ denotes Hermitian conjugate. We use Suzuki-Trotter formula [22] as our simulation method. The Trotter terms to be implemented are of the form $e^{i\hat{D}^{(M)}_{\vec{n}}t}, e^{i\hat{D}^{(E)}_{\vec{n}}t}, e^{i\hat{T}^{(K)}_{\vec{n}}t}, e^{i\hat{L}^{(B)}_{\vec{n}}t}$, where t is a sufficiently small number to ensure the Trotter error incurred is within a pre-specified tolerance. In the remaining part of this subsection, we discuss synthesizing circuits for each of the four Trotter terms.

Mass term $e^{i\hat{D}_{\vec{n}}^{(M)}t}$

The implementation of this term is straightforward. A single-qubit $R_z(\theta) = \exp\Big(-i\theta\hat{Z}/2\Big)$ gate, where $\theta = -m(-1)^{\vec{n}}t$, applied to the qubit that corresponds to site $\vec{n}$ in the site register suffices. Note that the angles of rotation are the same for all even and odd sites, respectively, up to a sign. The sign difference can be rectified by conjugating the z-rotations with NOT gates. Then, a circuit with one layer of R_z gates with the same angle of rotation results. This circuit can be implemented efficiently using the weight-sum trick in [137, 138]. Briefly, consider applying the same angle R_z gates on p qubits simultaneously. This imparts a phase to an input state with the phase angle being proportional to the Hamming weight of the input. This can thus alternatively be implemented by first computing Weight(p) into an ancilla register, while incurring $p-$Weight(p) ancilla qubits and at most $4(p-\text{Weight}(p))$ T gates, where Weight denotes the number of ones in the binary expansion of the integer number p. Finally, we apply $\lfloor \log(p)+1 \rfloor$ R_z rotations to the ancilla register to impart the correct phase, and then uncompute the weight on the ancilla register. For a d-dimensional lattice with L^d lattice sites, $p = L^d$.

Electric term $e^{i\hat{D}_{\vec{n}}^{(E)}t}$

Here, we present a method to implement the electric term. The method modifies that presented in [7], and provides an improvement in gate counts. We import the steps detailed in [7] for the convenience of the readers. $\hat{D}_{\vec{n}}^{(E)}$ is a sum of d commuting terms, and hence, its evolution can be implemented exactly as a product of d sub-evolutions,

$$e^{it\hat{D}_{\vec{n}}^{(E)}} = \prod_{l=1}^{d} e^{i\frac{g^2 t}{2a^{d-2}}\hat{E}^2(\vec{n},l)}. \tag{4.21}$$

We will discuss the implementation of only one sub-evolution without loss of generality. We herein drop the link location index for notational convenience. The electric field operator and a qubit-encoded gauge field state obeys the eigenvalue relation

$$\hat{E}\,|j\rangle = (j - 2^{\eta-1})\,|j\rangle\,. \tag{4.22}$$

As such, the evolution of the electric part $e^{it\frac{g^2}{2a^{d-2}}\hat{E}^2}$ is given by

$$|j\rangle \mapsto e^{it\frac{g^2}{2a^{d-2}}(j-2^{\eta-1})^2}\,|j\rangle\,. \tag{4.23}$$

To implement the term for each link, we first compute $(j-2^{\eta-1})^2$ into an ancilla register, and then, impart the phase by applying an R_z gate on every qubit in the ancilla register. We perform the arithmetic operations by first computing $j-2^{\eta-1}$, using an out-of-place adder, which incurs

$4(\eta-2)$ T gates and η reusable ancilla qubits [137], and then squaring the $(\eta+1)-$bit ancilla state, which costs $4\eta(12\eta-3\lfloor\log(\eta+1)\rfloor-2)$ T gates with the multiplier proposed in [7]. We induce approximate phases (described below) and then finally uncompute the ancilla register. Therefore, the entire arithmetic operations cost $8(\eta-2)+8\eta(12\eta-3\lfloor\log(\eta+1)\rfloor-2)$ T gates. Here, we choose to perform the arithmetic operations in series to reduce the ancilla-qubit count. Since there are dL^d links on an L^d-site d-dimensional lattice, the arithmetic operations on all links cost at most $8dL^d[(\eta-2)+\eta(12\eta-3\lfloor\log(\eta+1)\rfloor-2)]$ T gates, $3(\eta+1)dL^d$ ancilla qubits to store $\left|j-2^{\eta+1}\right\rangle$ and $\left|(j-2^{\eta+1})^2\right\rangle$, and $3(\eta+1)-\lfloor\log(\eta+1)\rfloor-1$ reusable workspace ancilla qubits [7]. If we choose to optimize the T-depth, we can parallelize the squaring operations, at the cost of increasing the workspace ancilla-qubit count.

We now discuss the phase induction. The correct phase can be induced by applying $R_z(2^k\theta)$, where $\theta=\frac{g^2t}{2a^{d-2}}$, on the kth qubit of the $2(\eta+1)-$bit ancilla state, $\left|(j-2^{\eta+1})^2\right\rangle$. Hence, there are $2(\eta+1)$ sets of dL^d same-angle R_z rotations to implement, where each set can be effected using the weight-sum trick. Once again, we first compute Weight(dL^d) into the ancilla register, incurring $4(dL^d-\text{Weight}(dL^d))$ T gates and $dL^d-\text{Weight}(dL^d)$ ancilla qubits, and then, applying $\lfloor\log\left(dL^d\right)+1\rfloor$ R_z gates to the ancilla register to induce the right phase.

There is an alternative method for simulations with a fixed Trotter step t, d and g^2, where a can be chosen such that $\frac{g^2t}{2a^{d-2}}=\frac{\pi}{2^M}$ with $M>\eta$. The electric evolution is then given by

$$|j\rangle\mapsto e^{i\frac{\pi}{2^M}(j-2^{\eta-1})^2}|j\rangle\,. \tag{4.24}$$

Once again, we first compute $(j-2^{\eta-1})^2$ into the ancilla register. Then, we impart the phase by a phase gradient operation, which consists of an M-bit addition on a specially prepared phase gradient state [143]

$$|\psi_M\rangle=\frac{1}{\sqrt{2^M}}\sum_{b=0}^{2^M-1}e^{-2\pi ib/2^M}|b\rangle\,, \tag{4.25}$$

incurring $4M+O(1)$ T gates due to the $M-$bit adder [137]. Here, we perform the arithmetic operations and phase gradient operation on one link at a time. Since $M=\log\left(\frac{2\pi a^{d-2}}{g^2t}\right)$, the number of T gates required by the adders operations on all the links is $4dL^d\log\left(\frac{2\pi a^{d-2}}{g^2t}\right)+O(dL^d)$. In order to synthesize the phase gradient state, which can be reused for all phase gradient operations, $M-1$ Z^α phase-shift rotation gates, defined by

$$Z^\alpha=\begin{pmatrix}1&0\\0&e^{i\pi\alpha}\end{pmatrix}, \tag{4.26}$$

are needed [138]. Each Z^α can be synthesized by using RUS circuits [135].

Kinetic term $e^{i\hat{T}^{(K)}_{\vec{n}}t}$

Here we present two different methods to implement the kinetic term. The first method is a small modification of the method in [7], so we import the steps detailed in [7] for the convenience of the readers. The second method is based on the diagonalization of $\hat{U}$ operators. Herein, we drop the exact site and link position dependence and instead use r and $r+1$ to denote two sites without loss of generality.

Method 1: Block-diagonal decomposition — In order to decompose the off-diagonal term into elementary gates, we write

$$\hat{U} + \hat{U}^\dagger = \hat{A} + \hat{\tilde{A}}, \tag{4.27}$$

where $\hat{A} = \hat{I} \otimes \hat{I} ... \otimes \hat{X}$ and $\hat{\tilde{A}} = \hat{U}^\dagger \hat{A} \hat{U}$, and similarly,

$$i(\hat{U} - \hat{U}^\dagger) = \hat{B} + \hat{\tilde{B}}, \tag{4.28}$$

where $\hat{B} = \hat{I} \otimes \hat{I} ... \otimes \hat{Y}$ and $\hat{\tilde{B}} = \hat{U}^\dagger \hat{B} \hat{U}$.

Furthermore, we define

$$\begin{aligned} \hat{P}_r &= \hat{X}_r \hat{X}_{r+1} + \hat{Y}_r \hat{Y}_{r+1}, \\ \hat{\tilde{P}}_r &= \hat{X}_r \hat{Y}_{r+1} - \hat{Y}_r \hat{X}_{r+1}. \end{aligned} \tag{4.29}$$

To simulate the off-diagonal term, we approximate

$$e^{-i\frac{t}{8a}[(\hat{A}+\hat{\tilde{A}})\otimes\hat{P}_r + (\hat{B}+\hat{\tilde{B}})\otimes\hat{\tilde{P}}_r]} \approx e^{-it(\hat{T}^{(2)}_r + \hat{T}^{(3)}_r)/2} e^{-it(\hat{T}^{(1)}_r + \hat{T}^{(4)}_r)/2}, \tag{4.30}$$

where

$$\hat{T}^{(1)}_r = (\hat{A} \otimes \hat{P}_r)/4a, \tag{4.31}$$

$$\begin{aligned} \hat{T}^{(2)}_r &= (\hat{\tilde{A}} \otimes \hat{P}_r)/4a \\ &= \hat{U}^\dagger T^{(1)}_r \hat{U}, \end{aligned} \tag{4.32}$$

$$\begin{aligned} \hat{T}^{(3)}_r &= (\hat{\tilde{B}} \otimes \hat{\tilde{P}}_r)/4a \\ &= \hat{U}^\dagger \hat{T}^{(4)}_r \hat{U}, \end{aligned} \tag{4.33}$$

$$\hat{T}^{(4)}_r = (\hat{B} \otimes \hat{\tilde{P}}_r)/4a. \tag{4.34}$$

In contrast to [7], wherein the Trotterization was performed for individual $\hat{T}$ terms in the order of $\hat{T}^{(1)}_r$, $\hat{T}^{(2)}_r$, $\hat{T}^{(3)}_r$, and $\hat{T}^{(4)}_r$, here, we Trotterize them into two terms (see (4.30)). We do this

since there is an efficient circuit known to implement $e^{-it(\hat{T}_r^{(1)}+\hat{T}_r^{(4)})/2}$ and $e^{-it(\hat{T}_r^{(2)}+\hat{T}_r^{(3)})/2}$ [144]. Briefly, the circuit is a doubly-controlled R_x gate whose angle is four times the angle of rotation in the Trotter term written in the Pauli basis, conjugated by a simple CNOT network – in this particular case the network is a CNOT gate with control on fermion site $r+1$ and target on fermion site r, followed by another CNOT gate with the same control but the target being the zeroth bit of the Bosonic link in between. See Fig. 4.1. The doubly-controlled R_x gate can be implemented using two uncontrolled R_z gates and two relative-phase Toffoli gates, which cost 4 T gates each [145]. Note that the angles of rotation here, one minus and one plus per r are the same, for all choices of r. Conjugated by a pair of NOT gates, the negative angle rotations become positive. As such, the emergent two subcircuits, each being a layer of individual R_z gates associated with each r, have the same angle of rotation. As in the mass term, we can use the weight-sum trick to implement the kinetic term.

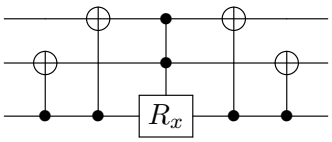

Figure 4.1: Circuit for an individual kinetic term. Top: the zeroth qubit of the bosonic gauge field between fermionic sites r and $r+1$. Middle/Bottom: fermionic sites r and $r+1$. Conjugation of this circuit by controlled-Z gates with the target on the bottom qubit addresses the JW string, and with the control on a qubit in the JW string.

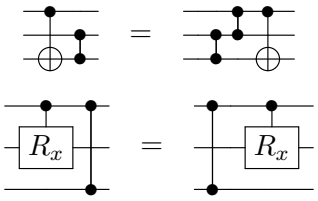

Figure 4.2: Commutation and cancellation rules used to parallelize the $U(1)$ kinetic term implementation. Note two closed circles connected by a line indicates a controlled-Z gate. A collision of two controlled-Z gates on the same two-qubit lines cancel each other (not shown). Two gates acting on two disjoint set of qubits commute (not shown).

However, unlike the mass term, we cannot implement the kinetic terms of all the sites in parallel due to two reasons. First, the kinetic terms for nearest-neighbors do not commute. As such, we have to evolve the odd and even sites separately. Second, the evolution operator includes the multi-site Pauli-z operators $\hat{\zeta}$, shown in (4.19), due to the JW transformation. Unless two

nearest-neighbor sites are connected on the JW path, the multi-site Pauli-z operators need to be taken into account. Note on a d-dimensional L^d-site lattice, there are dL^d individual kinetic terms to implement. In the following, we construct a circuit that implements these individual terms in parallel whenever possible.

We start with the JW transformation. Specifically, we follow a zigzag pattern. On a one-dimensional lattice, this path is simply a line. On a two-dimensional L^2-site lattice, one can draw L lines of length L in the x-direction, for instance, and connect the neighboring lines to form a zigzagging path. This zigzagging JW path can be generalized to d-dimensional lattices.

We next consider the terms in the bulk and on the edges of the lattice separately. The edges are $(d-1)$-dimensional hyperplanes, on which the terms are connected with periodic boundary conditions, but not with open boundary conditions. There are dL^{d-1} terms on the edges. The terms in the bulk are connected in both periodic and open boundary conditions. There are $d(L^d - L^{d-1})$ terms in the bulk.

We implement the evolution of the bulk- and edge-terms one orthogonal direction at a time. For each direction, we use a template circuit in Fig. 4.1, modified to accommodate for $\hat{\zeta}$. This is straightforwardly done by a conjugation of the circuit by controlled-Z gates [144].

We parallelize the circuit that implements the kinetic term for each direction as follows. Denote the subcircuit that is to the left of the doubly controlled R_x, including the aforementioned controlled-Z gates, as a circuit prefix P. Denote the subcircuit that appears to the right of the doubly controlled R_x, including the aforementioned controlled-Z gates, as a circuit suffix S. We can gather all of the Ps, in the order of their appearance, to the left end of the circuit. Similarly, we can collect all of the Ss to the right end of the circuit. Note that this process requires applications of gate commutation and cancellation rules. We report these in Fig. 4.2.

The resulting, parallelized circuit has a layer of doubly controlled R_x gates in the middle. We discussed earlier how to implement a doubly-controlled R_x gate using two R_z gates in parallel. With all angles of rotation being the same, we can employ the weight-sum trick to reduce the gate complexity.

We now gather everything. Recall we have four different levels to consider: (i) $\hat{T}^{(1/4)}$ vs $\hat{T}^{(2/3)}$, (ii) even vs odd sites, (iii) bulk vs edge terms, and (iv) each orthogonal directions $i = 1, .., d$ in the d-dimensional lattice. Levels (i) and (ii) imply that we apply four stages of circuits per given levels (iii) and (iv). Consider a single stage. For the bulk terms, for each direction i, the number of controlled-Z gates required in the parallelized circuit is $O(L^{i-1})$, assuming our zigzag pattern is formed in the ascending order of i. The number of doubly-controlled R_x gates implemented in parallel is $N_B = (L^d - L^{d-1})/2$. Our implementation requires $8N_B$ T gates to detach the double controls from R_x gates, N_B ancilla qubits to parallelize the R_z implementations, and additional $2N_B - \text{Weight}(2N_B)$ ancilla qubits and $4(2N_B - \text{Weight}(2N_B))$ T gates to compute the weight into the ancilla register, after which $\lfloor \log(2N_B) + 1 \rfloor$ R_z gates are applied to the ancilla

register. For the edge terms, for each direction i, the number of controlled-Z gates required in the parallelized circuit is $O(L^i)$. The number of doubly-controlled R_x gates implemented in parallel is $N_E = L^{d-1}/2$. The resource required is the same as above, where all occurrences of N_B is replaced by N_E.

To be complete, for level (i), note $e^{-it(\hat{T}_r^{(2)}+\hat{T}_r^{(3)})/2}$ has an extra incrementer and decrementer. This incurs an additional cost of $8(\eta-2)$ T gates and η reusable ancilla qubits [7], when using the compute-uncompute trick for logical ANDs in [137] and the Toffoli construction in [146].

Method 2: Diagonalization of $\hat{U}$ — Here we consider an alternative method to implement the kinetic term. We first consider an η-qubit quantum Fourier transform (QFT) $\mathcal{F}$ defined according to

$$\mathcal{F} = \frac{1}{\sqrt{2^\eta}} \sum_{j,k=0}^{2^\eta-1} e^{\frac{2\pi i jk}{2^\eta}} |k\rangle \langle j| . \tag{4.35}$$

Conjugating $\hat{U}^\dagger$ with the QFT, we obtain

$$\begin{aligned}
\mathcal{F}(\hat{U}^\dagger)\mathcal{F}^\dagger &= \frac{1}{2^\eta} \sum_{l,j,k,j',k'=0}^{2^\eta-1} e^{\frac{2\pi i(jk-j'k')}{2^\eta}} |k\rangle \langle j|l-1\rangle \langle l|j'\rangle \langle k'| \\
&= \frac{1}{2^\eta} \sum_{l,j,k,j',k'=0}^{2^\eta-1} e^{\frac{2\pi i(jk-j'k')}{2^\eta}} |k\rangle\langle k'| \, \delta_{j,l-1}\delta_{l,j'} \\
&= \frac{1}{2^\eta} \sum_{l,k,k'=0}^{2^\eta-1} e^{\frac{2\pi i(l-1)k}{2^\eta}} e^{\frac{-2\pi i l k'}{2^\eta}} |k\rangle\langle k'| \\
&= \frac{1}{2^\eta} \sum_{l,k,k'=0}^{2^\eta-1} e^{\frac{2\pi i(k-k')l}{2^\eta}} e^{\frac{-2\pi i k}{2^\eta}} |k\rangle\langle k'| \\
&= \sum_{k,k'=0}^{2^\eta-1} \delta_{k,k'} e^{\frac{-2\pi i k}{2^\eta}} |k\rangle\langle k'| \\
&= \sum_{k=0}^{2^\eta-1} e^{\frac{-2\pi i k}{2^\eta}} |k\rangle\langle k| .
\end{aligned} \tag{4.36}$$

Taking the Hermitian conjugate,

$$\mathcal{F}(\hat{U})\mathcal{F}^\dagger = \sum_{k=0}^{2^\eta-1} e^{\frac{2\pi i k}{2^\eta}} |k\rangle\langle k| . \tag{4.37}$$

By linearity, we obtain

$$\begin{aligned}\mathcal{F}(\hat{U}+\hat{U}^\dagger)\mathcal{F}^\dagger &= \sum_{k=0}^{2^\eta-1}(e^{\frac{2\pi ik}{2^\eta}}+e^{\frac{-2\pi ik}{2^\eta}})\,|k\rangle\langle k| \\ &= \sum_{k=0}^{2^\eta-1} 2\cos\left(\frac{2\pi k}{2^\eta}\right)|k\rangle\langle k| \equiv \hat{D}_c, \qquad (4.38)\\ \mathcal{F}i(\hat{U}-\hat{U}^\dagger)\mathcal{F}^\dagger &= \sum_{k=0}^{2^\eta-1} i(e^{\frac{2\pi ik}{2^\eta}}-e^{\frac{-2\pi ik}{2^\eta}})\,|k\rangle\langle k| \\ &= \sum_{k=0}^{2^\eta-1} -2\sin\left(\frac{2\pi k}{2^\eta}\right)|k\rangle\langle k| \equiv \hat{D}_s, \qquad (4.39)\end{aligned}$$

where $\hat{D}_c$ and $\hat{D}_s$ are diagonal. The fermionic operators $\hat{P}_r, \hat{\tilde{P}}_r$ can also be diagonalized. Define the basis as,

$$|\beta_{ab}\rangle = \frac{1}{\sqrt{2}}(|0b\rangle + (-1)^a\,|1\bar{b}\rangle), \qquad (4.40)$$

where $\bar{b}$ is the binary negation of b. Let $\hat{U}_{Bell}$ be

$$\sum_{a,b=0}^{1}|\beta_{ab}\rangle\langle ab|\,. \qquad (4.41)$$

Then,

$$\begin{aligned}\hat{P}_r &= \hat{U}_{Bell}\sum_{a,b=0}^{1}2b(-1)^a\,|ab\rangle\langle ab|\,\hat{U}_{Bell}^\dagger \\ &\equiv \hat{U}_{Bell}\hat{D}^f\hat{U}_{Bell}^\dagger \qquad (4.42)\end{aligned}$$

and

$$\begin{aligned}\hat{\tilde{P}}_r &= (\hat{S}^\dagger\otimes\hat{I})\hat{P}_r(\hat{S}\otimes\hat{I}) \\ &\equiv (\hat{S}^\dagger\otimes\hat{I})\hat{U}_{Bell}\hat{D}^f\hat{U}_{Bell}^\dagger(\hat{S}\otimes\hat{I}). \qquad (4.43)\end{aligned}$$

Note $\hat{D}^f$ is diagonal. As such, the kinetic term can be written as a sum of two diagonalizable operators

$$\begin{aligned}&\frac{1}{8a}[(\hat{U}+\hat{U}^\dagger)\otimes\hat{P}_r + i(\hat{U}-\hat{U}^\dagger)\otimes\hat{\tilde{P}}_r] \\ &= \frac{1}{8a}[\mathcal{F}^\dagger\otimes\hat{U}_{Bell}(\hat{D}_c\otimes\hat{D}^f)\mathcal{F}\otimes\hat{U}_{Bell}^\dagger + \mathcal{F}^\dagger\otimes(\hat{S}_r^{f\dagger}\hat{U}_{Bell})(\hat{D}_s\otimes\hat{D}^f)\mathcal{F}\otimes(\hat{U}_{Bell}^\dagger\hat{S}_r^f)]. \qquad (4.44)\end{aligned}$$

To first order, the Trotterization of the kinetic term is then

$$
\begin{aligned}
& e^{i\frac{t}{8a}[(\hat{U}+\hat{U}^\dagger)\otimes\hat{P}_r+i(\hat{U}-\hat{U}^\dagger)\otimes\hat{\tilde{P}}_r]} \\
\approx\ & e^{i\frac{t}{8a}(\hat{U}+\hat{U}^\dagger)\otimes\hat{P}_r}e^{i\frac{t}{8a}i(\hat{U}-\hat{U}^\dagger)\otimes\hat{\tilde{P}}_r} \\
=\ & [\mathcal{F}^\dagger\otimes\hat{U}_{Bell}e^{i\frac{t}{8a}(\hat{D}_c\otimes\hat{D}^f)}\mathcal{F}\otimes\hat{U}_{Bell}^\dagger][\mathcal{F}^\dagger\otimes(\hat{S}_r^{f\dagger}\hat{U}_{Bell})e^{i\frac{t}{8a}(\hat{D}_s\otimes\hat{D}^f)}\mathcal{F}\otimes(\hat{U}_{Bell}^\dagger\hat{S}_r^f)] \\
=\ & \mathcal{F}^\dagger\otimes\hat{U}_{Bell}e^{i\frac{t}{8a}(\hat{D}_c\otimes\hat{D}^f)}\hat{I}\otimes(\hat{U}_{Bell}^\dagger\hat{S}_r^{f\dagger}\hat{U}_{Bell})e^{i\frac{t}{8a}(\hat{D}_s\otimes\hat{D}^f)}\mathcal{F}\otimes(\hat{U}_{Bell}^\dagger\hat{S}_r^f),
\end{aligned}
\tag{4.45}
$$

where the first equality is due to $e^{it\hat{U}\hat{D}\hat{U}^\dagger}=\hat{U}e^{it\hat{D}}\hat{U}^\dagger$, with $\hat{U}$ and $\hat{D}$ being a unitary and a diagonal operator, respectively. Since the circuit implementation of the QFT and its inverse is known [109], the implementation of the kinetic term hinges upon the syntheses of $e^{i\frac{t}{8a}(\hat{D}_c\otimes\hat{D}^f)}$ and $e^{i\frac{t}{8a}(\hat{D}_s\otimes\hat{D}^f)}$. Expanding $\hat{D}_c\otimes\hat{D}^f$, we obtain the relation

$$
e^{i\frac{t}{8a}(\hat{D}_c\otimes\hat{D}^f)}=\hat{I}\otimes|00\rangle\langle 00|+e^{i\frac{t}{4a}\hat{D}_c}\otimes|01\rangle\langle 01|+\hat{I}\otimes|10\rangle\langle 10|+e^{-i\frac{t}{4a}\hat{D}_c}\otimes|11\rangle\langle 11|\,,
\tag{4.46}
$$

which can be implemented via applications of $\hat{U}_c\equiv e^{i\frac{t}{4a}\hat{D}_c}$ controlled upon the fermionic state. Similarly, $e^{i\frac{t}{4a}(\hat{D}_s\otimes\hat{D}^f)}$ can be implemented by controlled applications of $\hat{U}_s\equiv e^{i\frac{t}{4a}\hat{D}_s}$.

We next show that both $\hat{U}_c$ and $\hat{U}_s$ can be implemented efficiently via Quantum Signal Processing (QSP) [25]. First, we rewrite them in the form of $\sum_\lambda e^{-i\tau\sin(\theta_\lambda)}|u_\lambda\rangle\langle u_\lambda|$:

$$
\hat{U}_s=\sum_k e^{-i\frac{t}{2a}\sin\left(\frac{2\pi k}{2^\eta}\right)}|k\rangle\langle k|\,,
\tag{4.47}
$$

$$
\hat{U}_c=\sum_k e^{-i\frac{t}{2a}\sin\left(\frac{2\pi k}{2^\eta}+\frac{\pi}{2}\right)}|k\rangle\langle k|\,,
\tag{4.48}
$$

where $\tau=\frac{t}{2a}$. QSP implements an operator in such form with N queries of an oracle $\hat{U}_\phi$, which is defined as

$$
\hat{U}_\phi=(e^{-i\phi\hat{Z}/2}\otimes\hat{I})\hat{U}_0(e^{i\phi\hat{Z}/2}\otimes\hat{I}),
\tag{4.49}
$$

$$
\hat{U}_0=|+\rangle\langle+|\otimes\hat{I}+|-\rangle\langle-|\otimes\hat{W},
\tag{4.50}
$$

$$
\hat{W}=\sum_\lambda e^{i\theta_\lambda}|u_\lambda\rangle\langle u_\lambda|\,.
\tag{4.51}
$$

In this case, for both $\hat{U}_c$ and $\hat{U}_s$, the $\hat{W}$ oracle is given by

$$
\hat{W}=\sum_{k=0}^{2^\eta-1}e^{i\frac{2\pi k}{2^\eta}}|k\rangle\langle k|\,,
\tag{4.52}
$$

which can be implemented with an $\eta-$qubit phase gradient at the cost of $4\eta+O(1)$ T gates. The $\hat{W}$ oracle needs to be controlled by three qubits, one due to the QSP oracle in (4.50) and

two from the fermionic register. See (4.46). This can be accomplished by applying a relative phase Toffoli on an ancilla, controlled by the three qubits, then applying a $\hat{W}$ controlled by the ancilla, and then uncomputing the Toffoli gate. The controlled-$\hat{W}$ operation can be effected by a controlled phase gradient, which can be synthesized with $8\eta + O(1)$ T gates [147], and each triply-controlled relative-phase Toffoli costs 8 T gates [145], which adds a constant overhead to the triply-controlled-$\hat{W}$.

Now we consider the simulation of an individual kinetic term, which is a diagonal norm-one Hamiltonian. In this case, the QSP query complexity depends on only the simulation length τ, and error ϵ. Since the simulation length is fixed to be $\tau = \frac{t}{2a} = \frac{\pi}{g^2 2^M}$, which is much smaller than one, as required by the phase gradient operation for the electric term, we expect that a small number of query is enough to implement $\hat{\tilde{U}}_g$ with $g \in \{c, s\}$. In particular, since our error is bounded by $\frac{4\tau^q}{2^q q!}$, where $t \leq q-1$ and the number of queries is $2(q-1)$ [25], with small τ, $q = 2$ is likely sufficient.

We emphasize in passing that, when the cutoff is severe, the effects of the unwanted periodic wrapping terms in our implementation of $\hat{U}_r$ and $\hat{U}_r^\dagger$, which connect $|-\Lambda\rangle = |00...0\rangle, |\Lambda - 1\rangle = |11...1\rangle$, are no longer negligible. For instance, an application of the kinetic term, which can be expressed as $e^{\frac{it}{2a}(\hat{U}_r \hat{\sigma}_r^- \hat{\sigma}_{r+1}^+ + h.c.)}$, on a link in the state $|\Lambda - 1\rangle = |11...1\rangle$ will introduce a superposition between $|-\Lambda\rangle$ and $|\Lambda - 2\rangle$ because $\hat{U}_r |\Lambda - 1\rangle = |-\Lambda\rangle$ and $\hat{U}_r^\dagger |\Lambda - 1\rangle = |\Lambda - 2\rangle$. However, in the original U(1) LGT, $|-\Lambda\rangle$ will not arise because $|\Lambda - 1\rangle$ is in the null space of $\hat{U}_r$. This effect can be reversed by the evolution $e^{\frac{-it}{2a}(\otimes_{i=0}^{\eta-1} \hat{\sigma}_i^- \hat{\sigma}_r^- \hat{\sigma}_{r+1}^+ + h.c.)}$. This can be implemented using $2(\eta + 1)$ CNOTs, two Hadamard gates, and two R_z gates.

Magnetic term $e^{i\hat{L}_{\vec{n}}^{(B)} t}$

Here, we extend the two methods used to implement the kinetic term to implement the magnetic term. Once again, we drop the location indices for brevity.

Method 1: Block-diagonal decomposition — First, we decompose the ladder operators into the following off-diagonal operators:

$$\hat{U} = \hat{R} + \hat{U}^\dagger \hat{R} \hat{U}, \tag{4.53}$$

$$\hat{U}^\dagger = \hat{R}^\dagger + \hat{U}^\dagger \hat{R}^\dagger \hat{U}, \tag{4.54}$$

where $\hat{R} = \hat{I} \otimes \hat{I} \otimes ... \otimes \hat{\sigma}^+$ and $\hat{U}^\dagger \hat{R} \hat{U}$ are raising operators for $|E\rangle$ when E is odd and even, respectively, and similarly, $\hat{R}^\dagger = \hat{I} \otimes \hat{I} ... \otimes \hat{\sigma}^-$ and $\hat{U}^\dagger \hat{R}^\dagger \hat{U}$ are lowering operators for $|E\rangle$ when E is even and odd, respectively.

Defining

$$\hat{R}_\square = \hat{R}\hat{R}\hat{R}^\dagger \hat{R}^\dagger + \hat{R}^\dagger \hat{R}^\dagger \hat{R}\hat{R}, \tag{4.55}$$

each plaquette operator in $\hat{L}^{(B)}$ can then be expressed as

$$\begin{aligned}
&\hat{U}^{(1)}\hat{U}^{(2)}\hat{U}^{(3)\dagger}\hat{U}^{(4)\dagger} + \hat{U}^{(1)\dagger}\hat{U}^{(2)\dagger}\hat{U}^{(3)}\hat{U}^{(4)} \\
&= (\hat{R} + \hat{U}^{(1)\dagger}\hat{R}\hat{U}^{(1)})(\hat{R} + \hat{U}^{(2)\dagger}\hat{R}\hat{U}^{(2)})(\hat{R}^\dagger + \hat{U}^{(3)\dagger}\hat{R}^\dagger\hat{U}^{(3)})(\hat{R}^\dagger + \hat{U}^{(4)\dagger}\hat{R}^\dagger\hat{U}^{(4)}) + h.c. \\
&= \sum_{i,j,k,l=0}^{1} \hat{U}^{(1)\dagger i}\hat{U}^{(2)\dagger j}\hat{U}^{(3)\dagger k}\hat{U}^{(4)\dagger l}\hat{R}_\square\hat{U}^{(1)i}\hat{U}^{(2)j}\hat{U}^{(3)k}\hat{U}^{(4)l},
\end{aligned} \tag{4.56}$$

where the superscripts in the parentheses are used to denote the links around a plaquette, and the sum is over the powers to which the gauge field ladder operators are raised. In order to maximize the cancellation of $\hat{U}$ and $\hat{U}^\dagger$ in the plaquette operator's first-order Trotter evolution, we order the sum using the Gray code. The Gray code is a binary encoding where two successive values differ in only one bit. In particular, we first label each term by a vector of the ladder operators' powers (i, j, k, l), and then, arrange the labels in the Gray code ordering of the integers $0 - 15$. The first-order Trotterization of the evolution is thus given by

$$\begin{aligned}
&e^{-i\frac{t}{2a^{4-d}g^2}(\hat{U}^{(1)}\hat{U}^{(2)}\hat{U}^{(3)\dagger}\hat{U}^{(4)\dagger}+h.c.)} \\
&\approx \prod_{(i,j,k,l)=GC(0)}^{GC(15)} \hat{U}^{(1)\dagger i}\hat{U}^{(2)\dagger j}\hat{U}^{(3)\dagger k}\hat{U}^{(4)\dagger l}e^{-i\frac{t}{2a^{4-d}g^2}\hat{R}_\square}\hat{U}^{(1)i}\hat{U}^{(2)j}\hat{U}^{(3)k}\hat{U}^{(4)l},
\end{aligned} \tag{4.57}$$

where $GC(n)$ is the Gray code encoding of an integer n. There are 16 sub-evolutions, and between each consecutive sub-evolutions, there will be one $\hat{U}$ or $\hat{U}^\dagger$ that needs to be implemented in this ordering. Including the one $\hat{U}^\dagger$ operator at the end, there will be 16 $\hat{U}$ and $\hat{U}^\dagger$ operators in the evolution. $\hat{U}$ and $\hat{U}^\dagger$ can be implemented as an $\eta-$qubit binary incrementer and decrementer, respectively, each of which costs $4(\eta - 2)$ T gates and η reusable ancilla qubits [7]. Furthermore, each $e^{-i\frac{t}{2a^{4-d}g^2}\hat{R}_\square}$ operator costs two relative-phase triply-controlled Toffoli gates, which take 16 T gates in total to construct, and two R_z gates [144].

Briefly, any operator U that is of the form $e^{-i(\theta\otimes_k\sigma_k+h.c.)/2}$, where $\sigma_k \in \{\sigma^+, \sigma^-\}$ and $k = 1, 2, .., k_{\max}$ can be diagonalized by C as CDC^{-1}, where C is composed of a CNOT network with $k - 1$ CNOTs and a Hadamard gate and D is a diagonal operator. Without loss of generality, consider a case where there are p σ^+'s and $k_{\max} - p$ σ^-'s. Further pick an arbitrary qubit index, say, $k_{\max}$ and $\sigma_{k_{\max}} = \sigma^+$. We apply NOTs to $k_{\max} - p$ σ^-, all controlled on the same qubit $k_{\max}$. We now pick one of the $k_{\max} - p$ qubits with σ^-, say k'. We apply NOTs to the σ^+ qubits except for the $k_{\max}$ qubit, of which there are $p - 1$, all controlled on k'. Applying a Hadamard gate on the $k_{\max}$'th qubit diagonalizes U, i.e., D would now be an $n - 1$-controlled R_z gate with target on $k_{\max}$. A standard method to detach the controls results in two uncontrolled R_z gates.

Note the R_z gates have the same rotation angles, up to a sign, for each and every plaquette. This means, once again, just as in mass and kinetic terms, we can use the weight-sum trick to

reduce the number of R_z gates to be implemented. Since the magnetic terms for nearest-neighbors act on overlapping links, their evolutions are difficult to implement in parallel. Similar to the case of the kinetic term, we implement the magnetic evolutions for the even and odd sites along each two-dimensional plane, separately, in parallel.

Without loss of generality, we assume the number of odd and even sites are $\frac{L^d}{2}$ each. Hence, for each two-dimensional plane, there are $\frac{L^d}{2}$ plaquette evolutions to apply in parallel for even and odd sites, respectively. Consider just the even sites on one plane, the relative-phase triply-controlled Toffoli gates contribute $\frac{L^d}{2} \cdot 16 \cdot 16$ T gates. Further, there are L^d equal-angle R_z gates to implement in parallel for 16 times. Once again, we employ the weight-sum trick to effect the equal-angle R_z gates. The first step of computing $\text{Weight}(L^d)$ costs $4(L^d - \text{Weight}(L^d))$ T gates and $L^d - \text{Weight}(L^d)$ ancilla qubits. Then, we apply $\lfloor \log\left(L^d\right) + 1 \rfloor$ R_z rotations for 16 times. Lastly, the incrementers and decrementers cost $\frac{L^d}{2} \cdot 16 \cdot 4(\eta - 2)$ T gates and η ancilla qubits [7].

Method 2: Diagonalization of $\hat{U}$ — We can diagonalize the plaquette operator $\hat{L}^{(B)}$ by taking tensor products of Eqs. (4.36) and (4.37), i.e.,

$$\begin{aligned}
&\mathcal{F}^{\otimes 4}(\hat{U}^{(1)}\hat{U}^{(2)}\hat{U}^{(3)\dagger}\hat{U}^{(4)\dagger})\mathcal{F}^{\dagger\otimes 4} \\
&= \mathcal{F}(\hat{U}^{(1)})\mathcal{F}^\dagger \otimes \mathcal{F}(\hat{U}^{(2)})\mathcal{F}^\dagger \otimes \mathcal{F}(\hat{U}^{(3)\dagger})\mathcal{F}^\dagger \otimes \mathcal{F}(\hat{U}^{(4)\dagger})\mathcal{F}^\dagger \\
&= \sum_{k_1,k_2,k_3,k_4=0}^{2^\eta-1} e^{\frac{-2\pi i k_1}{2^\eta}} |k_1\rangle\langle k_1| \otimes e^{\frac{-2\pi i k_2}{2^\eta}} |k_2\rangle\langle k_2| \otimes e^{\frac{2\pi i k_3}{2^\eta}} |k_3\rangle\langle k_3| \otimes e^{\frac{2\pi i k_4}{2^\eta}} |k_4\rangle\langle k_4| \\
&= \sum_{k_1,k_2,k_3,k_4=0}^{2^\eta-1} e^{\frac{-2\pi i (k_1+k_2-k_3-k_4)}{2^\eta}} |k_1,k_2,k_3,k_4\rangle\langle k_1,k_2,k_3,k_4| \,. \qquad (4.58)
\end{aligned}$$

Again, by linearity,

$$\begin{aligned}
&\mathcal{F}^{\otimes 4}(\hat{U}^{(1)}\hat{U}^{(2)}\hat{U}^{(3)\dagger}\hat{U}^{(4)\dagger} + \hat{U}^{(1)\dagger}\hat{U}^{(2)\dagger}\hat{U}^{(3)}\hat{U}^{(4)})\mathcal{F}^{\dagger\otimes 4} \\
&= \sum_{k_1,k_2,k_3,k_4=0}^{2^\eta-1} 2\cos\left(\frac{2\pi(k_1+k_2-k_3-k_4)}{2^\eta}\right) |k_1,k_2,k_3,k_4\rangle\langle k_1,k_2,k_3,k_4| \equiv D_\square. \qquad (4.59)
\end{aligned}$$

Now we show that the evolution operator implied by the magnetic term, all of which are of the form,

$$e^{-i\frac{t}{2a^{4-d}g^2}(\hat{U}^{(1)}\hat{U}^{(2)}\hat{U}^{(3)\dagger}\hat{U}^{(4)\dagger}+h.c.)},$$

where $h.c.$ denotes the Hermitian conjugate, can also be diagonalized by a tensor product of four

QFTs. Taylor expanding the evolution operator, we get

$$
\begin{aligned}
& e^{-i\frac{t}{2a^{4-d}g^2}(\hat{U}^{(1)}\hat{U}^{(2)}\hat{U}^{(3)\dagger}\hat{U}^{(4)\dagger}+h.c.)} \\
&= 1+(\frac{-it}{2a^{4-d}g^2})\mathcal{F}^{\dagger\otimes 4}\hat{D}_{\square}\mathcal{F}^{\otimes 4}+\frac{1}{2}(\frac{-it}{2a^{4-d}g^2})^2\mathcal{F}^{\dagger\otimes 4}\hat{D}_{\square}\mathcal{F}^{\otimes 4}\mathcal{F}^{\dagger\otimes 4}\hat{D}_{\square}\mathcal{F}^{\otimes 4}+... \\
&= 1+(\frac{-it}{2a^{4-d}g^2})\mathcal{F}^{\dagger\otimes 4}\hat{D}_{\square}\mathcal{F}^{\otimes 4}+\frac{1}{2}(\frac{-it}{2a^{4-d}g^2})^2\mathcal{F}^{\dagger\otimes 4}\hat{D}^2_{\square}\mathcal{F}^{\otimes 4}+\frac{1}{3!}(\frac{-it}{2a^{4-d}g^2})^3\mathcal{F}^{\dagger\otimes 4}\hat{D}^3_{\square}\mathcal{F}^{\otimes 4}+... \\
&= \mathcal{F}^{\dagger\otimes 4}e^{-i\frac{t}{2a^{4-d}g^2}\hat{D}_{\square}}\mathcal{F}^{\otimes 4}\equiv\mathcal{F}^{\dagger\otimes 4}\hat{U}_{\square}\mathcal{F}^{\otimes 4}.
\end{aligned}
\tag{4.60}
$$

Since the circuit implementation of the QFT and its inverse is known [109], all that remains is to find a circuit that implements $\hat{U}_{\square}$.

To implement $\hat{U}_{\square}$, we consider its action on the input state $|k_1,k_2,k_3,k_4\rangle$, i.e.,

$$
\hat{U}_{\square}\,|k_1,k_2,k_3,k_4\rangle = e^{-i\frac{t}{2a^{4-d}g^2}\hat{D}_{\square}}\,|k_1,k_2,k_3,k_4\rangle = e^{-i\frac{t}{a^{4-d}g^2}\cos\left(\frac{2\pi(k_1+k_2-k_3-k_4)}{2^\eta}\right)}\,|k_1,k_2,k_3,k_4\rangle\,. \tag{4.61}
$$

Similar to the kinetic term implementation, we use QSP to implement the evolution of the plaquette term. As explained in the kinetic term section, it boils down to synthesizing a controlled $\hat{W}$ operator, which is given by

$$
\hat{W}=\sum_{k_1,k_2,k_3,k_4} e^{i\frac{2\pi(k_1+k_2-k_3-k_4)}{2^\eta}}\,|k_1,k_2,k_3,k_4\rangle\langle k_1,k_2,k_3,k_4|\,. \tag{4.62}
$$

The controlled $\hat{W}$ operator can be effected by first computing $k_1+k_2-k_3-k_4$ into an ancilla register, then performing a controlled phase gradient operation on the ancilla, and finally uncomputing the ancilla. We can compute $k_1+k_2-k_3-k_4$ using two out-of-place $\eta-$bit adders and one out-of-place $(\eta+1)$-bit adder proposed in [148]. The two $\eta-$bit adders compute $|k_1\rangle|k_2\rangle|k_3\rangle|k_4\rangle\mapsto|k_1\rangle|k_2\rangle|k_3\rangle|k_4\rangle|k_1+k_2\rangle|k_3+k_4\rangle$, using $2\cdot(5\eta-3\lfloor\log(\eta)\rfloor)-4)$ Toffoli gates and at most $\eta-\lfloor\log(\eta)\rfloor-1$ ancillas. The $(\eta+1)$-bit adder computes $|k_1\rangle|k_2\rangle|k_3\rangle|k_4\rangle|k_1+k_2\rangle|k_3+k_4\rangle\mapsto|k_1\rangle|k_2\rangle|k_3\rangle|k_4\rangle|k_1+k_2\rangle|k_3+k_4\rangle|k_1+k_2-k_3-k_4\rangle$, where $|k_1+k_2\rangle$ and $|k_3+k_4\rangle$ are $(\eta+1)-$qubit registers, and $|k_1+k_2-k_3-k_4\rangle$ is an $(\eta+2)-$qubit registers. This operation requires $5(\eta+1)-3\lfloor\log(\eta+1)\rfloor-4$ Toffoli gates and $(\eta+1)-\lfloor\log(\eta+1)\rfloor-1$ ancillas. As such, the computation and uncomputation of $k_1+k_2-k_3-k_4$ each costs $4\cdot(15\eta-3\lfloor\log(\eta+1)\rfloor-6\lfloor\log(\eta)\rfloor-7)$ T gates, using the Toffoli construction in [146], where each Toffoli gate costs four T gates and an ancilla qubit. As such, $\eta-\lfloor\log(\eta+1)\rfloor$ workspace ancilla qubits are used, and $3\eta+4$ qubits are needed to store the outputs $|k_1+k_2-k_3-k_4\rangle|k_3+k_4\rangle$.

We consider the simulation of an individual magnetic term, which is a diagonal norm-one Hamiltonian. As in the case of kinetic term, the QSP query complexity is determined by the simulation length $\tau=\frac{t}{a^{4-d}g^2}$, shown in (4.61). In order to keep the trotter error small, t, and

hence $\frac{t}{a^{4-d}g^2}$, must be much smaller than one. Once again, we expect that two queries are enough to implement $\hat{\hat{U}}_{\square}$. Therefore, the evolution of a magnetic term requires three serial R_z gates due to the concatenated phase oracle, which is an improvement over method 1, which needs 16 serial pairs of parallel R_z gates. As for the entire magnetic Hamiltonian evolution, we adopt the same parallelization strategy as in method 1, and achieve factors of 32/3 and 16/3 improvement in the total number and layers of R_z gates, respectively.

As in the kinetic term, when the cutoff is severe, the effects of the unwanted periodic wrapping terms of the operators $\hat{U}^{(\dagger)}$, which connect $|-\Lambda\rangle = |00...0\rangle, |\Lambda-1\rangle = |11...1\rangle$, are no longer negligible. Suppose we want to undo the periodic wrapping effect on the ith link of the plaquette. Then, we implement the evolution $e^{\frac{it}{2a^{4-d}g^2}(\otimes_{q=0}^{\eta-1}\hat{\sigma}_q^- \hat{U}^{(j)}\hat{U}^{(k)\dagger}\hat{U}^{(l)\dagger}+h.c.)}$, where the Pauli ladder operators act on the ith link. This evolution can be implemented using both the block-diagonal decomposition method and the diagonalization method. Using the block-diagonal method, the evolution can be implemented by

$$\begin{aligned}
&e^{\frac{it}{2a^{4-d}g^2}(\otimes_{q=0}^{\eta-1}\hat{\sigma}_q^- \hat{U}^{(j)}\hat{U}^{(k)^\dagger}\hat{U}^{(l)^\dagger}+h.c.)} \\
\approx &\prod_{(\alpha,\beta,\gamma)=GC(0)}^{GC(7)} \hat{U}^{(j)\dagger\alpha}\hat{U}^{(k)\dagger\beta}\hat{U}^{(l)\dagger\gamma} e^{\frac{it}{2a^{4-d}g^2}(\otimes_{q=0}^{\eta-1}\hat{\sigma}_q^- \hat{R}\hat{R}^\dagger\hat{R}^\dagger+h.c.)} \hat{U}^{(j)\alpha}\hat{U}^{(k)\beta}\hat{U}^{(l)\gamma},
\end{aligned} \tag{4.63}$$

where $\hat{R}$ is defined in (4.53), and $e^{\frac{it}{2a^{4-d}g^2}(\otimes_{q=0}^{\eta-1}\hat{\sigma}_q^- \hat{R}\hat{R}^\dagger\hat{R}^\dagger+h.c.)}$ can be effected using $2(\eta+2)$ CNOTs, two Hamadard gates and two R_z gates. Using the diagonalization method, we first diagonalize the evolution by applying CNOTs and Hadamards on the ith link to diagonalize the Pauli ladder operators. Next, we apply QFT on links j,k,l to diagonalize the remaining part of the evolution, and obtain

$$\begin{aligned}
&\sum_{m_i,m_j,m_k,m_l} e^{\frac{it}{2a^{4-d}g^2}[(-1)^{b_0}\prod_{q=1}^{\eta-1} b_q \cdot 2\cos\left(\frac{2\pi(m_j-m_k-m_l)}{2^\eta}\right)]} |m_i,m_j,m_k,m_l\rangle\langle m_i,m_j,m_k,m_l| \\
&= |11...1\rangle\langle 11...1| \otimes \sum_{m_j,m_k,m_l} e^{\frac{-it}{a^{4-d}g^2}\cos\left(\frac{2\pi(m_j-m_k-m_l)}{2^\eta}\right)} |m_j,m_k,m_l\rangle\langle m_j,m_k,m_l| \\
&\quad + |01...1\rangle\langle 01...1| \otimes \sum_{m_j,m_k,m_l} e^{\frac{it}{a^{4-d}g^2}\cos\left(\frac{2\pi(m_j-m_k-m_l)}{2^\eta}\right)} |m_j,m_k,m_l\rangle\langle m_j,m_k,m_l|,
\end{aligned} \tag{4.64}$$

where b_q is the bit-value of the qth qubit of the ith link register $|m_i\rangle$. Once again, the evolution can be implemented using two controlled QSP, as in the diagonalization method for the kinetic term. Now suppose we are to undo the periodic wrapping effect on two links, e.g. jth and kth links. Then, we implement the evolution $e^{\frac{it}{2a^{4-d}g^2}(\hat{U}^{(i)}\otimes_{q=0}^{\eta-1}\hat{\sigma}_q^- \otimes_{r=0}^{\eta-1}\hat{\sigma}_r^+\hat{U}^{(l)\dagger}+h.c.)}$, using either the

block-diagonal or diagonalization method. This technique can be straightforwardly generalized to undo the periodic wrapping effect on all combinations of links on each plaquette.

4.3.3 Resource requirement estimates

In this section, we analyze the algorithmic and synthesis errors for our simulations. In Sec. 4.3.3 we compute the algorithmic error for the Suzuki-Trotter formula for our U(1) Hamiltonian. Therein we show our result first, then show a full derivation of it for completeness. In Sec. 4.3.3 we compute the R_z synthesis error. In Sec. 4.3.3 we combine the two errors discussed in Secs. 4.3.3 and 4.3.3 to report the gate complexity and ancilla requirements.

Trotter errors

Simulating quantum dynamics can be boiled down to compiling the evolution generated by a Hamiltonian into a sequence of implementable quantum gates. Commonly used efficient quantum simulation algorithms include Trotter-Suzuki product formulas (PF) [22, 20], linear combinations of unitaries (LCU) [149, 24], and quantum signal processing (QSP) [25]. Here, we choose to employ the second-order PF over LCU and QSP. The reasons for this choice is given in [7], and we import them here for the convenience of the readers. The main reason is that the second-order PF achieves a quadratically better scaling, up to polylogarithmic factors, in the electric truncation Λ, when compared to the other algorithms.

Therefore, we as well choose to use the second-order PF as our simulation algorithm, just as in [7], and evaluate the commutator bound for the error given in (2.8). The result is

$$||e^{-i\hat{H}T} - \hat{U}_2^r(t)|| \leq r\left(\frac{T}{r}\right)^3 \rho \equiv \epsilon_{Trotter}, \tag{4.65}$$

where

$$\rho = \frac{1}{12}[\frac{4dL^d m^2}{a} + dL^d \frac{g^4}{4a^{2d-3}}(4\Lambda^2-1) + \frac{2L^d d(d-1)g^2(2\Lambda-1)^2}{a^d} + \frac{4d(d-1)L^d}{a^{6-d}g^2}$$
$$+ \frac{(8d^2-3d)L^d + (16d^2-8d)L^{d-1}}{2a^3}] + \frac{1}{24}[\frac{mg^2}{2a^{d-1}}(2\Lambda-1)dL^d + \frac{mL^d(16d^2-8d)}{a^2}$$
$$+ \frac{(4d^2-2d)L^d g^2(2\Lambda+1)}{a^d} + \frac{mL^d 8d(d-1)}{g^2 a^{5-d}} + \frac{2d(d-1)L^d}{a^3}(2\Lambda+1) + \frac{L^d d(d-1)(16\Lambda-8)}{a^3}$$
$$+ \frac{L^d d(d-1)(8d-11)(4\Lambda-2)}{g^2 a^{6-d}} + \frac{L^d}{a^3}(\frac{32}{3}d^3 - 4d^2 + \frac{11}{6}d) + \frac{L^{d-1}}{a^3}(\frac{160}{3}d^3 - 20d^2 - \frac{16}{3}d)$$
$$+ \frac{L^{d-2}}{a^3}(2d^2-2d) + \frac{2L^{d-3}}{3a^3}(d^3-3d^2+2d) + \frac{L^d}{g^2 a^{6-d}}(48d^3-102d^2+54d)$$
$$+ \frac{L^{d-1}}{g^2 a^{6-d}}(96d^3-232d^2+136d) + \frac{L^d}{g^2 a^{6-d}}(16d^3-10d^2-6d) + \frac{L^{d-1}}{g^2 a^{6-d}}(32d^3-56d^2+24d)$$
$$+ \frac{L^d(224d^3-544d^2+320d)}{a^{9-2d}g^4}] + L^d \frac{d(d-1)}{2}\frac{8}{a^{12-3d}g^6}. \tag{4.66}$$

For completeness, we show below a full derivation of the results shown above. Readers interested in how the results compare with the size of the synthesis error and how, together, they affect our simulation gate complexity should proceed to Secs. 4.3.3 and 4.3.3.

We start our derivation by first ordering the terms in the Hamiltonian $\hat{H}$. Consider an ordered list $\{\hat{H}_x\}_{x=1}^{x_{\max}}$ of $x_{\max}$-many individual Hamiltonian terms H_x, i.e.,

$$\{\hat{H}_x\}_{x=1}^{d^2+7d+2} = \{\sum_{\vec{n}} \hat{D}^{(M)}_{\vec{n}}, \sum_{\vec{n}} \hat{D}^{(E)}_{\vec{n}}, \sum_{\{\vec{n}_{e,1}\}} \frac{\hat{T}^{(1)}_{\vec{n}_{e,1}} + \hat{T}^{(4)}_{\vec{n}_{e,1}}}{2}, \sum_{\{\vec{n}_{e,1}\}} \frac{\hat{T}^{(2)}_{\vec{n}_{e,1}} + \hat{T}^{(3)}_{\vec{n}_{e,1}}}{2}, \sum_{\{\vec{n}_{o,1}\}} \frac{\hat{T}^{(1)}_{\vec{n}_{o,1}} + \hat{T}^{(4)}_{\vec{n}_{o,1}}}{2}$$
$$, \sum_{\{\vec{n}_{o,1}\}} \frac{\hat{T}^{(2)}_{\vec{n}_{o,1}} + \hat{T}^{(3)}_{\vec{n}_{o,1}}}{2}, ..., \sum_{\{\vec{n}_{e,2d}\}} \frac{\hat{T}^{(1)}_{\vec{n}_{e,2d}} + \hat{T}^{(4)}_{\vec{n}_{e,2d}}}{2}, \sum_{\{\vec{n}_{e,2d}\}} \frac{\hat{T}^{(2)}_{\vec{n}_{e,2d}} + \hat{T}^{(3)}_{\vec{n}_{e,2d}}}{2}, \sum_{\{\vec{n}_{o,2d}\}} \frac{\hat{T}^{(1)}_{\vec{n}_{o,2d}} + \hat{T}^{(4)}_{\vec{n}_{o,2d}}}{2}$$
$$, \sum_{\{\vec{n}_{o,2d}\}} \frac{\hat{T}^{(2)}_{\vec{n}_{o,2d}} + \hat{T}^{(3)}_{\vec{n}_{o,2d}}}{2}, \sum_{\{\vec{n}_{e,1}\}} \hat{L}^{(B)}_{\vec{n}_{e,1}}, \sum_{\{\vec{n}_{o,1}\}} \hat{L}^{(B)}_{\vec{n}_{o,1}}, ..., \sum_{\{\vec{n}_{e,\frac{d(d-1)}{2}}\}} \hat{L}^{(B)}_{\vec{n}_{e,\frac{d(d-1)}{2}}}, \sum_{\{\vec{n}_{o,\frac{d(d-1)}{2}}\}} \hat{L}^{(B)}_{\vec{n}_{o,\frac{d(d-1)}{2}}}\}, \tag{4.67}$$

where the grouping of terms as they appear in the list is motivated by the commutation so that each element in the list does not commute with at least one of the elements in the ordered set. For convenience, we group all the mass terms and electric terms (the first two in the list) into one term each, since the grouping incurs no Trotter error as the individual mass / electric terms

commute with one another. The set of subindices on each kinetic term $\{\vec{n}_{i,p}\}$ denotes the set of even or odd sites, i.e., $i \in \{e, o\}$, and the different directions, i.e., $p = 1, 2, .., 2d$. Note $p = 1, ..., d$ are the directions for the edge terms, and $p = d+1, ..., 2d$ are the directions for the bulk terms. In relation to (4.31-4.34), each kinetic term $\hat{T}^{(a)}_{\vec{n}_{i,p}}$, where $a \in \{1, 2, 3, 4\}$, acts on a link in direction p, which originate from either an odd or even site, depending on i, in either the bulk or edge, depending on the value of p. Furthermore, the sum of all kinetic terms is equivalent to $\sum_{\vec{n}} \hat{T}^{(K)}_{\vec{n}}$, defined in (4.19). The set of subindices on each magnetic term $\{\vec{n}_{k,\square}\}$, with $k \in \{e, o\}$, stands for the set of even or odd sites, respectively, on a two-dimensional plane denoted by $\square$. In relation to (4.20), each $\square$ corresponds to a specific pair of directions (i, j). For a d-dimensional lattice, there are $\frac{d(d-1)}{2}$ two-dimensional planes and plaquette operators in the magnetic term at each site. Moreover, note that the sum of all magnetic terms yields $\sum_{\vec{n}} \hat{L}^{(B)}_{\vec{n}}$, as defined in (4.20).

We now proceed to evaluate the Trotter error incurred by the second-order PF. First, we focus on the first sum in (2.8), i.e.,

$$\sum_i ||[[\hat{H}_i, \sum_{j>i} \hat{H}_j], \hat{H}_i]|| \leq \sum_{k=1}^{7} ||C_{1,k}||, \tag{4.68}$$

where

$$\begin{aligned}
C_{1,1} =& [[\sum_{\vec{n}} \hat{D}^{(M)}_{\vec{n}}, \sum_{\vec{n}'} \hat{D}^{(E)}_{\vec{n}'}], \sum_{\vec{n}} \hat{D}^{(M)}_{\vec{n}}], \\
C_{1,2} =& [[\sum_{\vec{n}} \hat{D}^{(M)}_{\vec{n}}, \sum_{\vec{n}'} \hat{T}^{(K)}_{\vec{n}'}], \sum_{\vec{n}} \hat{D}^{(M)}_{\vec{n}}], \\
C_{1,3} =& [[\sum_{\vec{n}} \hat{D}^{(M)}_{\vec{n}}, \sum_{\vec{n}'} \hat{L}^{(B)}_{\vec{n}'}], \sum_{\vec{n}} \hat{D}^{(M)}_{\vec{n}}], \\
C_{1,4} =& [[\sum_{\vec{n}} \hat{D}^{(E)}_{\vec{n}}, \sum_{\vec{n}'} \hat{T}^{(K)}_{\vec{n}'}], \sum_{\vec{n}} \hat{D}^{(E)}_{\vec{n}}], \\
C_{1,5} =& [[\sum_{\vec{n}} \hat{D}^{(E)}_{\vec{n}}, \sum_{\vec{n}'} \hat{L}^{(B)}_{\vec{n}'}], \sum_{\vec{n}} \hat{D}^{(E)}_{\vec{n}}], \\
C_{1,6} =& \sum_{i=e}^{o} \sum_{p=1}^{2d} \sum_{(a,b)=(1,4)}^{(2,3)} [[\sum_{\{\vec{n}_{i,p}\}} \frac{\hat{T}^{(a)}_{\vec{n}_{i,p}} + \hat{T}^{(b)}_{\vec{n}_{i,p}}}{2}, \sum_{\vec{n}'} \hat{L}^{(B)}_{\vec{n}'}], \sum_{\{\vec{n}_{i,p}\}} \frac{\hat{T}^{(a)}_{\vec{n}_{i,p}} + \hat{T}^{(b)}_{\vec{n}_{i,p}}}{2}], \\
C_{1,7} =& \sum_{i=e}^{o} \sum_{p=1}^{2d} \sum_{(a,b)=(1,4)}^{(2,3)} [[\sum_{\{\vec{n}_{i,p}\}} \frac{\hat{T}^{(a)}_{\vec{n}_{i,p}} + \hat{T}^{(b)}_{\vec{n}_{i,p}}}{2}, \sum_{\substack{j,p',(c,d),\\ \{\vec{n}_{j,p'}\}}} \frac{\hat{T}^{(c)}_{\vec{n}_{j,p'}} + \hat{T}^{(d)}_{\vec{n}_{j,p'}}}{2}], \sum_{\{\vec{n}_{i,p}\}} \frac{\hat{T}^{(a)}_{\vec{n}_{i,p}} + \hat{T}^{(b)}_{\vec{n}_{i,p}}}{2}].
\end{aligned} \tag{4.69}$$

In $C_{1,7}$, $(\hat{T}^{(c)}_{\vec{n}_{j,p'}} + \hat{T}^{(d)}_{\vec{n}_{j,p'}})/2$ is listed in (4.67) after and hence, implemented after $(\hat{T}^{(a)}_{\vec{n}_{i,p}} + \hat{T}^{(b)}_{\vec{n}_{i,p}})/2$.

It remains to evaluate in the following each term $C_{1,n}$. Note the following expressions will be useful in the foregoing evaluations of the terms:

$$||[[A,B],C]|| \leq 4||A|| \cdot ||B|| \cdot ||C||, \tag{4.70}$$

$$||\hat{D}^{(M)}_{\vec{n}} + \hat{D}^{(M)}_{\vec{n}+\hat{l}}|| \leq m, \tag{4.71}$$

which follows from (4.17),

$$||\hat{T}^{(b)}_{\vec{n}_{i,p}}|| \leq \frac{1}{2a}, \tag{4.72}$$

which is due to (4.31-4.34),

$$||\sum_{b=1}^{4} \frac{\hat{T}^{(b)}_{\vec{n},l}}{2}|| = ||\hat{K}(\vec{n},l)|| \leq \frac{1}{a}, \tag{4.73}$$

where we define

$$\begin{aligned}\hat{K}(\vec{n},l) = \frac{1}{8a}[&(\hat{U}(\vec{n},l) + \hat{U}^{\dagger}(\vec{n},l))(\hat{X}(\vec{n})\hat{X}(\vec{n}+\hat{l}) + \hat{Y}(\vec{n})\hat{Y}(\vec{n}+\hat{l}))\hat{\zeta}_{\vec{n},l} \\ &+ i(\hat{U}(\vec{n},l) - \hat{U}^{\dagger}(\vec{n},l))(\hat{X}(\vec{n})\hat{Y}(\vec{n}+\hat{l}) - \hat{Y}(\vec{n})\hat{X}(\vec{n}+\hat{l}))\hat{\zeta}_{\vec{n},l}],\end{aligned} \tag{4.74}$$

and use

$$||\hat{U}|| = ||\hat{U}^{\dagger}|| \leq 1, \tag{4.75}$$

$$||\hat{U} + \hat{U}^{\dagger}|| \leq 2. \tag{4.76}$$

Lastly,

$$||\hat{L}^{(B)}_{\vec{n}_k,\Box}|| = ||\frac{1}{2g^2a^{4-d}}(\hat{U}\hat{U}\hat{U}^{\dagger}\hat{U}^{\dagger} + h.c.)|| = \frac{1}{g^2a^{4-d}}, \tag{4.77}$$

where $\vec{n}_k$ may be an arbitrary position vector. Whenever these useful expressions are used, we use them without explicit references for brevity.

$C_{1,1}$ is straightforward to evaluate, since the mass and electric terms commute, i.e.,

$$[[\sum_{\vec{n}} \hat{D}^{(M)}_{\vec{n}}, \sum_{\vec{n}'} \hat{D}^{(E)}_{\vec{n}'}], \sum_{\vec{n}'} \hat{D}^{(M)}_{\vec{n}'}] = 0. \tag{4.78}$$

$C_{1,2}$ is bounded by

$$
\begin{aligned}
&|||[\sum_{\vec{n}} \hat{D}^{(M)}_{\vec{n}}, \sum_{\vec{n}} \hat{T}^{(K)}_{\vec{n}}], \sum_{\vec{n}} \hat{D}^{(M)}_{\vec{n}}]||| \\
&= |||[\sum_{\vec{n}} \sum_{l=1}^{d} [\hat{D}^{(M)}_{\vec{n}} + \hat{D}^{(M)}_{\vec{n}+\hat{l}}, \hat{K}(\vec{n}, l)], \hat{D}^{(M)}_{\vec{n}} + \hat{D}^{(M)}_{\vec{n}+\hat{l}}]||| \\
&\leq \sum_{\vec{n}} \sum_{l=1}^{d} |||[[\hat{D}^{(M)}_{\vec{n}} + \hat{D}^{(M)}_{\vec{n}+\hat{l}}, \hat{K}(\vec{n}, l)], \hat{D}^{(M)}_{\vec{n}} + \hat{D}^{(M)}_{\vec{n}+\hat{l}}]||| \\
&\leq \frac{4dL^d m^2}{a}.
\end{aligned} \tag{4.79}
$$

The first equality in (4.79) is due to the fact that each kinetic term at site $\vec{n}$ couples two sites, $\vec{n}$ and $\vec{n} + \hat{l}$ with l denoting the direction considered. The inequality that immediately follows from it is due to the triangle inequality. This is because, although the kinetic operators have $\hat{\zeta}$ JW strings, mass terms are diagonal, and thus they commute with the JW strings. The second inequality is due to (4.70). In the last inequality, the bound for the mass and kinetic terms are due to (4.17) and (4.31-4.34), respectively.

$C_{1,3}$ is straightforward to evaluate since mass and magnetic terms commute and hence,

$$
[[\sum_{\vec{n}} \hat{D}^{(M)}_{\vec{n}}, \sum_{\vec{n}} \hat{L}^{(B)}_{\vec{n}}], \sum_{\vec{n}} \hat{D}^{(M)}_{\vec{n}}] = 0. \tag{4.80}
$$

Before we evaluate the commutator between the electric and kinetic terms ($C_{1,4}$), we provide a couple useful properties about the kinetic operators $\hat{K}(\vec{n}, l)$. Acting on the fermionic space, a kinetic operator takes a computational basis state to another basis state. Acting on the gauge field on a link, it takes $|E\rangle \mapsto |E \pm 1\rangle$, where $E \in [-\Lambda, \Lambda - 1]$, up to a multiplicative constant. Therefore, if we consider an electric and a kinetic operator acting on the same link, we obtain

$$
\begin{aligned}
&|||[\frac{g^2}{2a^{d-2}} \hat{E}^2(\vec{n}, l), \hat{K}(\vec{n}, l)]|| \\
&= \frac{g^2}{2a^{d-2}} ||\hat{E}^2(\vec{n}, l)\hat{K}(\vec{n}, l) - \hat{K}(\vec{n}, l)\hat{E}^2(\vec{n}, l)|| \\
&\mapsto \frac{g^2}{2a^{d-2}} ||(E \pm 1)^2 \hat{K}(\vec{n}, l) - \hat{K}(\vec{n}, l) l^2||, \\
&= \frac{g^2}{2a^{d-2}} ||\hat{K}(\vec{n}, l)(\pm 2E + 1)|| \\
&\leq \frac{g^2}{2a^{d-2}} (2\Lambda + 1) ||\hat{K}(\vec{n}, l)|| \\
&\leq \frac{g^2}{2a^{d-2}} (2\Lambda + 1) \frac{1}{a} = \frac{g^2}{2a^{d-1}} (2\Lambda + 1),
\end{aligned} \tag{4.81}
$$

where we used $\hat{E}^2(\vec{n},l)$ to denote an electric term for the link $(\vec{n},l)$ up to a multiplicative constant, and

$$\begin{aligned}
&|||[[\frac{g^2}{2a^{d-2}}\hat{E}^2,\hat{K}(\vec{n},l)],\frac{g^2}{2a^{d-2}}\hat{E}^2]|||\\
&\mapsto ||\frac{g^2}{2a^{d-2}}(E^2-\hat{E}^2)[\frac{g^2}{2a^{d-2}}\hat{E}^2,\hat{K}(\vec{n},l)]||\\
&\mapsto ||\frac{g^2}{2a^{d-2}}(E^2-(E\pm 1)^2)[\frac{g^2}{2a^{d-2}}\hat{E}^2,\hat{K}(\vec{n},l)]||\\
&\mapsto ||\frac{g^2}{2a^{d-2}}(\mp 2E-1)[\frac{g^2}{2a^{d-2}}\hat{E}^2,\hat{K}(\vec{n},l)]||\\
&\leq \frac{g^2}{2a^{d-2}}(2\Lambda-1)|||[\frac{g^2}{2a^{d-2}}\hat{E}^2,\hat{K}(\vec{n},l)]|||\\
&\leq \frac{g^2}{2a^{d-2}}(2\Lambda-1)\frac{g^2}{2a^{d-1}}(2\Lambda+1)\\
&= \frac{g^4}{4a^{2d-3}}(4\Lambda^2-1).
\end{aligned} \tag{4.82}$$

Using these equations, we evaluate the bound of $C_{1,4}$ and obtain

$$\begin{aligned}
&|||[[\sum_{\vec{n}}\hat{D}^{(E)}_{\vec{n}},\sum_{\vec{n}}\hat{T}^{(K)}_{\vec{n}'}],\sum_{\vec{n}}\hat{D}^{(E)}_{\vec{n}}]|||\\
&= |||[[\sum_{\vec{n}}\hat{D}^{(E)}_{\vec{n}},\sum_{\vec{n}}\sum_{l=1}^{d}\hat{K}(\vec{n},l)],\sum_{\vec{n}}\hat{D}^{(E)}_{\vec{n}}]|||\\
&\leq \sum_{\vec{n}}\sum_{l=1}^{d}|||[[\frac{g^2}{2a^{d-2}}\hat{E}^2(\vec{n},l),\hat{K}(\vec{n},l)],\frac{g^2}{2a^{d-2}}\hat{E}^2(\vec{n},l)]|||\\
&\leq dL^d\frac{g^4}{4a^{2d-3}}(4\Lambda^2-1).
\end{aligned} \tag{4.83}$$

Next, we evaluate the commutators between the electric and plaquette operators ($C_{1,5}$), which are trivial unless the operators act on a common link. For the sake of brevity, we let the plaquette operator act on links $1,2,3,4$, and let the electric field operator act on link 1. The commutators

are then

$$
\begin{aligned}
&|||[\frac{g^2}{2a^{d-2}}\hat{E}_1^2, \frac{-1}{2g^2a^{4-d}}\hat{U}_1\hat{U}_2\hat{U}_3^\dagger\hat{U}_4^\dagger]||| \\
&= |||[\frac{g^2}{2a^{d-2}}\hat{E}_1^2, \frac{-1}{2g^2a^{4-d}}\hat{U}_1]|| \cdot ||\hat{U}_2\hat{U}_3^\dagger\hat{U}_4^\dagger|| \\
&\leq |||[\frac{g^2}{2a^{d-2}}\hat{E}_1^2, \frac{-1}{2g^2a^{4-d}}\hat{U}_1]||| \\
&= ||\frac{-1}{4a^2}(\hat{E}^2\hat{U} - \hat{U}\hat{E}^2)|| \\
&= ||\frac{-1}{4a^2}(\sum_E E^2 \left|E\right\rangle\!\left\langle E\right| \hat{U} - \hat{U}\sum_E E^2 \left|E\right\rangle\!\left\langle E\right|)|| \\
&= ||\frac{-1}{4a^2}(\sum_E E^2 \left|E\right\rangle\!\left\langle E-1\right| - \sum_E E^2 \left|E+1\right\rangle\!\left\langle E\right|)|| \\
&= ||\frac{-1}{4a^2}\sum_E \left[(E+1)^2 - E^2\right] \left|E+1\right\rangle\!\left\langle E\right| || \\
&= ||\frac{-1}{4a^2}\sum_E (2E+1) \left|E+1\right\rangle\!\left\langle E\right| || \\
&\leq ||\frac{-1}{4a^2}(-2\Lambda+1)|| = \frac{2\Lambda-1}{4a^2}
\end{aligned} \tag{4.84}
$$

and

$$
\begin{aligned}
&|||[\frac{g^2}{2a^{d-2}}\hat{E}_1^2, \frac{-1}{2g^2a^{4-d}}\hat{U}_1^\dagger\hat{U}_2^\dagger\hat{U}_3\hat{U}_4]||| \\
&\leq |||[\frac{g^2}{2a^{d-2}}\hat{E}_1^2, \frac{-1}{2g^2a^{4-d}}\hat{U}_1^\dagger]||| \\
&= ||\frac{-1}{4a^2}(\hat{E}^2\hat{U}^\dagger - \hat{U}^\dagger\hat{E}^2)|| \\
&= ||\frac{-1}{4a^2}(\sum_E E^2 \left|E\right\rangle\!\left\langle E+1\right| - \sum_E (E+1)^2 \left|E\right\rangle\!\left\langle E+1\right|)|| \\
&= ||\frac{1}{4a^2}\sum_E (2E+1) \left|E\right\rangle\!\left\langle E+1\right| || \\
&\leq ||\frac{1}{4a^2}(2(\Lambda-1)+1)|| = \frac{2\Lambda-1}{4a^2}.
\end{aligned} \tag{4.85}
$$

Combining the two commutators, we obtain

$$
\begin{aligned}
&|||[\frac{g^2}{2a^{d-2}}\sum_{i=1}^{4}\hat{E}_i^2, \frac{-1}{2g^2a^{4-d}}(\hat{U}_1\hat{U}_2\hat{U}_3^\dagger\hat{U}_4^\dagger + h.c.)]|||\\
&\leq 4|||[\frac{g^2}{2a^{d-2}}\hat{E}_1^2, \frac{-1}{2g^2a^{4-d}}(\hat{U}_1\hat{U}_2\hat{U}_3^\dagger\hat{U}_4^\dagger + h.c.)]|||\\
&= 4||\frac{1}{4a^2}[\sum_E (2E+1)\left|E\right\rangle\!\left\langle E+1\right| - (2E+1)\left|E+1\right\rangle\!\left\langle E\right|]|||\\
&\leq \frac{4\Lambda-2}{a^2}.
\end{aligned}
\tag{4.86}
$$

We are now equipped to evaluate the bound of $C_{1,5}$. The bound is

$$
\begin{aligned}
&|||[[\sum_{\vec{n}}\hat{D}_{\vec{n}}^{(E)}, \sum_{\vec{n}}\hat{L}_{\vec{n}}^{(B)}], \sum_{\vec{n}}\hat{D}_{\vec{n}}^{(E)}]|||\\
&\leq \frac{L^d d(d-1)}{2}|||[[\frac{g^2}{2a^{d-2}}\sum_{i=1}^{4}\hat{E}_i^2, \frac{-1}{2g^2a^{4-d}}(\hat{U}_1\hat{U}_2\hat{U}_3^\dagger\hat{U}_4^\dagger + h.c.)], \frac{g^2}{2a^{d-2}}\sum_{i=1}^{4}\hat{E}_i^2]|||\\
&= \frac{L^d d(d-1)}{2}||\frac{g^2}{2a^{d-2}}\sum_{i=1}^{4}(E_i^2 - \hat{E}_i^2)[\frac{g^2}{2a^{d-2}}\sum_{i=1}^{4}\hat{E}_i^2, \frac{-1}{2g^2a^{4-d}}(\hat{U}_1\hat{U}_2\hat{U}_3^\dagger\hat{U}_4^\dagger + h.c.)]||\\
&\mapsto \frac{L^d d(d-1)}{2}||\frac{g^2}{2a^{d-2}}\sum_{i=1}^{4}(E_i^2 - (E_i \pm 1)^2)[\frac{g^2}{2a^{d-2}}\sum_{i=1}^{4}\hat{E}_i^2, \frac{-1}{2g^2a^{4-d}}(\hat{U}_1\hat{U}_2\hat{U}_3^\dagger\hat{U}_4^\dagger + h.c.)]||\\
&= \frac{L^d d(d-1)}{2}||\frac{g^2}{2a^{d-2}}\sum_{i=1}^{4}(\mp 2E_i - 1)[\frac{g^2}{2a^{d-2}}\sum_{i=1}^{4}\hat{E}_i^2, \frac{-1}{2g^2a^{4-d}}(\hat{U}_1\hat{U}_2\hat{U}_3^\dagger\hat{U}_4^\dagger + h.c.)]||\\
&\leq \frac{L^d d(d-1)}{2}\frac{g^2}{2a^{d-2}}4(2\Lambda-1)|||[\frac{g^2}{2a^{d-2}}\sum_{i=1}^{4}\hat{E}_i^2, \frac{-1}{2g^2a^{4-d}}(\hat{U}_1\hat{U}_2\hat{U}_3^\dagger\hat{U}_4^\dagger + h.c.)]|||\\
&\leq \frac{L^d d(d-1)}{2}\frac{g^2}{2a^{d-2}}4(2\Lambda-1)\frac{4\Lambda-2}{a^2}\\
&= \frac{2L^d d(d-1)g^2(2\Lambda-1)^2}{a^d},
\end{aligned}
\tag{4.87}
$$

where in the second line, we have used the fact that there are $L^d\frac{d(d-1)}{2}$ plaquette terms in the sum $\sum_{\vec{n}}\hat{L}_{\vec{n}}^{(B)}$.

Considering $C_{1,6}$, we first fix the evenness and oddness of the sites. We consider the bulk and edge terms separately, although the required analysis is similar. We use p to denote the direction of the links acted on by the kinetic term. The commutator is trivially zero if the magnetic part

and kinetic part act on different links. Thus we consider the case where each plaquette operator in the magnetic part acts on links that the kinetic operators also act on. For direction p, we then have

$$
\begin{aligned}
&|||[\sum_{\{\vec{n}_{i,p}\}} \frac{\hat{T}^{(a)}_{\vec{n}_{i,p}} + \hat{T}^{(b)}_{\vec{n}_{i,p}}}{2}, \sum_{\vec{n}_{j,\square}} \hat{L}^{(B)}_{\vec{n}_{j,\square}}], \sum_{\{\vec{n}_{i,p}\}} \frac{\hat{T}^{(a)}_{\vec{n}_{i,p}} + \hat{T}^{(b)}_{\vec{n}_{i,p}}}{2}]|||\\
&= |||[\sum_{\{\vec{n}_{i,p}\}} [\frac{\hat{T}^{(a)}_{\vec{n}_{i,p}} + \hat{T}^{(b)}_{\vec{n}_{i,p}}}{2}, \sum_{\vec{n}_{j,\square}} \hat{L}^{(B)}_{\vec{n}_{j,\square}}], \sum_{\{\vec{n}_{i,p}\}} \frac{\hat{T}^{(a)}_{\vec{n}_{i,p}} + \hat{T}^{(b)}_{\vec{n}_{i,p}}}{2}]|||\\
&= |||[N_k[\frac{\hat{T}^{(a)}_{\vec{n}_{i,p}} + \hat{T}^{(b)}_{\vec{n}_{i,p}}}{2}, \hat{L}^{(B)}_{\vec{n}_{i,\square}}], \frac{\hat{T}^{(a)}_{\vec{n}_{i,p}} + \hat{T}^{(b)}_{\vec{n}_{i,p}}}{2}]|||\\
&\leq 4N_k||\frac{\hat{T}^{(a)}_{\vec{n}_{i,p}} + \hat{T}^{(b)}_{\vec{n}_{i,p}}}{2}||^2||\frac{-1}{2a^{4-d}g^2}(\hat{U}\hat{U}\hat{U}^\dagger\hat{U}^\dagger + h.c.)||\\
&\leq 4N_k\frac{1}{4a^2}\frac{1}{a^{4-d}g^2} = \frac{N_k}{a^{6-d}g^2},
\end{aligned}
\tag{4.88}
$$

where $N_k \in \{N_B, N_E\}$ is the number of odd or even sites in the bulk or on the edges in each direction. Recall that $N_B = (L^d - L^{d-1})/2$, and $N_E = L^{d-1}/2$. In the third line of (4.88), we have used the fact that for each kinetic term, there is a plaquette operator, of the type $\vec{n}_{i,\square}$, acting on the same link. Expanding this to include all sites, all directions, and all plaquette and kinetic operators, we obtain

$$
\begin{aligned}
&C_{1,6}\\
&\leq \sum_{i,j=e}^{o}\sum_{p=1}^{2d}\sum_{\square=1}^{d(d-1)/2}\sum_{(a,b)=(1,4)}^{(2,3)} |||[\sum_{\{\vec{n}_{i,p}\}} \frac{\hat{T}^{(a)}_{\vec{n}_{i,p}} + \hat{T}^{(b)}_{\vec{n}_{i,p}}}{2}, \sum_{\vec{n}_{j,\square}} \hat{L}^{(B)}_{\vec{n}_{j,\square}}], \sum_{\{\vec{n}_{i,p}\}} \frac{\hat{T}^{(a)}_{\vec{n}_{i,p}} + \hat{T}^{(b)}_{\vec{n}_{i,p}}}{2}]|||\\
&\leq 8d(d-1)(N_E + N_B)\frac{1}{a^{6-d}g^2} = \frac{4d(d-1)L^d}{a^{6-d}g^2},
\end{aligned}
\tag{4.89}
$$

where in the last inequality, the factor d comes from the fact that there are d directions each for the bulk and edges of the lattice. Further, for each direction p, there are $d-1$ two-dimensional planes $\square$ that contain links in that direction, hence the factor $d-1$.

Now, we compute $C_{1,7}$, which consists of the commutators between kinetic terms. There are three types of commutators; those between (i) two bulk terms, (ii) two edge terms, and (iii) a bulk and an edge term. We analyze case (i) first. We reiterate that there are $4d$ bulk terms of the form $\mathcal{T}^{(a,b)}_{\vec{n}_{i,p}} = \sum_{\{\vec{n}_{i,p}\}} \frac{\hat{T}^{(a)}_{\vec{n}_{i,p}} + \hat{T}^{(b)}_{\vec{n}_{i,p}}}{2}$ in total (we remind the readers that there are even / odd sites, then $\hat{T}^{(1)} + \hat{T}^{(4)}$ and $\hat{T}^{(2)} + \hat{T}^{(3)}$), where $\{\vec{n}_{i,p}\}$ runs over all sites for a given parity i, with

fixed direction p. Notice that, in a non-vanishing commutator, two bulk terms must either act on the same set of links and sites, or they overlap on one of the fermionic sites. This is so since, in all other scenarios, either the two kinetic terms simply act on disjoint Hilbert spaces (they act on two disjoint sets of qubit registers) or a kinetic term's JW string $\hat{\zeta}$ always commutes with the other kinetic term in our zig-zag JW path. To illustrate, consider a number system with basis d, where a number here encodes a fermionic site. A kinetic term is defined over picking a pair of two numbers that are different by one digit, with the difference of that digit being one. Consider two pairs of these numbers. The two pairs have two different ranges of numbers, over which the JW string acts. The former scenario of disjointedness arises when the two ranges do not overlap. The latter scenario arises when one range is inside the other range. Since operators $\hat{P}_r$ and $\hat{\tilde{P}}_r$ in (4.29) that act on fermion registers that collide with the JW string commute with the string, the latter scenario does not contribute to the commutator bound.

Since we always implement $\sum_{\{\vec{n}_{i,p}\}} \frac{\hat{T}^{(1)}_{\vec{n}_{i,p}} + \hat{T}^{(4)}_{\vec{n}_{i,p}}}{2}$ before $\sum_{\{\vec{n}_{i,p}\}} \frac{\hat{T}^{(2)}_{\vec{n}_{i,p}} + \hat{T}^{(3)}_{\vec{n}_{i,p}}}{2}$, as shown in (4.67), for each $\vec{n}_{i,p}$, we know that $\hat{H}_i = \sum_{\{\vec{n}_{i,p}\}} \frac{\hat{T}^{(1)}_{\vec{n}_{i,p}} + \hat{T}^{(4)}_{\vec{n}_{i,p}}}{2}$ and $\hat{H}_j = \sum_{\{\vec{n}_{i,p}\}} \frac{\hat{T}^{(2)}_{\vec{n}_{i,p}} + \hat{T}^{(3)}_{\vec{n}_{i,p}}}{2}$. Hence, the commutator for the case where two bulk terms act on the same set of links and sites is

$$
\begin{aligned}
&|||[\sum_{\{\vec{n}_{i,p}\}} \frac{\hat{T}^{(1)}_{\vec{n}_{i,p}} + \hat{T}^{(4)}_{\vec{n}_{i,p}}}{2}, \sum_{\{\vec{n}_{i,p}\}} \frac{\hat{T}^{(2)}_{\vec{n}_{i,p}} + \hat{T}^{(3)}_{\vec{n}_{i,p}}}{2}], \sum_{\{\vec{n}_{i,p}\}} \frac{\hat{T}^{(1)}_{\vec{n}_{i,p}} + \hat{T}^{(4)}_{\vec{n}_{i,p}}}{2}]||| \\
&\leq || \sum_{\{\vec{n}_{i,p}\}} [[\frac{\hat{T}^{(1)}_{\vec{n}_{i,p}} + \hat{T}^{(4)}_{\vec{n}_{i,p}}}{2}, \frac{\hat{T}^{(2)}_{\vec{n}_{i,p}} + \hat{T}^{(3)}_{\vec{n}_{i,p}}}{2}], \frac{\hat{T}^{(1)}_{\vec{n}_{i,p}} + \hat{T}^{(4)}_{\vec{n}_{i,p}}}{2}]|| \leq 4N_B || \frac{\hat{T}^{(a)}_{\vec{n}_{i,p}} + \hat{T}^{(b)}_{\vec{n}_{i,p}}}{2} ||^3 \\
&\leq 4N_B (\frac{1}{2a})^3 = \frac{N_B}{2a^3}.
\end{aligned} \tag{4.90}
$$

The first inequality is due to the fact that the kinetic terms acting on different sites and links commute. We used (4.70) for the second inequality. In the case where the two bulk terms overlap on one of the fermionic sites, the commutator is given by

$$
\begin{aligned}
&|||[\sum_{\{\vec{n}_{j,p'}\}} \frac{\hat{T}^{(a)}_{\vec{n}_{j,p'}} + \hat{T}^{(b)}_{\vec{n}_{j,p'}}}{2}, \sum_{\{\vec{n}_{i,p}\}} \sum_{c=1}^{4} \frac{\hat{T}^{(c)}_{\vec{n}_{i,p}}}{2}], \sum_{\{\vec{n}_{j,p'}\}} \frac{\hat{T}^{(a)}_{\vec{n}_{j,p'}} + \hat{T}^{(b)}_{\vec{n}_{j,p'}}}{2}]||| \\
&\leq \sum_{\{\vec{n}_{i,p}\}} 4 || 2 \frac{\hat{T}^{(a)}_{\vec{n}_{i,p}} + \hat{T}^{(b)}_{\vec{n}_{i,p}}}{2} ||^2 ||\hat{K}(\vec{n}_i, p)|| \\
&\leq \frac{4N_B}{a^3},
\end{aligned} \tag{4.91}
$$

where we once again used (4.70) and the fact that each term at site $\vec{n}_{i,p}$ has two neighboring kinetic terms acting on the sites $\vec{n}_{i,p}$ or $\vec{n}_{i,p} + \hat{p}$. We now compute the number of occurrences of

the commutators considered in (4.90) and (4.91). Since there are d directions, and two parities, there are $2d$ terms of the form (4.90). For (4.91), since each term $\mathcal{T}^{(a,b)}_{\vec{n}_{i,p}}$ commutes with itself, but not with the terms that are implemented afterwards, there are

$$2[(2d-1)+(2d-2)+...+1+0] = (2d-1)2d = 4d^2-2d, \tag{4.92}$$

where a factor of 2 is due to the fact that there are two (a,b)-combinations, non-vanishing commutators in total. We have also used the fact that there are $2d$ combinations of parity and direction, i.e., i and p, in the bulk. As such, the sum of the commutators between all the bulk terms is bounded by

$$(4d^2-2d)\frac{4N_B}{a^3} + 2d\frac{N_B}{2a^3} = (16d^2-6d)\frac{N_B}{a^3}. \tag{4.93}$$

Using similar arguments, we obtain the bound for the sum of the commutators between all the edge terms, $(16d^2-6d)\frac{N_E}{a^3}$.

Lastly, we evaluate the commutators between a term $\hat{K}(\vec{n}_j,p')$ from the bulk and a term $\mathcal{T}^{(a,b)}_{\vec{n}_{i,p}}$ from the edge. Each $\mathcal{T}^{(a,b)}_{\vec{n}_{i,p}}$ on an edge link has two $\hat{K}(\vec{n}_j,p')$ terms from the bulk acting on the same sites, and hence, the commutator between a bulk and edge term is bounded by $\frac{4N_E}{a^3}$, where we have replaced N_B with the smaller N_E in (4.91). Since there are $2d$ $\hat{K}(\vec{n}_j,p')$ terms from the bulk, and $4d$ $\mathcal{T}^{(a,b)}_{\vec{n}_{i,p}}$ terms from the edge, there are in total $8d^2$ commutators between bulk and edge terms. The bulk and edge terms that act on links along the same direction and sites with the same parity commute, and there are $4d$ pairs of such terms. Hence, the sum of such commutators is upper-bounded by $(8d^2-4d)\frac{4N_E}{a^3}$. In total, $C_{1,7}$ is bounded from above by

$$(16d^2-6d)\frac{N_E+N_B}{a^3} + (32d^2-16d)\frac{N_E}{a^3} = \frac{(8d^2-3d)L^d + (16d^2-8d)L^{d-1}}{a^3}. \tag{4.94}$$

Next, we analyze the second sum in (2.8), which is given by

$$\sum_i ||[[\hat{H}_i, \sum_{j>i}\hat{H}_j], \sum_{k>i}\hat{H}_k]|| \leq \sum_{n=1}^{11}||C_{2,n}||, \tag{4.95}$$

where

$$
\begin{aligned}
C_{2,1} =&[[\sum_{\vec{n}} \hat{D}^{(M)}_{\vec{n}}, \sum_{\vec{n}'} \hat{T}^{(K)}_{\vec{n}'}], \sum_{\vec{n}''} \hat{D}^{(E)}_{\vec{n}''}] \\
C_{2,2} =&[[\sum_{\vec{n}} \hat{D}^{(M)}_{\vec{n}}, \sum_{\vec{n}'} \hat{T}^{(K)}_{\vec{n}'}, \sum_{\vec{n}''} \hat{T}^{(K)}_{\vec{n}''}] \\
C_{2,3} =&[[\sum_{\vec{n}} \hat{D}^{(M)}_{\vec{n}}, \sum_{\vec{n}'} \hat{T}^{(K)}_{\vec{n}'}, \sum_{\vec{n}''} \hat{L}^{(B)}_{\vec{n}''}] \\
C_{2,4} =&[[\sum_{\vec{n}} \hat{D}^{(E)}_{\vec{n}}, \sum_{\vec{n}'} \hat{T}^{(K)}_{\vec{n}'}], \sum_{\vec{n}''} \hat{T}^{(K)}_{\vec{n}''}] \\
C_{2,5} =&[[\sum_{\vec{n}} \hat{D}^{(E)}_{\vec{n}}, \sum_{\vec{n}'} \hat{T}^{(K)}_{\vec{n}'}], \sum_{\vec{n}'} \hat{L}^{(B)}_{\vec{n}''}] \\
C_{2,6} =&[[\sum_{\vec{n}} \hat{D}^{(E)}_{\vec{n}}, \sum_{\vec{n}'} \hat{L}^{(B)}_{\vec{n}'}], \sum_{\vec{n}''} \hat{T}^{(K)}_{\vec{n}''}] \\
C_{2,7} =&[[\sum_{\vec{n}} \hat{D}^{(E)}_{\vec{n}}, \sum_{\vec{n}'} \hat{L}^{(B)}_{\vec{n}'}], \sum_{\vec{n}''} \hat{L}^{(B)}_{\vec{n}''}] \\
C_{2,8} =&\sum_{i=e}^{o} \sum_{p=1}^{2d} \sum_{(a,b)=(1,4)}^{(2,3)} [[\sum_{\{\vec{n}_{i,p}\}} \frac{\hat{T}^{(a)}_{\vec{n}_{i,p}} + \hat{T}^{(b)}_{\vec{n}_{i,p}}}{2}, \sum_{\substack{j,p',(c,d),\\ \{\vec{n}_{j,p'}\}}} \frac{\hat{T}^{(c)}_{\vec{n}_{j,p'}} + \hat{T}^{(d)}_{\vec{n}_{j,p'}}}{2}], \sum_{\substack{k,p'',(e,f),\\ \{\vec{n}_{k,p''}\}}} \frac{\hat{T}^{(e)}_{\vec{n}_{k,p''}} + \hat{T}^{(f)}_{\vec{n}_{k,p''}}}{2}] \\
C_{2,9} =&\sum_{i=e}^{o} \sum_{p=1}^{2d} \sum_{(a,b)=(1,4)}^{(2,3)} [[\sum_{\{\vec{n}_{i,p}\}} \frac{\hat{T}^{(a)}_{\vec{n}_{i,p}} + \hat{T}^{(b)}_{\vec{n}_{i,p}}}{2}, \sum_{\substack{j,p',(c,d),\\ \{\vec{n}_{j,p'}\}}} \frac{\hat{T}^{(c)}_{\vec{n}_{j,p'}} + \hat{T}^{(d)}_{\vec{n}_{j,p'}}}{2}], \sum_{\vec{n}''} \hat{L}^{(B)}_{\vec{n}''}] \\
C_{2,10} =&\sum_{i=e}^{o} \sum_{p=1}^{2d} \sum_{(a,b)=(1,4)}^{(2,3)} [[\sum_{\{\vec{n}_{i,p}\}} \frac{\hat{T}^{(a)}_{\vec{n}_{i,p}} + \hat{T}^{(b)}_{\vec{n}_{i,p}}}{2}, \sum_{\vec{n}'} \hat{L}^{(B)}_{\vec{n}'}], \sum_{\substack{j,p',(c,d),\\ \{\vec{n}_{j,p'}\}}} \frac{\hat{T}^{(c)}_{\vec{n}_{j,p'}} + \hat{T}^{(d)}_{\vec{n}_{j,p'}}}{2}] \\
C_{2,11} =&\sum_{i=e}^{o} \sum_{p=1}^{2d} \sum_{(a,b)=(1,4)}^{(2,3)} [[\sum_{\{\vec{n}_{i,p}\}} \frac{\hat{T}^{(a)}_{\vec{n}_{i,p}} + \hat{T}^{(b)}_{\vec{n}_{i,p}}}{2}, \sum_{\vec{n}'} \hat{L}^{(B)}_{\vec{n}'}], \sum_{\vec{n}''} \hat{L}^{(B)}_{\vec{n}''}]], \qquad (4.96)
\end{aligned}
$$

where we have implicitly assumed in $C_{2,8}$, $C_{2,9}$ and $C_{2,10}$ that $(\hat{T}^{(c)}_{\vec{n}_{j,p'}} + \hat{T}^{(d)}_{\vec{n}_{j,p'}})/2$ and $(\hat{T}^{(e)}_{\vec{n}_{k,p''}} + \hat{T}^{(f)}_{\vec{n}_{k,p''}})/2$ are listed in (4.67) after and hence, implemented after $(\hat{T}^{(a)}_{\vec{n}_{i,p}} + \hat{T}^{(b)}_{\vec{n}_{i,p}})/2$. We have removed any trivially vanishing terms, which involve commutators between mass and electric terms, mass and magnetic terms, and two magnetic terms, since in each respective case the operators commute with each other. In the following, we evaluate the bounds for each $C_{2,n}$.

For $C_{2,1}$, we obtain the bound

$$
\begin{aligned}
&|||[\sum_{\vec{n}} \hat{D}^{(M)}_{\vec{n}}, \sum_{\vec{n}'} \hat{T}^{(K)}_{\vec{n}'}], \sum_{\vec{n}''} \hat{D}^{(E)}_{\vec{n}''}]||| \\
&\leq |||[\sum_{\vec{n}} \sum_{l=1}^{d} [\hat{D}^{(M)}_{\vec{n}} + \hat{D}^{(M)}_{\vec{n}+\hat{l}}, \hat{K}(\vec{n},l)], \frac{g^2}{2a^{d-2}} \hat{E}^2(\vec{n},l)]||| \\
&\mapsto ||\frac{g^2}{2a^{d-2}}(E^2 - \hat{E}^2) \sum_{\vec{n}} \sum_{l=1}^{d} [\hat{D}^{(M)}_{\vec{n}} + \hat{D}^{(M)}_{\vec{n}+\hat{l}}, \hat{K}(\vec{n},l)]|| \\
&\mapsto ||\frac{g^2}{2a^{d-2}}(E^2 - (E \pm 1)^2) \sum_{\vec{n}} \sum_{l=1}^{d} [\hat{D}^{(M)}_{\vec{n}} + \hat{D}^{(M)}_{\vec{n}+\hat{l}}, \hat{K}(\vec{n},l)]|| \\
&= ||\frac{g^2}{2a^{d-2}}(\mp 2E - 1) \sum_{\vec{n}} \sum_{l=1}^{d} [\hat{D}^{(M)}_{\vec{n}} + \hat{D}^{(M)}_{\vec{n}+\hat{l}}, \hat{K}(\vec{n},l)]|| \\
&\leq \frac{g^2}{2a^{d-2}}(2\Lambda - 1)|| \sum_{\vec{n}} \sum_{l=1}^{d} [\hat{D}^{(M)}_{\vec{n}} + \hat{D}^{(M)}_{\vec{n}+\hat{l}}, \hat{K}(\vec{n},l)]|| \\
&\leq \frac{g^2}{2a^{d-2}}(2\Lambda - 1) dL^d ||\hat{D}^{(M)}_{\vec{n}} + \hat{D}^{(M)}_{\vec{n}+\hat{l}}|| \cdot ||\hat{K}(\vec{n},l)|| \\
&= \frac{mg^2}{2a^{d-1}}(2\Lambda - 1) dL^d,
\end{aligned}
\tag{4.97}
$$

where in the first inequality, we have used the fact that each kinetic term $\hat{K}(\vec{n},l)$ acts on the sites $\vec{n}$ and $\vec{n}+\hat{l}$, and the link $(\vec{n},l)$. The term does not commute with the mass and electric terms acting on the same space, but commutes with the rest.

For $C_{2,2}$, we obtain the bound

$$
\begin{aligned}
&|||[\sum_{\vec{n}} \hat{D}^{(M)}_{\vec{n}}, \sum_{\vec{n}'} \hat{T}^{(K)}_{\vec{n}'}], \sum_{\vec{n}''} \hat{T}^{(K)}_{\vec{n}''}]||| \\
&\leq || \sum_{\vec{n}} \sum_{l=1}^{d} [[\hat{D}^{(M)}_{\vec{n}} + \hat{D}^{(M)}_{\vec{n}+\hat{l}}, \hat{K}(\vec{n},l)], \sum_{\vec{n}''} \hat{T}^{(K)}_{\vec{n}''}]|| \\
&\leq 4dL^d ||\hat{D}^{(M)}_{\vec{n}} + \hat{D}^{(M)}_{\vec{n}+\hat{l}}|| \cdot ||\hat{K}(\vec{n},l)|| \cdot ||(4d-2)\hat{K}(\vec{n},l)|| \\
&= \frac{mL^d(16d^2 - 8d)}{a^2},
\end{aligned}
\tag{4.98}
$$

where the factor of $(4d-2)$ in the third norm term of the second inequality is due to the fact that there are $(4d-2)$ kinetic terms of the type $\hat{K}(\vec{n},l)$ acting on the same fermionic sites as $\hat{K}(\vec{n},l)$.

Using a similar method, we evaluate the bound of the $C_{2,4}$ term (we consider the $C_{2,3}$ term right afterwards). The only difference from the $C_{2,2}$ term is that the mass term is replaced by the electric term. As such, we obtain the upper bound of $C_{2,4}$,

$$\begin{aligned}
&|||[\sum_{\vec{n}} \hat{D}^{(E)}_{\vec{n}}, \sum_{\vec{n}'} \hat{T}^{(K)}_{\vec{n}'}], \sum_{\vec{n}''} \hat{T}^{(K)}_{\vec{n}''}]||| \\
&\leq || \sum_{\vec{n}} \sum_{l=1}^{d} [[\frac{g^2}{2a^{d-2}} \hat{E}^2(\vec{n}, l), \hat{K}(\vec{n}, l)], \sum_{\vec{n}''} \hat{T}^{(K)}_{\vec{n}''}]|| \\
&\leq 2dL^d || [\frac{g^2}{2a^{d-2}} \hat{E}^2(\vec{n}, l), \hat{K}(\vec{n}, l)]|| \cdot || \sum_{\vec{n}''} \hat{T}^{(K)}_{\vec{n}''}|| \\
&\leq 2dL^d || \frac{g^2}{2a^{d-1}} (2\Lambda + 1)|| \cdot ||(4d-2)\hat{K}(\vec{n}, l)|| \\
&\leq 2dL^d \frac{g^2}{2a^{d-1}} (2\Lambda + 1) \frac{4d-2}{a} = \frac{(4d^2 - 2d) L^d g^2 (2\Lambda + 1)}{a^d},
\end{aligned} \tag{4.99}$$

where in the first inequality, we have used the fact that the electric terms acting on different links as the kinetic terms commute, and in the third inequality, we used the bound in (4.81).

Moving onto the $C_{2,3}$ term in (4.95), we evaluate its bound as follows:

$$\begin{aligned}
&|||[\sum_{\vec{n}} \hat{D}^{(M)}_{\vec{n}}, \sum_{\vec{n}'} \hat{T}^{(K)}_{\vec{n}'}], \sum_{\vec{n}''} \hat{L}^{(B)}_{\vec{n}''}]||| \\
&\leq |||[\sum_{\vec{n}} \sum_{l=1}^{d} [\hat{D}^{(M)}_{\vec{n}} + \hat{D}^{(M)}_{\vec{n}+\hat{l}}, \hat{K}(\vec{n}, l)], \sum_{\vec{n}''} \hat{L}^{(B)}_{\vec{n}''}]||| \\
&\leq \sum_{\vec{n}} \sum_{l=1}^{d} 4 || \hat{D}^{(M)}_{\vec{n}} + \hat{D}^{(M)}_{\vec{n}+\hat{l}}|| \cdot ||\hat{K}(\vec{n}, l)|| \cdot ||2(d-1)\hat{L}^{(B)}_{\vec{n}_{i,\square}}|| \\
&\leq \frac{mL^d 8d(d-1)}{g^2 a^{5-d}},
\end{aligned} \tag{4.100}$$

where in the second inequality, we have used the fact that there is one kinetic and $2(d-1)$ magnetic operators acting on the same link.

We bound the $C_{2,5}$ term using a similar method, but with the mass term replaced by the

electric term. We evaluate its bound as follows:

$$
\begin{aligned}
&|||[\sum_{\vec{n}} \hat{D}^{(E)}_{\vec{n}}, \sum_{\vec{n}'} \hat{T}^{(K)}_{\vec{n}'}], \sum_{\vec{n}''} \hat{L}^{(B)}_{\vec{n}''}]||| \\
&\leq ||\sum_{\vec{n}} \sum_{l=1}^{d} [[\frac{g^2}{2a^{d-2}} \hat{E}^2(\vec{n}, \hat{l}), \hat{K}(\vec{n}, l)], \sum_{\vec{n}''} \hat{L}^{(B)}_{\vec{n}''}]|| \\
&\leq 2dL^d |||[\frac{g^2}{2a^{d-2}} \hat{E}^2(\vec{n}, \hat{l}), \hat{K}(\vec{n}, l)]|| \cdot ||2(d-1)\hat{L}^{(B)}_{\vec{n}_{i,\square}}|| \\
&\leq 2dL^d \frac{g^2}{2a^{d-1}}(2\Lambda + 1)\frac{2(d-1)}{g^2 a^{4-d}} = \frac{2d(d-1)L^d}{a^3}(2\Lambda + 1),
\end{aligned} \tag{4.101}
$$

where we have used (4.81).

Each commutator in the $C_{2,6}$ term contains an electric, magnetic, and kinetic term. Evaluating the bound, we have

$$
\begin{aligned}
&|||[\sum_{\vec{n}} \hat{D}^{(E)}_{\vec{n}}, \sum_{\vec{n}'} \hat{L}^{(B)}_{\vec{n}'}], \sum_{\vec{n}''} \hat{T}^{(K)}_{\vec{n}''}]||| \\
&= ||\sum_{\vec{n}} \sum_{i,j\neq i} [\frac{g^2}{2a^{d-2}}(\hat{E}^2(\vec{n}, i) + \hat{E}^2(\vec{n} + \hat{i}, j) + \hat{E}^2(\vec{n} + \hat{j}, i) + \hat{E}^2(\vec{n}, j)), \\
&\quad \frac{-1}{2a^{4-d}g^2}(\hat{U}(\vec{n}, i)\hat{U}(\vec{n} + \hat{i}, j)\hat{U}^\dagger(\vec{n} + \hat{j}, i)\hat{U}^\dagger(\vec{n}, j) + h.c.)] \\
&\quad , \hat{K}(\vec{n}, i) + \hat{K}(\vec{n} + \hat{i}, j) + \hat{K}(\vec{n} + \hat{j}, i) + \hat{K}(\vec{n}, j)]|| \\
&\leq L^d \frac{d(d-1)}{2} 2|||[\frac{g^2}{2a^{d-2}}(\hat{E}^2(\vec{n}, i) + \hat{E}^2(\vec{n} + \hat{i}, j) + \hat{E}^2(\vec{n} + \hat{j}, i) + \hat{E}^2(\vec{n}, j)), \\
&\quad \frac{-1}{2a^{4-d}g^2}(\hat{U}(\vec{n}, i)\hat{U}(\vec{n} + \hat{i}, j)\hat{U}^\dagger(\vec{n} + \hat{j}, i)\hat{U}^\dagger(\vec{n}, j) + h.c.)]|| \cdot \\
&\quad ||\hat{K}(\vec{n}, i) + \hat{K}(\vec{n} + \hat{i}, j) + \hat{K}(\vec{n} + \hat{j}, i) + \hat{K}(\vec{n}, j)|| \\
&\leq L^d \frac{d(d-1)}{2} 2||\frac{4\Lambda - 2}{a^2}|| \cdot ||\frac{4}{a}|| \\
&= \frac{L^d d(d-1)(16\Lambda - 8)}{a^3},
\end{aligned} \tag{4.102}
$$

where we used the fact that terms not acting on the same links always commute, and in the second inequality, we used the bound in (4.86).

We now evaluate the bound of the $C_{2,7}$ term, which contains two magnetic terms, using a

similar method,

$$
\begin{aligned}
&|||[[\sum_{\vec{n}} \hat{D}^{(E)}_{\vec{n}}, \sum_{\vec{n}'} \hat{L}^{(B)}_{\vec{n}'}], \sum_{\vec{n}''} \hat{L}^{(B)}_{\vec{n}''}]||| \\
&= || \sum_{\vec{n}} \sum_{i,j\neq i} [\frac{g^2}{2a^{d-2}} (\hat{E}^2(\vec{n}, i) + \hat{E}^2(\vec{n} + \hat{i}, j) + \hat{E}^2(\vec{n} + \hat{j}, i) + \hat{E}^2(\vec{n}, j)), \\
&\quad \frac{-1}{2a^{4-d}g^2} (\hat{U}(\vec{n}, i)\hat{U}(\vec{n} + \hat{i}, j)\hat{U}^\dagger(\vec{n} + \hat{j}, i)\hat{U}^\dagger(\vec{n}, j) + h.c.)], \sum_{\vec{n}''} \hat{L}^{(B)}_{\vec{n}''}]|| \\
&\leq 2\frac{d(d-1)}{2} L^d || \frac{4\Lambda - 2}{a^2} || \cdot || \frac{8d-11}{a^{4-d}g^2} || \\
&\leq \frac{L^d d(d-1)(8d-11)(4\Lambda - 2)}{g^2 a^{6-d}},
\end{aligned} \tag{4.103}
$$

where in the first inequality, we used the bound in (4.86) for the first norm term, and the fact that there are $8d-11$ magnetic operators acting on the same plaquette as the magnetic operator in the inner commutator for the second norm term. The factor $8d-8$ is due to the fact that each of the four links on a plaquette is acted on by $2(d-1)$ magnetic terms, but 3 out of the $8d-8$ have been overcounted.

$C_{2,8}$ is a sum of commutators between three kinetic terms, which we label as $\hat{H}_i, \hat{H}_j$, and $\hat{H}_k$. We remind the readers that the edge terms are evolved before the bulk terms, as indicated by (4.67). As such, we divide up the tuples $(\hat{H}_i, \hat{H}_j, \hat{H}_k)$ into five types: (i) all three terms are bulk terms, (ii) all three terms are edge terms, (iii) $\hat{H}_i$ and $\hat{H}_j$ are edge terms, and $\hat{H}_k$ is a bulk term, (iv) $\hat{H}_i$ and $\hat{H}_k$ are edge terms, and $\hat{H}_j$ is a bulk term, and (v) $\hat{H}_i$ is an edge term, and $\hat{H}_j$ and $\hat{H}_k$ are bulk terms.

We consider the type-(i) terms, and further divide it into six separate cases. In the first case, we consider a scenario where $\hat{H}_i$ and $\hat{H}_j$ act on the same links and $\hat{H}_k = \hat{H}_j$. There are a total of $2d$ of such instances with even/odd parities and d directions. Since we always implement $\sum_{\{\vec{n}_{i,p}\}} \frac{\hat{T}^{(1)}_{\vec{n}_{i,p}} + \hat{T}^{(4)}_{\vec{n}_{i,p}}}{2}$ before $\sum_{\{\vec{n}_{i,p}\}} \frac{\hat{T}^{(2)}_{\vec{n}_{i,p}} + \hat{T}^{(3)}_{\vec{n}_{i,p}}}{2}$, as shown in (4.67), for each $\vec{n}_{i,p}$, we know that $\hat{H}_i = \sum_{\{\vec{n}_{i,p}\}} \frac{\hat{T}^{(1)}_{\vec{n}_{i,p}} + \hat{T}^{(4)}_{\vec{n}_{i,p}}}{2}$ and $\hat{H}_j = \sum_{\{\vec{n}_{i,p}\}} \frac{\hat{T}^{(2)}_{\vec{n}_{i,p}} + \hat{T}^{(3)}_{\vec{n}_{i,p}}}{2}$. Hence, the bound for each of the

instance is given by

$$
\begin{aligned}
&|||[\sum_{\{\vec{n}_{i,p}\}} \frac{\hat{T}^{(1)}_{\vec{n}_{i,p}} + \hat{T}^{(4)}_{\vec{n}_{i,p}}}{2}, \sum_{\{\vec{n}_{i,p}\}} \frac{\hat{T}^{(2)}_{\vec{n}_{i,p}} + \hat{T}^{(3)}_{\vec{n}_{i,p}}}{2}], \sum_{\{\vec{n}_{i,p}\}} \frac{\hat{T}^{(2)}_{\vec{n}_{i,p}} + \hat{T}^{(3)}_{\vec{n}_{i,p}}}{2}]|| \\
&= || \sum_{\{\vec{n}_{i,p}\}} [[\frac{\hat{T}^{(1)}_{\vec{n}_{i,p}} + \hat{T}^{(4)}_{\vec{n}_{i,p}}}{2}, \frac{\hat{T}^{(2)}_{\vec{n}_{i,p}} + \hat{T}^{(3)}_{\vec{n}_{i,p}}}{2}], \frac{\hat{T}^{(2)}_{\vec{n}_{i,p}} + \hat{T}^{(3)}_{\vec{n}_{i,p}}}{2}]|| \\
&\leq 4N_B || \frac{\hat{T}^{(1)}_{\vec{n}_{i,p}} + \hat{T}^{(4)}_{\vec{n}_{i,p}}}{2} ||^3 = \frac{N_B}{2a^3},
\end{aligned} \tag{4.104}
$$

where the first equality is due to the fact that kinetic operators acting on different links and sites commute, and we have used (4.70) for the inequality. The second case we consider is when $\hat{H}_i$ and $\hat{H}_j$ act on the same links and $\hat{H}_k \neq \hat{H}_j$. There are in total $2d^2 - d$ of such instances. This is so because a link can have $2d$ combinations of parity and direction, and if $\hat{H}_i$ and $\hat{H}_j$ act on the link labelled by the nth combination, then $\hat{H}_k$ can act on links with $2d-n$ different combinations, since $k > i$ and $\hat{H}_k \neq \hat{H}_j$. Thus, we obtain $(2d-1) + (2d-2) + ... + 1 = 2d^2 - d$ for the total number of instances. We consider one of such instance, where we fix $\hat{H}_k = \sum_{\{\vec{n}_{k,p'}\}} \sum_{a=1}^{4} \frac{\hat{T}^{(a)}_{\vec{n}_{k,p'}}}{2}$, and obtain its bound

$$
\begin{aligned}
&|||[\sum_{\{\vec{n}_{i,p}\}} \frac{\hat{T}^{(1)}_{\vec{n}_{i,p}} + \hat{T}^{(4)}_{\vec{n}_{i,p}}}{2}, \sum_{\{\vec{n}_{i,p}\}} \frac{\hat{T}^{(2)}_{\vec{n}_{i,p}} + \hat{T}^{(3)}_{\vec{n}_{i,p}}}{2}], \sum_{\{\vec{n}_{k,p'}\}} \sum_{a=1}^{4} \frac{\hat{T}^{(a)}_{\vec{n}_{k,p'}}}{2}]|| \\
&= |||[\sum_{\{\vec{n}_{i,p}\}} [\frac{\hat{T}^{(1)}_{\vec{n}_{i,p}} + \hat{T}^{(4)}_{\vec{n}_{i,p}}}{2}, \frac{\hat{T}^{(2)}_{\vec{n}_{i,p}} + \hat{T}^{(3)}_{\vec{n}_{i,p}}}{2}], \sum_{\{\vec{n}_{k,p'}\}} \sum_{a=1}^{4} \frac{\hat{T}^{(a)}_{\vec{n}_{k,p'}}}{2}]|| \\
&\leq 4N_B || \frac{\hat{T}^{(1)}_{\vec{n}_{i,p}} + \hat{T}^{(4)}_{\vec{n}_{i,p}}}{2} ||^2 || 2 \sum_{a=1}^{4} \frac{\hat{T}^{(a)}_{\vec{n}_{k,p'}}}{2} || \\
&= \frac{2N_B}{a^3},
\end{aligned} \tag{4.105}
$$

where in the first inequality, the extra factor two in the second norm expression is due to the fact that there are two choices of sites in $\{\vec{n}_{k,p'}\}$ for $\hat{H}_k$ that result in non-vanishing commutator with $\hat{H}_i$ and $\hat{H}_j$ due to their collisions on the two fermionic sites that sit at the two ends of a link that $\hat{H}_i$ and $\hat{H}_j$ act on. Similarly, in the third case, $\hat{H}_i$ and $\hat{H}_k$ act on the same links, while $\hat{H}_j \neq \hat{H}_k$ act on links of a different parity in the same direction. Since $(1,4)$ is implemented after $(2,3)$, and even terms are implemented before odd terms, $\hat{H}_i$, $\hat{H}_j$ and $\hat{H}_k$ are of the forms $\sum_{\{\vec{n}_{e,p}\}} \frac{\hat{T}^{(1)}_{\vec{n}_{e,p}} + \hat{T}^{(4)}_{\vec{n}_{e,p}}}{2}$,

$\sum_{\{\vec{n}_{o,p}\}}\sum_{a=1}^{4}\frac{\hat{T}^{(a)}_{\vec{n}_{o,p}}}{2}$ and $\sum_{\{\vec{n}_{e,p}\}}\frac{\hat{T}^{(2)}_{\vec{n}_{e,p}}+\hat{T}^{(3)}_{\vec{n}_{e,p}}}{2}$, respectively. There are d such instances. We consider one of such instance, and obtain its bound

$$\begin{aligned}
&|||[\sum_{\{\vec{n}_{e,p}\}}\frac{\hat{T}^{(1)}_{\vec{n}_{e,p}}+\hat{T}^{(4)}_{\vec{n}_{e,p}}}{2},\sum_{\{\vec{n}_{o,p}\}}\sum_{a=1}^{4}\frac{\hat{T}^{(a)}_{\vec{n}_{o,p}}}{2}],\sum_{\{\vec{n}_{e,p}\}}\frac{\hat{T}^{(2)}_{\vec{n}_{e,p}}+\hat{T}^{(3)}_{\vec{n}_{e,p}}}{2}]|||\\
&=|||[\sum_{\{\vec{n}_{e,p}\}}[\frac{\hat{T}^{(1)}_{\vec{n}_{e,p}}+\hat{T}^{(4)}_{\vec{n}_{e,p}}}{2},\sum_{\{\vec{n}_{o,p}\}}\sum_{a=1}^{4}\frac{\hat{T}^{(a)}_{\vec{n}_{o,p}}}{2}],\frac{\hat{T}^{(2)}_{\vec{n}_{e,p}}+\hat{T}^{(3)}_{\vec{n}_{e,p}}}{2}]|||\\
&\leq 4N_B||\frac{\hat{T}^{(1)}_{\vec{n}_{e,p}}+\hat{T}^{(4)}_{\vec{n}_{e,p}}}{2}||\cdot||2\sum_{a=1}^{4}\frac{\hat{T}^{(a)}_{\vec{n}_{o,p}}}{2}||\cdot||3\frac{\hat{T}^{(2)}_{\vec{n}_{e,p}}+\hat{T}^{(3)}_{\vec{n}_{e,p}}}{2}||\\
&=\frac{6N_B}{a^3},
\end{aligned}\tag{4.106}$$

where in the first inequality, the factor two in the second norm term is due to the fact that there are two choices of sites in $\{\vec{n}_{o,p}\}$ for $\hat{H}_j$ that result in collisions on two sites with $\hat{H}_i$. Further, there are three $\hat{H}_k$ terms that collide with the inner commutator, which acts on three links and four sites, i.e. $\hat{H}_k$ and $\hat{H}_i$ act on the same link, and $\hat{H}_k$ collides with $\hat{H}_j$ on two sites. We consider the fourth case where now $\hat{H}_j$ acts on links in a different direction. There are $2d^2-2d$ such instances. This is so because a link can have d different directions, and if $\hat{H}_i$ and $\hat{H}_k$ act on the link with the nth direction, then $\hat{H}_j$ can act on links in $d-n$ directions. Thus, we obtain $4[(d-1)+(d-2)...+1]=2d^2-2d$ for the total number of instances, where the factor of 4 is because there are two parities for $\hat{H}_i$ and $\hat{H}_k$, and $\hat{H}_j$. We consider one of such instance, where we fix $\hat{H}_j=\sum_{\{\vec{n}_{k,p'}\}}\sum_{a=1}^{4}\frac{\hat{T}^{(a)}_{\vec{n}_{k,p'}}}{2}$, and obtain its bound

$$\begin{aligned}
&|||[\sum_{\{\vec{n}_{i,p}\}}\frac{\hat{T}^{(1)}_{\vec{n}_{i,p}}+\hat{T}^{(4)}_{\vec{n}_{i,p}}}{2},\sum_{\{\vec{n}_{k,p'}\}}\sum_{a=1}^{4}\frac{\hat{T}^{(a)}_{\vec{n}_{k,p'}}}{2}],\sum_{\{\vec{n}_{i,p}\}}\frac{\hat{T}^{(2)}_{\vec{n}_{i,p}}+\hat{T}^{(3)}_{\vec{n}_{i,p}}}{2}]|||\\
&=|||[\sum_{\{\vec{n}_{i,p}\}}[\frac{\hat{T}^{(1)}_{\vec{n}_{i,p}}+\hat{T}^{(4)}_{\vec{n}_{i,p}}}{2},\sum_{\{\vec{n}_{k,p'}\}}\sum_{a=1}^{4}\frac{\hat{T}^{(a)}_{\vec{n}_{k,p'}}}{2}],\frac{\hat{T}^{(2)}_{\vec{n}_{i,p}}+\hat{T}^{(3)}_{\vec{n}_{i,p}}}{2}]|||\\
&\leq 4N_B||\frac{\hat{T}^{(1)}_{\vec{n}_{i,p}}+\hat{T}^{(4)}_{\vec{n}_{i,p}}}{2}||\cdot||2\sum_{a=1}^{4}\frac{\hat{T}^{(a)}_{\vec{n}_{k,p'}}}{2}||\cdot||\frac{\hat{T}^{(2)}_{\vec{n}_{i,p}}+\hat{T}^{(3)}_{\vec{n}_{i,p}}}{2}||\\
&=\frac{2N_B}{a^3},
\end{aligned}\tag{4.107}$$

where the factor two in the second norm expression of the third line is due to the fact that there are two choices of sites in $\{\vec{n}_{k,p'}\}$ for $\hat{H}_j$ that collide on two sites with $\hat{H}_i$ and $\hat{H}_k$. The fifth case

we consider is when $\hat{H}_i$ and $\hat{H}_j$ act on different links, and $\hat{H}_j = \hat{H}_k = \sum_{\{\vec{n}_{j,p'}\}} \sum_{a=1}^{4} \frac{\hat{T}^{(a)}_{\vec{n}_{j,p'}}}{2}$ act on the same links. In total, there are $4d^2 - 2d$ of such instances, which is two times that of the second case because $\hat{H}_i$ can be labelled by both $(1,4)$ and $(2,3)$. Each instance is bounded by

$$\begin{aligned}
&|||[\sum_{\{\vec{n}_{i,p}\}} \frac{\hat{T}^{(a)}_{\vec{n}_{i,p}} + \hat{T}^{(b)}_{\vec{n}_{i,p}}}{2}, \sum_{\{\vec{n}_{j,p'}\}} \sum_{a=1}^{4} \frac{\hat{T}^{(a)}_{\vec{n}_{j,p'}}}{2}], \sum_{\{\vec{n}_{j,p'}\}} \sum_{a=1}^{4} \frac{\hat{T}^{(a)}_{\vec{n}_{j,p'}}}{2}]|||\\
&= |||[\sum_{\{\vec{n}_{j,p'}\}} [\sum_{\{\vec{n}_{i,p}\}} \frac{\hat{T}^{(a)}_{\vec{n}_{i,p}} + \hat{T}^{(b)}_{\vec{n}_{i,p}}}{2}, \sum_{a=1}^{4} \frac{\hat{T}^{(a)}_{\vec{n}_{j,p'}}}{2}], \sum_{a=1}^{4} \frac{\hat{T}^{(a)}_{\vec{n}_{j,p'}}}{2}]|||\\
&\leq 4N_B ||2\frac{\hat{T}^{(a)}_{\vec{n}_{i,p}} + \hat{T}^{(b)}_{\vec{n}_{i,p}}}{2}|| \cdot ||\sum_{a=1}^{4} \frac{\hat{T}^{(a)}_{\vec{n}_{j,p'}}}{2}||^2\\
&= \frac{4N_B}{a^3},
\end{aligned} \tag{4.108}$$

where, once again, in the first inequality, we have used the fact that there are two kinetic operators in $\hat{H}_i$ acting on the same sites as each term in $\hat{H}_j$ and $\hat{H}_k$. In the last case, $\hat{H}_i$, $\hat{H}_j$ and $\hat{H}_k$ all act on different links. There are $\frac{8}{3}(2d^3 - 3d^2 + d)$ such instances. This is so because if $\hat{H}_i$ acts on links with the nth parity-direction label, then $\hat{H}_j$ and $\hat{H}_k$ can act on links with $2d - n$ and $2d - n - 1$ different labels, respectively. As such, we obtain $2[(2d-1)(2d-2) + (2d-2)(2d-3) + ... + 2 \cdot 1] = \frac{8}{3}(2d^3 - 3d^2 + d)$ for the total number of instances, where the factor of two is because $\hat{H}_i$ can be labelled by $(1,4)$ and $(2,3)$. Each instance is bounded by

$$\begin{aligned}
&|||[\sum_{\{\vec{n}_{i,p}\}} \frac{\hat{T}^{(a)}_{\vec{n}_{i,p}} + \hat{T}^{(b)}_{\vec{n}_{i,p}}}{2}, \sum_{\{\vec{n}_{j,p'}\}} \sum_{c=1}^{4} \frac{\hat{T}^{(c)}_{\vec{n}_{j,p'}}}{2}], \sum_{\{\vec{n}_{k,p''}\}} \sum_{e=1}^{4} \frac{\hat{T}^{(e)}_{\vec{n}_{k,p''}}}{2}]|||\\
&= |||[\sum_{\{\vec{n}_{i,p}\}} [\frac{\hat{T}^{(a)}_{\vec{n}_{i,p}} + \hat{T}^{(b)}_{\vec{n}_{i,p}}}{2}, \sum_{\{\vec{n}_{j,p'}\}} \sum_{c=1}^{4} \frac{\hat{T}^{(c)}_{\vec{n}_{j,p'}}}{2}], \sum_{\{\vec{n}_{k,p''}\}} \sum_{e=1}^{4} \frac{\hat{T}^{(e)}_{\vec{n}_{k,p''}}}{2}]|||\\
&\leq 4N_B ||\frac{\hat{T}^{(a)}_{\vec{n}_{i,p}} + \hat{T}^{(b)}_{\vec{n}_{i,p}}}{2}|| \cdot ||2\frac{\hat{T}^{(c)}_{\vec{n}_{j,p'}}}{2}|| \cdot ||4\frac{\hat{T}^{(e)}_{\vec{n}_{k,p''}}}{2}||\\
&= \frac{4N_B}{a^3},
\end{aligned} \tag{4.109}$$

where the factor of two in the second norm term of the first inequality is due to the fact that there are two kinetic operators from $\hat{H}_j$ acting on the same sites as each kinetic operator in $\hat{H}_i$. Note the inner commutator acts on four sites, connecting three links in total. Then, there are

four operators in $\hat{H}_k$, acting on the four sites. This explains the factor of four in the third norm term of the first inequality. All together, the type-(i) bound is given by

$$\frac{N_B}{a^3}(\frac{64}{3}d^3 - 8d^2 + \frac{11}{3}d). \tag{4.110}$$

For type-(ii) terms, we divide them into five distinct cases. Case-(i) terms are those where $\hat{H}_i$ and $\hat{H}_j$ act on the same links and $\hat{H}_j = \hat{H}_k$. The bound for each of the $2d$ instances in case (i) is $\frac{N_E}{2a^3}$, which we have obtained by replacing the N_B with N_E in (4.104). Case (ii) contains terms, where $\hat{H}_i$ and $\hat{H}_j$ act on the same links, and $\hat{H}_k$ acts on links in different directions. In order to obtain a nontrivial commutator, $\hat{H}_k$ must collide with $\hat{H}_i$ and $\hat{H}_j$. Since there is only one link in each direction per site in the edge, $\hat{H}_k$ cannot share a direction with $\hat{H}_i$ and $\hat{H}_j$. Thus, $\hat{H}_k$ shares the same parity with $\hat{H}_i$ and $\hat{H}_j$, because otherwise, $\hat{H}_k$ will act on the bulk connected to the sites acted on by $\hat{H}_i$ and $\hat{H}_j$. As such, $\hat{H}_k$ acts on links in different directions but of the same parity as those acted on by $\hat{H}_i$ and $\hat{H}_j$. There are $d^2 - d$ of such instances. This is so because if $\hat{H}_i$ and $\hat{H}_j$ act on links labelled by the nth direction, then $\hat{H}_k$ can act on links in $d - n$ different directions. Thus, we obtain $2[(d-1) + (d-2) + ... + 1] = d^2 - d$ for the total number of instances, where the factor of 2 is because there are two parity degrees of freedom. Moreover, since each edge is a $(d-1)-$dimensional surface, $\hat{H}_i$, $\hat{H}_j$, and $\hat{H}_k$ will collide on a $(d-2)$-dimensional surface, containing $\frac{L^{d-2}}{2}$ sites for each parity. As such, we consider one of such commutator in this case, and obtain its bound

$$\begin{aligned}
&|||[\sum_{\{\vec{n}_{i,p}\}} \frac{\hat{T}^{(1)}_{\vec{n}_{i,p}} + \hat{T}^{(4)}_{\vec{n}_{i,p}}}{2}, \sum_{\{\vec{n}_{i,p}\}} \frac{\hat{T}^{(2)}_{\vec{n}_{i,p}} + \hat{T}^{(3)}_{\vec{n}_{i,p}}}{2}], \sum_{\{\vec{n}_{i,p'}\}} \sum_{a=1}^{4} \frac{\hat{T}^{(a)}_{\vec{n}_{i,p'}}}{2}]|||\\
&= |||[\sum_{\{\vec{n}_{i,p}\}} [\frac{\hat{T}^{(1)}_{\vec{n}_{i,p}} + \hat{T}^{(4)}_{\vec{n}_{i,p}}}{2}, \frac{\hat{T}^{(2)}_{\vec{n}_{i,p}} + \hat{T}^{(3)}_{\vec{n}_{i,p}}}{2}], \sum_{\{\vec{n}_{i,p'}\}} \sum_{a=1}^{4} \frac{\hat{T}^{(a)}_{\vec{n}_{i,p'}}}{2}]|||\\
&\leq 4\frac{L^{d-2}}{2} ||\frac{\hat{T}^{(1)}_{\vec{n}_{i,p}} + \hat{T}^{(4)}_{\vec{n}_{i,p}}}{2}||^2 ||\sum_{a=1}^{4} \frac{\hat{T}^{(a)}_{\vec{n}_{i,p'}}}{2}||\\
&= \frac{L^{d-2}}{2a^3}.
\end{aligned} \tag{4.111}$$

Similarly, in the third case, $\hat{H}_i$ and $\hat{H}_k$ act on the same links, while $\hat{H}_j$ acts on links in a different direction of the same parity. There are $d^2 - d$ of such instances, as in the second case, and each instance is bounded by $\frac{L^{d-2}}{2a^3}$, following similar arguments in (4.111). The fourth case we consider is when $\hat{H}_i$ and $\hat{H}_j$ act on links in a different direction of the same parity, and $\hat{H}_k = \hat{H}_j = \sum_{\{\vec{n}_{j,p'}\}} \sum_{a=1}^{4} \frac{\hat{T}^{(a)}_{\vec{n}_{j,p'}}}{2}$. There are twice as many instances as the second case, i.e. $2d^2 - 2d$, because

$\hat{H}_i$ can be of the kinds $(1,4)$ or $(2,3)$. Once again, each instance is bounded by $\frac{L^{d-2}}{2a^3}$, following similar arguments in (4.111). We now consider the fifth case, where $\hat{H}_i$, $\hat{H}_j$, and $\hat{H}_k$ all act on links of different directions, but the same parity. There are $\frac{2}{3}(d^3-3d^2+2d)$ such instances. This is so because if $\hat{H}_i$ acts on links in the nth direction, then $\hat{H}_j$ and $\hat{H}_k$ can act on links in $d-n$ and $d-n-1$ different directions. Thus, we obtain $2[(d-1)(d-2)+(d-2)(d-3)+...+2]=\frac{2}{3}(d^3-3d^2+2d)$ for the total number of instances, where the factor of two is due to the two parity degrees of freedom. Furthermore, since each edge is a $(d-1)-$dimensional surface, $\hat{H}_i$, $\hat{H}_j$, and $\hat{H}_k$ will collide on a $(d-3)$-dimensional surface, containing $\frac{L^{d-3}}{2}$ sites for each parity. As such, we consider one of such commutator in this case, and obtain its bound

$$\begin{aligned}
&|||[\sum_{\{\vec{n}_{i,p}\}}\frac{\hat{T}^{(a)}_{\vec{n}_{i,p}}+\hat{T}^{(b)}_{\vec{n}_{i,p}}}{2},\sum_{\{\vec{n}_{i,p'}\}}\sum_{c=1}^{4}\frac{\hat{T}^{(c)}_{\vec{n}_{i,p'}}}{2}],\sum_{\{\vec{n}_{i,p''}\}}\sum_{d=1}^{4}\frac{\hat{T}^{(d)}_{\vec{n}_{i,p''}}}{2}]|||\\
&\leq 4\frac{L^{d-3}}{2}||\frac{\hat{T}^{(a)}_{\vec{n}_{i,p}}+\hat{T}^{(b)}_{\vec{n}_{i,p}}}{2}||\cdot||\sum_{c=1}^{4}\frac{\hat{T}^{(c)}_{\vec{n}_{i,p'}}}{2}||^2\\
&=\frac{L^{d-3}}{a^3}.
\end{aligned}\tag{4.112}$$

All together, the type-(ii) bound is given by

$$\frac{N_E}{2a^3}2d+\frac{2L^{d-2}}{a^3}(d^2-d)+\frac{2L^{d-3}}{3a^3}(d^3-3d^2+2d).\tag{4.113}$$

Now, we consider type-(iii) terms. We divide the terms into two cases. In the first case, the edge terms, $\hat{H}_i$ and $\hat{H}_j$, act on the same links. There are $4d^2$ of $[[\hat{H}_i,\hat{H}_j],\hat{H}_k]$ commutators, in this case, since there are $2d$ choices for $\hat{H}_i$ and $\hat{H}_j$ pairs and another factor of $2d$ for $\hat{H}_k$, but $2d$ of them are trivially zero. This is so since for a given parity and direction for $\hat{H}_i$ and $\hat{H}_j$, there is one $\hat{H}_k$ term, of the type $\sum_{a=1}^{4}\frac{\hat{T}^{(a)}}{2}$, with the same parity and direction as $\hat{H}_i$ and $\hat{H}_j$, that commute with $\hat{H}_i$ and $\hat{H}_j$. Therefore, there are $4d^2-2d$ non-vanishing commutators in this case, and each is bounded by $\frac{2N_E}{a^3}$, where we have replaced N_B with the smaller N_E in (4.105). In the second case, $\hat{H}_i$ and $\hat{H}_j$ act on different links. There are $4d^2-2d$ such pairs of $\hat{H}_i$ and $\hat{H}_j$. Since, there are $2d$ choices of $\hat{H}_k$, there are $8d^3-4d^2$ terms in this case, and each of which is bounded by $\frac{4N_E}{a^3}$, using (4.109). Therefore, we obtain the bound for the sum of all type-(iii) terms to be

$$\frac{N_E}{a^3}(32d^3-8d^2-4d).\tag{4.114}$$

Note for type-(iv) terms, the same bound can be obtained along similar lines of reasoning, with the only difference being $\hat{H}_j$ is in the bulk, and $\hat{H}_k$ is in the edge.

Lastly, type-(v) terms can be separated into two cases. The first case is when the bulk terms $\hat{H}_j = \hat{H}_k = \sum_{\{\vec{n}_{j,p'}\}} \sum_{a=1}^{4} \frac{\hat{T}^{(a)}_{\vec{n}_{j,p'}}}{2}$ are acting on the same links. For each choice of $\hat{H}_i$, there are $(2d-1)$ choices of $\hat{H}_j$ that yields a non-zero commutator, with the subtraction by one arising from the same parity and direction. Since there are $4d$ choices of $\hat{H}_i$, there are then $4d(2d-1) = 8d^2-4d$ instances in this first case. The bound of each instance is obtained as,

$$\begin{aligned}
&|||[\sum_{\{\vec{n}_{i,p}\}} \frac{\hat{T}^{(a)}_{\vec{n}_{i,p}} + \hat{T}^{(b)}_{\vec{n}_{i,p}}}{2}, \sum_{\{\vec{n}_{j,p'}\}} \sum_{c=1}^{4} \frac{\hat{T}^{(c)}_{\vec{n}_{j,p'}}}{2}], \sum_{\{\vec{n}_{j,p'}\}} \sum_{c=1}^{4} \frac{\hat{T}^{(c)}_{\vec{n}_{j,p'}}}{2}]|||\\
&= || \sum_{\{\vec{n}_{j,p'}\}} [[\sum_{\{\vec{n}_{i,p}\}} \frac{\hat{T}^{(a)}_{\vec{n}_{i,p}} + \hat{T}^{(b)}_{\vec{n}_{i,p}}}{2}, \sum_{c=1}^{4} \frac{\hat{T}^{(c)}_{\vec{n}_{j,p'}}}{2}], \sum_{c=1}^{4} \frac{\hat{T}^{(c)}_{\vec{n}_{j,p'}}}{2}]||\\
&\leq 4N_E || \frac{\hat{T}^{(a)}_{\vec{n}_{i,p}} + \hat{T}^{(b)}_{\vec{n}_{i,p}}}{2} || \cdot ||2 \sum_{c=1}^{4} \frac{\hat{T}^{(c)}_{\vec{n}_{j,p'}}}{2}||^2\\
&= \frac{8N_E}{a^3}.
\end{aligned} \tag{4.115}$$

In the second case, $\hat{H}_j$ and $\hat{H}_k$ act on different links. Now, for each non-trivial pair of $\hat{H}_i$ and $\hat{H}_j$, there are $2d-2$ choices of $\hat{H}_k$. Thus, there are $4d(2d-1)(2d-2)$ such terms, each of which is bounded by $\frac{4N_E}{a^3}$, using (4.109). Therefore, type-(v) terms are bounded by

$$\frac{N_E}{a^3}(64d^3 - 32d^2). \tag{4.116}$$

As such, $C_{2,8}$ is bounded by

$$\frac{L^d}{a^3}(\frac{32}{3}d^3 - 4d^2 + \frac{11}{6}d) + \frac{L^{d-1}}{a^3}(\frac{160}{3}d^3 - 20d^2 - \frac{16}{3}d) + \frac{L^{d-2}}{a^3}(2d^2 - 2d) + \frac{2L^{d-3}}{3a^3}(d^3 - 3d^2 + 2d). \tag{4.117}$$

Now we consider the $C_{2,9}$ term, where $\hat{H}_i$ and $\hat{H}_j$ are kinetic terms, and $\hat{H}_k$ is a magnetic term. The terms can be separated into three types. Type (i): the terms where $\hat{H}_i$ and $\hat{H}_j$ are both of an edge kind. Type (ii): the terms where $\hat{H}_i$ and $\hat{H}_j$ are both of a bulk kind. The terms where $\hat{H}_i$ is in the edge and $\hat{H}_j$ is in the bulk belong to type (iii). We further divide type (i) into three cases. The first case is when $\hat{H}_i$ and $\hat{H}_j$ act on the same link. There are $2d$ such pairs of $\hat{H}_i$ and $\hat{H}_j$, and for each pair, there are $2(d-1)$ magnetic terms that act on links in the same

direction. As such, there are $4d^2 - 4d$ commutators in this case, each of which is bounded by

$$\begin{aligned}
&|||[\sum_{\{\vec{n}_{i,p}\}} \frac{\hat{T}^{(1)}_{\vec{n}_{i,p}} + \hat{T}^{(4)}_{\vec{n}_{i,p}}}{2}, \sum_{\{\vec{n}_{i,p}\}} \frac{\hat{T}^{(2)}_{\vec{n}_{i,p}} + \hat{T}^{(3)}_{\vec{n}_{i,p}}}{2}], \sum_{\vec{n}} \hat{L}^{(B)}_{\vec{n}}]|| \\
&\leq || \sum_{\{\vec{n}_{i,p}\}} [[\frac{\hat{T}^{(1)}_{\vec{n}_{i,p}} + \hat{T}^{(4)}_{\vec{n}_{i,p}}}{2}, \frac{\hat{T}^{(2)}_{\vec{n}_{i,p}} + \hat{T}^{(3)}_{\vec{n}_{i,p}}}{2}], \hat{L}^{(B)}_{\vec{n}_{i,\square}}]|| \\
&\leq 4N_E || \frac{\hat{T}^{(1)}_{\vec{n}_{i,p}} + \hat{T}^{(4)}_{\vec{n}_{i,p}}}{2} ||^2 \cdot || \frac{-1}{2g^2 a^{4-d}} (\hat{U}\hat{U}\hat{U}^\dagger \hat{U}^\dagger + h.c.)|| \\
&= \frac{N_E}{g^2 a^{6-d}},
\end{aligned} \tag{4.118}$$

where in step two, we have used the fact that only kinetic and magnetic operators that act on the same links yield non-zero commutators. The bound for all the terms in this case is then

$$\frac{4N_E}{g^2 a^{6-d}}(d^2 - d). \tag{4.119}$$

The second case is when $\hat{H}_i$ and $\hat{H}_j$ act on different links, but in the same direction. $\hat{H}_i$ and $\hat{H}_j$ have to be even and odd, respectively, due to the ordering. Since the links in the edge for any given direction are not connected, $\hat{H}_i$ and $\hat{H}_j$ must commute. Therefore, the bound for this case is zero.

In the third case, $\hat{H}_i$ and $\hat{H}_j$ act on links in different directions. There are $4d^2 - 4d$ pairs in this case. This is so because if $\hat{H}_i$ acts on links in the nth direction, then $\hat{H}_j$ can act on links in $d - n$ different directions. Thus, we obtain $8[(d-1) + (d-2) + ... + 1] = 4d^2 - 4d$, where the factor of 8 is due to the fact that $\hat{H}_i$ can be of the kinds $(1, 4)$ or $(2, 3)$, and each of $\hat{H}_i$ and $\hat{H}_j$ can be of two parities. For each pair of $\hat{H}_i$ and $\hat{H}_j$, there are 2 magnetic terms that do not commute with both, since the two directions from the pair form a plane, and for each plane the magnetic terms can be of different parities. Each inner commutator acts on three links, due to the fact that there are two $\hat{H}_j$ terms acting on the same sites as an $\hat{H}_i$ term. For each of such triple-link configuration, there are $2(d-2)$ magnetic terms acting on each single link, where the factor of two comes from the two parities, and the factor of $(d-2)$ is due to the fact that each magnetic term do not act on both links at the same time. Therefore, for each pair of $\hat{H}_i$ and $\hat{H}_j$,

the commutator is bounded by

$$
\begin{aligned}
&|||[\sum_{\{\vec{n}_{i,p}\}} \frac{\hat{T}^{(a)}_{\vec{n}_{i,p}} + \hat{T}^{(b)}_{\vec{n}_{i,p}}}{2}, \sum_{\{\vec{n}_{j,p}\}} \sum_{c=1}^{4} \frac{\hat{T}^{(c)}_{\vec{n}_{j,p'}}}{2}], \sum_{\vec{n}} \hat{L}^{(B)}_{\vec{n}}]|||\\
&\leq 4N_E || \frac{\hat{T}^{(a)}_{\vec{n}_{i,p}} + \hat{T}^{(b)}_{\vec{n}_{i,p}}}{2} || \cdot || 2 \sum_{c=1}^{4} \frac{\hat{T}^{(c)}_{\vec{n}_{j,p'}}}{2} || \cdot || \frac{-(2 + 3 \cdot 2(d-2))}{2g^2 a^{4-d}} (\hat{U}\hat{U}\hat{U}^\dagger \hat{U}^\dagger + h.c.) ||\\
&= \frac{(24d - 40) N_E}{g^2 a^{6-d}}.
\end{aligned} \tag{4.120}
$$

Therefore, the third case is bounded by

$$
\frac{N_E}{g^2 a^{6-d}} (24d - 40)(4d^2 - 4d). \tag{4.121}
$$

Finally, the bound for type-(i) terms is then

$$
\frac{N_E}{g^2 a^{6-d}} (96d^3 - 252d^2 + 156d). \tag{4.122}
$$

Similarly, we separate type-(ii) terms into three cases, and obtain the bounds for case (i) and (iii) as

$$
\frac{4N_B}{g^2 a^{6-d}} (d^2 - d) \tag{4.123}
$$

and

$$
\frac{N_B}{g^2 a^{6-d}} (24d - 40)(4d^2 - 4d), \tag{4.124}
$$

respectively. In the second case, $\hat{H}_i$ and $\hat{H}_j$ act on different links, but in the same direction. There are $2d$ such pairs of $\hat{H}_i$ and $\hat{H}_j$ because $\hat{H}_i$ and $\hat{H}_j$ have to be even and odd, respectively, due to the ordering, and $\hat{H}_i$ can be either $(1, 4)$ or $(2, 3)$, while $\hat{H}_j$ is of the form $\sum_{a=1}^{4} \frac{\hat{T}^{(a)}}{2}$. For each pairs of $\hat{H}_i$ and $\hat{H}_j$, the commutator is bounded by

$$
\begin{aligned}
&|||[\sum_{\{\vec{n}_{e,p}\}} \frac{\hat{T}^{(a)}_{\vec{n}_{e,p}} + \hat{T}^{(b)}_{\vec{n}_{e,p}}}{2}, \sum_{\{\vec{n}_{o,p}\}} \sum_{c=1}^{4} \frac{\hat{T}^{(c)}_{\vec{n}_{o,p}}}{2}], \sum_{\vec{n}} \hat{L}^{(B)}_{\vec{n}}]|||\\
&\leq 4N_B || \frac{\hat{T}^{(a)}_{\vec{n}_{e,p}} + \hat{T}^{(b)}_{\vec{n}_{e,p}}}{2} || \cdot || 2 \sum_{c=1}^{4} \frac{\hat{T}^{(c)}_{\vec{n}_{o,p}}}{2} || \cdot || \frac{-3 \cdot 2(d-1)}{2g^2 a^{4-d}} (\hat{U}\hat{U}\hat{U}^\dagger \hat{U}^\dagger + h.c.) ||\\
&= \frac{24(d-1) N_B}{g^2 a^{6-d}},
\end{aligned} \tag{4.125}
$$

where the factor two in the second norm term of the first inequality is because of the fact that there are two elements $\vec{n}_{o,p}$ that result in non-vanishing inner commutator due to collision of sites for a given $\vec{n}_{e,p}$. Further, for each inner commutator, which acts on three links, there are $3 \cdot 2(d-1)$ magnetic terms that overlap on these links. As such, the second case is bounded by

$$\frac{48N_B}{g^2a^{6-d}}(d^2-d). \tag{4.126}$$

Thus, the bound of type-(ii) terms is

$$\frac{N_B}{g^2a^{6-d}}(96d^3-204d^2+108d). \tag{4.127}$$

Now we consider type (iii), where $\hat{H}_i$ and $\hat{H}_j$ are from the edge and bulk, respectively. Once again, we divide the terms up into three cases. In the first case, $\hat{H}_i$ and $\hat{H}_j$ act on links in the same direction and sites of the same parity. There are $4d$ such pairs, and they commute with each other. The second case is where $\hat{H}_i$ and $\hat{H}_j$ act on links in the same direction, but sites of different parities. There are $4d$ such pairs, and there are $3(2d-2)$ magnetic terms that do not commute with each pair. Therefore, for each pair of $\hat{H}_i$ and $\hat{H}_j$, the bound for the commutator is $\frac{(24d-24)N_E}{g^2a^{6-d}}$, using similar arguments as (4.125). The third case contains commutators, in which $\hat{H}_i$ and $\hat{H}_j$ act on links in different directions. There are $8d^2-8d$ such pairs. This is so because there are $4d$ $\hat{H}_i$ and for each $\hat{H}_i$, $\hat{H}_j$ can be of $(d-1)$ directions and 2 parities. Further, there are $6d-10$ magnetic terms that do not commute with each pair, following similar arguments in (4.120). Once again, for each pair of $\hat{H}_i$ and $\hat{H}_j$, the bound for the commutator is $\frac{(24d-40)N_E}{g^2a^{6-d}}$, using similar arguments as (4.120). As such the bound for type-(iii) terms is given by

$$\frac{N_E}{g^2a^{6-d}}(192d^3-416d^2+224d). \tag{4.128}$$

Summing up the bounds for type-(i), -(ii), and -(iii) terms, we obtain the bound for $C_{2,9}$ as

$$\frac{L^d}{g^2a^{6-d}}(48d^3-102d^2+54d)+\frac{L^{d-1}}{g^2a^{6-d}}(96d^3-232d^2+136d). \tag{4.129}$$

Now for $C_{2,10}$, we can use a similar approach. The only difference is that in each case, we only need to consider the magnetic terms, $\hat{H}_j$, that do not commute with the first kinetic term, $\hat{H}_i$. This is because if $[\hat{H}_i,\hat{H}_j]=0$, $[[\hat{H}_i,\hat{H}_j],\hat{H}_k]=0$. If we divide up the terms into cases based on the kinetic terms $\hat{H}_i$ and $\hat{H}_k$ as we did for $C_{2,9}$, and use the fact that there are $2(d-1)$ magnetic terms $\hat{H}_j$ that do not commute with each $\hat{H}_i$, we can compute the bound for each case. For case (i) of type (i) and (ii), we obtain the bound

$$\frac{N_E+N_B}{g^2a^{6-d}}(2d)2(d-1). \tag{4.130}$$

For case (ii) of type (i), there are $2d$ pairs of $\hat{H}_i$ and $\hat{H}_k$ because there d directions and $\hat{H}_i$ can be of type $(1,4)$ or $(2,3)$. For each pair, the commutator is bounded by

$$\begin{aligned}
&|||[\sum_{\{\vec{n}_{e,p}\}} \frac{\hat{T}^{(a)}_{\vec{n}_{e,p}} + \hat{T}^{(b)}_{\vec{n}_{e,p}}}{2}, \sum_{\vec{n}_{k,\square}} \hat{L}^{(B)}_{\vec{n}_{k,\square}}], \sum_{\{\vec{n}_{o,p}\}} \sum_{c=1}^{4} \frac{\hat{T}^{(c)}_{\vec{n}_{o,p}}}{2}]||| \\
&\leq 4N_E || \frac{\hat{T}^{(a)}_{\vec{n}_{e,p}} + \hat{T}^{(b)}_{\vec{n}_{e,p}}}{2} || \cdot || \frac{-2(d-1)}{2g^2 a^{4-d}} (\hat{U}\hat{U}\hat{U}^\dagger \hat{U}^\dagger + h.c.) || \cdot || 2 \sum_{c=1}^{4} \frac{\hat{T}^{(c)}_{\vec{n}_{o,p}}}{2} || \\
&= \frac{8(d-1)N_E}{g^2 a^{6-d}},
\end{aligned} \tag{4.131}$$

where in the second line, the factor of 2 in the third norm term is because of the fact that for a given $\vec{n}_{e,p}$, there are two odd kinetic terms, of the type $\vec{n}_{o,p}$, that collide on two links with the magnetic term. For case (ii) of type (ii), once again, there are $2d$ pairs of $\hat{H}_i$ and $\hat{H}_k$. For each pair, the commutator is bounded by

$$\begin{aligned}
&|||[\sum_{\{\vec{n}_{e,p}\}} \frac{\hat{T}^{(a)}_{\vec{n}_{e,p}} + \hat{T}^{(b)}_{\vec{n}_{e,p}}}{2}, \sum_{\vec{n}_{k,\square}} \hat{L}^{(B)}_{\vec{n}_{k,\square}}], \sum_{\{\vec{n}_{o,p}\}} \sum_{c=1}^{4} \frac{\hat{T}^{(c)}_{\vec{n}_{o,p}}}{2}]||| \\
&\leq 4N_E || \frac{\hat{T}^{(a)}_{\vec{n}_{e,p}} + \hat{T}^{(b)}_{\vec{n}_{e,p}}}{2} || \cdot || \frac{-2(d-1)}{2g^2 a^{4-d}} (\hat{U}\hat{U}\hat{U}^\dagger \hat{U}^\dagger + h.c.) || \cdot || 4 \sum_{c=1}^{4} \frac{\hat{T}^{(c)}_{\vec{n}_{o,p}}}{2} || \\
&= \frac{16(d-1)N_B}{g^2 a^{6-d}},
\end{aligned} \tag{4.132}$$

where in the second line, the factor of 4 in the third norm term is because of the fact that each even kinetic term of the type $\vec{n}_{e,p}$ collides with two odd kinetic terms of the type $\vec{n}_{o,p}$, and each magnetic term collides with two odd kinetic terms. Thus, for case (ii) of type (i) and (ii), we obtain the bound

$$\frac{4N_E + 8N_B}{g^2 a^{6-d}} 2d \cdot 2(d-1). \tag{4.133}$$

For case (iii) of type (i) and (ii), we obtain the bound

$$\frac{4N_E + 4N_B}{g^2 a^{6-d}} 2(d-1)(4d^2 - 4d), \tag{4.134}$$

by replacing the number of non-commuting magnetic terms. Next, there are $4d$ pairs of $\hat{H}_i$ and $\hat{H}_k$ in case (ii) of type (iii), and the commutator bound for each pair has the same bound as (4.131), $\frac{8(d-1)N_E}{g^2 a^{6-d}}$. For case (iii) of type (iii), there are $(8d^2 - 8d)$ pairs of $\hat{H}_i$ and $\hat{H}_k$ in case (ii)

of type (iii), and the commutator bound for each pair has the same bound as (4.131), $\frac{8(d-1)N_E}{g^2a^{6-d}}$. Thus, for type (iii), we obtain the bound

$$\frac{4N_E}{g^2a^{6-d}}(8d^2-4d)2(d-1), \tag{4.135}$$

by replacing the number of non-commuting magnetic terms. By summing up the bounds for all cases, we obtain the bound for $C_{2,10}$,

$$\begin{aligned}
&\frac{N_E+N_B}{g^2a^{6-d}}[(2d)(2d-2)+8d\cdot 2(d-1)+8(d-1)(4d^2-4d)]\\
&+\frac{N_E}{g^2a^{6-d}}(8d^2-4d)(8d-8)+\frac{N_B}{g^2a^{6-d}}8d(2d-2)\\
&=\frac{L^d}{g^2a^{6-d}}(16d^3-10d^2-6d)+\frac{L^{d-1}}{g^2a^{6-d}}(32d^3-56d^2+24d).
\end{aligned} \tag{4.136}$$

Lastly, we consider $C_{2,11}$, where $\hat{H}_i$ is a kinetic term, and $\hat{H}_j$ and $\hat{H}_k$ are magnetic terms. We evaluate its bound as follows:

$$\begin{aligned}
&\sum_{i=e}^{o}\sum_{p=1}^{2d}\sum_{(a,b)=(1,4)}^{(2,3)}|||[\sum_{\{\vec{n}_{i,p}\}}\frac{\hat{T}^{(a)}_{\vec{n}_{i,p}}+\hat{T}^{(b)}_{\vec{n}_{i,p}}}{2},\sum_{\vec{n}}\hat{L}^{(B)}_{\vec{n}}],\sum_{\vec{n}'}\hat{L}^{(B)}_{\vec{n}'}]]||\\
&\leq 32d(N_E+N_B)||\frac{\hat{T}^{(a)}_{\vec{n}_{i,p}}+\hat{T}^{(b)}_{\vec{n}_{i,p}}}{2}||\cdot||\frac{-2(d-1)}{2a^{4-d}g^2}(\hat{U}\hat{U}\hat{U}^\dagger\hat{U}^\dagger+h.c.)||\cdot||\frac{-(14d-20)}{2a^{4-d}g^2}(\hat{U}\hat{U}\hat{U}^\dagger\hat{U}^\dagger+h.c.)||\\
&=\frac{L^d((224d^3-544d^2+320d))}{a^{9-2d}g^4},
\end{aligned} \tag{4.137}$$

where in the second line, the factor of $2(d-1)$ in the second norm term is the number of magnetic terms that act on the same link as the kinetic term, since there are $(d-1)$ planes that share a direction with the kinetic term, and on each plane, there is a pair of magnetic terms of two different parities. For each pair of such magnetic terms, there are 8 colliding magnetic terms on the same plane, and $7\cdot 2(d-2)$ colliding magnetic terms on different planes, where 7 is the number of links acted on by the pair and $2(d-2)$ is the number of colliding magnetic terms on each of the 7 links. This explains the factor of $8+7\cdot 2(d-2)=14d-20$.

As a final step, we include the second-order Trotter error for the magnetic term, of which the ordering is given by (4.57). We use (4.70) to bound both the commutators $[[\hat{H}_i,\sum_{j>i}\hat{H}_j],\hat{H}_i]$ and $[[\hat{H}_i,\sum_{j>i}\hat{H}_j],\sum_{k>i}\hat{H}_k]$. We remind the readers that each $\hat{H}_i$ is of the form

$$\frac{-1}{2a^{4-d}g^2}\hat{U}^{(1)^\dagger\alpha}\hat{U}^{(2)\dagger\beta}\hat{U}^{(3)\dagger\gamma}\hat{U}^{(4)^\dagger\delta}\hat{R}_\square\hat{U}^{(1)\alpha}\hat{U}^{(2)\beta}\hat{U}^{(3)\gamma}\hat{U}^{(4)\delta}, \tag{4.138}$$

where $(\alpha, \beta, \gamma, \delta) \in S_{GC} \equiv \{GC(0), GC(1), ..., GC(15)\}$. Excluding the prefactor $\frac{-1}{2a^{4-d}g^2}$, the norm of the operator is two. Furthermore, $\hat{H}_i$ operators with different values of $\alpha, \beta, \gamma, \delta$ are submatrices, which act on disjoint sets of states and have no overlapping elements, of

$$\frac{-1}{2a^{4-d}g^2}(\hat{U}\hat{U}\hat{U}^\dagger\hat{U}^\dagger + h.c.), \tag{4.139}$$

of which the norm is two, excluding the prefactor $\frac{-1}{2a^{4-d}g^2}$. Therefore, we obtain the inequality

$$||\sum_{(\alpha,\beta,\gamma,\delta)\in b; b\subseteq S_{GC}} \frac{-1}{2a^{4-d}g^2}\hat{U}^{(1)^\dagger\alpha}\hat{U}^{(2)\dagger\beta}\hat{U}^{(3)\dagger\gamma}\hat{U}^{(4)^\dagger\delta}\hat{R}_\square\hat{U}^{(1)\alpha}\hat{U}^{(2)\beta}\hat{U}^{(3)\gamma}\hat{U}^{(4)\delta}|| \leq \frac{1}{a^{4-d}g^2}. \tag{4.140}$$

Using this relation, we evaluate the bound for the latter type of commutator

$$[[\hat{H}_i, \sum_{j>i}\hat{H}_j], \sum_{k>i}\hat{H}_k] \leq 4||\frac{1}{a^{4-d}g^2}||^3 = \frac{4}{a^{12-3d}g^6}. \tag{4.141}$$

As such, in accordance to (2.8) and a straightforward counting argument, the error of the magnetic term is given by

$$\frac{1}{12}\sum_i |||[[\hat{H}_i, \sum_{j>i}\hat{H}_j], \hat{H}_i]|| + \frac{1}{24}\sum_i |||[[\hat{H}_i, \sum_{j>i}\hat{H}_j], \sum_{k>i}\hat{H}_k]|| \leq L^d\frac{d(d-1)}{2}\frac{8}{a^{12-3d}g^6}, \tag{4.142}$$

where L^d is the number of sites, $\frac{d(d-1)}{2}$ is the number of plaquettes per site, and $\frac{1}{a^{12-3d}g^6}$ is the Trotter error per plaquette.

Synthesis errors

Here, we compute the synthesis errors for R_z gates required for each of the four terms, i.e., $e^{i\hat{D}_{\vec{n}}^{(M)}t}, e^{i\hat{D}_{\vec{n}}^{(E)}t}, e^{i\hat{T}_{\vec{n}}^{(K)}t}, e^{i\hat{L}_{\vec{n}}^{(B)}t}$, that were described in detail in Sec. 4.3.2. To start, we consider the mass term. In this term, we have $\lfloor\log\left(L^d\right)+1\rfloor$ R_z gates to implement. Therefore, we incur for each mass term $\lfloor\log\left(L^d\right)+1\rfloor \cdot \epsilon(R_z)$ amount of error, where $\epsilon(R_z)$ denotes the error per R_z gate.

Next, we consider the electric term, which has $2(\eta+1)\lfloor\log\left(dL^d\right)+1\rfloor$ R_z gates. Therefore, each electric term incurs $2(\eta+1)\lfloor\log\left(dL^d\right)+1\rfloor \cdot \epsilon(R_z)$ amount of error. If we instead use the phase gradient operation, once the gadget state $|\psi_M\rangle$ in (4.25) is prepared, each quantum adder call to implement the operation does not incur any synthesis error. We come back to the error incurred in preparing the gadget state itself in the next section.

For the kinetic term, there are $4d(\lfloor\log\big(L^d - L^{d-1}\big) + 1\rfloor + \lfloor\log\big(L^{d-1}\big) + 1\rfloor)$ R_z gates to apply in total. Therefore, the total error per kinetic term is $4d(\lfloor\log\big(L^d - L^{d-1}\big) + 1\rfloor + \lfloor\log\big(L^{d-1}\big) + 1\rfloor) \cdot \epsilon(R_z)$.

For the magnetic term, there are $16d(d-1)\lfloor\log\big(L^d\big) + 1\rfloor$ R_z gates to apply. Hence, the amount of error per magnetic term is $16d(d-1) \cdot \lfloor\log\big(L^d\big) + 1\rfloor \cdot \epsilon(R_z)$.

Lastly, we compute the total synthesis error $\epsilon_{\text{synthesis}}$. Note that each term appears twice per Trotter step in the second-order product formula in (2.7). However, the implementation of the diagonal terms can be optimized. In particular, the diagonal mass and electric terms applied at the beginning (end) of each Trotter step can be applied together with the terms at the end (beginning) of the previous (next) Trotter step, unless the terms are at the very beginning or end of the simulation. As such, there are $r+1$ diagonal mass and electric terms, and $2r$ off-diagonal kinetic and magnetic terms to implement in total. Thus, $\epsilon_{\text{synthesis}}$ is given by

$$\begin{aligned}\epsilon_{\text{synthesis}} = \{(r+1) \cdot [\lfloor\log\Big(L^d\Big) + 1\rfloor + 2(\eta+1)\lfloor\log\Big(dL^d\Big) + 1\rfloor] + 2r \cdot [(16d^2 - 16d) \cdot \lfloor\log\Big(L^d\Big) + 1\rfloor \\ + 4d(\lfloor\log\Big(L^d - L^{d-1}\Big) + 1\rfloor + \lfloor\log\Big(L^{d-1}\Big) + 1\rfloor)]\} \cdot \epsilon(R_z),\end{aligned} \tag{4.143}$$

where r, to reiterate for the convenience of the readers, is the total number of Trotter steps.

Complexity analysis

Having computed both the Trotter and synthesis errors in the two previous sections, we are now ready to perform the complexity analysis for the U(1) LGT.

The total error is given by

$$\epsilon_{\text{total}} = \epsilon_{\text{synthesis}} + \epsilon_{\text{Trotter}}. \tag{4.144}$$

Here, we evenly distribute the total error between the synthesis and Trotter errors. Focusing on the Trotter error, we obtain the number of Trotter steps by

$$\epsilon_{\text{Trotter}} = \frac{\epsilon_{\text{total}}}{2} \implies r = \lceil \frac{T^{3/2} 2^{1/2} \rho^{1/2}}{\epsilon_{\text{total}}^{1/2}} \rceil. \tag{4.145}$$

As such, we can compute the error each R_z gate can incur by

$$\begin{aligned}&\epsilon_{\text{synthesis}} = \frac{\epsilon_{\text{total}}}{2} \implies \\ &\epsilon(R_z) = \frac{\epsilon_{\text{total}}}{2}\{(\lceil \frac{T^{3/2} 2^{1/2} \rho^{1/2}}{\epsilon_{\text{total}}^{1/2}} \rceil + 1) \cdot [\lfloor\log\Big(L^d\Big) + 1\rfloor + 2(\eta+1)\lfloor\log\Big(dL^d\Big) + 1\rfloor] + \lceil \frac{T^{3/2} 2^{1/2} \rho^{1/2}}{\epsilon_{\text{total}}^{1/2}} \rceil \\ &\cdot 2[(16d^2 - 16d) \cdot \lfloor\log\Big(L^d\Big) + 1\rfloor + 4d(\lfloor\log\Big(L^d - L^{d-1}\Big) + 1\rfloor + \lfloor\log\Big(L^{d-1}\Big) + 1\rfloor)]\}^{-1}.\end{aligned} \tag{4.146}$$

With this, we obtain the number of T gates required to synthesize each R_z gate using RUS circuit [135],

$$\text{Cost}(R_z) = 1.15 \log\left(\frac{1}{\epsilon(R_z)}\right). \tag{4.147}$$

Combining the T gates required for implementation of R_z gates and the T gates used elsewhere in the circuit, we obtain the total number of T gates for the entire circuit as

$$\begin{aligned}
&\{(\lceil \frac{T^{3/2}2^{1/2}\rho^{1/2}}{\epsilon_{\text{total}}^{1/2}} \rceil + 1) \cdot [\lfloor \log\left(L^d\right) + 1 \rfloor + 2(\eta+1)\lfloor \log\left(dL^d\right) + 1 \rfloor] + 2\lceil \frac{T^{3/2}2^{1/2}\rho^{1/2}}{\epsilon_{\text{total}}^{1/2}} \rceil \cdot [(16d^2 \\
&- 16d) \cdot \lfloor \log\left(L^d\right) + 1 \rfloor + 4d(\lfloor \log\left(L^d - L^{d-1}\right) + 1 \rfloor + \lfloor \log\left(L^{d-1}\right) + 1 \rfloor)]\} \cdot \text{Cost}(R_z) \\
&+ (\lceil \frac{T^{3/2}2^{1/2}\rho^{1/2}}{\epsilon_{\text{total}}^{1/2}} \rceil + 1)[4(L^d - \text{Weight}(L^d)) + 8dL^d(\eta - 2) + 8dL^d\eta(12\eta - 3\lfloor \log(\eta+1) \rfloor - 2) \\
&+ 8(\eta+1)(dL^d - \text{Weight}(dL^d))] + 2\lceil \frac{T^{3/2}2^{1/2}\rho^{1/2}}{\epsilon_{\text{total}}^{1/2}} \rceil \cdot [16d(2L^d - \text{Weight}(L^d - L^{d-1}) \\
&- \text{Weight}(L^{d-1}) + L^d(\eta - 2)) + 16d(d-1)(L^d[8 + 2\eta] - 4\text{Weight}(L^d))].
\end{aligned} \tag{4.148}$$

The size of the ancilla register is given by the ancilla qubits required by the electric Hamiltonian, since it requires the most out of all circuit elements. Taking this into account, we obtain the total number of qubits required for the simulation by summing up those in the ancilla, fermionic and gauge-field registers, which is given by

$$L^d + \eta dL^d + 3(\eta+1)dL^d + dL^d - \text{Weight}(dL^d) = [4d(\eta+1) + 1]L^d - \text{Weight}(dL^d). \tag{4.149}$$

Note that in the case where the electric term is implemented using phase gradient operation, the T-gate count changes by

$$\begin{aligned}
&(\lceil \frac{T^{3/2}2^{1/2}\rho^{1/2}}{\epsilon_{total}^{1/2}} \rceil + 1) \cdot [4dL^d \log\left(\frac{2\pi a^{d-2}}{g^2 t}\right) + O(dL^d) - 2(\eta+1)\lfloor \log\left(dL^d\right) + 1 \rfloor \cdot \text{Cost}(R_z) \\
&- 8(\eta+1)(dL^d - \text{Weight}(dL^d))] + \text{Cost}(|\psi_M\rangle),
\end{aligned} \tag{4.150}$$

where the $\text{Cost}(R_z)$ needs to be modified, since $\epsilon(R_z)$ has changed to

$$\begin{aligned}
\epsilon(R_z) = \frac{\epsilon_{\text{total}}}{2}\{(\lceil \frac{T^{3/2}2^{1/2}\rho^{1/2}}{\epsilon_{\text{total}}^{1/2}} \rceil + 1) \cdot \lfloor \log\left(L^d\right) + 1 \rfloor + 2\lceil \frac{T^{3/2}2^{1/2}\rho^{1/2}}{\epsilon_{\text{total}}^{1/2}} \rceil \cdot [(16d^2 - 16d) \\
\cdot \lfloor \log\left(L^d\right) + 1 \rfloor + 4d(\lfloor \log\left(L^d - L^{d-1}\right) + 1 \rfloor + \lfloor \log\left(L^{d-1}\right) + 1 \rfloor)]\}^{-1}.
\end{aligned} \tag{4.151}$$

Further, $\text{Cost}(|\psi_M\rangle)$, which denotes the one-time synthesis costs of the phase gradient gadget state. Here, we choose to use the synthesis method delineated in [147]. Briefly, we apply

Hadamard gates to the register $|00...0\rangle$, and then apply gates $Z, Z^{-1/2}, ..., Z^{-1/2^{M-1}}$. Each Z^{α} gates are synthesized using RUS circuits [135]. Let δ be the error of preparing the gadget state $|\psi_M\rangle$. Then, each gate can incur at most M/δ error, and thus, costs $1.15\log(M/\delta)$, using RUS circuits [135]. Thus, the gadget state preparation costs $1.15M\log(M/\delta)$.

Finally, in this case, the ancilla-qubit count is given by that of the magnetic term and the phase gradient state. As such, the total qubit count is given by

$$L^d + dL^d\eta + (L^d - \text{Weight}(L^d)) + \eta + \log\left(\frac{2\pi a^{d-2}}{g^2 t}\right) = L^d(2+d\eta) + \eta - \text{Weight}(L^d) + \log\left(\frac{2\pi a^{d-2}}{g^2 t}\right). \tag{4.152}$$

4.4 Methodology for Simulating SU(2) Lattice Gauge Theory

In this section, we introduce the non-Abelian SU(2) lattice gauge theory. We follow the same format as in the U(1) case to guide the readers.

4.4.1 Preliminaries

Once again, we aim to simulate our system, governed by four types of Hamiltonian, i.e., the electric Hamiltonian H_E, magnetic Hamiltonian H_B, mass Hamiltonian H_M and kinetic Hamiltonian H_K. Just as in the U(1) case, H_E and H_B act on the links that connect two fermionic sites, H_M acts on the fermions themselves, and H_K acts on nearest pairs of fermionic sites and the links that connect the pairs. Thus, we consider two different types of qubit registers, one for the fields (H_E, H_B, H_K) and the other for the fermions (H_M, H_K).

To simulate this system, we need to choose a good basis for each register, as in the U(1) case. For the fermionic register, we consider an occupation basis. Note however though, in the current case of SU(2), the fermions may assume two different colors in the fundamental representation. As such, the mass Hamiltonian is now of the form

$$\hat{H}_M = m\sum_{\vec{n}}\sum_{\alpha=1}^{2}(-1)^{\vec{n}}\hat{\psi}_{\alpha}^{\dagger}(\vec{n})\hat{\psi}_{\alpha}(\vec{n}), \tag{4.153}$$

where $\alpha \in \{1, 2\}$ denotes the color. This means that we have two subregisters, each for the two different colors, that comprise the full fermion register. For concreteness and simplicity, we use the JW transformation [142] for the rest of this section to map the fermion operators to the qubit operators.

For the link register, just as in the U(1) theory, we need to write down Gauss' law. For SU(2), we have

$$\hat{G}^a(\vec{n}) = \sum_k (\hat{E}^a_L(\vec{n},k) + \hat{E}^a_R(\vec{n},k)) + \hat{Q}^a(\vec{n}), \tag{4.154}$$

where $\hat{G}^a$ is the Gauss operator for the projection axis a. The charge operator for the projection axis a is

$$\hat{Q}^a(\vec{n}) = \sum_{\alpha,\beta=1}^{2} \hat{\psi}^\dagger_\alpha \frac{1}{2} \sigma^a_{\alpha\beta} \hat{\psi}_\beta, \tag{4.155}$$

and it satisfies the SU(2) algebra

$$[\hat{Q}^a, \hat{\psi}_\alpha] = -\frac{1}{2} \sum_{\beta=1}^{2} \sigma^a_{\alpha\beta} \hat{\psi}_\beta. \tag{4.156}$$

$\hat{E}^a_L(\vec{n},k)$ and $\hat{E}^a_R(\vec{n},k)$ are the left and right chromoelectric field operators for the projection axis a, whose mathematical properties will be discussed later. Here, σ^a are Pauli-a matrices, $a \in \{1,2,3\}$ for the three different kinds, which generate the fundamental representation of SU(2). $\hat{\psi}^\dagger_\alpha$ and $\hat{\psi}_\alpha$ are the fermion creation and annihilation operators of different colors α. Similar to the U(1) lattice gauge theory, the SU(2) Hamiltonian commutes with all of the Gauss operators $\hat{G}^a(\vec{n})$, implied by gauge invariance.

The physical, gauge-invariant Hilbert space $\mathcal{H}_G$ is defined through the eigenstates of the Gauss operator:

$$\mathcal{H}_G = \{|\Psi\rangle \in \mathcal{H}_G \,|\, \hat{G}^a(\vec{n})\,|\Psi\rangle = 0,\ \forall \vec{n}, a\}. \tag{4.157}$$

Based on the U(1) case, one may be tempted to write the field terms in the eigenbasis of the chromoelectric field operators. However, as can be straightforwardly checked, the chromoelectric field and Gauss operators do not all commute. Indeed, the complete set of commuting observables on a link is conventionally taken to be $\{\hat{E}^2, \hat{E}^3_L, \hat{E}^3_R\}$, where $\hat{E}^2$ is the total electric field squared, known as the Casimir operator [150], and $\hat{E}^3_L$ and $\hat{E}^3_R$ are the third component of the left and right chromoelectric fields, respectively. Specifically, on each link, the left and right electric fields each forms SU(2) Lie algebras, and they obey the commutation relations

$$[\hat{E}^a_L, \hat{E}^b_L] = i \sum_{c=1}^{3} \epsilon^{abc} \hat{E}^c_L, \tag{4.158}$$

$$[\hat{E}^a_R, \hat{E}^b_R] = i \sum_{c=1}^{3} \epsilon^{abc} \hat{E}^c_R, \tag{4.159}$$

$$[\hat{E}^a_L, \hat{E}^b_R] = 0, \tag{4.160}$$

where ϵ^{abc} is the Levi-Civita symbol. While the left and right field operators commute, we note that they are not independent, and are related by a unitary change of reference frame [105]. Consequently, the squared fields on either side are equal:

$$\hat{E}^2 \equiv \sum_{a=1}^{3} \hat{E}_L^a \hat{E}_L^a = \sum_{a=1}^{3} \hat{E}_R^a \hat{E}_R^a. \tag{4.161}$$

The eigenbasis for this set of operators is an angular momentum basis that describes the quantum state of a link by its irreducible representation or total angular momentum, j, and associated third-component projections at the left (m^L) and right (m^R) end of the link, $\left|j, m^L, m^R\right\rangle$. In this basis, the eigenvalues are given by [151]

$$\hat{E}^2 \left|j, m^L, m^R\right\rangle = j(j+1) \left|j, m^L, m^R\right\rangle, \; j = n/2, \; n \in \mathbb{N}, \tag{4.162}$$

$$\hat{E}^3_{L/R} \left|j, m^L, m^R\right\rangle = m^{L/R} \left|j, m^L, m^R\right\rangle, \; m^{L/R} = -j, -j+1, ..., j. \tag{4.163}$$

Lastly, we express the SU(2) parallel transporters, $\hat{U}_{\alpha\beta}$, in the above angular momentum basis. Dropping the link position index for notational brevity, they are defined according to

$$\begin{aligned}\hat{U}_{\alpha\beta} \left|j, m^L, m^R\right\rangle = \sum_{J=|j-1/2|}^{j+1/2} \sqrt{\frac{2j+1}{2J+1}} \left\langle J, M_L \middle| j, m^L; \frac{1}{2}, \alpha' \right\rangle \left\langle J, M_R \middle| j, m^R; \frac{1}{2}, \beta' \right\rangle \\ \times \left|J, M_L = m^L + \alpha', M_R = m^R + \beta'\right\rangle,\end{aligned} \tag{4.164}$$

where $\langle J, M | j, m, 1/2, \Delta m\rangle$ are the Clebsch–Gordan coefficients for SU(2) in the fundamental representation, and $\alpha'/\beta' = \frac{1}{2}(-\frac{1}{2})$ for $\alpha/\beta = 1(2)$. Note that the Clebsch-Gordan coefficients $c_{\alpha\beta}$ can be evualated using the formulas provided in Table 4.4. The above definition of $\hat{U}_{\alpha\beta}$ operators can be used to directly verify the proper commutation relations

$$[\hat{E}_L^a, \hat{U}_{\alpha\beta}] = \sum_{\gamma=1}^{2} -\frac{1}{2} \sigma^a_{\alpha\gamma} \hat{U}_{\gamma\beta}, \tag{4.165}$$

$$[\hat{E}_R^a, \hat{U}_{\alpha\beta}] = \sum_{\gamma=1}^{2} \frac{1}{2} \hat{U}_{\alpha\gamma} \sigma^a_{\gamma\beta}, \tag{4.166}$$

where α, β, γ, $\delta \in \{1, 2\}$, required by the SU(2) lattice gauge theory. These operators follow the commutation relations of

$$[\hat{U}_{\alpha\beta}, \hat{U}_{\gamma\delta}] = [\hat{U}_{\alpha\beta}, \hat{U}^\dagger_{\gamma\delta}] = 0, \tag{4.167}$$

$$\hat{U}_{22} = \hat{U}^\dagger_{11}, \;\; \hat{U}_{21} = -\hat{U}^\dagger_{12}, \tag{4.168}$$

where $\alpha\beta \neq \gamma\delta$.

Coefficient	Δj	Δm	Formula
c_{11}	$1/2$	$1/2$	$\sqrt{\frac{j+m+1}{2j+1}}$
c_{12}	$1/2$	$-1/2$	$\sqrt{\frac{j-m+1}{2j+1}}$
c_{21}	$-1/2$	$1/2$	$-\sqrt{\frac{j-m}{2j+1}}$
c_{22}	$-1/2$	$-1/2$	$\sqrt{\frac{j+m}{2j+1}}$

Table 4.4: The formulas for Clebsch-Gordan coefficients $\left\langle J=j+\Delta j, M=m+\Delta m \middle| j,m;\frac{1}{2},\Delta m\right\rangle$. They can be efficiently computed classically [8, 9].

4.4.2 Simulation circuit synthesis

Following the encoding described in [6], the infinite-dimensional gauge-field register consists of three subregisters, $|j\rangle, \left|m^L\right\rangle, \left|m^R\right\rangle$, each representing a quantum number. As in the U(1) case, we impose a cutoff on the electric field. In particular, for a given link, $j \in \{0, \frac{1}{2}, ..., \Lambda\}$ and $m^L, m^R \in \{-\Lambda, -\Lambda+\frac{1}{2}, ..., \Lambda\}$. In this basis, we import the definitions of the following useful operators from [6] and slightly modify them for our discussion:

$$\hat{J}^{\pm} = \sum_{j=0}^{\Lambda} \left| j \pm \frac{1}{2} \right\rangle\!\left\langle j \right|, \tag{4.169}$$

$$\hat{N}_{\alpha} = \begin{cases} \sum_{j=0}^{\Lambda} \sqrt{\frac{2j+1}{2j+2}}\, |j\rangle\langle j|, & \alpha = 1, \\ \sum_{j=0}^{\Lambda} \sqrt{\frac{2j+1}{2j}}\, |j\rangle\langle j|, & \alpha = 2, \end{cases} \tag{4.170}$$

$$\hat{M}_{\alpha}^{L/R} = \begin{cases} \sum_{m^{L/R}=-\Lambda}^{\Lambda} \left| m^{L/R} + \frac{1}{2} \right\rangle\!\left\langle m^{L/R} \right|, & \alpha = 1, \\ \sum_{m^{L/R}=-\Lambda}^{\Lambda} \left| m^{L/R} - \frac{1}{2} \right\rangle\!\left\langle m^{L/R} \right|, & \alpha = 2, \end{cases} \tag{4.171}$$

$$\hat{c}_{\alpha\beta}^{L/R} = \sum_{j=0}^{\Lambda} \sum_{m^{L/R}=-\Lambda}^{\Lambda} c_{\alpha\beta}(j, m^{L/R})\, |j\rangle\langle j| \otimes \left| m^{L/R} \right\rangle\!\left\langle m^{L/R} \right|, \tag{4.172}$$

where the quantum numbers j, m^L and m^R are incremented and decremented by $\frac{1}{2}$ at a time, $c_{\alpha\beta}$ are Clebsch-Gordon coefficients, as provided in Table 4.4, $\hat{N}_{\alpha}$ is the normalization operator. The formulas in Table 4.4 could evaluate to complex numbers, if the quantum numbers are outside the ranges given in (4.162) and (4.163), i.e., $\left| j \leq \Lambda, -j \leq m^L \leq j, -j \leq m^R \leq j \right\rangle$. However, the coefficients are real if the quantum numbers are within the allowed ranges. Thus, we set the elements, which correspond to the disallowed states, of the diagonal Clebsch-Gordan operator in (4.172) to zeros, thereby ensuring its Hermiticity. Using the operators defined above, we can

express the $\hat{U}_{\alpha\beta}$ operators in the new basis as

$$\hat{U}_{\alpha\beta} \equiv \hat{M}^L_\alpha \hat{M}^R_\beta [\hat{J}^+ \hat{c}^L_{1\alpha} \hat{c}^R_{1\beta} \hat{N}_1 + \hat{J}^- \hat{c}^L_{2\alpha} \hat{c}^R_{2\beta} \hat{N}_2], \tag{4.173}$$

which can straightforwardly be shown to satisfy (4.168). Note that the encoded $\hat{U}_{\alpha\beta}$ operator in (4.173) only maps states with the allowed quantum numbers to each other, and the disallowed states are in the operator's null space. In order to conveniently represent them on a quantum computer, we map j, m^L, m^R to positive full integers. Thus, $j \in \{0, 1, ..., 2\Lambda\}$ and $m^L, m^R \in \{0, 1, ..., 4\Lambda\}$. Using the binary computational basis, the number of qubits on the subregister $|j\rangle$ is $\eta = \log(2\Lambda + 1)$, and that on the subregisters $\left|m^L\right\rangle$ and $\left|m^R\right\rangle$ is $\eta + 1$. Then, the operators in the qubit basis are written as

$$\hat{J}^\pm \to \sum_{j=0}^{2\Lambda} |j \pm 1\rangle\langle j| \,, \tag{4.174}$$

$$\hat{N}_\alpha \to \begin{cases} \sum_{j=0}^{2\Lambda} \sqrt{\frac{j+1}{j+2}} \, |j\rangle\langle j| \,, & \alpha = 1, \\ \sum_{j=0}^{2\Lambda} \sqrt{\frac{j+1}{j}} \, |j\rangle\langle j| \,, & \alpha = 2, \end{cases} \tag{4.175}$$

$$\hat{M}^{L/R}_\alpha \to \begin{cases} \sum_{m^{L/R}=0}^{4\Lambda} \left|m^{L/R} + 1\right\rangle\left\langle m^{L/R}\right| \,, & \alpha = 1, \\ \sum_{m^{L/R}=0}^{4\Lambda} \left|m^{L/R} - 1\right\rangle\left\langle m^{L/R}\right| \,, & \alpha = 2, \end{cases} \tag{4.176}$$

$$\hat{c}^{L/R}_{\alpha\beta} \to \sum_{j=0}^{2\Lambda} \sum_{m^{L/R}=0}^{4\Lambda} c_{\alpha\beta}(\frac{j}{2}, \frac{m^{L/R}}{2} - \Lambda) \, |j\rangle\langle j| \otimes \left|m^{L/R}\right\rangle\left\langle m^{L/R}\right| . \tag{4.177}$$

The slight modification from the original definitions in [6] is that we have introduced a periodic-wrapping term to each of $\hat{J}^+, \hat{M}^{L/R}_1$, which are now numerically equivalent to the $\hat{U}$ operators from the U(1) model, and can be represented as binary incrementers. Similarly, $\hat{J}^-, \hat{M}^{L/R}_2$, like the $\hat{U}^\dagger$ operators from the U(1) model, and can be represented as binary decrementers. The undesirable effect of the periodic-wrapping terms can be removed by applying circuits that include multiply controlled gates, similar to the U(1) case. On the other hand, the fermionic register is different from the U(1) case in that we now have two different colors of fermions or anti-fermions to consider for each site. We thus allocate two qubits per site, each qubit corresponding to a different color.

Equipped with all the necessary operator definitions and qubit register structure, we now decompose the Hamiltonian into separate parts. Just as in U(1), we have for SU(2) LGT

$$\hat{H} = \sum_{\vec{n}} \left[\hat{D}^{(M)}_{\vec{n}} + \hat{D}^{(E)}_{\vec{n}} + \hat{T}^{(K)}_{\vec{n}} + \hat{L}^{(B)}_{\vec{n}} \right], \tag{4.178}$$

where

$$\hat{D}_{\vec{n}}^{(M)} = \frac{m}{2}(-1)^{\vec{n}}(\hat{Z}_1(\vec{n}) + \hat{Z}_2(\vec{n})), \tag{4.179}$$

$$\hat{D}_{\vec{n}}^{(E)} = \frac{g^2}{2a^{d-2}} \sum_{l=1}^{d} \hat{E}^2(\vec{n}, l) \tag{4.180}$$

are diagonal operators, where $\hat{Z}_i(\vec{n})$, with $i \in \{1, 2\}$, are Pauli-z operators that act on the fermion of color i at site $\vec{n}$, and $(-1)^{\vec{n}}$, is either $+1$ or -1 depending on whether $\vec{n}$ is a fermion or anti-fermion site, respectively, reflective of the use of staggered fermions [105], and

$$\hat{T}_{\vec{n}}^{(K)} = \frac{1}{2a} \sum_{l=1}^{d} \sum_{\alpha,\beta=1}^{2} [\hat{U}_{\alpha\beta}(\vec{n}, l)\hat{\sigma}_{\alpha}^{-}(\vec{n})\hat{\sigma}_{\beta}^{+}(\vec{n} + \hat{l})\hat{\zeta}_{\alpha\beta,\vec{n},l} + h.c.] \tag{4.181}$$

is an off-diagonal operator, which corresponds to kinetic Hamiltonian. The operators $\hat{\sigma}_{\alpha}^{\pm}(\vec{n})$ are Pauli raising and lowering operators on the fermion of color α at site $\vec{n}$. Further, the operators $\hat{\zeta}_{\alpha\beta,\vec{n},l}$ tensor products of $\hat{Z}$, which arise from the JW transformation and have an additional color-dependence when compared to the U(1) case. If we consider a d-dimensional L^d-site lattice, the length of each $\hat{\zeta}_{\alpha\beta,\vec{n},l}$ is $O((2L)^{d-1})$. For brevity, we suppress the $\hat{\zeta}_{\alpha\beta,\vec{n},l}$ operators in the remaining part of the section. The second off-diagonal operator that corresponds to the magnetic Hamiltonian is given by

$$\hat{L}_{\vec{n}}^{(B)} = -\frac{1}{2a^{4-d}g^2} \sum_{i=1}^{d} \sum_{j\neq i;j=1}^{d} \sum_{\alpha,\beta,\delta,\gamma=1}^{2} (\hat{U}_{\alpha\beta}(\vec{n}, i)\hat{U}_{\beta\gamma}(\vec{n} + \hat{i}, j)\hat{U}_{\gamma\delta}^{\dagger}(\vec{n} + \hat{j}, i)\hat{U}_{\delta\alpha}^{\dagger}(\vec{n}, j) + h.c.). \tag{4.182}$$

Assuming we use Suzuki-Trotter formula [22] as our simulation method, each Trotter terms to be implemented then are of the form $e^{i\hat{D}_{\vec{n}}^{(M)}t}, e^{i\hat{D}_{\vec{n}}^{(E)}t}, e^{i\hat{T}_{\vec{n}}^{(K)}t}, e^{i\hat{L}_{\vec{n}}^{(B)}t}$, where t is a sufficiently small number to ensure the Trotter error incurred is within a pre-specified tolerance. In the remaining part of this subsection, we discuss circuit syntheses for each of the four Trotter terms.

Mass term $e^{i\hat{D}_{\vec{n}}^{(M)}t}$

The implementation of this term is straightforward. Two single-qubit $R_z(\theta) = \exp\Big(-i\theta\hat{Z}/2\Big)$ gates, where $\theta = -m(-1)^{\vec{n}}t$, applied to the two qubits, which correspond to the two fermions at site $\vec{n}$, in the site register suffice. As in the implementation of U(1) mass term, we once again use the weight-sum trick [137, 138], except for SU(2), the number of same angle R_z gates increased by a factor of two. Again, briefly, if the original subcircuit applies the same angle R_z gates on p qubits simultaneously, we can reduce the number of R_z gates to $\lfloor \log(p) + 1 \rfloor$, while incurring $p - \text{Weight}(p)$ ancilla qubits and at most $4(p - \text{Weight}(p))$ T gates. For a d-dimensional lattice with L^d lattice sites, $p = 2L^d$.

Electric term $e^{i\hat{D}_{\vec{n}}^{(E)}t}$

Here, we present a method to implement the electric term. $\hat{D}_{\vec{n}}^{(E)}$ is a sum of d commuting terms, and thus, its evolution can be implemented exactly as a product of d sub-evolutions,

$$e^{i\hat{D}_{\vec{n}}^{(E)}t} = \prod_{l=1}^{d} e^{i\frac{g^2t}{2a^{d-2}}\hat{E}^2(\vec{n},l)}. \tag{4.183}$$

Without loss of generality, we only discuss one sub-evolution. For notational convenience, we drop the link location index. Since the eigenvalue equation

$$\begin{aligned}\hat{E}^2\left|j,m^L,m^R\right\rangle &= \frac{j}{2}(\frac{j}{2}+1)\left|j,m^L,m^R\right\rangle \\ &= \frac{1}{4}[(j+1)^2-1]\left|j,m^L,m^R\right\rangle\end{aligned} \tag{4.184}$$

only depends on the subregister $|j\rangle$, and not on the subregisters $\left|m^L\right\rangle$ and $\left|m^R\right\rangle$, we will implement the operator $e^{it\frac{g^2t}{2a^{d-2}}\hat{E}^2}$ according to the eigenvalue equation,

$$e^{i\frac{g^2t}{2a^{d-2}}\hat{E}^2}\left|j\right\rangle = e^{i\frac{g^2t}{8a^{d-2}}(j+1)^2}\left|j\right\rangle, \tag{4.185}$$

where the global phase of $-\frac{g^2t}{8a^{d-2}}$ has been neglected. As in the U(1) electric term, we implement the term by first computing $(j+1)^2$ into an ancilla register, then impart the phase on all links in parallel, using the weight-sum trick, and finally, uncomputing the ancilla register. The T-gate and ancilla-qubit counts for the arithmetic operations are the same as that for the U(1) electric term. Thus, we will simply state the arithmetic costs: $8dL^d[(\eta-2)+\eta(12\eta-3\lfloor\log(\eta+1)\rfloor-2)]$ T gates, $3(\eta+1)dL^d$ ancilla qubits to store $|j+1\rangle$ and $\left|(j+1)^2\right\rangle$ for all links, and $3(\eta+1)-\lfloor\log(\eta+1)\rfloor-1$ reusable workspace ancilla qubits. For more details on the implementation, we refer the readers to Sec. 4.3.2. We now discuss the phase induction. The correct phase can be induced by applying $R_z(2^k\theta)$, where $\theta=\frac{g^2t}{8a^{d-2}}$, on the kth qubit of the $2(\eta+1)-$bit ancilla state, $\left|(j+1)^2\right\rangle$. Hence, there are $2(\eta+1)$ sets of dL^d same-angle R_z rotations to implement, where each set can be effected using the weight-sum trick. Once again, we first compute Weight(dL^d) into the ancilla register, incurring $4(dL^d-\text{Weight}(dL^d))$ T gates and $dL^d-\text{Weight}(dL^d)$ ancilla qubits, and then, applying $\lfloor\log\left(dL^d\right)+1\rfloor$ R_z gates to the ancilla register to induce the right phase.

Alternatively, for simulations with a fixed g^2, d and t, where a can be chosen such that $\frac{g^2t}{8a^{d-2}}=\frac{\pi}{2^M}$ with $M>1$. Then, the electric evolution can be implemented as

$$|j\rangle \mapsto e^{i\frac{\pi}{2^M}(j+1)^2}\left|j\right\rangle. \tag{4.186}$$

Once again, as in U(1), we implement this by first computing $(j+1)^2$ into the ancilla register, and then, impart the phase one link at a time, using the phase gradient operation.

Note that the operations required for the electric term evolution here are almost the same as that in the U(1) case. The only difference is the size of the adders required for the phase gradient operations. The number of T gates needed for the phase gradient adders is $4dL^d \log\left(\frac{8a^{d-2}\pi}{g^2 t}\right) + O(dL^d)$. We refer the readers to 4.3.2 for a detailed discussion on the synthesis costs of the phase-gradient operation.

Kinetic term $e^{i\hat{T}^{(K)}_{\vec{n}}t}$

Here we present a method to implement the kinetic term. This method takes advantage of the fact that the $\hat{U}_{\alpha\beta}$ operators are block-diagonal, just as in method 1 for the U(1) kinetic and magnetic term. For brevity, we drop the site location indices. We rewrite the $\hat{U}_{\alpha\beta}$ operators as follows:

$$\hat{U}_{11} = \sum_{j=0}^{2^\eta-1} \sum_{m^L,m^R=0}^{2^{\eta+1}-1} \sum_{\Delta j=-1}^{1} f_{11}(j,\Delta j,m^L,m^R)\,|j+\Delta j\rangle\langle j| \otimes \left|m^L+1\right\rangle\left\langle m^L\right| \otimes \left|m^R+1\right\rangle\left\langle m^R\right|, \tag{4.187}$$

$$\hat{U}_{12} = \sum_{j=0}^{2^\eta-1} \sum_{m^L,m^R=0}^{2^{\eta+1}-1} \sum_{\Delta j=-1}^{1} f_{12}(j,\Delta j,m^L,m^R)\,|j+\Delta j\rangle\langle j| \otimes \left|m^L+1\right\rangle\left\langle m^L\right| \otimes \left|m^R-1\right\rangle\left\langle m^R\right|, \tag{4.188}$$

$$\hat{U}_{21} = \sum_{j=0}^{2^\eta-1} \sum_{m^L,m^R=0}^{2^{\eta+1}-1} \sum_{\Delta j=-1}^{1} f_{21}(j,\Delta j,m^L,m^R)\,|j+\Delta j\rangle\langle j| \otimes \left|m^L-1\right\rangle\left\langle m^L\right| \otimes \left|m^R+1\right\rangle\left\langle m^R\right|, \tag{4.189}$$

$$\hat{U}_{22} = \sum_{j=0}^{2^\eta-1} \sum_{m^L,m^R=0}^{2^{\eta+1}-1} \sum_{\Delta j=-1}^{1} f_{22}(j,\Delta j,m^L,m^R)\,|j+\Delta j\rangle\langle j| \otimes \left|m^L-1\right\rangle\left\langle m^L\right| \otimes \left|m^R-1\right\rangle\left\langle m^R\right|, \tag{4.190}$$

where

$$f_{11}(j,1,m^L,m^R)=\sqrt{\frac{(\frac{j+m^L}{2}-\Lambda+1)(\frac{j+m^R}{2}-\Lambda+1)}{(j+1)(j+2)}},$$
$$f_{11}(j,-1,m^L,m^R)=\sqrt{\frac{(\frac{j-m^L}{2}+\Lambda)(\frac{j-m^R}{2}+\Lambda)}{j(j+1)}},$$
$$f_{12}(j,1,m^L,m^R)=\sqrt{\frac{(\frac{j+m^L}{2}-\Lambda+1)(\frac{j-m^R}{2}+\Lambda+1)}{(j+1)(j+2)}},$$
$$f_{12}(j,-1,m^L,m^R)=-\sqrt{\frac{(\frac{j-m^L}{2}+\Lambda)(\frac{j+m^R}{2}-\Lambda)}{j(j+1)}},$$
$$f_{21}(j,1,m^L,m^R)=\sqrt{\frac{(\frac{j-m^L}{2}+\Lambda+1)(\frac{j+m^R}{2}-\Lambda+1)}{(j+1)(j+2)}},$$
$$f_{21}(j,-1,m^L,m^R)=-\sqrt{\frac{(\frac{j+m^L}{2}-\Lambda)(\frac{j-m^R}{2}+\Lambda)}{j(j+1)}},$$
$$f_{22}(j,1,m^L,m^R)=\sqrt{\frac{(\frac{j-m^L}{2}+\Lambda+1)(\frac{j-m^R}{2}+\Lambda+1)}{(j+1)(j+2)}},$$
$$f_{22}(j,-1,m^L,m^R)=\sqrt{\frac{(\frac{j+m^L}{2}-\Lambda)(\frac{j+m^R}{2}-\Lambda)}{j(j+1)}}. \tag{4.191}$$

The operators $\hat{U}_{\alpha\beta}$ are similar to the U(1) plaquette operator $\hat{U}\hat{U}\hat{U}^\dagger\hat{U}^\dagger$ in that both of them raise and lower multiple registers simultaneously. The main difference between them is that the matrix elements of $\hat{U}_{\alpha\beta}$ are not all ones. However, we can still employ the trick of splitting the sums over all j,m^L,m^R into series of even and odd j,m^L,m^R, i.e.,

$$\sum_{j=0}^{2^\eta-1}\sum_{m^L,m^R=0}^{2^{\eta+1}-1}=\sum_{j,m^L,m^R\in\{even,odd\}}, \tag{4.192}$$

where $j = 0, 1, ..., 2^\eta - 1$ and $m^{L/R} = 0, 1, ..., 2^{\eta+1} - 1$. Without loss of generality, we consider the all-even series of $\hat{U}_{11}$ with $\Delta j = 1$, i.e.,

$$\begin{aligned}
&\sum_{j,m^L,m^R\ even} f_{11}(j,1,m^L,m^R)\,|j+1\rangle\langle j|\otimes\left|m^L+1\right\rangle\left\langle m^L\right|\otimes\left|m^R+1\right\rangle\left\langle m^R\right| \\
&= \sum_{j,m^L,m^R\ even} f_{11}(j,1,m^L,m^R)\,|j_{\eta-1}...j_1\rangle\langle j_{\eta-1}...j_1|\otimes|j_0=1\rangle\langle j_0=0|\otimes\left|m_\eta^L...m_1^L\right\rangle\left\langle m_\eta^L...m_1^L\right| \\
&\otimes\left|m_0^L=1\right\rangle\left\langle m_0^L=0\right|\otimes\left|m_\eta^R...m_1^R\right\rangle\left\langle m_\eta^R...m_1^R\right|\otimes\left|m_0^R=1\right\rangle\left\langle m_0^R=0\right| \\
&\equiv \hat{D}_{11}(\Delta j=1)\otimes\hat{\sigma}^+\hat{\sigma}^+\hat{\sigma}^+, \qquad (4.193)
\end{aligned}$$

where j_i denotes the ith binary digit of j, likewise for m^L and m^R, and the diagonal part $\hat{D}_{11}(\Delta j = 1)$ is defined via the operator

$$\begin{aligned}
\hat{D}_{\alpha\beta}(\Delta j) = &\sum_{\substack{j_{\eta-1}...j_1\\ m_\eta^L...m_1^L=0\\ m_\eta^R...m_1^R}}^{1} f_{\alpha\beta}(j,\Delta j,m^L,m^R)\,|j_{\eta-1}...j_1\rangle\langle j_{\eta-1}...j_1|\otimes\left|m_\eta^L...m_1^L\right\rangle\left\langle m_\eta^L...m_1^L\right| \\
&\otimes\left|m_\eta^R...m_1^R\right\rangle\left\langle m_\eta^R...m_1^R\right|, \qquad (4.194)
\end{aligned}$$

where $\alpha, \beta \in \{1, 2\}$, $\Delta j \in \{-1, 1\}$, and the zeroth digits of j, m^L, m^R are classically known. The remaining digits can be gleaned from the qubits, and thus, with an abuse of notation for j, $f_{\alpha\beta}(j, \Delta j, m^L, m^R)$ can be evaluated on a quantum computer. By conjugating (4.193) with binary decrementers and incrementers, the three sub-registers of different parities can be addressed, as

shown by the following expressions for $\hat{U}_{11}, \hat{U}_{12}, \hat{U}_{21}$ and $\hat{U}_{22}$:

$$\begin{aligned}\hat{U}_{11} = \sum_{a,b,c=0}^{1} (\hat{J}^+)^a (\hat{M}_1^L)^b (\hat{M}_1^R)^c [\hat{D}_{11}(\Delta j = 1) \otimes \hat{\sigma}^+ \hat{\sigma}^+ \hat{\sigma}^+ \\ + \hat{D}_{11}(\Delta j = -1) \otimes \hat{\sigma}^- \hat{\sigma}^+ \hat{\sigma}^+] (\hat{J}^-)^a (\hat{M}_2^L)^b (\hat{M}_2^R)^c \end{aligned} \tag{4.195}$$

$$\begin{aligned}\hat{U}_{12} = \sum_{a,b,c=0}^{1} (\hat{J}^+)^a (\hat{M}_1^L)^b (\hat{M}_1^R)^c [\hat{D}_{12}(\Delta j = 1) \otimes \hat{\sigma}^+ \hat{\sigma}^+ \hat{\sigma}^- \\ + \hat{D}_{12}(\Delta j = -1) \otimes \hat{\sigma}^- \hat{\sigma}^+ \hat{\sigma}^-] (\hat{J}^-)^a (\hat{M}_2^L)^b (\hat{M}_2^R)^c \end{aligned} \tag{4.196}$$

$$\begin{aligned}\hat{U}_{21} = \sum_{a,b,c=0}^{1} (\hat{J}^+)^a (\hat{M}_1^L)^b (\hat{M}_1^R)^c [\hat{D}_{21}(\Delta j = 1) \otimes \hat{\sigma}^+ \hat{\sigma}^- \hat{\sigma}^+ \\ + \hat{D}_{21}(\Delta j = -1) \otimes \hat{\sigma}^- \hat{\sigma}^- \hat{\sigma}^+] (\hat{J}^-)^a (\hat{M}_2^L)^b (\hat{M}_2^R)^c \end{aligned} \tag{4.197}$$

$$\begin{aligned}\hat{U}_{22} = \sum_{a,b,c=0}^{1} (\hat{J}^+)^a (\hat{M}_1^L)^b (\hat{M}_1^R)^c [\hat{D}_{22}(\Delta j = 1) \otimes \hat{\sigma}^+ \hat{\sigma}^- \hat{\sigma}^- \\ + \hat{D}_{22}(\Delta j = -1) \otimes \hat{\sigma}^- \hat{\sigma}^- \hat{\sigma}^-] (\hat{J}^-)^a (\hat{M}_2^L)^b (\hat{M}_2^R)^c, \end{aligned} \tag{4.198}$$

where, as defined in (4.174) and (4.176), $(\hat{J}^+)^\dagger = \hat{J}^-$ and $(\hat{M}_1^{L/R})^\dagger = \hat{M}_2^{L/R}$. We simplify the notation and express $\hat{U}_{\alpha\beta}$ as

$$\hat{U}_{\alpha\beta} + h.c. = \sum_{a,b,c=0}^{1} (\hat{J}^+)^a (\hat{M}_1^L)^b (\hat{M}_1^R)^c [\sum_{\Delta j=-1}^{1} \hat{D}_{\alpha\beta}(\Delta j) \otimes (\hat{P}_{\alpha\beta}(\Delta j) + h.c.)] (\hat{J}^-)^a (\hat{M}_2^L)^b (\hat{M}_2^R)^c, \tag{4.199}$$

where $\hat{P}_{\alpha\beta}(\Delta j)$ are Pauli operators of the form $\otimes_{i=0}^{2} \hat{\sigma}_i^{\pm}$ that depend on α, β, and Δj.

Using α, r and $\beta, r+1$ to denote two colors α, β at two sites $r, r+1$, without loss of generality, we write

$$\hat{U}_{\alpha\beta} \hat{\sigma}_{\alpha,r}^- \hat{\sigma}_{\beta,r+1}^+ + h.c. = \sum_{a,b,c=0}^{1} (\hat{J}^+)^a (\hat{M}_1^L)^b (\hat{M}_1^R)^c [\sum_{\Delta j=-1}^{1} \hat{D}_{\alpha\beta}(\Delta j) \otimes \hat{F}_{\alpha\beta}(\Delta j)] (\hat{J}^-)^a (\hat{M}_2^L)^b (\hat{M}_2^R)^c, \tag{4.200}$$

where $\hat{F}_{\alpha\beta}(\Delta j) = \hat{P}_{\alpha\beta}(\Delta j) \hat{\sigma}_{\alpha,r}^- \hat{\sigma}_{\beta,r+1}^+ + h.c.$ acts on both the gauge field and fermionic registers.

We may now approximate the kinetic evolution $e^{it\hat{T}_r^{(K)}}$ as

$$e^{it\hat{T}_r^{(K)}} \approx \prod_{(c,b,a)=GC(0)}^{GC(7)} (\hat{J}^+)^a (\hat{M}_1^L)^b (\hat{M}_1^R)^c \left[\prod_{\alpha,\beta=0}^{1} \prod_{\Delta j=-1}^{1} e^{i\frac{t}{2a}\hat{D}_{\alpha\beta}(\Delta j)\hat{F}_{\alpha\beta}(\Delta j)} \right] (\hat{J}^-)^a (\hat{M}_2^L)^b (\hat{M}_2^R)^c, \tag{4.201}$$

where we have minimized the number of binary incrementers and decrementers using the Gray code. In particular, the number of binary incrementers or decrementers is reduced to eight, i.e., four acting on the $\eta-$bit $|j\rangle$ register and four acting on the $(\eta+1)-$bit $\left|m^L\right\rangle$ and $\left|m^R\right\rangle$ registers, which cost $4\cdot 4(\eta-2)+4\cdot 4(\eta+1-2)=32\eta-48$ T gates and $\eta+1$ reuseable ancilla qubits in total [7].

The operators $e^{i\frac{t}{2a}\hat{D}_{\alpha\beta}\hat{F}_{\alpha\beta}(\Delta j)}$ can be implemented by first diagonalizing $\hat{F}_{\alpha\beta}(\Delta j)$ with CNOT gates and two Hadamard gates, just as in the U(1) case. Let us denotes $\hat{\mathcal{D}}_{\alpha\beta}(\Delta)$ as the diagonalized $\hat{F}_{\alpha\beta}(\Delta j)$. In order to understand the action of the diagonalized evolution $e^{i\frac{t}{2a}\hat{D}_{\alpha\beta}\hat{\mathcal{D}}_{\alpha\beta}(\Delta)}$, it is instrumental to first consider a hypothetical scenario where the operator $\hat{D}_{\alpha\beta}$ is an identity operator. Then, in the exponent of $e^{i\frac{t}{2a}\hat{D}_{\alpha\beta}\hat{F}_{\alpha\beta}(\Delta j)}$, we are left with $\hat{F}_{\alpha\beta}(\Delta j)$, i.e. a string of Pauli ladder operators of the kind $\otimes_{i=0}^{4}\sigma_i^{\pm}+h.c.$, which can be reduced to a quadruply-controlled R_x gate with 8 CNOT gates. When we diagonalize the quadruply-controlled R_x gate with a pair of Hadamard gates on the target qubit, the resulting quadruply-controlled R_z gate imparts phases to the states $|11110\rangle$ and $|11111\rangle$, assuming the last qubit is the target. Now, we return to the original case with the operator $\hat{D}_{\alpha\beta}$ restored. Here, instead of the multiply-controlled R_z gate, we have a multiply-controlled diagonal gate. We can implement this via a phase oracle $\hat{O}_{\alpha\beta}^{(\Delta j)}$, which is defined according to

$$\begin{aligned}
&\hat{O}_{\alpha\beta}^{(\Delta j)} \left|j'\right\rangle \left|m^{L\prime}\right\rangle \left|m^{R\prime}\right\rangle \left|f'_{\alpha,r}\right\rangle \left|f'_{\beta,r+1}\right\rangle \\
&\mapsto e^{if_{\alpha\beta}(j',\Delta j,m^{L\prime},m^{R\prime})[\frac{t}{2a}(-1)^{j'_0}m_0^{L\prime}m_0^{R\prime}f'_{\alpha,r}f'_{\beta,r+1}]} \left|j'\right\rangle \left|m^{L\prime}\right\rangle \left|m^{R\prime}\right\rangle \left|f'_{\alpha,r}\right\rangle \left|f'_{\beta,r+1}\right\rangle,
\end{aligned} \tag{4.202}$$

where $j'_0, m_0^{L\prime}, m_0^{R\prime}$ are the zeroth digits of $j', m^{L\prime}, m^{R\prime}$, the first three registers of qubits are for a link, and the latter two registers of length one each denote the fermions of colors α and β that sit at sites r and $r+1$, respectively. This oracle can be implemented efficiently with qRAM [152] in polylogarithmic time. Alternatively, we choose to synthesize this oracle directly as a diagonal gate, which imparts the phase $(-1)^{j'_0}f_{\alpha\beta}(j,\Delta j,m^L,m^R)\frac{t}{2a}$, controlled by $m_0^{L\prime}, m_0^{R\prime}, f'_{\alpha,r}f'_{\beta,r+1}$. In particular, for each link, $f_{\alpha\beta}(j,\Delta j,m^L,m^R)$ can be computed efficiently using fixed point arithmetic circuits [136], and the phases can be induced using R_z gates. We refer readers to sec. 4.4.3 for the detailed implementation.

Hereafter, we assume in our resource analysis that the oracles with different values of $\alpha,\beta,\Delta j$ have the same cost $\mathcal{C}^{(K)}$ per query. Then, the implementation of the kinetic term for a pair of

nearest-neightbor sites and the link joining them costs $32\eta - 48$ T gates and $64\mathcal{C}^{(K)}$. Note that the neglected $\hat{\zeta}$ multi-site Pauli-z operators can be straightforwardly accommodated by conjugating the circuit with controlled-Z gates, as in the U(1) kinetic term. The $\hat{\zeta}$ operators arise from the JW transformation. In order to account for the two fermions per site in the JW transformation, we slightly modify the zigzagging JW path by assigning two nodes, instead of one node in the case of U(1), per lattice site. In total, there are dL^d links, and thus, the cost of implementing the kinetic term on all links is $dL^d(32\eta - 48)$ T gates and $64dL^d\mathcal{C}^{(K)}$.

Magnetic term $e^{i\hat{L}_{\vec{n}}^{(B)}t}$

Here, we extend the block-diagonal decomposition method used for the kinetic term to implement the magnetic term. Once again, we drop the location indices for brevity. The magnetic term for a single plaquette is given by

$$\hat{L}_r^{(B)} = -\frac{1}{2a^{4-d}g^2} \sum_{\alpha\beta\delta\gamma=1}^{2} (\hat{U}_{\alpha\beta}\hat{U}_{\beta\gamma}\hat{U}_{\gamma\delta}^{\dagger}\hat{U}_{\delta\alpha}^{\dagger} + h.c.). \tag{4.203}$$

Now, we rewrite one term in (4.203) as

$$\begin{aligned}
&\hat{U}_{\alpha\beta}\hat{U}_{\beta\gamma}\hat{U}_{\gamma\delta}^{\dagger}\hat{U}_{\delta\alpha}^{\dagger} + h.c. \\
=& \sum_{q_1,q_2,\ldots,q_{12}=0}^{1} (\hat{J}^{(1)+})^{q_1}(\hat{M}_1^{(1),L})^{q_2}(\hat{M}_1^{(1),R})^{q_3}\ldots(\hat{J}^{(4)+})^{q_{10}}(\hat{M}_1^{(4),L})^{q_{11}}(\hat{M}_1^{(4),R})^{q_{12}} \\
&[\sum_{\Delta j_1,\ldots,\Delta j_4=-1}^{1} \hat{D}_{\alpha\beta}(\Delta j_1)\hat{P}_{\alpha\beta}(\Delta j_1)\hat{D}_{\beta\gamma}(\Delta j_2)\hat{P}_{\beta\gamma}(\Delta j_2)\hat{D}_{\gamma\delta}(\Delta j_3)\hat{P}_{\gamma\delta}^{\dagger}(\Delta j_3)\hat{D}_{\delta\alpha}(\Delta j_4)\hat{P}_{\delta\alpha}^{\dagger}(\Delta j_4) + h.c.] \\
&(\hat{J}^{(1)-})^{q_1}(\hat{M}_2^{(1),L})^{q_2}(\hat{M}_2^{(1),R})^{q_3}\ldots(\hat{J}^{(4)-})^{q_{10}}(\hat{M}_2^{(4),L})^{q_{11}}(\hat{M}_2^{(4),R})^{q_{12}} \\
\equiv& \sum_{q_1,q_2,\ldots,q_{12}=0}^{1} (\hat{J}^{(1)+})^{q_1}(\hat{M}_1^{(1),L})^{q_2}\ldots(\hat{M}_1^{(4),R})^{q_{12}} \\
&[\sum_{\Delta j_1,\ldots,\Delta j_4=-1}^{1} \hat{D}_{\alpha\beta\gamma\delta}(\Delta j_1,\Delta j_2,\Delta j_3,\Delta j_4)\hat{P}_{\alpha\beta\gamma\delta}(\Delta j_1,\Delta j_2,\Delta j_3,\Delta j_4)] \\
&(\hat{J}^{(1)-})^{q_1}(\hat{M}_2^{(1),L})^{q_2}\ldots(\hat{M}_2^{(4),R})^{q_{12}},
\end{aligned} \tag{4.204}$$

where the superscript (i) and subindex i of Δj_i are used to differentiate between the four links of a plaquette. Once again, in the implementation $e^{i\hat{L}_r^{(B)}t}$, we can minimize the number of binary

incrementers and decrementers using the Gray code, i.e.,

$$
\begin{aligned}
& e^{i\hat{L}_r^{(B)}t} \\
\approx & \prod_{(q_1,q_2,...q_{12})=GC(0)}^{GC(2^{12}-1)} (\hat{J}^{(1)+})^{q_1}(\hat{M}_1^{(1),L})^{q_2}...(\hat{M}_1^{(4),R})^{q_{12}} \\
& \left[\prod_{\alpha,\beta,\delta,\gamma=1}^{2}\prod_{\Delta j_1,...,\Delta j_4=-1}^{1} e^{it\frac{-1}{2ag^2}\hat{D}_{\alpha\beta\gamma\delta}(\Delta j_1,\Delta j_2,\Delta j_3,\Delta j_4)\hat{P}_{\alpha\beta\gamma\delta}(\Delta j_1,\Delta j_2,\Delta j_3,\Delta j_4)}\right] \\
& (\hat{J}^{(1)-})^{q_1}(\hat{M}_2^{(1),L})^{q_2}...(\hat{M}_2^{(4),R})^{q_{12}}.
\end{aligned} \tag{4.205}
$$

Since $\hat{P}_{\alpha\beta\gamma\delta}$ is a twelve-qubit Pauli operator of the form $\otimes_{i=0}^{11}\hat{\sigma}_i^{\pm} + h.c.$, $e^{it\frac{-1}{2a^{4-d}g^2}\hat{D}_{\alpha\beta\gamma\delta}\hat{P}_{\alpha\beta\gamma\delta}}$ can be diagonalized using twenty-two CNOT and two Hadamard gates into an operator of the form

$$
e^{it\frac{-1}{2a^{4-d}g^2}\hat{D}_{\alpha\beta\gamma\delta}(\Delta j_1,\Delta j_2,\Delta j_3,\Delta j_4)\hat{\mathcal{D}}_{\alpha\beta\gamma\delta}(\Delta j_1,\Delta j_2,\Delta j_3,\Delta j_4)}, \tag{4.206}
$$

where $\hat{\mathcal{D}}_{\alpha\beta\gamma\delta}$ is the diagonalized Pauli part of the operator. Before defining the oracle, we define some useful notations. We denote the state of a plaquette as $\otimes_{i=1}^{4}|j_i\rangle\left|m_i^L\right\rangle\left|m_i^R\right\rangle$, where the values of i represent the four links of a plaquette. Next, the zeroth digits of j_i, m_i^L, m_i^R are denoted as $j_{i,0}, m_{i,0}^L, m_{i,0}^R$, respectively. Further, we define

$$
f_{\alpha\beta\gamma\delta} = f_{\alpha\beta}(j_1,\Delta j_1,m_1^L,m_1^R)f_{\beta\gamma}(j_2,\Delta j_2,m_2^L,m_2^R)f_{\gamma\delta}(j_3,\Delta j_3,m_3^L,m_3^R)f_{\delta\alpha}(j_4,\Delta j_4,m_4^L,m_4^R). \tag{4.207}
$$

As such, the phase oracle is defined as

$$
\begin{aligned}
& \hat{O}_{\alpha\beta\gamma\delta}^{(\Delta j_1,\Delta j_2,\Delta j_3,\Delta j_4)} \otimes_{i=1}^{4}\left|j_i'\right\rangle\left|m_i^{L\prime}\right\rangle\left|m_i^{R\prime}\right\rangle \\
\mapsto & e^{if_{\alpha\beta\gamma\delta}[(\frac{-1}{2a^{4-d}g^2}(-1)^{j_{1,0}'}m_{1,0}^{L\prime}m_{1,0}^{R\prime}j_{2,0}'m_{2,0}^{L\prime}m_{2,0}^{R\prime}j_{3,0}'m_{3,0}^{L\prime}m_{3,0}^{R\prime}j_{4,0}'m_{4,0}^{L\prime}m_{4,0}^{R\prime})]}\otimes_{i=1}^{4}\left|j_i'\right\rangle\left|m_i^{L\prime}\right\rangle\left|m_i^{R\prime}\right\rangle,
\end{aligned} \tag{4.208}
$$

where the primed states are the states that have been acted on by the diagonalization circuit consisting of CNOT and Hadamard gates, and $\left|j_{1,0}'\right\rangle$ is the target qubit of the diagonalized Pauli part of the operator. As in the kinetic term implementation, we can implement this diagonal operator as a phase oracle using qRAM, or directly synthesize it using quantum arithmetic circuits. Once again, we compute $\pm f_{\alpha\beta\gamma\delta}$ using fixed point arithmetic circuits [136], and induce the approximate phases using R_z gates. See 4.4.3 for the implementation details.

Assuming the cost of the oracle $\mathcal{C}^{(B)}$ is the same for all parameters choices, we calculate the implementation cost of $e^{i\hat{L}_r^{(B)}t}$. First, it incurs 2^{12} incrementers or decrementers, of which a significant portion act on the $\eta-$bit $|j\rangle$, but, without affecting complexity arguments, we assume that all the incrementers or decrementers are for the larger register of size $\eta+1$ qubits. As such,

they cost $2^{12}\cdot 4(\eta-1)$ T gates, and $\eta+1$ reusable ancilla qubits. Second, it needs $2^{12}\cdot 16^2 = 1048576$ oracle queries to account for the different combinations of α, β, γ, δ, and Δj_i. In order to obtain the cost of the entire magnetic term, we need to multiply both the T-gate count and the number of oracle queries by the number of plaquettes, $\frac{d(d-1)}{2}L^d$.

4.4.3 Resource requirement estimates

In this section, we analyze the algorithmic and synthesis errors for our simulations. In Sec. 4.4.3 we compute the algorithmic error for the Suzuki-Trotter formula for our SU(2) Hamiltonian. Therein we show our result first, then show a full derivation of it for completeness. In, Sec. 4.4.3, we calculate the error incurred by the arithmetic circuits used to synthesize the oracles. In Sec. 4.4.3 we compute the R_z synthesis error. In Sec. 4.4.3 we combine the two errors discussed in Secs. 4.4.3 and 4.4.3 to report the gate and query complexity, and ancilla requirements.

Trotter errors

As in the U(1) case, we choose to use the second-order PF as our simulation algorithm, and evaluate the commutator bound for the error given in (2.8). The result is

$$||e^{-i\hat{H}T} - \hat{U}_2^r(t)|| \leq r\left(\frac{T}{r}\right)^3 \rho \equiv \epsilon_{Trotter}, \tag{4.209}$$

where

$$\begin{aligned}
\rho = \frac{1}{12}\Big[&\frac{16dL^dm^2}{a} + \frac{dL^dg^4(4\Lambda+3)^2}{32a^{2d-3}} + \frac{2L^dd(d-1)g^2(4\Lambda+3)^2}{a^d} + \frac{8192d(d-1)L^d}{a^{6-d}g^2} \\
&+ \frac{(2048d^2-48d)L^d}{a^3} + \frac{L^d}{a^{12-3d}g^6}(134217728d^3 - 301990160d^2 + 167772432d)\Big] \\
&+ \frac{1}{24}\Big[\frac{mdL^dg^2(4\Lambda+3)}{a^{d-1}} + \frac{(128d^2-16d)mL^d}{a^2} + \frac{256mL^d(d^2-d)}{a^{5-d}g^2} + \frac{8d^2L^dg^2(4\Lambda+3)}{a^d} \\
&+ \frac{32d(d-1)L^d(4\Lambda+3)}{a^3} + \frac{128d(d-1)L^d(4\Lambda+3)}{a^3} + \frac{L^d(4\Lambda+3)}{a^{6-d}g^2}(1024d^3 - 2432d^2 + 1408d) \\
&+ (131072\frac{d^3}{3} - 25728d^2 + 52528\frac{d}{3})\frac{L^d}{a^3} + \frac{L^d}{a^{6-d}g^2}(81920d^3 - 148992d^2 + 67072d) \\
&+ (32768d^3 + 6656d^2 - 39424d)\frac{L^d}{a^{6-d}g^2} + \frac{L^d}{a^{9-2d}g^4}(1835008d^3 - 4456448d^2 + 2621440d) \\
&+ \frac{L^d}{a^{12-3d}g^6}(17179869184\frac{d^5}{5} - 17179869184\frac{d^4}{3} + 49392123904\frac{d^3}{3} - 322659435248\frac{d^2}{3} \\
&+ 1207422766768\frac{d}{15} - 8589934592)\Big].
\end{aligned} \tag{4.210}$$

For completeness, we show below a full derivation of the results shown above. Readers interested in how the results compare with the size of the synthesis error and how, together, they affect our simulation gate complexity should proceed to Secs. 4.4.3 and 4.4.3.

We start our derivation by first ordering the terms in the Hamiltonian $\hat{H}$. As in the U(1) case, we implement the diagonal mass and electric terms first, then the off-diagonal kinetic and magnetic terms. We consider only the kinetic terms for the moment. As in the U(1) case, nearest-neighbor terms do not commute as they collide on fermionic sites. Therefore, we choose to group together the commuting terms, which originate from sites of the same parity, and act on links of the same direction. In particular, using (p, l) to indicate the parity- and direction-dependence of each kinetic term, we order the kinetic terms according to the ordered list, i.e.,

$$\{(p,l)\} \equiv \{(e,1),(o,1),(e,2),(o,2),...,(e,d),(o,d)\}, \tag{4.211}$$

where $p = e, o$ labels the even and odd sites, respectively. For a fixed (p, l), the kinetic terms also depend on the parameters $a, b, c, \Delta j, \alpha, \beta$, which are defined in (4.200). For instance, a, b, c are the exponents on the incrementers and decrementers, which are ordered according to the Gray code, i.e.,

$$\{a,b,c\} \equiv \{GC(q)\}_{q=1}^{7}. \tag{4.212}$$

Each of the remaining parameters, i.e., $\Delta j, \alpha, \beta$, can take on two values. Thus, we order them according to the standard binary code. Representing each kinetic term with the label (p,l,a,b,c,Δj, α,β), the ordering of the kinetic term is then given by the ordered list, i.e.,

$$\mathbb{T} = \{(p,l)\} \times \{a,b,c\} \times \{\Delta j, \alpha, \beta\}, \tag{4.213}$$

where $\times$ is an order-preserving Cartesian product, such that l and β are the variables that vary the slowest and fastest in $\mathbb{T}$, respectively. We denote an element in $\mathbb{T}$ as $\hat{h}_T$, and an element that is implemented after $\hat{h}_T$ as $\hat{h}_{T'}$ with $T' > T$. Each $\hat{h}_T$ with a fixed set of parameters is a sum of $\frac{L^d}{2}$ all even or odd kinetic operators, each of which acts on a link in the fixed direction l originated from an even or odd site $\vec{n}_p$, respectively, and the sites connected by the link, and is represented with $\hat{h}_T(\vec{n}_p, l)$. Moreover, the number of elements in $\mathbb{T}$ is given by

$$|\mathbb{T}| = |\{(p,l)\}| \cdot |\{a,b,c\}| \cdot |\{\Delta j, \alpha, \beta\}| = 2d \cdot 2^3 \cdot 2^3 = 2^7 d. \tag{4.214}$$

We proceed to describe the ordering for the magnetic terms. Magnetic terms acting on neighboring plaquettes do not commute in general. Therefore, we group together the terms that originate from sites of the same parity and act on the same two-dimensional plane. Further, we order the magnetic terms according to the ordered list,

$$\{(p,j,k)\} = \{(e,1,2),(o,1,2),(e,1,3),(o,1,3),...(o,1,d),(e,2,3),...,(e,d-1,d),(o,d-1,d)\}, \tag{4.215}$$

where $p = e, o$ labels the parity, the two directions of a given plane are represented by $j = 1, 2, ..., d-1$ and $k = j+1, ..., d$, and p is the fastest-varying parameter in the list. We represent each magnetic term with a tuple of its parameters, $(p, j, k, q_1, q_2, ..., q_{12}, \Delta j_1, \Delta j_2, \Delta j_3, \Delta j_4, \alpha, \beta, \gamma, \delta)$, as defined in (4.204), and order the magnetic terms according to the following ordered list,

$$\mathbb{L} = \{(p, j, k)\} \times \{q_1, q_2, ..., q_{12}\} \times \{\Delta j_1, \Delta j_2, \Delta j_3, \Delta j_4\} \times \{\alpha, \beta, \gamma, \delta\}, \tag{4.216}$$

where $q_1, q_2, ..., q_{12}$ are ordered using the Gray code, $\Delta j_1, \Delta j_2, \Delta j_3, \Delta j_4$ and $\alpha, \beta, \gamma, \delta$ are ordered according to the binary code. We denote an element in $\mathbb{L}$ as $\hat{h}_L$, and an element that is implemented after $\hat{h}_L$ as $\hat{h}_{L'}$ with $L' > L$. Each $\hat{h}_L$ with a fixed set of parameters is a sum of $\frac{L^d}{2}$ all even or odd magnetic operators, each of which acts on a plaquette on a fixed plane (j, k) originated from an even or odd site $\vec{n}_p$, respectively, and is represented with $\hat{h}_L(\vec{n}_p, j, k)$. Further, the number of elements in $\mathbb{L}$ is given by

$$\begin{aligned} |\mathbb{L}| &= |\{(p, j, k)\}| \cdot |\{q_1, q_2, ..., q_{12}\}| \cdot |\{\Delta j_1, \Delta j_2, \Delta j_3, \Delta j_4\}| \cdot |\{\alpha, \beta, \gamma, \delta\}| \\ &= 2\frac{d(d-1)}{2} \cdot 2^{12} \cdot 2^4 \cdot 2^4 = 2^{20} d(d-1). \end{aligned} \tag{4.217}$$

Finally, the ordering of the terms in the Hamiltonian $\hat{H}$ is given by the following ordered list:

$$\{\hat{H}_x\} = \{\sum_{\vec{n}} \hat{D}_{\vec{n}}^{(M)}, \sum_{\vec{n}} \hat{D}_{\vec{n}}^{(E)}\} \cup \mathbb{T} \cup \mathbb{L}, \tag{4.218}$$

where $\cup$ is denotes the order-preserving union.

We now proceed to evaluate the Trotter error incurred by the second-order PF. First, we focus on the first sum in (2.8), i.e.,

$$\sum_i ||[[\hat{H}_i, \sum_{j>i} \hat{H}_j], \hat{H}_i]|| \leq \sum_{k=1}^{8} ||C_{1,k}||, \tag{4.219}$$

where

$$
\begin{aligned}
C_{1,1} =&[[\sum_{\vec{n}} \hat{D}^{(M)}_{\vec{n}}, \sum_{\vec{n}'} \hat{D}^{(E)}_{\vec{n}'}], \sum_{\vec{n}} \hat{D}^{(M)}_{\vec{n}}], \\
C_{1,2} =&[[\sum_{\vec{n}} \hat{D}^{(M)}_{\vec{n}}, \sum_{\vec{n}'} \hat{T}^{(K)}_{\vec{n}'}], \sum_{\vec{n}} \hat{D}^{(M)}_{\vec{n}}], \\
C_{1,3} =&[[\sum_{\vec{n}} \hat{D}^{(M)}_{\vec{n}}, \sum_{\vec{n}'} \hat{L}^{(B)}_{\vec{n}'}], \sum_{\vec{n}} \hat{D}^{(M)}_{\vec{n}}], \\
C_{1,4} =&[[\sum_{\vec{n}} \hat{D}^{(E)}_{\vec{n}}, \sum_{\vec{n}'} \hat{T}^{(K)}_{\vec{n}'}], \sum_{\vec{n}} \hat{D}^{(E)}_{\vec{n}}], \\
C_{1,5} =&[[\sum_{\vec{n}} \hat{D}^{(E)}_{\vec{n}}, \sum_{\vec{n}'} \hat{L}^{(B)}_{\vec{n}'}], \sum_{\vec{n}} \hat{D}^{(E)}_{\vec{n}}], \\
C_{1,6} =& \sum_{\hat{h}_T \in \mathbb{T}} [[\hat{h}_T, \sum_{\vec{n}} \hat{L}^{(B)}_{\vec{n}}], \hat{h}_T], \\
C_{1,7} =& \sum_{\hat{h}_T \in \mathbb{T}} [[\hat{h}_T, \sum_{\hat{h}_{T'} \in \mathbb{T}; T' > T} \hat{h}_{T'}], \hat{h}_T], \\
C_{1,8} =& \sum_{\hat{h}_L \in \mathbb{L}} [[\hat{h}_L, \sum_{\hat{h}_{L'} \in \mathbb{L}; L' > L} \hat{h}_{L'}], \hat{h}_L].
\end{aligned} \tag{4.220}
$$

Note the following expressions will be useful in the foregoing evaluations of the terms:

$$
||\hat{U}_{\alpha\beta}|| \leq 1, \tag{4.221}
$$

which follows from the fact that in the original, untruncated theory, $\hat{U}_{\alpha\beta}$ are elements of a matrix in the considered unitary gauge group SU(2) in the so-called group element basis [3] [153, 106, 107]. (4.221) still holds after the truncation because of two reasons. First, for all input state $|\psi\rangle$ such that the output state $|\phi\rangle = \hat{U}_{\alpha\beta}|\psi\rangle$ are within the truncated space, the truncated and untruncated $\hat{U}_{\alpha\beta}$ produce the same output. Second, if in the untruncated theory, $|\phi\rangle$ contains any basis state $\left|j, m^L, m^R\right\rangle$ that lies outside the truncated space, $\left|j, m^L, m^R\right\rangle$ will be replaced by 0 in the truncated theory. Thus, the norm of any output state of $\hat{U}_{\alpha\beta}$ in the truncated theory is upper-bounded by that in the untruncated theory.

Using (4.221), we straightforwardly obtain

$$
||\hat{U}_{\alpha\beta} + \hat{U}^{\dagger}_{\alpha\beta}|| \leq 2, \tag{4.222}
$$

$$
||\hat{U}_{\alpha\beta}\hat{\sigma}^{-}_{\alpha}\hat{\sigma}^{+}_{\beta} + \hat{U}^{\dagger}_{\alpha\beta}\hat{\sigma}^{+}_{\alpha}\hat{\sigma}^{-}_{\beta}|| \leq 2. \tag{4.223}
$$

[3] The basis used in this chapter and the group element basis are related via a generalized, non-Abelian Fourier transform [106].

We note that the norm of each term in the block-diagonal decomposition of $\hat{U}_{\alpha\beta}\hat{\sigma}^-_\alpha\hat{\sigma}^+_\beta + \hat{U}^\dagger_{\alpha\beta}\hat{\sigma}^+_\alpha\hat{\sigma}^-_\beta$, as shown in (4.200), is upper-bounded by 2. The reason is that, for each term in the decomposition, the norms of the incrementers, decrementers and Pauli ladder operators are bounded from above by one, and that of the diagonal part $\hat{D}_{\alpha\beta}$, of which the elements are defined via $f_{\alpha\beta}$, is also upper-bounded by one. This implies that

$$||\hat{h}_T(\vec{n}_p, l)|| \leq \frac{1}{a}, \tag{4.224}$$

because $\hat{h}_T(\vec{n}_p, l)$ is, up to a multiplicative factor of $\frac{1}{2a}$, a term in the block-diagonal decomposition.

Furthermore, we consider the terms $\hat{h}_T(\vec{n}, l)$, which act on a pair of nearest-neighbor sites and the link that connects them, i.e., $(\vec{n}, l)$. We denote this set of terms as $\mathbb{T}|_{(\vec{n},l)}$. Then,

$$\sum_{\hat{h}_T(\vec{n},l)\in\mathbb{T}|_{(\vec{n},l)}} \hat{h}_T(\vec{n}, l) = \frac{1}{2a}\sum_{\alpha,\beta=1}^{2} \hat{U}_{\alpha\beta}(\vec{n}, l)\hat{\sigma}^-_\alpha(\vec{n})\hat{\sigma}^+_\beta(\vec{n}+\hat{l}) + h.c., \tag{4.225}$$

which we combine with (4.223) to obtain

$$||\sum_{\substack{\hat{h}_T(\vec{n},l)\in S;\\ S\subseteq\mathbb{T}|_{(\vec{n},l)}}} \hat{h}_T(\vec{n}, l)|| \leq ||\frac{1}{2a}\sum_{\alpha,\beta=1}^{2} \hat{U}_{\alpha\beta}(\vec{n}, l)\hat{\sigma}^-_\alpha(\vec{n})\hat{\sigma}^+_\beta(\vec{n}+\hat{l}) + h.c.|| \leq \frac{4}{a}. \tag{4.226}$$

Similarly, for the magnetic term, we obtain the following bound:

$$||\hat{U}_{\alpha\beta}\hat{U}_{\beta\gamma}\hat{U}^\dagger_{\gamma\delta}\hat{U}^\dagger_{\delta\alpha} + h.c.|| \leq 2||\hat{U}_{\alpha\beta}\hat{U}_{\beta\gamma}\hat{U}^\dagger_{\gamma\delta}\hat{U}^\dagger_{\delta\alpha}|| \leq 2||\hat{U}_{\alpha\beta}||^4 \leq 2, \tag{4.227}$$

where we have used (4.221) for the last equality. As in the kinetic term, the norm of each term in the block-diagonal decomposition of $\hat{U}_{\alpha\beta}\hat{U}_{\beta\gamma}\hat{U}^\dagger_{\gamma\delta}\hat{U}^\dagger_{\delta\alpha} + h.c.$, as shown in (4.204), is bounded by 2. The reason is that the norms of the incrementers, decrementers and Pauli ladder operators are bounded from above by one, and that of the diagonal part $\hat{D}_{\alpha\beta\gamma\delta}$, of which the elements are defined via $f_{\alpha\beta\gamma\delta}$, as defined in (4.207), is also upper-bounded by one. This implies that

$$||\hat{h}_L(\vec{n}_p, i, j)|| \leq \frac{1}{a^{4-d}g^2} \tag{4.228}$$

because each $\hat{h}_L(\vec{n}_p, i, j)$ is a product between $\frac{-1}{2a^{4-d}g^2}$ and a term in (4.204).

Lastly, we consider the terms $\hat{h}_L(\vec{n}, i, j)$, which act on a single plaquette, denoted by $(\vec{n}, i, j)$. Let these terms form a set $\mathbb{L}|_{(\vec{n},i,j)}$. Then,

$$\sum_{\hat{h}_L(\vec{n},i,j)\in\mathbb{L}|_{(\vec{n},i,j)}} \hat{h}_L(\vec{n}, i, j) = \frac{-1}{2a^{4-d}g^2}\sum_{\alpha,\beta,\gamma,\delta=1}^{2} \hat{U}_{\alpha\beta}(\vec{n}, i)\hat{U}_{\beta\gamma}(\vec{n}+\hat{i}, j)\hat{U}^\dagger_{\gamma\delta}(\vec{n}+\hat{j}, i)\hat{U}^\dagger_{\delta\alpha}(\vec{n}, j) + h.c.. \tag{4.229}$$

Using the above relation and (4.227), we obtain

$$||\sum_{\substack{\hat{h}_L(\vec{n},i,j)\in S;\\ S\subseteq\mathbb{L}|_{(\vec{n},i,j)}}}\hat{h}_L(\vec{n},i,j)|| \leq ||\frac{-1}{2a^{4-d}g^2}\sum_{\alpha,\beta,\gamma,\delta=1}^{2}\hat{U}_{\alpha\beta}(\vec{n},i)\hat{U}_{\beta\gamma}(\vec{n}+\hat{i},j)\hat{U}^{\dagger}_{\gamma\delta}(\vec{n}+\hat{j},i)\hat{U}^{\dagger}_{\delta\alpha}(\vec{n},j)+h.c.||$$

$$\leq \frac{16}{a^{4-d}g^2}. \tag{4.230}$$

Whenever these useful expressions (4.221-4.230) are used, we use them without explicit references for brevity.

We now evaluate in the following each term $C_{1,n}$. First, $C_{1,1}$ and $C_{1,3}$ both evaluate to zero because the mass term commutes with both the electric and magnetic terms. $C_{1,2}$ is bounded by

$$\begin{aligned}
&|||[[\sum_{\vec{n}}\hat{D}^{(M)}_{\vec{n}},\sum_{\vec{n}'}\hat{T}^{(K)}_{\vec{n}'}],\sum_{\vec{n}}\hat{D}^{(M)}_{\vec{n}}]|||\\
&\leq \sum_{\vec{n}}\sum_{l=1}^{d}|||[[\hat{D}^{(M)}_{\vec{n}}+\hat{D}^{(M)}_{\vec{n}+\hat{l}},\frac{1}{2a}\sum_{\alpha,\beta=1}^{2}(\hat{U}_{\alpha\beta}(\vec{n},l)\hat{\sigma}^{-}_{\alpha}(\vec{n})\hat{\sigma}^{+}_{\beta}(\vec{n}+\hat{l})+h.c.)],\hat{D}^{(M)}_{\vec{n}}+\hat{D}^{(M)}_{\vec{n}+\hat{l}}]|||\\
&\leq dL^d\sum_{\alpha,\beta=1}^{2}|||[[\frac{m}{2}((-1)^{\vec{n}}\hat{Z}_{\alpha}(\vec{n})+(-1)^{\vec{n}+\hat{l}}\hat{Z}_{\beta}(\vec{n}+\hat{l})),\frac{1}{2a}(\hat{U}_{\alpha\beta}(\vec{n},l)\hat{\sigma}^{-}_{\alpha}(\vec{n})\hat{\sigma}^{+}_{\beta}(\vec{n}+\hat{l})+h.c.)]\\
&\quad,\frac{m}{2}((-1)^{\vec{n}}\hat{Z}_{\alpha}(\vec{n})+(-1)^{\vec{n}+\hat{l}}\hat{Z}_{\beta}(\vec{n}+\hat{l}))]|||\\
&\leq 4dL^d\cdot 4||m||^2||\frac{1}{a}|| = \frac{16dL^dm^2}{a},
\end{aligned} \tag{4.231}$$

where in the first two inequalities, we have used the fact that only the fermionic sites of colors α,β at $\vec{n},\vec{n}+\hat{l}$, respectively, are acted on by the kinetic term with color indices $\alpha\beta$.

Before evaluating $C_{1,4}$, we provide some useful properties about the kinetic operators $\frac{1}{2a}(\hat{U}_{\alpha\beta}(\vec{n},l)\hat{\sigma}^{-}_{\alpha}(\vec{n})\hat{\sigma}^{+}_{\beta}(\vec{n}+\hat{l})+h.c.)$. At the fermionic sites $\vec{n}$ and $\vec{n}+\hat{l}$ of colors α and β, respectively, the kinetic operator takes a computational basis state to another basis state. Acting on the gauge field on the link $(\vec{n},l)$, it maps the subregister $|j\rangle \mapsto |j\pm 1\rangle$, where $j\in[0,2\Lambda]$, up to a multiplicative constant. Therefore, if we evaluate the commutator between an electric and kinetic operator acting on the same link, we obtain

$$\begin{aligned}
&|||[\frac{g^2}{2a^{d-2}}\hat{E}^2(\vec{n},l),\frac{1}{2a}(\hat{U}_{\alpha\beta}(\vec{n},l)\hat{\sigma}^{-}_{\alpha}(\vec{n})\hat{\sigma}^{+}_{\beta}(\vec{n}+\hat{l})+h.c.)]||\\
&\mapsto \frac{g^2}{2a^{d-2}}\frac{1}{4}[(j+1\pm 1)^2-(j+1)^2]||\frac{1}{2a}(\hat{U}_{\alpha\beta}(\vec{n},l)\hat{\sigma}^{-}_{\alpha}(\vec{n})\hat{\sigma}^{+}_{\beta}(\vec{n}+\hat{l})+h.c.)||\\
&\leq \frac{g^2}{8a^{d-2}}(2j+3)\frac{1}{a}\leq\frac{g^2}{8a^{d-1}}(4\Lambda+3),
\end{aligned} \tag{4.232}$$

where in the second line, we have used the eigenvalue equation in (4.184). Using this relation, we evaluate the bound for $C_{1,4}$, and obtain

$$
\begin{aligned}
&|||[[\sum_{\vec{n}} \hat{D}^{(E)}_{\vec{n}}, \sum_{\vec{n}} \hat{T}^{(K)}_{\vec{n}'}], \sum_{\vec{n}} \hat{D}^{(E)}_{\vec{n}}]||| \\
&\leq \sum_{\vec{n}} \sum_{l=1}^{d} \sum_{\alpha,\beta=1}^{2} |||[[\frac{g^2}{2a^{d-2}} \hat{E}^2(\vec{n},l), \frac{1}{2a}(\hat{U}_{\alpha\beta}(\vec{n},l)\hat{\sigma}^-_\alpha(\vec{n})\hat{\sigma}^+_\beta(\vec{n}+\hat{l}) + h.c.)], \frac{g^2}{2a^{d-2}} \hat{E}^2(\vec{n},l)]|| \\
&\mapsto \sum_{\vec{n}} \sum_{l=1}^{d} \sum_{\alpha,\beta=1}^{2} \frac{g^2}{8a^{d-2}}[(j+1\pm 1)^2 - (j+1)^2] \\
&\quad \cdot |||[\frac{g^2}{2a^{d-2}} \hat{E}^2(\vec{n},l), \frac{1}{2a}(\hat{U}_{\alpha\beta}(\vec{n},l)\hat{\sigma}^-_\alpha(\vec{n})\hat{\sigma}^+_\beta(\vec{n}+\hat{l}) + h.c.)]|| \\
&\leq 4dL^d \frac{g^2}{8a^{d-2}}(4\Lambda+3)|||[\frac{g^2}{2a^{d-2}} \hat{E}^2(\vec{n},l), \frac{1}{2a}(\hat{U}_{\alpha\beta}(\vec{n},l)\hat{\sigma}^-_\alpha(\vec{n})\hat{\sigma}^+_\beta(\vec{n}+\hat{l}) + h.c.)]|| \\
&\leq 4dL^d \frac{g^2}{8a^{d-2}}(4\Lambda+3)\frac{g^2}{8a^{d-1}}(4\Lambda+3) = \frac{dL^d g^4 (4\Lambda+3)^2}{32a^{2d-3}}.
\end{aligned}
\tag{4.233}
$$

Next, we evaluate the commutators between the electric and magnetic terms, which are trivial unless the operators act on the same link. Thus, we evaluate the bound for the commutator between the electric and magnetic operators acting on a single plaquette as follows:

$$
\begin{aligned}
&|||[\frac{g^2}{2a^{d-2}}(\hat{E}^2(\vec{n},i) + \hat{E}^2(\vec{n}+\hat{i},j) + \hat{E}^2(\vec{n}+\hat{j},i) + \hat{E}^2(\vec{n},j)) \\
&\quad , -\frac{1}{2a^{4-d}g^2} \sum_{\alpha,\beta,\delta,\gamma=1}^{2} (\hat{U}_{\alpha\beta}(\vec{n},i)\hat{U}_{\beta\gamma}(\vec{n}+\hat{i},j)\hat{U}^\dagger_{\gamma\delta}(\vec{n}+\hat{j},i)\hat{U}^\dagger_{\delta\alpha}(\vec{n},j) + h.c.)]|| \\
&\leq 4 \sum_{\alpha,\beta,\delta,\gamma=1}^{2} |||[\frac{g^2}{2a^{d-2}} \hat{E}^2, -\frac{1}{2a^{4-d}g^2}(\hat{U}_{\alpha\beta}\hat{U}_{\beta\gamma}\hat{U}^\dagger_{\gamma\delta}\hat{U}^\dagger_{\delta\alpha} + h.c.)]|| \\
&\leq 4 \cdot 2^4 \frac{g^2}{2a^{d-2}} \frac{1}{4}[(j+1\pm 1)^2 - (j+1)^2]||\frac{1}{2a^{4-d}g^2}(\hat{U}_{\alpha\beta}\hat{U}_{\beta\gamma}\hat{U}^\dagger_{\gamma\delta}\hat{U}^\dagger_{\delta\alpha} + h.c.)|| \\
&\leq \frac{8}{a^2}(4\Lambda+3),
\end{aligned}
\tag{4.234}
$$

where in the first inequality, we have dropped the location indices for brevity, since the commutator between any of the four electric terms and the magnetic terms shares the same bound, and in the last inequality, we have used (4.227). Now we use the above relation to compute the bound

for $C_{1,5}$, and obtain

$$
\begin{aligned}
&|||[[\sum_{\vec{n}} \hat{D}^{(E)}_{\vec{n}}, \sum_{\vec{n}'} \hat{L}^{(B)}_{\vec{n}'}], \sum_{\vec{n}} \hat{D}^{(E)}_{\vec{n}}]||| \\
&\leq || \sum_{\vec{n}} \sum_{i=1}^{d} \sum_{j\neq i; j=1}^{d} [[\frac{g^2}{2a^{d-2}}(\hat{E}^2(\vec{n},i) + \hat{E}^2(\vec{n}+\hat{i},j) + \hat{E}^2(\vec{n}+\hat{j},i) + \hat{E}^2(\vec{n},j)) \\
&\quad , -\frac{1}{2a^{4-d}g^2} \sum_{\alpha,\beta,\delta,\gamma=1}^{2} (\hat{U}_{\alpha\beta}(\vec{n},i)\hat{U}_{\beta\gamma}(\vec{n}+\hat{i},j)\hat{U}^{\dagger}_{\gamma\delta}(\vec{n}+\hat{j},i)\hat{U}^{\dagger}_{\delta\alpha}(\vec{n},j) + h.c.)] \\
&\quad , \frac{g^2}{2a^{d-2}}(\hat{E}^2(\vec{n},i) + \hat{E}^2(\vec{n}+\hat{i},j) + \hat{E}^2(\vec{n}+\hat{j},i) + \hat{E}^2(\vec{n},j))]|| \\
&\leq L^d \frac{d(d-1)}{2} 4 || \frac{g^2}{2a^{d-2}} \frac{1}{4} [(j+1\pm 1)^2 - (j+1)^2] [\frac{g^2}{2a^{d-2}}(\hat{E}^2(\vec{n},i) + \hat{E}^2(\vec{n}+\hat{i},j) + \hat{E}^2(\vec{n}+\hat{j},i) \\
&\quad + \hat{E}^2(\vec{n},j)), -\frac{1}{2a^{4-d}g^2} \sum_{\alpha,\beta,\delta,\gamma=1}^{2} (\hat{U}_{\alpha\beta}(\vec{n},i)\hat{U}_{\beta\gamma}(\vec{n}+\hat{i},j)\hat{U}^{\dagger}_{\gamma\delta}(\vec{n}+\hat{j},i)\hat{U}^{\dagger}_{\delta\alpha}(\vec{n},j) + h.c.)]|| \\
&\leq L^d \frac{d(d-1)}{2} \frac{g^2}{2a^{d-2}} (4\Lambda+3) \frac{8}{a^2} (4\Lambda+3) = \frac{2L^d d(d-1) g^2 (4\Lambda+3)^2}{a^d},
\end{aligned} \tag{4.235}
$$

where in the second equality, we have used the fact that there are $L^d \frac{d(d-1)}{2}$ plaquettes on the lattice, and in the last inequality, we have used (4.234).

Now, we move on to $C_{1,6}$, which is bounded from above by

$$
\begin{aligned}
&\sum_{\hat{h}_T \in \mathbb{T}} |||[[\hat{h}_T, \sum_{\vec{n}} \hat{L}^{(B)}_{\vec{n}}], \hat{h}_T]||| \\
&\leq \sum_{\hat{h}_T \in \mathbb{T}} |||[[\sum_{\vec{n}_p} \hat{h}_T(\vec{n}_p, l), \sum_{\vec{n}} \hat{L}^{(B)}_{\vec{n}}], \sum_{\vec{n}_p} \hat{h}_T(\vec{n}_p, l)]||| \\
&\leq 2^7 d \frac{L^d}{2} 4 ||\hat{h}_T(\vec{n}_p, l)|| \cdot || \frac{2(d-1)}{2a^{4-d}g^2} \sum_{\alpha,\beta,\gamma,\delta=1}^{2} (\hat{U}_{\alpha\beta}\hat{U}_{\beta\gamma}\hat{U}^{\dagger}_{\gamma\delta}\hat{U}^{\dagger}_{\delta\alpha} + h.c.)|| \cdot ||\hat{h}_T(\vec{n}_p, l)|| \\
&\leq 2^8 L^d d || \frac{1}{a} ||^2 || \frac{32(d-1)}{a^{4-d}g^2} || = \frac{8192 d(d-1) L^d}{a^{6-d} g^2},
\end{aligned} \tag{4.236}
$$

where in the first inequality, the factor of $2^7 d$ outside the norm expression is the cardinality of $\mathbb{T}$, and in the second inequality, the factor $\frac{L^d}{2}$ is the number of even or odd sites $\vec{n}_p$, the factor of $2(d-1)$ is due to the fact that each link $(\vec{n}_p, l)$ is acted on concurrently by a kinetic term and $2(d-1)$ plaquette operators, and we have used (4.70).

Now we consider $C_{1,7}$, which consists of the commutators between kinetic terms. There are two types of commutators; those between (i) terms acting on the same link, and (ii) terms acting

on neighboring links that are connected via the sites. We begin with the analysis of case (i). First, we denote the subset of $\mathbb{T}$ that consists of elements with a fixed parity and direction by $\mathbb{T}|_{(p,l)}$. The number of elements in $\mathbb{T}|_{(p,l)}$ is 2^6, which is the number of remaining free parameters, $a, b, c, \Delta j, \alpha, \beta$. We consider the bound of the commutator, where $\hat{h}_T$ is one of the first $2^6 - 4$ elements of $\mathbb{T}|_{(p,l)}$, and obtain

$$\begin{aligned}
&||[[\hat{h}_T(\vec{n}_p, l), \sum_{\hat{h}_{T'} \in \mathbb{T}|_{(p,l)}; T' > T} \hat{h}_{T'}], \hat{h}_T(\vec{n}_p, l)]|| \\
&\leq 4 \cdot ||\hat{h}_T(\vec{n}_p, l)||^2 || \sum_{\hat{h}_{T'} \in \mathbb{T}|_{(p,l)}; T' > T} \hat{h}_{T'}|| \\
&\leq 4 \cdot ||\hat{h}_T(\vec{n}_p, l)||^2 || \frac{1}{2a} \sum_{\alpha,\beta=1}^{2} (\hat{U}_{\alpha\beta}(\vec{n}_p, l) \hat{\sigma}_\alpha^-(\vec{n}_p) \hat{\sigma}_\beta^+(\vec{n}_p + \hat{l}) + h.c.)|| \\
&\leq 4 \cdot ||\frac{1}{a}||^2 || \frac{4}{a}|| = \frac{16}{a^3},
\end{aligned} \tag{4.237}$$

where in the second inequality, we used (4.226) to obatin the second norm expression. The last 4 elements of $\mathbb{T}|_{(p,l)}$ have the same $a, b, c, \Delta j$. The terms with $\alpha\beta = 11, 22, (12, 21)$ commute with each other, but not with terms with $\alpha\beta = 12, 21, (11, 22)$. Therefore, for the last four $\hat{h}_T \in \mathbb{T}|_{(p,l)}$, which are implemented in the order of $\alpha\beta = 11, 12, 21, 22$, there are four non-trivial commutators, each of which is bounded by

$$4||\frac{1}{a}||^3 = \frac{4}{a^3} \tag{4.238}$$

Therefore, the bound for the commutators that belong to type (i) is given by

$$2d \frac{L^d}{2} [(2^6 - 4)\frac{16}{a^3} + \frac{16}{a^3}] = \frac{976 d L^d}{a^3}, \tag{4.239}$$

where $2d$ is the number of different (p, l), and $\frac{L^d}{2}$ is the number of sites of a given parity. Next, we analyze type (ii), which we further divide into two cases. Case (i) consists of commutators where $\hat{h}_T, \hat{h}_{T'}$ act on links in the same direction, but sites of different parities. Since we implement even terms before odd terms, there are d commutators in case (i). In case (ii), $\hat{h}_T, \hat{h}_{T'}$ act on links in different directions. Let $\hat{h}_T$ and $\hat{h}_{T'}$ be labelled by (p, l) and (p', l'). Then, there are $\sum_{p',p=e}^{o} \sum_{l=1}^{d} \sum_{l'>l,l'=1}^{d} = 4\frac{d(d-1)}{2} = 2d^2 - 2d$ commutators in case (ii). In both types, $\hat{h}_T, \hat{h}_{T'}$ could collide on one or two sites, depending on their respective color indices. If $\hat{h}_T$ and $\hat{h}_{T'}$ are labelled by $\alpha\beta$ and $\beta\alpha$, respectively, then each $\hat{h}_T$ will collide with two $\hat{h}_{T'}$ on sites of both colors α and β. If $\hat{h}_T$ is labelled by $\alpha\beta$, and $\hat{h}_{T'}$ by $\beta\beta$ ($\alpha\alpha$), then each $\hat{h}_T$ will collide with one $\hat{h}_{T'}$ on the site of color β (α). In the former scenario, where collisions occur at two sites, the bound for each commutator is

$$4 \cdot ||\hat{h}_T(\vec{n}_p, l)||^2 \cdot ||2 \cdot \frac{1}{2a} (\hat{U}_{\beta\alpha} \hat{\sigma}_\beta^- \hat{\sigma}_\alpha^+ + h.c.)|| \leq \frac{8}{a^3}. \tag{4.240}$$

In the latter scenario, where there is a collision on one site, the bound for each commutator is

$$4 \cdot ||\hat{h}_T(\vec{n}_p, l)||^2 \cdot ||\frac{1}{2a} \sum_{\alpha'\beta'=\beta\beta}^{\alpha\alpha} (\hat{U}_{\alpha'\beta'} \hat{\sigma}^-_{\alpha'} \hat{\sigma}^+_{\beta'} + h.c.)|| \leq \frac{8}{a^3}. \tag{4.241}$$

The bound for the commutators in type (ii) is thus

$$\frac{(8+8)}{a^3} 2^6 \cdot (2d^2 - 2d + d) \frac{L^d}{2} = \frac{(2048d^2 - 1024d)L^d}{a^3}. \tag{4.242}$$

As such, the bound for $C_{1,7}$ is

$$\frac{(2048d^2 - 48d)L^d}{a^3}. \tag{4.243}$$

Finally, we consider $C_{1,8}$, which consists of the commutators between magnetic terms. We separate the terms into two cases: cases (i) and (ii), respectively, consist of intra- and inter-plaquette commutators, where $\hat{h}_L$ and $\hat{h}_{L'}$ act on the same and different plaquettes, respectively. We first examine case (i). We denote the subset of $\mathbb{L}$ that consists of elements with a fixed parity and two-dimensional plane by $\mathbb{L}|_{(p,j,k)}$. As such, the number of elements in $\mathbb{L}|_{(p,j,k)}$, 2^{20}, is the number of remaining free parameters. We compute the bound of the commutator, in which $\hat{h}_L$ is amongst the first $2^{20} - 16$ elements of $\mathbb{L}|_{(p,j,k)}$, and obtain

$$\begin{aligned} &|||[\hat{h}_L(p,j,k), \sum_{\hat{h}_{L'} \in \mathbb{L}|_{(p,j,k)}; L' > L} \hat{h}_{L'}], \hat{h}_L(p,j,k)]|| \\ &\leq 4||\hat{h}_L(\vec{n}_p, j, k)||^2 \cdot ||\frac{-1}{2a^{4-d}g^2} (\sum_{\alpha,\beta,\gamma,\delta=1}^{2} \hat{U}_{\alpha\beta} \hat{U}_{\beta\gamma} \hat{U}^\dagger_{\gamma\delta} \hat{U}^\dagger_{\delta\alpha} + h.c.)|| = \frac{4 \cdot 16}{a^{12-3d}g^6} = \frac{64}{a^{12-3d}g^6}. \end{aligned} \tag{4.244}$$

Since the last sixteen terms all have different color indices $\alpha\beta\gamma\delta$, they do not commute with each other in general. Thus, the bound for the last 16 terms is

$$\sum_{q=15}^{1} 4 \cdot ||\hat{h}_L(\vec{n}_p, j, k)|| \cdot ||q \cdot \hat{h}_{L'}(\vec{n}_p, j, k)|| \cdot ||\hat{h}_L(\vec{n}_p, j, k)|| = 480||\hat{h}_L(\vec{n}_p, j, k)||^3 = \frac{480}{a^{12-3d}g^6} \tag{4.245}$$

Therefore, the bound for case-(i) terms is

$$L^d \frac{d(d-1)}{2} [(2^{20} - 16) \frac{64}{a^{12-3d}g^6} + \frac{480}{a^{12-3d}g^6}] = \frac{33554160 L^d d(d-1)}{a^{12-3d}g^6}, \tag{4.246}$$

We divide case (ii) into two types; those where (i) $\hat{h}_L$ and $\hat{h}_{L'}$ act on neighboring plaquettes with different parities on the same two-dimensional plane, and those where (ii) $\hat{h}_L$ and $\hat{h}_{L'}$ act

(p,k,l), $k<l$	colliding tuples	# tuples
1	(p,k,j), $j>l$	$d-l$
2	(p,l,j), $j>l$	$d-l$
3	(p,j,l), $k<j<l$	$l-k-1$
4	(p',k,j), $j>l$	$d-l$
5	(p',l,j), $j>l$	$d-l$
6	(p',j,l), $k<j<l$	$l-k-1$

Table 4.5: The number of tuples that share a dimension with (p,k,l) and are implemented after (p,k,l) in the ordered list $\mathbb{L}$. Each term $\hat{h}_L \in \mathbb{L}$ partially labelled by (p,k,l) collides on two links with two $\hat{h}_{L'}$ terms, respectively, labelled with tuples in the second column. Here, $p,p' \in \{even, odd\}$ and $p \neq p'$. Therefore, the total number colliding tuples is given by $\sum_{k=1}^{d-1}\sum_{l>k}^{d} 8d - 4(l+k) - 4 = 2d^3 - 6d^2 + 4d$.

on plaquettes that share only one common dimension. In type (i), the number of pairs of $\hat{h}_L$ and $\hat{h}_{L'}$ is the number of two-dimensional planes, $\frac{d(d-1)}{2}$. Since we have chosen to implement even terms before odd terms, each commutator is bounded by

$$4 \cdot ||\hat{h}_L(\vec{n}_e, j, k)||^2 \cdot ||4 \cdot 16\hat{h}_{L'}(\vec{n}_o, j, k)|| = \frac{256}{a^{12-3d}g^6}, \tag{4.247}$$

where in the second norm expression, the factor of 4 is due to the fact that there are four $\hat{h}_{L'}(\vec{n}_o)$ terms acting on the four links, which form the plaquette that $\hat{h}_L(\vec{n}_e)$ acts on, and the factor of 16 is the number of different color indices of the magnetic operators. There are $2d^3 - 6d^2 + 4d$ pairs of $\hat{h}_L$ and $\hat{h}_{L'}$ in type (ii). See Table 4.5 for the explanation. Each commutator is bounded by

$$4 \cdot ||\hat{h}_L(\vec{n}_p, j, k)||^2 \cdot ||2 \cdot 16\hat{h}_{L'}(\vec{n}'_p, j', k')|| = \frac{128}{a^{12-3d}g^6}, \tag{4.248}$$

where in the second norm expression, the factor of 2 is due to the fact that there are two $\hat{h}_{L'}$ that collide with each $\hat{h}_L$. Therefore, the bound for case-(ii) terms is given by

$$2^{20}\frac{L^d}{2}[\frac{256}{a^{12-3d}g^6}\frac{d(d-1)}{2} + \frac{128}{a^{12-3d}g^6}(2d^3 - 6d^2 + 4d)] = \frac{67108864L^d}{a^{12-3d}g^6}(2d^3 - 5d^2 + 3d) \tag{4.249}$$

In total, $C_{1,8}$ is bounded by

$$\frac{L^d}{a^{12-3d}g^6}(134217728d^3 - 301990160d^2 + 167772432d). \tag{4.250}$$

Next, we analyze the second sum in (2.8), which is given by

$$\sum_i ||[[\hat{H}_i, \sum_{j>i}\hat{H}_j], \sum_{k>i}\hat{H}_k]|| \leq \sum_{n=1}^{12} ||C_{2,n}||, \tag{4.251}$$

where

$$
\begin{aligned}
C_{2,1} =&[[\sum_{\vec{n}} \hat{D}^{(M)}_{\vec{n}}, \sum_{\vec{n}'} \hat{T}^{(K)}_{\vec{n}'}], \sum_{\vec{n}''} \hat{D}^{(E)}_{\vec{n}''}], \\
C_{2,2} =&[[\sum_{\vec{n}} \hat{D}^{(M)}_{\vec{n}}, \sum_{\vec{n}'} \hat{T}^{(K)}_{\vec{n}'}], \sum_{\vec{n}''} \hat{T}^{(K)}_{\vec{n}''}], \\
C_{2,3} =&[[\sum_{\vec{n}} \hat{D}^{(M)}_{\vec{n}}, \sum_{\vec{n}'} \hat{T}^{(K)}_{\vec{n}'}], \sum_{\vec{n}''} \hat{L}^{(B)}_{\vec{n}''}], \\
C_{2,4} =&[[\sum_{\vec{n}} \hat{D}^{(E)}_{\vec{n}}, \sum_{\vec{n}'} \hat{T}^{(K)}_{\vec{n}'}], \sum_{\vec{n}''} \hat{T}^{(K)}_{\vec{n}''}], \\
C_{2,5} =&[[\sum_{\vec{n}} \hat{D}^{(E)}_{\vec{n}}, \sum_{\vec{n}'} \hat{T}^{(K)}_{\vec{n}'}], \sum_{\vec{n}''} \hat{L}^{(B)}_{\vec{n}''}], \\
C_{2,6} =&[[\sum_{\vec{n}} \hat{D}^{(E)}_{\vec{n}}, \sum_{\vec{n}'} \hat{L}^{(B)}_{\vec{n}'}], \sum_{\vec{n}''} \hat{T}^{(K)}_{\vec{n}''}], \\
C_{2,7} =&[[\sum_{\vec{n}} \hat{D}^{(E)}_{\vec{n}}, \sum_{\vec{n}'} \hat{L}^{(B)}_{\vec{n}'}], \sum_{\vec{n}''} \hat{L}^{(B)}_{\vec{n}''}], \\
C_{2,8} =& \sum_{\hat{h}_T \in \mathbb{T}} [[\hat{h}_T, \sum_{\hat{h}_{T'} \in \mathbb{T}; T' > T} \hat{h}_{T'}], \sum_{\hat{h}_{T''} \in \mathbb{T}; T'' > T} \hat{h}_{T''}], \\
C_{2,9} =& \sum_{\hat{h}_T \in \mathbb{T}} [[\hat{h}_T, \sum_{\hat{h}_{T'} \in \mathbb{T}; T' > T} \hat{h}_{T'}], \sum_{\vec{n}} \hat{L}^{(B)}_{\vec{n}}], \\
C_{2,10} =& \sum_{\hat{h}_T \in \mathbb{T}} [[\hat{h}_T, \sum_{\vec{n}'} \hat{L}^{(B)}_{\vec{n}'}], \sum_{\hat{h}_{T'} \in \mathbb{T}; T' > T} \hat{h}_{T'}], \\
C_{2,11} =& \sum_{\hat{h}_T \in \mathbb{T}} [[\hat{h}_T, \sum_{\vec{n}} \hat{L}^{(B)}_{\vec{n}}], \sum_{\vec{n}'} \hat{L}^{(B)}_{\vec{n}'}], \\
C_{2,12} =& \sum_{\hat{h}_L \in \mathbb{L}} [[\hat{h}_L, \sum_{\hat{h}_{L'} \in \mathbb{L}; L' > L} \hat{h}_{L'}], \sum_{\hat{h}_{L''} \in \mathbb{L}; L'' > L} \hat{h}_{L''}].
\end{aligned} \tag{4.252}
$$

For $C_{2,1}$, we obtain the bound

$$
\begin{aligned}
&|||[\sum_{\vec{n}} \hat{D}^{(M)}_{\vec{n}}, \sum_{\vec{n}'} \hat{T}^{(K)}_{\vec{n}'}], \sum_{\vec{n}''} \hat{D}^{(E)}_{\vec{n}''}]||| \\
&\leq ||\sum_{\vec{n}} \sum_{l=1}^{d} \sum_{\alpha,\beta=1}^{2} [[\frac{m}{2}((-1)^{\vec{n}} \hat{Z}_\alpha(\vec{n}) + (-1)^{\vec{n}+\hat{l}} \hat{Z}_\beta(\vec{n}+\hat{l})), \frac{1}{2a}(\hat{U}_{\alpha\beta}(\vec{n},l)\hat{\sigma}^-_\alpha(\vec{n})\hat{\sigma}^+_\beta(\vec{n}) + h.c.)] \\
&\quad , \frac{g^2}{2a^{d-2}} \hat{E}^2(\vec{n},l)]|| \\
&\leq 4dL^d || \frac{g^2}{2a^{d-2}} \frac{1}{4}[(j+1\pm 1)^2 - (j+1)^2][\frac{m}{2}((-1)^{\vec{n}} \hat{Z}_\alpha(\vec{n}) + (-1)^{\vec{n}+\hat{l}} \hat{Z}_\beta(\vec{n}+\hat{l})) \\
&\quad , \frac{1}{2a}(\hat{U}_{\alpha\beta}(\vec{n},l)\hat{\sigma}^-_\alpha(\vec{n})\hat{\sigma}^+_\beta(\vec{n}) + h.c.)]|| \\
&\leq 4dL^d \frac{g^2}{8a^{d-2}}(4\Lambda+3)|||[\frac{m}{2}((-1)^{\vec{n}} \hat{Z}_\alpha(\vec{n}) + (-1)^{\vec{n}+\hat{l}} \hat{Z}_\beta(\vec{n}+\hat{l})), \frac{1}{2a}(\hat{U}_{\alpha\beta}(\vec{n},l)\hat{\sigma}^-_\alpha(\vec{n})\hat{\sigma}^+_\beta(\vec{n}) + h.c.)]|| \\
&\leq \frac{dL^d g^2(4\Lambda+3)}{2a^{d-2}} 2||m|| \cdot ||\frac{1}{a}|| = \frac{mdL^d g^2(4\Lambda+3)}{a^{d-1}},
\end{aligned} \tag{4.253}
$$

where, in the first inequality, we used the fact that the mass terms at $\vec{n}, \vec{n}+\hat{l}$, of which the respective colors are not α, β, commute with the kinetic term with color indices $\alpha\beta$.

For $C_{2,2}$, we divide the commutators up into two types; type (i) where the kinetic terms in the inner commutator $\hat{T}^{(K)}_{\vec{n}'}$, and outer commutator $\hat{T}^{(K)}_{\vec{n}''}$ act on the same links, and type (ii) where $\hat{T}^{(K)}_{\vec{n}'}$ and $\hat{T}^{(K)}_{\vec{n}''}$ act on different links. We evaluate the bound for type (i), and obtain

$$
\begin{aligned}
&||\sum_{\vec{n}} \sum_{l=1}^{d} \sum_{\alpha,\beta=1}^{2} [[\frac{m}{2}((-1)^{\vec{n}} \hat{Z}_\alpha(\vec{n}) + (-1)^{\vec{n}+\hat{l}} \hat{Z}_\beta(\vec{n}+\hat{l})), \frac{1}{2a}(\hat{U}_{\alpha\beta}(\vec{n},l)\hat{\sigma}^-_\alpha(\vec{n})\hat{\sigma}^+_\beta(\vec{n}+\hat{l}) + h.c.)] \\
&, \frac{1}{2a} \sum_{\alpha'\beta'} (\hat{U}_{\alpha',\beta'}(\vec{n},l)\hat{\sigma}^-_{\alpha'}(\vec{n})\hat{\sigma}^+_{\beta'}(\vec{n}+\hat{l}) + h.c.)]|| \leq 4dL^d \cdot 4||m|| \cdot ||\frac{1}{a}|| \cdot ||3\frac{1}{a}|| = \frac{48mdL^d}{a^2},
\end{aligned} \tag{4.254}
$$

where the factor of three in the third norm expression in the last line is due to the fact that one of the four kinetic terms commute with the inner commutator. In particular, if $\alpha' = \alpha$ or $\beta' = \beta$, then the fermionic part of the outer kinetic term does not commute with the mass term. However, if $\alpha'\beta'$ and $\alpha\beta$ do not share any common color, then the fermionic operators in the inner and outer commutators act on different registers representing fermionic sites of different colors, the two gauge field operators commute due to (4.168), and thus the commutator vanishes.

We split type (ii) into two cases. Suppose the color indices of $\hat{T}^{(K)}_{\vec{n}'}$ is $\alpha\beta$. Then, in case (i), $\hat{T}^{(K)}_{\vec{n}''}$ has color indices $\beta\alpha$, and in case (ii), $\hat{T}^{(K)}_{\vec{n}''}$ has color indices $\beta\beta$ or $\alpha\alpha$. The bound for case

(i) is as follows:

$$||\sum_{\vec{n}}\sum_{l=1}^{d}\sum_{\alpha,\beta=1}^{2}[[\frac{m}{2}((-1)^{\vec{n}}\hat{Z}_{\alpha}(\vec{n})+(-1)^{\vec{n}+\hat{l}}\hat{Z}_{\beta}(\vec{n}+\hat{l})),\frac{1}{2a}(\hat{U}_{\alpha\beta}(\vec{n},l)\hat{\sigma}^{-}_{\alpha}(\vec{n})\hat{\sigma}^{+}_{\beta}(\vec{n}+\hat{l})+h.c.)]$$
$$,\frac{4d-2}{2a}(\hat{U}_{\beta\alpha}\hat{\sigma}^{-}_{\beta}\hat{\sigma}^{+}_{\alpha}+h.c.)]||| \leq 4dL^{d}\cdot 4||m||\cdot||\frac{1}{a}||\cdot||\frac{(4d-2)}{a}|| = \frac{(64d^{2}-32d)mL^{d}}{a^{2}}, \quad (4.255)$$

where the factor of $4d-2$, in front of the third term of the commutator, is the number of $\hat{U}_{\beta\alpha}\hat{\sigma}^{-}_{\beta}\hat{\sigma}^{+}_{\alpha}+h.c.$ that collide with each $\hat{U}_{\alpha\beta}\hat{\sigma}^{-}_{\alpha}\hat{\sigma}^{+}_{\beta}+h.c.$. The bound for case (ii) is

$$||\sum_{\vec{n}}\sum_{l=1}^{d}\sum_{\alpha,\beta=1}^{2}[[\frac{m}{2}((-1)^{\vec{n}}\hat{Z}_{\alpha}(\vec{n})+(-1)^{\vec{n}+\hat{l}}\hat{Z}_{\beta}(\vec{n}+\hat{l})),\frac{1}{2a}(\hat{U}_{\alpha\beta}(\vec{n},l)\hat{\sigma}^{-}_{\alpha}(\vec{n})\hat{\sigma}^{+}_{\beta}(\vec{n}+\hat{l})+h.c.)]$$
$$,\frac{2d-1}{2a}\sum_{\alpha'\beta'=\beta\beta}^{\alpha\alpha}(\hat{U}_{\alpha'\beta'}\hat{\sigma}^{-}_{\alpha'}\hat{\sigma}^{+}_{\beta'}+h.c.)]|| \leq 4dL^{d}\cdot 4||m||\cdot||\frac{1}{a}||\cdot||\frac{2(2d-1)}{a}|| = \frac{(64d^{2}-32d)mL^{d}}{a^{2}}, \quad (4.256)$$

where the factor of $2d-1$, in front of the third term of the commutator, is the number of $\hat{U}_{\alpha'\beta'}\hat{\sigma}^{-}_{\alpha'}\hat{\sigma}^{+}_{\beta'}+h.c.$, with $\alpha'\beta'=\beta\beta$ or $\alpha\alpha$, that collide with each $\hat{U}_{\alpha\beta}\hat{\sigma}^{-}_{\alpha}\hat{\sigma}^{+}_{\beta}+h.c.$. Adding up the bounds for type (i) and (ii), we obtain the bound for the $C_{2,2}$ as follows:

$$\frac{(128d^{2}-16d)mL^{d}}{a^{2}}. \quad (4.257)$$

The bound for $C_{2,3}$ is given by

$$|||[[\sum_{\vec{n}}\hat{D}^{(M)}_{\vec{n}},\sum_{\vec{n}'}\hat{T}^{(K)}_{\vec{n}'}],\sum_{\vec{n}''}\hat{L}^{(B)}_{\vec{n}''}]|||$$
$$\leq ||\sum_{\vec{n}}\sum_{l=1}^{d}\sum_{\alpha,\beta=1}^{2}[[\frac{m}{2}((-1)^{\vec{n}}\hat{Z}_{\alpha}(\vec{n})+(-1)^{\vec{n}+\hat{l}}\hat{Z}_{\beta}(\vec{n}+\hat{l})),\frac{1}{2a}(\hat{U}_{\alpha\beta}(\vec{n},l)\hat{\sigma}^{-}_{\alpha}(\vec{n})\hat{\sigma}^{+}_{\beta}(\vec{n}+\hat{l})+h.c.)]$$
$$,\sum_{\vec{n}''}\hat{L}^{(B)}_{\vec{n}''}]||| \quad (4.258)$$
$$\leq 4dL^{d}\cdot 4||m||\cdot||\frac{1}{a}||\cdot||\frac{2(d-1)}{2a^{4-d}g^{2}}\sum_{\alpha,\beta,\gamma,\delta=1}^{2}(\hat{U}_{\alpha\beta}\hat{U}_{\beta\gamma}\hat{U}^{\dagger}_{\gamma\delta}\hat{U}^{\dagger}_{\delta\alpha}+h.c.)|| \leq \frac{256mL^{d}(d^{2}-d)}{a^{5-d}g^{2}},$$

where $2(d-1)$ is the number of plaquettes that consist of the link $(\vec{n},l)$.

Next, we consider $C_{2,4}$. We divide the commutators up into two cases the same way we did for $C_{2,2}$. The bound for case (i), where the kinetic terms act on the same links, is given by

$$\begin{aligned}
&||\sum_{\vec{n}}\sum_{l=1}^{d}\sum_{\alpha,\beta=1}^{2}[[\frac{g^2}{2a^{d-2}}\hat{E}^2(\vec{n},l),\frac{1}{2a}(\hat{U}_{\alpha\beta}(\vec{n},l)\hat{\sigma}^-_{\alpha}(\vec{n})\hat{\sigma}^+_{\beta}(\vec{n}+\hat{l})+h.c.)]\\
&,\frac{1}{2a}\sum_{\alpha',\beta'=1}^{2}(\hat{U}_{\alpha'\beta'}(\vec{n},l)\hat{\sigma}^-_{\alpha'}(\vec{n})\hat{\sigma}^+_{\beta'}(\vec{n}+\hat{l})+h.c.)]||\\
&\leq 4dL^d\cdot 2||[\frac{g^2}{2a^{d-2}}\hat{E}^2(\vec{n},l),\frac{1}{2a}(\hat{U}_{\alpha\beta}(\vec{n},l)\hat{\sigma}^-_{\alpha}(\vec{n})\hat{\sigma}^+_{\beta}(\vec{n}+\hat{l})+h.c.)]||\\
&\quad\cdot||\frac{1}{2a}\sum_{\alpha',\beta'=1}^{2}(\hat{U}_{\alpha'\beta'}(\vec{n},l)\hat{\sigma}^-_{\alpha'}(\vec{n})\hat{\sigma}^+_{\beta'}(\vec{n}+\hat{l})+h.c.)||\\
&\leq 8dL^d\frac{g^2}{8a^{d-1}}(4\Lambda+3)\cdot\frac{4}{a}=\frac{4g^2dL^d(4\Lambda+3)}{a^d},
\end{aligned}\tag{4.259}$$

where we have used (4.232) to evaluate the first norm expression in the first inequality. As in $C_{2,2}$, we separate case (ii), where the kinetic terms act on different links, into two types. The bound for type (i), where the color indices for the outer kinetic term is $\beta\alpha$, is given by

$$\begin{aligned}
&||\sum_{\vec{n}}\sum_{l=1}^{d}\sum_{\alpha,\beta=1}^{2}[[\frac{g^2}{2a^{d-2}}\hat{E}^2(\vec{n},l),\frac{1}{2a}(\hat{U}_{\alpha\beta}(\vec{n},l)\hat{\sigma}^-_{\alpha}(\vec{n})\hat{\sigma}^+_{\beta}(\vec{n}+\hat{l})+h.c.)]\\
&,\frac{4d-2}{2a}(\hat{U}_{\beta\alpha}\hat{\sigma}^-_{\beta}\hat{\sigma}^+_{\alpha}+h.c.)]||\\
&\leq 4dL^d\cdot 2\frac{g^2}{8a^{d-1}}(4\Lambda+3)\cdot\frac{4d-2}{a}=\frac{(4d^2-2d)L^dg^2(4\Lambda+3)}{a^d}.
\end{aligned}\tag{4.260}$$

For type (ii), where the color indices for the outer kinetic term is $\beta\beta$ or $\alpha\alpha$, we obtain the following bound:

$$\begin{aligned}
&||\sum_{\vec{n}}\sum_{l=1}^{d}\sum_{\alpha,\beta=1}^{2}[[\frac{g^2}{2a^{d-2}}\hat{E}^2(\vec{n},l),\frac{1}{2a}(\hat{U}_{\alpha\beta}(\vec{n},l)\hat{\sigma}^-_{\alpha}(\vec{n})\hat{\sigma}^+_{\beta}(\vec{n}+\hat{l})+h.c.)]\\
&,\frac{2d-1}{2a}\sum_{\alpha'\beta'=\beta\beta}^{\alpha\alpha}(\hat{U}_{\alpha'\beta'}\hat{\sigma}^-_{\alpha'}\hat{\sigma}^+_{\beta'}+h.c.)]||\\
&\leq 4dL^d\cdot 2\frac{g^2}{8a^{d-1}}(4\Lambda+3)\cdot\frac{2(2d-1)}{a}=\frac{(4d^2-2d)L^dg^2(4\Lambda+3)}{a^d}.
\end{aligned}\tag{4.261}$$

Therefore, the bound for $C_{2,4}$ is

$$\frac{8d^2L^dg^2(4\Lambda+3)}{a^d}.\tag{4.262}$$

We proceed to evaluate the bound for $C_{2,5}$ as follows:

$$
\begin{aligned}
&[[\sum_{\vec{n}} \hat{D}^{(E)}_{\vec{n}}, \sum_{\vec{n}'} \hat{T}^{(K)}_{\vec{n}'}], \sum_{\vec{n}''} \hat{L}^{(B)}_{\vec{n}''}] \\
&\leq || \sum_{\vec{n}} \sum_{l=1}^{d} \sum_{\alpha,\beta=1}^{2} [[\frac{g^2}{2a^{d-2}} \hat{E}^2(\vec{n},l), \frac{1}{2a}(\hat{U}_{\alpha\beta}(\vec{n},l)\hat{\sigma}^-_{\alpha}(\vec{n})\hat{\sigma}^+_{\beta}(\vec{n}+\hat{l}) + h.c.)], \sum_{\vec{n}''} \hat{L}^{(B)}_{\vec{n}''}]|| \\
&\leq 4dL^d \cdot 2 || [\frac{g^2}{2a^{d-2}} \hat{E}^2(\vec{n},l), \frac{1}{2a}(\hat{U}_{\alpha\beta}(\vec{n},l)\hat{\sigma}^-_{\alpha}(\vec{n})\hat{\sigma}^+_{\beta}(\vec{n}+\hat{l}) + h.c.)]|| \\
&\quad \cdot || \frac{2(d-1)}{2a^{4-d}g^2} \sum_{\alpha,\beta,\gamma,\delta=1}^{2} (\hat{U}_{\alpha\beta}\hat{U}_{\beta\gamma}\hat{U}^{\dagger}_{\gamma\delta}\hat{U}^{\dagger}_{\delta\alpha} + h.c.)|| \\
&\leq 4dL^d \cdot 2 \frac{g^2}{8a^{d-1}}(4\Lambda+3) \cdot \frac{32(d-1)}{a^{4-d}g^2} = \frac{32d(d-1)L^d(4\Lambda+3)}{a^3},
\end{aligned} \tag{4.263}
$$

where in the second inequality, we have used (4.232) and the fact that there are $2(d-1)$ plaquettes consisting of the link $(\vec{n}, l)$. The bound for the $C_{2,6}$ is given by

$$
\begin{aligned}
&|||[\sum_{\vec{n}} \hat{D}^{(E)}_{\vec{n}}, \sum_{\vec{n}'} \hat{L}^{(B)}_{\vec{n}'}], \sum_{\vec{n}''} \hat{T}^{(K)}_{\vec{n}''}]|| \\
&= ||[\sum_{\vec{n}} \sum_{i=1}^{d} \sum_{j\neq i;j=1}^{d} [\frac{g^2}{2a^{d-2}}(\hat{E}^2(\vec{n},i) + \hat{E}^2(\vec{n}+\hat{i},j) + \hat{E}^2(\vec{n}+\hat{j},i) + \hat{E}^2(\vec{n},j)) \\
&\quad , \frac{-1}{2a^{4-d}g^2} \sum_{\alpha,\beta,\gamma,\delta=1}^{2} (\hat{U}_{\alpha\beta}(\vec{n},i)\hat{U}_{\beta\gamma}(\vec{n}+\hat{i},j)\hat{U}^{\dagger}_{\gamma\delta}(\vec{n}+\hat{j},i)\hat{U}^{\dagger}_{\delta\alpha}(\vec{n},j) + h.c.)] \\
&\quad , \frac{1}{2a} \sum_{\alpha',\beta'=1}^{2} [\hat{U}_{\alpha'\beta'}(\vec{n},i)\hat{\sigma}^-_{\alpha'}(\vec{n})\hat{\sigma}^+_{\beta'}(\vec{n}+\hat{i}) + \hat{U}_{\alpha'\beta'}(\vec{n}+\hat{i},j)\hat{\sigma}^-_{\alpha'}(\vec{n}+\hat{i})\hat{\sigma}^+_{\beta'}(\vec{n}+\hat{i}+\hat{j}) \\
&\quad + \hat{U}_{\alpha'\beta'}(\vec{n}+\hat{j},i)\hat{\sigma}^-_{\alpha'}(\vec{n}+\hat{j})\hat{\sigma}^+_{\beta'}(\vec{n}+\hat{j}+\hat{i}) + \hat{U}_{\alpha'\beta'}(\vec{n},j)\hat{\sigma}^-_{\alpha'}(\vec{n})\hat{\sigma}^+_{\beta'}(\vec{n}+\hat{j}) + h.c.]]|| \\
&\leq L^d \frac{d(d-1)}{2} \cdot 2 \cdot || \frac{8(4\Lambda+3)}{a^2} || \cdot 4 || \frac{1}{2a} \sum_{\alpha',\beta'=1}^{2} (\hat{U}_{\alpha'\beta'}\hat{\sigma}^-_{\alpha'}\hat{\sigma}^+_{\beta'} + h.c.)|| \\
&\leq L^d \frac{d(d-1)}{2} \cdot 2 \cdot || \frac{8(4\Lambda+3)}{a^2} || \cdot 4 || \frac{4}{a} || = \frac{128d(d-1)L^d(4\Lambda+3)}{a^3},
\end{aligned} \tag{4.264}
$$

where we have used (4.234) to evaluate the first norm expression of the first inequality. The

bound for $C_{2,7}$ is given by

$$
\begin{aligned}
&|||[\sum_{\vec{n}} \hat{D}^{(E)}_{\vec{n}}, \sum_{\vec{n}'} \hat{L}^{(B)}_{\vec{n}'}], \sum_{\vec{n}''} \hat{L}^{(B)}_{\vec{n}''}]||| \\
&\leq |||[\sum_{\vec{n}} \sum_{i=1}^{d} \sum_{j\neq i; j=1}^{d} [\frac{g^2}{2a^{d-2}}(\hat{E}^2(\vec{n},i) + \hat{E}^2(\vec{n}+\hat{i},j) + \hat{E}^2(\vec{n}+\hat{j},i) + \hat{E}^2(\vec{n},j)) \\
&\quad , \frac{-1}{2a^{4-d}g^2} \sum_{\alpha,\beta,\gamma,\delta=1}^{2} (\hat{U}_{\alpha\beta}(\vec{n},i)\hat{U}_{\beta\gamma}(\vec{n}+\hat{i},j)\hat{U}^{\dagger}_{\gamma\delta}(\vec{n}+\hat{j},i)\hat{U}^{\dagger}_{\delta\alpha}(\vec{n},j) + h.c.)], \sum_{\vec{n}''} \hat{L}^{(B)}_{\vec{n}''}]||| \\
&\leq L^d \frac{d(d-1)}{2} \cdot 2 || \frac{8(4\Lambda+3)}{a^2} || \cdot || \frac{8d-11}{2a^{4-d}g^2} \sum_{\alpha,\beta,\gamma,\delta=1}^{2} (\hat{U}_{\alpha\beta}\hat{U}_{\beta\gamma}\hat{U}^{\dagger}_{\gamma\delta}\hat{U}^{\dagger}_{\delta\alpha} + h.c.)|| \\
&\leq L^d \frac{d(d-1)8(4\Lambda+3)}{a^2} \cdot \frac{(8d-11)16}{a^{4-d}g^2} = \frac{(1024d^3 - 2432d^2 + 1408d)L^d(4\Lambda+3)}{a^{6-d}g^2}, \qquad (4.265)
\end{aligned}
$$

where in the second inequality, we have used (4.234) to evaluate the first norm expression, and the factor of $8d-11$ in the second norm term is the number of plaquettes that collide on links with the plaquette acted on by the magnetic operators in the inner commutator, as explained in the paragraph below (4.103).

Next we consider $C_{2,8}$, and divide the commutators up into five cases: (i) $\hat{h}_T$, $\hat{h}_{T'}$ and $\hat{h}_{T''}$ all act on the same links, (ii) $\hat{h}_T$ and $\hat{h}_{T'}$ act on the same links, while $\hat{h}_{T''}$ acts on neighboring links that are connected via the fermionic sites, (iii) $\hat{h}_T$ and $\hat{h}_{T''}$ act on the same links, while $\hat{h}_{T'}$ acts on neighboring links that are connected via the fermionic sites, (iv) $\hat{h}_{T'}$ and $\hat{h}_{T''}$ act on the same links, while $\hat{h}_T$ acts on neighboring links that are connected via the fermionic sites, and (v) $\hat{h}_T$, $\hat{h}_{T'}$ and $\hat{h}_{T''}$ all act on different but connected links. We begin with case (i) by considering $\hat{h}_T$, $\hat{h}_{T'}$ and $\hat{h}_{T''}$ that act on one link $(\vec{n}_p, l)$ only. There are 2^6 such $\hat{h}_T$ terms, each with different parameters $a, b, c, \Delta j, \alpha, \beta$ in $\mathbb{T}$. Since $\hat{h}_{T'}$ and $\hat{h}_{T''}$ are terms that succeed $\hat{h}_T$ in $\mathbb{T}$, they can have different or same color indices α, β as $\hat{h}_T$, if $\hat{h}_T$ is among the first $2^6 - 4$ terms of $\mathbb{T}$, in which

case the bound is given by

$$(2^6-4)\sum_{p=e}^{o}\sum_{l=1}^{d}||[[\sum_{\vec{n}_p}\hat{h}_T(\vec{n}_p,l),\sum_{\hat{h}_{T'}\in\mathbb{T};T'>T}\sum_{\vec{n}_p}\hat{h}_{T'}(\vec{n}_p,l)],\sum_{\hat{h}_{T''}\in\mathbb{T};T''>T}\sum_{\vec{n}_p}\hat{h}_{T''}(\vec{n}_p,l)]||$$
$$\leq (2^6-4)2d\sum_{\vec{n}_p}4||\hat{h}_T(\vec{n}_p,l)||\cdot||\sum_{\hat{h}_{T'}\in\mathbb{T};T'>T}\hat{h}_{T'}(\vec{n}_p,l)||\cdot||\sum_{\hat{h}_{T''}\in\mathbb{T};T''>T}\hat{h}_{T''}(\vec{n}_p,l)]||$$
$$\leq 240dL^d||\frac{1}{a}||\cdot||\frac{1}{2a}\sum_{\alpha,\beta=1}^{2}(\hat{U}_{\alpha\beta}(\vec{n}_p,l)\hat{\sigma}_\alpha^-(\vec{n}_p)\hat{\sigma}_\beta^+(\vec{n}_p+\hat{l})+h.c.)||^2$$
$$\leq \frac{240dL^d}{a}(\frac{4}{a})^2=\frac{3840dL^d}{a^3}. \tag{4.266}$$

If $\hat{h}_T$ is one of the last four terms of $\mathbb{T}$, then $\hat{h}_{T'}$ and $\hat{h}_{T''}$ must have different color indices. As a result of (4.168), if $\hat{h}_T$ is the fourth-to-last term, which has $\alpha\beta=11$, then the commutator $[[\hat{h}_T(\vec{n}_p,l),\hat{h}_{T'}(\vec{n}_p,l)],\hat{h}_{T''}(\vec{n}_p,l)]$ is non-zero if both $\hat{h}_{T'},\hat{h}_{T''}$ have color indices equal to either 12 or 21, in which case the bound is given by

$$dL^d\cdot 4||\frac{1}{a}||\cdot||2\frac{1}{a}||^2, \tag{4.267}$$

where the factor of two outside the fraction in the second norm expression reflects the fact that $\hat{h}_{T'},\hat{h}_{T''}$ can have $\alpha\beta=12,21$. If $\hat{h}_T$ is the second- and third-to-last terms, which have $\alpha\beta=12,21$, respectively, then the commutator $[[\hat{h}_T(\vec{n}_p,l),\hat{h}_{T'}(\vec{n}_p,l)],\hat{h}_{T''}(\vec{n}_p,l)]$ is non-zero if $\hat{h}_{T'},\hat{h}_{T''}$ have color indices equal to 22, in which each case the bound is given by

$$dL^d\cdot 4||\frac{1}{a}||^3. \tag{4.268}$$

As such, the bound for case (i) is

$$\frac{3920dL^d}{a^3}. \tag{4.269}$$

Similarly, for case (ii), we analyze the first 2^6-4 and last 4 $\hat{h}_T\in\mathbb{T}$ separately. The bound for

the first 2^6-4 terms is

$$
\begin{aligned}
&(2^6-4)\sum_{p=e}^{o}\sum_{l=1}^{d}|||[\sum_{\vec{n}_p}\hat{h}_T(\vec{n}_p,l),\sum_{\hat{h}_{T'}\in\mathbb{T};T'>T}\sum_{\vec{n}_p}\hat{h}_{T'}(\vec{n}_p,l)],\sum_{\hat{h}_{T''}\in\mathbb{T};T''>T}\hat{h}_{T''}]|||\\
&\leq(2^6-4)2d\sum_{\vec{n}_p}4||\hat{h}_T(\vec{n}_p,l)||\cdot||\sum_{\hat{h}_{T'}\in\mathbb{T};T'>T}\hat{h}_{T'}(\vec{n}_p,l)||\cdot||\sum_{\hat{h}_{T''}\in\mathbb{T};T''>T}\hat{h}_{T''}||\\
&\leq 240dL^d||\frac{1}{a}||\cdot||\frac{1}{2a}\sum_{\alpha,\beta=1}^{2}(\hat{U}_{\alpha\beta}(\vec{n}_p,l)\hat{\sigma}^-_\alpha(\vec{n}_p)\hat{\sigma}^+_\beta(\vec{n}_p+\hat{l})+h.c.)||\cdot||\frac{4d-1}{2a}\sum_{\alpha,\beta=1}^{2}(\hat{U}_{\alpha\beta}\hat{\sigma}^-_\alpha\hat{\sigma}^+_\beta+h.c.)||\\
&\leq\frac{240dL^d}{a}\frac{4}{a}\frac{4(4d-1)}{a}=\frac{(15360d^2-3840d)L^d}{a^3},
\end{aligned}
\tag{4.270}
$$

where the factor of $4d-1$ in the third norm expression of the second inequality is the number of links connected to $(\vec{n}_p,l)$, via the fermionic sites on both its ends. We admit that the constants can be improved slightly by optimizing over the color indices. For instance, if the inner commutator consists of only terms with $\alpha\beta=11$, then it commutes with $\hat{h}_{T''}$ with $\alpha\beta=22$, as they do act on fermions of different colors on the ends of $(\vec{n}_p,l)$, and it commutes with $\hat{h}_{T''}$ with $\alpha\beta=12,21$ on one of the fermionic sites on the ends of $(\vec{n}_p,l)$. Hereafter, we neglect this type of optimization, unless specified. We now consider the fourth-to-last $\hat{h}_T\in\mathbb{T}$, with $\alpha\beta=11$, and compute its bound in the following:

$$
4dL^d||\frac{1}{a}||\cdot||\frac{2}{a}||\cdot||\frac{2d-1}{a}8||=\frac{(128d^2-64d)L^d}{a^3},
\tag{4.271}
$$

where the 2 in the numerator of the second norm expression is due to the fact that $\hat{h}_T$ does not commute with two of the remaining terms, with $\alpha\beta=12,21$. For the the second- and third-to-last $\hat{h}_T\in\mathbb{T}$, with $\alpha\beta=12,21$, we compute the bound for each term as follows:

$$
4dL^d||\frac{1}{a}||\cdot||\frac{1}{a}||\cdot||\frac{2d-1}{a}8||=\frac{(64d^2-32d)L^d}{a^3},
\tag{4.272}
$$

where the second norm expression is due to the fact that $\hat{h}_T$ does not commute with the remaining term with $\alpha\beta=22$. Therefore, the case (ii) is bounded by

$$
\frac{(15616d^2-3968d)L^d}{a^3}.
\tag{4.273}
$$

We separate case (iii) into two types: type (i) consists of commutators where $\hat{h}_{T'}$ acts on links in the same direction, but of different parity, as $\hat{h}_T,\hat{h}_{T''}$; type (ii) consists of commutators where

$\hat{h}_{T'}$ acts on links in different directions from $\hat{h}_T, \hat{h}_{T''}$. Consider type (i), since we implement the even terms before the odd terms, the commutator bound for the first $2^6 - 4$ $\hat{h}_T$ is

$$\begin{aligned}
&(2^6-4)\sum_{l=1}^{d}|||[[\sum_{\vec{n}_e}\hat{h}_T(\vec{n}_e,l), \sum_{\hat{h}_{T'}\in\mathbb{T};T'>T}\sum_{\vec{n}_o}\hat{h}_{T'}(\vec{n}_o,l)], \sum_{\hat{h}_{T''}\in\mathbb{T};T''>T}\sum_{\vec{n}_e}\hat{h}_{T''}(\vec{n}_e,l)]|||\\
&\leq (2^6-4)d\sum_{\vec{n}_e}4||\hat{h}_T(\vec{n}_e,l)||\cdot||2\frac{1}{2a}\sum_{\alpha,\beta=1}^{2}(\hat{U}_{\alpha\beta}(\vec{n}_o,l)\hat{\sigma}_\alpha^-(\vec{n}_o)\hat{\sigma}_\beta^+(\vec{n}_o+\hat{l})+h.c.)||\\
&\quad\cdot||3\frac{1}{2a}\sum_{\alpha,\beta=1}^{2}(\hat{U}_{\alpha\beta}(\vec{n}_e,l)\hat{\sigma}_\alpha^-(\vec{n}_e)\hat{\sigma}_\beta^+(\vec{n}_e+\hat{l})+h.c.)]||\\
&\leq 240d\frac{L^d}{2}||\frac{1}{a}||\cdot||\frac{8}{a}||\cdot||\frac{12}{a}|| = \frac{11520dL^d}{a^3},
\end{aligned} \tag{4.274}$$

where in the first inequality, the factor of 2 in the second norm expression is the number of odd links that are connected to each $(\vec{n}_e, l)$, and the factor of 3 in the third norm expression is the number of links that collide with the original link, and are connected with the two odd links connected to the original link. There are four non-trivial commutators for the last 4 $\hat{h}_T$; if $\hat{h}_T$ has $\alpha\beta = 11$, then $\hat{h}_{T'}$ must have $\alpha\beta = 12, 21$; if $\hat{h}_T$ has $\alpha\beta = 12, 21$, then $\hat{h}_{T'}$ must have $\alpha\beta = 22$. Thus, each of the last four commutators is bounded by

$$\begin{aligned}
&\sum_{l=1}^{d}\sum_{\vec{n}_e}4||\hat{h}_T(\vec{n}_e,l)||\cdot||2\frac{1}{2a}(\hat{U}_{\alpha\beta}(\vec{n}_o,l)\hat{\sigma}_\alpha^-(\vec{n}_o)\hat{\sigma}_\beta^+(\vec{n}_o+\hat{l})+h.c.)||\\
&\cdot||3\frac{1}{2a}\sum_{\alpha,\beta=1}^{2}(\hat{U}_{\alpha\beta}(\vec{n}_e,l)\hat{\sigma}_\alpha^-(\vec{n}_e)\hat{\sigma}_\beta^+(\vec{n}_e+\hat{l})+h.c.)]|| = \frac{48dL^d}{a^3},
\end{aligned} \tag{4.275}$$

and thus, type (i) is bounded by

$$\frac{11712dL^d}{a^3}. \tag{4.276}$$

Similarly, we obtain bound for the first 2^6-4 terms in type (ii) as follows

$$
\begin{aligned}
&(2^6-4)\sum_{p,p'=e}^{o}\sum_{l'>l}\sum_{l=1}^{d}|||[[\sum_{\vec{n}_p}\hat{h}_T(\vec{n}_p,l),\sum_{\hat{h}_{T'}\in\mathbb{T};T'>T}\sum_{\vec{n}_{p'}}\hat{h}_{T'}(\vec{n}_{p'},l')],\sum_{\hat{h}_{T''}\in\mathbb{T};T''>T}\sum_{\vec{n}_p}\hat{h}_{T''}(\vec{n}_p,l)]|||\\
&\leq(2^6-4)4\frac{d(d-1)}{2}\sum_{\vec{n}_p}4||\hat{h}_T(\vec{n}_p,l)||\cdot||2\frac{1}{2a}\sum_{\alpha,\beta=1}^{2}(\hat{U}_{\alpha\beta}(\vec{n}'_p,l')\hat{\sigma}^-_\alpha(\vec{n}'_p)\hat{\sigma}^+_\beta(\vec{n}'_p+\hat{l}')+h.c.)||\\
&\quad\cdot||\frac{1}{2a}\sum_{\alpha,\beta=1}^{2}(\hat{U}_{\alpha\beta}(\vec{n}_p,l)\hat{\sigma}^-_\alpha(\vec{n}_p)\hat{\sigma}^+_\beta(\vec{n}_p+\hat{l})+h.c.)]||\\
&\leq 240d(d-1)L^d||\frac{1}{a}||\cdot||\frac{8}{a}||\cdot||\frac{4}{a}||=\frac{7680(d^2-d)L^d}{a^3},
\end{aligned}
\tag{4.277}
$$

where in the first inequality, the factor of 2 in the second norm expression is the number of links $(\vec{n}_{p'},l)$ that are connected to each $(\vec{n}_p,l)$. The bound for each of the last four commutators is bounded by

$$
\begin{aligned}
&\sum_{p,p'=e}^{o}\sum_{l'>l}\sum_{l=1}^{d}|||[[\sum_{\vec{n}_p}\hat{h}_T(\vec{n}_p,l),\sum_{\hat{h}_{T'}\in\mathbb{T};T'>T}\sum_{\vec{n}_{p'}}\hat{h}_{T'}(\vec{n}_{p'},l')],\sum_{\hat{h}_{T''}\in\mathbb{T};T''>T}\sum_{\vec{n}_p}\hat{h}_{T''}(\vec{n}_p,l)]|||\\
&\leq 4\frac{d(d-1)}{2}\sum_{\vec{n}_p}4||\hat{h}_T(\vec{n}_p,l)||\cdot||2\frac{1}{2a}(\hat{U}_{\alpha\beta}(\vec{n}'_p,l')\hat{\sigma}^-_\alpha(\vec{n}'_p)\hat{\sigma}^+_\beta(\vec{n}'_p+\hat{l}')+h.c.)||\\
&\quad\cdot||\frac{1}{2a}\sum_{\alpha,\beta=1}^{2}(\hat{U}_{\alpha\beta}(\vec{n}_p,l)\hat{\sigma}^-_\alpha(\vec{n}_p)\hat{\sigma}^+_\beta(\vec{n}_p+\hat{l})+h.c.)]||\\
&\leq 4d(d-1)L^d||\frac{1}{a}||\cdot||\frac{2}{a}||\cdot||\frac{4}{a}||=\frac{32(d^2-d)L^d}{a^3}.
\end{aligned}
\tag{4.278}
$$

Therefore, the bound for case (iii) is given by

$$
\frac{L^d}{a^3}(7808d^2+3904d). \tag{4.279}
$$

We divide case (iv) into two types: type-(i) commutators are those where $\hat{h}_T$, $\hat{h}_{T'}$ and $\hat{h}_{T''}$ act on links in the same direction; and type-(ii) commutators are those where $\hat{h}_T$, $\hat{h}_{T'}$ and $\hat{h}_{T''}$ act on links in different directions. We consider type (i) first. Since even terms are implemented before

odd terms, we obtain its bound as follows

$$
\begin{aligned}
&2^6\sum_{l=1}^{d}|||[[\sum_{\vec{n}_e}\hat{h}_T(\vec{n}_e,l),\sum_{\hat{h}_{T'}\in\mathbb{T};T'>T}\sum_{(\vec{n}_o,l)}\hat{h}_{T'}(\vec{n}_o,l)],\sum_{\hat{h}_{T''}\in\mathbb{T};T''>T}\sum_{(\vec{n}_o,l)}\hat{h}_{T''}(\vec{n}_o,l)]|||\\
&\leq 2^6 d\cdot\sum_{\vec{n}_e}4||\hat{h}_T(\vec{n}_e,l)||\cdot||\frac{2}{2a}\sum_{\alpha,\beta=1}^{2}(\hat{U}_{\alpha\beta}(\vec{n}_o,l)\hat{\sigma}_\alpha^-(\vec{n}_o)\hat{\sigma}_\beta^+(\vec{n}_o+\hat{l})+h.c.)||^2\\
&\leq \frac{2^6dL^d}{2}4||\frac{1}{a}||\cdot||\frac{8}{a}||^2=\frac{8192dL^d}{a^2},
\end{aligned}
\tag{4.280}
$$

where the factor of 2 in the numerator of the second norm expression of the second line is due to the fact that $(\vec{n}_e,l)$ is connected to two $(\vec{n}_o,l)$. Next, we evaluate the bound for type (ii) as follows:

$$
\begin{aligned}
&2^6\sum_{p,p'=e}^{o}\sum_{l=1}^{d}\sum_{l'>l}|||[[\sum_{\vec{n}_p}\hat{h}_T(\vec{n}_p,l),\sum_{\hat{h}_{T'}\in\mathbb{T};T'>T}\sum_{(\vec{n}_{p'},l')}\hat{h}_{T'}(\vec{n}_{p'},l')],\sum_{\hat{h}_{T''}\in\mathbb{T};T''>T}\sum_{(\vec{n}_{p'},l')}\hat{h}_{T''}(\vec{n}_{p'},l')]|||\\
&\leq 2^6\cdot 4\frac{d(d-1)}{2}\cdot 4\sum_{\vec{n}_p}||\hat{h}_T(\vec{n}_p,l)||\cdot||\frac{2}{2a}\sum_{\alpha\beta}(\hat{U}_{\alpha\beta}(\vec{n}_{p'},l')\hat{\sigma}_\alpha^-(\vec{n}_{p'})\hat{\sigma}_\beta^+(\vec{n}_{p'}+\hat{l}')+h.c.)||^2\\
&\leq 2^7d(d-1)\frac{L^d}{2}4||\frac{1}{a}||\cdot||\frac{8}{a}||^2=\frac{16384(d^2-d)L^d}{a^3},
\end{aligned}
\tag{4.281}
$$

where the factor of 2 in the numerator of the second norm expression of the second line is due to the fact that the link $(\vec{n}_p,l)$, acted on by $\hat{h}_T$, is connected to two links $(\vec{n}_{p'},l')$, acted on by $\hat{h}_{T'}$ and $\hat{h}_{T''}$. Therefore, case (iv) is bounded by

$$
\frac{(16384d^2-8192d)L^d}{a^3}. \tag{4.282}
$$

Lastly, we obtain the bound for case (v)

$$
\begin{aligned}
&2^6\sum_{(p,l)}\sum_{\substack{(p',l');\\(p',l')>(p,l)}}\sum_{\substack{(p'',l'');\\(p'',l'')>(p',l')}}|||[[\sum_{\vec{n}_p}\hat{h}_T(\vec{n}_p,l),\sum_{\substack{\hat{h}_{T'}\in\mathbb{T};\\T'>T}}\sum_{(\vec{n}_{p'},l')}\hat{h}_{T'}(\vec{n}_{p'},l')],\sum_{\substack{\hat{h}_{T''}\in\mathbb{T};\\T''>T}}\sum_{(\vec{n}_{p''},l'')}\hat{h}_{T''}(\vec{n}_{p''},l'')]|||\\
&\leq 2^6\frac{4}{3}(2d^3-3d^2+d)\cdot 4\sum_{\vec{n}_p}||\hat{h}_T(\vec{n}_p,l)||\cdot||\frac{2}{2a}\sum_{\alpha\beta}(\hat{U}_{\alpha\beta}(\vec{n}_{p'},l')\hat{\sigma}_\alpha^-(\vec{n}_{p'})\hat{\sigma}_\beta^+(\vec{n}_{p'}+\hat{l}')+h.c.)||\\
&\quad\cdot||\frac{4}{2a}\sum_{\alpha\beta}(\hat{U}_{\alpha\beta}(\vec{n}_{p''},l'')\hat{\sigma}_\alpha^-(\vec{n}_{p''})\hat{\sigma}_\beta^+(\vec{n}_{p''}+\hat{l}'')+h.c.)||\\
&=\frac{2^9L^d}{3a}(2d^3-3d^2+d)||\frac{8}{a}||\cdot||\frac{16}{a}||=\frac{L^d}{3a^3}(131072d^3-196608d^2+65536d),
\end{aligned}
\tag{4.283}
$$

where $(p', l') > (p, l)$ means that (p', l') appears after (p, l) in $\mathbb{T}$, and since there are $2d$ (p, l), the triple sum outside the norm expression in the first line evaluates to

$$\sum_{q=1}^{2d}(2d-q)(2d-q-1) = \frac{4}{3}(2d^3 - 3d^2 + d). \tag{4.284}$$

In the inequality, the factor of 2 in the numerator of the second norm expression is because of the fact that $(\vec{n}_p, l)$ is connected to at most 2 $(\vec{n}_{p'}, l')$, and thus, each of the inner commutators acts on at most three links and four sites. Further, each of these four sites are connected to at most one $(\vec{n}_{p''}, l'')$, hence the factor of 4 in the numerator of the third norm expression. Note that the constants can be further tightened by considering the color indices of the fermionic operators. Finally, adding the bounds for all cases, we arrive at the bound for $C_{2,8}$

$$(131072\frac{d^3}{3} - 25728d^2 + 52528\frac{d}{3})\frac{L^d}{a^3}. \tag{4.285}$$

Now for $C_{2,9}$, we separate the commutators into three cases. Case-(i) commutators consists of $\hat{h}_T$ and $\hat{h}_{T'}$ that act on the same links. Case-(ii) commutators consists of $\hat{h}_T$ and $\hat{h}_{T'}$ that act on links in the same directions, but of different parities. Case-(iii) commutators consists of $\hat{h}_T$ and $\hat{h}_{T'}$ that act on links in different directions, but connected via fermionic sites. For case (i), once again, we consider the first $2^6 - 4$ and last 4 $\hat{h}_T$ terms in $\mathbb{T}$ separately. The bound for the first $2^6 - 4$ $\hat{h}_T$ terms is given by

$$\begin{aligned}
&(2^6-4)\sum_{p=e}^{o}\sum_{l=1}^{d}[[\sum_{\vec{n}_p}\hat{h}_T(\vec{n}_p, l), \sum_{\hat{h}_{T'}\in\mathbb{T};T'>T}\sum_{\vec{n}_p}\hat{h}_{T'}(\vec{n}_p, l)], \sum_{\vec{n}}\hat{L}_{\vec{n}}^{(B)}] \\
&\leq (2^6-4)2d\sum_{\vec{n}_p} 4||\hat{h}_T(\vec{n}_p, l)|| \cdot ||\frac{1}{2a}\sum_{\alpha\beta}(\hat{U}_{\alpha\beta}(\vec{n}_p, l)\hat{\sigma}_\alpha^-(\vec{n}_p)\hat{\sigma}_\beta^+(\vec{n}_p + \hat{l}) + h.c.)|| \\
&\quad \cdot ||\frac{2(d-1)}{2a^{4-d}g^2}\sum_{\alpha,\beta,\gamma,\delta=1}^{2}(\hat{U}_{\alpha\beta}\hat{U}_{\beta\gamma}\hat{U}_{\gamma\delta}^\dagger\hat{U}_{\delta\alpha}^\dagger + h.c.)|| \\
&\leq 60dL^d \cdot 4||\frac{1}{a}|| \cdot ||\frac{4}{a}|| \cdot ||\frac{32(d-1)}{a^{4-d}g^2}|| = \frac{(30720d^2 - 30720d)L^d}{a^{6-d}g^2},
\end{aligned} \tag{4.286}$$

where in the first inequality, the numerator $2(d-1)$ in the third norm term is the number of magnetic operators that act on link $(\vec{n}_p, l)$. The last four $\hat{h}_T$ terms contribute four commutators,

each of which is bounded by

$$\begin{aligned}
&4dL^d||\hat{h}_T(\vec{n}_p,l)||\cdot||\frac{1}{2a}(\hat{U}_{\alpha\beta}(\vec{n}_p,l)\hat{\sigma}^-_\alpha(\vec{n}_p)\hat{\sigma}^+_\beta(\vec{n}_p+\hat{l})+h.c.)||\\
&\cdot||\frac{2(d-1)}{2a^{4-d}g^2}\sum_{\alpha,\beta,\gamma,\delta=1}^{2}(\hat{U}_{\alpha\beta}\hat{U}_{\beta\gamma}\hat{U}^\dagger_{\gamma\delta}\hat{U}^\dagger_{\delta\alpha}+h.c.)||\\
&\leq\frac{128(d^2-d)L^d}{a^{6-d}g^2}.
\end{aligned}\tag{4.287}$$

As such, the bound for case-(i) commutators is

$$\frac{31232(d^2-d)L^d}{a^{6-d}g^2}.\tag{4.288}$$

For case (ii), there are two types of commutators; those where (i) $\hat{h}_T$ and $\hat{h}_{T'}$ have color indices $\alpha\beta$ and $\beta\alpha$, respectively, and thus, collide on two fermionic sites, and where (ii) $\hat{h}_T$ and $\hat{h}_{T'}$ have color indices $\alpha\beta$ and $\beta\beta$ or $\alpha\alpha$, respectively, and thus, collide on one fermionic sites. Thus, considering type (i), the inner commutators act on three links, which collide with $3\cdot 2(d-1)$ magnetic operators. Since we implement the even terms before the odd terms, we obtain the bound for the type-(i) commutators as follows:

$$\begin{aligned}
&2^6\sum_{l=1}^{d}4\sum_{\vec{n}_e}||\hat{h}_T(\vec{n}_e,l)||\cdot||\frac{2}{2a}(\hat{U}_{\beta\alpha}(\vec{n}_o,l)\hat{\sigma}^-_\beta(\vec{n}_o)\hat{\sigma}^+_\alpha(\vec{n}_o+\hat{l})+h.c.)||\\
&\cdot||\frac{6(d-1)}{2a^{4-d}g^2}\sum_{\alpha,\beta,\gamma,\delta=1}^{2}(\hat{U}_{\alpha\beta}\hat{U}_{\beta\gamma}\hat{U}^\dagger_{\gamma\delta}\hat{U}^\dagger_{\delta\alpha}+h.c.)||\\
&\leq 2^7dL^d||\frac{1}{a}||\cdot||\frac{2}{a}||\cdot||\frac{96(d-1)}{a^{4-d}g^2}||=\frac{24576(d^2-d)L^d}{a^{6-d}g^2}.
\end{aligned}\tag{4.289}$$

For type (ii), the inner commutators act on two links, and thus collide with $2\cdot 2(d-1)$ magnetic operators. We obtain the bound for the type-(ii) commutators as follows:

$$\begin{aligned}
&2^6\sum_{l=1}^{d}4\sum_{\vec{n}_e}||\hat{h}_T(\vec{n}_e,l)||\cdot||\frac{1}{2a}\sum_{\alpha'\beta'=\beta\beta}^{\alpha\alpha}(\hat{U}_{\alpha'\beta'}(\vec{n}_o,l)\hat{\sigma}^-_{\alpha'}(\vec{n}_o)\hat{\sigma}^+_{\beta'}(\vec{n}_o+\hat{l})+h.c.)||\\
&\cdot||\frac{4(d-1)}{2a^{4-d}g^2}\sum_{\alpha,\beta,\gamma,\delta=1}^{2}(\hat{U}_{\alpha\beta}\hat{U}_{\beta\gamma}\hat{U}^\dagger_{\gamma\delta}\hat{U}^\dagger_{\delta\alpha}+h.c.)||\\
&\leq 2^7dL^d||\frac{1}{a}||\cdot||\frac{2}{a}||\cdot||\frac{64(d-1)}{a^{4-d}g^2}||=\frac{16384(d^2-d)L^d}{a^{6-d}g^2}.
\end{aligned}\tag{4.290}$$

Thus, for case (ii), we obtain the bound

$$\frac{40960(d^2-d)L^d}{a^{6-d}g^2}. \tag{4.291}$$

In the third case, $\hat{h}_T$ and $\hat{h}_{T'}$ act on links in different directions. As in the second case, we divide up case (iii) based on the color indices of $\hat{h}_T$ and $\hat{h}_{T'}$. Focusing on the first type, the inner commutators act on three links, which collide with $2+3\cdot 2(d-2)=6d-10$ magnetic operators, where two of them act on all three links, and there are $2(d-2)$ magnetic operators acting on each one link, but not the other two links. Thus, we obtain the bound for type (i) commutators as follows:

$$\begin{aligned}
&2^6\sum_{p,p'=e}^{o}\sum_{l=1}^{d}\sum_{l'>l}4\sum_{\vec{n}_p}||\hat{h}_T(\vec{n}_p,l)||\cdot||\frac{2}{2a}(\hat{U}_{\beta\alpha}(\vec{n}_{p'},l')\hat{\sigma}^-_{\beta}(\vec{n}_{p'})\hat{\sigma}^+_{\alpha}(\vec{n}_{p'}+\hat{l}')+h.c.)||\\
&\cdot||\frac{6d-10}{2a^{4-d}g^2}\sum_{\alpha,\beta,\gamma,\delta=1}^{2}(\hat{U}_{\alpha\beta}\hat{U}_{\beta\gamma}\hat{U}^\dagger_{\gamma\delta}\hat{U}^\dagger_{\delta\alpha}+h.c.)||\\
&\leq 2^6\cdot 4\frac{d(d-1)}{2}\cdot 4\frac{L^d}{2}||\frac{1}{a}||\cdot||\frac{2}{a}||\cdot||\frac{32(3d-5)}{a^{4-d}g^2}||=(49152d^3-131072d^2+81920d)\frac{L^d}{a^{6-d}g^2}.
\end{aligned} \tag{4.292}$$

Moving onto the second type, the inner commutators act on two links, which collide with $1+2\cdot 2(d-2)=4d-7$ magnetic operators, where one of them acts on both links, and there are $2(d-2)$ magnetic operators acting on each one link, but not the other. Hence, we evaluate the bound for type (ii), and obtain,

$$\begin{aligned}
&2^6\sum_{p,p'=e}^{o}\sum_{l=1}^{d}\sum_{l'>l}4\sum_{\vec{n}_p}||\hat{h}_T(\vec{n}_p,l)||\cdot||\frac{1}{2a}\sum_{\alpha'\beta'=\beta\gamma}^{\gamma\alpha}(\hat{U}_{\alpha'\beta'}(\vec{n}_{p'},l)\hat{\sigma}^-_{\alpha'}(\vec{n}_{p'})\hat{\sigma}^+_{\beta'}(\vec{n}_{p'}+\hat{l})+h.c.)||\\
&\cdot||\frac{4d-7}{2a^{4-d}g^2}\sum_{\alpha,\beta,\gamma,\delta=1}^{2}(\hat{U}_{\alpha\beta}\hat{U}_{\beta\gamma}\hat{U}^\dagger_{\gamma\delta}\hat{U}^\dagger_{\delta\alpha}+h.c.)||\\
&\leq 2^6\cdot 4\frac{d(d-1)}{2}\cdot 4\frac{L^d}{2}||\frac{1}{a}||\cdot||\frac{2}{a}||\cdot||\frac{16(4d-7)}{a^{4-d}g^2}||=(32768d^3-90112d^2+57344d)\frac{L^d}{a^{6-d}g^2}.
\end{aligned} \tag{4.293}$$

Therefore, the bound for case (iii) is

$$(81920d^3-221184d^2+139264d)\frac{L^d}{a^{6-d}g^2}. \tag{4.294}$$

Summing up the bounds for all three cases, we obtain the bound for $C_{2,9}$

$$(81920d^3 - 148992d^2 + 67072d)\frac{L^d}{a^{6-d}g^2}. \tag{4.295}$$

Now for $C_{2,10}$, we divide the commutators up into cases and types, as we have done for $C_{2,9}$. The bound for case (i) of both the $C_{2,9}$ and $C_{2,10}$ is the same, and is given by

$$\frac{31232(d^2-d)L^d}{a^{6-d}g^2}. \tag{4.296}$$

The bound for case (ii) can be obtained from the case-(ii) bounds for $C_{2,9}$ after some slight modifications. First, since the kinetic operator $\hat{h}_T$ only acts on one link, there are only $2(d-1)$ plaquette operators in the inner commutator that do not commute with each $\hat{h}_T$ because the plaquettes may lie on $d-1$ two-dimensional planes and can be of two different parities. Second, the kinetic operators $\hat{h}_{T'}$ not only collide with $\hat{h}_T$ via fermionic sites, but also with the magnetic operators on links. Thus, we obtain the bound for type (i) of case (ii)

$$\begin{aligned}
&2^6\sum_{l=1}^{d}4\sum_{\vec{n}_e}||\hat{h}_T(\vec{n}_e,l)||\cdot||\frac{2(d-1)}{2a^{4-d}g^2}\sum_{\alpha,\beta,\gamma,\delta=1}^{2}(\hat{U}_{\alpha\beta}\hat{U}_{\beta\gamma}\hat{U}^\dagger_{\gamma\delta}\hat{U}^\dagger_{\delta\alpha}+h.c.)||\\
&\cdot||\frac{4}{2a}(\hat{U}_{\beta\alpha}(\vec{n}_o,l)\hat{\sigma}^-_\beta(\vec{n}_o)\hat{\sigma}^+_\alpha(\vec{n}_o+\hat{l})+h.c.)||\\
&\leq 2^7dL^d||\frac{1}{a}||\cdot||\frac{32(d-1)}{a^{4-d}g^2}||\cdot||\frac{4}{a}||=\frac{16384(d^2-d)L^d}{a^{6-d}g^2},
\end{aligned} \tag{4.297}$$

where a factor of 4 in the numerator of the third norm expression is due to the fact that two $\hat{h}_{T'}$, of color indices $\beta\alpha$, collide with each of $\hat{h}_T$, of color indices $\alpha\beta$, and the pair of plaquette operators that lie on the same plane. The bound for the second type of case (ii) is

$$\begin{aligned}
&2^6\sum_{l=1}^{d}4\sum_{\vec{n}_e}||\hat{h}_T(\vec{n}_e,l)||\cdot||\frac{2(d-1)}{2a^{4-d}g^2}\sum_{\alpha,\beta,\gamma,\delta=1}^{2}(\hat{U}_{\alpha\beta}\hat{U}_{\beta\gamma}\hat{U}^\dagger_{\gamma\delta}\hat{U}^\dagger_{\delta\alpha}+h.c.)||\\
&\cdot||\frac{3}{2a}\sum_{\alpha'\beta'=\beta\beta}^{\alpha\alpha}(\hat{U}_{\alpha'\beta'}(\vec{n}_o,l)\hat{\sigma}^-_{\alpha'}(\vec{n}_o)\hat{\sigma}^+_{\beta'}(\vec{n}_o+\hat{l})+h.c.)||\\
&\leq 2^7dL^d||\frac{1}{a}||\cdot||\frac{32(d-1)}{a^{4-d}g^2}||\cdot||\frac{6}{a}||=\frac{24576(d^2-d)L^d}{a^{6-d}g^2},
\end{aligned} \tag{4.298}$$

where the numerator 3 in the third norm expression is due to the fact that each $\hat{h}_{T'}$, of color indices $\alpha\alpha$ or $\beta\beta$, collides with $\hat{h}_T$, of color indices $\alpha\beta$, and two $\hat{h}_{T'}$ collide with the pair of magnetic operators that lie on the same plane. Thus, for case (ii), the bound is given by

$$\frac{40960(d^2-d)L^d}{a^{6-d}g^2}. \tag{4.299}$$

Now we consider the third case. Once again, we modify the case-(iii) bounds of $C_{2,9}$. Thus, we obtain the respective bounds for type (i) and (ii) commutators as follows:

$$\begin{aligned}
&2^6 \sum_{p,p'=e}^{o} \sum_{l=1}^{d} \sum_{l'>l} 4 \sum_{\vec{n}_p} ||\hat{h}_T(\vec{n}_p, l)|| \cdot ||\frac{2(d-1)}{2a^{4-d}g^2} \sum_{\alpha,\beta,\gamma,\delta=1}^{2} (\hat{U}_{\alpha\beta}\hat{U}_{\beta\gamma}\hat{U}^{\dagger}_{\gamma\delta}\hat{U}^{\dagger}_{\delta\alpha} + h.c.)|| \\
&\cdot ||\frac{2}{2a}(\hat{U}_{\beta\alpha}(\vec{n}_{p'}, l')\hat{\sigma}^{-}_{\beta}(\vec{n}_{p'})\hat{\sigma}^{+}_{\alpha}(\vec{n}_{p'} + \hat{l}') + h.c.)|| \\
&\leq 2^6 \cdot 4\frac{d(d-1)}{2} \cdot 4\frac{L^d}{2}||\frac{1}{a}|| \cdot ||\frac{32(d-1)}{a^{4-d}g^2}|| \cdot ||\frac{2}{a}|| = (16384d^3 - 32768d^2 + 16384d)\frac{L^d}{a^{6-d}g^2},
\end{aligned} \tag{4.300}$$

and

$$\begin{aligned}
&2^6 \sum_{p,p'=e}^{o} \sum_{l=1}^{d} \sum_{l'>l} 4 \sum_{\vec{n}_p} ||\hat{h}_T(\vec{n}_p, l)|| \cdot ||\frac{2(d-1)}{2a^{4-d}g^2} \sum_{\alpha,\beta,\gamma,\delta=1}^{2} (\hat{U}_{\alpha\beta}\hat{U}_{\beta\gamma}\hat{U}^{\dagger}_{\gamma\delta}\hat{U}^{\dagger}_{\delta\alpha} + h.c.)|| \\
&\cdot ||\frac{1}{2a} \sum_{\alpha'\beta'=\beta\gamma}^{\gamma\alpha} (\hat{U}_{\alpha'\beta'}(\vec{n}_{p'}, l)\hat{\sigma}^{-}_{\alpha'}(\vec{n}_{p'})\hat{\sigma}^{+}_{\beta'}(\vec{n}_{p'} + \hat{l}) + h.c.)|| \\
&\leq 2^6 \cdot 4\frac{d(d-1)}{2} \cdot 4\frac{L^d}{2}||\frac{1}{a}|| \cdot ||\frac{32(d-1)}{a^{4-d}g^2}|| \cdot ||\frac{2}{a}|| = (16384d^3 - 32768d^2 + 16384d)\frac{L^d}{a^{6-d}g^2}.
\end{aligned} \tag{4.301}$$

Therefore, the bound for case (iii) is

$$(32768d^3 - 65536d^2 + 32768d)\frac{L^d}{a^{6-d}g^2}. \tag{4.302}$$

Summing up the bounds for all cases, we obtain the bound for $C_{2,10}$

$$(32768d^3 + 6656d^2 - 39424d)\frac{L^d}{a^{6-d}g^2}. \tag{4.303}$$

We compute the bound for $C_{2,11}$, and obtain

$$\begin{aligned}
&\sum_{\hat{h}_T\in\mathbb{T}} |||[\hat{h}_T, \sum_{\vec{n}} \hat{L}^{(B)}_{\vec{n}}], \sum_{\vec{n}'} \hat{L}^{(B)}_{\vec{n}'}]||| \\
&\leq 2^7 d\frac{L^d}{2}\cdot 4||\hat{h}_T(\vec{n}_p,l)||\cdot||\frac{2(d-1)}{2a^{4-d}g^2}\sum_{\alpha,\beta,\gamma,\delta=1}^{2}(\hat{U}_{\alpha\beta}\hat{U}_{\beta\gamma}\hat{U}^\dagger_{\gamma\delta}\hat{U}^\dagger_{\delta\alpha}+h.c.)|| \\
&\quad\cdot||\frac{14d-20}{2a^{4-d}g^2}\sum_{\alpha,\beta,\gamma,\delta=1}^{2}(\hat{U}_{\alpha\beta}\hat{U}_{\beta\gamma}\hat{U}^\dagger_{\gamma\delta}\hat{U}^\dagger_{\delta\alpha}+h.c.)|| \\
&\leq \frac{2^8 dL^d}{a}\frac{32(d-1)}{a^{4-d}g^2}\frac{16(14d-20)}{a^{4-d}g^2} = \frac{(1835008d^3-4456448d^2+2621440d)L^d}{a^{9-2d}g^4},
\end{aligned} \tag{4.304}$$

where in the first inequality, the factors of $2(d-1)$ and $14d-20$ are explained in the paragraph below (4.137).

Lastly, we consider $C_{2,12}$, which consists of commutators between only magnetic operators. The commutators are either *intra-plaquette* or *inter-plaquette*, where $\hat{h}_L$, $\hat{h}_{L'}$ and $\hat{h}_{L''}$ act on the same or different plaquettes, respectively. We consider intra-plaquette terms first. We remind the readers that there are 2^{20} $\hat{h}_L(\vec{n}_p,j,k)$ terms acting on each plaquette $(\vec{n}_p,j,k)$. We analyze the commutators, where $\hat{h}_T(\vec{n}_p,j,k)$ is among the first $2^{20}-16$, and last 16 terms, separately. When $\hat{h}_T(\vec{n}_p,j,k)$ is among the first $2^{20}-16$ terms, the bound is given by

$$\begin{aligned}
&(2^{20}-16)\sum_{k\neq j;k=1}^{d}\sum_{j=1}^{d}\sum_{\vec{n}_p}\sum_{p=e}^{o}|||[\hat{h}_L(\vec{n}_p,j,k), \sum_{\hat{h}_{L'}\in\mathbb{L};L'>L}\hat{h}_{L'}(\vec{n}_p,j,k)], \sum_{\hat{h}_{L''}\in\mathbb{L};L''>L}\hat{h}_{L''}(\vec{n}_p,j,k)]||| \\
&\leq \frac{(2^{20}-16)d(d-1)L^d}{2}4||\hat{h}_L(\vec{n}_p,j,k)||\cdot||\frac{1}{2a^{4-d}g^2}\sum_{\alpha,\beta,\gamma,\delta=1}^{2}(\hat{U}_{\alpha\beta}\hat{U}_{\beta\gamma}\hat{U}^\dagger_{\gamma\delta}\hat{U}^\dagger_{\delta\alpha}+h.c.)||^2 \\
&\leq (2^{21}-32)d(d-1)L^d||\frac{1}{a^{4-d}g^2}||\cdot||\frac{16}{a^{4-d}g^2}||^2 = \frac{536862720(d^2-d)L^d}{a^{12-3d}g^6}.
\end{aligned} \tag{4.305}$$

When $\hat{h}_L(\vec{n}_p,j,k)$ is among the last 16 terms, the bound is given by

$$\frac{d(d-1)L^d}{2}4||\frac{1}{a^{4-d}g^2}||\cdot\sum_{q=15}^{1}||\frac{16q}{a^{4-d}g^2}||^2 = \frac{2480(d^2-d)L^d}{a^{12-3d}g^6}. \tag{4.306}$$

Thus, the bound for the intra-plaquette commutators is

$$\frac{536865200(d^2-d)L^d}{a^{12-3d}g^6}. \tag{4.307}$$

We now proceed to analyze the inter-plaquette commutators. Since each $\hat{h}_{L''}$ operator is non-zero, the inner commutator $[\hat{h}_L, \sum_{\hat{h}_{L'} \in \mathbb{L}; L' > L} \hat{h}_{L'}]$ must be non-zero to guarantee a non-trivial triple commutator

$$[[\hat{h}_L, \sum_{\hat{h}_{L'} \in \mathbb{L}; L' > L} \hat{h}_{L'}], \sum_{\hat{h}_{L''} \in \mathbb{L}; L'' > L} \hat{h}_{L''}].$$

Given a non-zero inner commutator, we further divide the inter-plaquette commutators into three types. Type (i) commutators satisfy

$$[\hat{h}_L, \sum_{\hat{h}_{L'} \in \mathbb{L}; L' > L} \hat{h}_{L'}] \neq 0, \; [\hat{h}_L, \sum_{\hat{h}_{L''} \in \mathbb{L}; L'' > L} \hat{h}_{L''}] \neq 0, \; [\sum_{\hat{h}_{L'} \in \mathbb{L}; L' > L} \hat{h}_{L'}, \sum_{\hat{h}_{L''} \in \mathbb{L}; L'' > L} \hat{h}_{L''}] \neq 0. \quad (4.308)$$

Type (ii) commutators satisfy

$$[\hat{h}_L, \sum_{\hat{h}_{L'} \in \mathbb{L}; L' > L} \hat{h}_{L'}] \neq 0, \; [\hat{h}_L, \sum_{\hat{h}_{L''} \in \mathbb{L}; L'' > L} \hat{h}_{L''}] \neq 0, \; [\sum_{\hat{h}_{L'} \in \mathbb{L}; L' > L} \hat{h}_{L'}, \sum_{\hat{h}_{L''} \in \mathbb{L}; L'' > L} \hat{h}_{L''}] = 0. \quad (4.309)$$

Type (iii) commutators satisfy

$$[\hat{h}_L, \sum_{\hat{h}_{L'} \in \mathbb{L}; L' > L} \hat{h}_{L'}] \neq 0, \; [\hat{h}_L, \sum_{\hat{h}_{L''} \in \mathbb{L}; L'' > L} \hat{h}_{L''}] = 0, \; [\sum_{\hat{h}_{L'} \in \mathbb{L}; L' > L} \hat{h}_{L'}, \sum_{\hat{h}_{L''} \in \mathbb{L}; L'' > L} \hat{h}_{L''}] \neq 0. \quad (4.310)$$

In order to facilitate the counting of the commutators in each case, we provide a geometric interpretation to the conditions for each type. For instance, the condition satisfied by all three cases $[\hat{h}_L, \sum_{\hat{h}_{L'} \in \mathbb{L}; L' > L} \hat{h}_{L'}] \neq 0$ implies that, some or all of the links of each plaquette, which is acted on by $\hat{h}_L$, must also be acted on by each $\hat{h}_{L'}$. As such, we can further infer that the plaquettes acted on by $\hat{h}_L$ and $\hat{h}_{L'}$ share at least one dimension. We extend this geometric interpretation to compute the number of non-trivial commutators in each type.

For type (i), the plaquettes acted on by $\hat{h}_L$, collide with those acted on by $\hat{h}_{L'}$ and $\hat{h}_{L''}$, and those acted on by $\hat{h}_{L'}$ also collide with those acted on by $\hat{h}_{L''}$. Suppose $\hat{h}_L$ is labelled by (p, k, l). The possible parity-location tuples that label $\hat{h}_{L'}$ and $\hat{h}_{L''}$ are given in Table 4.6 and 4.7 for $p =$ *even* and *odd*, respectively. Consider first the case where $p =$ *even*, and $\hat{h}_L$ and $\hat{h}_{L'}$ are labelled by items $1-4$, 6 and 7 in Table 4.6. Then, each plaquette acted on by $\hat{h}_L$ is acted on by two $\hat{h}_{L'}$ as they share one dimension. Further, the plaquettes acted on by $\hat{h}_L$ and $\hat{h}_{L'}$ are acted on by either $2, 4, 6$ or 8 $\hat{h}_{L''}$. In particular, if the plaquettes acted on by $\hat{h}_{L''}$ (i) share one common dimension with $\hat{h}_L$, and two common dimensions and parity with $\hat{h}_{L'}$, or (ii) share one common dimension with $\hat{h}_L$ and a different dimension with $\hat{h}_{L'}$, then $\hat{h}_L$ and $\hat{h}_{L'}$ collide with two $\hat{h}_{L''}$. We compute the number of combinations of parity-location labels that satisfy these conditions using Table 4.6, and obtain

$$\sum_{l>k} \sum_{k=1}^{d-1} 12(d-l) + 2(l-k-1) = \frac{7}{3}(d^3 - 3d^2 + 2d). \quad (4.311)$$

The bound in this case is given by

$$
\begin{aligned}
&2^{20}|||[\sum_{\vec{n}_e}\hat{h}_L(e,k,l),\sum_{\hat{h}_{L'}\in\mathbb{L};L'>L}\hat{h}_{L'}],\sum_{\hat{h}_{L''}\in\mathbb{L};L''>L}\hat{h}_{L''}]|||\\
&\leq\frac{2^{20}\cdot 7}{3}(d^3-3d^2+2d)\sum_{\vec{n}_e}4\cdot||\hat{h}_L(e,k,l)||\cdot||\frac{2}{2a^{4-d}g^2}\sum_{\alpha,\beta,\gamma,\delta=1}^{2}(\hat{U}_{\alpha\beta}\hat{U}_{\beta\gamma}\hat{U}^\dagger_{\gamma\delta}\hat{U}^\dagger_{\delta\alpha}+h.c.)||\\
&\quad\cdot||\frac{2}{2a^{4-d}g^2}\sum_{\alpha,\beta,\gamma,\delta=1}^{2}(\hat{U}_{\alpha\beta}\hat{U}_{\beta\gamma}\hat{U}^\dagger_{\gamma\delta}\hat{U}^\dagger_{\delta\alpha}+h.c.)||\\
&=\frac{L^d}{3a^{12-3d}g^6}15032385536(d^3-3d^2+2d),
\end{aligned}
\tag{4.312}
$$

where 2^{20} is the number of $\hat{h}_L$ terms per plaquette.

If the plaquettes acted on by $\hat{h}_{L''}$ share only one dimension with both $\hat{h}_L$ and $\hat{h}_{L'}$, then $\hat{h}_L$ and $\hat{h}_{L'}$ collide with four $\hat{h}_{L''}$. Using Table 4.6, we find the number of combinations of parity-location labels that satisfy this condition, i.e.

$$
\begin{aligned}
&\sum_{l>k}\sum_{k=1}^{d-1}(d-l)[8(d-l-1)+4(l-k-1)]+(l-k-1)[4(d-l)+4(l-k-2)]\\
&=\frac{4}{3}(d^4-6d^3+11d^2-6d).
\end{aligned}
\tag{4.313}
$$

The bound in this case is given by

$$
\begin{aligned}
&2^{20}|||[\sum_{\vec{n}_e}\hat{h}_L(e,k,l),\sum_{\hat{h}_{L'}\in\mathbb{L};L'>L}\hat{h}_{L'}],\sum_{\hat{h}_{L''}\in\mathbb{L};L''>L}\hat{h}_{L''}]|||\\
&\leq\frac{2^{20}\cdot 4}{3}(d^4-6d^3+11d^2-6d)\sum_{\vec{n}_e}4\cdot||\hat{h}_L(e,k,l)||\cdot||\frac{2}{2a^{4-d}g^2}\sum_{\alpha,\beta,\gamma,\delta=1}^{2}(\hat{U}_{\alpha\beta}\hat{U}_{\beta\gamma}\hat{U}^\dagger_{\gamma\delta}\hat{U}^\dagger_{\delta\alpha}+h.c.)||\\
&\quad\cdot||\frac{4}{2a^{4-d}g^2}\sum_{\alpha,\beta,\gamma,\delta=1}^{2}(\hat{U}_{\alpha\beta}\hat{U}_{\beta\gamma}\hat{U}^\dagger_{\gamma\delta}\hat{U}^\dagger_{\delta\alpha}+h.c.)||\\
&=\frac{L^d}{3a^{12-3d}g^6}17179869184(d^4-6d^3+11d^2-6d).
\end{aligned}
\tag{4.314}
$$

If the plaquettes acted on by $\hat{h}_{L''}$ share only one dimension with $\hat{h}_{L'}$, and share both dimensions, but not the parity, with $\hat{h}_L$, then $\hat{h}_L$ and $\hat{h}_{L'}$ collide with six $\hat{h}_{L''}$. Once again, we use Table

4.6 to obtain the number of combinations of parity-location labels that satisfy this condition, i.e.

$$\sum_{l>k}\sum_{k=1}^{d-1} 4(d-l)+2(l-k-1) = (d^3-3d^2+2d). \tag{4.315}$$

The bound in this case is given by

$$\begin{aligned}
&2^{20}|||[[\sum_{\vec{n}_e}\hat{h}_L(e,k,l), \sum_{\hat{h}_{L'}\in\mathbb{L};L'>L}\hat{h}_{L'}], \sum_{\hat{h}_{L''}\in\mathbb{L};L''>L}\hat{h}_{L''}]|||\\
&\leq 2^{20}(d^3-3d^2+2d)\sum_{\vec{n}_e} 4\cdot||\hat{h}_L(e,k,l)||\cdot||\frac{2}{2a^{4-d}g^2}\sum_{\alpha,\beta,\gamma,\delta=1}^{2}(\hat{U}_{\alpha\beta}\hat{U}_{\beta\gamma}\hat{U}^\dagger_{\gamma\delta}\hat{U}^\dagger_{\delta\alpha}+h.c.)||\\
&\quad\cdot||\frac{6}{2a^{4-d}g^2}\sum_{\alpha,\beta,\gamma,\delta=1}^{2}(\hat{U}_{\alpha\beta}\hat{U}_{\beta\gamma}\hat{U}^\dagger_{\gamma\delta}\hat{U}^\dagger_{\delta\alpha}+h.c.)||\\
&= \frac{L^d}{a^{12-3d}g^6}6442450944(d^3-3d^2+2d).
\end{aligned} \tag{4.316}$$

If the plaquettes acted on by $\hat{h}_{L''}$ share only one dimension with $\hat{h}_L$, and share both dimensions, but not the parity, with $\hat{h}_{L'}$, then $\hat{h}_L$ and $\hat{h}_{L'}$ collide with eight $\hat{h}_{L''}$. Once again, we use Table 4.6 to obtain the number of combinations of parity-location labels that satisfy this condition, i.e.

$$\sum_{l>k}\sum_{k=1}^{d-1} 4(d-l)+2(l-k-1) = (d^3-3d^2+2d). \tag{4.317}$$

The bound in this case is given by

$$\begin{aligned}
&2^{20}|||[[\sum_{\vec{n}_e}\hat{h}_L(e,k,l), \sum_{\hat{h}_{L'}\in\mathbb{L};L'>L}\hat{h}_{L'}], \sum_{\hat{h}_{L''}\in\mathbb{L};L''>L}\hat{h}_{L''}]|||\\
&\leq 2^{20}(d^3-3d^2+2d)\sum_{\vec{n}_e} 4\cdot||\hat{h}_L(e,k,l)||\cdot||\frac{2}{2a^{4-d}g^2}\sum_{\alpha,\beta,\gamma,\delta=1}^{2}(\hat{U}_{\alpha\beta}\hat{U}_{\beta\gamma}\hat{U}^\dagger_{\gamma\delta}\hat{U}^\dagger_{\delta\alpha}+h.c.)||\\
&\quad\cdot||\frac{8}{2a^{4-d}g^2}\sum_{\alpha,\beta,\gamma,\delta=1}^{2}(\hat{U}_{\alpha\beta}\hat{U}_{\beta\gamma}\hat{U}^\dagger_{\gamma\delta}\hat{U}^\dagger_{\delta\alpha}+h.c.)||\\
&= \frac{L^d}{a^{12-3d}g^6}8589934592(d^3-3d^2+2d).
\end{aligned} \tag{4.318}$$

If $\hat{h}_{L''}$ acts on plaquettes that share only one dimension with $\hat{h}_L$ and $\hat{h}_{L'}$, then $\hat{h}_L$ and $\hat{h}_{L'}$ collide with eight $\hat{h}_{L''}$. There are

$$\sum_{l>k}\sum_{k=1}^{d-1} 4(d-l)+2(l-k-1) = d^3-3d^2+2d \tag{4.319}$$

combinations of parity-location labels that satisfy this condition. The bound in this case is given by

$$\begin{aligned}
&2^{20}||[[\sum_{\vec{n}_e}\hat{h}_L(e,k,l), \sum_{\hat{h}_{L'}\in\mathbb{L};L'>L}\hat{h}_{L'}], \sum_{\hat{h}_{L''}\in\mathbb{L};L''>L}\hat{h}_{L''}]|| \\
&\leq 2^{20}(d-1)\sum_{\vec{n}_e} 4\cdot||\hat{h}_L(e,k,l)||\cdot||\frac{4}{2a^{4-d}g^2}\sum_{\alpha,\beta,\gamma,\delta=1}^{2}(\hat{U}_{\alpha\beta}\hat{U}_{\beta\gamma}\hat{U}^\dagger_{\gamma\delta}\hat{U}^\dagger_{\delta\alpha}+h.c.)|| \\
&\quad\cdot||\frac{8}{2a^{4-d}g^2}\sum_{\alpha,\beta,\gamma,\delta=1}^{2}(\hat{U}_{\alpha\beta}\hat{U}_{\beta\gamma}\hat{U}^\dagger_{\gamma\delta}\hat{U}^\dagger_{\delta\alpha}+h.c.)|| \\
&= \frac{L^d}{a^{12-3d}g^6}17179869184(d^3-3d^2+2d).
\end{aligned} \tag{4.320}$$

Consider now the case where $\hat{h}_L$ and $\hat{h}_{L'}$ collide on two dimensions, but have different parities, i.e., item 5 in Table 4.6. Since we implement even terms before odd ones, the parities of $\hat{h}_L$ and $\hat{h}_{L'}$ are even and odd, respectively. Moreover, $\hat{h}_L$ acting on a plaquette collides with four $\hat{h}_{L'}$ on the four links. If $\hat{h}_{L''}$ act on plaquettes that share one dimension with $\hat{h}_L$, and both dimensions and the parity with those acted on by $\hat{h}_{L'}$, then $\hat{h}_L$ and $\hat{h}_{L'}$ collide with four $\hat{h}_{L''}$. There are

$$\sum_{k=1}^{d-1} 1 = d-1 \tag{4.321}$$

combinations of parity-location labels that satisfy this condition. The bound in this case is given by

$$\begin{aligned}
&2^{20}||[[\sum_{\vec{n}_e}\hat{h}_L(e,k,l), \sum_{\hat{h}_{L'}\in\mathbb{L};L'>L}\hat{h}_{L'}], \sum_{\hat{h}_{L''}\in\mathbb{L};L''>L}\hat{h}_{L''}]|| \\
&\leq 2^{20}(d-1)\sum_{\vec{n}_e} 4\cdot||\hat{h}_L(e,k,l)||\cdot||\frac{4}{2a^{4-d}g^2}\sum_{\alpha,\beta,\gamma,\delta=1}^{2}(\hat{U}_{\alpha\beta}\hat{U}_{\beta\gamma}\hat{U}^\dagger_{\gamma\delta}\hat{U}^\dagger_{\delta\alpha}+h.c.)|| \\
&\quad\cdot||\frac{4}{2a^{4-d}g^2}\sum_{\alpha,\beta,\gamma,\delta=1}^{2}(\hat{U}_{\alpha\beta}\hat{U}_{\beta\gamma}\hat{U}^\dagger_{\gamma\delta}\hat{U}^\dagger_{\delta\alpha}+h.c.)|| \\
&= \frac{L^d}{a^{12-3d}g^6}8589934592(d-1).
\end{aligned} \tag{4.322}$$

Therefore, type-(i) commutators, where $\hat{h}_L$ acts on even plaquettes are bounded by

$$(17179869184\frac{d^4}{3}+8589934592\frac{d^3}{3}-146028888064\frac{d^2}{3}+146028888064\frac{d}{3}-8589934592)\frac{L^d}{a^{12-3d}g^6}. \tag{4.323}$$

Similarly, we obtain the bound for the commutators where $\hat{h}_L$ acts on odd plaquettes, i.e.,

$$(17179869184\frac{d^4}{3}-10737418240\frac{d^3}{3}-88046829568\frac{d^2}{3}+81604378624\frac{d}{3})\frac{L^d}{a^{12-3d}g^6}, \tag{4.324}$$

by considering separately the cases, in which $\hat{h}_L$ and $\hat{h}_{L'}$ collide with 2, 4, or 8 $\hat{h}_{L''}$, listed in Table 4.7. Thus, the bound for all type-(i) commutators is

$$(34359738368\frac{d^4}{3}-2147483648\frac{d^3}{3}-234075717632\frac{d^2}{3}+227633266688\frac{d}{3}-8589934592)\frac{L^d}{a^{12-3d}g^6}. \tag{4.325}$$

We proceed to analyze type-(ii) commutators. By definition, $\hat{h}_L$ does not commute with both $\hat{h}_{L'}$ and $\hat{h}_{L''}$, but $\hat{h}_{L'}$ and $\hat{h}_{L''}$ commute with each other. On the lattice, this implies that $\hat{h}_L$ shares one common dimension each with $\hat{h}_{L'}$ and $\hat{h}_{L''}$, but $\hat{h}_{L'}$ and $\hat{h}_{L''}$ share no common dimension. Thus, each plaquette acted on by $\hat{h}_L$ is also acted on by two $\hat{h}_{L'}$ and $\hat{h}_{L''}$. Using table 4.8, we obtain the number of combinations of parity-location labels that satisfy this condition as follows

$$\sum_{l>k}\sum_{k=1}^{d-1}2(d-l)[4(l-k-1)+8(d-l-1)]+8(l-k-1)(d-l)=2d^4-12d^3+11d^2-6d. \tag{4.326}$$

Hence, the bound for all type-(ii) commutators is

$$\begin{aligned}
&2^{20}\sum_{p=e}^{o}||[[\sum_{\vec{n}_p}\hat{h}_L(p,k,l),\sum_{\hat{h}_{L'}\in\mathbb{L};L'>L}\hat{h}_{L'}],\sum_{\hat{h}_{L''}\in\mathbb{L};L''>L}\hat{h}_{L''}]||\\
&\leq 2^{21}(2d^4-12d^3+11d^2-6d)\sum_{\vec{n}_p}4\cdot||\hat{h}_L(p,k,l)||\cdot||\frac{2}{2a^{4-d}g^2}\sum_{\alpha,\beta,\gamma,\delta=1}^{2}(\hat{U}_{\alpha\beta}\hat{U}_{\beta\gamma}\hat{U}^\dagger_{\gamma\delta}\hat{U}^\dagger_{\delta\alpha}+h.c.)||\\
&\quad\cdot||\frac{2}{2a^{4-d}g^2}\sum_{\alpha,\beta,\gamma,\delta=1}^{2}(\hat{U}_{\alpha\beta}\hat{U}_{\beta\gamma}\hat{U}^\dagger_{\gamma\delta}\hat{U}^\dagger_{\delta\alpha}+h.c.)||\\
&=\frac{L^d}{a^{12-3d}g^6}4294967296(2d^4-12d^3+11d^2-6d).
\end{aligned} \tag{4.327}$$

Last but not least, for type (iii) commutators, $\hat{h}_{L'}$ does not commute with both $\hat{h}_L$ and $\hat{h}_{L''}$, but $\hat{h}_L$ and $\hat{h}_{L''}$ commute with each other. On the lattice, this implies that $\hat{h}_{L'}$ share one

common dimension each with $\hat{h}_L$ and $\hat{h}_{L''}$, but $\hat{h}_L$ and $\hat{h}_{L''}$ share no common dimension. Thus, each plaquette acted on by $\hat{h}_L$ is also acted on by two $\hat{h}_{L'}$, and each plaquette acted on by $\hat{h}_{L'}$ is in turn acted on by two $\hat{h}_{L''}$. Using table 4.9, we evaluate the number of combinations of parity-location labels that satisfy this condition, and obtain

$$\sum_{\substack{j>l;\\ l>k}}\sum_{k=1}^{d-1} 16(d-l)(d-j+l-k-1)+8(l-k-1)[(l-j-1)+(j-k-1)] = \frac{2}{5}(2d^5-15d^4+40d^3-45d^2+18d). \tag{4.328}$$

Hence, the bound for all type-(iii) commutators is

$$\begin{aligned}
&2^{20}\sum_{p=e}^{o} |||[[\sum_{\vec{n}_p}\hat{h}_L(p,k,l), \sum_{\hat{h}_{L'}\in\mathbb{L};L'>L}\hat{h}_{L'}], \sum_{\hat{h}_{L''}\in\mathbb{L};L''>L}\hat{h}_{L''}]|||\\
&\leq \frac{2^{22}}{5}(2d^5-15d^4+40d^3-45d^2+18d)\sum_{\vec{n}_p} 4\cdot||\hat{h}_L(p,k,l)||\cdot\\
&\quad\cdot||\frac{2}{2a^{4-d}g^2}\sum_{\alpha,\beta,\gamma,\delta=1}^{2}(\hat{U}_{\alpha\beta}\hat{U}_{\beta\gamma}\hat{U}^\dagger_{\gamma\delta}\hat{U}^\dagger_{\delta\alpha}+h.c.)||\cdot||\frac{2}{2a^{4-d}g^2}\sum_{\alpha,\beta,\gamma,\delta=1}^{2}(\hat{U}_{\alpha\beta}\hat{U}_{\beta\gamma}\hat{U}^\dagger_{\gamma\delta}\hat{U}^\dagger_{\delta\alpha}+h.c.)||\\
&= \frac{L^d}{a^{12-3d}g^6}\frac{8589934592}{5}(2d^5-15d^4+40d^3-45d^2+18d).
\end{aligned} \tag{4.329}$$

Finally, summing up the bounds for all three types of commutators, we obtain the bound for $C_{2,12}$,

$$(17179869184\frac{d^5}{5}-17179869184\frac{d^4}{3}+49392123904\frac{d^3}{3}-322659435248\frac{d^2}{3}+1207422766768\frac{d}{15}-8589934592)\frac{L^d}{a^{12-3d}g^6}. \tag{4.330}$$

Table 4.6: The number of tuples, which label $\hat{h}_{L'}$ and $\hat{h}_{L''}$, such that (4.308) holds and $\hat{h}_L$ is labelled by $(even, k, l)$ with $k < l$. The tuples that label $\hat{h}_{L'}$ are given in the numerically labelled rows. The alphabetical rows, which immediately follow each numerically labelled row, but precede the next one, list the tuples that label $\hat{h}_{L''}$. The number of tuples that label $\hat{h}_{L'}$ for each $\hat{h}_L$, satisfying $L' > L$, and that label $\hat{h}_{L''}$ for each pair of $\hat{h}_L$ and $\hat{h}_{L'}$, satisfying $L'' > L$, are given in the fifth column. The sixth column indicates the number of common dimensions $\hat{h}_{L'}$ or $\hat{h}_{L''}$ at each row share with $\hat{h}_L$. The seventh column denotes whether $\hat{h}_{L'}$ or $\hat{h}_{L''}$ at each row acts on plaquettes of the same parity as $\hat{h}_L$ do. The eighth column indicates the number of common dimensions $\hat{h}_{L''}$ at each row shares with $\hat{h}_{L'}$. The seventh column denotes whether $\hat{h}_{L''}$ at each row acts on plaquettes of the same parity as $\hat{h}_{L'}$ does. Combining the information in the sixth to ninth columns, one can straightforwardly compute, for each combination of tuples that label $\hat{h}_L$, $\hat{h}_{L'}$ and $\hat{h}_{L''}$, the number of links $\hat{h}_L$, $\hat{h}_{L'}$ and $\hat{h}_{L''}$ collide on.

$\hat{h}_L$	$(even, k, l), k < l$			# tuples	# common dimensions	same parity		
1	$\hat{h}_{L'}$	$(even, k, j), j > l$		$d - l$	1	Y	# common dimensions	same parity
	a	$\hat{h}_{L''}$	$(even, k, i), i = j$	1	1	Y	2	Y
	b		$(even, k, i), i > l, i \neq j$	$d-l-1$	1	Y	1	Y
	c		$(even, l, i), i = j$	1	1	Y	1	Y
	d		$(odd, k, i), i = j$	1	1	N	2	N
	e		$(odd, k, i), i = l$	1	2	N	1	N
	f		$(odd, k, i), i > l, i \neq j$	$d-l-1$	1	N	1	N
	g		$(odd, l, i), i = j$	1	1	N	1	N
2	$\hat{h}_{L'}$	$(even, l, j), j > l$		$d - l$	1	Y		
	a	$\hat{h}_{L''}$	$(even, k, i), i = j$	1	1	Y	1	Y
	b		$(even, i, l), k < i < l$	$l-k-1$	1	Y	1	Y
	c		$(even, l, i), i = j$	1	1	Y	2	Y
	d		$(even, l, i), i > l, i \neq j$	$d-l-1$	1	Y	1	Y

Continued on next page

Table 4.6 – continued from previous page

$\hat{h}_L$	$(even, k, l), k < l$			# tuples	# common dimensions	same parity		
	e		$(odd, k, i), i = l$	1	2	N	1	N
	f		$(odd, k, i), i = j$	1	1	N	1	N
	g		$(odd, l, i), i = j$	1	1	N	2	N
	h		$(odd, l, i), i > l, i \neq j$	$d-l-1$	1	N	1	N
	i		$(odd, i, l), k < i < l$	$l-k-1$	1	N	1	N
3	$\hat{h}_{L'}$	$(even, j, l), k < j < l$		$l-k-1$	1	Y		
	a	$\hat{h}_{L''}$	$(even, l, i), i > l$	$d-l$	1	Y	1	Y
	b		$(even, i, l), i = j$	1	1	Y	2	Y
	c		$(even, i, l), k < i < l, i \neq j$	$l-k-2$	1	Y	1	Y
	d		$(odd, l, i), i > l$	$d-l$	1	Y	1	Y
	e		$(odd, k, i), i = l$	1	2	N	1	N
	f		$(odd, i, l), i = j$	1	1	N	2	N
	g		$(odd, i, l), k < i < l, i \neq j$	$l-k-2$	1	N	1	N
4	$\hat{h}_{L'}$	$(odd, k, j), j > l$		$d-l$	1	N		
	a	$\hat{h}_{L''}$	$(even, k, i), i = j$	1	1	Y	2	N
	b		$(even, k, i), i > l, i \neq j$	$d-l-1$	1	Y	1	N
	c		$(even, l, i), i = j$	1	1	Y	1	N
	d		$(odd, k, i), i = j$	1	1	N	2	Y
	e		$(odd, k, i), i = l$	1	2	N	1	Y
	f		$(odd, k, i), i > l, i \neq j$	$d-l-1$	1	N	1	Y
	g		$(odd, l, i), i = j$	1	1	N	1	Y
5	$\hat{h}_{L'}$	$(odd, k, j), j = l$		1	2	N		
	a	$\hat{h}_{L''}$	$(even, k, i), i > l$	$d-l$	1	Y	1	N
	b		$(even, l, i), i > l$	$d-l$	1	Y	1	N
	c		$(even, i, l), k < i < l$	$l-k-1$	1	Y	1	N
	d		$(odd, k, i), i = l$	1	2	N	2	Y
	e		$(odd, k, i), i > l$	$d-l$	1	N	1	Y
	f		$(odd, l, i), i > l$	$d-l$	1	N	1	Y
	g		$(odd, i, l), k < i < l$	$l-k-1$	1	N	1	Y
6	$\hat{h}_{L'}$	$(odd, l, j), j > l$		$d-l$	1	N		

Continued on next page

Table 4.6 – continued from previous page

$\hat{h}_L$	$(even, k, l), k < l$			# tuples	# common dimensions	same parity		
	a	$\hat{h}_{L''}$	$(even, k, i), i = j$	1	1	Y	1	N
	b		$(even, i, l), k < i < l$	$l-k-1$	1	Y	1	N
	c		$(even, l, i), i = j$	1	1	Y	2	N
	d		$(even, l, i), i > l, i \neq j$	$d-l-1$	1	Y	1	N
	e		$(odd, k, i), i = l$	1	2	N	1	Y
	f		$(odd, k, i), i = j$	1	1	N	1	Y
	g		$(odd, l, i), i = j$	1	1	N	2	Y
	h		$(odd, l, i), i > l, i \neq j$	$d-l-1$	1	N	1	Y
	i		$(odd, i, l), k < i < l$	$l-k-1$	1	N	1	Y
7	$\hat{h}_{L'}$	$(odd, j, l), k < j < l$		$l-k-1$	1	N		
	a	$\hat{h}_{L''}$	$(even, l, i), i > l$	$d-l$	1	Y	1	N
	b		$(even, i, l), i = j$	1	1	Y	2	N
	c		$(even, i, l), k < i < l, i \neq j$	$l-k-2$	1	Y	1	N
	d		$(odd, l, i), i > l$	$d-l$	1	N	1	Y
	e		$(odd, k, i), i = l$	1	2	N	1	Y
	f		$(odd, i, l), i = j$	1	1	N	2	Y
	g		$(odd, i, l), k < i < l, i \neq j$	$l-k-2$	1	N	1	Y

Table 4.7: The number of tuples, which label $\hat{h}_{L'}$ and $\hat{h}_{L''}$, such that (4.308) holds and $\hat{h}_L$ is labelled by (odd, k, l) with $k < l$.

$\hat{h}_L$	$(odd, k, l), k < l$			# tuples	# common dimensions	same parity		
1	$\hat{h}_{L'}$	$(even, k, j), j > l$		$d - l$	1	N	# common dimensions	same parity
	a	$\hat{h}_{L''}$	$(even, k, i), i = j$	1	1	N	2	Y
	b		$(even, k, i), i > l, i \neq j$	$d-l-1$	1	N	1	Y
	c		$(even, l, i), i = j$	1	1	N	1	Y
	d		$(odd, k, i), i = j$	1	1	Y	2	N
	e		$(odd, k, i), i > l, i \neq j$	$d-l-1$	1	Y	1	N
	f		$(odd, l, i), i = j$	1	1	Y	1	N
2	$\hat{h}_{L'}$	$(even, l, j), j > l$		$d - l$	1	N		
	a	$\hat{h}_{L''}$	$(even, k, i), i = j$	1	1	N	1	Y
	b		$(even, i, l), k < i < l$	$l-k-1$	1	N	1	Y
	c		$(even, l, i), i = j$	1	1	N	2	Y
	d		$(even, l, i), i > l, i \neq j$	$d-l-1$	1	N	1	Y
	e		$(odd, k, i), i = j$	1	1	Y	1	N
	f		$(odd, l, i), i = j$	1	1	Y	2	N
	g		$(odd, l, i), i > l, i \neq j$	$d-l-1$	1	Y	1	N
	h		$(odd, i, l), k < i < l$	$l-k-1$	1	Y	1	N
3	$\hat{h}_{L'}$	$(even, j, l), k < j < l$		$l-k-1$	1	N		
	a	$\hat{h}_{L''}$	$(even, l, i), i > l$	$d - l$	1	N	1	Y
	b		$(even, i, l), i = j$	1	1	N	2	Y
	c		$(even, i, l), k < i < l, i \neq j$	$l-k-2$	1	N	1	Y
	d		$(odd, l, i), i > l$	$d - l$	1	Y	1	N
	e		$(odd, i, l), i = j$	1	1	Y	2	N
	f		$(odd, i, l), k < i < l, i \neq j$	$l-k-2$	1	Y	1	N

Continued on next page

Table 4.7 – continued from previous page

$\hat{h}_L$	$(odd, k, l), k < l$			# tuples	# common dimensions	same parity		
4	$\hat{h}_{L'}$	$(odd, k, j), j > l$		$d - l$	1	Y		
	a	$\hat{h}_{L''}$	$(even, k, i), i = j$	1	1	N	2	N
	b		$(even, k, i), i > l, i \neq j$	$d-l-1$	1	N	1	N
	c		$(even, l, i), i = j$	1	1	N	1	N
	d		$(odd, k, i), i = j$	1	1	Y	2	Y
	e		$(odd, k, i), i > l, i \neq j$	$d-l-1$	1	Y	1	Y
	f		$(odd, l, i), i = j$	1	1	Y	1	Y
5	$\hat{h}_{L'}$	$(odd, l, j), j > l$		$d - l$	1	Y		
	a	$\hat{h}_{L''}$	$(even, k, i), i = j$	1	1	N	1	N
	b		$(even, i, l), k < i < l$	$l-k-1$	1	N	1	N
	c		$(even, l, i), i = j$	1	1	N	2	N
	d		$(even, l, i), i > l, i \neq j$	$d-l-1$	1	N	1	N
	e		$(odd, k, i), i = j$	1	1	Y	1	Y
	f		$(odd, l, i), i = j$	1	1	Y	2	Y
	g		$(odd, l, i), i > l, i \neq j$	$d-l-1$	1	Y	1	Y
	h		$(odd, i, l), k < i < l$	$l-k-1$	1	Y	1	Y
6	$\hat{h}_{L'}$	$(odd, j, l), k < j < l$		$l-k-1$	1	Y		
	a	$\hat{h}_{L''}$	$(even, l, i), i > l$	$d - l$	1	N	1	N
	b		$(even, i, l), i = j$	1	1	N	2	N
	c		$(even, i, l), k < i < l, i \neq j$	$l-k-2$	1	N	1	N
	d		$(odd, l, i), i > l$	$d - l$	1	Y	1	Y
	e		$(odd, i, l), i = j$	1	1	Y	2	Y
	f		$(odd, i, l), k < i < l, i \neq j$	$l-k-2$	1	Y	1	Y

Oracle errors

Here, we describe the direct syntheses of the kinetic and magnetic oracles, and compute the errors incurred by the fixed point arithmetic circuits.

Syntheses of the kinetic oracles: The kinetic oracle, defined in (4.202), can be directly synthesized as two controlled-diagonal gates, which impart the phases $(-1)^{j'_0} f_{\alpha\beta}(j, \Delta j, m^L, m^R) \frac{t}{2a}$,

$\hat{h}_L$	$(p,k,l), k<l$			# tuples
1	$\hat{h}_{L'}$	$(p',k,j), j>l$		$d-l$
	a	$\hat{h}_{L''}$	$(p,i,l), k<i<l$	$l-k-1$
	b		$(p,l,i), i>l, i\neq j$	$d-l-1$
	c		$(p',i,l), k<i<l$	$l-k-1$
	d		$(p',l,i), i>l, i\neq j$	$d-l-1$
2	$\hat{h}_{L'}$	$(p',l,j), j>l$		$d-l$
	a	$\hat{h}_{L''}$	$(p',k,i), i>l, i\neq j$	$d-l-1$
	b		$(p,k,i), i>l, i\neq j$	$d-l-1$
3	$\hat{h}_{L'}$	$(p',j,l), k<j<l$		$l-k-1$
	a	$\hat{h}_{L''}$	$(p',k,i), i>l$	$d-l$
	b		$(p,k,i), i>l$	$d-l$
4	$\hat{h}_{L'}$	$(p,k,j), j>l$		$d-l$
	a	$\hat{h}_{L''}$	$(p,i,l), k<i<l$	$l-k-1$
	b		$(p,l,i), i>l, i\neq j$	$d-l-1$
	c		$(p',i,l), k<i<l$	$l-k-1$
	d		$(p',l,i), i>l, i\neq j$	$d-l-1$
5	$\hat{h}_{L'}$	$(p,l,j), j>l$		$d-l$
	a	$\hat{h}_{L''}$	$(p',k,i), i>l, i\neq j$	$d-l-1$
	b		$(p,k,i), i>l, i\neq j$	$d-l-1$
6	$\hat{h}_{L'}$	$(p,j,l), k<j<l$		$l-k-1$
	a	$\hat{h}_{L''}$	$(p',k,i), i>l$	$d-l$
	b		$(p,k,i), i>l$	$d-l$

Table 4.8: The number of tuples, which label $\hat{h}_{L'}$ and $\hat{h}_{L''}$, such that (4.309) holds and $\hat{h}_L$ is labelled by (p,k,l) with $k<l$. Here, $p\neq p'$.

where $f_{\alpha\beta}(\cdot)$ is defined in (4.191), for $j'_0=0,1$, if the control bits $m_0^{L\prime}, m_0^{R\prime}, f'_{\alpha,r}$, and $f'_{\beta,r+1}$ are all ones. Without loss of generality, we consider the case where $j'_0=0$. The implementation of the diagonal phase gate is similar to that of the electric term. Before providing the details, we provide a high-level description of the implementation. We begin by computing $f_{\alpha\beta}(j,\Delta j,m^L,m^R)$ into an ancilla register, conditioned upon the values of the control bits. Then, by applying R_z gates to the ancilla state $\left|f_{\alpha\beta}(j,\Delta j,m^L,m^R)\right\rangle$, we induce the correct phase. Finally, we uncompute $\left|f_{\alpha\beta}(j,\Delta j,m^L,m^R)\right\rangle$. The computation of $f_{\alpha\beta}(j,\Delta j,m^L,m^R)$, each of which is the square root of a fraction as defined in (4.191), can be broken down into five steps. In the first and second steps, we compute the numerator and denominator, respectively. In the third step, we approximate the inverse of the denominator, using the circuits in [136]. In the fourth step, we approximate the argument of the square-root by multiplying together the numerator and the inverse of the

$\hat{h}_L$	$(p,k,l), k<l$			# tuples
1	$\hat{h}_{L'}$	$(p',k,j), j>l$		$d-l$
	a	$\hat{h}_{L''}$	$(p,j,i), j<i$	$d-j$
	b		$(p',j,i), j<i$	$d-j$
	c		$(p,i,j), k<i<l$	$l-k-1$
	d		$(p',i,j), k<i<l$	$l-k-1$
2	$\hat{h}_{L'}$	$(p',l,j), j>l$		$d-l$
	a	$\hat{h}_{L''}$	$(p,j,i), j<i$	$d-j$
	b		$(p',j,i), j<i$	$d-j$
	c		$(p,i,j), k<i<l$	$l-k-1$
	d		$(p',i,j), k<i<l$	$l-k-1$
3	$\hat{h}_{L'}$	$(p',j,l), k<j<l$		$l-k-1$
	a	$\hat{h}_{L''}$	$(p,j,i), j<i<l$	$l-j-1$
	b		$(p',j,i), j<i<l$	$l-j-1$
	c		$(p,i,j), k<i<j$	$j-k-1$
	d		$(p',i,j), k<i<j$	$j-k-1$
4	$\hat{h}_{L'}$	$(p,k,j), j>l$		$d-l$
	a	$\hat{h}_{L''}$	$(p,j,i), j<i$	$d-j$
	b		$(p',j,i), j<i$	$d-j$
	c		$(p,i,j), k<i<l$	$l-k-1$
	d		$(p',i,j), k<i<l$	$l-k-1$
5	$\hat{h}_{L'}$	$(p,l,j), j>l$		$d-l$
	a	$\hat{h}_{L''}$	$(p,j,i), j<i$	$d-j$
	b		$(p',j,i), j<i$	$d-j$
	c		$(p,i,j), k<i<l$	$l-k-1$
	d		$(p',i,j), k<i<l$	$l-k-1$
6	$\hat{h}_{L'}$	$(p,j,l), k<j<l$		$l-k-1$
	a	$\hat{h}_{L''}$	$(p,j,i), j<i<l$	$l-j-1$
	b		$(p',j,i), j<i<l$	$l-j-1$
	c		$(p,i,j), k<i<j$	$j-k-1$
	d		$(p',i,j), k<i<j$	$j-k-1$

Table 4.9: The number of tuples, which label $\hat{h}_{L'}$ and $\hat{h}_{L''}$, such that (4.310) holds and $\hat{h}_L$ is labelled by (p,k,l) with $k<l$. Here, $p \neq p'$.

denominator. Lastly, we approximate the square-root, using the circuits in [136]. Only the third and last steps incur approximation errors. Hereafter, we use the logarithmic depth out-of-place

adder developed in [148], unless one of the inputs is classically known in which case we use the adder proposed in [137], and the multiplier proposed in [7].

We consider the computation of the numerator. First, we perform two additions or subtractions between j and m^L, and j and m^R, which requires two $(\eta+1)$-bit adders. They cost $40(\eta+1)-24\lfloor\log(\eta+1)\rfloor-8$ T gates. Next, we divide the outputs by 2, which is accomplished by shifting the decimal point. Then, for each output, we add or subtract an η-bit classically known number, costing $4(\eta-1)$ T gates. At this point, we have two numbers with at most $(\eta+3)$ bits, which we need to multiply together. We need to guarantee that both numbers are positive, which implies the realness of the Clebsch-Gordan coefficients, and that the quantum numbers are within the allowed ranges given in (4.162) and (4.163), i.e., $j \leq \Lambda, -j \leq m^L \leq j, -j \leq m^R \leq j$. This can be accomplished by applying a Toffoli to an ancilla bit, controlled by the bits representing the signs of the two numbers, and then, apply the multiplication, conditioned upon the value of the ancilla bit. The singly-controlled multiplication operation is implemented in two stages. First, we copy one of the numbers into an ancilla register, controlled by the ancilla bit, which costs $(\eta+3)$ Toffoli gates and ancilla qubits. The Toffoli gates can be synthesized with $4\eta+16$ T gates [146]. Second, we apply a multiplier to the register that holds the controlled-copy, and the uncopied number. This requires one $(\eta+3)$-bit multiplier, which costs $4(\eta+2)(12\eta-3\lfloor\log(\eta+3)\rfloor+23)+4$ T gates. The number of ancilla qubits required to store the outputs is $5\eta+15$, and that required for the workspace is $3(\eta+3)-\lfloor\log(\eta+3)\rfloor-1$. For the computation of the denominator, we have to add a classical number to j with at most 2 bits twice, costing $8(\eta-2)$ in total and resulting in two $(\eta+1)$-bit numbers. Then, we multiply them together, which costs $4\eta(12\eta-3\lfloor\log(\eta+1)\rfloor)+4$ T gates. The number of ancilla qubits required to store the outputs is $4\eta+4$, and that required for the workspace is $3(\eta+1)-\lfloor\log(\eta+1)\rfloor-1$.

Next, we consider the third step, where we compute the inverse of the denominator using the algorithm in [136]. Briefly, the algorithm takes a fixed precision n-bit binary number $w \geq 1$, with the first m bits representing the integer part, and approximates $\frac{1}{w}$ by applying Newton's root-finding algorithm to $f(x) = \frac{1}{w} - x$. This produces a sequence of estimates, according to the recurrence equation

$$x_i = -w\tilde{x}_{i-1}^2 + 2\tilde{x}_{i-1},\ i = 1, 2, ..., s, \tag{4.331}$$

where $\tilde{x}_{i-1}$ is obtained by truncating x_{i-1} to $b \geq n$ bits after the decimal point. If the initial estimate $\tilde{x}_0 = 2^{-p}$ with $p \in \mathbb{N}$ and $2^p > w \geq 2^{p-1}$, and $s = \lceil\log(b)\rceil$, then the approximation error is

$$|\tilde{x}_s - \frac{1}{w}| \leq \frac{2+\log(b)}{2^b}. \tag{4.332}$$

Since the input w, in this case, is the denominator, at most an $(2\eta+2)-$bit integer, the algorithmic parameters $n = m = 2\eta+2$. Thus, the preparation of the initial estimate requires $2\eta+1$ Toffoli gates, which cost 4 T gates each [146], and one triply-controlled Toffoli gate, which costs 15 T gates [145]. The evaluation of each iteration can be split into four steps: (i) squaring $\tilde{x}_{i-1}$; (ii) multiplying w and $\tilde{x}_{i-1}^2$; (iii) appending a 0 to $\tilde{x}_{i-1}$ to obtain $2\tilde{x}_{i-1}$; and (iv) adding $2\tilde{x}_{i-1}$ to

the negated $w\tilde{x}_{i-1}^2$. Using the fact that each estimate $\tilde{x}_i \leq \frac{1}{w} \leq 1$ is at most a $b-$bit number, we obtain the T-gate count for inverting the denominator, i.e., $\lceil \log(b) \rceil \cdot [48b^2 + 96b(2\eta+2) - 12(b-1)\lfloor \log(b) \rfloor - 12(2\eta+1)\lfloor \log(b) \rfloor - 152b - 32(2\eta+2) - 12\lfloor \log(2b+2\eta+2) \rfloor + 104] + 8\eta + 19$. Furthermore, the number of storage and workspace ancilla qubits required are $\lceil \log(b) \rceil \cdot (4\eta + 7b + 6)$ and $6b - \lfloor \log(6b) \rfloor - 1$, respectively.

In the fourth step, we multiply the numerator and the inverse of the denominator, which are at most $(2\eta+6)-$bit and $b-$bit numbers, respectively, to obtain the fraction. Assuming $b \geq 2\eta + 6$, this costs $4b + 4(2\eta+5)(12b - 3\lfloor \log(b) \rfloor - 13)$ T gates, $b + 2\eta + 6$ storage ancilla qubits, and $3b - \lfloor \log(b) \rfloor - 1$ workspace ancilla qubits. In the fifth step, we compute the square-root of the fraction using the algorithm in [136]. Briefly, given an $n-$bit input $w \geq 1$ with an m-bit integer part, the algorithm first calls the inverse algorithm to obtain $\tilde{x}_s \approx \frac{1}{w}$. Then, it applies Newton's root-finding algorithm to $f(y) = \frac{1}{y^2} - \frac{1}{w}$ to approximate $\sqrt{w}$ via the recursive relation

$$y_j = \frac{1}{2}(3\tilde{y}_{j-1} - \tilde{x}_s \tilde{y}_{j-1}^3),\ j = 1, 2, ..., s, \tag{4.333}$$

where $\tilde{y}_{j-1}$ is obtained by truncating y_{j-1} to $c \geq \max\{2m, 4\}$ bits after the decimal point. If $\tilde{y}_0 = 2^{\lfloor (q-1)/2 \rfloor}$ with $q \in \mathbb{N}$ and $2^{1-q} > \tilde{x}_s \geq 2^{-q}$, and $s = \lceil \log(c) \rceil$, then the approximation error is

$$|\tilde{y}_s - \sqrt{w}| \leq \left(\frac{3}{4}\right)^{c-2m} (2 + c + \log(c)). \tag{4.334}$$

The output of the fourth step is at most a $(b + 4\eta + 6)-$bit fraction that is bounded above and below by 1 and 0, respectively. Since the square-root algorithm requires an input $w \geq 1$, we shift the decimal point of the fraction $(b + 4\eta + 6)$ times to obtain a $(b + 4\eta + 6)-$bit integer $w \geq 1$, and shift it back $(b + 4\eta + 6)/2$ times once we obtain the root. We assume without loss of generality that we have chosen an even b in the third step. We divide the fifth step into three stages: calling the inverse algorithm, preparing $|\tilde{y}_0\rangle$, and Newton's iteration for $|\tilde{y}_s\rangle$. The costs of the inverse algorithm has been discussed above. The second stage requires $\lceil \frac{3c}{2} \rceil$ storage ancilla qubits, $\lceil \frac{c}{2} \rceil$ Toffoli gates, $\lceil \frac{c}{2} \rceil - 1$ triply-controlled Toffoli gates, and one quadruply-controlled Toffoli gates. We further divide the third stage into four steps: (i) multiplying $\tilde{x}_s$ and $\tilde{y}_0$; (ii) multiplying $\tilde{x}_s\tilde{y}_0$ and $\tilde{y}_0$; (iii) add 3 to the negated $\tilde{x}_s\tilde{y}_0^2$; and (iv) multiplying $3 - \tilde{x}_s\tilde{y}_0^3$ by $\tilde{y}_0$ and then, $\frac{1}{2}$. We use the fact that each estimate $\tilde{y}_i$ is at most a $\lceil \frac{3c}{2} \rceil-$bit number to obtain the total T-gate count, i.e., $\lceil \log(c) \rceil \cdot [528c^2 + 96bc + 384c\eta - c(12\lfloor \log(c) \rfloor + 12\lfloor \log(\lceil \frac{3c}{2} \rceil) \rfloor + 12\lfloor \log(\lceil \frac{5c}{2} \rceil) \rfloor + 18\lfloor \log(1+4c) \rfloor) - 12b\lfloor \log(2c) \rfloor - 48\eta\lfloor \log(2c) \rfloor + 12(\lfloor \log(c) \rfloor + \lfloor \log(\lceil \frac{3c}{2} \rceil) \rfloor) - 60\lfloor \log(2c) \rfloor + 12\lfloor \log(\lceil \frac{5c}{2} \rceil) \rfloor + 12\lfloor \log(1+4c) \rfloor - 12\lfloor \log(2c+b+4\eta+6) \rfloor + 50c - 32b - 128\eta - 28] + \lceil \frac{19c}{2} \rceil + 4b + 16\eta + 43$. The number of storage and workspace ancilla qubits required are $\lceil \log(c) \rceil \cdot (\lceil \frac{51c}{2} \rceil + 8\eta + 2b + 17)$ and $12c - \lfloor \log(4c+2) \rfloor + 5$, respectively.

We impart the phase by applying $R_z(2^{k-c}\theta)$, where c is the number of digits after the decimal point in the output of the square-root functions, and $\theta = \frac{t}{2a}$, to the kth qubit of the ancilla state

$\left|f_{\alpha\beta}(j,\Delta j,m^L,m^R)\right\rangle$. In order to implement the controlled version of this phase gate, we control each R_z gate by the four control bits and the ancilla bit that checks the realness of the Clebsch-Gordan coefficients. Each quintuply-controlled R_z gate requires two quintuply-controlled Toffoli gates, which cost 31 T gates each [145], two R_z gates and one ancilla qubit [144]. Since the state has at most $\lceil\frac{3c}{2}\rceil$ qubits and there are dL^d links on the lattice, there are $\lceil\frac{3c}{2}\rceil dL^d$ multi-controlled R_z gates to be applied.

We sum up the T-gate requirements for all the steps, and multiply the outcome by two to account for the uncomputation costs. Conjugating each controlled R_z gate with a pair of CNOT gates, where j_0' is the control bit, addresses both $j_0'=0,1$. As such, the T-gate count for one oracle call, i.e.,

$$\begin{aligned}\mathcal{T}^{(K)} = 2\lceil\log(c)\rceil\cdot[&528c^2+96bc+384c\eta-c(12\lfloor\log(c)\rfloor+12\lfloor\log\left(\lceil\frac{3c}{2}\rceil\right)\rfloor+12\lfloor\log\left(\lceil\frac{5c}{2}\rceil\right)\rfloor\\&+18\lfloor\log(1+4c)\rfloor)-12b\lfloor\log(2c)\rfloor-48\eta\lfloor\log(2c)\rfloor+12(\lfloor\log(c)\rfloor+\lfloor\log\left(\lceil\frac{3c}{2}\rceil\right)\rfloor)\\&-60\lfloor\log(2c)\rfloor+12\lfloor\log\left(\lceil\frac{5c}{2}\rceil\right)\rfloor+12\lfloor\log(1+4c)\rfloor-12\lfloor\log(2c+b+4\eta+6)\rfloor+50c\\&-32b-128\eta-28]+19c+8b+32\eta+86+2\lceil\log(b)\rceil\cdot[48b^2+96b(2\eta+2)\\&-12(b-1)\lfloor\log(b)\rfloor-12(2\eta+1)\lfloor\log(b)\rfloor-152b-32(2\eta+2)-12\lfloor\log(2b+2\eta+2)\rfloor\\&+104]+16\eta+38+8b+8(2\eta+5)(12b-3\lfloor\log(b)\rfloor-13)+88\eta-48\lfloor\log(\eta+1)\rfloor\\&+(8\eta+16)(12\eta-3\lfloor\log(\eta+3)\rfloor+23)+8\eta(12\eta-3\lfloor\log(\eta+1)\rfloor)+74+186c+32\eta-48.\end{aligned}\tag{4.335}$$

The number of storage ancilla qubits required is

$$\lceil\log(c)\rceil\cdot(\lceil\frac{49c}{2}\rceil+2b+8\eta+17)+\lceil\log(b)\rceil\cdot(4\eta+7b+6)+b+9\eta+19,\tag{4.336}$$

and the number of workspace ancilla qubits required is

$$12c-\lfloor\log(4c+1)\rfloor+5.\tag{4.337}$$

There are two types of syntheses errors, i.e., arithmetic approximation errors and R_z syntheses errors. The latter will be analyzed in Sec. 4.4.3. The arithmetic approximation errors per step is given by

$$\frac{2+\log(b)}{2^b}+\left(\frac{3}{4}\right)^{c-(2b+8\eta+12)}(2+c+\log(c)).\tag{4.338}$$

In total, the approximation errors are

$$\epsilon^{(K)}=r\cdot 64dL^d[\frac{2+\log(b)}{2^b}+\left(\frac{3}{4}\right)^{c-(2b+8\eta+12)}(2+c+\log(c))],\tag{4.339}$$

where r is the number of Trotter steps, and $64dL^d$ is the number of oracle calls. We divide the approximation errors evenly such that

$$\epsilon_b^{(K)} = \frac{\epsilon^{(K)}}{2r \cdot 64dL^d},\ \epsilon_c^{(K)} = \frac{\epsilon^{(K)}}{2r \cdot 64dL^d}, \tag{4.340}$$

and

$$\epsilon_b^{(K)} \geq \frac{2 + \log(b)}{2^b}, \tag{4.341}$$

$$\epsilon_c^{(K)} \geq \left(\frac{3}{4}\right)^{c-(2b+8\eta+12)} (2 + c + \log(c)). \tag{4.342}$$

Note that this is not the optimal division of approximation errors. We let $b = \log\left(\frac{8}{\epsilon_b^{(K)}}\right)$. Then, (4.341) is always satisfied for $0 < \epsilon_b^{(K)} < 1$. We proceed to compute the upper bound for c. Since $c \geq 2b + 8\eta + 12 \geq 12\eta + 24$, and $\eta \geq 1$, $\frac{44}{36}c \geq 2 + c + \log(c)$. Inserting this relation and our choice of b into (4.342), we obtain

$$\epsilon_c^{(K)} \geq \left(\frac{3}{4}\right)^{c-\left(2\log\left(8/\epsilon_b^{(K)}\right)+8\eta+12\right)} \frac{44}{36}c. \tag{4.343}$$

Let

$$\tilde{\epsilon}_c^{(K)} = \epsilon_c^{(K)} \cdot \left(\frac{3}{4}\right)^{2\log\left(8/\epsilon_b^{(K)}\right)+8\eta+12} \frac{36}{44}. \tag{4.344}$$

Then, we want to find a c such that

$$c\left(\frac{3}{4}\right)^c \leq \tilde{\epsilon}_c^{(K)}. \tag{4.345}$$

Assuming that $0 < \tilde{\epsilon}_c^{(K)} < 1$, the choice

$$c = \log_{\frac{3}{4}}\left(\frac{\frac{\tilde{\epsilon}_c^{(K)}}{2.28}}{\log_{\frac{3}{4}}\left(\frac{\tilde{\epsilon}_c^{(K)}}{2.28}\right)}\right) \tag{4.346}$$

satisfies (4.345). We have verified numerically with Mathematica that for $0 < \tilde{\epsilon}_{\text{oracle}} < 1$, $\tilde{\epsilon}_{\text{oracle}} - c\left(\frac{3}{4}\right)^c$ never exceeds 0.0431937, given our choice of c.

We mention in passing that the phase-inducing step can be parallelized. As in U(1), we first divide the kinetic terms up into bulk and edge terms. Then, for each direction of the bulk or edge terms, we implement $O(L^d - L^{d-1})$ or $O(L^{d-1})$ $R_z(2^{k-c}\theta)$ in parallel, using the weight-sum

trick, and thus, exponentially reducing the number of R_z gates required to $O(cd\log(L^d))$. In this work, we focus on the resource analysis of the serial implementation, and will leave that of the parallel implementation for future work.

Syntheses of the magnetic oracles: Similar to the implementation of the kinetic oracle, we directly synthesize the magnetic oracle, defined in (4.208), as two controlled-diagonal gates, which impart the phases $\frac{-f_{\alpha\beta\gamma\delta}}{2a^{4-d}g^2}(-1)^{j'_{1,0}}$ for $j'_{1,0}=0,1$, if the control bits $m^{L\prime}_{1,0}$, $m^{R\prime}_{1,0}$, $j'_{2,0}$, $m^{L\prime}_{2,0}$, $m^{R\prime}_{2,0}$, $j'_{3,0}$, $m^{L\prime}_{3,0}$, $m^{R\prime}_{3,0}$, $j'_{4,0}$, $m^{L\prime}_{4,0}$, and $m^{R\prime}_{4,0}$ are all ones. The function $f_{\alpha\beta\gamma\delta}$ is defined in (4.207) as a product of four functions, $f_{\alpha\beta}(j_1,\Delta j_1,m_1^L,m_1^R)$, $f_{\beta\gamma}(j_2,\Delta j_2,m_2^L,m_2^R)$, $f_{\gamma\delta}(j_3,\Delta j_3,m_3^L,m_3^R)$, and $f_{\delta\alpha}(j_4,\Delta j_4,m_4^L,m_4^R)$, where $\left|j_i,m_i^L,m_i^R\right\rangle$ represents the state for the ith link on a plaquette. Without loss of generality, we consider the case where $j'_{1,0}=0$. We begin by computing $f_{\alpha\beta\gamma\delta}$ into an ancilla register, conditioned upon the values of the control bits. Then, we induce the correct phase by applying R_z gates to the ancilla state $|f_{\alpha\beta\gamma\delta}\rangle$. Finally, we uncompute $|f_{\alpha\beta\gamma\delta}\rangle$. The computation of $f_{\alpha\beta\gamma\delta}$ can be broken down into five steps. In the first and second steps, we compute the numerator and denominator, respectively. In the third step, we approximate the inverse of the denominator, using the circuits in [136]. In the fourth step, we approximate the argument of the square-root by multiplying together the numerator and the inverse of the denominator. Lastly, we approximate the square-root, using the circuits in [136]. Only the third and last steps incur approximation errors. Hereafter, we use the logarithmic depth out-of-place adder developed in [148], unless one of the inputs is classically known in which case we use the adder proposed in [137], and the multiplier proposed in [7].

First, we consider the computation of the numerator. We start with computing the numerators in the four functions that constitute $f_{\alpha\beta\gamma\delta}$. This costs four times as many T gates and storage ancilla qubits as those required for the computation of the numerator in a kinetic oracle, i.e., $16(\eta+2)(12\eta-3\lfloor\log(\eta+3)\rfloor+23)+240\eta-96\lfloor\log(\eta+1)\rfloor+208$ and $20\eta+60$, respectively, while the reusable workspace ancilla qubit requirement remains the same, i.e., $3(\eta+3)-\lfloor\log(\eta+3)\rfloor-1$. The multiplication of the four numerators costs two $(2\eta+6)$-bit multipliers, and one $(4\eta+12)-$bit multiplier. In total, the multipliers cost $(16\eta+44)(48\eta-3\lfloor\log(4\eta+12)\rfloor+131)+(8\eta+20)(24\eta-3\lfloor\log(2\eta+6)\rfloor+59)+(32\eta+96)$ T gates, $16\eta+48$ storage ancilla qubits, and $12\eta-\lfloor\log(4\eta+12)\rfloor+35$ workspace ancilla qubits. Next, we compute the denominator. First, we perform two additions of a classical number to an $\eta-$bit j_i, for each $i\in\{1,2,3,4\}$, which costs $32(\eta-2)$T gates, and then, multiply together eight $(\eta+1)-$bit numbers, which requires four $(\eta+1)-$bit multipliers, two $(2\eta+2)-$bit multipliers, and one $(4\eta+4)-$bit multiplier. This costs $(16\eta+12)(48\eta-3\lfloor\log(4\eta+4)\rfloor+35)+(16\eta+8)(24\eta-3\lfloor\log(2\eta+2)\rfloor+11)+16\eta(12\eta-3\lfloor\log(\eta+1)\rfloor-1)+(48\eta+48)$ T gates, $32\eta+32$ storage ancilla qubits, and $12\eta-\lfloor\log(4\eta+4)\rfloor+11$ workspace ancilla qubits.

We now proceed to compute the inverse of the denominator using the algorithm in [136]. We refer readers to the kinetic oracle implementation for a detailed overview of the algorithm. Here, we simply state the algorithmic parameters and costs. The input w is at most an $(8\eta+8)$-bit integer. Truncating at $b\geq 8\eta+8$ bits after the decimal point, the approximation error is

bounded from above by $\frac{2+\log(b)}{2^b}$. The T-gate count is $\lceil\log(b)\rceil\cdot(48b^2+768b\eta-(12b+96\eta-12)\lfloor\log(b)\rfloor+616b-256\eta-12\lfloor\log(2b+8\eta+8)\rfloor-84\lfloor\log(2b)\rfloor-152)+32\eta+43$. The required number of storage ancilla qubits is $\lceil\log(b)\rceil\cdot(7b+16\eta+18)$, and that of workspace ancilla qubits is $6b-\lfloor\log(2b)\rfloor-1$. Next, we multiply the numerator, an $8\eta+24$-bit number, and the inverse of the denominator, a b-bit number to obtain the fraction. Assuming that $b\geq 8\eta+24$, this costs $384b\eta-96\eta\lfloor\log(b)\rfloor+1108b-416\eta-276\lfloor\log(b)\rfloor-1196$ T gates, $b+8\eta+24$ storage ancilla qubits, and $3b-\lfloor\log(b)\rfloor-1$ workspace ancilla qubits. Lastly, we compute the square-root function. The output of the previous step is a $(b+8\eta+24)$-bit fraction, bounded above and below by 1 and 0, respectively. As in the kinetic oracle implementation, we shift it by $b+8\eta+24$ bits to obtain an integer input w, and shift it back by $(b+8\eta+24)/2$ bits once we obtain the root, assuming without loss of generality that b is even. Let $c\geq 2b+16\eta+48$. Then, we approximate $\sqrt{w}$, up to $\left(\frac{3}{4}\right)^{c-2m}(2+c+\log(c))$ error. This costs $\lceil\log(c)\rceil\cdot[528c^2+96bc+768c\eta-c(12\lfloor\log(c)\rfloor+12\lfloor\log\left(\lceil\frac{3c}{2}\rceil\right)\rfloor+12\lfloor\log\left(\lceil\frac{5c}{2}\rceil\right)\rfloor+18\lfloor\log(1+4c)\rfloor)-12b\lfloor\log(2c)\rfloor-96n\lfloor\log(2c)\rfloor+12\lfloor\log(c)\rfloor+12\lfloor\log\left(\lceil\frac{3c}{2}\rceil\right)\rfloor-276\lfloor\log(2c)\rfloor+12\lfloor\log\left(\lceil\frac{5c}{2}\rceil\right)\rfloor+12\lfloor\log(1+4c)\rfloor-12\lfloor\log(2c+b+8n+24)\rfloor+1778c-32b-256\eta-604]+\lceil\frac{19c}{2}\rceil+4b+32\eta+115$ T gates, $\lceil\log(c)\rceil\cdot(\lceil\frac{51c}{2}\rceil+2b+16\eta+53)$ storage ancilla qubits, and $12c-\lfloor\log(4c+1)\rfloor+5$ workspace ancilla qubits.

We impart the phase by applying $R_z(2^{k-c}\theta)$, where c is the number of digits after the decimal in the output of the square-root function, and $\theta=\frac{-1}{2a^{4-d}g^2}$, to the kth qubit of the ancilla state $|f_{\alpha\beta\gamma\delta}\rangle$. In order to implement the controlled version of this phase gate, we control each R_z gate by the eleven control bits and the four ancilla bits that check the realness of the Clebsch-Gordan coefficients. Each multi-controlled R_z gate requires two Toffoli gates with fifteen controls, which cost 119 T gates each [145], two R_z gates and one ancilla qubit [144]. Since the state has at most $\lceil\frac{3c}{2}\rceil$ qubits and there are $L^d\frac{d(d-1)}{2}$ plaquettes on the lattice, there are $3cL^d\frac{d(d-1)}{2}$ multi-controlled R_z gates to be applied.

We sum up the T-gate requirements for all the steps, and multiply the outcome by two to account for the uncomputation costs. Conjugating each controlled R_z gate with a pair of CNOT gates, where j_0' is the control bit, addresses both $j_0'=0,1$. As such, the T-gate count for one

oracle call, i.e.,

$$\begin{aligned}\mathcal{T}^{(B)} &= 1248\eta^2 - 12\eta(\lceil\log(2\eta+6)\rceil - 2\lceil\log(2\eta+2)\rceil - 2\lceil\log(\eta+3)\rceil + 2\lceil\log(\eta)\rceil \\ &\quad + 2\lceil\log(4\eta+12)\rceil + \lceil\log(4\eta+4)\rceil) + 3844\eta - 6(2\lceil\log(2\eta+2)\rceil + 8\lceil\log(\eta+1)\rceil \\ &\quad + 8\lceil\log(\eta+3)\rceil + 5\lceil\log(2\eta+6)\rceil + 3\lceil\log(4\eta+4)\rceil + 11\lceil\log(4\eta+12)\rceil) + 4270 \\ &\quad + 2\lceil\log(b)\rceil \cdot (48b^2 + 768b\eta - (12b + 96\eta - 12)\lfloor\log(b)\rfloor + 616b - 256\eta \\ &\quad - 12\lfloor\log(2b+8\eta+8)\rfloor - 84\lfloor\log(2b)\rfloor - 152) + 64\eta + 86 \\ &\quad + 768b\eta - 192\eta\lfloor\log(b)\rfloor + 2216b - 832\eta - 552\lfloor\log(b)\rfloor - 3624 \\ &\quad + 2\lceil\log(c)\rceil \cdot [528c^2 + 96bc + 768c\eta - c(12\lfloor\log(c)\rfloor + 12\lfloor\log\left(\lceil\frac{3c}{2}\rceil\right)\rfloor + 12\lfloor\log\left(\lceil\frac{5c}{2}\rceil\right)\rfloor \\ &\quad + 18\lfloor\log(2+4c)\rfloor) - 12b\lfloor\log(2c)\rfloor - 96\eta\lfloor\log(2c)\rfloor + 12\lfloor\log(c)\rfloor + 12\lfloor\log\left(\lceil\frac{3c}{2}\rceil\right)\rfloor \\ &\quad - 276\lfloor\log(2c)\rfloor + 12\lfloor\log\left(\lceil\frac{5c}{2}\rceil\right)\rfloor + 12\lfloor\log(2+4c)\rfloor - 12\lfloor\log(2c+b+8\eta+24)\rfloor \\ &\quad + 1762c - 32b - 256\eta - 596] + 19c + 8b + 64\eta + 96 + 714c + 192\eta - 320. \end{aligned} \tag{4.347}$$

The number of storage ancilla qubits required is

$$\lceil\log(c)\rceil \cdot (\lceil\frac{49c}{2}\rceil + 4b + 32\eta + 101) + \lceil\log(b)\rceil \cdot (7b + 16\eta + 18) + b + 76\eta + 164, \tag{4.348}$$

and the number of workspace ancilla qubits required is

$$12c - \lfloor\log(4c+1)\rfloor + 5. \tag{4.349}$$

There are two types of syntheses errors, i.e., arithmetic approximation errors and R_z syntheses errors. The latter will be analyzed in Sec. 4.4.3. The arithmetic approximation errors per step is given by

$$\frac{2+\log(b)}{2^b} + \left(\frac{3}{4}\right)^{c-(2b+16\eta+48)}(2 + c + \log(c)). \tag{4.350}$$

In total, the approximation errors are

$$\epsilon^{(B)} = r \cdot 1048576 \cdot \frac{d(d-1)}{2} L^d (\frac{2+\log(b)}{2^b} + \left(\frac{3}{4}\right)^{c-(2b+16\eta+48)}(2 + c + \log(c))), \tag{4.351}$$

where r is the number of Trotter steps, and $1048576 \cdot \frac{d(d-1)}{2} L^d$ is the number of oracle calls. We divide the approximation errors evenly such that

$$\epsilon_b^{(B)} = \frac{\epsilon^{(B)}}{r \cdot 1048576 d(d-1) L^d}, \; \epsilon_c^{(B)} = \frac{\epsilon^{(B)}}{r \cdot 1048576 d(d-1) L^d}, \tag{4.352}$$

and

$$\epsilon_b^{(B)} \geq \frac{2+\log(b)}{2^b}, \tag{4.353}$$

$$\epsilon_c^{(B)} \geq \left(\frac{3}{4}\right)^{c-(2b+16\eta+48)} (2+c+\log(c)). \tag{4.354}$$

Note that this is not the optimal division of approximation errors. We let $b = \log\left(\frac{8}{\epsilon_b^{(B)}}\right)$. Then, (4.353) is always satisfied for $0 < \epsilon_b^{(B)} < 1$. We proceed to compute the upper bound for c. Since $c \geq 2b + 16\eta + 48 \geq 32\eta + 96$, and $\eta \geq 1$, $\frac{137}{128}c \geq 2 + c + \log(c)$. Inserting this relation and our choice of b into (4.354), we obtain

$$\epsilon_c^{(B)} \geq \left(\frac{3}{4}\right)^{c-(2\log\left(8/\epsilon_b^{(B)}\right)+16\eta+48)} \frac{137}{128}c. \tag{4.355}$$

Let

$$\tilde{\epsilon}_c^{(B)} = \epsilon_c^{(B)} \cdot \left(\frac{3}{4}\right)^{(2\log\left(8/\epsilon_b^{(B)}\right)+16\eta+48)} \frac{128}{137}. \tag{4.356}$$

Then, we want to find a c such that

$$c\left(\frac{3}{4}\right)^c \leq \tilde{\epsilon}_c^{(B)}. \tag{4.357}$$

Assuming that $0 < \tilde{\epsilon}_c^{(B)} < 1$, the choice

$$c = \log_{\frac{3}{4}}\left(\frac{\frac{\tilde{\epsilon}_c^{(B)}}{2.28}}{\log_{\frac{3}{4}}\left(\frac{\tilde{\epsilon}_c^{(B)}}{2.28}\right)}\right) \tag{4.358}$$

satisfies (4.357).

We mention in passing that the phase-inducing step can be parallelized. As in U(1), we can implement the magnetic terms acting on the odd and even plaquettes on a given two dimensional plane in parallel. In particular, we effect $O(L^d)$ same-angle R_z gates, using the weight-sum trick, for each bit of the ancilla state $|\pm f_{\alpha\beta\gamma\delta}\rangle$. Thus, the parallel implementation exponentially reduces the R_z-gate count to $O(cd^2\log(L^d))$. In this work, we focus on the resource analysis of the serial implementation, and will leave that of the parallel implementation for future work.

We divide the oracle error ϵ_{oracle} evenly between the kinetic and magnetic oracles, i.e.,

$$\epsilon^{(K)} = \frac{\epsilon_{\text{oracle}}}{2},\ \epsilon^{(B)} = \frac{\epsilon_{\text{oracle}}}{2} \implies \epsilon_{\text{oracle}} = \epsilon^{(K)} + \epsilon^{(B)}. \tag{4.359}$$

Synthesis errors

Here, we compute the synthesis errors for R_z gates required for the mass and electric term, separately from those for the oracles required for the kinetic and magnetic terms. To start, we consider the mass term. In this term, we have $\lfloor \log\left(2L^d\right) + 1 \rfloor$ R_z gates to implement. Therefore, we incur for each mass term $\lfloor \log\left(2L^d\right) + 1 \rfloor \cdot \epsilon(R_z)$ amount of error, where $\epsilon(R_z)$ denotes the error per R_z gate.

Next, we consider the electric term, which has $2(\eta+1)\lfloor \log\left(dL^d\right) + 1 \rfloor$ R_z gates. Therefore, each electric term incurs $2(\eta+1)\lfloor \log\left(dL^d\right) + 1 \rfloor \cdot \epsilon(R_z)$ amount of error. If we instead use the phase gradient operation, once the gadget state $|\psi_M\rangle$ in (4.25) is prepared, each quantum adder call to implement the operation does not incur any synthesis error. We come back to the error incurred in preparing the gadget state itself in the next section.

The errors per Trotter step due to the R_z gates for the kinetic and magnetic terms are $64dL^d \cdot \lceil \frac{3c^{(K)}}{2} \rceil \cdot \epsilon(R_z)$ and $1048576 \cdot \frac{d(d-1)}{2} L^d \cdot \lceil \frac{3c^{(B)}}{2} \rceil \cdot \epsilon(R_z)$, where we have and will continue to denote the approximation parameter c for the kinetic and magnetic oracles as $c^{(K)}$ and $c^{(B)}$, respectively.

We add the error incurred for the four terms to obtain the synthesis error $\epsilon_{\text{synthesis}}$. Note that, as in the U(1) case, the implementation of the diagonal mass and electric terms can be optimized. As in the U(1) case, there are $r+1$ diagonal mass and electric terms, and $2r$ off-diagonal kinetic and magnetic terms to implement in total. Thus, $\epsilon_{\text{synthesis}}$ is given by

$$\begin{aligned}\epsilon_{\text{synthesis}} = \{(r+1) \cdot [\lfloor \log\Big(2L^d\Big) + 1 \rfloor + 2(\eta+1)\lfloor \log\Big(dL^d\Big) + 1 \rfloor] \\ + 2r \cdot [96c^{(K)}dL^d + 786432c^{(B)}d(d-1)L^d]\} \cdot \epsilon(R_z), \quad (4.360)\end{aligned}$$

where r, to reiterate for the convenience of the readers, is the total number of Trotter steps.

Complexity analysis

Having computed the Trotter, oracle and synthesis errors, we proceed to perform the complexity analysis for the SU(2) LGT.

The total error is given by

$$\epsilon_{\text{total}} = \epsilon_{\text{Trotter}} + \epsilon_{\text{oracle}} + \epsilon_{\text{synthesis}}. \quad (4.361)$$

We choose to evenly distribute the total error between the Trotter, oracle, and synthesis errors. Focusing on the Trotter error, we obtain the number of Trotter steps by

$$\epsilon_{\text{Trotter}} = \frac{\epsilon_{\text{total}}}{3} \implies r = \lceil \frac{T^{3/2} 3^{1/2} \rho^{1/2}}{\epsilon_{\text{total}}^{1/2}} \rceil. \quad (4.362)$$

Next, we use the above relation and $\epsilon_{\text{oracle}} = \frac{\epsilon_{\text{total}}}{3}$ to obtain the expressions for $c^{(K)}$ and $c^{(B)}$. $c^{(K)}$ is given by (4.346), where

$$\tilde{\epsilon}_c^{(K)} = \frac{\epsilon_{\text{total}}}{12r \cdot 64dL^d} \left(\frac{3}{4}\right)^{2\log\left(8\frac{12r\cdot 64dL^d}{\epsilon_{\text{total}}}\right)+8\eta+12} \frac{36}{44}. \tag{4.363}$$

$c^{(B)}$ is given by (4.358), where

$$\tilde{\epsilon}_c^{(B)} = \frac{\epsilon_{\text{total}}}{6r \cdot 1048576d(d-1)L^d} \left(\frac{3}{4}\right)^{2\log\left(8\frac{6r\cdot 1048576d(d-1)L^d}{\epsilon_{\text{total}}}\right)+16\eta+48} \frac{128}{137}. \tag{4.364}$$

Finally, we compute the error each R_z gate can incur by

$$\begin{aligned}
&\epsilon_{\text{synthesis}} = \frac{\epsilon_{\text{total}}}{3} \implies \\
&\epsilon(R_z) = \frac{\epsilon_{\text{total}}}{3}\{(\lceil \frac{T^{3/2}3^{1/2}\rho^{1/2}}{\epsilon_{\text{total}}^{1/2}} \rceil + 1) \cdot [\lfloor \log\left(2L^d\right) + 1 \rfloor + 2(\eta+1)\lfloor \log\left(dL^d\right) + 1 \rfloor] \\
&\quad + 2\lceil \frac{T^{3/2}3^{1/2}\rho^{1/2}}{\epsilon_{\text{total}}^{1/2}} \rceil \cdot [96c^{(K)}dL^d + 786432c^{(B)}d(d-1)L^d]\}^{-1}.
\end{aligned} \tag{4.365}$$

With this, we obtain the number of T gates required to synthesize each R_z gate using RUS circuit [135],

$$\text{Cost}(R_z) = 1.15 \log\left(\frac{1}{\epsilon(R_z)}\right). \tag{4.366}$$

Combining the T gates required for implementation of R_z gates and the T gates used elsewhere in the circuit, we obtain the total number of T gates for the entire circuit as

$$\begin{aligned}
&\{(\lceil \frac{T^{3/2}3^{1/2}\rho^{1/2}}{\epsilon_{\text{total}}^{1/2}} \rceil + 1) \cdot [\lfloor \log\left(2L^d\right) + 1 \rfloor + 2(\eta+1)\lfloor \log\left(dL^d\right) + 1 \rfloor] + 2\lceil \frac{T^{3/2}3^{1/2}\rho^{1/2}}{\epsilon_{\text{total}}^{1/2}} \rceil \cdot [96c^{(K)}dL^d \\
&+ 786432c^{(B)}d(d-1)L^d]\}\text{Cost}(R_z) + (\lceil \frac{T^{3/2}3^{1/2}\rho^{1/2}}{\epsilon_{\text{total}}^{1/2}} \rceil + 1) \cdot [4(2L^d - \text{Weight}(2L^d)) + 8dL^d(\eta-2) \\
&+ 8dL^d\eta(12\eta - 3\lfloor \log(\eta+1) \rfloor - 2) + (8\eta+8)(dL^d - \text{Weight}(dL^d)) + dL^d(32\eta - 48)] + 2\lceil \frac{T^{3/2}3^{1/2}\rho^{1/2}}{\epsilon_{\text{total}}^{1/2}} \rceil \\
&\cdot [64dL^d\mathcal{T}^{(K)} + 2^{13}d(d-1)L^d + 524288d(d-1)L^d\mathcal{T}^{(B)}],
\end{aligned} \tag{4.367}$$

where $\mathcal{T}^{(K)}, \mathcal{T}^{(B)}$ are given in (4.335,4.347), respectively. The size of the ancilla register is given by the maximum between the ancilla qubits required by the electric and magnetic Hamiltonian,

i.e.,

$$Q_{\max} = \max\{(3\eta+1)dL^d + 3(\eta+1) - \lfloor \log(\eta+1) \rfloor - 1 + dL^d - \text{Weight}(dL^d),$$
$$\lceil \log(c) \rceil \cdot (\lceil \frac{49c}{2} \rceil + 4b + 32\eta + 101) + \lceil \log(b) \rceil \cdot (7b + 16\eta + 18) + b + 76\eta + 12c - \lfloor \log(4c+1) \rfloor + 169\}. \tag{4.368}$$

Taking this into account, we obtain the total number of qubits required for the simulation by summing up those in the ancilla, fermionic and gauge-field registers, which is given by

$$2L^d + (3\eta+2)dL^d + Q_{\max}. \tag{4.369}$$

Note that in the case where the electric term is implemented using phase gradient operation, the T-gate count changes by

$$(\lceil \frac{T^{3/2}3^{1/2}\rho^{1/2}}{\epsilon_{total}^{1/2}} \rceil + 1) \cdot [4dL^d \log\left(\frac{8\pi a^{d-2}}{g^2 t}\right) + O(dL^d) - 2(\eta+1)\lfloor \log\left(dL^d\right) + 1 \rfloor \cdot \text{Cost}(R_z)$$
$$- (8\eta+8)(dL^d - \text{Weight}(dL^d))] + \text{Cost}(|\psi_M\rangle), \tag{4.370}$$

where the $\text{Cost}(R_z)$ needs to be modified, since $\epsilon(R_z)$ has changed to

$$\epsilon(R_z) = \frac{\epsilon_{\text{total}}}{3}\{(\lceil \frac{T^{3/2}3^{1/2}\rho^{1/2}}{\epsilon_{\text{total}}^{1/2}} \rceil + 1) \cdot \lfloor \log\left(2L^d\right) + 1 \rfloor$$
$$+ 2\lceil \frac{T^{3/2}3^{1/2}\rho^{1/2}}{\epsilon_{\text{total}}^{1/2}} \rceil \cdot [192c^{(K)}dL^d + 1572864c^{(B)}d(d-1)L^d]\}^{-1}. \tag{4.371}$$

Further, $\text{Cost}(|\psi_M\rangle)$, which denotes the one-time synthesis costs of the phase gradient gadget state. Here, we choose to use the synthesis method delineated in [147]. Briefly, we apply Hadamard gates to the register $|00...0\rangle$, and then apply gates $Z, Z^{-1/2}, ..., Z^{-1/2^{M-1}}$. Each Z^α gates are synthesized using RUS circuits [135]. Let δ be the error of preparing the gadget state $|\psi_M\rangle$. Then, each gate can incur at most M/δ error, and thus, costs $1.15\log(M/\delta)$, using RUS circuits [135]. Thus, the gadget state preparation costs $1.15M\log(M/\delta)$.

Finally, in this case, the ancilla-qubit count is given by that of the maximum between the mass term and the phase gradient state, and the magnetic term, i.e.,

$$Q_{\max} = \max\{(2L^d - \text{Weight}(2L^d)) + \log\left(\frac{8\pi a^{d-2}}{g^2 t}\right), \lceil \log(c) \rceil \cdot (\lceil \frac{49c}{2} \rceil + 4b + 32\eta + 101)$$
$$+ \lceil \log(b) \rceil \cdot (7b + 16\eta + 18) + b + 76\eta + 12c - \lfloor \log(4c+1) \rfloor + 169\}. \tag{4.372}$$

As such, the total qubit count is given by

$$2L^d + dL^d(3\eta+2) + Q_{\max}. \tag{4.373}$$

4.5 Methodology for Simulating SU(3) Lattice Gauge Theory

In this section, we introduce the non-Abelian SU(3) lattice gauge theory, or lattice QCD. We follow the same format as in the SU(2) case to guide the readers.

4.5.1 Preliminaries

As in the cases of U(1) and SU(2), we aim to simulate our system, governed by four types of Hamiltonian, i.e., the electric Hamiltonian H_E, magnetic Hamiltonian H_B, mass Hamiltonian H_M and kinetic Hamiltonian H_K. Once again, H_E and H_B act on the links that connect two fermionic sites, H_M acts on the fermions themselves, and H_K act on nearest pairs of fermionic sites and the links that connect the pairs. Thus, we consider two different types of qubit registers, one for the fields (H_E, H_B, H_K) and the other for the fermions (H_M, H_K).

To simulate this system, we again need to choose a good basis for each register, as in the SU(2) case. For the fermionic register, we consider an occupation basis. Note however though, in the current case of SU(3), the fermions may assume three different colors in the fundamental representation. For instance, the mass Hamiltonian is now of the form

$$\hat{H}_M = m \sum_{\vec{n}} \sum_{\alpha=1}^{3} (-1)^{\vec{n}} \hat{\psi}_\alpha^\dagger(\vec{n}) \hat{\psi}_\alpha(\vec{n}), \tag{4.374}$$

where $\alpha \in \{1, 2, 3\}$ denotes the color. This means that we have three subregisters, each for the three different colors, that comprise the full fermion register. For concreteness and simplicity, we use the JW transformation [142] for the rest of this section to map the fermion operators to the qubit operators.

For the link register, we once again write down the Gauss' law,

$$\hat{G}^a(\vec{n}) = \sum_k (\hat{E}_L^a(\vec{n}, k) + \hat{E}_R^a(\vec{n}, k)) + \hat{Q}^a(\vec{n}), \tag{4.375}$$

which, up to the charge operator, has the same form as the one for SU(2). The SU(3) charge operator for the projection axis a is given by

$$\hat{Q}^a(\vec{n}) = \sum_{\alpha,\beta=1}^{3} \hat{\psi}_\alpha^\dagger \tau_{\alpha\beta}^a \hat{\psi}_\beta, \tag{4.376}$$

where τ^a, $a = 1, ..., 8$, are the eight generators of the fundamental representation of SU(3), which satisfy

$$[\tau^a, \tau^b] = i \sum_{c=1}^{8} f^{abc} \tau^c, \ \mathrm{Tr}[\tau^a \tau^b] = \frac{1}{2} \delta_{ab}, \tag{4.377}$$

where f^{abc} are the group structure constants of SU(3), the $\hat{\psi}_\alpha^\dagger$ and $\hat{\psi}_\alpha$ are the fermion creation and annihilation operators of color α. Similar to the SU(2) case, the charge operators at each vertex satisfy the SU(3) algebra

$$[\hat{Q}^a, \hat{\psi}_\alpha] = \sum_{\beta=1}^{3} -\tau^a_{\alpha\beta}\hat{\psi}_\beta. \tag{4.378}$$

On each link, the left and right electric fields each also forms SU(3) Lie algebras, and they commute with each other, according to

$$[\hat{E}^a_L, \hat{E}^b_L] = i\sum_{c=1}^{8} f^{abc}\hat{E}^c_L, \tag{4.379}$$

$$[\hat{E}^a_R, \hat{E}^b_R] = i\sum_{c=1}^{8} f^{abc}\hat{E}^c_R, \tag{4.380}$$

$$[\hat{E}^a_L, \hat{E}^b_R] = 0. \tag{4.381}$$

Once again, due to gauge-invariance, the SU(3) Hamiltonian commutes with all of the Gauss operators $\hat{G}^a(\vec{n})$.

The physical, gauge-invariant Hilbert space $\mathcal{H}_G$ is defined through the eigenstates of the Gauss operator:

$$\mathcal{H}_G = \{|\Psi\rangle \in \mathcal{H}_G \,|\, \hat{G}^a(\vec{n})\,|\Psi\rangle = 0,\ \forall \vec{n}, a\}. \tag{4.382}$$

Due to the non-Abelian nature of SU(3), the electric fields and Gauss operators do not all commute. Conventionally, the complete set of commuting observables on a link is given by $\{\hat{E}^2, \hat{T}_L, \hat{T}^z_L, \hat{Y}_L, \hat{T}_R, \hat{T}^z_R, \hat{Y}_R\}$, where $\hat{T}_i, \hat{T}^z_i, \hat{Y}_i$, with $i = L, R$ for left and right, are physical quantities, known as the isospin, z-component of the isospin, and hypercharge [154, 155], and $\hat{E}^2$ is the Casimir operator defined by

$$\hat{E}^2 \equiv \sum_{a=1}^{8} \hat{E}^a_L\hat{E}^a_L = \sum_{a=1}^{8} \hat{E}^a_R\hat{E}^a_R. \tag{4.383}$$

In this basis, the states are labelled by eight quantum numbers

$$|p, q, T_L, T^z_L, Y_L, T_R, T^z_R, Y_R\rangle\,, \tag{4.384}$$

where p and q label the representation [155]. The eigenvalues of the Casimir operator are a function of p and q given by [156]

$$\hat{E}^2\,|p, q\rangle = \frac{1}{3}[p^2 + q^2 + pq + 3(p + q)]\,|p, q\rangle\,;\ p, q \in \mathbb{N}, \tag{4.385}$$

where the isospin and hypercharge labels are omitted for brevity.

Finally, we can define the SU(3) parallel transporters, $\hat{U}_{\alpha\beta}$, in the basis defined above. Dropping the link position index for notational convenience, they are given by

$$\begin{aligned}
&\hat{U}_{\alpha\beta}\,|p,q,T_L,T_L^z,Y_L,T_R,T_R^z,Y_R\rangle \\
&= \sum_{(p',q')}\sum_{T_L'=|T_L-t_L|}^{T_L+t_L}\sum_{T_R'=|T_R-t_R|}^{T_R+t_R}\sqrt{\frac{\dim(p,q)}{\dim(p',q')}}\,\langle p',q',T_L',T_L^{z\prime},Y_L'|p,q,T_L,T_L^z,Y_L;1,0,t_L,t_L^z,y_L\rangle \\
&\quad\times\langle p',q',T_R',T_R^{z\prime},Y_R'|p,q,T_R,T_R^z,Y_R;1,0,t_R,t_R^z,y_R\rangle\,|p',q',T_L',T_L^{z\prime},Y_L',T_R',T_R^{z\prime},Y_R'\rangle\,, \quad (4.386)
\end{aligned}$$

where $(p',q')\in\{(p+1,q),(p-1,q+1),(p,q-1)\}$, $\langle p',q',T_i',T_i^{z\prime},Y_i'|p,q,T_i,T_i^z,Y_i;1,0,t_i,t_i^z,y_i\rangle$, with $i=L,R$, are the Clebsch-Gordan coefficients for SU(3) in the fundamental representation, i.e., $(p=1,q=0)$, as provided in Table 4.11, the dimension of the representation (p,q) is given by

$$\dim(p,q)=(1+p)(1+q)(1+\frac{p+q}{2}), \quad (4.387)$$

and the left and right isospin and hypercharge values $(t_i,t_i^z,y_i)_{i=L,R}$ depend on α,β, respectively, as follows:

$$(t_{L/R},t_{L/R}^z,y_{L/R})=\begin{cases}(\frac{1}{2},\frac{1}{2},\frac{1}{3}),\alpha/\beta=1,\\(\frac{1}{2},-\frac{1}{2},\frac{1}{3}),\alpha/\beta=2,\\(0,0,-\frac{2}{3}),\alpha/\beta=3.\end{cases} \quad (4.388)$$

Further, the hypercharge Y_i' and z-component isospin $T_i^{z\prime}$ values are obtained by

$$Y_i'=Y_i+y_i, \quad (4.389)$$

$$T_i^{z\prime}=T_i^z+t_i^z, \quad (4.390)$$

for $i=L,R$. Lastly, the ranges of values for the quantum numbers are given by

$$p=n,\ q=m;\ n,m\in\mathbb{N}, \quad (4.391)$$

$$T_i=0,\frac{1}{2},...,\frac{1}{2}(p+q), \quad (4.392)$$

$$T_i^z=-\frac{1}{2}(p+q),-\frac{1}{2}(p+q)+\frac{1}{2},...,\frac{1}{2}(p+q), \quad (4.393)$$

$$Y_i=-\frac{1}{3}(q+2p),-\frac{1}{3}(q+2p)+\frac{1}{3},...,\frac{1}{3}(p+2q), \quad (4.394)$$

where $i=L,R$.

The above definition of $\hat{U}_{\alpha\beta}$ operators can be used to directly verify the proper commutation

relations

$$[\hat{E}^a_L, \hat{U}_{\alpha\beta}] = -\sum_{\gamma=1}^{3} \tau^a_{\alpha\gamma} \hat{U}_{\gamma\beta}, \tag{4.395}$$

$$[\hat{E}^a_R, \hat{U}_{\alpha\beta}] = \sum_{\gamma=1}^{3} \hat{U}_{\alpha\gamma} \tau^a_{\gamma\beta}, \tag{4.396}$$

where α, β, γ, $\delta \in \{1, 2, 3\}$, required by the SU(3) lattice gauge theory. Note that $\hat{U}_{\alpha\beta}$ are elements of the unitary operator-valued matrix $\hat{\mathbf{U}}$. Denoting the $\alpha\beta$th element of $\hat{\mathbf{U}}$ as $[\hat{\mathbf{U}}]_{\alpha\beta}$, the operators $\hat{U}_{\alpha\beta}$ are related to $\hat{\mathbf{U}}$ by $[\hat{\mathbf{U}}]_{\alpha\beta} = \hat{U}_{\alpha\beta}$ and thus, $[\hat{\mathbf{U}}^\dagger]_{\alpha\beta} = \hat{U}^\dagger_{\beta\alpha}$. It can be shown that in the fundamental representation of SU(3), the parallel transporters satisfy the relation [156, 157]

$$\langle 0| [\hat{\mathbf{U}}]_{\alpha\beta} [\hat{\mathbf{U}}^\dagger]_{\gamma\delta} |0\rangle = \langle 0| \hat{U}_{\alpha\beta} \hat{U}^\dagger_{\delta\gamma} |0\rangle = \frac{1}{3} \delta_{\alpha\gamma} \delta_{\beta\delta}, \tag{4.397}$$

where $|0\rangle$ here is used to denote the basis state in (4.383) with all eight quantum numbers being zeros.

Coefficient	Formula
I_{11}	$\sqrt{\frac{\Omega_1^+(\Omega_2^++6)}{\Gamma_1\Upsilon_1}}$
I_{12}	$-\sqrt{\frac{-\Omega_1^-(\Omega_2^-+6)(\Omega_3^-+6)}{\Gamma_1\Upsilon_2}}$
I_{13}	$\sqrt{\frac{\Omega_1^-\Omega_1^+}{\Gamma_1\Upsilon_3}}$
I_{21}	$-\sqrt{\frac{(6-\Omega_1^-)\Omega_2^-(\Omega_3^++6)}{\Gamma_2\Upsilon_1}}$
I_{22}	$-\sqrt{\frac{(\Omega_1^+-6)\Omega_2^+(\Omega_3^-+6)}{\Gamma_2\Upsilon_2}}$
I_{23}	$\sqrt{\frac{-\Omega_2^-\Omega_2^+}{\Gamma_2\Upsilon_3}}$
I_{31}	$-\sqrt{\frac{(\Omega_1^--6)(\Omega_2^++6)\Omega_3^-}{\Gamma_3\Upsilon_1}}$
I_{32}	$\sqrt{\frac{-(\Omega_1^+-6)(\Omega_2^-+6)\Omega_3^+}{\Gamma_3\Upsilon_2}}$
I_{33}	$\sqrt{\frac{\Omega_3^+\Omega_3^-}{\Gamma_3\Upsilon_3}}$

Table 4.10: The formulas for the Isoscalar factors $I_{\alpha\beta}$ in the fundamental SU(3) representation, where $\Omega_1^\pm = 4p+2q\pm6T_i-3Y_i+9\pm3$, $\Omega_2^\pm = 2p-2q\pm6T_i+3Y_i-3\pm3$, $\Omega_3^\pm = 2p+4q\pm6T_i+3Y_i+3\pm3$, $\Gamma_1 = (1+p)(2+p+q)$, $\Gamma_2 = (1+p)(1+q)$, $\Gamma_3 = (1+q)(2+p+q)$, $\Upsilon_1 = 432(1+T_i)$, $\Upsilon_2 = 432T_i$, and $\Upsilon_3 = 36$, taken from [6], whose authors obtained these formulas efficiently classically with methods developed in [8, 9].

Coefficient	Δp	Δq	ΔT	ΔT^z	ΔY	Formula
$C_{11}^{(a)}$	1	0	$\frac{1}{2}$	$\frac{1}{2}$	$\frac{1}{3}$	$I_{11}c_{11}$
$C_{11}^{(b)}$	1	0	$-\frac{1}{2}$	$\frac{1}{2}$	$\frac{1}{3}$	$I_{12}c_{21}$
$C_{12}^{(a)}$	1	0	$\frac{1}{2}$	$-\frac{1}{2}$	$\frac{1}{3}$	$I_{11}c_{12}$
$C_{12}^{(b)}$	1	0	$-\frac{1}{2}$	$-\frac{1}{2}$	$\frac{1}{3}$	$I_{12}c_{22}$
C_{13}	1	0	0	0	$-\frac{2}{3}$	I_{13}
$C_{21}^{(a)}$	-1	1	$\frac{1}{2}$	$\frac{1}{2}$	$\frac{1}{3}$	$I_{21}c_{11}$
$C_{21}^{(b)}$	-1	1	$-\frac{1}{2}$	$\frac{1}{2}$	$\frac{1}{3}$	$I_{22}c_{21}$
$C_{22}^{(a)}$	-1	1	$\frac{1}{2}$	$-\frac{1}{2}$	$\frac{1}{3}$	$I_{21}c_{12}$
$C_{22}^{(b)}$	-1	1	$-\frac{1}{2}$	$-\frac{1}{2}$	$\frac{1}{3}$	$I_{22}c_{22}$
C_{23}	-1	1	0	0	$-\frac{2}{3}$	I_{23}
$C_{31}^{(a)}$	0	-1	$\frac{1}{2}$	$\frac{1}{2}$	$\frac{1}{3}$	$I_{31}c_{11}$
$C_{31}^{(b)}$	0	-1	$-\frac{1}{2}$	$\frac{1}{2}$	$\frac{1}{3}$	$I_{32}c_{21}$
$C_{32}^{(a)}$	0	-1	$\frac{1}{2}$	$-\frac{1}{2}$	$\frac{1}{3}$	$I_{31}c_{12}$
$C_{32}^{(b)}$	0	-1	$-\frac{1}{2}$	$-\frac{1}{2}$	$\frac{1}{3}$	$I_{32}c_{22}$
C_{33}	0	-1	0	0	$-\frac{2}{3}$	I_{33}

Table 4.11: The formulas for Clebsch-Gordan coefficients $\langle p+\Delta p, q+\Delta q, T_i+\Delta T, T_i^z+\Delta T^z, Y_i+\Delta Y|\ p, q, T_i, T_i^z, Y_i; 1, 0, \Delta T, \Delta T^z, \Delta Y\rangle$ may be obtained by combining the SU(2) Clebsch-Gordan coefficients $c_{\alpha\beta}$ and Isoscalar factors $I_{\alpha\beta}$ from Tables 4.4 and 4.10, respectively. When evaluating $c_{\alpha\beta}$, $\Delta T, \Delta T^z$ are inserted in place of $\Delta j, \Delta m$, respectively. See [6] for details, where the authors computed these formulas classically efficiently with the methods developed in [8, 9].

4.5.2 Simulation circuit synthesis

The infinite-dimensional gauge-field register consists of eight subregisters, each representing a quantum number. We import the encodings for $|p\rangle$, $|q\rangle$, $|T_L\rangle$, $|T_L^z\rangle$, $|Y_L\rangle$, $|T_R\rangle$, $|T_R^z\rangle$ and $|Y_R\rangle$ from [6]. In order to represent them on a finite quantum computer, we impose a cutoff on the electric field. In particular, for a given link, we truncate both p and q at Λ, i.e.,

$$p, q \in \{0, 1, ..., \Lambda\},\ T_i \in \{0, \frac{1}{2}, ..., \Lambda\},$$
$$T_i^z \in \{-\Lambda, -\Lambda + \frac{1}{2}, ..., \Lambda\},\ Y_i = \{-\Lambda, -\Lambda + \frac{1}{3}, ..., \Lambda\}, \tag{4.398}$$

where $i = L, R$. In this basis, in order to import the encoding of the parallel transporters $\hat{U}_{\alpha\beta}$ from [6], we import and will slightly modify the definitions of the following useful operators from

[6]:

$$\hat{P}^{\pm} = \sum_{p=0}^{\Lambda} |p \pm 1\rangle\langle p| \,, \; \hat{Q}^{\pm} = \sum_{q=0}^{\Lambda} |q \pm 1\rangle\langle q| \,,$$
$$\hat{T}_i^{\pm} = \sum_{T_i=0}^{\Lambda} \left|T_i \pm \frac{1}{2}\right\rangle\left\langle T_i\right| \,, \; \hat{T}_i^{z\pm} = \sum_{T_i^z=-\Lambda}^{\Lambda} \left|T_i^z \pm \frac{1}{2}\right\rangle\left\langle T_i^z\right| \,,$$
$$\hat{Y}_i^{\pm} = \sum_{Y_i=-\Lambda}^{\Lambda} \left|Y_i \pm \frac{1}{3}\right\rangle\left\langle Y_i\right| \,, \tag{4.399}$$

where $i = L, R$, and the quantum numbers p and q, T_i and T_i^z, and Y_i are incremented and decremented by 1, $\frac{1}{2}$ and $\frac{1}{3}$ at a time, respectively. The slight modification from the original definitions in [6] is that we have introduced a periodic-wrapping term to the above ladder operators, such that they can be implemented as binary incrementers and decrementers on a quantum computer. The undesirable effect of the periodic-wrapping terms can be removed by applying circuits that include multiply controlled gates, similar to the U(1) case. We further import the following diagonal Clebsch-Gordan operators,

$$\hat{C}_{\alpha\beta}^{i(a)} = \sum_{p,q,T_i,T_i^z,Y_i} C_{\alpha\beta}^{(a)}(p,q,T_i,T_i^z,Y_i,\Delta p,\Delta q,\Delta T_i,\Delta T_i^z,\Delta Y_i)\,|p,q,T_i,T_i^z,Y_i\rangle\langle p,q,T_i,T_i^z,Y_i| \,,$$
$$\text{for } \beta = 1,2,$$
$$\hat{C}_{\alpha\beta}^{i(b)} = \sum_{p,q,T_i,T_i^z,Y_i} C_{\alpha\beta}^{(b)}(p,q,T_i,T_i^z,Y_i,\Delta p,\Delta q,\Delta T_i,\Delta T_i^z,\Delta Y_i)\,|p,q,T_i,T_i^z,Y_i\rangle\langle p,q,T_i,T_i^z,Y_i| \,,$$
$$\text{for } \beta = 1,2,$$
$$\hat{C}_{\alpha\beta}^{i} = \sum_{p,q,T_i,T_i^z,Y_i} C_{\alpha\beta}(p,q,T_i,T_i^z,Y_i,\Delta p,\Delta q,\Delta T_i,\Delta T_i^z,\Delta Y_i)\,|p,q,T_i,T_i^z,Y_i\rangle\langle p,q,T_i,T_i^z,Y_i| \,,$$
$$\text{for } \beta = 3, \tag{4.400}$$

where $C_{\alpha\beta}^{i(a)}$, $C_{\alpha\beta}^{i(b)}$, and $C_{\alpha\beta}^{i}$ are the SU(3) Clebsch-Gordan coefficients evaluated using the formulas in Table 4.11, $\alpha \in \{1,2,3\}$, $i = L, R$, the sums of p, q, T_i, T_i^z, Y_i are over the ranges defined in (4.398), and $|p,q,T_i,T_i^z,Y_i\rangle$ is a tensor product of $|p\rangle$, $|q\rangle$, $|T_i\rangle$, $|T_i^z\rangle$, $|Y_i\rangle$. Further, the SU(3) Clebsch-Gordan coefficients shown in Table 4.11 are real [154, 158]. However, since we are summing over the ranges in (4.398), which include unphysical quantum numbers that violate (4.391-4.394), the formulas in Table 4.11 could result in complex numbers. Thus, we set the complex elements of the diagonal Clebsch-Gordan operator in (4.400) to zeros, thereby ensuring

its Hermiticity. Next, using (4.399) and (4.400), the following operators can be defined:

$$\hat{\mathcal{C}}^i_{\alpha\beta} = \begin{cases} \hat{T}^+_i \hat{C}^{i(a)}_{\alpha\beta} + \hat{T}^-_i \hat{C}^{i(b)}_{\alpha\beta}, \text{ for } \beta = 1,2, \\ \hat{C}^i_{\alpha\beta}, \text{ for } \beta = 3, \end{cases} \tag{4.401}$$

$$\hat{M}^i_\alpha = \begin{cases} \hat{T}^{z+}_i \hat{Y}^+_i, \text{ for } \alpha = 1, \\ \hat{T}^{z-}_i \hat{Y}^+_i, \text{ for } \alpha = 2, \\ (\hat{Y}^-_i)^2, \text{ for } \alpha = 3, \end{cases} \tag{4.402}$$

where $i = L, R$. Moreover, the diagonal normalization operators are defined as

$$\hat{N}_\alpha = \begin{cases} \sum_{p,q} \sqrt{\frac{\dim(p,q)}{\dim(p+1,q)}} \left|p,q\right\rangle\!\left\langle p,q\right|, \text{ for } \alpha = 1, \\ \sum_{p,q} \sqrt{\frac{\dim(p,q)}{\dim(p-1,q+1)}} \left|p,q\right\rangle\!\left\langle p,q\right|, \text{ for } \alpha = 2, \\ \sum_{p,q} \sqrt{\frac{\dim(p,q)}{\dim(p,q-1)}} \left|p,q\right\rangle\!\left\langle p,q\right|, \text{ for } \alpha = 3, \end{cases} \tag{4.403}$$

where $\dim(p,q)$ are given in (4.387). Finally, using (4.399), (4.400) and (4.403), we import the encoding for $\hat{U}_{\alpha\beta}$ from [6],

$$\hat{U}_{\alpha\beta} = \hat{M}^L_\alpha \hat{M}^R_\beta [\hat{P}^+ \hat{\mathcal{C}}^L_{1\alpha} \hat{\mathcal{C}}^R_{1\beta} \hat{N}_1 + \hat{P}^- \hat{Q}^+ \hat{\mathcal{C}}^L_{2\alpha} \hat{\mathcal{C}}^R_{2\beta} \hat{N}_2 + \hat{Q}^- \hat{\mathcal{C}}^L_{3\alpha} \hat{\mathcal{C}}^R_{3\beta} \hat{N}_3], \tag{4.404}$$

which can be straightforwardly shown to satisfy (4.386).

In order to implement these operators on a quantum computer, we need to map the non-integer quantum numbers T_i, T^z_i, Y_i with $i = L, R$ to positive full integers:

$$T_i \mapsto 2T_i,\ T^z_i \mapsto 2(T^z_i + \Lambda),\ Y_i \mapsto 3(Y_i + \Lambda), \tag{4.405}$$

such that

$$T_i \in \{0, 1, ..., 2\Lambda\},\ T^z_i \in \{0, 1, ..., 4\Lambda\},\ Y_i = \{0, 1, ..., 6\Lambda\}, \tag{4.406}$$

and

$$\hat{T}^\pm_i \mapsto \sum_{T_i=0}^{2\Lambda} \left|T_i \pm 1\right\rangle\!\left\langle T_i\right|, \hat{T}^{z\pm}_i \mapsto \sum_{T^z_i=0}^{4\Lambda} \left|T^z_i \pm 1\right\rangle\!\left\langle T^z_i\right|, \hat{Y}^\pm_i \mapsto \sum_{Y_i=0}^{6\Lambda} \left|Y_i \pm 1\right\rangle\!\left\langle Y_i\right|. \tag{4.407}$$

Thus, if the number of qubits required for each of $|p\rangle$ and $|q\rangle$ is $\eta = \log(\Lambda + 1)$, then that for $|T_i\rangle$, $|T^z_i\rangle$ and $|Y_i\rangle$ are $\eta + 1$, $\eta + 2$ and $\lceil \log(6\Lambda + 1) \rceil = \eta + 3$. Since the quantum numbers have been scaled, we have to apply the inverse of (4.405), i.e.,

$$T_i \mapsto \frac{T_i}{2},\ T^z_i \mapsto \frac{T^z_i}{2} - \Lambda,\ Y_i \mapsto \frac{Y_i}{3} - \Lambda, \tag{4.408}$$

before evaluating the Clebsch-Gordan coefficients in (4.400).

Equipped with all the necessary operator definitions and qubit register structure, we now decompose the Hamiltonian into separate parts. Specifically, just as in SU(2), we have for SU(3) LGT

$$\hat{H} = \sum_{\vec{n}} \left[\hat{D}_{\vec{n}}^{(M)} + \hat{D}_{\vec{n}}^{(E)} + \hat{T}_{\vec{n}}^{(K)} + \hat{L}_{\vec{n}}^{(B)} \right], \tag{4.409}$$

where

$$\hat{D}_{\vec{n}}^{(M)} = \frac{m}{2}(-1)^{\vec{n}}(\hat{Z}_1(\vec{n}) + \hat{Z}_2(\vec{n}) + \hat{Z}_3(\vec{n})), \tag{4.410}$$

$$\hat{D}_{\vec{n}}^{(E)} = \frac{g^2}{2a^{d-2}} \sum_{l=1}^{d} \hat{E}^2(\vec{n}, l) \tag{4.411}$$

are diagonal operators, where $\hat{Z}_i(\vec{n})$, with $i \in \{1, 2, 3\}$, are Pauli-z operators that act on the fermion of color i at site $\vec{n}$, and $(-1)^{\vec{n}}$, is either $+1$ or -1 depending on whether $\vec{n}$ is a fermion or anti-fermion site, respectively, reflective of the use of staggered fermions [105], and

$$\hat{T}_{\vec{n}}^{(K)} = \frac{1}{2a} \sum_{l=1}^{d} \sum_{\alpha,\beta=1}^{3} [\hat{U}_{\alpha\beta}(\vec{n}, l)\hat{\sigma}_{\alpha}^{-}(\vec{n})\hat{\sigma}_{\beta}^{+}(\vec{n} + \hat{l})\hat{\zeta}_{\alpha\beta,\vec{n},l} + h.c.] \tag{4.412}$$

is an off-diagonal operator, which corresponds to kinetic Hamiltonian. The operators $\hat{\sigma}_{\alpha}^{\pm}(\vec{n})$ are Pauli raising and lowering operators on the fermion of color α at site $\vec{n}$. Further, the operators $\hat{\zeta}_{\alpha\beta,\vec{n},l}$ are tensor products of $\hat{Z}$, which arise from the JW transformation and have an additional color-dependence when compared to the U(1) case. If we consider a d-dimensional L^d-site lattice, the length of each $\hat{\zeta}_{\alpha\beta,\vec{n},l}$ is $O((3L)^{d-1})$. For brevity, we suppress the $\hat{\zeta}_{\alpha\beta,\vec{n},l}$ operators in the remaining part of the section. The second off-diagonal operator that corresponds to the magnetic Hamiltonian is given by

$$\hat{L}_{\vec{n}}^{(B)} = -\frac{1}{2a^{4-d}g^2} \sum_{i=1}^{d} \sum_{j\neq i;j=1}^{d} \sum_{\alpha,\beta,\delta,\gamma=1}^{3} (\hat{U}_{\alpha\beta}(\vec{n}, i)\hat{U}_{\beta\gamma}(\vec{n} + \hat{i}, j)\hat{U}_{\gamma\delta}^{\dagger}(\vec{n} + \hat{j}, i)\hat{U}_{\delta\alpha}^{\dagger}(\vec{n}, j) + h.c.). \tag{4.413}$$

Assuming we use Suzuki-Trotter formula [22] as our simulation method, each Trotter terms to be implemented then are of the form $e^{i\hat{D}_{\vec{n}}^{(M)}t}, e^{i\hat{D}_{\vec{n}}^{(E)}t}, e^{i\hat{T}_{\vec{n}}^{(K)}t}, e^{i\hat{L}_{\vec{n}}^{(B)}t}$, where t is a sufficiently small number to ensure the Trotter error incurred is within a pre-specified tolerance. In the remaining part of this subsection, we discuss circuit synthesis for each of the four Trotter terms.

Mass term $e^{i\hat{D}_{\vec{n}}^{(M)}t}$

The implementation of this term is straightforward. Three single-qubit $R_z(\theta) = \exp\left(-i\theta\hat{Z}/2\right)$ gate, where $\theta = -m(-1)^{\vec{n}}t$, applied to the three qubits, which correspond to the three fermions

at site $\vec{n}$, in the site register suffices. As in the implementation of U(1) mass term, we once again use the weight-sum trick [137, 138], except for SU(3), the number of same-angle R_z gates increased by a factor of three. Again, briefly, if the original subcircuit applies the same angle R_z gates on p qubits simultaneously, we can reduce the number of R_z gates to $\lfloor \log(p) + 1 \rfloor$, while incurring $p - \text{Weight}(p)$ ancilla qubits and at most $4(p - \text{Weight}(p))$ T gates. For a d-dimensional lattice with L^d lattice sites, $p = 3L^d$.

Electric term $e^{i\hat{D}^{(E)}_{\vec{n}}t}$

Here, we present a method to implement the electric term, $\hat{D}^{(E)}_{\vec{n}}$. It is a sum of d commuting terms, and thus, its evolution can be implemented exactly as a product of d sub-evolutions,

$$e^{i\hat{D}^{(E)}_{\vec{n}}t} = \prod_{l=1}^{d} e^{i\frac{g^2t}{2a^{d-2}}\hat{E}^2(\vec{n},l)}. \tag{4.414}$$

Without loss of generality, we restrict our discussion to one sub-evolution. For notational convenience, we drop the link location index. Since the eigenvalue equation in (4.385) only depends on the subregisters $|p\rangle$ and $|q\rangle$, we implement the operator $e^{i\frac{g^2t}{2a^{d-2}}\hat{E}^2}$ according to the eigenvalue equation,

$$\begin{aligned} e^{i\frac{g^2t}{2a^{d-2}}\hat{E}^2}|p\rangle|q\rangle &= e^{i\frac{g^2t}{6a^{d-2}}[p^2+q^2+pq+3(p+q)]}|p\rangle|q\rangle \\ &= e^{i\frac{g^2t}{6a^{d-2}}[(p+q)(p+q+3)-pq]}|p\rangle|q\rangle. \end{aligned} \tag{4.415}$$

Similar to the SU(2) electric term implementation, we first compute $(p+q)(p+q+3)-pq$ into an ancilla register, then induce the phase on all links in parallel, using the weight-sum trick, and finally uncomputing the ancilla register. The initial arithmetic operations create $|p+q\rangle$ and $|-pq\rangle$ with an $\eta-$bit adder and multiplier, respectively, incurring $4(5\eta - 3\lfloor\log(\eta)\rfloor - 4)$ and $4(\eta-1)(12\eta-3\lfloor\log(\eta)\rfloor-12)+4$ T gates, respectively [148, 7]. Next, we compute $|p+q+3\rangle$ into the ancilla register by copying $|p+q\rangle$ and then adding 3 with a 2η-bit adder, incurring $4(2\eta-2)$ T gates. Finally, we compute $(p+q)(p+q+3)-pq$ with a multiplier and $(2\eta+3)$-bit adder, incurring $4\eta(12\eta-3\lfloor\log(\eta+2)\rfloor+10)+4$ and $4(10\eta-3\lfloor\log(2\eta+3)\rfloor+11)$ T gates, respectively. In total, the number of T gates required for computing and uncomputing of $(p+q)(p+q+3)-pq$ on all the links is $8dL^d[(8\eta-8)+(5\eta-3\lfloor\log(\eta)\rfloor-4)+(\eta-1)(12\eta-3\lfloor\log(\eta)\rfloor-12)+1+\eta(12\eta-3\lfloor\log(\eta+2)\rfloor+10)+1+(10\eta-3\lfloor\log(2\eta+3)\rfloor+11)]$. The number of ancilla qubits used to store $|p+q\rangle$, $|-pq\rangle$, $|p+q+3\rangle$, $|(p+q)(p+q+3)\rangle$ and $|(p+q)(p+q+3)-pq\rangle$ for all the links is $dL^d(8\eta+10)$. The number of reusable workspace ancilla qubits is $3(\eta+2)-\lfloor\log(\eta+2)\rfloor$, as required by the most expensive arithmetic step, the last multiplier.

We now discuss the phase induction. The correct phase can be induced by applying $R_z(2^k\theta)$, where $\theta = \frac{g^2t}{6a^{d-2}}$, on the kth qubit of the $(2\eta+4)-$bit ancilla state, $|(p+q)(p+q+3)-pq\rangle$.

Hence, there are $(2\eta+4)$ sets of dL^d same-angle R_z rotations to implement, where each set can be effected using the weight sum trick. Once again, we first compute $\text{Weight}(dL^d)$ into the ancilla register, incurring $4(dL^d - \text{Weight}(dL^d))$ T gates and $dL^d - \text{Weight}(dL^d)$ ancilla qubits, and then, applying $\lfloor \log\left(dL^d\right) + 1 \rfloor$ R_z gates to the ancilla register to induce the right phase. Thus, the number of R_z gates required to impart the phase is $(2\eta+4)\lfloor \log\left(dL^d\right) + 1 \rfloor$.

As in the cases of U(1) and SU(2) electric terms, for simulations with a fixed t, d and g^2, where a can be chosen such that $\frac{g^2 t}{6a^{d-2}} = \frac{\pi}{2^M}$ with a sufficiently large $M > 1$. Then, the electric evolution can be implemented by

$$|p\rangle\,|q\rangle \mapsto e^{-i\frac{\pi}{2^M}[(p+q)(p+q+3)-pq]}\,|p\rangle\,|q\rangle\,. \tag{4.416}$$

First, we compute $[(p+q)(p+q+3)-pq]$ into an ancilla register, then impart the phase by a phase gradient operation, consisting of an $M-$bit addition on the phase gradient state in (4.25), on the ancilla register, and finally uncompute the ancilla register. The arithmetic operations are carried out one link at a time, and hence, the number of storage ancilla qubits is $8\eta+10$. The phase gradient operations on all links cost $4dL^d \log\left(\frac{6a^{d-2}\pi}{g^2 t}\right) + O(dL^d)$ T gates in total.

Kinetic term $e^{i\hat{T}^{(K)}_{\vec{n}}t}$

In order to facilitate the circuit syntheses of terms involving the $\hat{U}_{\alpha\beta}$ operators, we rewrite them as

$$\begin{aligned}
\hat{U}_{11} = & \sum_{p,q=0}^{\Lambda} \sum_{T_L,T_R=0}^{2\Lambda} \sum_{T^z_L,T^z_R=0}^{4\Lambda} \sum_{Y_L,Y_R=0}^{6\Lambda} \sum_{\Delta T_L,\Delta T_R\in\{-1,1\}} \sum_{(\Delta p,\Delta q)} \\
& f_{11}(p,q,T_L,T^z_L,Y_L,T_R,T^z_R,Y_R,\Delta p,\Delta q,\Delta T_L,\Delta T_R) \\
& |p+\Delta p, q+\Delta q, T_L+\Delta T_L, T^z_L+1, Y_L+1, \\
& T_R+\Delta T_R, T^z_R+1, Y_R+1\rangle \langle p,q,T_L,T^z_L,Y_L,T_R,T^z_R,Y_R| \qquad (4.417) \\
\hat{U}_{12} = & \sum_{p,q=0}^{\Lambda} \sum_{T_L,T_R=0}^{2\Lambda} \sum_{T^z_L,T^z_R=0}^{4\Lambda} \sum_{Y_L,Y_R=0}^{6\Lambda} \sum_{\Delta T_L,\Delta T_R\in\{-1,1\}} \sum_{(\Delta p,\Delta q)} \\
& f_{12}(p,q,T_L,T^z_L,Y_L,T_R,T^z_R,Y_R,\Delta p,\Delta q,\Delta T_L,\Delta T_R) \\
& |p+\Delta p, q+\Delta q, T_L+\Delta T_L, T^z_L+1, Y_L+1, \\
& T_R+\Delta T_R, T^z_R-1, Y_R+1\rangle \langle p,q,T_L,T^z_L,Y_L,T_R,T^z_R,Y_R| \qquad (4.418) \\
\hat{U}_{13} = & \sum_{p,q=0}^{\Lambda} \sum_{T_L,T_R=0}^{2\Lambda} \sum_{T^z_L,T^z_R=0}^{4\Lambda} \sum_{Y_L,Y_R=0}^{6\Lambda} \sum_{\Delta T_L\in\{-1,1\}} \sum_{(\Delta p,\Delta q)} \\
& f_{13}(p,q,T_L,T^z_L,Y_L,T_R,T^z_R,Y_R,\Delta p,\Delta q,\Delta T_L,\Delta T_R=0) \\
& |p+\Delta p, q+\Delta q, T_L+\Delta T_L, T^z_L+1, Y_L+1, \\
& T_R, T^z_R, Y_R-2\rangle \langle p,q,T_L,T^z_L,Y_L,T_R,T^z_R,Y_R| \qquad (4.419) \\
\hat{U}_{21} = & \sum_{p,q=0}^{\Lambda} \sum_{T_L,T_R=0}^{2\Lambda} \sum_{T^z_L,T^z_R=0}^{4\Lambda} \sum_{Y_L,Y_R=0}^{6\Lambda} \sum_{\Delta T_L,\Delta T_R\in\{-1,1\}} \sum_{(\Delta p,\Delta q)} \\
& f_{21}(p,q,T_L,T^z_L,Y_L,T_R,T^z_R,Y_R,\Delta p,\Delta q,\Delta T_L,\Delta T_R) \\
& |p+\Delta p, q+\Delta q, T_L+\Delta T_L, T^z_L-1, Y_L+1, \\
& T_R+\Delta T_R, T^z_R+1, Y_R+1\rangle \langle p,q,T_L,T^z_L,Y_L,T_R,T^z_R,Y_R| \qquad (4.420) \\
\hat{U}_{22} = & \sum_{p,q=0}^{\Lambda} \sum_{T_L,T_R=0}^{2\Lambda} \sum_{T^z_L,T^z_R=0}^{4\Lambda} \sum_{Y_L,Y_R=0}^{6\Lambda} \sum_{\Delta T_L,\Delta T_R\in\{-1,1\}} \sum_{(\Delta p,\Delta q)} \\
& f_{22}(p,q,T_L,T^z_L,Y_L,T_R,T^z_R,Y_R,\Delta p,\Delta q,\Delta T_L,\Delta T_R) \\
& |p+\Delta p, q+\Delta q, T_L+\Delta T_L, T^z_L-1, Y_L+1, \\
& T_R+\Delta T_R, T^z_R-1, Y_R+1\rangle \langle p,q,T_L,T^z_L,Y_L,T_R,T^z_R,Y_R| \qquad (4.421)
\end{aligned}$$

$$\hat{U}_{23} = \sum_{p,q=0}^{\Lambda} \sum_{T_L,T_R=0}^{2\Lambda} \sum_{T_L^z,T_R^z=0}^{4\Lambda} \sum_{Y_L,Y_R=0}^{6\Lambda} \sum_{\Delta T_L \in \{-1,1\}} \sum_{(\Delta p,\Delta q)}$$
$$f_{23}(p,q,T_L,T_L^z,Y_L,T_R,T_R^z,Y_R,\Delta p,\Delta q,\Delta T_L,\Delta T_R=0)$$
$$|p+\Delta p,q+\Delta q,T_L+\Delta T_L,T_L^z-1,Y_L+1,$$
$$T_R,T_R^z,Y_R-2\rangle\langle p,q,T_L,T_L^z,Y_L,T_R,T_R^z,Y_R| \tag{4.422}$$
$$\hat{U}_{31} = \sum_{p,q=0}^{\Lambda} \sum_{T_L,T_R=0}^{2\Lambda} \sum_{T_L^z,T_R^z=0}^{4\Lambda} \sum_{Y_L,Y_R=0}^{6\Lambda} \sum_{\Delta T_R \in \{-1,1\}} \sum_{(\Delta p,\Delta q)}$$
$$f_{31}(p,q,T_L,T_L^z,Y_L,T_R,T_R^z,Y_R,\Delta p,\Delta q,\Delta T_L=0,\Delta T_R)$$
$$|p+\Delta p,q+\Delta q,T_L,T_L^z,Y_L-2,T_R+\Delta T_R,$$
$$T_R^z+1,Y_R+1\rangle\langle p,q,T_L,T_L^z,Y_L,T_R,T_R^z,Y_R| \tag{4.423}$$
$$\hat{U}_{32} = \sum_{p,q=0}^{\Lambda} \sum_{T_L,T_R=0}^{2\Lambda} \sum_{T_L^z,T_R^z=0}^{4\Lambda} \sum_{Y_L,Y_R=0}^{6\Lambda} \sum_{\Delta T_R \in \{-1,1\}} \sum_{(\Delta p,\Delta q)}$$
$$f_{32}(p,q,T_L,T_L^z,Y_L,T_R,T_R^z,Y_R,\Delta p,\Delta q,\Delta T_L=0,\Delta T_R)$$
$$|p+\Delta p,q+\Delta q,T_L,T_L^z,Y_L-2,T_R+\Delta T_R,$$
$$T_R^z-1,Y_R+1\rangle\langle p,q,T_L,T_L^z,Y_L,T_R,T_R^z,Y_R| \tag{4.424}$$
$$\hat{U}_{33} = \sum_{p,q=0}^{\Lambda} \sum_{T_L,T_R=0}^{2\Lambda} \sum_{T_L^z,T_R^z=0}^{4\Lambda} \sum_{Y_L,Y_R=0}^{6\Lambda} \sum_{(\Delta p,\Delta q)}$$
$$f_{33}(p,q,T_L,T_L^z,Y_L,T_R,T_R^z,Y_R,\Delta p,\Delta q,\Delta T_L=0,\Delta T_R=0)$$
$$|p+\Delta p,q+\Delta q,T_L,T_L^z,Y_L-2,T_R,T_R^z,Y_R-2\rangle$$
$$\langle p,q,T_L,T_L^z,Y_L,T_R,T_R^z,Y_R|\,, \tag{4.425}$$

where the tuple $(\Delta p,\Delta q)$ is summed over the elements in $\{(1,0),(-1,1),(0,1)\}$. Hereafter, we will omit some of the arguments of $f_{\alpha\beta}$ for brevity, whenever the context is clear. As in SU(2), we split the sums over all the quantum numbers into series of even and odd quantum numbers,

and define the operators $\hat{U}_{\alpha\beta}$ using the diagonal operators,

$$\begin{aligned}
&\hat{D}_{\alpha\beta}(p,q,T_L,T_L^z,Y_L,T_R,T_R^z,Y_R,\Delta p,\Delta q,\Delta T_L,\Delta T_R)\\
=&\sum_{\substack{p_{\eta-1}\ldots p_1\\ q_{\eta-1}\ldots q_1}=0}^{1}\sum_{\substack{T_{L;\eta}\ldots T_{L;1}\\ T_{R;\eta}\ldots T_{R;1}}=0}^{1}\sum_{\substack{T^z_{L;\eta+1}\ldots T^z_{L;1}\\ T^z_{R;\eta+1}\ldots T^z_{R;1}}=0}^{1}\sum_{\substack{Y_{L;\eta+2}\ldots Y_{L;2}Y_{L;k}\\ Y_{R;\eta+2}\ldots Y_{R;2}Y_{R;k}}=0}^{1}\\
&f_{\alpha\beta}(p,q,T_L,T_L^z,Y_L,T_R,T_R^z,Y_R,\Delta p,\Delta q,\Delta T_L,\Delta T_R)\\
&|p_{\eta-1}\ldots p_1\rangle\langle p_{\eta-1}\ldots p_1|\otimes|q_{\eta-1}\ldots q_1\rangle\langle q_{\eta-1}\ldots q_1|\\
&\otimes|T_{L;\eta}\ldots T_{L;1}\rangle\langle T_{L;\eta}\ldots T_{L;1}|\otimes\left|T^z_{L;\eta+1}\ldots T^z_{L;1}\right\rangle\left\langle T^z_{L;\eta+1}\ldots T^z_{L;1}\right|\\
&\otimes|Y_{L;\eta+2}\ldots Y_{L;2}Y_{L;k}\rangle\langle Y_{L;\eta+2}\ldots Y_{L;2}Y_{L;k}|\otimes|T_{R;\eta}\ldots T_{R;1}\rangle\langle T_{R;\eta}\ldots T_{R;1}|\\
&\otimes\left|T^z_{R;\eta+1}\ldots T^z_{R;1}\right\rangle\left\langle T^z_{R;\eta+1}\ldots T^z_{R;1}\right|\otimes|Y_{R;\eta+2}\ldots Y_{R;2}Y_{R;k}\rangle\langle Y_{R;\eta+2}\ldots Y_{R;2}Y_{R;k}|\,,
\end{aligned}\tag{4.426}$$

where $\alpha,\beta\in\{1,2,3\}$, $\Delta p,\Delta q,\Delta T_L,\Delta T_R\in\{1,0,-1\}$, and

$$Y_{L/R;k}=\begin{cases}Y_{L/R;1}\text{ if }\alpha/\beta=1,2,\\ Y_{L/R;0}\text{ if }\alpha/\beta=3.\end{cases}\tag{4.427}$$

Because we consider all possible bit-strings that consist the zeroth digits of p,q,T_L,T_L^z,T_R,T_R^z and kth digits of Y_L,Y_R separately one at a time, these bit-strings are classically known, and the remaining digits are obtained from the qubits, and thus $f_{\alpha\beta}$ can be evaluated on a quantum computer. In particular, $f_{\alpha\beta}$, whose formula can be straightforwardly obtained from (4.404), are products of the Clebsch-Gordan coefficients in Table 4.11, and normalization factors in (4.403). For brevity, we hereafter write the operator and diagonal elements in (4.426) as $\hat{D}_{\alpha\beta}(\Delta p,\Delta q,\Delta T_L,\Delta T_R)$, whenever the context is clear. Next, similar to the SU(2) kinetic term, we express the operators $\hat{U}_{\alpha\beta}$ in terms of the diagonal operators in (4.426), Pauli ladder operators, which act on the zeroth qubits of p,q,T_L,T_L^z,T_R,T_R^z and kth qubits of Y_L,Y_R, and binary incrementers and decrementers acting on the eight subregisters as follows:

$$\begin{aligned}
\hat{U}_{\alpha\beta}+h.c.=&\sum_{n_1,n_2,\ldots,n_8=0}^{1}(\hat{P}^+)^{n_1}(\hat{Q}^+)^{n_2}(\hat{T}_L^+)^{n_3}(\hat{T}_L^{z+})^{n_4}(\hat{Y}_L^+)^{\delta_{\alpha,3}+n_5}(\hat{T}_R^+)^{n_6}(\hat{T}_R^{z+})^{n_7}(\hat{Y}_R^+)^{\delta_{\beta,3}+n_8}\\
&[\sum_{(\Delta p,\Delta q)}\sum_{\Delta T_L,\Delta T_R}\hat{D}_{\alpha\beta}(\Delta p,\Delta q,\Delta T_L,\Delta T_R)\hat{P}_{\alpha\beta}(\Delta p,\Delta q,\Delta T_L,\Delta T_R)+h.c.]\\
&(\hat{P}^-)^{n_1}(\hat{Q}^-)^{n_2}(\hat{T}_L^-)^{n_3}(\hat{T}_L^{z-})^{n_4}(\hat{Y}_L^-)^{\delta_{\alpha,3}+n_5}(\hat{T}_R^-)^{n_6}(\hat{T}_R^{z-})^{n_7}(\hat{Y}_R^-)^{\delta_{\beta,3}+n_8},
\end{aligned}\tag{4.428}$$

where $(\Delta p,\Delta q)\in\{(1,0),(-1,1),(0,1)\}$, $\Delta T_L,\Delta T_R\in\{-1,1\}$ for $\alpha,\beta=1,2$, respectively, and $\Delta T_L,\Delta T_R=0$ if $\alpha,\beta=3$. Further,

$$\hat{P}_{\alpha\beta}(\Delta p,\Delta q,\Delta T_L,\Delta T_R)=\otimes_{i=0}^{7}\hat{\sigma}_i,\tag{4.429}$$

where the operator $\hat{\sigma}_i \in \{\hat{\sigma}^+, \hat{\sigma}^-, \hat{I}\}$ depends on α, β, Δp, Δq, ΔT_L, and ΔT_R. In particular, $\hat{\sigma}_0, \hat{\sigma}_1, \hat{\sigma}_2, \hat{\sigma}_5 = \hat{\sigma}^+, \hat{\sigma}^-, \hat{I}$ if $\Delta p, \Delta q, \Delta T_L, \Delta T_R = 1, -1, 0$, respectively. Moreover, $\hat{\sigma}_3\hat{\sigma}_4$ $(\hat{\sigma}_6\hat{\sigma}_7) = \hat{\sigma}^+\hat{\sigma}^+$, $\hat{\sigma}^-\hat{\sigma}^+$, $\hat{I}\hat{\sigma}^+$ if α $(\beta) = 1, 2, 3$, respectively. Note that when $\hat{\sigma}_i = \hat{I}$, the corresponding gauge-field subregister's incrementer and decrementer cancel out. When α or $\beta = 3$, $\hat{U}_{\alpha\beta}$ lowers Y_L or Y_R by two, respectively. Hence, when $\alpha/\beta = 3$, $\hat{U}_{\alpha\beta}$ has an extra pair of incrementer and decrementer, and the Pauli ladder operators act on the first bit of $Y_{L/R}$.

Using α, r and $\beta, r+1$ to denote two colors α, β at two sites $r, r+1$, without loss of generality, we write

$$\begin{aligned}\hat{U}_{\alpha\beta}\hat{\sigma}^-_{\alpha,r}\hat{\sigma}^+_{\beta,r+1} + h.c. = &\sum_{n_1,n_2,\ldots,n_8=0}^{1} (\hat{P}^+)^{n_1}(\hat{Q}^+)^{n_2}(\hat{T}^+_L)^{n_3}(\hat{T}^{z+}_L)^{n_4}(\hat{Y}^+_L)^{n_5}(\hat{T}^+_R)^{n_6}(\hat{T}^{z+}_R)^{n_7}(\hat{Y}^+_R)^{n_8} \\ &[\sum_{(\Delta p,\Delta q)}\sum_{\Delta T_L,\Delta T_R} \hat{D}_{\alpha\beta}(\Delta p,\Delta q,\Delta T_L,\Delta T_R)\hat{F}_{\alpha\beta}(\Delta p,\Delta q,\Delta T_L,\Delta T_R)] \\ &(\hat{P}^-)^{n_1}(\hat{Q}^-)^{n_2}(\hat{T}^-_L)^{n_3}(\hat{T}^{z-}_L)^{n_4}(\hat{Y}^-_L)^{\delta_{\alpha,3}+n_5}(\hat{T}^-_R)^{n_6}(\hat{T}^{z-}_R)^{n_7}(\hat{Y}^-_R)^{\delta_{\beta,3}+n_8},\end{aligned} \tag{4.430}$$

where $\hat{F}_{\alpha\beta} = \hat{P}_{\alpha\beta}\hat{\sigma}^-_{\alpha,r}\hat{\sigma}^+_{\beta,r+1} + h.c.$ act on both the gauge field and fermionic registers, of which the gauge field part is defined via $\hat{P}_{\alpha\beta}$. Further, for notational convenience, we have dropped, and will hereafter drop the arguments of $\hat{D}_{\alpha\beta}$, whenever the context is clear, since they are implied by those of $\hat{P}_{\alpha\beta}$ or $\hat{F}_{\alpha\beta}$. We approximate the kinetic evolution $e^{it\hat{T}^{(K)}_r}$ as

$$\begin{aligned}&e^{it\hat{T}^{(K)}_r} \\ \approx &\prod_{(n_1,n_2,\ldots,n_8)=GC(0)}^{GC(2^8-1)} (\hat{P}^+)^{n_1}(\hat{Q}^+)^{n_2}(\hat{T}^+_L)^{n_3}(\hat{T}^{z+}_L)^{n_4}(\hat{Y}^+_L)^{n_5}(\hat{T}^+_R)^{n_6}(\hat{T}^{z+}_R)^{n_7}(\hat{Y}^+_R)^{n_8} \prod_{\alpha=1}^{2+(1\oplus OR(n_3,n_4))} \\ &\prod_{\beta=1}^{2+(1\oplus OR(n_6,n_7))} \{(\hat{Y}^+_L)^{\delta_{\alpha,3}}(\hat{Y}^+_R)^{\delta_{\beta,3}}[\prod_{\substack{(\Delta p,\Delta q),\\ \Delta T_L,\Delta T_R}} e^{i\frac{t}{2a}\hat{D}_{\alpha\beta}(\Delta p,\Delta q,\Delta T_L,\Delta T_R)\hat{F}_{\alpha\beta}(\Delta p,\Delta q,\Delta T_L,\Delta T_R)}] \\ &(\hat{Y}^-_L)^{\delta_{\alpha,3}}(\hat{Y}^-_R)^{\delta_{\beta,3}}\}(\hat{P}^-)^{n_1}(\hat{Q}^-)^{n_2}(\hat{T}^-_L)^{n_3}(\hat{T}^{z-}_L)^{n_4}(\hat{Y}^-_L)^{n_5}(\hat{T}^-_R)^{n_6}(\hat{T}^{z-}_R)^{n_7}(\hat{Y}^-_R)^{n_8},\end{aligned} \tag{4.431}$$

where we have minimized the number of binary incrementers and decrementers using the Gray code encoding. Furthermore, the evolution operators with $\alpha = 3$, $\beta = 3$ are included only when $1 \oplus OR(n_3, n_4) = 1$, $1 \oplus OR(n_6, n_7) = 1$, respectively, where $OR(\cdot)$ is the bitwise OR function, and $\oplus$ is the binary addition. This is because if $\alpha/\beta = 3$, then $\Delta T_{L/R}, \Delta T^z_{L/R} = 0$, meaning that $\left|T_{L/R,0}\right\rangle, \left|T^z_{L/R,0}\right\rangle$ are not acted on by Pauli ladder operators. Here we adopt the same implementation strategy for the SU(2) kinetic term. Briefly, the strategy diagonalizes the

Pauli ladder operators with CNOT and Hadamard gates, and then implements the diagonalized operators as a phase oracle using either qRAM or quantum arithmetic circuits. The number of oracle queries is determined by the number of terms in each $\hat{U}_{\alpha\beta}$, whereas the T-gate count is decided by the number of binary incrementers and decrementers. Conjugated by the incrementers and decrementers is a product of operators of the form

$$e^{i\frac{t}{2a}\hat{D}_{\alpha\beta}\hat{F}_{\alpha\beta}(\Delta p,\Delta q,\Delta T_L,\Delta T_R)}. \tag{4.432}$$

Once again, as in the SU(2) case, we diagonalize the Pauli part $\hat{F}_{\alpha\beta}$ using a CNOT network and two Hadamard gates, mapping (4.432) to

$$e^{i\frac{t}{2a}\hat{D}_{\alpha\beta}\hat{\mathcal{D}}_{\alpha\beta}(\Delta p,\Delta q,\Delta T_L,\Delta T_R)}, \tag{4.433}$$

where $\hat{\mathcal{D}}_{\alpha\beta}(\Delta p, \Delta q, \Delta T_L, \Delta T_R)$ refers to the diagonalized Pauli part. As in the SU(2) kinetic term implementation, we implement the diagonalized operator as a phase oracle. Before defining the oracle, we define the following useful notations and function. We denote a set of qubits of the gauge-field registers by $S_0 \equiv \{|p_0\rangle, |q_0\rangle, |T_{L,0}\rangle, \left|T^z_{L,0}\right\rangle, |Y_{L,k}\rangle, |T_{R,0}\rangle, \left|T^z_{R,0}\right\rangle, |Y_{R,k}\rangle\}$, where $Y_{L/R,k}$ are defined in (4.427), and the fermionic states by $|f_{\alpha,r}\rangle$, $|f_{\beta,r+1}\rangle$. Further, we define

$$B(\hat{\mathcal{D}}_{\alpha\beta}(\Delta p, \Delta q, \Delta T_L, \Delta T_R)) = (-1)^{f_{\alpha,r}} f_{\beta,r+1} \prod_j b_j, \tag{4.434}$$

where $\{|b_j\rangle\} \subseteq S_0$ is the set of qubits in the gauge-field registers that are acted on nontrivially by $\hat{\mathcal{D}}_{\alpha\beta}(\Delta p, \Delta q, \Delta T_L, \Delta T_R)$. Now we can define the phase oracle used to implement (4.433) as

$$\begin{aligned}
&\hat{O}^{(\Delta p,\Delta q,\Delta T_L,\Delta T_R)}_{\alpha\beta} \left|p'_0\right\rangle \left|q'_0\right\rangle \left|T'_{L,0}\right\rangle \left|T^{z\prime}_{L,0}\right\rangle \left|Y'_{L,k}\right\rangle \left|T'_{R,0}\right\rangle \left|T^{z\prime}_{R,0}\right\rangle \left|Y'_{R,k}\right\rangle \left|f'_{\alpha,r}\right\rangle \left|f'_{\beta,r+1}\right\rangle \\
&\mapsto e^{if_{\alpha\beta}[\frac{t}{2a}B(\hat{\mathcal{D}}_{\alpha\beta}(\Delta p,\Delta q,\Delta T_L,\Delta T_R))]} \left|p'_0\right\rangle \left|q'_0\right\rangle \left|T'_{L,0}\right\rangle \left|T^{z\prime}_{L,0}\right\rangle \left|Y'_{L,k}\right\rangle \left|T'_{R,0}\right\rangle \left|T^{z\prime}_{R,0}\right\rangle \left|Y'_{R,k}\right\rangle \left|f'_{\alpha,r}\right\rangle \left|f'_{\beta,r+1}\right\rangle,
\end{aligned} \tag{4.435}$$

where the function $f_{\alpha\beta}$ is defined in (4.426), and the primes are used to indicate that the states have been acted on by the diagonalization circuit consisting of CNOT and Hadamard gates. Note that we have chosen $f_{\alpha,r}$ to be the target of the diagonalization circuit for concreteness. Further, we note that the bit-value product, i.e. $f_{\beta,r+1}\prod_j b_j$, from the function $B(\cdot)$ in the phase implies that the qubits $|f_{\beta,r+1}\rangle$ and $|b_j\rangle \in S_0$ are the controls of the oracle, since the phase is zero if any of $|f_{\beta,r+1}\rangle$ and $|b_j\rangle \in S_0$ is in the zero state. This phase oracle can be implemented either using qRAM or quantum arithmetic circuits. As in the SU(2) case, we choose to synthesize this oracle directly as a diagonal gate, which imparts the phase $(-1)^{f_{\alpha,r}} f_{\alpha\beta}\frac{t}{2a}$, controlled by $f_{\beta,r+1}, \{b_j\}$. In particular, for each link, $f_{\alpha\beta}$ can be computed efficiently using fixed point arithmetic circuits [136], and the phases can be induced using R_z gates. We refer readers to sec. 4.5.3 for the detailed implementation.

We proceed with the cost analysis of the kinetic term. We assume that the oracle incurs the same costs $\mathcal{C}^{(K)}$. We first consider a pair of the nearest-neighbor fermionic sites and the link joining them. The number of binary incrementers and decrementers required is $2^8+4\cdot2\cdot2^6+4\cdot2^4 = 832$, out of which 2^8 come from the outermost incrementers and decrementers in (4.431), $4\cdot2\cdot2^6$ are due to the fact that there are 4 tuples (α,β) with either α or $\beta = 3$, each of which leads to 2 additional $\hat{Y}^{\pm}_{L/R}$ for each of the 2^6 tuples $(n_1, n_2, ..., n_8)$ that satisfy either $OR(n_3, n_4)$ or $OR(n_6, n_7)$, respectively, and $4\cdot2^4$ is due to the fact that there is a tuple (α,β) with $\alpha,\beta = 3$, which requires 2 extra $\hat{Y}^{\pm}_{L}$ and $\hat{Y}^{\pm}_{R}$, for each of the 2^4 tuples $(n_1, n_2, ..., n_8)$ that satisfy $OR(n_3, n_4)$ and $OR(n_6, n_7)$. Without affecting complexity arguments, we assume that all the incrementers or decrementers act on the largest registers of size $\eta+3$ qubits, and hence, each of them costs $4(\eta+1)$ T gates [7]. In total, the incrementers and decrementers require at most $3328(\eta+1)$ T gates and $\eta+3$ reusable ancilla qubits. Now, we calculate the number of oracle queries needed. $12\cdot2^8$ queries are required for when both α and $\beta \neq 3$, since in these cases, there are twelve combinations of $(\Delta p, \Delta q), \Delta T_L, \Delta T_R$ for each $(n_1, n_2, ..., n_8)$. When either α or $\beta = 3$, $6\cdot2^6$ queries are needed because there are six combinations of $(\Delta p, \Delta q), \Delta T_L, \Delta T_R$ for each $(n_1, n_2, ..., n_8)$ satisfying one of the two conditions, $1 \oplus OR(n_3, n_4) = 1$ and $1 \oplus OR(n_6, n_7) = 1$. When both α and $\beta = 3$, $3\cdot2^4$ queries are needed because there are three combinations of $(\Delta p, \Delta q), \Delta T_L, \Delta T_R$ for each $(n_1, n_2, ..., n_8)$ satisfying both $1\oplus OR(n_3, n_4) = 1$ and $1\oplus OR(n_6, n_7) = 1$. Therefore, the number of oracle queries is $4\cdot12\cdot2^8 + 4\cdot6\cdot2^6 + 3\cdot2^4 = 13872$. Finally, we multiply both the T-gate count and the number of oracle queries by the number of links dL^d in order to obtain the costs of the entire kinetic term.

Magnetic term $e^{i\hat{L}^{(B)}_{\vec{n}}t}$

Here, we provide the implementation of the magnetic term, which is similar to that of the SU(2) magnetic term. Once again, we drop the location indices for brevity. The magnetic term for a single plaquette is given by

$$\hat{L}^{(B)}_r = -\frac{1}{2a^{4-d}g^2}\sum_{\alpha\beta\delta\gamma=1}^{3}(\hat{U}_{\alpha\beta}\hat{U}_{\beta\gamma}\hat{U}^{\dagger}_{\gamma\delta}\hat{U}^{\dagger}_{\delta\alpha} + h.c.), \tag{4.436}$$

where $\hat{U}_{\alpha\beta}$ is defined in (4.428). We now write express a single term in (4.436) as

$$\begin{aligned}\hat{U}_{\alpha\beta}\hat{U}_{\beta\gamma}\hat{U}^{\dagger}_{\gamma\delta}\hat{U}^{\dagger}_{\delta\alpha} = &\sum_{n_1,n_2,...,n_{32}=0}^{1} (\hat{P}_1^+)^{n_1}(\hat{Q}_1^+)^{n_2}(\hat{T}_{L,1}^+)^{n_3}(\hat{T}_{L,1}^{z+})^{n_4}(\hat{Y}_{L,1}^+)^{\delta_{\alpha,3}+n_5}...(\hat{T}_{R,4}^+)^{n_{30}}(\hat{T}_{R,4}^{z+})^{n_{31}} \\ &(\hat{Y}_{R,4}^+)^{\delta_{\alpha,3}+n_{32}} \left[\sum_{\vec{\theta}_1,\vec{\theta}_2,\vec{\theta}_3,\vec{\theta}_4} \hat{D}_{\alpha\beta\gamma\delta}(\vec{\theta}_1,\vec{\theta}_2,\vec{\theta}_3,\vec{\theta}_4)\hat{P}_{\alpha\beta\gamma\delta}(\vec{\theta}_1,\vec{\theta}_2,\vec{\theta}_3,\vec{\theta}_4)\right] \\ &(\hat{P}_1^-)^{n_1}(\hat{Q}_1^-)^{n_2}(\hat{T}_{L,1}^-)^{n_3}(\hat{T}_{L,1}^{z-})^{n_4}(\hat{Y}_{L,1}^-)^{\delta_{\alpha,3}+n_5}...(\hat{T}_{R,4}^-)^{n_{30}}(\hat{T}_{R,4}^{z-})^{n_{31}}(\hat{Y}_{R,4}^-)^{\delta_{\alpha,3}+n_{32}},\end{aligned} \tag{4.437}$$

where the subindices $i = 1, 2, 3, 4$ denote the four links around a plaquette, $\vec{\theta}_i$ are the parameters $(\Delta p, \Delta q, \Delta T_L, \Delta T_R)$ for link i, and the definitions of $\hat{D}_{\alpha\beta\gamma\delta}$ and $\hat{P}_{\alpha\beta\gamma\delta}$ are given by

$$\hat{D}_{\alpha\beta\gamma\delta}(\vec{\theta}_1,\vec{\theta}_2,\vec{\theta}_3,\vec{\theta}_4) = \hat{D}_{\alpha\beta}(\vec{\theta}_1)\hat{D}_{\beta\gamma}(\vec{\theta}_2)\hat{D}_{\gamma\delta}(\vec{\theta}_3)\hat{D}_{\delta\alpha}(\vec{\theta}_4), \tag{4.438}$$

where $\hat{D}_{\alpha\beta}$ is defined in (4.426), and

$$\hat{P}_{\alpha\beta\gamma\delta}(\vec{\theta}_1,\vec{\theta}_2,\vec{\theta}_3,\vec{\theta}_4) = \hat{P}_{\alpha\beta}(\vec{\theta}_1)\hat{P}_{\beta\gamma}(\vec{\theta}_2)\hat{P}_{\gamma\delta}(\vec{\theta}_3)\hat{P}_{\delta\alpha}(\vec{\theta}_4) + h.c., \tag{4.439}$$

where $\hat{P}_{\alpha\beta}$ is a Pauli operator of the form $\otimes_i \hat{\sigma}_i^{\pm}$, which acts on at most eight qubits, as defined in (4.429). Similar to the kinetic term, we can minimize the number of binary incrementers and decrementers in the implementation of $e^{i\hat{L}_r^{(B)}t}$ using the Gray code ordering, i.e.,

$$\begin{aligned}&e^{i\hat{L}_r^{(B)}t} \\ \approx &\prod_{(n_1,n_2,...,n_{32})=GC(0)}^{GC(2^{32}-1)} (\hat{P}_1^+)^{n_1}(\hat{Q}_1^+)^{n_2}(\hat{T}_{L,1}^+)^{n_3}(\hat{T}_{L,1}^{z+})^{n_4}(\hat{Y}_{L,1}^+)^{n_5}...(\hat{T}_{R,4}^+)^{n_{30}}(\hat{T}_{R,4}^{z+})^{n_{31}}(\hat{Y}_{R,4}^+)^{n_{32}} \\ &\prod_{\alpha=1}^{N(n_{30},n_{31},n_3,n_4)} \prod_{\beta=1}^{N(n_6,n_7,n_{11},n_{12})} \prod_{\gamma=1}^{N(n_{14},n_{15},n_{19},n_{20})} \prod_{\delta=1}^{N(n_{22},n_{23},n_{27},n_{28})} \\ &\{(\hat{Y}_{L,1}^+)^{\delta_{\alpha,3}}(\hat{Y}_{R,1}^+)^{\delta_{\beta,3}}(\hat{Y}_{L,2}^+)^{\delta_{\beta,3}}(\hat{Y}_{R,2}^+)^{\delta_{\gamma,3}}(\hat{Y}_{L,3}^+)^{\delta_{\gamma,3}}(\hat{Y}_{R,3}^+)^{\delta_{\delta,3}}(\hat{Y}_{L,4}^+)^{\delta_{\delta,3}}(\hat{Y}_{R,4}^+)^{\delta_{\alpha,3}} \\ &\left[\prod_{\vec{\theta}_1,\vec{\theta}_2,\vec{\theta}_3,\vec{\theta}_4} e^{i\frac{-t}{2a^4-dg^2}\hat{D}_{\alpha\beta\gamma\delta}\hat{P}_{\alpha\beta\gamma\delta}(\vec{\theta}_1,\vec{\theta}_2,\vec{\theta}_3,\vec{\theta}_4)}\right] \\ &(\hat{Y}_{L,1}^-)^{\delta_{\alpha,3}}(\hat{Y}_{R,1}^-)^{\delta_{\beta,3}}(\hat{Y}_{L,2}^-)^{\delta_{\beta,3}}(\hat{Y}_{R,2}^-)^{\delta_{\gamma,3}}(\hat{Y}_{L,3}^-)^{\delta_{\gamma,3}}(\hat{Y}_{R,3}^-)^{\delta_{\delta,3}}(\hat{Y}_{L,4}^-)^{\delta_{\delta,3}}(\hat{Y}_{R,4}^-)^{\delta_{\alpha,3}}\} \\ &(\hat{P}_1^-)^{n_1}(\hat{Q}_1^-)^{n_2}(\hat{T}_{L,1}^-)^{n_3}(\hat{T}_{L,1}^{z-})^{n_4}(\hat{Y}_{L,1}^-)^{n_5}...(\hat{T}_{R,4}^-)^{n_{30}}(\hat{T}_{R,4}^{z-})^{n_{31}}(\hat{Y}_{R,4}^-)^{n_{32}},\end{aligned} \tag{4.440}$$

where the function $N(n_i, n_j, n_k, n_l) = 2 + (1 \oplus OR(OR(n_i, n_j), OR(n_k, n_l)))$ evaluates to 3 if and only if all of $n_i, n_j, n_k, n_l = 0$. Since the operator $\hat{P}_{\alpha\beta\gamma\delta}$ is a Pauli operator of the form

$\otimes_i \hat{\sigma}_i^{\pm} + h.c.$, $e^{it\frac{-1}{2a^{4-d}g^2}\hat{D}_{\alpha\beta\gamma\delta}\hat{P}_{\alpha\beta\gamma\delta}}$ can be diagonalized efficiently using CNOT and Hadamard gates into an operator of the form

$$e^{it\frac{-1}{2a^{4-d}g^2}\hat{D}_{\alpha\beta\gamma\delta}\hat{\mathcal{D}}_{\alpha\beta\gamma\delta}(\vec{\theta}_1,\vec{\theta}_2,\vec{\theta}_3,\vec{\theta}_4)}, \tag{4.441}$$

where $\hat{\mathcal{D}}_{\alpha\beta\gamma\delta}$ is the diagonalized $\hat{P}_{\alpha\beta\gamma\delta}$. As in the case of SU(2), we implement this diagonal operator, using either qRAM or quantum arithmetic circuits. Before defining the oracle, we define some useful notations. We denote the state of a plaquette as

$$\otimes_{i=1}^{4} \left|p_i, q_i, T_{L,i}, T^z_{L,i}, Y_{L,i}, T_{R,i}, T^z_{R,i}, Y_{R,i}\right\rangle, \tag{4.442}$$

where the values of i represent the four links around a plaquette. We denote a set of qubits of the subregisters by $S_0^{\square} \equiv \{|p_{i,0}\rangle, |q_{i,0}\rangle, |T_{L,i,0}\rangle, \left|T^z_{L,i,0}\right\rangle, |Y_{L,i,k}\rangle, |T_{R,i,0}\rangle, \left|T^z_{R,i,0}\right\rangle, |Y_{R,i,k}\rangle\}_{i=1}^4$, where $\left|Y_{L/R,i,k}\right\rangle$ is the kth qubit of $\left|Y_{L/R,i}\right\rangle$ as defined in (4.427). Further, we define

$$B(\hat{\mathcal{D}}_{\alpha\beta\gamma\delta}(\vec{\theta}_1,\vec{\theta}_2,\vec{\theta}_3,\vec{\theta}_4)) = (-1)^{b_i}\prod_j b_j, \tag{4.443}$$

where $\{|b_i\rangle, |b_j\rangle\} \subseteq S_0^{\square}$ are acted on nontrivially by $\hat{\mathcal{D}}_{\alpha\beta\gamma\delta}(\vec{\theta}_1,\vec{\theta}_2,\vec{\theta}_3,\vec{\theta}_4)$, and

$$f_{\alpha\beta\gamma\delta} = f_{\alpha\beta}(\vec{\theta}_1)f_{\beta\gamma}(\vec{\theta}_2)f_{\gamma\delta}(\vec{\theta}_3)f_{\delta\alpha}(\vec{\theta}_4). \tag{4.444}$$

As such, the phase oracle is defined as

$$\begin{aligned}&\hat{O}^{(\vec{\theta}_1,\vec{\theta}_2,\vec{\theta}_3,\vec{\theta}_4)}_{\alpha\beta\gamma\delta} \otimes_{i=1}^{4} \left|p'_i, q'_i, T'_{L,i}, T^{z\prime}_{L,i}, Y'_{L,i}, T'_{R,i}, T^{z\prime}_{R,i}, Y'_{R,i}\right\rangle \\ &\mapsto e^{if_{\alpha\beta\gamma\delta}[(\frac{-1}{2a^{4-d}g^2}B(\hat{\mathcal{D}}_{\alpha\beta\gamma\delta}(\vec{\theta}_1,\vec{\theta}_2,\vec{\theta}_3,\vec{\theta}_4)))]} \otimes_{i=1}^{4} \left|p'_i, q'_i, T'_{L,i}, T^{z\prime}_{L,i}, Y'_{L,i}, T'_{R,i}, T^{z\prime}_{R,i}, Y'_{R,i}\right\rangle,\end{aligned} \tag{4.445}$$

where the primed states are the states that have been acted on by the diagonalization circuit consisting of CNOT and Hadamard gates. As in the kinetic term implementation, we can implement this diagonal operator as a phase oracle using qRAM, or directly synthesize it using quantum arithmetic circuits. Once again, we compute $\pm f_{\alpha\beta\gamma\delta}$ into the ancilla register, conditioned upon the values of the control bits, and induce the approximate phases using R_z gates. See 4.5.3 for the implementation details.

We proceed with the resource analysis of magnetic term. We first focus on a single plaquette. The number of binary incrementers and decrementers outside the braces in (4.440) is 2^{32}, while the number of incrementers and decrementers inside the brackets depends on the values of $\alpha, \beta, \gamma, \delta$. Let $c(n)$ be the number of tuples $(\alpha, \beta, \gamma, \delta)$ with n entries equal to 3. Then, the number of incrementers and decrementers inside the bracket for a given n is given by $c(n) \cdot 2^{32-4n} \cdot 4n$. This is so because for every $(\alpha, \beta, \gamma, \delta)$ with n entries equal to 3, there are $2n$ incrementers and decrementers with exponents equal to one, whereas the rest have exponents equal to zero, and they

are iterated over 2^{32-4n} tuples $(n_1, n_2, ..., n_{32})$ that satisfy the $N(\cdot)$ functions in the upperbound of the products over $\alpha, \beta, \gamma, \delta$. As such, the number of binary incrementers and decrementers is given by $2^{32} + \sum_n c(n) \cdot 2^{32-4n} \cdot 4n = 2^{32} + 32 \cdot 2^{28} \cdot 4 + 24 \cdot 2^{24} \cdot 8 + 8 \cdot 2^{20} \cdot 12 + 2^{16} \cdot 16 = 41977643008$. We assume without affecting complexity arguments that all the incrementers and decrementers act on the largest register with $\eta + 3$ qubits. Then, each incrementer or decrementer costs $4(\eta + 1)$ T gates. Thus, the binary incrementers and decrementers required for a single plaquette incurs at most $167910572032(\eta + 1)$ T gates, and $\eta + 3$ reusable ancilla qubits. Assuming the costs of the oracle, $\mathcal{C}^{(B)}$, are the same for all parameters, we compute the number of oracle queries. Once again, we consider separate cases based on the number of entries, n, in $(\alpha, \beta, \gamma, \delta)$ that are equal to 3 because the number of parameters $\vec{\theta}_i$ and tuples $(n_1, n_2, ..., n_{32})$ that are iterated over depend on n. For $n = 0$, there are 16 tuples $(\alpha, \beta, \gamma, \delta)$. For each tuple, the pairs (α, β), (β, γ), (γ, δ) and (δ, α) lead to 12 $\vec{\theta}_i$ with $i \in \{1, 2, 3, 4\}$, as explained in (4.426) and (4.428), and hence, 12^4 tuples $(\vec{\theta}_1, \vec{\theta}_2, \vec{\theta}_3, \vec{\theta}_4)$. As such, there are 12^4 distinct $e^{i \frac{-t}{2a^{4-d} g^2} \hat{D}_{\alpha\beta\gamma\delta} \hat{P}_{\alpha\beta\gamma\delta}(\vec{\theta}_1, \vec{\theta}_2, \vec{\theta}_3, \vec{\theta}_4)}$ that need to be applied, which are then iterated over 2^{32} tuples $(n_1, n_2, ..., n_{32})$. Thus, for $n = 0$, $16 \cdot (12 \cdot 2^8)^4$ oracle queries are needed. For $n = 1$, there are 32 tuples $(\alpha, \beta, \gamma, \delta)$, each of which gives rise to $6^2 \cdot 12^2$ tuples $(\vec{\theta}_1, \vec{\theta}_2, \vec{\theta}_3, \vec{\theta}_4)$ and hence, $e^{i \frac{-t}{2a^{4-d} g^2} \hat{D}_{\alpha\beta\gamma\delta} \hat{P}_{\alpha\beta\gamma\delta}(\vec{\theta}_1, \vec{\theta}_2, \vec{\theta}_3, \vec{\theta}_4)}$ that are iterated over 2^{28} tuples $(\alpha, \beta, \gamma, \delta)$. Thus, for $n = 1$, $32 \cdot (6 \cdot 2^6)^2 \cdot (12 \cdot 2^8)^2$ oracle queries are needed. For $n = 2$, there are 16 tuples $(\alpha, \beta, \gamma, \delta)$ such that one of the pairs (α, β), (β, γ), (γ, δ) and (δ, α) has both entries equal to 3, in which case there are $3 \cdot 6^2 \cdot 12$ tuples $(\vec{\theta}_1, \vec{\theta}_2, \vec{\theta}_3, \vec{\theta}_4)$. Further, there are 8 tuples $(\alpha, \beta, \gamma, \delta)$ such that all (α, β), (β, γ), (γ, δ) and (δ, α) have one entry equal to 3, in which case there are 6^4 tuples $(\vec{\theta}_1, \vec{\theta}_2, \vec{\theta}_3, \vec{\theta}_4)$. All $e^{i \frac{-t}{2a^{4-d} g^2} \hat{D}_{\alpha\beta\gamma\delta} \hat{P}_{\alpha\beta\gamma\delta}(\vec{\theta}_1, \vec{\theta}_2, \vec{\theta}_3, \vec{\theta}_4)}$ with $n = 2$ are iterated over 2^{24} tuples $(n_1, n_2, ..., n_{32})$. Thus, for $n = 2$, $(16 \cdot 3 \cdot 6^2 \cdot 12 + 8 \cdot 6^4) \cdot 2^{24}$ oracle queries are required. Similarly, we obtain the number of oracle queries for $n = 3, 4$ as $8 \cdot 3^2 \cdot 6^2 \cdot 2^{20}$, $3^4 \cdot 2^{16}$, respectively. We sum up the number of oracle queries for $n = 1 - 4$ to obtain that for a single plaquette: 1470021852266496. In order to obtain the T-gate count and oracle queries required for the entire magentic term, we multiply the costs of a single plaquette by the number of plaquettes, $L^d \frac{d(d-1)}{2}$.

4.5.3 Resource requirement estimates

In this section, we analyze the algorithmic and synthesis errors for our simulations. In Sec. 4.5.3 we compute the algorithmic error for the Suzuki-Trotter formula for our SU(3) Hamiltonian. Therein we show our result first, then show a full derivation of it for completeness. In Sec. 4.5.3 we compute the R_z synthesis error. In Sec. 4.5.3 we combine the two errors discussed in Secs. 4.5.3 and 4.5.3 to report the gate and query complexity, and ancilla requirements.

Trotter errors

As in the simulation algorithms for U(1) and SU(2), we choose to use the second-order PF as our simulation algorithm, and evaluate the commutator bound for the error given in (2.8). The result is

$$||e^{-i\hat{H}T} - \hat{U}_2^r(t)|| \leq r\left(\frac{T}{r}\right)^3 \rho \equiv \epsilon_{Trotter}, \tag{4.446}$$

where

$$\begin{aligned}
\rho = \frac{1}{12}\Big[&\frac{36dL^d m^2}{a} + \frac{dL^d g^4(4+3\Lambda)^2}{4a^{2d-3}} + \frac{18L^d(d^2-d)g^2(4+3\Lambda)^2}{a^d} + \frac{L^d}{a^{6-d}g^2}8989056(d^2-d) \\
&+ \frac{(332928d^2+832320d)L^d}{a^3} + \frac{L^d}{a^{12-3d}g^6}(476287080134344704d^3 - 11907177003358617 60d^2 \\
&+ 714430620201517056d)\Big] + \frac{1}{24}\Big[\frac{3mdL^d g^2(4+3\Lambda)}{a^{d-1}} + \frac{(432d^2+108d)mL^d}{a^2} + \frac{5832mL^d(d^2-d)}{a^{5-d}g^2} \\
&+ \frac{(36d^2+9d)L^d g^2(4\Lambda+3)}{a^d} + \frac{486d(d-1)L^d(4\Lambda+3)}{a^3} + \frac{1944d(d-1)L^d(3\Lambda+4)}{a^3} + (34992d^3 \\
&- 83106d^2 + 48114d)\frac{L^d(3\Lambda+4)}{a^{6-d}g^2} + \frac{(143824896d^3 - 170792064d^2 + 85396032d)L^d}{a^3} \\
&+ \frac{(125846784d^3 - 197759232d^2 + 71912448d)L^d}{a^{6-d}g^2} + \frac{(53934336d^3 + 44945280d^2 - 98879616d)L^d}{a^{6-d}g^2} \\
&+ (10193589504d^3 - 24755860224d^2 + 14562270720d)\frac{L^d}{a^{9-2d}g^4} + (3086340279270553681 92\frac{d^5}{5} \\
&- 10287800930901845606 4d^4 + 2957742767634280611 84d^3 - 1932177612335002877952d^2 \\
&+ 723039509174945336524 8\frac{d}{5} - 154317013963527684096)\frac{L^d}{a^{12-3d}g^6}\Big].
\end{aligned} \tag{4.447}$$

For completeness, we show below a full derivation of the results shown above. Readers interested in how the results compare with the size of the synthesis error and how, together, they affect our simulation gate complexity should proceed to Secs. 4.5.3 and 4.5.3.

We start our derivation by first ordering the terms in the Hamiltonian $\hat{H}$. As in the U(1) and SU(2) simulations, we implement the diagonal mass and electric terms first, then the off-diagonal kinetic and magnetic terms. Due to the similarity between the SU(2) and SU(3) simulation algorithms, we adopt the same notation used in Sec. 4.4.3. We first discuss the kinetic terms. The ordering of the kinetic term is given by the ordered list, i.e.

$$\mathbb{T} = \{(p,l)\} \times \{n_1, n_2, ..., n_8\} \times \{(\Delta p, \Delta q), \Delta T_L, \Delta T_R\} \times \{\alpha, \beta\}, \tag{4.448}$$

where $\times$ is an order-preserving Cartesian product. Further, the exponents of the incrementers and decrementers $n_1, n_2, ..., n_8$ are ordered by the Gray code, and the color indices $\alpha, \beta \in \{1, 2, 3\}$ are ordered simply in the ascending order in the ternary representation of a three-digit number. Here, the values that the parameters $(\Delta p, \Delta q), \Delta T_L, \Delta T_R$ and $n_1, n_2, ..., n_8$ can assume depend on the values of α, β. Suppose $\alpha, \beta \neq 3$. There are 4 of such tuples (α, β). The elements $\hat{h}_T$ that satisfy $\alpha, \beta \neq 3$ can assume 12 combinations of $(\Delta p, \Delta q), \Delta T_L, \Delta T_R$, and 2^8 combinations of $n_1, n_2, ..., n_8$. Thus, the number of elements $\hat{h}_T$ in $\mathbb{T}$ with $\alpha, \beta \neq 3$ is

$$|\mathbb{T}|_{\alpha,\beta\neq 3} = 2d \cdot 2^8 \cdot 12 \cdot 4 = 24576d. \tag{4.449}$$

Suppose either α or β is 3. There are 4 such tuples. The elements $\hat{h}_T$ that satisfy α or $\beta = 3$ can assume 6 combinations of $(\Delta p, \Delta q), \Delta T_L, \Delta T_R$, and 2^6 combinations of $n_1, n_2, ..., n_8$. Thus, the number of elements in $\mathbb{T}$ with α or $\beta = 3$ is

$$|\mathbb{T}|_{\alpha/\beta=3} = 2d \cdot 2^6 \cdot 6 \cdot 4 = 3072d. \tag{4.450}$$

Suppose $(\alpha, \beta) = (3, 3)$. The elements $\hat{h}_T$ that satisfy $(\alpha, \beta) = (3, 3)$ can assume 3 combinations of $(\Delta p, \Delta q), \Delta T_L, \Delta T_R$, and 2^4 combinations of $n_1, n_2, ..., n_8$. Thus, the number of elements in $\mathbb{T}$ with $(\alpha, \beta) = (3, 3)$ is

$$|\mathbb{T}|_{\alpha,\beta=3} = 2d \cdot 2^4 \cdot 3 = 96d. \tag{4.451}$$

Therefore, the total number of elements in $\mathbb{T}$ is given by

$$|\mathbb{T}| = |\mathbb{T}|_{\alpha,\beta\neq 3} + |\mathbb{T}|_{\alpha/\beta=3} + |\mathbb{T}|_{\alpha,\beta=3} = 27744d. \tag{4.452}$$

The ordering of the magnetic terms is given by the following ordered list,

$$\mathbb{L} = \{(p, j, k)\} \times \{n_1, n_2, ..., n_{32}\} \times \{\Delta\vec{\theta}_1, \Delta\vec{\theta}_2, \Delta\vec{\theta}_3, \Delta\vec{\theta}_4\} \times \{\alpha, \beta, \gamma, \delta\}, \tag{4.453}$$

where the exponents of the incrementers and decrementers $q_1, q_2, ..., q_{32}$ are ordered using the Gray code, and the color indices $\alpha, \beta, \gamma, \delta$ are ordered in the ascending order in the ternary representation of a three-digit number. We remind the readers that $\Delta\vec{\theta}_i$ denotes the parameters $(\Delta p, \Delta q), \Delta T_L, \Delta T_R$ for the ith link on each plaquette. Similar to the kinetic terms, the values that the parameters $\Delta\vec{\theta}_i$, with $i = 1, 2, 3, 4$, and $n_1, n_2, ..., n_{32}$ can assume depend on the values of the color indices $\alpha, \beta, \gamma, \delta$. Let n be the number of color indices that are equal to 3. First, we consider the tuples $(\alpha, \beta, \gamma, \delta)$ with $n = 0$. The number of such tuples is 16. Each element $\hat{h}_L$ with $n = 0$ can assume 12^4 combinations of $\Delta\vec{\theta}_i$ with $i = 1, 2, 3, 4$, and 2^{32} combinations of $n_1, n_2, ..., n_{32}$. Thus, the number of elements $\hat{h}_L$ in $\mathbb{L}$ with $n = 0$ is

$$|\mathbb{L}|_{n=0} = 2 \cdot \frac{d(d-1)}{2} \cdot 16 \cdot 12^4 \cdot 2^{32}. \tag{4.454}$$

The number of tuples $(\alpha, \beta, \gamma, \delta)$ with $n = 1$ is 32. Each element $\hat{h}_L$ with $n = 1$ can assume $6^2 \cdot 12^2$ combinations of $\Delta\vec{\theta}_i$ with $i = 1, 2, 3, 4$, and 2^{28} combinations of $n_1, n_2, ..., n_{32}$. Thus, the number of elements $\hat{h}_L$ in $\mathbb{L}$ with $n = 1$ is

$$|\mathbb{L}|_{n=1} = 2 \cdot \frac{d(d-1)}{2} \cdot 32 \cdot 6^2 \cdot 12^2 \cdot 2^{28}. \tag{4.455}$$

We now consider the tuples $(\alpha, \beta, \gamma, \delta)$ with $n = 2$, which can be separated into two cases. The first case consists of the tuples, where one of the pairs (α, β), (β, γ), (γ, δ), and (δ, α) has both entries equal to 3. There are 16 of such tuples. Moreover, each element $\hat{h}_L$ labelled by these tuples can assume $3 \cdot 6^2 \cdot 12$ combinations of $\Delta\vec{\theta}_i$ with $i = 1, 2, 3, 4$, and 2^{24} combinations of $n_1, n_2, ..., n_{32}$. For each tuples in the second case, each pair (α, β), (β, γ), (γ, δ), and (δ, α) has one entry equal to 3. There are 8 of such tuples. Moreover, each element $\hat{h}_L$ labelled by these tuples can assume 6^4 combinations of $\Delta\vec{\theta}_i$ with $i = 1, 2, 3, 4$, and 2^{24} combinations of $n_1, n_2, ..., n_{32}$. Thus, the number of elements $\hat{h}_L$ in $\mathbb{L}$ with $n = 2$ is

$$|\mathbb{L}|_{n=2} = 2 \cdot \frac{d(d-1)}{2} \cdot (16 \cdot 3 \cdot 6^2 \cdot 12 + 8 \cdot 6^4) \cdot 2^{24}. \tag{4.456}$$

There are 8 tuples with $n = 3$. Each element labelled by these tuples can assume $3^2 \cdot 6^2$ combinations $\Delta\vec{\theta}_i$ with $i = 1, 2, 3, 4$, and 2^{20} combinations of $n_1, n_2, ..., n_{32}$. Then, the number of elements $\hat{h}_L$ in $\mathbb{L}$ with $n = 3$ is

$$|\mathbb{L}|_{n=3} = 2 \cdot \frac{d(d-1)}{2} \cdot 8 \cdot 3^2 \cdot 6^2 \cdot 2^{20}. \tag{4.457}$$

Lastly, there is 1 tuple with $n = 4$. Each element labelled by this tuple can assume 3^4 combinations $\Delta\vec{\theta}_i$ with $i = 1, 2, 3, 4$, and 2^{16} combinations of $n_1, n_2, ..., n_{32}$. Then, the number of elements $\hat{h}_L$ in $\mathbb{L}$ with $n = 4$ is

$$|\mathbb{L}|_{n=4} = 2 \cdot \frac{d(d-1)}{2} \cdot 3^4 \cdot 2^{16}. \tag{4.458}$$

Thus, the number of elements in $\mathbb{L}$ is given by

$$|\mathbb{L}| = \sum_{k=0}^{4} |\mathbb{L}|_{n=k} = 2 \cdot \frac{d(d-1)}{2} \cdot 735010926133248. \tag{4.459}$$

Finally, the ordering of the terms in the Hamiltonian $\hat{H}$ is given by the following ordered list:

$$\{\hat{H}_x\} = \{\sum_{\vec{n}} \hat{D}_{\vec{n}}^{(M)}, \sum_{\vec{n}} \hat{D}_{\vec{n}}^{(E)}\} \cup \mathbb{T} \cup \mathbb{L}, \tag{4.460}$$

where $\cup$ is denotes the order-preserving union.

We now evaluate the Trotter error incurred by the second-order PF, which is given in (2.8). Due to the similarities between the SU(2) and SU(3) simulation algorithms, throughout the

following analysis, we will make use of the notations and relevant results from the SU(2) analysis, and highlight the differences whenever necessary.

In the following, we derive useful expressions, similar to (4.221-4.230) in the SU(2) case. As in SU(2) LGTs, we have

$$||\hat{U}_{\alpha\beta}|| \leq 1, \tag{4.461}$$

$$||\hat{U}_{\alpha\beta} + \hat{U}^{\dagger}_{\alpha\beta}|| \leq 2, \tag{4.462}$$

$$||\hat{U}_{\alpha\beta}\hat{\sigma}^{-}_{\alpha}\hat{\sigma}^{+}_{\beta} + \hat{U}^{\dagger}_{\alpha\beta}\hat{\sigma}^{+}_{\alpha}\hat{\sigma}^{-}_{\beta}|| \leq 2. \tag{4.463}$$

We note that the norm of each term in the block-diagonal decomposition of $\hat{U}_{\alpha\beta}\hat{\sigma}^{-}_{\alpha}\hat{\sigma}^{+}_{\beta} + \hat{U}^{\dagger}_{\alpha\beta}\hat{\sigma}^{+}_{\alpha}\hat{\sigma}^{-}_{\beta}$, as shown in (4.430), is upper-bounded by 2. The reason is that, for each term in the decomposition, the norms of the incrementers, decrementers and Pauli ladder operators are bounded from above by one, and that of the diagonal part $\hat{D}_{\alpha\beta}$, of which the elements are defined via $f_{\alpha\beta}$, is also upper-bounded by one. This implies that

$$||\hat{h}_T(\vec{n}_p, l)|| \leq \frac{1}{a}, \tag{4.464}$$

because $\hat{h}_T(\vec{n}_p, l)$ is, up to a multiplicative factor of $\frac{1}{2a}$, a term in the block-diagonal decomposition.

Furthermore, we consider the terms $\hat{h}_T(\vec{n}, l)$, which act on a pair of nearest-neighbor sites and the link that connects them, i.e., $(\vec{n}, l)$. We denote this set of terms as $\mathbb{T}|_{(\vec{n},l)}$. Then,

$$\sum_{\hat{h}_T(\vec{n},l)\in\mathbb{T}|_{(\vec{n},l)}} \hat{h}_T(\vec{n}, l) = \frac{1}{2a}\sum_{\alpha,\beta=1}^{3} \hat{U}_{\alpha\beta}(\vec{n}, l)\hat{\sigma}^{-}_{\alpha}(\vec{n})\hat{\sigma}^{+}_{\beta}(\vec{n} + \hat{l}) + h.c., \tag{4.465}$$

which we combine with (4.463) to get

$$||\sum_{\substack{\hat{h}_T(\vec{n},l)\in S;\\ S\subseteq\mathbb{T}|_{(\vec{n},l)}}} \hat{h}_T(\vec{n}, l)|| \leq ||\frac{1}{2a}\sum_{\alpha,\beta=1}^{3} \hat{U}_{\alpha\beta}(\vec{n}, l)\hat{\sigma}^{-}_{\alpha}(\vec{n})\hat{\sigma}^{+}_{\beta}(\vec{n} + \hat{l}) + h.c.|| \leq \frac{9}{a}. \tag{4.466}$$

Similarly, for the magnetic term, we obtain the following bound:

$$||\hat{U}_{\alpha\beta}\hat{U}_{\beta\gamma}\hat{U}^{\dagger}_{\gamma\delta}\hat{U}^{\dagger}_{\delta\alpha} + h.c.|| \leq 2||\hat{U}_{\alpha\beta}\hat{U}_{\beta\gamma}\hat{U}^{\dagger}_{\gamma\delta}\hat{U}^{\dagger}_{\delta\alpha}|| \leq 2||\hat{U}_{\alpha\beta}||^4 \leq 2, \tag{4.467}$$

As in the kinetic term, the norm of each term in the block-diagonal decomposition of $\hat{U}_{\alpha\beta}\hat{U}_{\beta\gamma}\hat{U}^{\dagger}_{\gamma\delta}\hat{U}^{\dagger}_{\delta\alpha} + h.c.$, as shown in (4.430), is bounded by 2. The reason is that the norms of the incrementers,

decrementers and Pauli ladder operators are bounded from above by one, and that of the diagonal part $\hat{D}_{\alpha\beta\gamma\delta}$, of which the elements are defined via $f_{\alpha\beta\gamma\delta}$, as defined in (4.444), is also upper-bounded by one. This implies that

$$||\hat{h}_L(\vec{n}_p, i, j)|| \leq \frac{1}{a^{4-d}g^2} \tag{4.468}$$

because each $\hat{h}_L(\vec{n}_p, i, j)$ is a product between $\frac{1}{2a^{4-d}g^2}$ and a term in (4.430).

Lastly, we consider the terms $\hat{h}_L(\vec{n}, i, j)$, which act on a single plaquette, denoted by $(\vec{n}, i, j)$. Let these terms form a set $\mathbb{L}|_{(\vec{n},i,j)}$. Then,

$$\sum_{\hat{h}_L(\vec{n},i,j)\in\mathbb{L}|_{(\vec{n},i,j)}} \hat{h}_L(\vec{n}, i, j) = \frac{1}{2a^{4-d}g^2} \sum_{\alpha,\beta,\gamma,\delta=1}^{3} \hat{U}_{\alpha\beta}(\vec{n}, i)\hat{U}_{\beta\gamma}(\vec{n} + \hat{i}, j)\hat{U}^{\dagger}_{\gamma\delta}(\vec{n} + \hat{j}, i)\hat{U}^{\dagger}_{\delta\alpha}(\vec{n}, j) + h.c.. \tag{4.469}$$

Using the above relation and (4.467), we obtain

$$\begin{aligned}
||\sum_{\substack{\hat{h}_L(\vec{n},i,j)\in S;\\ S\subseteq\mathbb{L}|_{(\vec{n},i,j)}}} \hat{h}_L(\vec{n}, i, j)|| &\leq ||\frac{1}{2a^{4-d}g^2} \sum_{\alpha,\beta,\gamma,\delta=1}^{3} \hat{U}_{\alpha\beta}(\vec{n}, i)\hat{U}_{\beta\gamma}(\vec{n} + \hat{i}, j)\hat{U}^{\dagger}_{\gamma\delta}(\vec{n} + \hat{j}, i)\hat{U}^{\dagger}_{\delta\alpha}(\vec{n}, j) + h.c.|| \\
&\leq \frac{1}{2a^{4-d}g^2} \sum_{\alpha,\beta,\gamma,\delta=1}^{3} ||\hat{U}_{\alpha\beta}(\vec{n}, i)\hat{U}_{\beta\gamma}(\vec{n} + \hat{i}, j)\hat{U}^{\dagger}_{\gamma\delta}(\vec{n} + \hat{j}, i)\hat{U}^{\dagger}_{\delta\alpha}(\vec{n}, j) + h.c.|| \\
&\leq \frac{1}{2a^{4-d}g^2} 81 \cdot 2 = \frac{81}{a^{4-d}g^2}.
\end{aligned} \tag{4.470}$$

Whenever these expressions are used, we use them without explicit references for brevity.

Next, we analyze the first sum in (2.8), which is a sum of eight terms, i.e., $||C_{1,n}||$ with $n = 1, ..., 8$, according to (4.219,4.220). First, $C_{1,1}$ and $C_{1,3}$ both evaluate to zero because the mass term commutes with both the electric and mass terms. $C_{1,2}$ is bounded by

$$\begin{aligned}
&|||[\sum_{\vec{n}} \hat{D}^{(M)}_{\vec{n}}, \sum_{\vec{n}'} \hat{T}^{(K)}_{\vec{n}'}], \sum_{\vec{n}} \hat{D}^{(M)}_{\vec{n}}]||| \\
&\leq \sum_{\vec{n}} \sum_{l=1}^{d} |||[[\hat{D}^{(M)}_{\vec{n}} + \hat{D}^{(M)}_{\vec{n}+\hat{l}}, \frac{1}{2a} \sum_{\alpha,\beta=1}^{3} (\hat{U}_{\alpha\beta}(\vec{n}, l)\hat{\sigma}^{-}_{\alpha}(\vec{n})\hat{\sigma}^{+}_{\beta}(\vec{n} + \hat{l}) + h.c.)], \hat{D}^{(M)}_{\vec{n}} + \hat{D}^{(M)}_{\vec{n}+\hat{l}}]|||} \\
&\leq dL^d \sum_{\alpha,\beta=1}^{3} |||[[\frac{m}{2}((-1)^{\vec{n}}\hat{Z}_{\alpha}(\vec{n}) + (-1)^{\vec{n}+\hat{l}}\hat{Z}_{\beta}(\vec{n} + \hat{l})), \frac{1}{2a}(\hat{U}_{\alpha\beta}(\vec{n}, l)\hat{\sigma}^{-}_{\alpha}(\vec{n})\hat{\sigma}^{+}_{\beta}(\vec{n} + \hat{l}) + h.c.)] \\
&\quad , \frac{m}{2}((-1)^{\vec{n}}\hat{Z}_{\alpha}(\vec{n}) + (-1)^{\vec{n}+\hat{l}}\hat{Z}_{\beta}(\vec{n} + \hat{l}))] \leq dL^d \cdot 4||m||^2 \cdot \frac{9}{a} = \frac{36dL^d m^2}{a},
\end{aligned} \tag{4.471}$$

where in the first two inequalities, we have used the fact that only the fermionic sites of colors α, β at $\vec{n}, \vec{n}+\hat{l}$, respectively, acted on by the kinetic term with color indices $\alpha\beta$.

Before evaluating $C_{1,4}$, we provide some useful properties about the kinetic operators $\frac{1}{2a}(\hat{U}_{\alpha\beta}(\vec{n},l)\hat{\sigma}^-_\alpha(\vec{n})\hat{\sigma}^+_\beta(\vec{n}+\hat{l})+h.c.)$. At the fermionic sites $\vec{n}$ and $\vec{n}+\hat{l}$ of color α and β, respectively, the kinetic operator takes a computational basis state to another basis state. Acting on the gauge field on the link $(\vec{n},l)$, it maps the subregisters $|p\rangle|q\rangle \mapsto \{|p\pm1\rangle|q\rangle, |p\mp1\rangle|q\pm1\rangle, |p\rangle|q\pm1\rangle\}$, where $j \in [0,\Lambda]$, up to a multiplicative constant. Therefore, if we evaluate the commutator between an electric and kinetic operator acting on the same link, we obtain

$$
\begin{aligned}
&|||[\frac{g^2}{2a^{d-2}}\hat{E}^2(\vec{n},l), \frac{1}{2a}\sum_{\alpha,\beta=1}^{3}(\hat{U}_{\alpha\beta}(\vec{n},l)\hat{\sigma}^-_\alpha(\vec{n})\hat{\sigma}^+_\beta(\vec{n}+\hat{l})+h.c.)]|||\\
&\mapsto \begin{cases}
\frac{g^2}{6a^{d-2}}[(p\pm1+q)(p\pm1+q+3)-(p\pm1)q-(p+q)(p+q+3)+pq]\\
\cdot\sum_{\alpha,\beta=1}^{3}||\frac{1}{2a}(\hat{U}_{\alpha\beta}(\vec{n},l)\hat{\sigma}^-_\alpha(\vec{n})\hat{\sigma}^+_\beta(\vec{n}+\hat{l})+h.c.)||, \text{ if } |p\rangle|q\rangle\mapsto|p\pm1\rangle|q\rangle\\
\frac{g^2}{6a^{d-2}}[(p\pm1+q\mp1)(p\pm1+q\mp1+3)-(p\pm1)(q\mp1)-(p+q)(p+q+3)+pq]\\
\cdot\sum_{\alpha,\beta=1}^{3}||\frac{1}{2a}(\hat{U}_{\alpha\beta}(\vec{n},l)\hat{\sigma}^-_\alpha(\vec{n})\hat{\sigma}^+_\beta(\vec{n}+\hat{l})+h.c.)||, \text{ if } |p\rangle|q\rangle\mapsto|p\pm1\rangle|q\mp1\rangle\\
\frac{g^2}{6a^{d-2}}[(p+q\pm1)(p+q\pm1+3)-p(q\pm1)-(p+q)(p+q+3)+pq]\\
\cdot\sum_{\alpha,\beta=1}^{3}||\frac{1}{2a}(\hat{U}_{\alpha\beta}(\vec{n},l)\hat{\sigma}^-_\alpha(\vec{n})\hat{\sigma}^+_\beta(\vec{n}+\hat{l})+h.c.)||, \text{ if } |p\rangle|q\rangle\mapsto|p\rangle|q\pm1\rangle
\end{cases}\\
&\leq \begin{cases}
\frac{g^2}{6a^{d-1}}||4+2p+q||\cdot\frac{9}{a}, \text{ if } |p\rangle|q\rangle\mapsto|p+1\rangle|q\rangle\\
\frac{g^2}{6a^{d-1}}||4+p+2q||\cdot\frac{9}{a}, \text{ if } |p\rangle|q\rangle\mapsto|p\rangle|q+1\rangle
\end{cases}\\
&= \frac{3g^2}{2a^{d-1}}(4+3\Lambda),
\end{aligned}
\tag{4.472}
$$

where for the first inequality, we have used (4.415) and listed the cases where the norm is maximized. Using this equation, we evaluate the bound for $C_{1,4}$, and obtain

$$
\begin{aligned}
&|||[[\sum_{\vec{n}}\hat{D}^{(E)}_{\vec{n}}, \sum_{\vec{n}}\hat{T}^{(K)}_{\vec{n}'}], \sum_{\vec{n}}\hat{D}^{(E)}_{\vec{n}}]|||\\
&\leq \sum_{\vec{n}}\sum_{l=1}^{d}\sum_{\alpha,\beta=1}^{3}|||[[\frac{g^2}{2a^{d-2}}\hat{E}^2(\vec{n},l), \frac{1}{2a}(\hat{U}_{\alpha\beta}(\vec{n},l)\hat{\sigma}^-_\alpha(\vec{n})\hat{\sigma}^+_\beta(\vec{n}+\hat{l})+h.c.)], \frac{g^2}{2a^{d-2}}\hat{E}^2(\vec{n},l)]|||\\
&\mapsto \sum_{\vec{n}}\sum_{l=1}^{d}\sum_{\alpha,\beta=1}^{3}\frac{g^2}{6a^{d-2}}(4+3\Lambda)|||[\frac{g^2}{2a^{d-2}}\hat{E}^2(\vec{n},l), \frac{1}{2a}(\hat{U}_{\alpha\beta}(\vec{n},l)\hat{\sigma}^-_\alpha(\vec{n})\hat{\sigma}^+_\beta(\vec{n}+\hat{l})+h.c.)]|||\\
&\leq dL^d\frac{g^2}{6a^{d-2}}(4+3\Lambda)\frac{3g^2}{2a^{d-1}}(4+3\Lambda)\\
&= \frac{dL^dg^4(4+3\Lambda)^2}{4a^{2d-3}},
\end{aligned}
\tag{4.473}
$$

where we have used (4.472) for the last inequality.

In order to compute the bound for $C_{1,5}$, it is useful to evaluate the bound for the commutator between the electric and magnetic operators acting on a single plaquette, which is given by

$$\begin{aligned}
&|||[\frac{g^2}{2a^{d-2}}(\hat{E}^2(\vec{n},i)+\hat{E}^2(\vec{n}+\hat{i},j)+\hat{E}^2(\vec{n}+\hat{j},i)+\hat{E}^2(\vec{n},j)) \\
&,-\frac{1}{2a^{4-d}g^2}\sum_{\alpha,\beta,\delta,\gamma=1}^{3}(\hat{U}_{\alpha\beta}(\vec{n},i)\hat{U}_{\beta\gamma}(\vec{n}+\hat{i},j)\hat{U}^{\dagger}_{\gamma\delta}(\vec{n}+\hat{j},i)\hat{U}^{\dagger}_{\delta\alpha}(\vec{n},j)+h.c.)]|||\\
\leq\ & 4\sum_{\alpha,\beta,\delta,\gamma=1}^{3}|||[\frac{g^2}{2a^{d-2}}\hat{E}^2,-\frac{1}{2a^{4-d}g^2}(\hat{U}_{\alpha\beta}\hat{U}_{\beta\gamma}\hat{U}^{\dagger}_{\gamma\delta}\hat{U}^{\dagger}_{\delta\alpha}+h.c.)]|||\\
\leq\ & 4\sum_{\alpha,\beta,\delta,\gamma=1}^{3}||\frac{4+3\Lambda}{12a^2}(\hat{U}_{\alpha\beta}\hat{U}_{\beta\gamma}\hat{U}^{\dagger}_{\gamma\delta}\hat{U}^{\dagger}_{\delta\alpha}+h.c.)||\\
\leq\ & \frac{54}{a^2}(4+3\Lambda),
\end{aligned}\tag{4.474}$$

where in the first inequality, we have dropped the location indices for brevity, since the commutator between any of the four electric terms and the magnetic terms shares the same bound, in the second inequality, we have used (4.472), and in the last inequality, we have used (4.470). Now we use the above relation to compute the bound for $C_{1,5}$, and obtain

$$\begin{aligned}
&|||[[\sum_{\vec{n}}\hat{D}^{(E)}_{\vec{n}},\sum_{\vec{n}'}\hat{L}^{(B)}_{\vec{n}'}],\sum_{\vec{n}}\hat{D}^{(E)}_{\vec{n}}]|||\\
\leq\ & ||\sum_{\vec{n}}\sum_{i=1}^{d}\sum_{j\neq i;j=1}^{d}[[\frac{g^2}{2a^{d-2}}(\hat{E}^2(\vec{n},i)+\hat{E}^2(\vec{n}+\hat{i},j)+\hat{E}^2(\vec{n}+\hat{j},i)+\hat{E}^2(\vec{n},j))\\
&,-\frac{1}{2a^{4-d}g^2}\sum_{\alpha,\beta,\delta,\gamma=1}^{3}(\hat{U}_{\alpha\beta}(\vec{n},i)\hat{U}_{\beta\gamma}(\vec{n}+\hat{i},j)\hat{U}^{\dagger}_{\gamma\delta}(\vec{n}+\hat{j},i)\hat{U}^{\dagger}_{\delta\alpha}(\vec{n},j)+h.c.)]\\
&,\frac{g^2}{2a^{d-2}}(\hat{E}^2(\vec{n},i)+\hat{E}^2(\vec{n}+\hat{i},j)+\hat{E}^2(\vec{n}+\hat{j},i)+\hat{E}^2(\vec{n},j))]||\\
\leq\ & L^d\frac{d(d-1)}{2}4||\frac{g^2}{6a^{d-2}}(4+3\Lambda)[\frac{g^2}{2a^{d-2}}(\hat{E}^2(\vec{n},i)+\hat{E}^2(\vec{n}+\hat{i},j)+\hat{E}^2(\vec{n}+\hat{j},i)+\hat{E}^2(\vec{n},j))\\
&,-\frac{1}{2a^{4-d}g^2}\sum_{\alpha,\beta,\delta,\gamma=1}^{3}(\hat{U}_{\alpha\beta}(\vec{n},i)\hat{U}_{\beta\gamma}(\vec{n}+\hat{i},j)\hat{U}^{\dagger}_{\gamma\delta}(\vec{n}+\hat{j},i)\hat{U}^{\dagger}_{\delta\alpha}(\vec{n},j)+h.c.)]||\\
\leq\ & L^d\frac{d(d-1)}{2}4\frac{g^2}{6a^{d-2}}(4+3\Lambda)\frac{54}{a^2}(4+3\Lambda)=\frac{18L^d d(d-1)g^2(4+3\Lambda)^2}{a^d},
\end{aligned}\tag{4.475}$$

where in the second inequality, we have used the fact that there are $L^d \frac{d(d-1)}{2}$ plaquettes on the lattice, and in the last inequality, we have used (4.474).

Next, we evaluate the bound for $C_{1,6}$, and obtain

$$\begin{aligned}
&\sum_{\hat{h}_T \in \mathbb{T}} |||[[\hat{h}_T, \sum_{\vec{n}} \hat{L}_{\vec{n}}^{(B)}], \hat{h}_T]||| \\
&\leq \sum_{\hat{h}_T \in \mathbb{T}} |||[[\sum_{\vec{n}_p} \hat{h}_T(\vec{n}_p, l), \sum_{\vec{n}} \hat{L}_{\vec{n}}^{(B)}], \sum_{\vec{n}_p} \hat{h}_T(\vec{n}_p, l)]||| \\
&\leq 27744d \frac{L^d}{2} 4 ||\hat{h}_T(\vec{n}_p, l)|| \cdot ||\frac{2(d-1)}{2a^{4-d}g^2} \sum_{\alpha,\beta,\gamma,\delta=1}^{3} (\hat{U}_{\alpha\beta}\hat{U}_{\beta\gamma}\hat{U}_{\gamma\delta}^\dagger \hat{U}_{\delta\alpha}^\dagger + h.c.)|| \cdot ||\hat{h}_T(\vec{n}_p, l)|| \\
&\leq 27744d \cdot 2L^d ||\frac{1}{a}||^2 \cdot ||162 \frac{d-1}{a^{4-d}g^2}|| = \frac{8989056d(d-1)L^d}{a^{6-d}g^2},
\end{aligned} \tag{4.476}$$

where in the second inequality, the factor of $27744d$ outside the norm expression is the cardinality of $\mathbb{T}$, $\frac{L^d}{2}$ is the number of even or odd sites $\vec{n}_p$, $2(d-1)$ is due to the fact that each link $(\vec{n}_p, l)$ is acted on concurrently by a kinetic term and $2(d-1)$ plaquette operators, and we have used (4.70).

Next, we analyze $C_{1,7}$. As in the SU(2) case, we divide the commutators up into two types; those between (i) terms acting on the same link, and (ii) terms acting on neighboring links that are connected via the sites. We denote the subset of $\mathbb{T}$ that consists of elements with a fixed parity and direction by $\mathbb{T}|_{(p,l)}$. The number of elements in $\mathbb{T}|_{(p,l)}$ is the number of free parameters: 13872. Then, for type (i), the bound is given by

$$\begin{aligned}
&13872 || \sum_{p=e}^{o} \sum_{l=1}^{d} [[\sum_{\vec{n}_p} \hat{h}_T(\vec{n}_p, l), \sum_{\hat{h}_{T'} \in \mathbb{T}|_{(p,l)}; T' > T} \hat{h}_{T'}], \hat{h}_T(\vec{n}_p, l)]|| \\
&\leq 13872 \cdot 2d \cdot 4 \cdot ||\hat{h}_T(\vec{n}_p, l)||^2 \cdot || \sum_{\hat{h}_{T'} \in \mathbb{T}|_{(p,l)}; T' > T} \hat{h}_{T'} || \\
&\leq 13872 \cdot 2d \cdot 4 \cdot ||\hat{h}_T(\vec{n}_p, l)||^2 \cdot ||\frac{1}{2a} \sum_{\alpha,\beta=1}^{3} (\hat{U}_{\alpha\beta}(\vec{n}_p, l) \hat{\sigma}_\alpha^-(\vec{n}_p) \hat{\sigma}_\beta^+(\vec{n}_p + \hat{l}) + h.c.)|| \\
&\leq 13872 \cdot 2d \cdot 4 \cdot ||\frac{1}{a}||^2 \cdot ||\frac{9}{a}|| = \frac{998784d}{a^3},
\end{aligned} \tag{4.477}$$

where in the second inequality, we used (4.466), and the fact that each $\hat{h}_T(\vec{n}_p, l)$ collides on a link with at most nine kinetic operators of different color indices to obtain the second norm expression. Next, we analyze type (ii), which we further divide into two cases. Case (i) consists of d commutators, where $\hat{h}_T, \hat{h}_{T'}$ act on links in the same direction, but sites of different parities, whereas $\hat{h}_T, \hat{h}_{T'}$, in case (ii), act on links in different directions. There are

$\sum_{p',p=e}^{o}\sum_{l=1}^{d}\sum_{l'>l,l'=1}^{d} = 2d^2-2d$ commutators in case (ii). In both types, $\hat{h}_T$ and $\hat{h}_{T'}$ could collide on one or two sites, depending on their respective color indices. If $\hat{h}_T$ and $\hat{h}_{T'}$ are labelled by $\alpha\beta$ and $\beta\alpha$, respectively, then each $\hat{h}_T$ collides with two $\hat{h}_{T'}$ on sites of both colors α,β. If $\hat{h}_T$ is lablled by $\alpha\beta$, and $\hat{h}_{T'}$ is labelled by $\beta\gamma$ with $\gamma\neq\beta$, or $\gamma\alpha$ with $\gamma\neq\alpha$, then each $\hat{h}_T$ collides with one $\hat{h}_{T'}$, on the site labelled by β or α, respectively. For each $\hat{h}_T$ labelled by $\alpha\beta$, there is one $\beta\alpha$, two $\beta\gamma$ with $\gamma\neq\alpha$, and two $\gamma\alpha$ with $\gamma\neq\beta$ that label $\hat{h}_{T'}$. Thus, the bound for each commutator, where there is a collision on two sites, is

$$4\cdot||\hat{h}_T(\vec{n}_p,l)||^2\cdot||2\cdot\frac{1}{2a}(\hat{U}_{\beta\alpha}\hat{\sigma}^-_\beta\hat{\sigma}^+_\alpha+h.c.)||\leq\frac{8}{a^3}, \tag{4.478}$$

The bound for each commutator, where there is a collision on one site, is

$$4\cdot||\hat{h}_T(\vec{n}_p,l)||^2\cdot||\frac{1}{2a}\sum_{\alpha'\beta'=\beta\gamma}^{\gamma\alpha}(\hat{U}_{\alpha'\beta'}\hat{\sigma}^-_{\alpha'}\hat{\sigma}^+_{\beta'}+h.c.)||\leq\frac{16}{a^3}. \tag{4.479}$$

The bound for the commutators in type (ii) is thus

$$\frac{8+16}{a^3}|\mathbb{T}|_{(p,l)}\cdot(2d^2-2d+d)\frac{L^d}{2}=\frac{24}{a^3}13872\cdot(2d^2-d)\frac{L^d}{2}=\frac{(332928d^2-166464d)L^d}{a^3}. \tag{4.480}$$

As such, the bound for $C_{1,7}$ is

$$\frac{(332928d^2+832320d)L^d}{a^3}. \tag{4.481}$$

Finally, we consider $C_{1,8}$, which consists of the commutators between magnetic terms. As in the SU(2) case, we separate the terms into two cases: case (i) and (ii) consists of intra- and inter-plaquette commutators. We first examine case (i). We denote the subset of $\mathbb{L}$ that consists of elements with a fixed parity and two-dimensional plane by $\mathbb{L}|_{(p,j,k)}$. As such, the number of elements in $\mathbb{L}|_{(p,j,k)}$, 735010926133248, is the number of remaining free parameters. We compute the bound of the commutators in case (i), and obtain

$$\begin{aligned}
&735010926133248L^d\frac{d(d-1)}{2}|||[\hat{h}_L(\vec{n}_p,j,k),\sum_{\hat{h}_{L'}\in\mathbb{L}|_{(p,j,k)};L'>L}\hat{h}_{L'}],\hat{h}_L(\vec{n}_p,j,k)]|||\\
&\leq 735010926133248L^d\frac{d(d-1)}{2}\cdot 4\cdot||\hat{h}_L(\vec{n}_p,j,k)||^2||\frac{-1}{2a^{4-d}g^2}\sum_{\alpha,\beta,\gamma,\delta=1}^{3}\hat{U}_{\alpha\beta}\hat{U}_{\beta\gamma}\hat{U}^\dagger_{\gamma\delta}\hat{U}^\dagger_{\delta\alpha}+h.c.||\\
&=735010926133248L^d\frac{d(d-1)}{2}\cdot\frac{4\cdot 81}{a^{12-3d}g^6}=\frac{11907177003358617 6(d^2-d)L^d}{a^{12-3d}g^6},
\end{aligned} \tag{4.482}$$

where in the second norm expression in the first inequality, we have used the fact that each $\hat{h}_L(\vec{n}_p,j,k)$ can collide with at most 81 magnetic operators with different color indices.

We divide case (ii) into two types; those where (i) $\hat{h}_L$ and $\hat{h}_{L'}$ act on neighboring plaquettes with different parities on the same two-dimensional plane, and those where (ii) $\hat{h}_L$ and $\hat{h}_{L'}$ act on plaquettes that share one common dimension. In type (i), there are $\frac{d(d-1)}{2}$ pairs of $\hat{h}_L$ and $\hat{h}_{L'}$, which is the same as the number of two-dimensional planes. Since we have chosen to implement even terms before odd terms, each commutator is bounded by

$$4 \cdot ||\hat{h}_L(\vec{n}_e, j, k)||^2 \cdot ||4 \cdot \sum_{\hat{h}_{L'} \in \mathbb{L}|_{(o,j,k)}; L' > L} \hat{h}_{L'}(\vec{n}_o, j, k)|| = \frac{16 \cdot 81}{a^{12-3d} g^6} = \frac{1296}{a^{12-3d} g^6}, \tag{4.483}$$

where in the second norm expression, the factor of 4 is due to the fact that there are four $\hat{h}_{L'}(\vec{n}_o)$ terms acting on the four links, which form the plaquette that $\hat{h}_L(\vec{n}_e)$ acts on, and the factor of 81 is the number of different color indices of the magnetic operators. There are $2d^3 - 6d^2 + 4d$ type-(ii) pairs of $\hat{h}_L$ and $\hat{h}_{L'}$. See Table 4.5. Each commutator is bounded by

$$4 \cdot ||\hat{h}_L(\vec{n}_p, j, k)||^2 \cdot ||2 \cdot \sum_{\hat{h}_{L'} \in \mathbb{L}|_{(p',j',k')}; L' > L} \hat{h}_{L'}(\vec{n}'_p, j', k')|| = \frac{8 \cdot 81}{a^{12-3d} g^6} = \frac{648}{a^{12-3d} g^6}, \tag{4.484}$$

where in the second norm expression, the factor of 2 is due to the fact that there are two $\hat{h}_{L'}$ that collide with $\hat{h}_L$ on a link. Therefore, the bound for case-(ii) terms is given by

$$\begin{aligned} &735010926133248 \frac{L^d}{2} [\frac{1296}{a^{12-3d} g^6} \frac{d(d-1)}{2} + \frac{648}{a^{12-3d} g^6} (2d^3 - 6d^2 + 4d)] \\ &= \frac{L^d}{a^{12-3d} g^6} 238143540067172352 (2d^3 - 5d^2 + 3d). \end{aligned} \tag{4.485}$$

In total, $C_{1,8}$ is bounded by

$$\frac{L^d}{a^{12-3d} g^6} (476287080134344704 d^3 - 1190717700335861760 d^2 + 714430620201517056 d). \tag{4.486}$$

Next, we analyze the second sum in (2.8), which is a sum of twelve terms, i.e. $||C_{2,n}||$ with $n = 1, ..., 12$, according to (4.251,4.252). For $C_{2,1}$, we obtain the bound

$$\begin{aligned} &|||[\sum_{\vec{n}} \hat{D}^{(M)}_{\vec{n}}, \sum_{\vec{n}'} \hat{T}^{(K)}_{\vec{n}'}], \sum_{\vec{n}''} \hat{D}^{(E)}_{\vec{n}''}]||| \\ &\leq || \sum_{\vec{n}} \sum_{l=1}^{d} \sum_{\alpha,\beta=1}^{3} [[\frac{m}{2}((-1)^{\vec{n}} \hat{Z}_\alpha(\vec{n}) + (-1)^{\vec{n}+\hat{l}} \hat{Z}_\beta(\vec{n}+\hat{l})), \frac{1}{2a}(\hat{U}_{\alpha\beta}(\vec{n}, l) \hat{\sigma}^-_\alpha(\vec{n}) \hat{\sigma}^+_\beta(\vec{n}) + h.c.)], \frac{g^2}{2a^{d-2}} \hat{E}^2(\vec{n}, l)]|| \\ &\leq dL^d \frac{g^2}{6a^{d-2}} (4 + 3\Lambda) \sum_{\alpha,\beta=1}^{3} |||[\frac{m}{2}((-1)^{\vec{n}} \hat{Z}_\alpha(\vec{n}) + (-1)^{\vec{n}+\hat{l}} \hat{Z}_\beta(\vec{n}+\hat{l})), \frac{1}{2a}(\hat{U}_{\alpha\beta}(\vec{n}, l) \hat{\sigma}^-_\alpha(\vec{n}) \hat{\sigma}^+_\beta(\vec{n}) + h.c.)]|| \\ &\leq \frac{dL^d g^2 (4 + 3\Lambda)}{6a^{d-2}} 2||m|| \cdot \frac{9}{a} = \frac{3mdL^d g^2 (4 + 3\Lambda)}{a^{d-1}}, \end{aligned} \tag{4.487}$$

where in the second inequality, we used the fact that the mass terms at $\vec{n}, \vec{n}+\hat{l}$, of which the respective colors are not α, β, commute with the kinetic term with color indices $\alpha\beta$.

For $C_{2,2}$, we divide the commutators up into two types as in the SU(2) analysis. We evaluate the bound for type (i), where the kinetic terms act on the same links, and obtain

$$
\begin{aligned}
&||\sum_{\vec{n}}\sum_{l=1}^{d}\sum_{\alpha,\beta=1}^{3}[[\frac{m}{2}((-1)^{\vec{n}}\hat{Z}_{\alpha}(\vec{n})+(-1)^{\vec{n}+\hat{l}}\hat{Z}_{\beta}(\vec{n}+\hat{l})),\frac{1}{2a}(\hat{U}_{\alpha\beta}(\vec{n},l)\hat{\sigma}^{-}_{\alpha}(\vec{n})\hat{\sigma}^{+}_{\beta}(\vec{n}+\hat{l})+h.c.)] \\
&,\frac{1}{2a}\sum_{\alpha',\beta'=1}^{3}(\hat{U}_{\alpha',\beta'}(\vec{n},l)\hat{\sigma}^{-}_{\alpha'}(\vec{n})\hat{\sigma}^{+}_{\beta'}(\vec{n}+\hat{l})+h.c.)]|| \\
&\leq dL^{d}\cdot 4||m||\cdot||\frac{9}{a}||\cdot||\frac{9}{a}||=\frac{324mdL^{d}}{a^{2}}. \qquad (4.488)
\end{aligned}
$$

We split type (ii) into two cases. Suppose the color indices of $\hat{T}^{(K)}_{\vec{n}'}$ is $\alpha\beta$. Then, in case (i), $\hat{T}^{(K)}_{\vec{n}''}$ has color indices $\beta\alpha$, and in case (ii), it has color indices $\beta\gamma$ with $\gamma\neq\alpha$, or $\gamma\alpha$ with $\gamma\neq\beta$. The bound for case (i) is as follows:

$$
\begin{aligned}
&||\sum_{\vec{n}}\sum_{l=1}^{d}\sum_{\alpha,\beta=1}^{3}[[\frac{m}{2}((-1)^{\vec{n}}\hat{Z}_{\alpha}(\vec{n})+(-1)^{\vec{n}+\hat{l}}\hat{Z}_{\beta}(\vec{n}+\hat{l})),\frac{1}{2a}(\hat{U}_{\alpha\beta}(\vec{n},l)\hat{\sigma}^{-}_{\alpha}(\vec{n})\hat{\sigma}^{+}_{\beta}(\vec{n}+\hat{l})+h.c.)] \\
&,\frac{4d-2}{2a}(\hat{U}_{\beta\alpha}\hat{\sigma}^{-}_{\beta}\hat{\sigma}^{+}_{\alpha}+h.c.)]|| \\
&\leq 4dL^{d}\sum_{\alpha,\beta=1}^{3}||m||\cdot||\frac{1}{2a}(\hat{U}_{\alpha\beta}(\vec{n},l)\hat{\sigma}^{-}_{\alpha}(\vec{n})\hat{\sigma}^{+}_{\beta}(\vec{n}+\hat{l})+h.c.)||\cdot||\frac{4d-2}{2a}(\hat{U}_{\beta\alpha}(\vec{n},l)\hat{\sigma}^{-}_{\beta}(\vec{n})\hat{\sigma}^{+}_{\alpha}(\vec{n}+\hat{l})+h.c.)|| \\
&=(16d-8)dL^{d}m\sum_{\alpha,\beta=1}^{3}||\frac{1}{2a}(\hat{U}_{\alpha\beta}(\vec{n},l)\hat{\sigma}^{-}_{\alpha}(\vec{n})\hat{\sigma}^{+}_{\beta}(\vec{n}+\hat{l})+h.c.)||^{2} \\
&=(16d-8)dL^{d}m\frac{9}{a^{2}}=\frac{(144d^{2}-72d)mL^{d}}{a^{2}}, \qquad (4.489)
\end{aligned}
$$

where the factor of $4d-2$, in front of the third term of the commutator, is the number of

$\hat{U}_{\beta\alpha}\hat{\sigma}^-_\beta\hat{\sigma}^+_\alpha + h.c.$ that collide with each $\hat{U}_{\alpha\beta}\hat{\sigma}^-_\alpha\hat{\sigma}^+_\beta + h.c.$. The bound for case (ii) is

$$
\begin{aligned}
&||\sum_{\vec{n}}\sum_{l=1}^{d}\sum_{\alpha,\beta=1}^{3}[[\frac{m}{2}((-1)^{\vec{n}}\hat{Z}_\alpha(\vec{n})+(-1)^{\vec{n}+\hat{l}}\hat{Z}_\beta(\vec{n}+\hat{l})),\frac{1}{2a}(\hat{U}_{\alpha\beta}(\vec{n},l)\hat{\sigma}^-_\alpha(\vec{n})\hat{\sigma}^+_\beta(\vec{n}+\hat{l})+h.c.)]\\
&,\frac{2d-1}{2a}\sum_{\alpha'\beta'=\beta\gamma}^{\gamma\alpha}(\hat{U}_{\alpha'\beta'}\hat{\sigma}^-_{\alpha'}\hat{\sigma}^+_{\beta'}+h.c.)]||\\
&=dL^d\cdot 4(2d-1)||m||\sum_{\alpha,\beta=1}^{3}||\frac{1}{2a}(\hat{U}_{\alpha\beta}(\vec{n},l)\hat{\sigma}^-_\alpha(\vec{n})\hat{\sigma}^+_\beta(\vec{n}+\hat{l})+h.c.)||\cdot||\frac{1}{2a}\sum_{\alpha'\beta'=\beta\gamma}^{\gamma\alpha}(\hat{U}_{\alpha'\beta'}\hat{\sigma}^-_{\alpha'}\hat{\sigma}^+_{\beta'}+h.c.)||\\
&=mL^d(8d^2-4d)\cdot 9\cdot\frac{1}{a}\frac{4\cdot 2}{2a}=\frac{mL^d(288d^2-144d)}{a^2}
\end{aligned}
\tag{4.490}
$$

where the factor of $2d-1$, in front of the third term of the nested commutator, is the number of $\hat{U}_{\alpha'\beta'}\hat{\sigma}^-_{\alpha'}\hat{\sigma}^+_{\beta'} + h.c.$, with $\alpha'\beta' = \beta\gamma$ or $\gamma\alpha$, that collide with each $\hat{U}_{\alpha\beta}\hat{\sigma}^-_\alpha\hat{\sigma}^+_\beta + h.c.$. In the last equality, we have accounted for the different bounds of $\hat{U}_{\alpha\beta}\hat{\sigma}^-_\alpha\hat{\sigma}^+_\beta + h.c.$ for each $\alpha\beta$, and the number of $\alpha'\beta' = \beta\gamma$ or $\gamma\alpha$, where $\gamma \neq \alpha, \beta$. Adding up the bounds for type (i) and (ii), we obtain the bound for the $C_{2,2}$ as follows:

$$
\frac{(432d^2+108d)mL^d}{a^2}. \tag{4.491}
$$

The bound for $C_{2,3}$ is given by

$$
\begin{aligned}
&|||[[\sum_{\vec{n}}\hat{D}^{(M)}_{\vec{n}},\sum_{\vec{n}'}\hat{T}^{(K)}_{\vec{n}'}],\sum_{\vec{n}''}\hat{L}^{(B)}_{\vec{n}''}]|||\\
&\leq||\sum_{\vec{n}}\sum_{l=1}^{d}\sum_{\alpha,\beta=1}^{3}[[\frac{m}{2}((-1)^{\vec{n}}\hat{Z}_\alpha(\vec{n})+(-1)^{\vec{n}+\hat{l}}\hat{Z}_\beta(\vec{n}+\hat{l})),\frac{1}{2a}(\hat{U}_{\alpha\beta}(\vec{n},l)\hat{\sigma}^-_\alpha(\vec{n})\hat{\sigma}^+_\beta(\vec{n}+\hat{l})+h.c.)],\sum_{\vec{n}''}\hat{L}^{(B)}_{\vec{n}''}]||\\
&\leq dL^d\cdot 4||m||\cdot\frac{9}{a}\cdot||\frac{2(d-1)}{2a^{4-d}g^2}\sum_{\alpha,\beta,\gamma,\delta=1}^{3}(\hat{U}_{\alpha\beta}\hat{U}_{\beta\gamma}\hat{U}^\dagger_{\gamma\delta}\hat{U}^\dagger_{\delta\alpha}+h.c.)||\leq\frac{5832mL^d(d^2-d)}{a^{5-d}g^2}.
\end{aligned}
\tag{4.492}
$$

Now we consider $C_{2,4}$. We divide the commutators up into two cases the same way we did

$C_{2,2}$. The bound for case (i), where the kinetic terms act on the same links, is given by

$$
\begin{aligned}
&||\sum_{\vec{n}}\sum_{l=1}^{d}\sum_{\alpha,\beta=1}^{3}[[\frac{g^2}{2a^{d-2}}\hat{E}^2(\vec{n},l),\frac{1}{2a}(\hat{U}_{\alpha\beta}(\vec{n},l)\hat{\sigma}_{\alpha}^{-}(\vec{n})\hat{\sigma}_{\beta}^{+}(\vec{n}+\hat{l})+h.c.)]\\
&,\frac{1}{2a}\sum_{\alpha',\beta'=1}^{3}(\hat{U}_{\alpha'\beta'}(\vec{n},l)\hat{\sigma}_{\alpha'}^{-}(\vec{n})\hat{\sigma}_{\beta'}^{+}(\vec{n}+\hat{l})+h.c.)]||| \\
&\leq dL^d\cdot 2\sum_{\alpha,\beta=1}^{3}|||[\frac{g^2}{2a^{d-2}}\hat{E}^2(\vec{n},l),\frac{1}{2a}(\hat{U}_{\alpha\beta}(\vec{n},l)\hat{\sigma}_{\alpha}^{-}(\vec{n})\hat{\sigma}_{\beta}^{+}(\vec{n}+\hat{l})+h.c.)]|||\\
&\cdot||\frac{1}{2a}\sum_{\alpha',\beta'=1}^{3}(\hat{U}_{\alpha'\beta'}(\vec{n},l)\hat{\sigma}_{\alpha'}^{-}(\vec{n})\hat{\sigma}_{\beta'}^{+}(\vec{n}+\hat{l})+h.c.)||\leq 2dL^d\frac{3g^2}{2a^{d-1}}(3\Lambda+4)\cdot\frac{9}{a}=\frac{27g^2dL^d(3\Lambda+4)}{a^d},
\end{aligned}
\tag{4.493}
$$

where we have used (4.472) to evaluate the first norm expression in the first inequality. As in $C_{2,2}$, we separate case (ii), where the kinetic terms act on different links, into two types. The bound for type (i), where the color indices for the outer kinetic term is $\beta\alpha$, is given by

$$
\begin{aligned}
&||\sum_{\vec{n}}\sum_{l=1}^{d}\sum_{\alpha,\beta=1}^{3}[[\frac{g^2}{2a^{d-2}}\hat{E}^2(\vec{n},l),\frac{1}{2a}(\hat{U}_{\alpha\beta}(\vec{n},l)\hat{\sigma}_{\alpha}^{-}(\vec{n})\hat{\sigma}_{\beta}^{+}(\vec{n}+\hat{l})+h.c.)],\frac{4d-2}{2a}(\hat{U}_{\beta\alpha}\hat{\sigma}_{\beta}^{-}\hat{\sigma}_{\alpha}^{+}+h.c.)]||| \\
&\leq dL^d\cdot 2\frac{g^2}{6a^{d-2}}(4+3\Lambda)\cdot\sum_{\alpha,\beta=1}^{3}||\frac{1}{2a}(\hat{U}_{\alpha\beta}\hat{\sigma}_{\alpha}^{-}\hat{\sigma}_{\beta}^{+}+h.c.)||\cdot||\frac{4d-2}{2a}(\hat{U}_{\beta\alpha}\hat{\sigma}_{\beta}^{-}\hat{\sigma}_{\alpha}^{+}+h.c.)|| \\
&\leq\frac{(4d^2-2d)L^dg^2(3\Lambda+4)}{3a^{d-2}}\sum_{\alpha,\beta=1}^{3}||\frac{1}{2a}(\hat{U}_{\alpha\beta}\hat{\sigma}_{\alpha}^{-}\hat{\sigma}_{\beta}^{+}+h.c.)||^2 \\
&\leq\frac{(4d^2-2d)L^dg^2(3\Lambda+4)}{3a^{d-2}}\frac{9}{a^2}=\frac{(12d^2-6d)L^dg^2(3\Lambda+4)}{3a^d}.
\end{aligned}
\tag{4.494}
$$

For type (ii), where the color indices for the outer kinetic term is $\beta\gamma$ with $\gamma\neq\alpha$, or $\gamma\alpha$ with

$\gamma \neq \beta$, we obtain the following bound:

$$
\begin{aligned}
&||\sum_{\vec{n}}\sum_{l=1}^{d}\sum_{\alpha,\beta=1}^{3}[[\frac{g^2}{2a^{d-2}}\hat{E}^2(\vec{n},l),\frac{1}{2a}(\hat{U}_{\alpha\beta}(\vec{n},l)\hat{\sigma}_{\alpha}^{-}(\vec{n})\hat{\sigma}_{\beta}^{+}(\vec{n}+\hat{l})+h.c.)],\frac{2d-1}{2a}\sum_{\alpha'\beta'=\beta\gamma}^{\gamma\alpha}(\hat{U}_{\alpha'\beta'}\hat{\sigma}_{\alpha'}^{-}\hat{\sigma}_{\beta'}^{+}+h.c.)]||\\
&\leq dL^d\cdot 2\frac{g^2}{6a^{d-2}}(4+3\Lambda)\cdot\sum_{\alpha,\beta=1}^{3}||\frac{1}{2a}(\hat{U}_{\alpha\beta}\hat{\sigma}_{\alpha}^{-}\hat{\sigma}_{\beta}^{+}+h.c.)||\cdot||\frac{2d-1}{2a}\sum_{\alpha'\beta'=\beta\gamma}^{\gamma\alpha}(\hat{U}_{\alpha'\beta'}\hat{\sigma}_{\alpha'}^{-}\hat{\sigma}_{\beta'}^{+}+h.c.)||\\
&\leq \frac{(2d^2-d)L^dg^2}{3a^{d-2}}(4+3\Lambda)\cdot\sum_{\alpha,\beta=1}^{3}||\frac{1}{2a}(\hat{U}_{\alpha\beta}\hat{\sigma}_{\alpha}^{-}\hat{\sigma}_{\beta}^{+}+h.c.)||\cdot||\frac{1}{2a}\sum_{\alpha'\beta'=\beta\gamma}^{\gamma\alpha}(\hat{U}_{\alpha'\beta'}\hat{\sigma}_{\alpha'}^{-}\hat{\sigma}_{\beta'}^{+}+h.c.)||\\
&\leq \frac{(2d^2-d)L^dg^2}{3a^{d-2}}(4+3\Lambda)\cdot 9\cdot\frac{1}{a}\cdot\frac{4}{a}=\frac{(24d^2-12d)L^dg^2}{a^d}(4+3\Lambda). \qquad (4.495)
\end{aligned}
$$

Therefore, the bound for $C_{2,4}$ is

$$\frac{(36d^2+9d)L^dg^2(4\Lambda+3)}{a^d}. \qquad (4.496)$$

We proceed to evaluate the bound for $C_{2,5}$ as follows:

$$
\begin{aligned}
&[[\sum_{\vec{n}}\hat{D}_{\vec{n}}^{(E)},\sum_{\vec{n}'}\hat{T}_{\vec{n}'}^{(K)}],\sum_{\vec{n}''}\hat{L}_{\vec{n}''}^{(B)}]\\
&\leq||\sum_{\vec{n}}\sum_{l=1}^{d}\sum_{\alpha,\beta=1}^{3}[[\frac{g^2}{2a^{d-2}}\hat{E}^2(\vec{n},l),\frac{1}{2a}(\hat{U}_{\alpha\beta}(\vec{n},l)\hat{\sigma}_{\alpha}^{-}(\vec{n})\hat{\sigma}_{\beta}^{+}(\vec{n}+\hat{l})+h.c.)],\sum_{\vec{n}''}\hat{L}_{\vec{n}''}^{(B)}]||\\
&\leq dL^d\cdot 2\sum_{\alpha,\beta=1}^{3}||[\frac{g^2}{2a^{d-2}}\hat{E}^2(\vec{n},l),\frac{1}{2a}(\hat{U}_{\alpha\beta}(\vec{n},l)\hat{\sigma}_{\alpha}^{-}(\vec{n})\hat{\sigma}_{\beta}^{+}(\vec{n}+\hat{l})+h.c.)]||\\
&\quad\cdot||\frac{2(d-1)}{2a^{4-d}g^2}\sum_{\alpha,\beta,\gamma,\delta=1}^{3}(\hat{U}_{\alpha\beta}\hat{U}_{\beta\gamma}\hat{U}_{\gamma\delta}^{\dagger}\hat{U}_{\delta\alpha}^{\dagger}+h.c.)||\\
&\leq dL^d\cdot 2\frac{3g^2}{2a^{d-1}}(3\Lambda+4)\cdot\frac{162(d-1)}{a^{4-d}g^2}=\frac{486d(d-1)L^d(4\Lambda+3)}{a^3}, \qquad (4.497)
\end{aligned}
$$

where in the second inequality, we have used (4.472) and the fact that there are $2(d-1)$ plaquettes consisting of the link $(\vec{n},l)$ to evaluate the first norm expression. The bound for the $C_{2,6}$ is given

by

$$
\begin{aligned}
&[[\sum_{\vec{n}} \hat{D}^{(E)}_{\vec{n}}, \sum_{\vec{n}'} \hat{L}^{(B)}_{\vec{n}'}], \sum_{\vec{n}''} \hat{T}^{(K)}_{\vec{n}''}] \\
&= |||[\sum_{\vec{n}} \sum_{i=1}^{d} \sum_{j\neq i;j=1}^{d} [\frac{g^2}{2a^{d-2}}(\hat{E}^2(\vec{n},i) + \hat{E}^2(\vec{n}+\hat{i},j) + \hat{E}^2(\vec{n}+\hat{j},i) + \hat{E}^2(\vec{n},j)) \\
&\quad , \frac{-1}{2a^{4-d}g^2} \sum_{\alpha,\beta,\gamma,\delta=1}^{3} (\hat{U}_{\alpha\beta}(\vec{n},i)\hat{U}_{\beta\gamma}(\vec{n}+\hat{i},j)\hat{U}^{\dagger}_{\gamma\delta}(\vec{n}+\hat{j},i)\hat{U}^{\dagger}_{\delta\alpha}(\vec{n},j) + h.c.)] \\
&\quad , \frac{1}{2a} \sum_{\alpha',\beta'=1}^{3} [\hat{U}_{\alpha'\beta'}(\vec{n},i)\hat{\sigma}^{-}_{\alpha'}(\vec{n})\hat{\sigma}^{+}_{\beta'}(\vec{n}+\hat{i}) + \hat{U}_{\alpha'\beta'}(\vec{n}+\hat{i},j)\hat{\sigma}^{-}_{\alpha'}(\vec{n}+\hat{i})\hat{\sigma}^{+}_{\beta'}(\vec{n}+\hat{i}+\hat{j}) \\
&\quad + \hat{U}_{\alpha'\beta'}(\vec{n}+\hat{j},i)\hat{\sigma}^{-}_{\alpha'}(\vec{n}+\hat{j})\hat{\sigma}^{+}_{\beta'}(\vec{n}+\hat{j}+\hat{i}) + \hat{U}_{\alpha'\beta'}(\vec{n},j)\hat{\sigma}^{-}_{\alpha'}(\vec{n})\hat{\sigma}^{+}_{\beta'}(\vec{n}+\hat{j}) + h.c.]]|| \\
&\leq L^d \frac{d(d-1)}{2} \cdot 2 \cdot ||\frac{54}{a^2}(4+3\Lambda)|| \cdot 4||\frac{1}{2a} \sum_{\alpha',\beta'=1}^{3} (\hat{U}_{\alpha'\beta'}\hat{\sigma}^{-}_{\alpha'}\hat{\sigma}^{+}_{\beta'} + h.c.)|| \\
&\leq L^d \frac{d(d-1)}{2} \cdot 2 \cdot ||\frac{54}{a^2}(4+3\Lambda)|| \cdot 4||\frac{9}{a}|| = \frac{1944d(d-1)L^d(3\Lambda+4)}{a^3},
\end{aligned} \tag{4.498}
$$

where we have used (4.474) to evaluate the first norm expression of the first inequality. The bound for $C_{2,7}$ is given by

$$
\begin{aligned}
&|||[[\sum_{\vec{n}} \hat{D}^{(E)}_{\vec{n}}, \sum_{\vec{n}'} \hat{L}^{(B)}_{\vec{n}'}], \sum_{\vec{n}''} \hat{L}^{(B)}_{\vec{n}''}]|| \\
&\leq |||[\sum_{\vec{n}} \sum_{i=1}^{d} \sum_{j\neq i;j=1}^{d} [\frac{g^2}{2a^{d-2}}(\hat{E}^2(\vec{n},i) + \hat{E}^2(\vec{n}+\hat{i},j) + \hat{E}^2(\vec{n}+\hat{j},i) + \hat{E}^2(\vec{n},j)) \\
&\quad , \frac{-1}{2a^{4-d}g^2} \sum_{\alpha,\beta,\gamma,\delta=1}^{3} (\hat{U}_{\alpha\beta}(\vec{n},i)\hat{U}_{\beta\gamma}(\vec{n}+\hat{i},j)\hat{U}^{\dagger}_{\gamma\delta}(\vec{n}+\hat{j},i)\hat{U}^{\dagger}_{\delta\alpha}(\vec{n},j) + h.c.)], \sum_{\vec{n}''} \hat{L}^{(B)}_{\vec{n}''}]|| \\
&\leq L^d \frac{d(d-1)}{2} \cdot 2||\frac{54}{a^2}(4+3\Lambda)|| \cdot ||\frac{8d-11}{2a^{4-d}g^2} \sum_{\alpha,\beta,\gamma,\delta=1}^{3} (\hat{U}_{\alpha\beta}\hat{U}_{\beta\gamma}\hat{U}^{\dagger}_{\gamma\delta}\hat{U}^{\dagger}_{\delta\alpha} + h.c.)|| \\
&\leq L^d \frac{d(d-1)54(3\Lambda+4)}{a^2} \cdot \frac{81(8d-11)}{a^{4-d}g^2} = \frac{L^d(3\Lambda+4)}{a^{6-d}g^2}(34992d^3 - 83106d^2 + 48114d),
\end{aligned} \tag{4.499}
$$

where in the second inequality, we have used (4.474) to evaluate the first norm expression, and the factor of $8d-11$ in the second norm term is the number of plaquettes that collide on links with the plaquette acted on by the magnetic operators in the inner commutator, as explained in the paragraph below (4.103).

Next we consider $C_{2,8}$. As in the case of SU(2), we divide the commutators up into five cases: (i) $\hat{h}_T$, $\hat{h}_{T'}$ and $\hat{h}_{T''}$ all act on the same links, (ii) $\hat{h}_T$ and $\hat{h}_{T'}$ act on the same links, while $\hat{h}_{T''}$ acts on neighboring links that are connect via the fermionic sites, (iii) $\hat{h}_T$ and $\hat{h}_{T''}$ act on the same links, while $\hat{h}_{T'}$ acts on neighboring links that are connect via the fermionic sites, (iv) $\hat{h}_{T'}$ and $\hat{h}_{T''}$ act on the same links, while $\hat{h}_T$ acts on neighboring links that are connect via the fermionic sites, (i) $\hat{h}_T$, $\hat{h}_{T'}$ and $\hat{h}_{T''}$ all act on different but connected links. We begin with case (i) by considering $\hat{h}_T$, $\hat{h}_{T'}$ and $\hat{h}_{T''}$ that act on one link $(\vec{n}_p, l)$ only. There are 13872 such $\hat{h}_T$ terms, each with different parameters $a, b, c, \Delta j, \alpha, \beta$, in $\mathbb{T}$. Thus, the bound for case (i) is given by

$$
\begin{aligned}
&13872 \sum_{p=e}^{o} \sum_{l=1}^{d} |||[\sum_{\vec{n}_p} \hat{h}_T(\vec{n}_p, l), \sum_{\hat{h}_{T'} \in \mathbb{T}; T' > T} \sum_{\vec{n}_p} \hat{h}_{T'}(\vec{n}_p, l)], \sum_{\hat{h}_{T''} \in \mathbb{T}; T'' > T} \sum_{\vec{n}_p} \hat{h}_{T''}(\vec{n}_p, l)]|||\\
&\leq 13872 \cdot 2d \sum_{\vec{n}_p} 4||\hat{h}_T(\vec{n}_p, l)|| \cdot || \sum_{\hat{h}_{T'} \in \mathbb{T}; T' > T} \hat{h}_{T'}(\vec{n}_p, l)|| \cdot || \sum_{\hat{h}_{T''} \in \mathbb{T}; T'' > T} \hat{h}_{T''}(\vec{n}_p, l)]||\\
&\leq 55488 dL^d || \frac{1}{2a} || \cdot || \frac{1}{a} \sum_{\alpha,\beta=1}^{3} (\hat{U}_{\alpha\beta}(\vec{n}_p, l) \hat{\sigma}_\alpha^-(\vec{n}_p) \hat{\sigma}_\beta^+(\vec{n}_p + \hat{l}) + h.c.)||^2\\
&\leq \frac{55488 dL^d}{a} (\frac{9}{a})^2 = \frac{4494528 dL^d}{a^3}.
\end{aligned}
\tag{4.500}
$$

The bound for case (ii) is

$$
\begin{aligned}
&13872 \sum_{p=e}^{o} \sum_{l=1}^{d} |||[\sum_{\vec{n}_p} \hat{h}_T(\vec{n}_p, l), \sum_{\hat{h}_{T'} \in \mathbb{T}; T' > T} \sum_{\vec{n}_p} \hat{h}_{T'}(\vec{n}_p, l)], \sum_{\hat{h}_{T''} \in \mathbb{T}; T'' > T} \hat{h}_{T''}]|||\\
&\leq 13872 \cdot 2d \sum_{\vec{n}_p} 4||\hat{h}_T(\vec{n}_p, l)|| \cdot || \sum_{\hat{h}_{T'} \in \mathbb{T}; T' > T} \hat{h}_{T'}(\vec{n}_p, l)|| \cdot || \sum_{\hat{h}_{T''} \in \mathbb{T}; T'' > T} \hat{h}_{T''}||\\
&\leq \frac{55488 dL^d}{a} \cdot || \frac{1}{2a} \sum_{\alpha,\beta=1}^{3} (\hat{U}_{\alpha\beta}(\vec{n}_p, l) \hat{\sigma}_\alpha^-(\vec{n}_p) \hat{\sigma}_\beta^+(\vec{n}_p + \hat{l}) + h.c.)|| \cdot || \frac{4d-1}{2a} \sum_{\alpha,\beta=1}^{3} (\hat{U}_{\alpha\beta} \hat{\sigma}_\alpha^- \hat{\sigma}_\beta^+ + h.c.)||\\
&\leq \frac{55488 dL^d}{a} \frac{9}{a} \frac{9(4d-1)}{a} = \frac{4494528(4d^2 - d)L^d}{a^3},
\end{aligned}
\tag{4.501}
$$

where the factor of $4d-1$ in the third norm expression of the second inequality is the number of links connected to $(\vec{n}_p, l)$, via the fermionic sites on both its ends.

We separate case (iii) into two types: type (i) consists of commutators where $\hat{h}_{T'}$ act on links in the same direction, but of different parity, as $\hat{h}_T, \hat{h}_{T''}$; type (ii) consists of commutators where $\hat{h}_{T'}$ act on links in different directions from $\hat{h}_T, \hat{h}_{T''}$. Consider type (i), since we implement the

even terms before the odd terms, the commutator bound is

$$
\begin{aligned}
&13872\sum_{l=1}^{d}||[[\sum_{\vec{n}_e}\hat{h}_T(\vec{n}_e,l),\sum_{\hat{h}_{T'}\in\mathbb{T};T'>T}\sum_{\vec{n}_o}\hat{h}_{T'}(\vec{n}_o,l)],\sum_{\hat{h}_{T''}\in\mathbb{T};T''>T}\sum_{\vec{n}_e}\hat{h}_{T''}(\vec{n}_e,l)]||\\
&\leq 13872d\sum_{\vec{n}_e}4||\hat{h}_T(\vec{n}_e,l)||\cdot||2\frac{1}{2a}\sum_{\alpha,\beta=1}^{3}(\hat{U}_{\alpha\beta}(\vec{n}_o,l)\hat{\sigma}_\alpha^-(\vec{n}_o)\hat{\sigma}_\beta^+(\vec{n}_o+\hat{l})+h.c.)||\\
&\quad\cdot||3\frac{1}{2a}\sum_{\alpha,\beta=1}^{3}(\hat{U}_{\alpha\beta}(\vec{n}_e,l)\hat{\sigma}_\alpha^-(\vec{n}_e)\hat{\sigma}_\beta^+(\vec{n}_e+\hat{l})+h.c.)]||\\
&\leq 55488d\frac{L^d}{2}||\frac{1}{a}||\cdot||\frac{18}{a}||\cdot||\frac{27}{a}||=\frac{13483584dL^d}{a^3},
\end{aligned}
\tag{4.502}
$$

where in the first inequality, the factor of 2 in the second norm expression is the number of odd links that are connected to each $(\vec{n}_e,l)$, and the factor of 3 in the third norm expression is the number of links that collide with $(\vec{n}_e,l)$ or are connected with the two odd links connected to $(\vec{n}_e,l)$. Similarly, we obtain the bound for type (ii)

$$
\begin{aligned}
&13872\sum_{p,p'=e}^{o}\sum_{l'>l}\sum_{l=1}^{d}||[[\sum_{\vec{n}_p}\hat{h}_T(\vec{n}_p,l),\sum_{\hat{h}_{T'}\in\mathbb{T};T'>T}\sum_{\vec{n}_{p'}}\hat{h}_{T'}(\vec{n}_{p'},l')],\sum_{\hat{h}_{T''}\in\mathbb{T};T''>T}\sum_{\vec{n}_p}\hat{h}_{T''}(\vec{n}_p,l)]||\\
&\leq 13872\cdot 4\frac{d(d-1)}{2}\sum_{\vec{n}_p}4||\hat{h}_T(\vec{n}_p,l)||\cdot||2\frac{1}{2a}\sum_{\alpha,\beta=1}^{3}(\hat{U}_{\alpha\beta}(\vec{n}'_p,l')\hat{\sigma}_\alpha^-(\vec{n}'_p)\hat{\sigma}_\beta^+(\vec{n}'_p+\hat{l}')+h.c.)||\\
&\quad\cdot||\frac{1}{2a}\sum_{\alpha,\beta=1}^{3}(\hat{U}_{\alpha\beta}(\vec{n}_p,l)\hat{\sigma}_\alpha^-(\vec{n}_p)\hat{\sigma}_\beta^+(\vec{n}_p+\hat{l})+h.c.)]||\\
&\leq 55488d(d-1)L^d||\frac{1}{a}||\cdot||\frac{18}{a}||\cdot||\frac{9}{a}||=\frac{8989056(d^2-d)L^d}{a^3}.
\end{aligned}
\tag{4.503}
$$

Therefore, the bound for case (iii) is

$$
\frac{(8989056d^2+22472640d)L^d}{a^3}. \tag{4.504}
$$

We divide case (iv) into two types: type-(i) commutators are those where $\hat{h}_T$, $\hat{h}_{T'}$ and $\hat{h}_{T''}$ act on links in the same direction; and type-(ii) commutators are those where $\hat{h}_T$, $\hat{h}_{T'}$ and $\hat{h}_{T''}$ act on links in different directions. We consider type (i) first. Since even terms are implemented

before odd terms, we obtain its bound as follows

$$13872\sum_{l=1}^{d}|||[[\sum_{\vec{n}_e}\hat{h}_T(\vec{n}_e,l),\sum_{\hat{h}_{T'}\in\mathbb{T};T'>T}\sum_{(\vec{n}_o,l)}\hat{h}_{T'}(\vec{n}_o,l)],\sum_{\hat{h}_{T''}\in\mathbb{T};T''>T}\sum_{(\vec{n}_o,l)}\hat{h}_{T''}(\vec{n}_o,l)]|||$$

$$\leq 13872d\cdot\sum_{\vec{n}_e}4||\hat{h}_T(\vec{n}_e,l)||\cdot||\frac{2}{2a}\sum_{\alpha,\beta=1}^{3}(\hat{U}_{\alpha\beta}(\vec{n}_o,l)\hat{\sigma}_\alpha^-(\vec{n}_o)\hat{\sigma}_\beta^+(\vec{n}_o+\hat{l})+h.c.)||^2$$

$$\leq\frac{13872dL^d}{2}4||\frac{1}{a}||\cdot||\frac{18}{a}||^2=\frac{8989056dL^d}{a^2},\tag{4.505}$$

where the factor of 2 in the numerator of the second norm expression of the second line is due to the fact that $(\vec{n}_e,l)$ is connected to two $(\vec{n}_o,l)$. Next, we evaluate the bound for type (ii) as follows:

$$13872\sum_{p,p'=e}^{o}\sum_{l'>l}\sum_{l=1}^{d}|||[[\sum_{\vec{n}_p}\hat{h}_T(\vec{n}_p,l),\sum_{\hat{h}_{T'}\in\mathbb{T};T'>T}\sum_{(\vec{n}_{p'},l')}\hat{h}_{T'}(\vec{n}_{p'},l')],\sum_{\hat{h}_{T''}\in\mathbb{T};T''>T}\sum_{(\vec{n}_{p'},l')}\hat{h}_{T''}(\vec{n}_{p'},l')]|||$$

$$\leq 13872\cdot 4\frac{d(d-1)}{2}\cdot 4\sum_{\vec{n}_p}||\hat{h}_T(\vec{n}_p,l)||\cdot||\frac{2}{2a}\sum_{\alpha,\beta=1}^{3}(\hat{U}_{\alpha\beta}(\vec{n}_{p'},l')\hat{\sigma}_\alpha^-(\vec{n}_{p'})\hat{\sigma}_\beta^+(\vec{n}_{p'}+\hat{l}')+h.c.)||^2$$

$$\leq 27744d(d-1)\frac{L^d}{2}4||\frac{1}{a}||\cdot||\frac{18}{a}||^2=\frac{17978112(d^2-d)L^d}{a^3},\tag{4.506}$$

where the factor of 2 in the numerator of the second norm expression of the second line is due to the fact that the link $(\vec{n}_p,l)$, acted on by $\hat{h}_T$, is connected to two links $(\vec{n}_{p'},l')$, acted on by $\hat{h}_{T'}$ and $\hat{h}_{T''}$. Therefore, case (iv) is bounded by

$$\frac{8989056(2d^2-d)L^d}{a^3}.\tag{4.507}$$

Lastly, we obtain the bound for case (v)

$$13872\sum_{\substack{(p'',l'');\\(p'',l'')>(p',l')}}\sum_{\substack{(p',l');\\(p',l')>(p,l)}}\sum_{(p,l)}|||[[\sum_{\vec{n}_p}\hat{h}_T(\vec{n}_p,l),\sum_{\substack{\hat{h}_{T'}\in\mathbb{T};\\T'>T}}\sum_{(\vec{n}_{p'},l')}\hat{h}_{T'}(\vec{n}_{p'},l')],\sum_{\substack{\hat{h}_{T''}\in\mathbb{T};\\T''>T}}\sum_{(\vec{n}_{p''},l'')}\hat{h}_{T''}(\vec{n}_{p''},l'')]|||$$

$$\leq 13872\frac{4}{3}(2d^3-3d^2+d)\cdot 4\sum_{\vec{n}_p}||\hat{h}_T(\vec{n}_p,l)||\cdot||\frac{2}{2a}\sum_{\alpha,\beta=1}^{3}(\hat{U}_{\alpha\beta}(\vec{n}_{p'},l')\hat{\sigma}_\alpha^-(\vec{n}_{p'})\hat{\sigma}_\beta^+(\vec{n}_{p'}+\hat{l}')+h.c.)||$$

$$\cdot||\frac{4}{2a}\sum_{\alpha,\beta=1}^{3}(\hat{U}_{\alpha\beta}(\vec{n}_{p''},l'')\hat{\sigma}_\alpha^-(\vec{n}_{p''})\hat{\sigma}_\beta^+(\vec{n}_{p''}+\hat{l}'')+h.c.)||$$

$$=\frac{110976L^d}{a}(2d^3-3d^2+d)||\frac{18}{a}||\cdot||\frac{36}{a}||=\frac{L^d}{a^3}71912448(2d^3-3d^2+d),\tag{4.508}$$

where $(p', l') > (p, l)$ means that (p', l') appears after (p, l) in $\mathbb{T}$, and since there are $2d$ (p, l), the triple sum outside the norm expression in the first line evaluates to

$$\sum_{q=1}^{2d}(2d-q)(2d-q-1) = \frac{4}{3}(2d^3 - 3d^2 + d). \tag{4.509}$$

In the second inequality, the factor of 2 in the numerator of the second norm expression is because of the fact that $(\vec{n}_p, l)$ is connected to at most 2 $(\vec{n}_{p'}, l')$, and thus, each of the inner commutators acts on at most three links and four sites. Further, each of these four sites are connected to at most one $(\vec{n}_{p''}, l'')$, hence the factor of 4 in the numerator of the third norm expression. Note that constants can be further tightened by considering the color indices of the fermionic operators. Finally, adding the bounds for all cases, we arrive at the bound for $C_{2,8}$

$$(143824896d^3 - 170792064d^2 + 85396032d)\frac{L^d}{a^3}. \tag{4.510}$$

Now for $C_{2,9}$, we separate the commutators into three cases. Case-(i) commutators consists of $\hat{h}_T$ and $\hat{h}_{T'}$ that act on the same links. Case-(ii) commutators consists of $\hat{h}_T$ and $\hat{h}_{T'}$ that act on links in the same directions, but of different parities. Case-(iii) commutators consists of $\hat{h}_T$ and $\hat{h}_{T'}$ that act on links in different directions, but connected via fermionic sites. The bound for case (i) is given by

$$\begin{aligned}
&13872\sum_{p=e}^{o}\sum_{l=1}^{d}[[\sum_{\vec{n}_p}\hat{h}_T(\vec{n}_p, l), \sum_{\hat{h}_{T'}\in\mathbb{T};T'>T}\sum_{\vec{n}_p}\hat{h}_{T'}(\vec{n}_p, l)], \sum_{\vec{n}}\hat{L}_{\vec{n}}^{(B)}] \\
&\leq 13872\cdot 2d\sum_{\vec{n}_p} 4||\hat{h}_T(\vec{n}_p, l)||\cdot||\frac{1}{2a}\sum_{\alpha,\beta=1}^{3}(\hat{U}_{\alpha,\beta}(\vec{n}_p, l)\hat{\sigma}_\alpha^-(\vec{n}_p)\hat{\sigma}_\beta^+(\vec{n}_p+\hat{l}) + h.c.)|| \\
&\quad\cdot||\frac{2(d-1)}{2a^{4-d}g^2}\sum_{\alpha,\beta,\gamma,\delta=1}^{3}(\hat{U}_{\alpha\beta}\hat{U}_{\beta\gamma}\hat{U}_{\gamma\delta}^\dagger\hat{U}_{\delta\alpha}^\dagger + h.c.)|| \\
&\leq 13872dL^d\cdot 4||\frac{1}{a}||\cdot||\frac{9}{a}||\cdot||\frac{162(d-1)}{a^{4-d}g^2}|| = \frac{80901504(d^2-d)L^d}{a^{6-d}g^2},
\end{aligned} \tag{4.511}$$

where in the first inequality, the numerator $2(d-1)$ in the third norm term is the number of magnetic operators that act on link $(\vec{n}_p, l)$.

For case (ii), there are two types of commutators; those where (i) $\hat{h}_T$ and $\hat{h}_{T'}$ have color indices $\alpha\beta$ and $\beta\alpha$, respectively, and thus, collide on two fermionic sites, and where (ii) $\hat{h}_T$ and $\hat{h}_{T'}$ have color indices $\alpha\beta$ and $\beta\gamma$ with $\gamma \neq \alpha$ or $\gamma\alpha$ with $\gamma \neq \beta$, respectively, and thus, collide on one fermionic sites. Thus, considering type (i), the inner commutators act on three links, which

collide with $3 \cdot 2(d-1)$ magnetic operators. Since we implement the even terms before the odd terms, we obtain the bound for the type-(i) commutators as follows:

$$\begin{aligned} & 13872 \sum_{l=1}^{d} 4 \sum_{\vec{n}_e} ||\hat{h}_T(\vec{n}_e, l)|| \cdot ||\frac{2}{2a}(\hat{U}_{\beta\alpha}(\vec{n}_o, l)\hat{\sigma}_{\beta}^{-}(\vec{n}_o)\hat{\sigma}_{\alpha}^{+}(\vec{n}_o + \hat{l}) + h.c.)|| \\ & \cdot ||\frac{6(d-1)}{2a^{4-d}g^2} \sum_{\alpha,\beta,\gamma,\delta=1}^{3} (\hat{U}_{\alpha\beta}\hat{U}_{\beta\gamma}\hat{U}_{\gamma\delta}^{\dagger}\hat{U}_{\delta\alpha}^{\dagger} + h.c.)|| \\ & \leq 27744dL^d ||\frac{1}{a}|| \cdot ||\frac{2}{a}|| \cdot ||\frac{486(d-1)}{a^{4-d}g^2}|| = \frac{26967168(d^2-d)L^d}{a^{6-d}g^2}. \end{aligned} \tag{4.512}$$

For type (ii), the inner commutators act on two links, and thus collide with $2 \cdot 2(d-1)$ magnetic operators. We obtain the bound for the type-(ii) commutators as follows:

$$\begin{aligned} & 13872 \sum_{l=1}^{d} 4 \sum_{\vec{n}_e} ||\hat{h}_T(\vec{n}_e, l)|| \cdot ||\frac{1}{2a} \sum_{\alpha'\beta'=\beta\gamma}^{\gamma\alpha} (\hat{U}_{\alpha'\beta'}(\vec{n}_o, l)\hat{\sigma}_{\alpha'}^{-}(\vec{n}_o)\hat{\sigma}_{\beta'}^{+}(\vec{n}_o + \hat{l}) + h.c.)|| \\ & \cdot ||\frac{4(d-1)}{2a^{4-d}g^2} \sum_{\alpha,\beta,\gamma,\delta=1}^{3} (\hat{U}_{\alpha\beta}\hat{U}_{\beta\gamma}\hat{U}_{\gamma\delta}^{\dagger}\hat{U}_{\delta\alpha}^{\dagger} + h.c.)|| \\ & \leq 27744dL^d ||\frac{1}{a}|| \cdot ||\frac{4}{a}|| \cdot ||\frac{324(d-1)}{a^{4-d}g^2}|| = \frac{35956224(d^2-d)L^d}{a^{6-d}g^2}, \end{aligned} \tag{4.513}$$

where in the last inequality, the numerator 4 in the second norm expression in the number of $\alpha'\beta' = \beta\gamma$, or $\gamma\alpha$ with $\gamma \neq \alpha, \beta$. Thus, for case (ii), we obtain the bound

$$\frac{62923392(d^2-d)L^d}{a^{6-d}g^2}. \tag{4.514}$$

In the third case, $\hat{h}_T$ and $\hat{h}_{T'}$ act on links in different directions. As in the second case, we divide up case (iii) based on the color indices of $\hat{h}_T$ and $\hat{h}_{T'}$. Focusing on the first type, the inner commutators act on three links, which collide with $2 + 3 \cdot 2(d-2) = 6d - 10$ magnetic operators, where two of them act on all three links, and there are $2(d-2)$ magnetic operators acting on each one link, but not the other two links. Thus, we obtain the bound for type (i) commutators

as follows:

$$
\begin{aligned}
&13872 \sum_{p,p'=e}^{o} \sum_{l'>l} \sum_{l=1}^{d} 4 \sum_{\vec{n}_p} ||\hat{h}_T(\vec{n}_p, l)|| \cdot ||\frac{2}{2a}(\hat{U}_{\beta\alpha}(\vec{n}_{p'}, l')\hat{\sigma}^-_{\beta}(\vec{n}_{p'})\hat{\sigma}^+_{\alpha}(\vec{n}_{p'} + \hat{l}') + h.c.)|| \\
&\cdot ||\frac{6d-10}{2a^{4-d}g^2} \sum_{\alpha,\beta,\gamma,\delta=1}^{3} (\hat{U}_{\alpha\beta}\hat{U}_{\beta\gamma}\hat{U}^{\dagger}_{\gamma\delta}\hat{U}^{\dagger}_{\delta\alpha} + h.c.)|| \\
&\leq 13872 \cdot 4\frac{d(d-1)}{2} \cdot 4\frac{L^d}{2}||\frac{1}{a}|| \cdot ||\frac{2}{a}|| \cdot ||\frac{81(6d-10)}{a^{4-d}g^2}|| \\
&= (53934336d^3 - 143824896d^2 + 89890560d)\frac{L^d}{a^{6-d}g^2}.
\end{aligned} \tag{4.515}
$$

Moving onto the second type, the inner commutators act on two links, which collide with $1 + 2 \cdot 2(d-2) = 4d - 7$ magnetic operators, where one of them acts on both links, and there are $2(d-2)$ magnetic operators acting on each one link, but not the other. Hence, we evaluate the bound for type (ii), and obtain,

$$
\begin{aligned}
&13872 \sum_{p,p'=e}^{o} \sum_{l'>l} \sum_{l=1}^{d} 4 \sum_{\vec{n}_p} ||\hat{h}_T(\vec{n}_p, l)|| \cdot ||\frac{1}{2a} \sum_{\alpha'\beta'=\beta\gamma}^{\gamma\alpha} (\hat{U}_{\alpha'\beta'}(\vec{n}_{p'}, l)\hat{\sigma}^-_{\alpha'}(\vec{n}_{p'})\hat{\sigma}^+_{\beta'}(\vec{n}_{p'} + \hat{l}) + h.c.)|| \\
&\cdot ||\frac{4d-7}{2a^{4-d}g^2} \sum_{\alpha,\beta,\gamma,\delta=1}^{3} (\hat{U}_{\alpha\beta}\hat{U}_{\beta\gamma}\hat{U}^{\dagger}_{\gamma\delta}\hat{U}^{\dagger}_{\delta\alpha} + h.c.)|| \\
&\leq 13872 \cdot 4\frac{d(d-1)}{2} \cdot 4\frac{L^d}{2}||\frac{1}{a}|| \cdot ||\frac{4}{a}|| \cdot ||\frac{81(4d-7)}{a^{4-d}g^2}|| \\
&= (71912448d^3 - 197759232d^2 + 125846784d)\frac{L^d}{a^{6-d}g^2}.
\end{aligned} \tag{4.516}
$$

Therefore, the bound for case (iii) is

$$
(125846784d^3 - 341584128d^2 + 215737344d)\frac{L^d}{a^{6-d}g^2}. \tag{4.517}
$$

Summing up the bounds for all three cases, we obtain the bound for $C_{2,9}$

$$
(125846784d^3 - 197759232d^2 + 71912448d)\frac{L^d}{a^{6-d}g^2}. \tag{4.518}
$$

Now for $C_{2,10}$, we divide the commutators up into cases and types, as we have done for $C_{2,9}$. The bound for case (i) of both $C_{2,9}$ and $C_{2,10}$ is the same, and is given by

$$
\frac{80901504(d^2-d)L^d}{a^{6-d}g^2}. \tag{4.519}
$$

The bound for case (ii) can be obtained from the case-(ii) bounds for $C_{2,9}$ after some slight modifications. First, since the kinetic operator $\hat{h}_T$ only act on one link, there are only $2(d-1)$ plaquette operators in the inner commutator that do not commute with each $\hat{h}_T$ because the plaquettes may lie on $d-1$ two-dimensional planes and can be of two different parities. Second, the kinetic operators $\hat{h}_{T'}$ not only collide with $\hat{h}_T$ via fermionic sites, but also with the magnetic operators on links. Thus, we obtain the bound for type (i) of case (ii)

$$\begin{aligned}
&13872\sum_{l=1}^{d}4\sum_{\vec{n}_e}||\hat{h}_T(\vec{n}_e,l)||\cdot||\frac{2(d-1)}{2a^{4-d}g^2}\sum_{\alpha,\beta,\gamma,\delta=1}^{3}(\hat{U}_{\alpha\beta}\hat{U}_{\beta\gamma}\hat{U}^{\dagger}_{\gamma\delta}\hat{U}^{\dagger}_{\delta\alpha}+h.c.)||\\
&\cdot||\frac{4}{2a}(\hat{U}_{\beta\alpha}(\vec{n}_o,l)\hat{\sigma}^{-}_{\beta}(\vec{n}_o)\hat{\sigma}^{+}_{\alpha}(\vec{n}_o+\hat{l})+h.c.)||\\
&\leq 27744d(d-1)L^d||\frac{1}{a}||\cdot||\frac{162}{a^{4-d}g^2}||\cdot||\frac{4}{a}||=\frac{17978112(d^2-d)L^d}{a^{6-d}g^2},
\end{aligned}\tag{4.520}$$

where the numerator 4 in the third norm expression is due to the fact that two $\hat{h}_{T'}$ collides with each of $\hat{h}_T$, and the pair of magnetic operators that lie on the same plane. The bound for type (ii) of case (ii) is

$$\begin{aligned}
&13872\sum_{l=1}^{d}4\sum_{\vec{n}_e}||\hat{h}_T(\vec{n}_e,l)||\cdot||\frac{2(d-1)}{2a^{4-d}g^2}\sum_{\alpha,\beta,\gamma,\delta=1}^{3}(\hat{U}_{\alpha\beta}\hat{U}_{\beta\gamma}\hat{U}^{\dagger}_{\gamma\delta}\hat{U}^{\dagger}_{\delta\alpha}+h.c.)||\\
&\cdot||\frac{3}{2a}\sum_{\alpha'\beta'=\beta\gamma}^{\gamma\alpha}(\hat{U}_{\alpha'\beta'}(\vec{n}_o,l)\hat{\sigma}^{-}_{\alpha'}(\vec{n}_o)\hat{\sigma}^{+}_{\beta'}(\vec{n}_o+\hat{l})+h.c.)||\\
&\leq 27744d(d-1)L^d||\frac{1}{a}||\cdot||\frac{162}{a^{4-d}g^2}||\cdot||\frac{3\cdot 4}{a}||=\frac{53934336(d^2-d)L^d}{a^{6-d}g^2},
\end{aligned}\tag{4.521}$$

where the numerator 3 in the third norm expression is due to the fact that for a fixed pair of color indices $\alpha'\beta'$, one $\hat{h}_{T'}$ collides with $\hat{h}_T$, and two with the pair of magnetic operators that lie on the same plane. Thus, for case (ii), the bound is given by

$$\frac{71912448(d^2-d)L^d}{a^{6-d}g^2}.\tag{4.522}$$

Now we consider the third case. Once again, we modify the case-(iii) bounds of $C_{2,9}$. Thus, we

obtain the respective bounds for type (i) and (ii) commutators as follows:

$$
\begin{aligned}
&13872\sum_{p,p'=e}^{o}\sum_{l'>l}\sum_{l=1}^{d}4\sum_{\vec{n}_p}||\hat{h}_T(\vec{n}_p,l)||\cdot||\frac{2(d-1)}{2a^{4-d}g^2}\sum_{\alpha,\beta,\gamma,\delta=1}^{3}(\hat{U}_{\alpha\beta}\hat{U}_{\beta\gamma}\hat{U}^{\dagger}_{\gamma\delta}\hat{U}^{\dagger}_{\delta\alpha}+h.c.)||\\
&\cdot||\frac{2}{2a}(\hat{U}_{\beta\alpha}(\vec{n}_{p'},l')\hat{\sigma}^{-}_{\beta}(\vec{n}_{p'})\hat{\sigma}^{+}_{\alpha}(\vec{n}_{p'}+\hat{l}')+h.c.)||\\
&\leq 13872\cdot 4\frac{d(d-1)}{2}\cdot 4\frac{L^d}{2}||\frac{1}{a}||\cdot||\frac{162(d-1)}{a^{4-d}g^2}||\cdot||\frac{2}{a}||=17978112(d^3-2d^2+d)\frac{L^d}{a^{6-d}g^2},
\end{aligned}
\tag{4.523}
$$

and

$$
\begin{aligned}
&13872\sum_{p,p'=e}^{o}\sum_{l'>l}\sum_{l=1}^{d}4\sum_{\vec{n}_p}||\hat{h}_T(\vec{n}_p,l)||\cdot||\frac{2(d-1)}{2a^{4-d}g^2}\sum_{\alpha,\beta,\gamma,\delta=1}^{3}(\hat{U}_{\alpha\beta}\hat{U}_{\beta\gamma}\hat{U}^{\dagger}_{\gamma\delta}\hat{U}^{\dagger}_{\delta\alpha}+h.c.)||\\
&\cdot||\frac{1}{2a}\sum_{\alpha'\beta'=\beta\gamma}^{\gamma\alpha}(\hat{U}_{\alpha'\beta'}(\vec{n}_{p'},l)\hat{\sigma}^{-}_{\alpha'}(\vec{n}_{p'})\hat{\sigma}^{+}_{\beta'}(\vec{n}_{p'}+\hat{l})+h.c.)||\\
&\leq 13872\cdot 4\frac{d(d-1)}{2}\cdot 4\frac{L^d}{2}||\frac{1}{a}||\cdot||\frac{162(d-1)}{a^{4-d}g^2}||\cdot||\frac{4}{a}||=35956224(d^3-2d^2+d)\frac{L^d}{a^{6-d}g^2}.
\end{aligned}
\tag{4.524}
$$

Therefore, the bound for case (iii) is

$$
53934336(d^3-2d^2+d)\frac{L^d}{a^{6-d}g^2}. \tag{4.525}
$$

Summing up the bounds for all cases, we obtain the bound for $C_{2,10}$

$$
(53934336d^3+44945280d^2-98879616d)\frac{L^d}{a^{6-d}g^2}. \tag{4.526}
$$

We compute the bound for $C_{2,11}$, and obtain

$$
\begin{aligned}
&\sum_{\hat{h}_T\in\mathbb{T}}|||[\hat{h}_T,\sum_{\vec{n}}\hat{L}^{(B)}_{\vec{n}}],\sum_{\vec{n}'}\hat{L}^{(B)}_{\vec{n}'}]|||\\
&\leq 13872dL^d\cdot 4||\hat{h}_T(\vec{n}_p,l)||\cdot||\frac{2(d-1)}{2a^{4-d}g^2}\sum_{\alpha,\beta,\gamma,\delta=1}^{3}(\hat{U}_{\alpha\beta}\hat{U}_{\beta\gamma}\hat{U}^{\dagger}_{\gamma\delta}\hat{U}^{\dagger}_{\delta\alpha}+h.c.)||\\
&\cdot||\frac{14d-20}{2a^{4-d}g^2}\sum_{\alpha,\beta,\gamma,\delta=1}^{3}(\hat{U}_{\alpha\beta}\hat{U}_{\beta\gamma}\hat{U}^{\dagger}_{\gamma\delta}\hat{U}^{\dagger}_{\delta\alpha}+h.c.)||\\
&\leq \frac{55488dL^d}{a}\frac{162(d-1)}{a^{4-d}g^2}\frac{162(7d-10)}{a^{4-d}g^2}=\frac{(10193589504d^3-24755860224d^2+14562270720d)L^d}{a^{9-2d}g^4},
\end{aligned}
\tag{4.527}
$$

where in the first inequality, the factors of $2(d-1)$ and $14d-20$ are explained in the paragraph below (4.137).

Lastly, we consider $C_{2,12}$, which consists of commutators between only magnetic operators. The commutators are either *intra-plaquette* or *inter-plaquette*, where $\hat{h}_L$, $\hat{h}_{L'}$ and $\hat{h}_{L''}$ act on the same or different plaquettes, respectively. We consider intra-plaquette terms first. We remind the readers that there are $N_L \equiv 735010926133248$ different $\hat{h}_L(\vec{n}_p, j, k)$ terms acting on each plaquette $(\vec{n}_p, j, k)$. The bound for the intra-plaquette commutators is given by

$$
\begin{aligned}
& N_L \sum_{k\neq j;k=1}^{d} \sum_{j=1}^{d} \sum_{\vec{n}_p} \sum_{p=e}^{o} |||[\hat{h}_L(\vec{n}_p,j,k), \sum_{\hat{h}_{L'}\in\mathbb{L};L'>L} \hat{h}_{L'}(\vec{n}_p,j,k)], \sum_{\hat{h}_{L''}\in\mathbb{L};L''>L} \hat{h}_{L''}(\vec{n}_p,j,k)]||| \\
& \leq \frac{N_L d(d-1)L^d}{2} 4||\hat{h}_L(\vec{n}_p,j,k)|| \cdot ||\frac{1}{2a^{4-d}g^2} \sum_{\alpha,\beta,\gamma,\delta=1}^{3} (\hat{U}_{\alpha\beta}\hat{U}_{\beta\gamma}\hat{U}^{\dagger}_{\gamma\delta}\hat{U}^{\dagger}_{\delta\alpha} + h.c.)||^2 \\
& \leq 2N_L d(d-1)L^d ||\frac{1}{a^{4-d}g^2}|| \cdot ||\frac{81}{a^{4-d}g^2}||^2 \\
& = \frac{L^d}{a^{12-3d}g^6} 9644813372720480256(d^2-d). \qquad (4.528)
\end{aligned}
$$

We now proceed to analyze the inter-plaquette commutators. Since each $\hat{h}_{L''}$ operator is non-zero, the inner commutator $[\hat{h}_L, \sum_{\hat{h}_{L'}\in\mathbb{L};L'>L} \hat{h}_{L'}]$ must be non-zero to guarantee a non-trivial triple commutator

$$
[[\hat{h}_L, \sum_{\hat{h}_{L'}\in\mathbb{L};L'>L} \hat{h}_{L'}], \sum_{\hat{h}_{L''}\in\mathbb{L};L''>L} \hat{h}_{L''}].
$$

Given a non-zero inner commutator, we further divide the inter-plaquette commutators into three types. Type (i), (ii) and (iii) commutators satisfy (4.308),(4.309) and (4.310), respectively.

For type (i), the plaquettes acted on by $\hat{h}_L$, collide with those acted on by $\hat{h}_{L'}$ and $\hat{h}_{L''}$, and those acted on by $\hat{h}_{L'}$ also collide with those acted on by $\hat{h}_{L''}$. Suppose $\hat{h}_L$ is labelled by (p,k,l). The possible parity-location tuples that label $\hat{h}_{L'}$ and $\hat{h}_{L''}$ are given in Table 4.6 and 4.7 for $p =$ *even* and *odd*, respectively. Consider first the case where $p =$ *even*, and $\hat{h}_L$ and $\hat{h}_{L'}$ are labelled by items $1-4$, 6 and 7 in Table 4.6. Then, each plaquette acted on by $\hat{h}_L$ is acted on by two $\hat{h}_{L'}$ as they share one dimension. Further, the plaquettes acted on by $\hat{h}_L$ and $\hat{h}_{L'}$ are acted on by either $2, 4, 6$ or 8 $\hat{h}_{L''}$. In particular, if the plaquettes acted on by $\hat{h}_{L''}$ (i) share one common dimension with $\hat{h}_L$, and two common dimensions and parity with $\hat{h}_{L'}$, or (ii) share one dimension with $\hat{h}_L$ and a different dimension with $\hat{h}_{L'}$, then $\hat{h}_L$ and $\hat{h}_{L'}$ collide with two $\hat{h}_{L''}$. We compute the number of combinations of parity-location labels that satisfy these conditions using Table 4.6, and obtain

$$
\sum_{l>k} \sum_{k=1}^{d-1} 12(d-l) + 2(l-k-1) = \frac{7}{3}(d^3 - 3d^2 + 2d). \qquad (4.529)
$$

$$
\begin{aligned}
&N_L||[[\sum_{\vec{n}_e}\hat{h}_L(e,k,l),\sum_{\hat{h}_{L'}\in\mathbb{L};L'>L}\hat{h}_{L'}],\sum_{\hat{h}_{L''}\in\mathbb{L};L''>L}\hat{h}_{L''}]||| \\
&\leq\frac{N_L\cdot 7}{3}(d^3-3d^2+2d)\sum_{\vec{n}_e}4\cdot||\hat{h}_L(e,k,l)||\cdot||\frac{2}{2a^{4-d}g^2}\sum_{\alpha,\beta,\gamma,\delta=1}^{3}(\hat{U}_{\alpha\beta}\hat{U}_{\beta\gamma}\hat{U}^{\dagger}_{\gamma\delta}\hat{U}^{\dagger}_{\delta\alpha}+h.c.)|| \\
&\quad\cdot||\frac{2}{2a^{4-d}g^2}\sum_{\alpha,\beta,\gamma,\delta=1}^{3}(\hat{U}_{\alpha\beta}\hat{U}_{\beta\gamma}\hat{U}^{\dagger}_{\gamma\delta}\hat{U}^{\dagger}_{\delta\alpha}+h.c.)|| \\
&\leq\frac{L^d}{a^{12-3d}g^6}900182581453911490 56(d^3-3d^2+2d),
\end{aligned}
\tag{4.530}
$$

where N_L is the number of $\hat{h}_L$ terms per plaquette.

If the plaquettes acted on by $\hat{h}_{L''}$ share only one dimension with both $\hat{h}_L$ and $\hat{h}_{L'}$, then $\hat{h}_L$ and $\hat{h}_{L'}$ collide with four $\hat{h}_{L''}$. Using Table 4.6, we find the number of combinations of parity-location labels that satisfy this condition, i.e.

$$
\begin{aligned}
&\sum_{l>k}\sum_{k=1}^{d-1}(d-l)[8(d-l-1)+4(l-k-1)]+(l-k-1)[4(d-l)+4(l-k-2)] \\
&=\frac{4}{3}(d^4-6d^3+11d^2-6d).
\end{aligned}
\tag{4.531}
$$

The bound in this case is given by

$$
\begin{aligned}
&N_L||[[\sum_{\vec{n}_e}\hat{h}_L(e,k,l),\sum_{\hat{h}_{L'}\in\mathbb{L};L'>L}\hat{h}_{L'}],\sum_{\hat{h}_{L''}\in\mathbb{L};L''>L}\hat{h}_{L''}]||| \\
&\leq\frac{N_L\cdot 4}{3}(d^4-6d^3+11d^2-6d)\sum_{\vec{n}_e}4\cdot||\hat{h}_L(e,k,l)||\cdot||\frac{2}{2a^{4-d}g^2}\sum_{\alpha,\beta,\gamma,\delta=1}^{3}(\hat{U}_{\alpha\beta}\hat{U}_{\beta\gamma}\hat{U}^{\dagger}_{\gamma\delta}\hat{U}^{\dagger}_{\delta\alpha}+h.c.)|| \\
&\quad\cdot||\frac{4}{2a^{4-d}g^2}\sum_{\alpha,\beta,\gamma,\delta=1}^{3}(\hat{U}_{\alpha\beta}\hat{U}_{\beta\gamma}\hat{U}^{\dagger}_{\gamma\delta}\hat{U}^{\dagger}_{\delta\alpha}+h.c.)|| \\
&\leq\frac{L^d}{a^{12-3d}g^6}1028780093090184560 64(d^4-6d^3+11d^2-6d).
\end{aligned}
\tag{4.532}
$$

If the plaquettes acted on by $\hat{h}_{L''}$ share only one dimension with $\hat{h}_{L'}$, and share both dimensions, but not the parity, with $\hat{h}_L$, then $\hat{h}_L$ and $\hat{h}_{L'}$ collide with six $\hat{h}_{L''}$. Once again, we use Table 4.6 to obtain the number of combinations of parity-location labels that satisfy this condition, i.e.

$$
\sum_{l>k}\sum_{k=1}^{d-1}4(d-l)+2(l-k-1)=(d^3-3d^2+2d).
\tag{4.533}
$$

The bound in this case is given by

$$
\begin{aligned}
&N_L||[[\sum_{\vec{n}_e}\hat{h}_L(e,k,l),\sum_{\hat{h}_{L'}\in\mathbb{L};L'>L}\hat{h}_{L'}],\sum_{\hat{h}_{L''}\in\mathbb{L};L''>L}\hat{h}_{L''}]||\\
&\leq N_L(d^3-3d^2+2d)\sum_{\vec{n}_e}4\cdot||\hat{h}_L(e,k,l)||\cdot||\frac{2}{2a^{4-d}g^2}\sum_{\alpha,\beta,\gamma,\delta=1}^{3}(\hat{U}_{\alpha\beta}\hat{U}_{\beta\gamma}\hat{U}^{\dagger}_{\gamma\delta}\hat{U}^{\dagger}_{\delta\alpha}+h.c.)||\\
&\quad\cdot||\frac{6}{2a^{4-d}g^2}\sum_{\alpha,\beta,\gamma,\delta=1}^{3}(\hat{U}_{\alpha\beta}\hat{U}_{\beta\gamma}\hat{U}^{\dagger}_{\gamma\delta}\hat{U}^{\dagger}_{\delta\alpha}+h.c.)||\\
&\leq\frac{L^d}{a^{12-3d}g^6}115737760472645763072(d^3-3d^2+2d).
\end{aligned}
\tag{4.534}
$$

If the plaquettes acted on by $\hat{h}_{L''}$ share only one dimension with $\hat{h}_L$, and share both dimensions, but not the parity, with $\hat{h}_{L'}$, then $\hat{h}_L$ and $\hat{h}_{L'}$ collide with eight $\hat{h}_{L''}$. Once again, we use Table 4.6 to obtain the number of combinations of parity-location labels that satisfy this condition, i.e.

$$
\sum_{l>k}\sum_{k=1}^{d-1}4(d-l)+2(l-k-1)=(d^3-3d^2+2d).
\tag{4.535}
$$

The bound in this case is given by

$$
\begin{aligned}
&N_L||[[\sum_{\vec{n}_e}\hat{h}_L(e,k,l),\sum_{\hat{h}_{L'}\in\mathbb{L};L'>L}\hat{h}_{L'}],\sum_{\hat{h}_{L''}\in\mathbb{L};L''>L}\hat{h}_{L''}]||\\
&\leq N_L(d^3-3d^2+2d)\sum_{\vec{n}_e}4\cdot||\hat{h}_L(e,k,l)||\cdot||\frac{2}{2a^{4-d}g^2}\sum_{\alpha,\beta,\gamma,\delta=1}^{3}(\hat{U}_{\alpha\beta}\hat{U}_{\beta\gamma}\hat{U}^{\dagger}_{\gamma\delta}\hat{U}^{\dagger}_{\delta\alpha}+h.c.)||\\
&\quad\cdot||\frac{8}{2a^{4-d}g^2}\sum_{\alpha,\beta,\gamma,\delta=1}^{3}(\hat{U}_{\alpha\beta}\hat{U}_{\beta\gamma}\hat{U}^{\dagger}_{\gamma\delta}\hat{U}^{\dagger}_{\delta\alpha}+h.c.)||\\
&\leq\frac{L^d}{a^{12-3d}g^6}154317013963527684096(d^3-3d^2+2d).
\end{aligned}
\tag{4.536}
$$

If $\hat{h}_{L''}$ acts on plaquettes that share only one dimension with $\hat{h}_L$ and $\hat{h}_{L'}$, then $\hat{h}_L$ and $\hat{h}_{L'}$ collide with eight $\hat{h}_{L''}$. There are

$$
\sum_{l>k}\sum_{k=1}^{d-1}4(d-l)+2(l-k-1)=d^3-3d^2+2d
\tag{4.537}
$$

combinations of parity-location labels that satisfy this condition. The bound in this case is given by

$$
\begin{aligned}
& N_L||[[\sum_{\vec{n}_e} \hat{h}_L(e,k,l), \sum_{\hat{h}_{L'} \in \mathbb{L}; L' > L} \hat{h}_{L'}], \sum_{\hat{h}_{L''} \in \mathbb{L}; L'' > L} \hat{h}_{L''}]|| \\
& \leq N_L(d-1) \sum_{\vec{n}_e} 4 \cdot ||\hat{h}_L(e,k,l)|| \cdot ||\frac{4}{2a^{4-d}g^2} \sum_{\alpha,\beta,\gamma,\delta=1}^{2} (\hat{U}_{\alpha\beta}\hat{U}_{\beta\gamma}\hat{U}^{\dagger}_{\gamma\delta}\hat{U}^{\dagger}_{\delta\alpha} + h.c.)|| \\
& \quad \cdot ||\frac{8}{2a^{4-d}g^2} \sum_{\alpha,\beta,\gamma,\delta=1}^{2} (\hat{U}_{\alpha\beta}\hat{U}_{\beta\gamma}\hat{U}^{\dagger}_{\gamma\delta}\hat{U}^{\dagger}_{\delta\alpha} + h.c.)|| \\
& \leq \frac{L^d}{a^{12-3d}g^6} 308634027927055368192(d^3 - 3d^2 + 2d).
\end{aligned} \tag{4.538}
$$

Consider now the case where $\hat{h}_L$ and $\hat{h}_{L'}$ collide on two dimensions, but have different parities, i.e., item 5 in Table 4.6. Since we implement even terms before odd ones, the parities of $\hat{h}_L$ and $\hat{h}_{L'}$ are even and odd, respectively. Moreover, $\hat{h}_L$ acting on a plaquette collides with four $\hat{h}_{L'}$ on the four links. If $\hat{h}_{L''}$ act on plaquettes that share one dimension with $\hat{h}_L$, and both dimensions and the parity with those acted on by $\hat{h}_{L'}$, then $\hat{h}_L$ and $\hat{h}_{L'}$ collide with four $\hat{h}_{L''}$. There are

$$
\sum_{k=1}^{d-1} 1 = d - 1 \tag{4.539}
$$

combinations of parity-location labels that satisfy this condition. The bound in this case is given by

$$
\begin{aligned}
& N_L||[[\sum_{\vec{n}_e} \hat{h}_L(e,k,l), \sum_{\hat{h}_{L'} \in \mathbb{L}; L' > L} \hat{h}_{L'}], \sum_{\hat{h}_{L''} \in \mathbb{L}; L'' > L} \hat{h}_{L''}]|| \\
& \leq N_L(d-1) \sum_{\vec{n}_e} 4 \cdot ||\hat{h}_L(e,k,l)|| \cdot ||\frac{4}{2a^{4-d}g^2} \sum_{\alpha,\beta,\gamma,\delta=1}^{3} (\hat{U}_{\alpha\beta}\hat{U}_{\beta\gamma}\hat{U}^{\dagger}_{\gamma\delta}\hat{U}^{\dagger}_{\delta\alpha} + h.c.)|| \\
& \quad \cdot ||\frac{4}{2a^{4-d}g^2} \sum_{\alpha,\beta,\gamma,\delta=1}^{3} (\hat{U}_{\alpha\beta}\hat{U}_{\beta\gamma}\hat{U}^{\dagger}_{\gamma\delta}\hat{U}^{\dagger}_{\delta\alpha} + h.c.)|| \\
& \leq \frac{L^d}{a^{12-3d}g^6} 154317013963527684096(d-1).
\end{aligned} \tag{4.540}
$$

Therefore, type (i) commutators, where $\hat{h}_L$ acts on even plaquettes are bounded by

$$(10287800930901845606 4d^4 + 5143900465450922803 2d^3 - 8744630791266568765 44d^2 + 8744630791266568765 44d - 154317013963527684096)\frac{L^d}{a^{12-3d}g^6}. \quad (4.541)$$

Similarly, we obtain the bound for the commutators where $\hat{h}_L$ acts on odd plaquettes, i.e.,

$$(10287800930901845606 4d^4 - 6429875581813653504 0d^3 - 5272497977087195873 28d^2 + 4886705442178376663 04d)\frac{L^d}{a^{12-3d}g^6}. \quad (4.542)$$

by considering separately the cases, in which $\hat{h}_L$ and $\hat{h}_{L'}$ collide with 2, 4, or 8 $\hat{h}_{L''}$, listed in Table 4.7. Thus, the bound for all type-(i) commutators is

$$(20575601861803691212 8d^4 - 1285975116362730700 8d^3 - 1401712876835376463872d^2 + 1363133623344494542848d - 154317013963527684096)\frac{L^d}{a^{12-3d}g^6}. \quad (4.543)$$

We proceed to analyze type-(ii) commutators. By definition, $\hat{h}_L$ does not commute with both $\hat{h}_{L'}$ and $\hat{h}_{L''}$, but $\hat{h}_{L'}$ and $\hat{h}_{L''}$ commute with each other. On the lattice, this implies that $\hat{h}_L$ share one common dimension each with $\hat{h}_{L'}$ and $\hat{h}_{L''}$, but $\hat{h}_{L'}$ and $\hat{h}_{L''}$ share no common dimension. Thus, each plaquette acted on by $\hat{h}_L$ is also acted on by two $\hat{h}_{L'}$ and $\hat{h}_{L''}$. Using table 4.8, we obtain the number of combinations of parity-location labels that satisfy this condition as follows

$$\sum_{l>k}\sum_{k=1}^{d-1} 2(d-l)[4(l-k-1)+8(d-l-1)]+8(l-k-1)(d-l) = 2d^4-12d^3+11d^2-6d. \quad (4.544)$$

Hence, the bound for all type-(ii) commutators is

$$\begin{aligned}
&N_L\sum_{p=e}^{o}|||[[\sum_{\vec{n}_p}\hat{h}_L(p,k,l), \sum_{\hat{h}_{L'}\in\mathbb{L};L'>L}\hat{h}_{L'}], \sum_{\hat{h}_{L''}\in\mathbb{L};L''>L}\hat{h}_{L''}]|| \\
&\leq 2N_L(2d^4-12d^3+11d^2-6d)\sum_{\vec{n}_p} 4\cdot||\hat{h}_L(p,k,l)||\cdot||\frac{2}{2a^{4-d}g^2}\sum_{\alpha,\beta,\gamma,\delta=1}^{3}(\hat{U}_{\alpha\beta}\hat{U}_{\beta\gamma}\hat{U}^\dagger_{\gamma\delta}\hat{U}^\dagger_{\delta\alpha}+h.c.)|| \\
&\quad\cdot||\frac{2}{2a^{4-d}g^2}\sum_{\alpha,\beta,\gamma,\delta=1}^{3}(\hat{U}_{\alpha\beta}\hat{U}_{\beta\gamma}\hat{U}^\dagger_{\gamma\delta}\hat{U}^\dagger_{\delta\alpha}+h.c.)|| \\
&\leq \frac{L^d}{a^{12-3d}g^6}(154317013963527684096d^4 - 9259020837811661045 76d^3 \\
&\quad + 8487435767994022625 28d^2 - 4629510418905830522 88d). \quad (4.545)
\end{aligned}$$

Last but not least, for type (iii) commutators, $\hat{h}_{L'}$ does not commute with both $\hat{h}_L$ and $\hat{h}_{L''}$, but $\hat{h}_L$ and $\hat{h}_{L''}$ commute with each other. On the lattice, this implies that $\hat{h}_{L'}$ share one common dimension each with $\hat{h}_L$ and $\hat{h}_{L''}$, but $\hat{h}_L$ and $\hat{h}_{L''}$ share no common dimension. Thus, each plaquette acted on by $\hat{h}_L$ is also acted on by two $\hat{h}_{L'}$, and each plaquette acted on by $\hat{h}_{L'}$ is in turn acted on by two $\hat{h}_{L''}$. Using table 4.9, we evaluate the number of combinations of parity-location labels that satisfy this condition, and obtain

$$\sum_{j>l}\sum_{l>k}\sum_{k=1}^{d-1} 16(d-l)(d-j+l-k-1)+8(l-k-1)[(l-j-1)+(j-k-1)] = \frac{2}{5}(2d^5-15d^4+40d^3-45d^2+18d). \tag{4.546}$$

Hence, the bound for all type-(iii) commutators is

$$\begin{aligned}
&N_L \sum_{p=e}^{o} |||[[\sum_{\vec{n}_p} \hat{h}_L(p,k,l), \sum_{\hat{h}_{L'}\in\mathbb{L};L'>L} \hat{h}_{L'}], \sum_{\hat{h}_{L''}\in\mathbb{L};L''>L} \hat{h}_{L''}]|||\\
&\leq \frac{4N_L}{5}(2d^5-15d^4+40d^3-45d^2+18d)\sum_{\vec{n}_p} 4\cdot||\hat{h}_L(p,k,l)||\cdot||\frac{2}{2a^{4-d}g^2}\sum_{\alpha,\beta,\gamma,\delta=1}^{2}(\hat{U}_{\alpha\beta}\hat{U}_{\beta\gamma}\hat{U}^\dagger_{\gamma\delta}\hat{U}^\dagger_{\delta\alpha}+h.c.)||\\
&\quad\cdot||\frac{2}{2a^{4-d}g^2}\sum_{\alpha,\beta,\gamma,\delta=1}^{2}(\hat{U}_{\alpha\beta}\hat{U}_{\beta\gamma}\hat{U}^\dagger_{\gamma\delta}\hat{U}^\dagger_{\delta\alpha}+h.c.)||\\
&= (308634027927055368192\frac{d^5}{5} - 462951041890583052288d^4 + 123453611170822147276 8d^3\\
&- 138885312567174915686 4d^2 + 27777062513434983137 28\frac{d}{5})\frac{L^d}{a^{12-3d}g^6}.
\end{aligned} \tag{4.547}$$

Finally, summing up the bounds for the intra-plaquette and all three types of inter-plaquette commutators, we obtain the bound for $C_{2,12}$,

$$\begin{aligned}
&(308634027927055368192\frac{d^5}{5} - 102878009309018456064d^4 + 295774276763428061184d^3\\
&- 193217761233500287795 2d^2 + 723039509174945336524 8\frac{d}{5} - 154317013963527684096)\frac{L^d}{a^{12-3d}g^6}.
\end{aligned} \tag{4.548}$$

Oracle errors

Here, we describe the direct syntheses of the kinetic and magnetic oracles, and compute the errors incurred by the fixed point arithmetic circuits.

Syntheses of the kinetic oracles: The kinetic oracle, defined in (4.435), can be directly synthesized as two controlled-diagonal gates, which impart the phases $f_{\alpha\beta}\frac{t}{2a}(-1)^{f_{\alpha,r}}f_{\beta,r+1}\prod_j b_j$, for $f_{\alpha,r}=0,1$, if the control bits $f_{\beta,r+1}$ and b_j's are all ones. Recall that the function

$$f_{\alpha\beta}(p,q,T_L,T_L^z,Y_L,T_R,T_R^z,Y_R,\Delta p,\Delta q,\Delta T_L,\Delta T_R)$$

are the matrix elements of the diagonal operator defined in (4.426). The number of control bits, and costs of implementation for each oracle depend on the parameters of the function $f_{\alpha\beta}$. In order to estimate the implementation costs, we first construct $f_{\alpha\beta}$ from the Clebsch-Gordan coefficients in Table 4.11, and normalization factors in (4.403), and then, obtain its arguments using (4.408) to invert the encoding of the quantum numbers onto the registers. Here, for the sake of complexity analysis, we only estimate the costs of the most expensive oracle, where $\alpha\beta=11$, and $(\Delta p,\Delta q,\Delta T_L,\Delta T_R)=(0,-1,1,1)$. In terms of SU(3) Clebsch-Gordan coefficients and normalization factor, we write

$$f_{11}(p,q,T_L,T_L^z,Y_L,T_R,T_R^z,Y_R,0,-1,1,1)=C_{31}^L C_{31}^R N_3=I_{31}^L c_{11}^L I_{31}^R c_{11}^R N_3, \tag{4.549}$$

where C_{31} is a SU(3) Clebsch-Gordan coefficient from Table 4.11, I_{31} is an isoscalar factor defined in Table (4.10), c_{11} is a SU(2) Clebsch-Gordan coefficient from Table 4.4, and N_3 is a normalization factor in (4.403). Hereafter, we denote this function as $f_{11}(0,-1,1,1)$. Now we apply the mapping in (4.408) to obtain the relations

$$I_{31}^i=\sqrt{\frac{(4p+2q-3T_i-Y_i+3\Lambda)(2p-2q+3T_i+Y_i-3\Lambda+6)(2p+4q-3T_i+Y_i-3\Lambda)}{(1+q)(2+p+q)(432+216T_i)}} \tag{4.550}$$

$$c_{11}^i=\sqrt{\frac{\frac{(T_i+T_i^z)}{2}-\Lambda+1}{T_i+1}} \tag{4.551}$$

$$N_3=\sqrt{\frac{(1+q)(2+p+q)}{q(1+p+q)}}. \tag{4.552}$$

Without loss of generality, we consider the case where $f_{\alpha,r}=0$. Then, we implement the diagonal phase gate by computing $f_{11}(0,-1,1,1)$ into an ancilla register, conditioned upon the values of the control bits. Then, by applying R_z gates to the ancilla state $|f_{11}(0,-1,1,1)\rangle$, we induce the correct phase. Finally we uncompute $|f_{11}(0,-1,1,1)\rangle$. The computation of $f_{11}(0,-1,1,1)$, can be broken down into five steps. In the first and second steps, we compute the numerator and denominator, respectively. In the third step, we approximate the inverse of the denominator, using the fixed-point circuits in [136]. In the fourth step, we approximate the argument of the square-root by multiplying together the numerator and the inverse of the denominator. Lastly, we approximate the square-root, using the fixed-point circuits in [136]. Only the third and last

steps incur approximation errors. Hereafter, we use the logarithmic depth out-of-place adder developed in [148], unless one of the inputs is classically known in which case we use the adder proposed in [137], and the multiplier proposed in [7].

We consider the computation of the numerator. We compute the numerators of I_{31}^L, c_{11}^L, I_{31}^R, and c_{11}^R, separately. The numerator of N_3 cancels out with the part of the denominator of I_{31}^L. First, we compute the numerator of I_{31}^L. $|4p\rangle$ and $|2q\rangle$ can be computed by two ancilla qubits to $|p\rangle$ and one to $|q\rangle$, costing no T gates. $|3T_L\rangle$ can be computed by adding $|2T_L\rangle$ and $|T_L\rangle$, using an $(\eta+2)$-bit adder since T_L is an $(\eta+1)$-bit number. Computing $4p+2q$ and $3T_L - Y_L$ requires an $(\eta+2)$ and $(\eta+3)$-bit adder. Computing $4p+2q-3T_L-Y_L$ costs one $(\eta+4)$-bit adder, and adding 3Λ requires $4(\eta+3)$ T gates. Therefore, computing $(4p+2q-3T_L-Y_L+3\Lambda)$ costs $84\eta - 12(2\lfloor\log(\eta+2)\rfloor + \lfloor\log(\eta+3)\rfloor + \lfloor\log(\eta+4)\rfloor) + 216$ T gates, $5\eta+21$ storage ancilla qubits, and $\eta - \lfloor\log(\eta+4)\rfloor + 4$ workspace ancilla qubits. The computation of $(2p+4q-3T_L+Y_L-3\Lambda)$ has the same costs. Similarly, we compute $(2p+2q+3T_L+Y_L-3\Lambda+6)$, using $84\eta - 12(\lfloor\log(\eta+1)\rfloor + \lfloor\log(\eta+2)\rfloor + \lfloor\log(\eta+3)\rfloor + \lfloor\log(\eta+4)\rfloor) + 196$ T gates, $5\eta+20$ storage ancilla qubits, and $\eta - \lfloor\log(\eta+4)\rfloor + 4$ workspace ancilla qubits. Next, we multiply together these three $(\eta+5)$-bit numbers, using two multipliers, costing $(12\eta+60)+(4\eta+16)(36\eta - 3\lfloor\log(\eta+5)\rfloor - 3\lfloor\log(2\eta+10)\rfloor + 154$ T gates, $5\eta+25$ storage ancilla qubits, and $6\eta - \lfloor\log(2\eta+10)\rfloor + 29$ workspace ancilla qubits. The computation of the numerator for I_{31}^R incurs the same costs. The computation of the numerator of c_{11}^L requires an $(\eta+2)$-bit adder, since T_L^z is an $(\eta+2)$-bit number. The division by 2 is done by shifting the decimal point, and the addition of $-\Lambda+1$ requires $\eta+3$ ancilla qubits, and $4(\eta+1)$ T gates. Therefore, the total costs are $24\eta - 12\lfloor\log(\eta+2)\rfloor + 40$ T gates, $2\eta+6$ storage ancilla qubits, and $\eta - \lfloor\log(\eta+2)\rfloor + 2$ workspace ancilla qubits. The computation of the numerator for c_{11}^R incurs the same costs. We now have to multiply together two $(3\eta+15)$-bit numbers and two $(\eta+3)$-bit numbers to obtain the numerator of $f_{11}(0,-1,1,1)$, conditioned upon the fact that they are all positive. The positivity condition guarantees that the Clebsch-Gordan coefficients and isoscalar factors are real [154, 158], since in their definitions, the denominators in the square roots are positive. This can be implemented by controlling one of the three multiplications to be done by the sign bits of the four inputs. The first multiplication is between two $(3\eta+15)$-bit numbers; the second one is between two $(\eta+3)$-bit numbers; and the last one is between the outputs from the previous two multiplications, which result in a $(6\eta+30)$ and $(2\eta+6)$-bit number. The total costs of the three multipliers are $40\eta+192+4(2\eta+5)(12(6\eta+30)-3\lfloor\log(6\eta+30)\rfloor-13)+4(3\eta+14)(12(3\eta+15)-3\lfloor\log(3\eta+15)\rfloor-13)+4(\eta+3)(12(\eta+2)-12\lfloor\log(\eta+3)\rfloor-13)$ T gates, $16\eta+72$ storage ancilla qubits, and $3(6\eta+30)-\lfloor\log(6\eta+30)\rfloor-1$ workspace ancilla qubits. We control the multiplication of the second multiplier by the four sign bits. As discussed in the SU(2) oracle implementation, the quadruply-controlled multiplication additionally costs a quadruply-controlled Toffoli gate and $\eta+3$ Toffoli gates, which amount to $4\eta+35$ T gates, $\eta+3$ storage ancilla qubits, and a reusable workspace ancilla qubit.

Next, we consider the computation of the denominator, i.e., $(1+q)(2+p+q)(432+216T_L)(432+216T_R)(T_L+1)(T_R+1)q(1+p+q)$. Computing $p+q$ requires an η-bit adder, and then, adding 1

requires $\eta+2$ storage ancilla qubits and $4(\eta-1)$ T gates. We then obtain $q(1+p+q)$ by multiplying $(1+p+q)$ by q. The computation of $q(1+p+q)$ costs $4(\eta+2)+4(\eta-1)(12\eta-3\lfloor\log(\eta+2)\rfloor+11)$ T gates, $2\eta+2$ storage ancilla qubits, and $3\eta-\lfloor\log(\eta+2)\rfloor+5$ workspace ancilla qubits. We then compute $(1+q)(2+p+q)$ by adding $2+p+2q$ to $q(1+p+q)$. Computing $p+2q$ costs an $(\eta+1)$-bit adder, and the addition of 2 costs $(\eta+3)$ ancilla qubits and $4(\eta+1)$ T gates. Thus, adding $2+p+2q$ to $q(1+p+q)$ costs a $(2\eta+2)$-bit adder. Then, we multiply together $q(1+p+q)$ and $(1+q)(2+p+q)$. As such, calculating $q(1+p+q)(1+q)(2+p+q)$ incurs $(8\eta+4)(24\eta-3\lfloor\log(2\eta+3)\rfloor+23)+(4\eta-4)(12\eta-3\lfloor\log(\eta+2)\rfloor+11)+100\eta-12(\lfloor\log(\eta)\rfloor+\lfloor\log(\eta+1)\rfloor+\lfloor\log(2\eta+2)\rfloor)+68$ T gates, $12\eta+18$ storage ancilla qubits, and $6\eta-\lfloor\log(2\eta+3)\rfloor+8$ workspace ancilla qubits. Since $(432+216T_L)=2^3(2^5-2^2-2^0)(2+T_L)$, we obtain $(432+216T_L)$ in three steps. First, we compute $2+T_L$, incurring $\eta+2$ storage ancilla qubits and $4(\eta-1)$ T gates. Then, we compute $2^5(2+T_L)$ and $2^2(2+T_L)$ by copying $2+T_L$ to two ancilla registers, and then appending extra ancilla qubits for the multiplications. Finally, we use an $(\eta+4)$-bit adder and an $(\eta+7)$-bit adder to compute $(2^5-2^2-2^0)(2+T_L)$, and then, append three ancilla qubits to obtain the desired output. Thus, calculating $(432+216T_L)$ costs $48\eta-12(\lfloor\log(\eta+4)\rfloor+\lfloor\log(\eta+7)\rfloor)+204$ T gates, $5\eta+26$ storage ancilla qubits, and $\eta-\lfloor\log(\eta+7)\rfloor+7$ workspace ancilla qubits. Computing $(432+216T_R)$ incurs the same costs. $(432+216T_L)$ and $(432+216T_R)$ are both $(\eta+11)$-bit numbers. Thus, evaluating their product costs $4\eta+44+(4\eta+40)(12\eta-3\lfloor\log(\eta+11)\rfloor+119)$ T gates, $2\eta+22$ storage ancilla qubits, and $3\eta-\lfloor\log(\eta+11)\rfloor+30$ workspace ancilla qubits. Calculating (T_L+1) and (T_R+1) cost $2\eta+4$ storage ancilla qubits, and $8(\eta-1)$ T gates. We compute their product using $4\eta+8+(4\eta+4)(12\eta-3\lfloor\log(\eta+2)\rfloor+11)$ T gates, $2\eta+4$ storage ancilla qubits, and $3\eta-\lfloor\log(\eta+2)\rfloor+5$ workspace ancilla qubits. We then multiply together $(432+216T_L)(432+216T_R)$, a $(2\eta+22)$-bit number, and $(T_L+1)(T_R+1)$, a $(2\eta+4)$-bit number, which costs $(8\eta+12)(24\eta-3\lfloor\log(2\eta+22)\rfloor+251)+8\eta+88$ T gates, $4\eta+26$ storage ancilla qubits, and $6\eta-\lfloor\log(2\eta+22)\rfloor+65$ workspace ancilla qubits. Finally, we obtain the denominator by multiplying the $(4\eta+26)$-bit output to $q(1+p+q)(1+q)(2+p+q)$, a $(4\eta+5)$-bit number, which requires $(4\eta+16)(48\eta-3\lfloor\log(4\eta+26)\rfloor+299)+16\eta+104$ T gates, $8\eta+31$ storage ancilla qubits, and $12\eta-\lfloor\log(4\eta+26)\rfloor+77$ workspace ancilla qubits.

We proceed to compute the inverse of the denominator using the algorithm in [136]. We refer the readers to the SU(2) kinetic oracle implementation in Sec. 4.4.3 for a detailed overview of the algorithm. Here, we simply state the algorithmic parameters and costs. The input w is at most an $(8\eta+31)$-bit integer. Truncating at $b\geq 8\eta+31$ bits after the decimal point, the approximation error is bounded from above by $\frac{2+\log(b)}{2^b}$. The T-gate count is $\lceil\log(b)\rceil\cdot(48b^2+768b\eta-(12b+360\eta-12)\lfloor\log(b)\rfloor+2824b-256\eta-12\lfloor\log(2b+8\eta+31)\rfloor-96\lfloor\log(2b)\rfloor-888)+32\eta+135$. The required number of storage ancilla qubits is $\lceil\log(b)\rceil\cdot(7b+16\eta+64)$, and that of workspace ancilla qubits is $6b-\lfloor\log(2b)\rfloor-1$. Next, we multiply the numerator, an $8\eta+36$-bit number, and the inverse of the denominator, a b-bit number to obtain the fraction. Assuming that $b\geq 8\eta+36$, this costs $384b\eta-96\eta\lfloor\log(b)\rfloor+1684b-416\eta-420\lfloor\log(b)\rfloor-1820$ T gates, $b+8\eta+36$ storage ancilla qubits, and $3b-\lfloor\log(b)\rfloor-1$ workspace ancilla qubits. Lastly, we compute the square-root function. The

output of the previous step is a $(b+8\eta+36)$-bit fraction, bounded above and below by 1 and 0, respectively. Since the algorithm require an input that is larger than 1, we shift it by $b+8\eta+36$ bits to obtain an integer input w. Once we obtain the root, we shift it back by $(b+8\eta+36)/2$ bits, assuming without loss of generality that b is even. Let $c \geq 2b+16\eta+72$. Then, we approximate $\sqrt{w}$, up to $\left(\frac{3}{4}\right)^{c-(2b+16\eta+72)}(2+c+\log(c))$ error. This costs $\lceil\log(c)\rceil \cdot [528c^2+96bc+768c\eta - c(12\lfloor\log(c)\rfloor+12\lfloor\log\left(\lceil\frac{3c}{2}\rceil\right)\rfloor+12\lfloor\log\left(\lceil\frac{5c}{2}\rceil\right)\rfloor+18\lfloor\log(1+4c)\rfloor)-12b\lfloor\log(2c)\rfloor-96n\lfloor\log(2c)\rfloor+12(\lfloor\log(c)\rfloor+\lfloor\log\left(\lceil\frac{3c}{2}\rceil\right)\rfloor-35\lfloor\log(2c)\rfloor+\lfloor\log\left(\lceil\frac{5c}{2}\rceil\right)\rfloor+\lfloor\log(1+4c)\rfloor-\lfloor\log(2c+b+8n+36)\rfloor)+2930c-32b-256\eta-988]+\lceil\frac{19c}{2}\rceil+4b+32\eta+163$ T gates, $\lceil\log(c)\rceil\cdot(\lceil\frac{49c}{2}\rceil+2b+16\eta+77)$ storage ancilla qubits, and $12c-\lfloor\log(4c+1)\rfloor+5$ workspace ancilla qubits.

We impart the phase by applying $R_z(2^{k-c}\theta)$, where c is the number of digits after the decimal point in the output of the square-root functions, and $\theta=\frac{t}{2a}$, to the kth qubit of the ancilla state $|f_{\alpha\beta}\rangle$. In order to implement the controlled version of this phase gate, we control each R_z gate by nine control bits, as required by the costliest kinetic oracle, and the ancilla bit that checks the realness of the Clebsch-Gordan coefficients and isoscalar factors. Each R_z gate with ten controls requires two Toffoli gates with ten controls, which cost 71 T gates each [145], two R_z gates and one ancilla qubit [144]. Since the state has at most $\lceil\frac{3c}{2}\rceil$ qubits and there are dL^d links on the lattice, there are $\lceil\frac{3c}{2}\rceil dL^d$ multi-controlled R_z gates to be applied.

We sum up the T-gate requirements for all the steps, and multiply the outcome by two to account for the uncomputation costs. Conjugating each controlled R_z gate with a pair of CNOT gates, where $f_{\alpha,r}$ is the control bit, addresses both $f_{\alpha,r}=0,1$. As such, the T-gate count for one

oracle call, i.e.,

$$\begin{aligned}\mathcal{T}^{(K)} = 2\lceil\log(c)\rceil \cdot [528c^2 + 96bc + 768c\eta - c(12\lfloor\log(c)\rfloor + 12\lfloor\log\left(\lceil\frac{3c}{2}\rceil\right)\rfloor + 12\lfloor\log\left(\lceil\frac{5c}{2}\rceil\right)\rfloor \\ + 18\lfloor\log(1+4c)\rfloor) - 12b\lfloor\log(2c)\rfloor - 96\eta\lfloor\log(2c)\rfloor + 12(\lfloor\log(c)\rfloor + \lfloor\log\left(\lceil\frac{3c}{2}\rceil\right)\rfloor \\ - 35\lfloor\log(2c)\rfloor + \lfloor\log\left(\lceil\frac{5c}{2}\rceil\right)\rfloor + \lfloor\log(1+4c)\rfloor - \lfloor\log(2c+b+8\eta+36)\rfloor) + 2930c \\ - 32b - 256\eta - 980] + 19c + 8b + 64\eta + 326 \\ + 768b\eta - 192\eta\lfloor\log(b)\rfloor + 3368b - 832\eta - 840\lfloor\log(b)\rfloor - 3640 \\ + 2\lceil\log(b)\rceil \cdot (48b^2 + 768b\eta - (12b + 360\eta - 12)\lfloor\log(b)\rfloor + 2824b - 256\eta \\ - 12\lfloor\log(2b+8\eta+31)\rfloor - 96\lfloor\log(2b)\rfloor - 888) + 64\eta + 270 \\ + 4128\eta^2 - \eta(48\lfloor\log(2+\eta)\rfloor + 96\lfloor\log(3+\eta)\rfloor + 48\lfloor\log(5+\eta)\rfloor + 24\lfloor\log(11+\eta)\rfloor \\ + 48\lfloor\log(3+2\eta)\rfloor + 48\lfloor\log(10+2\eta)\rfloor + 48\lfloor\log(22+2\eta)\rfloor + 72\lfloor\log(15+3\eta)\rfloor \\ + 24\lfloor\log(26+4\eta)\rfloor + 48\lfloor\log(30+6\eta)\rfloor) - (24\lfloor\log(\eta)\rfloor + 72\lfloor\log(1+\eta)\rfloor \\ + 288\lfloor\log(2+\eta)\rfloor + 432\lfloor\log(3+\eta)\rfloor + 192\lfloor\log(4+\eta)\rfloor + 192\lfloor\log(5+\eta)\rfloor \\ + 48\lfloor\log(7+\eta)\rfloor + 240\lfloor\log(11+\eta)\rfloor + 24\lfloor\log(2+2\eta)\rfloor + 24\lfloor\log(3+2\eta)\rfloor \\ + 192\lfloor\log(10+2\eta)\rfloor + 72\lfloor\log(22+2\eta)\rfloor + 336\lfloor\log(15+3\eta)\rfloor + 96\lfloor\log(26+4\eta)\rfloor \\ + 120\lfloor\log(30+6\eta)\rfloor) + 30952\eta + 54156 + 426c + 96\eta + 80. \end{aligned} \tag{4.553}$$

The number of storage ancilla qubits required is

$$\lceil\log(c)\rceil \cdot (\lceil\frac{49c}{2}\rceil + 2b + 16\eta + 77) + \lceil\log(b)\rceil \cdot (16\eta + 7b + 64) + b + 89\eta + 667, \tag{4.554}$$

and the number of workspace ancilla qubits required is

$$12c - \lfloor\log(4c+1)\rfloor + 5. \tag{4.555}$$

There are two types of syntheses errors, i.e., arithmetic approximation errors and R_z syntheses errors. The latter will be analyzed in Sec. 4.5.3. The arithmetic approximation errors per step is given by

$$\frac{2+\log(b)}{2^b} + \left(\frac{3}{4}\right)^{c-(2b+16\eta+72)}(2 + c + \log(c)). \tag{4.556}$$

In total, the approximation errors are

$$\epsilon^{(K)} = r \cdot 13872dL^d[\frac{2+\log(b)}{2^b} + \left(\frac{3}{4}\right)^{c-(2b+16\eta+72)}(2 + c + \log(c))], \tag{4.557}$$

where r is the number of Trotter steps, and $13872dL^d$ is the number of oracle calls. We divide the approximation errors evenly such that

$$\epsilon_b^{(K)} = \frac{\epsilon^{(K)}}{2r \cdot 13872dL^d},\ \epsilon_c^{(K)} = \frac{\epsilon^{(K)}}{2r \cdot 13872dL^d}, \tag{4.558}$$

and

$$\epsilon_b^{(K)} \geq \frac{2 + \log(b)}{2^b}, \tag{4.559}$$

$$\epsilon_c^{(K)} \geq \left(\frac{3}{4}\right)^{c-(2b+16\eta+72)} (2 + c + \log(c)). \tag{4.560}$$

Note that this is not the optimal division of approximation errors. We let $b = \log\left(\frac{8}{\epsilon_b^{(K)}}\right)$. Then, (4.559) is always satisfied for $0 < \epsilon_b^{(K)} < 1$. We proceed to compute the upper bound for c. Since $c \geq 2b + 16\eta + 72 \geq 32\eta + 144$, and $\eta \geq 1$, $\frac{186}{176}c \geq 2 + c + \log(c)$. Inserting this relation and our choice of b into (4.560), we obtain

$$\epsilon_c^{(K)} \geq \left(\frac{3}{4}\right)^{c-\left(\log\left(8/\epsilon_b^{(K)}\right)+16\eta+72\right)} \frac{186}{176}c. \tag{4.561}$$

Let

$$\tilde{\epsilon}_c^{(K)} = \epsilon_c^{(K)} \cdot \left(\frac{3}{4}\right)^{\log\left(8/\epsilon_b^{(K)}\right)+16\eta+72} \frac{176}{186}. \tag{4.562}$$

Then, we want to find a c such that

$$c\left(\frac{3}{4}\right)^c \leq \tilde{\epsilon}_c^{(K)}. \tag{4.563}$$

Assuming that $0 < \tilde{\epsilon}_c^{(K)} < 1$, the choice

$$c = \log_{\frac{3}{4}}\left(\frac{\frac{\tilde{\epsilon}_c^{(K)}}{2.28}}{\log_{\frac{3}{4}}\left(\frac{\tilde{\epsilon}_c^{(K)}}{2.28}\right)}\right) \tag{4.564}$$

satisfies (4.563). We have verified numerically with Mathematica that for $0 < \tilde{\epsilon}_{\text{oracle}} < 1$, $\tilde{\epsilon}_{\text{oracle}} - c\left(\frac{3}{4}\right)^c$ never exceeds 0.0431937, given our choice of c.

We mention in passing that the phase-inducing step can be parallelized. As in U(1), we first divide the kinetic terms up into bulk and edge terms. Then, for each direction of the bulk or edge terms, we implement $O(L^d - L^{d-1})$ or $O(L^{d-1})$ $R_z(2^{k-c}\theta)$ in parallel, using the weight-sum

trick, and thus, exponentially reducing the number of R_z gates required to $O(cd\log(L^d))$. In this work, we focus on the resource analysis of the serial implementation, and will leave that of the parallel implementation for future work.

Syntheses of the magnetic oracles: Similar to the implementation of the kinetic oracle, we directly synthesize the magnetic oracle, defined in (4.445), as two controlled-diagonal gates, which impart the phases $\frac{-f_{\alpha\beta\gamma\delta}}{2a^{4-d}g^2}(-1)^{b_k}$ for $b_k = 0, 1$, if the control bits $\in \{|b_j\rangle\}$ are all ones. Recall that $\{|b_k\rangle, |b_j\rangle\} \subseteq S_0^{\square} \equiv \{\left|p'_{i,0}\right\rangle, \left|q'_{i,0}\right\rangle, \left|T'_{L,i,0}\right\rangle, \left|T^{z'}_{L,i,0}\right\rangle, \left|Y'_{L,i,k}\right\rangle, \left|T'_{R,i,0}\right\rangle, \left|T^{z'}_{R,i,0}\right\rangle, \left|Y'_{R,i,k}\right\rangle\}_{i=1}^{4}$, where i denotes the ith link on a plaquette, and $\left|Y'_{L/R,i,k}\right\rangle$ is the kth qubit of $\left|Y'_{L/R,i}\right\rangle$ as defined in (4.427). The function $f_{\alpha\beta\gamma\delta}$ is defined in (4.444) as a product of four functions, $f_{\alpha\beta}$, $f_{\beta\gamma}$, $f_{\gamma\delta}$, and $f_{\delta\alpha}$. Here, we consider the costliest $f_{\alpha\beta\gamma\delta}$, which is the product of four $f_{11}(0, -1, 1, 1)$ considered in the kinetic oracle. In this case, all registers are acted on, and thus, $\{|b_k\rangle, |b_j\rangle\} = S_0^{\square}$. We choose $b_k = p'_{1,0}$. Without loss of generality, we consider the case where $p'_{1,0} = 0$. We begin by computing $f_{\alpha\beta\gamma\delta}$ into an ancilla register, conditioned upon the values of the control bits. Then, we induce the correct phase by applying R_z gates to the ancilla state $|f_{\alpha\beta\gamma\delta}\rangle$. Finally, we uncompute $|f_{\alpha\beta\gamma\delta}\rangle$. The computation of $f_{\alpha\beta\gamma\delta}$ can be broken down into five steps. In the first and second steps, we compute the numerator and denominator, respectively. In the third step, we approximate the inverse of the denominator, using the circuits in [136]. In the fourth step, we approximate the argument of the square-root by multiplying together the numerator and the inverse of the denominator. Lastly, we approximate the square-root, using the circuits in [136]. Only the third and last steps incur approximation errors. Hereafter, we use the logarithmic depth out-of-place adder developed in [148], unless one of the inputs is classically known in which case we use the adder proposed in [137], and the multiplier proposed in [7].

First, we consider the computation of the numerator. We begin by computing the numerators in the four functions that constitute $f_{\alpha\beta\gamma\delta}$. This costs four times the T gates and storage ancilla qubits required for computing the numerator in a kinetic oracle, i.e.,

$$\begin{aligned}&5376\eta^2 - \eta(192\lfloor\log(\eta+3)\rfloor + 96\lfloor\log(\eta+5)\rfloor + 96\lfloor\log(2\eta+10)\rfloor + 144\lfloor\log(3\eta+15)\rfloor\\&+ 96\lfloor\log(6\eta+30)\rfloor) + 40656\eta - 96\lfloor\log(\eta+1)\rfloor - 576\lfloor\log(\eta+2)\rfloor - 864\lfloor\log(\eta+3)\rfloor\\&- 288\lfloor\log(\eta+4)\rfloor - 384\lfloor\log(\eta+5)\rfloor - 384\lfloor\log(2\eta+10)\rfloor - 672\lfloor\log(3\eta+15)\rfloor\\&- 240\lfloor\log(6\eta+30)\rfloor + 73340 + 96\eta + 224\end{aligned}$$

and $41\eta + 174$, respectively. We then multiply the four outputs with two $(8\eta + 36)$-bit multipliers, and one $(16\eta + 72)-$bit multiplier. The multipliers cost $18432\eta^2 - 192\eta(\lfloor\log(8\eta + 36)\rfloor + \lfloor\log(16\eta + 72)\rfloor) - 840\lfloor\log(8\eta + 36)\rfloor - 852\lfloor\log(16\eta + 72)\rfloor + 162816\eta + 359580$ T gates, $64\eta + 288$ storage ancilla qubits, and $48\eta - \lfloor\log(16\eta + 72)\rfloor + 215$ workspace ancilla qubits. We proceed to compute the denominator. First, we compute the denominators in the four functions that constitute $f_{\alpha\beta\gamma\delta}$. This costs four times the T gates and storage ancilla qubits required for computing

the denominator in a kinetic oracle, i.e.,

$$720\eta^2 - \eta(24\lfloor\log(\eta+2)\rfloor + 12\lfloor\log(\eta+11)\rfloor + \lfloor\log(2\eta+3)\rfloor + 24\lfloor\log(2\eta+22)\rfloor + 12\lfloor\log(4\eta+26)\rfloor) + 5312\eta - 12\lfloor\log(\eta)\rfloor - 12\lfloor\log(1+\eta)\rfloor - 24\lfloor\log(\eta+4)\rfloor - 24\lfloor\log(\eta+7)\rfloor - 120\lfloor\log(\eta+11)\rfloor - 12\lfloor\log(2\eta+2)\rfloor - 12\lfloor\log(2\eta+3)\rfloor - 36\lfloor\log(2\eta+22)\rfloor - 48\lfloor\log(4\eta+26)\rfloor + 8743,$$

and $160\eta + 628$, respectively. We then multiply the four outputs with two $(8\eta+31)$-bit multipliers, and one $(16\eta+62)-$bit multiplier. The multipliers cost $18432\eta^2 - 192\eta(\lfloor\log(8\eta+31)\rfloor + \lfloor\log(16\eta+62)\rfloor) - 720\lfloor\log(8\eta+31)\rfloor - 732\lfloor\log(16\eta+62)\rfloor + 139776\eta + 265020 + 96\eta - 96$ T gates, $64\eta + 248$ storage ancilla qubits, and $48\eta - \lfloor\log(16\eta+62)\rfloor + 185$ workspace ancilla qubits.

We now proceed to compute the inverse of the denominator using the algorithm in [136]. We refer the readers to the SU(2) kinetic oracle implementation in Sec. 4.4.3 for a detailed overview of the algorithm. Here, we simply state the algorithmic parameters and costs. The input w is at most an $(32\eta+124)$-bit integer. Truncating at $b \geq 32\eta + 124$ bits after the decimal point, the approximation error is bounded from above by $\frac{2+\log(b)}{2^b}$. The T-gate count is $\lceil\log(b)\rceil \cdot (48b^2 + 3072b\eta - (12b + 384\eta - 12)\lfloor\log(b)\rfloor + 11752b - 1024\eta - 12\lfloor\log(2b+32\eta+124)\rfloor - 1476\lfloor\log(2b)\rfloor - 3864) + 128\eta + 507$. The required number of storage ancilla qubits is $\lceil\log(b)\rceil \cdot (7b + 64\eta + 250)$, and that of workspace ancilla qubits is $6b - \lfloor\log(2b)\rfloor - 1$. Next, we multiply together the numerator, an $32\eta + 144$-bit number, and the inverse of the denominator, a b-bit number to obtain the fraction. Assuming that $b \geq 32\eta + 144$, this costs $1536b\eta - 384\eta\lfloor\log(b)\rfloor + 6868b - 1664\eta - 1716\lfloor\log(b)\rfloor - 7436$ T gates, $b + 32\eta + 144$ storage ancilla qubits, and $3b - \lfloor\log(b)\rfloor - 1$ workspace ancilla qubits. Lastly, we compute the square-root function. The output of the previous step is a $(b + 32\eta + 144)$-bit fraction, bounded above and below by 1 and 0, respectively. As in the kinetic oracle implementation, we shift it by $b + 32\eta + 144$ bits to obtain an integer input w, and shift it back by $(b + 32\eta + 144)/2$ bits once we obtain the root, assuming without loss of generality that b is even. Let $c \geq 2b + 64\eta + 288$. Then, we approximate $\sqrt{w}$, up to $\left(\frac{3}{4}\right)^{c-2m}(2 + c + \log(c))$ error. This costs $\lceil\log(c)\rceil \cdot [528c^2 + 96bc + 3072c\eta - c(12\lfloor\log(c)\rfloor + 12\lfloor\log\left(\lceil\frac{3c}{2}\rceil\right)\rfloor + 12\lfloor\log\left(\lceil\frac{5c}{2}\rceil\right)\rfloor + 18\lfloor\log(1+4c)\rfloor) - 12b\lfloor\log(2c)\rfloor - 384\eta\lfloor\log(2c)\rfloor + 12\lfloor\log(c)\rfloor + 12\lfloor\log\left(\lceil\frac{3c}{2}\rceil\right)\rfloor - 1716\lfloor\log(2c)\rfloor + 12\lfloor\log\left(\lceil\frac{5c}{2}\rceil\right)\rfloor + 12\lfloor\log(1+4c)\rfloor - 12\lfloor\log(2c+b+32n+144)\rfloor + 13298c - 32b - 1024\eta - 4444] + \lceil\frac{19c}{2}\rceil + 4b + 128\eta + 595$ T gates, $\lceil\log(c)\rceil \cdot (23c + 2b + 64\eta + 293)$ storage ancilla qubits, and $12c - \lfloor\log(4c+2)\rfloor + 5$ workspace ancilla qubits.

We impart the phase by applying $R_z(2^{k-c}\theta)$, where c is the number of digits after the decimal in the output of the square-root function, and $\theta = \frac{-1}{2a^{4-d}g^2}$, to the kth qubit of the ancilla state $|f_{\alpha\beta\gamma\delta}\rangle$. In order to implement the controlled version of this phase gate, we control each R_z gate by 31 control bits, as required by the costliest magnetic oracle, and the four ancilla bits that check the realness of the Clebsch-Gordan coefficients and isoscalar factors. Each multi-controlled R_z gate requires two Toffoli gates with 31 controls, which cost 239 T gates each [145], two R_z

gates and one ancilla qubit [144]. Since the state has at most $\lceil \frac{3c}{2} \rceil$ qubits and there are $L^d \frac{d(d-1)}{2}$ plaquettes on the lattice, there are $3cL^d \frac{d(d-1)}{2}$ multi-controlled R_z gates to be applied.

We sum up the T-gate requirements for all the steps, and multiply the outcome by two to account for the uncomputation costs. Conjugating each controlled R_z gate with a pair of CNOT gates, where $p_{1,0}$ is the control bit, addresses both $p_{1,0} = 0, 1$. As such, the T-gate count for one oracle call, i.e.,

$$\begin{aligned}
\mathcal{T}^{(B)} = 2 \cdot [&42960\eta^2 - \eta(192\lfloor\log(\eta+3)\rfloor + 96\lfloor\log(\eta+5)\rfloor + 96\lfloor\log(2\eta+10)\rfloor + 144\lfloor\log(3\eta+15)\rfloor \\
&+ 96\lfloor\log(6\eta+30)\rfloor + 192\lfloor\log(8\eta+36)\rfloor + 192\lfloor\log(16\eta+72)\rfloor + 24\lfloor\log(\eta+2)\rfloor \\
&+ 12\lfloor\log(\eta+11)\rfloor + \lfloor\log(2\eta+3)\rfloor + 24\lfloor\log(2\eta+22)\rfloor + 12\lfloor\log(4\eta+26)\rfloor \\
&+ 192\lfloor\log(8\eta+31)\rfloor + 192\lfloor\log(16\eta+62)\rfloor) + 348560\eta - 96\lfloor\log(\eta+1)\rfloor - 576\lfloor\log(\eta+2)\rfloor \\
&- 864\lfloor\log(\eta+3)\rfloor - 288\lfloor\log(\eta+4)\rfloor - 384\lfloor\log(\eta+5)\rfloor - 384\lfloor\log(2\eta+10)\rfloor \\
&- 672\lfloor\log(3\eta+15)\rfloor - 240\lfloor\log(6\eta+30)\rfloor - 840\lfloor\log(8\eta+36)\rfloor - 852\lfloor\log(16\eta+72)\rfloor \\
&- 12\lfloor\log(\eta)\rfloor - 12\lfloor\log(1+\eta)\rfloor - 24\lfloor\log(\eta+4)\rfloor - 24\lfloor\log(\eta+7)\rfloor - 120\lfloor\log(\eta+11)\rfloor \\
&- 12\lfloor\log(2\eta+2)\rfloor - 12\lfloor\log(2\eta+3)\rfloor - 36\lfloor\log(2\eta+22)\rfloor - 48\lfloor\log(4\eta+26)\rfloor \\
&- 720\lfloor\log(8\eta+31)\rfloor - 732\lfloor\log(16\eta+62)\rfloor + 706683] \\
&+ 2 \cdot \lceil\log(b)\rceil \cdot (48b^2 + 3072b\eta - (12b + 384\eta - 12)\lfloor\log(b)\rfloor + 11752b - 1024\eta \\
&- 12\lfloor\log(2b+32\eta+124)\rfloor - 1476\lfloor\log(2b)\rfloor - 3864) + 256\eta + 1014 \\
&+ 3072b\eta - 768\eta\lfloor\log(b)\rfloor + 13736b - 3328\eta - 3432\lfloor\log(b)\rfloor - 14872 \\
&+ 2 \cdot \lceil\log(c)\rceil \cdot [528c^2 + 96bc + 3072c\eta - c(12\lfloor\log(c)\rfloor + 12\lfloor\log\left(\lceil\frac{3c}{2}\rceil\right)\rfloor + 12\lfloor\log\left(\lceil\frac{5c}{2}\rceil\right)\rfloor \\
&+ 18\lfloor\log(1+4c)\rfloor) - 12b\lfloor\log(2c)\rfloor - 384\eta\lfloor\log(2c)\rfloor + 12\lfloor\log(c)\rfloor + 12\lfloor\log\left(\lceil\frac{3c}{2}\rceil\right)\rfloor \\
&- 1716\lfloor\log(2c)\rfloor + 12\lfloor\log\left(\lceil\frac{5c}{2}\rceil\right)\rfloor + 12\lfloor\log(1+4c)\rfloor - 12\lfloor\log(2c+b+32n+144)\rfloor \\
&+ 13298c - 32b - 1024\eta - 4444] + 19c + 8b + 256\eta + 694 + 372 + 384\eta + 320. \qquad (4.565)
\end{aligned}$$

The number of storage ancilla qubits required is

$$\lceil\log(c)\rceil \cdot (\lceil\frac{49c}{2}\rceil + 2b + 64\eta + 293) + \lceil\log(b)\rceil \cdot (7b + 64\eta + 250) + b + 361\eta + 1482, \qquad (4.566)$$

and the number of workspace ancilla qubits required is

$$12c - \lfloor\log(4c+1)\rfloor + 5. \qquad (4.567)$$

There are two types of syntheses errors, i.e., arithmetic approximation errors and R_z syntheses errors. The latter will be analyzed in Sec. 4.4.3. The arithmetic approximation errors per step

is given by

$$\frac{2+\log(b)}{2^b}+\left(\frac{3}{4}\right)^{c-(2b+64\eta+288)}(2+c+\log(c)). \tag{4.568}$$

In total, the approximation errors are

$$\epsilon^{(B)}=r\cdot 1470021852266496\cdot\frac{d(d-1)}{2}L^d(\frac{2+\log(b)}{2^b}+\left(\frac{3}{4}\right)^{c-(2b+64\eta+288)}(2+c+\log(c))), \tag{4.569}$$

where r is the number of Trotter steps, and $1470021852266496\cdot\frac{d(d-1)}{2}L^d$ is the number of oracle calls. We divide the approximation errors evenly such that

$$\epsilon_b^{(B)}=\frac{\epsilon^{(B)}}{r\cdot 1470021852266496d(d-1)L^d},\ \epsilon_c^{(B)}=\frac{\epsilon^{(B)}}{r\cdot 1470021852266496d(d-1)L^d}, \tag{4.570}$$

and

$$\epsilon_b^{(B)}\geq\frac{2+\log(b)}{2^b}, \tag{4.571}$$

$$\epsilon_c^{(B)}\geq\left(\frac{3}{4}\right)^{c-(2b+64\eta+288)}(2+c+\log(c)). \tag{4.572}$$

Note that this is not the optimal division of approximation errors. We let $b=\log\left(\frac{8}{\epsilon_b^{(B)}}\right)$. Then, (4.571) is always satisfied for $0<\epsilon_b^{(K)}<1$. We proceed to compute the upper bound for c. Since $c\geq 2b+64\eta+288\geq 128\eta+576$, and $\eta\geq 1$, $\frac{716}{704}c\geq 2+c+\log(c)$. Inserting this relation and our choice of b into (4.572), we obtain

$$\epsilon_c^{(B)}\geq\left(\frac{3}{4}\right)^{c-(\log\left(8/\epsilon_b^{(B)}\right)+64\eta+288)}\frac{716}{704}c. \tag{4.573}$$

Let

$$\tilde{\epsilon}_c^{(B)}=\epsilon_c^{(B)}\cdot\left(\frac{3}{4}\right)^{\log\left(8/\epsilon_b^{(B)}\right)+64\eta+288}\frac{704}{716}. \tag{4.574}$$

Then, we want to find a c such that

$$c\left(\frac{3}{4}\right)^c\leq\tilde{\epsilon}_c^{(B)}. \tag{4.575}$$

Assuming that $0<\tilde{\epsilon}_c^{(B)}<1$, the choice

$$c=\log_{\frac{3}{4}}\left(\frac{\frac{\tilde{\epsilon}_c^{(B)}}{2.28}}{\log_{\frac{3}{4}}(\frac{\tilde{\epsilon}_c^{(B)}}{2.28})}\right) \tag{4.576}$$

satisfies (4.575).

We mention in passing that the phase-inducing step can be parallelized. As in U(1), we can implement the magnetic terms acting on the odd and even plaquettes on a given two dimensional plane in parallel. In particular, we effect $O(L^d)$ same-angle R_z gates, using the weight-sum trick, for each bit of the ancilla state $|\pm f_{\alpha\beta\gamma\delta}\rangle$. Thus, the parallel implementation exponentially reduces the R_z-gate count to $O(cd^2 \log(L^d))$. In this work, we focus on the resource analysis of the serial implementation, and will leave that of the parallel implementation for future work.

We divide the oracle error ϵ_{oracle} evenly between the kinetic and magnetic oracles, i.e.,

$$\epsilon^{(K)} = \frac{\epsilon_{\text{oracle}}}{2},\ \epsilon^{(B)} = \frac{\epsilon_{\text{oracle}}}{2} \implies \epsilon_{\text{oracle}} = \epsilon^{(K)} + \epsilon^{(B)}. \tag{4.577}$$

Synthesis errors

Here, we compute the synthesis errors for R_z gates required for the mass and electric term, separately from those for the oracles required for the kinetic and magnetic terms. To start, we consider the mass term. In this term, we have $\lfloor \log(3L^d) + 1 \rfloor$ R_z gates to implement. Therefore, we incur for each Trotter step $\lfloor \log(3L^d) + 1 \rfloor \cdot \epsilon(R_z)$ amount of error, where $\epsilon(R_z)$ denotes the error per R_z gate.

Next, we consider the electric term, which has $(2\eta + 4)\lfloor \log(dL^d) + 1 \rfloor$ R_z gates. Therefore, each Trotter step incurs $(2\eta + 4)\lfloor \log(dL^d) + 1 \rfloor \cdot \epsilon(R_z)$ amount of error. If we instead use the phase gradient operation, once the gadget state $|\psi_M\rangle$ in (4.25) is prepared, each quantum adder call to implement the operation does not incur any synthesis error. We come back to the error incurred in preparing the gadget state itself in the next section.

The errors per Trotter step due to the R_z gates for the kinetic and magnetic terms are $13872dL^d \cdot \lceil \frac{3c^{(K)}}{2} \rceil \cdot \epsilon(R_z)$ and $1470021852266496 \cdot \frac{d(d-1)}{2} L^d \cdot \lceil \frac{3c^{(B)}}{2} \rceil \cdot \epsilon(R_z)$, where we have and will continue to denote the approximation parameter c for the kinetic and magnetic oracles as $c^{(K)}$ and $c^{(B)}$, respectively.

We add the error incurred for the four terms to obtain the synthesis error $\epsilon_{\text{synthesis}}$. Note that, as in the U(1) case, the implementation of the diagonal mass and electric terms can be optimized. As in the U(1) case, there are $r + 1$ diagonal mass and electric terms, and $2r$ off-diagonal kinetic and magnetic terms to implement in total. Thus, $\epsilon_{\text{synthesis}}$ is given by

$$\begin{aligned}\epsilon_{\text{synthesis}} = \{(r+1) \cdot [\lfloor \log\left(3L^d\right) + 1 \rfloor + (2\eta + 4)\lfloor \log\left(dL^d\right) + 1 \rfloor] + 2r \cdot [20808c^{(K)}dL^d \\ + 1102516389199872c^{(B)}d(d-1)L^d]\} \cdot \epsilon(R_z),\end{aligned} \tag{4.578}$$

where r, to reiterate for the convenience of the readers, is the total number of Trotter steps.

Complexity analysis

Having computed the Trotter, oracle and synthesis errors, we proceed to perform the complexity analysis for the SU(3) LGT.

The total error is given by

$$\epsilon_{\text{total}} = \epsilon_{\text{Trotter}} + \epsilon_{\text{oracle}} + \epsilon_{\text{synthesis}}. \tag{4.579}$$

We choose to evenly distribute the total error between the Trotter, oracle, and synthesis errors. Focusing on the Trotter error, we obtain the number of Trotter steps by

$$\epsilon_{\text{Trotter}} = \frac{\epsilon_{\text{total}}}{3} \implies r = \lceil \frac{T^{3/2} 3^{1/2} \rho^{1/2}}{\epsilon_{\text{total}}^{1/2}} \rceil. \tag{4.580}$$

Next, we use the above relation and $\epsilon_{\text{oracle}} = \frac{\epsilon_{\text{total}}}{3}$ to obtain the expressions for $c^{(K)}$ and $c^{(B)}$. $c^{(K)}$ is given by (4.564), where

$$\tilde{\epsilon}_c^{(K)} = \frac{\epsilon_{\text{total}}}{12r \cdot 13872 d L^d} \left(\frac{3}{4}\right)^{2\log\left(8\frac{12r\cdot 13872 dL^d}{\epsilon_{\text{total}}}\right)+16\eta+72} \frac{176}{186}. \tag{4.581}$$

$c^{(B)}$ is given by (4.576), where

$$\tilde{\epsilon}_c^{(B)} = \frac{\epsilon_{\text{total}}}{6r \cdot 1470021852266496 d(d-1) L^d} \left(\frac{3}{4}\right)^{2\log\left(8\frac{6r\cdot 1470021852266496 d(d-1)L^d}{\epsilon_{\text{total}}}\right)+64\eta+288} \frac{704}{716}. \tag{4.582}$$

Finally, we compute the error each R_z gate can incur by

$$\begin{aligned}
&\epsilon_{\text{synthesis}} = \frac{\epsilon_{\text{total}}}{3} \implies \\
&\epsilon(R_z) = \frac{\epsilon_{\text{total}}}{3} \{ (\lceil \frac{T^{3/2} 3^{1/2} \rho^{1/2}}{\epsilon_{\text{total}}^{1/2}} \rceil + 1) \cdot [\lfloor \log\left(3L^d\right) + 1 \rfloor + (2\eta+4) \lfloor \log\left(dL^d\right) + 1 \rfloor] \\
&+ 2 \lceil \frac{T^{3/2} 3^{1/2} \rho^{1/2}}{\epsilon_{\text{total}}^{1/2}} \rceil \cdot [20808 c^{(K)} dL^d + 1102516389199872 c^{(B)} d(d-1) L^d] \}^{-1}.
\end{aligned} \tag{4.583}$$

With this, we obtain the number of T gates required to synthesize each R_z gate using RUS circuit [135],

$$\text{Cost}(R_z) = 1.15 \log\left(\frac{1}{\epsilon(R_z)}\right). \tag{4.584}$$

Combining the T gates required for implementation of R_z gates and the T gates used elsewhere in the circuit, we obtain the total number of T gates for the entire circuit as

$$
\begin{aligned}
&(\lceil\frac{T^{3/2}3^{1/2}\rho^{1/2}}{\epsilon_{\text{total}}^{1/2}}\rceil+1)\cdot[\lfloor\log\Big(3L^d\Big)+1\rfloor+(2\eta+4)\lfloor\log\Big(dL^d\Big)+1\rfloor]+2\lceil\frac{T^{3/2}3^{1/2}\rho^{1/2}}{\epsilon_{\text{total}}^{1/2}}\rceil\\
&\cdot[20808c^{(K)}dL^d+1102516389199872c^{(B)}d(d-1)L^d]\cdot\text{Cost}(R_z)+(\lceil\frac{T^{3/2}3^{1/2}\rho^{1/2}}{\epsilon_{\text{total}}^{1/2}}\rceil+1)\\
&\cdot[4(3L^d-\text{Weight}(3L^d))+8dL^d[(8\eta-8)+(5\eta-3\lfloor\log(\eta)\rfloor-4)+(\eta-1)(12\eta-3\lfloor\log(\eta)\rfloor-12)\\
&+1+\eta(12\eta-3\lfloor\log(\eta+2)\rfloor+10)+1+(10\eta-3\lfloor\log(2\eta+3)\rfloor+11)]+(8\eta+16)(dL^d\\
&-\text{Weight}(dL^d))+3328(\eta+1)dL^d]+2\lceil\frac{T^{3/2}3^{1/2}\rho^{1/2}}{\epsilon_{\text{total}}^{1/2}}\rceil\cdot[13872dL^d\mathcal{T}^{(K)}\\
&+83955286016(\eta+1)L^dd(d-1)+735010926133248d(d-1)L^d\mathcal{T}^{(B)}],
\end{aligned}
\tag{4.585}
$$

where $\mathcal{T}^{(K)},\mathcal{T}^{(B)}$ are given in (4.553,4.565), respectively.

The size of the ancilla register is given by the maximum between the ancilla qubits required by the electric and magnetic Hamiltonian, i.e.,

$$
\begin{aligned}
&Q_{\max}=\max\{(8\eta+10)dL^d+3(\eta+2)-\lfloor\log(\eta+2)\rfloor+dL^d-\text{Weight}(dL^d),\\
&\lceil\log(c)\rceil\cdot(\lceil\frac{49c}{2}\rceil+2b+64\eta+293)+\lceil\log(b)\rceil\cdot(7b+64\eta+250)+b+361\eta+12c-\lfloor\log(4c+1)\rfloor+1487\}.
\end{aligned}
\tag{4.586}
$$

Taking this into account, we obtain the total number of qubits required for the simulation by summing up those in the ancilla, fermionic and gauge-field registers, which is given by

$$
3L^d+(8\eta+12)dL^d+Q_{\max}. \tag{4.587}
$$

Note that in the case where the electric term is implemented using phase gradient operation, the T-gate count changes by

$$
\begin{aligned}
&(\lceil\frac{T^{3/2}3^{1/2}\rho^{1/2}}{\epsilon_{total}^{1/2}}\rceil+1)\cdot[4dL^d\log\Big(\frac{6\pi a^{d-2}}{g^2t}\Big)+O(dL^d)-(2\eta+4)\lfloor\log\Big(dL^d\Big)+1\rfloor\cdot\text{Cost}(R_z)\\
&-4(2\eta+4)(dL^d-\text{Weight}(dL^d))]+\text{Cost}(|\psi_M\rangle),
\end{aligned}
\tag{4.588}
$$

where the $\text{Cost}(R_z)$ needs to be modified, since $\epsilon(R_z)$ has changed to

$$
\begin{aligned}
\epsilon(R_z)=\frac{\epsilon_{\text{total}}}{3}\{&(\lceil\frac{T^{3/2}3^{1/2}\rho^{1/2}}{\epsilon_{\text{total}}^{1/2}}\rceil+1)\cdot\lfloor\log\Big(3L^d\Big)+1\rfloor+2\lceil\frac{T^{3/2}3^{1/2}\rho^{1/2}}{\epsilon_{\text{total}}^{1/2}}\rceil\cdot[20808c^{(K)}dL^d\\
&+1102516389199872c^{(B)}d(d-1)L^d]\}^{-1}.
\end{aligned}
\tag{4.589}
$$

Further, $\text{Cost}(|\psi_M\rangle)$, which denotes the one-time synthesis costs of the phase gradient gadget state. Here, we choose to use the synthesis method delineated in [147]. Briefly, we apply Hadamard gates to the register $|00...0\rangle$, and then apply gates $Z, Z^{-1/2}, ..., Z^{-1/2^{M-1}}$. Each Z^α gates are synthesized using RUS circuits [135]. Let δ be the error of preparing the gadget state $|\psi_M\rangle$. Then, each gate can incur at most M/δ error, and thus, costs $1.15\log(M/\delta)$, using RUS circuits [135]. Thus, the gadget state preparation costs $1.15M\log(M/\delta)$.

Finally, in this case, the ancilla-qubit count is given by that of the maximum between the mass term and the phase gradient state, and the magnetic term, i.e.,

$$Q_{\max} = \max\{(3L^d - \text{Weight}(3L^d)) + \log\left(\frac{6\pi a^{d-2}}{g^2 t}\right), \lceil\log(c)\rceil \cdot (\lceil\frac{49c}{2}\rceil + 2b + 64\eta + 293) + \lceil\log(b)\rceil \cdot (7b + 64\eta + 250) + b + 361\eta + 12c - \lfloor\log(4c+1)\rfloor + 1487\}. \quad (4.590)$$

As such, the total qubit count is given by

$$3L^d + dL^d(8\eta + 12) + Q_{\max}. \quad (4.591)$$

4.6 Improvements over previous work

In this section, we demonstrate the algorithmic improvements achieved in this work over previous works, [6] and [7]. In particular, we use the asymptotic scaling, with respect to L, Λ, and ϵ, assuming d, a, g, and m are fixed, of T gates required for a single Trotter step as the comparison metric.

4.6.1 U(1) case:

Here we compare our algorithm with those proposed in [6] and [7]. We first provide a brief overview of the simulation methods in [6]. Similar to our method, as described in 4.3.2, the authors applied a truncation Λ to the electric eigenbasis $|E\rangle$ on each link such that $E \in \{-\Lambda, -\Lambda+1, ..., \Lambda\}$, and the gauge-field operators $\hat{E}$, $\hat{U}$, and $\hat{U}^\dagger$ become finite-dimensional. Then, they mapped $|E\rangle$ to qubits using an unary encoding. In particular, an integer $-\Lambda \leq j \leq \Lambda$ is represented on an unary $(2\Lambda+1)-$qubit register as the state where the jth qubit is $|0\rangle$ and the remaining qubits are all $|1\rangle$. As such, the gauge-field operators are represented as follows:

$$\hat{E} = \sum_{l=-\Lambda}^{\Lambda} l\frac{(\hat{Z}_l + \hat{I}_l)}{2}, \quad (4.592)$$

$$\hat{U} = \sum_{l=-\Lambda}^{\Lambda-1} \hat{\sigma}_l^+ \hat{\sigma}_{l+1}^-, \quad (4.593)$$

where the subscript l denotes the qubit index for each link register $|E\rangle$.

Using the above relations, the evolution of each link due to the electric Hamiltonian $e^{it\frac{g^2}{2a^{d-2}}\hat{E}^2}$ can be implemented, up to a global phase, as

$$\prod_{l=-\Lambda}^{\Lambda} e^{it\frac{g^2}{2a^{d-2}}\frac{i^2}{2}\hat{Z}_l}, \tag{4.594}$$

which requires $O(\Lambda)$ R_z gates. Therefore, for a d-dimensional cubic lattice with L^d sites, the evolution due to the electric Hamiltonian costs $O(dL^d\Lambda)$ R_z gates in total. Hereafter, we suppose an error budget ϵ is allocated for synthesizing all the required R_z gates, and we use RUS circuits [135] to synthesize them. Then, $O(dL^d\Lambda\log(dL^d\Lambda/\epsilon))$ T gates are needed. In comparison, our algorithm (see Sec. 4.3.2 for details) requires $O(\log(dL^d)\log(\Lambda))$ R_z gates and $O(dL^d(\log(\Lambda))^2)$ T gates. This amounts to $O(\log(dL^d)\log(\Lambda)\log(\log(dL^d)\log(\Lambda)/\epsilon) + dL^d(\log(\Lambda))^2)$ total T gates. As a result, our algorithm reduces the Λ-dependence from linear to quadratic logarithmic.

Next, we discuss the evolution of each plaquette due to the magnetic Hamiltonian $e^{-i\frac{t}{2a^{4-d}g^2}(\hat{U}\hat{U}\hat{U}^\dagger\hat{U}^\dagger+h.c.)}$, which can be Trotterized to first order as,

$$\prod_{j,k,l,m=-\Lambda}^{\Lambda-1} e^{-i\frac{t}{2a^{4-d}g^2}(\hat{\sigma}_j^+\hat{\sigma}_{j+1}^-\hat{\sigma}_k^+\hat{\sigma}_{k+1}^-\hat{\sigma}_l^-\hat{\sigma}_{l+1}^+\hat{\sigma}_m^-\hat{\sigma}_{m+1}^+ + h.c.)}. \tag{4.595}$$

This can be implemented as $O(\Lambda^4)$ unitary operations of the form $e^{-i\theta(\otimes_k\hat{\sigma}_k+h.c.)}$, each of which, as shown in Sec. 4.3.2, requires $O(1)$ R_z gate. The magnetic term for a d-dimensional lattice, where there are $O(d^2L^d)$ plaquettes, costs $O(d^2L^d\Lambda^4\log(d^2L^d\Lambda^4/\epsilon))$ T gates in total. In comparison, our algorithm (see Sec. 4.3.2 for details) requires $O(d^2\log(L^d))$ R_z gates and $O(d^2\log(\Lambda)L^d)$ T gates, which amount to $O(d^2[\log(L^d)\log(d^2\log(L^d)/\epsilon) + \log(\Lambda)L^d])$ total T gates. As such, our algorithm scales exponentially better in Λ.

In addition to the improvements in T gate count, our algorithm also scales more favorably in terms of qubit count. In particular, their method requires $O(dL^d\Lambda)$ qubits, whereas our algorithm requires $O(dL^d\log(\Lambda))$ qubits.

Next, we apply our algorithm to a one-dimensional lattice, and compare it to that in [7]. Both algorithms encode the gauge-field operators to qubits using binary encoding, and use Jordan-Wigner transformation to map fermions to qubits. The main difference is the parallelization techniques, i.e. , the weight-sum trick, used in our algorithm, which reduce the number of R_z gates incurred. Given the similarity between our algorithms, we simply report the T gate counts for a Trotter step due to each term of the Hamiltonian. Their algorithm requires $O(L\log(L/\epsilon))$, $O(L[\log(\Lambda)\log(L\log(\Lambda)/\epsilon) + (\log(\Lambda))^2])$, and $O(L[\log(L/\epsilon) + \log(\Lambda)])$ T gates for the mass, electric, and kinetic terms, respectively. Our algorithm requires $O(L + \log(L)\log(\log(L)/\epsilon))$, $O(\log(L)\log(\Lambda)\log(\log(L)\log(\Lambda)/\epsilon) + L(\log(\Lambda))^2)$, and $O(\log(L)\log(\log(L)/\epsilon) + L\log(\Lambda))$ T gates for the mass, electric, and kinetic terms, respectively.

4.6.2 SU(2) case:

Here we provide a comparison between our algorithm and that in [6]. Briefly, we describe the method in [6]. Similar to our algorithm, as described in Sec. 4.4.2, a truncation is applied to the basis $\left|j, m^L, m^R\right\rangle$, such that, for a given link, $j \in \{0, \frac{1}{2}, ..., \Lambda\}$ and $m^L, m^R \in \{-\Lambda, -\Lambda+\frac{1}{2}, ..., \Lambda\}$. As in the U(1) case, they map $|j\rangle$, $\left|m^L\right\rangle$, and $\left|m^R\right\rangle$ to qubit using an unary encoding. In particular, $k \in \{-\Lambda, -\Lambda+\frac{1}{2}, ..., \Lambda\}$ is represented on an unary $(4\Lambda+1)$-qubit register as the state where the $2k$th qubit is $|0\rangle$ and the remaining qubits are all $|1\rangle$. $k \in \{0, \frac{1}{2}, ..., \Lambda\}$ is represented similarly on a $(2\Lambda+1)$-qubit register.

Using this unary encoding, the operator $\hat{E}^2$, which satisfies the relation in (4.162), i.e., $\hat{E}^2 \left|j, m^L, m^R\right\rangle = j(j+1)\left|j, m^L, m^R\right\rangle$, can be represented as

$$\hat{E}^2 = \sum_{l=0}^{2\Lambda} l(l+1)\frac{(\hat{Z}_l + \hat{I}_l)}{2}, \tag{4.596}$$

where the subscript l denotes the qubit index in the register $|j\rangle$ for a given link. Then, the evolution of each link due to the electric Hamiltonian $e^{it\frac{g^2}{2a^{d-2}}\hat{E}^2}$ can be implemented, up to a global phase, with $O(\Lambda)$ R_z gates. Therefore, for a d-dimensional cubic lattice with L^d sites, the evolution due to the electric Hamiltonian costs $O(dL^d\Lambda)$ R_z gates in total, which, using RUS circuits, translate to $O(dL^d\Lambda \log(dL^d\Lambda/\epsilon))$ total T gates. In comparison, our algorithm (see Sec.4.4.2 for details) requires $O(\log(dL^d)\log(\Lambda))$ R_z gates and $O(dL^d(\log(\Lambda))^2)$ T gates, which amounts to $O(\log(dL^d)\log(\Lambda)\log(\log(dL^d)\log(\Lambda)/\epsilon) + dL^d(\log(\Lambda))^2)$ T gates in total. As in the U(1) case, our algorithm reduces the Λ-dependence from linear to quadratic logarithmic.

We now proceed to discuss the magnetic evolution for each plaquette, i.e., $e^{-i\frac{t}{2a^{4-d}g^2}(\hat{U}_{\alpha\beta}\hat{U}_{\beta\gamma}\hat{U}^\dagger_{\gamma\delta}\hat{U}^\dagger_{\delta\alpha}+h.c.)}$. Briefly, the $\hat{U}_{\alpha\beta}$ operators in (4.173) are defined in terms of raising and lowering operators on $|j\rangle$, and $\left|m^{L/R}\right\rangle$, which, in the unary encoding, are given by

$$\hat{J}^+ = \sum_{l=0}^{2\Lambda-1} \hat{\sigma}^+_l \hat{\sigma}^-_{l+1},\ \hat{J}^- = (\hat{J}^+)^\dagger \tag{4.597}$$

$$\hat{M}_1^{L/R} = \sum_{l=-2\Lambda}^{2\Lambda-1} \hat{\sigma}^+_l \hat{\sigma}^-_{l+1},\ \hat{M}_2^{L/R} = (\hat{M}_1^{L/R})^\dagger \tag{4.598}$$

respectively, where, l denotes the qubit index, and diagonal operators, $\hat{N}_\alpha$ in (4.170) and $\hat{c}^{L/R}_{\alpha\beta}$ in (4.172) that encode the normalization factors and SU(2) Clebsch-Gordan coefficients, respectively.

Then, the $\hat{U}_{\alpha\beta}$ operators can be expressed as

$$\begin{aligned}\hat{U}_{\alpha\beta} &= \hat{M}_\alpha^L \hat{M}_\beta^R [\hat{J}^+ \hat{c}_{1\alpha}^L \hat{c}_{1\beta}^R \hat{N}_1 + \hat{J}^- \hat{c}_{2\alpha}^L \hat{c}_{2\beta}^R \hat{N}_2] \\ &= \sum_{i,k=-2\Lambda}^{2\Lambda-1} \sum_{l=0}^{2\Lambda-1} \hat{\sigma}_i^s \hat{\sigma}_{i+1}^s \hat{\sigma}_k^q \hat{\sigma}_{k+1}^q [\hat{\sigma}_l^+ \hat{\sigma}_{l+1}^- \hat{c}_{1\alpha}^L \hat{c}_{1\beta}^R \hat{N}_1 + \hat{\sigma}_l^- \hat{\sigma}_{l+1}^+ \hat{c}_{2\alpha}^L \hat{c}_{2\beta}^R \hat{N}_2] \\ &= \sum_{i,k=-2\Lambda}^{2\Lambda-1} \sum_{l=0}^{2\Lambda-1} \hat{\sigma}_i^s \hat{\sigma}_{i+1}^s \hat{\sigma}_k^q \hat{\sigma}_{k+1}^q [c_{1\alpha}^L(\frac{l}{2}, \frac{i}{2}) c_{1\beta}^R(\frac{l}{2}, \frac{k}{2}) \sqrt{\frac{l+1}{l+2}} \hat{\sigma}_l^+ \hat{\sigma}_{l+1}^- \\ &\quad + c_{2\alpha}^L(\frac{l}{2}, \frac{i}{2}) c_{2\beta}^R(\frac{l}{2}, \frac{k}{2}) \sqrt{\frac{l+1}{l}} \hat{\sigma}_l^- \hat{\sigma}_{l+1}^+], \end{aligned} \tag{4.599}$$

where i, k, l are qubit indices for registers $\left|m^L\right\rangle$, $\left|m^R\right\rangle$, $|j\rangle$, respectively, and $s, q \in \{+, -\}$ depend on α, β, respectively. Moreover, in the third equality, we are able deduce the unique state each string of Pauli operators, i.e., $\bigotimes_r \hat{\sigma}^r$ with $r \in \{+, -\}$, acts on, and thus, the Clebsch-Gordan coefficient and normalization factor induced by the diagonal operators. Using this expression, there are $O(\Lambda^{12})$ $\bigotimes_r \hat{\sigma}^r + h.c.$ operators in each $\hat{U}_{\alpha\beta}\hat{U}_{\beta\gamma}\hat{U}_{\gamma\delta}^\dagger\hat{U}_{\delta\alpha}^\dagger + h.c.$ operator. Since each $e^{it(\otimes_r \hat{\sigma}^r + h.c.)}$ costs $O(1)$ R_z gate, each evolution operator $e^{-i\frac{t}{2a^{4-d}g^2}(\hat{U}_{\alpha\beta}\hat{U}_{\beta\gamma}\hat{U}_{\gamma\delta}^\dagger\hat{U}_{\delta\alpha}^\dagger + h.c.)}$ costs $O(\Lambda^{12})$ R_z gates. Therefore, the magnetic term for the entire d-dimensional lattice costs $O(d^2L^d\Lambda^{12}\log(d^2L^d\Lambda^{12}/\epsilon))$ T gates in total. In comparison, our algorithm requires $O(d^2L^d\log(\Lambda))$ T gates, $O(cd^2L^d)$ R_z gates, and $O(d^2L^d)$ queries to arithmetic oracles, each of which costs $O(c^2\log(c)+(\log(\Lambda))^2)$ T gates. From Sec. 4.4.3, we obtain that $c = O(\log\left(\frac{d^2L^d\Lambda}{\epsilon}\right)+\log\left(\log\left(\frac{d^2L^d\Lambda}{\epsilon}\right)\right))$. Hence, omitting $O(\log\log(\epsilon^{-1}))$ and $O(\log\log(\Lambda))$ factors, our algorithm has a quadratically worse ϵ^{-1}-dependence, i.e., $(\log(\epsilon^{-1}))^2$ versus $\log(\epsilon^{-1})$, but a superpolynomial improvement in the Λ-dependence, i.e, $(\log(\Lambda))^2$ versus Λ^{12}.

4.6.3 SU(3) case:

Once again, we provide a comparison between our algorithm and that in [6]. Briefly, we describe the method in [6]. Similar to our algorithm, as described in Sec. 4.5.2, a truncation is applied to the basis $|p, q, T_L, T_L^z, Y_L, T_R, T_R^z, Y_R\rangle$, such that, for a given link, $p, q \in \{0, 1, ..., \Lambda\}$, $T_i \in \{0, \frac{1}{2}, ..., \Lambda\}$, $T_i^z \in \{-\Lambda, -\Lambda + \frac{1}{2}, ..., \Lambda\}$, $Y_i = \{-\Lambda, -\Lambda + \frac{1}{3}, ..., \Lambda\}$, where $i = L, R$. As in the U(1) and SU(2) cases, they map $|p\rangle$, $|q\rangle$, $|T_i\rangle$, $|T_i^z\rangle$, and $|Y_i\rangle$ to qubit using an unary encoding. In particular, $k \in \{0, 1, ..., \Lambda\}$ is represented on an unary $(\Lambda + 1)$-qubit register as the state where the kth qubit is $|0\rangle$ and the remaining qubits are all $|1\rangle$. Similarly, $k \in \{-\Lambda, -\Lambda + \frac{1}{2}, ..., \Lambda\}$ is represented on an unary $(4\Lambda + 1)$-qubit register as the state where the $2k$th qubit is $|0\rangle$ and the remaining qubits are all $|1\rangle$, while $k \in \{0, \frac{1}{2}, ..., \Lambda\}$ is represented similarly on a $(2\Lambda + 1)$-qubit register. Finally, $k \in \{-\Lambda, -\Lambda + \frac{1}{3}, ..., \Lambda\}$ is represented on an unary $(6\Lambda + 1)$-qubit register as the state where the $3k$th qubit is $|0\rangle$ and the remaining qubits are all $|1\rangle$.

Using this unary encoding, the operator $\hat{E}^2$, which satisfies the relation in 4.385, i.e., $\hat{E}^2 |p,q\rangle = \frac{1}{3}[p^2+q^2+pq+3(p+q)]\,|p,q\rangle$, can be represented as

$$\hat{E}^2 = \sum_{l,m=0}^{\Lambda} \frac{1}{3}[l^2+m^2+lm+3(l+m)] \frac{(\hat{Z}_l+\hat{I}_l)}{2} \frac{(\hat{Z}_m+\hat{I}_m)}{2}, \tag{4.600}$$

where the subscripts l, m denote the qubit indices in the registers $|p\rangle$, $|q\rangle$, respectively, for a given link. Then, the evolution of each link due to the electric Hamiltonian $e^{it\frac{g^2}{2a^{d-2}}\hat{E}^2}$ can be implemented, up to a global phase, with $O(\Lambda^2)$ R_z gates. Therefore, for a d-dimensional cubic lattice with L^d sites, the electric term costs $O(dL^d\Lambda^2)$ R_z gates in total, which using RUS circuits, translate to $O(dL^d\Lambda^2 \log\big(dL^d\Lambda^2/\epsilon\big))$ total T gates. In comparison, our algorithm (see Sec.4.5.2 for details) requires $O(\log\big(dL^d\big)\log(\Lambda))$ R_z gates and $O(dL^d(\log(\Lambda))^2)$ T gates, which amounts to $O(\log\big(dL^d\big)\log(\Lambda)\log\big(\log\big(dL^d\big)\log(\Lambda)/\epsilon\big) + dL^d(\log(\Lambda))^2)$ T gates in total. Our algorithm reduces the Λ-dependence from quadratic to quadratic logarithmic.

Finally, we discuss the magnetic term for each plaquette, i.e., $e^{-i\frac{t}{2a^{4-d}g^2}(\hat{U}_{\alpha\beta}\hat{U}_{\beta\gamma}\hat{U}^\dagger_{\gamma\delta}\hat{U}^\dagger_{\delta\alpha}+h.c.)}$. Briefly, the $\hat{U}_{\alpha\beta}$ operators in (4.404) are defined in terms of raising and lowering operators on $|p\rangle$, $|q\rangle$, $|T_i\rangle$, $|T_i^z\rangle$, and $|Y_i\rangle$, where $i = L, R$, and diagonal operators that encode the normalization factors and SU(3) Clebsch-Gordan coefficients. As in the U(1) and SU(2) case, in the unary encoding, each raising and lowering operator is a sum $O(\Lambda)$ $\hat{\sigma}^+\hat{\sigma}^-$ operators. Similar to the SU(2) case, the $\hat{U}_{\alpha\beta}$ operators consist of $O(\Lambda^8)$ strings of Pauli operators, i.e., $\bigotimes_r \hat{\sigma}^r$ with $r \in \{+,-\}$. Hence, there are $O(\Lambda^{32})$ $\bigotimes_r \hat{\sigma}^r + h.c.$ in each $\hat{U}_{\alpha\beta}\hat{U}_{\beta\gamma}\hat{U}^\dagger_{\gamma\delta}\hat{U}^\dagger_{\delta\alpha} + h.c.$ operator. Since each $e^{it(\otimes_r\hat{\sigma}^r+h.c.)}$ costs $O(1)$ R_z gate, each evolution operator $e^{-i\frac{t}{2a^{4-d}g^2}(\hat{U}_{\alpha\beta}\hat{U}_{\beta\gamma}\hat{U}^\dagger_{\gamma\delta}\hat{U}^\dagger_{\delta\alpha}+h.c.)}$ costs $O(\Lambda^{32})$ R_z gates. Therefore, the magnetic term for the entire d-dimensional lattice costs $O(d^2L^d\Lambda^{32}\log\big(d^2L^d\Lambda^{32}/\epsilon\big))$ T gates in total. Our algorithm has the same scaling as in the SU(2) case. As such, it requires $O(d^2L^d\log(\Lambda))$ T gates, $O(cd^2L^d)$ R_z gates, and $O(d^2L^d)$ queries to arithmetic oracles, each of which costs $O(c^2\log(c) + (\log(\Lambda))^2)$ T gates, where $c = O(\log\Big(\frac{d^2L^d\Lambda}{\epsilon}\Big) + \log\Big(\log\Big(\frac{d^2L^d\Lambda}{\epsilon}\Big)\Big))$. Hence, omitting $O(\log\log\big(\epsilon^{-1}\big))$ and $O(\log\log(\Lambda))$ factors, our algorithm has a quadratically worse ϵ^{-1}-dependence, i.e., $(\log\big(\epsilon^{-1}\big))^2$ versus $\log\big(\epsilon^{-1}\big)$, but a superpolynomial improvement in the Λ-dependence, i.e, $(\log(\Lambda))^2$ versus Λ^{32}.

Chapter 5

A Resource-Efficient Approach for Quantum and Classical Simulations of U(1) Lattice Gauge Theories

In this chapter, we provide a resource-efficient approach that facilitates the quantum simulation of lattice gauge theories (LGTs) in more than one spatial dimension that would otherwise be out of reach for current and near-term quantum hardware. Indeed, our approach is crucial to our proposal for near-term quantum simulations in [1] and chapter 3. We aim to address the important problem of reaching the continuum limit, i.e., when the lattice spacing approaches zero, with finite computational resources. Taking the continuum limit is in general computationally expensive. MCMC methods, for instance, have an intrinsic problem of auto-correlations that become more and more severe at decreasingly small lattice spacing. This drawback in turn leads to a significant increase in the computational cost, and limits the smallest value of the lattice spacing that can be reached. While Hamiltonian-based approaches, such as quantum simulation, circumvent this problem, they face the challenge that for continuous (Abelian and non-Abelian) gauge groups, local gauge degrees of freedom are defined in an infinite dimensional Hilbert space. As a consequence, any simulation – classical or quantum – requires a truncation of the gauge fields.

We present a practical solution to overcome this crucial bottleneck and to allow for resource-efficient simulations of lattice quantum electrodynamics (QED) Hamiltonian. Although our approach is applicable to any dimension, we consider two-dimensional QED as a benchmark example. In lattice QED, truncation of the gauge fields is typically performed in the 'electric basis', i.e. the basis in which the electric Hamiltonian and Gauss' law are diagonal, as discussed in chapters 3 and 4. While a heavily truncated electric basis can result in an accurate description of the system in the strong-coupling regime, at weaker coupling or smaller lattice spacing, where the

magnetic contributions dominate, the number of states that have to be included in the electric basis grows dramatically. Therefore, truncation of the gauge fields is at conflict with continuum extrapolation.

A plausible solution to simulate the weak coupling regime is to use the so-called magnetic basis, i.e., the basis in which magnetic interactions are diagonal. The magnetic basis can be obtained by Fourier-transforming the electric basis over the considered gauge group [106, 159]. However, the fact that the magnetic degrees of freedom are continuous variables with a gapless spectrum poses intricate challenges for a resource-efficient truncation scheme, that have yet (to the best of our knowledge) to be addressed. In this work, we provide a practical solution in the case of lattice QED by combining state truncation with a gauge group discretisation that is dynamically adjusted to the value of the coupling. This approach allows for controlled simulations at all values of the bare coupling. As a proof-of-principle of this new approach and its ability to faithfully simulate non-perturbative phenomena, we target the renormalised coupling in QED in $2+1$ dimensions. In particular, as previously done in the pioneering work by Creutz [160], we study the bare coupling dependence of the local plaquette operator, which does not require large-scale simulations on both classical and quantum computers. This quantity allows us to benchmark our formalism and to demonstrate that a smooth connection between the weak and the strong coupling regimes can be established. In addition, our method allows for estimating the precision with which a given truncation approximates the untruncated results.

In Sec. 5.1, we review lattice QED in (2+1) dimensions with periodic boundary conditions. By eliminating redundant gauge degrees of freedom, we obtain an effective Hamiltonian description that allows for simulations at a low computational cost. In Sec. 5.2, we introduce a new magnetic representation of lattice QED that is equipped with a regularisation in terms of a $\mathbb{Z}_{2L+1}$ group and an efficient truncation scheme. In Sec. 5.3, we study the performance of our method and benchmark its precision by calculating the expectation value of the plaquette operator on a periodic plaquette. We show that both the truncation cut-off parameter, i.e. the number of basis states included in the simulation, and L, the dimension of the $\mathbb{Z}_{2L+1}$ group, can be used as adjustable variational parameters. Both are used to optimise the simulation and estimate its accuracy. In Sec. 5.4, we present the generalisation to an arbitrary, two-dimensional periodic lattice with dynamical matter. Finally, we outline the prospects of this method for classical and quantum simulations in Sec. 5.5

5.1 Minimal encoding of U(1) LGTs

We review the standard Kogut-Susskind Hamiltonian subject to Gauss' law (the local constraints ensuring gauge invariance) in Sec. 5.1.1, considering QED on a square lattice as a paradigmatic example. In Sec. 5.1.2, we proceed to provide a minimal formulation of the lattice QED Hamiltonian, in which redundant degrees of freedom have been removed.

5.1.1 QED in two dimensions

In LGTs [14], the charges occupy the sites $\boldsymbol{n} = (n_x, n_y)$ of the lattice while the electromagnetic fields are defined on the links. The links are denoted by their starting site $\boldsymbol{n}$ and their direction $\boldsymbol{e}_\mu$ ($\mu = x, y$), as shown in Fig. 5.1. The electric interactions are defined in terms of the electric field operator $\hat{E}_{\boldsymbol{n},\boldsymbol{e}_\mu}$, which acts on the link connecting the sites $\boldsymbol{n}$ and $\boldsymbol{n} + \boldsymbol{e}_\mu$. For each link, one further defines a parallel transport operator $\hat{U}_{\boldsymbol{n},\boldsymbol{e}_\mu}$, as the lowering operator for the electric field, $[\hat{E}_{\boldsymbol{n},\boldsymbol{e}_\mu}, \hat{U}_{\boldsymbol{n}',\boldsymbol{e}_\nu}] = -\delta_{\boldsymbol{n},\boldsymbol{n}'}\delta_{\mu,\nu}\hat{U}_{\boldsymbol{n},\boldsymbol{e}_\mu}$. The parallel transport operator measures the phase proportional to the bare coupling g acquired by a unit charge moved along the link $(\boldsymbol{n}, \boldsymbol{e}_\mu)$ of length a, i.e. $\hat{U}_{\boldsymbol{n},\boldsymbol{e}_\mu} \sim \exp\{iag\hat{A}_\mu(\boldsymbol{n})\}$. The magnetic interactions are given by (oriented) products of parallel transport operators on the links around the plaquettes of the lattice. These operators are used to construct the Kogut-Susskind Hamiltonian as $\hat{H} = \hat{H}_{\text{gauge}} + \hat{H}_{\text{matter}}$. Let us discuss first the pure gauge part

$$\begin{aligned} \hat{H}_{\text{gauge}} &= \hat{H}_E + \hat{H}_B, \\ \hat{H}_E &= \frac{g^2}{2}\sum_{\boldsymbol{n}}\left(\hat{E}^2_{\boldsymbol{n},\boldsymbol{e}_x} + \hat{E}^2_{\boldsymbol{n},\boldsymbol{e}_y}\right), \\ \hat{H}_B &= -\frac{1}{2g^2a^2}\sum_{\boldsymbol{n}}\left(\hat{P}_{\boldsymbol{n}} + \hat{P}^\dagger_{\boldsymbol{n}}\right). \end{aligned} \tag{5.1}$$

Here, the sums run over both components of the sites $\boldsymbol{n} = (n_x, n_y)$ and

$$\hat{P}_{\boldsymbol{n}} = \hat{U}_{\boldsymbol{n},\boldsymbol{e}_x}\hat{U}_{\boldsymbol{n}+\boldsymbol{e}_x,\boldsymbol{e}_y}\hat{U}^\dagger_{\boldsymbol{n}+\boldsymbol{e}_y,\boldsymbol{e}_x}\hat{U}^\dagger_{\boldsymbol{n},\boldsymbol{e}_y} \tag{5.2}$$

is the plaquette operator. It is easy to check that (5.1) reduces to the pure gauge U(1) Hamiltonian in the continuum, $\hat{H} \propto \int \mathrm{d}\boldsymbol{x} E(\boldsymbol{x})^2 + B(\boldsymbol{x})^2$, when the lattice spacing a is sent to zero [161]. The Hamiltonian in (5.1) is gauge-invariant as it commutes with the lattice version of Gauss' law

$$\left[\sum_{\mu=x,y}\left(\hat{E}_{\boldsymbol{n},\boldsymbol{e}_\mu} - \hat{E}_{\boldsymbol{n}-\boldsymbol{e}_\mu,\boldsymbol{e}_\mu}\right) - \hat{q}_{\boldsymbol{n}} - \hat{Q}_{\boldsymbol{n}}\right]|\Phi\rangle = 0\ \forall \boldsymbol{n} \iff |\Phi\rangle \in \{\text{physical states}\}, \tag{5.3}$$

that determines what states are physical for a given distribution of charges. Here, $\hat{q}_{\boldsymbol{n}}$ is the operator measuring the dynamical charge on the site $\boldsymbol{n}$ and $|\Phi\rangle$ represents the state of the whole lattice, including both links and sites. Furthermore, the operators $\hat{Q}_{\boldsymbol{n}}$ denote possible static charges which we set to zero in the following. The eigenstates of the electric field operators

$$\hat{E}_{\boldsymbol{n},\boldsymbol{e}_\mu}\left|E_{\boldsymbol{n},\boldsymbol{e}_\mu}\right\rangle = E_{\boldsymbol{n},\boldsymbol{e}_\mu}\left|E_{\boldsymbol{n},\boldsymbol{e}_\mu}\right\rangle, \quad E_{\boldsymbol{n},\boldsymbol{e}_\mu} \in \mathbb{Z} \tag{5.4}$$

form a basis for the link degrees of freedom. In particular, the physical states can be easily identified in this basis via (5.3).

In QED, charges are represented by Dirac fermions. In the staggered fermion representation [105], their Hamiltonian is $\hat{H}_{\text{matter}} = \hat{H}_M + \hat{H}_K$, where $\hat{H}_M$ and $\hat{H}_K$ are the mass and kinetic contributions, respectively

$$\hat{H}_M = m \sum_{\boldsymbol{n}} (-1)^{n_x+n_y} \hat{\Psi}^\dagger_{\boldsymbol{n}} \hat{\Psi}_{\boldsymbol{n}}, \tag{5.5}$$

$$\hat{H}_K = \kappa \sum_{\boldsymbol{n}} \sum_{\mu=x,y} \left[\hat{\Psi}^\dagger_{\boldsymbol{n}} \left(\hat{U}^\dagger_{\boldsymbol{n},\boldsymbol{e}_\mu} \right) \hat{\Psi}_{\boldsymbol{n}+\boldsymbol{e}_\mu} + h.c. \right]. \tag{5.6}$$

Here, m the fermionic mass parameter, κ the kinetic strength and $\hat{\Psi}^{(\dagger)}_{\boldsymbol{n}}$ the fermionic lowering (raising) operator for site $\boldsymbol{n}$. Since $\hat{H}_M$ identifies the Dirac vacuum with the state with all odd sites occupied, creating (destroying) a particle at even (odd) site is equivalent to creating a fermion (anti-fermion) in the Dirac vacuum. Thus, the gauge-invariant tunneling processes in the kinetic term correspond to the creation or annihilation of particle-antiparticle pairs and the corresponding change in the electric field connecting them. The charge operator $\hat{q}_{\boldsymbol{n}}$ is given by

$$\hat{q}_{\mathbf{n}} = \left(\hat{\Psi}^\dagger_{\mathbf{n}} \hat{\Psi}_{\mathbf{n}} - \frac{\mathbb{1}}{2} [1 - (-1)^{n_x+n_y}] \right). \tag{5.7}$$

5.1.2 QED Hamiltonian for physical states

As outlined in the previous section, gauge-invariance constrains the dynamics to the physical states only, i.e. those satisfying Gauss' law in (5.3). The unphysical states not only contaminate the spectrum of the Hamiltonan, but they also incur a memory overhead for classical and quantum simulations. They may be suppressed via energy penalties [66, 162, 163], in which case, the memory overhead remains. Alternatively, one can eliminate the redundant degrees of freedom by solving the constraint at each lattice site. In one dimension, such a procedure allows one to completely eliminate the gauge field, yielding an effective Hamiltonian containing only matter terms with long-range interactions [112, 81]. A similar approach is applicable in higher dimensions, with the difference that the gauge fields cannot be completely eliminated. Here, we show how to formulate an effective Hamiltonian that directly incorporates the Gauss' law constraints by employing a convenient parametrization of the physical states that yields an intuitive description of the system.

For the sake of clarity, we consider the minimal instance of a periodic two-dimensional lattice, namely, a square lattice formed by four lattice points. The generalisation to an arbitrary periodic two-dimensional lattice is derived in Sec. 5.4. Due to the periodic boundary conditions, this minimal system can equivalently be represented as a torus with four faces, or as four distinct plaquettes consisting of eight links [see Fig. 5.1(b)]. Due to charge conservation $\sum_{\boldsymbol{n}} \hat{q}_{\boldsymbol{n}} = 0$, only three out of the four constraints given by Gauss' law [(5.3)] are independent. Consequently, three

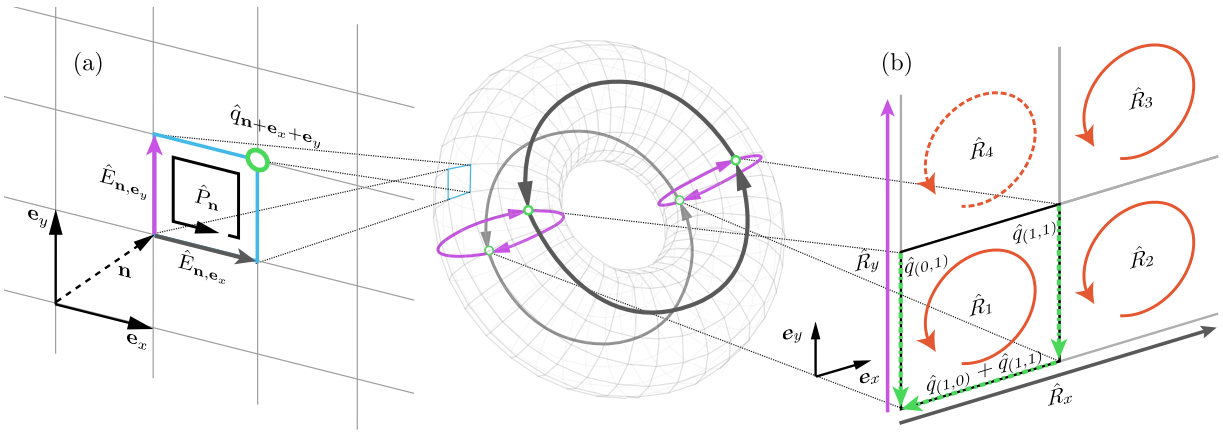

Figure 5.1: **Two-dimensional lattice gauge theory with periodic boundary conditions.** A single cell of the periodic 2D lattice in (a) is made of four links, oriented towards the positive x and y directions. Each lattice site is indicated by a unique vector $\boldsymbol{n}$, which marks the lower left corner of each single plaquette. The associated operator $\hat{P}_{\boldsymbol{n}}$ accounts for the electric field quanta circulating along the sketched path. The periodic lattice spans the surface of a torus, shown in the middle, whose minimal instance is assembled by four sites and the corresponding electric fields [thick lines, same color coding as in (a)]. Unwrapping this minimal torus yields the geometry shown in (b). We identify the strings $\hat{R}_x$ and $\hat{R}_y$ and the four rotators $\hat{R}_j$, $j = 1, 2, 3, 4$. The eigenstates of the strings and three of the rotators (we arbitrarily remove $\hat{R}_4$, dashed loop) form a basis for the physical states of the pure gauge theory. To describe the physical states for a generic charge configuration we add three charge strings (dotted green arrows) that correspond to a conventional physical state for the given charge configuration.

of the eight gauge fields on the lattice are redundant, and the Hamiltonian in (5.1) can be solely expressed in terms of the remaining five (see App. B.1 in [3] for details).

Describing the system in terms of these five gauge fields, however, entails serious drawbacks. The resulting effective Hamiltonian contains many-body interactions (see App. B.1 in [3]) which are prohibitively expensive to implementation using current quantum hardware. To circumvent this problem, we consider a natural basis for the physical states in terms of small loops around each plaquette, and large electric loops around the whole lattice. In such a basis, the electric and magnetic Hamiltonians take a simpler form, and are expressed in terms of a set of operators, *rotators* and *strings* (see Fig. 5.1), that are diagonal in the loop basis.

With the notation and conventions presented in Fig. 5.1, rotators and strings are given by

the relations

$$\begin{aligned}
\hat{E}_{(0,0),\boldsymbol{e}_x} &= \hat{R}_1 + \hat{R}_x - (\hat{q}_{(1,0)} + \hat{q}_{(1,1)}),\\
\hat{E}_{(1,0),\boldsymbol{e}_x} &= \hat{R}_2 - \hat{R}_3 + \hat{R}_x,\\
\hat{E}_{(1,0),\boldsymbol{e}_y} &= \hat{R}_1 - \hat{R}_2 - \hat{q}_{(1,1)},\\
\hat{E}_{(1,1),\boldsymbol{e}_y} &= -\hat{R}_3,\\
\hat{E}_{(0,1),\boldsymbol{e}_x} &= -\hat{R}_1,\\
\hat{E}_{(1,1),\boldsymbol{e}_x} &= \hat{R}_3 - \hat{R}_2,\\
\hat{E}_{(0,0),\boldsymbol{e}_y} &= \hat{R}_2 - \hat{R}_1 + \hat{R}_y - \hat{q}_{(0,1)},\\
\hat{E}_{(0,1),\boldsymbol{e}_y} &= \hat{R}_3 + \hat{R}_y,
\end{aligned} \tag{5.8}$$

where the charges $\hat{q}_{\boldsymbol{n}}$ are inserted to satisfy the Gauss' law. An intuitive way to understand the effect of the charge terms in (5.8) is to consider them as sources of additional electric strings , as displayed by the green lines in Fig. 5.1(b).

By recalling the plaquette operator $\hat{P}_{\boldsymbol{n}}$ in (5.2), it becomes clear why $\hat{R}_i$ and $\hat{R}_\mu$ are a convenient choice to represent the electric gauge field components. The operator $\hat{P}_{\boldsymbol{n}}$ increases the anticlockwise quanta of the electric field circulating in the $\boldsymbol{n}$-th plaquette. Consequently, it does not act on strings and takes the form of the lowering operator of the associated rotator. This fact can be formally proven by examining the raising and lowering operators of rotators and strings. From the commutation relations of the links and the relations shown in (5.8), it follows that

$$\begin{aligned}
\left[\hat{R}_i, \hat{P}_j\right] =& \delta_{i,j}\hat{P}_j,\\
\left[\hat{R}_x, \hat{U}_{(0,0),\boldsymbol{e}_x}\hat{U}_{(1,0),\boldsymbol{e}_x}\right] =& \hat{U}_{(0,0),\boldsymbol{e}_x}\hat{U}_{(1,0),\boldsymbol{e}_x} \equiv \hat{P}_x,\\
\left[\hat{R}_y, \hat{U}_{(0,0),\boldsymbol{e}_y}\hat{U}_{(0,1),\boldsymbol{e}_y}\right] =& \hat{U}_{(0,0),\boldsymbol{e}_y}\hat{U}_{(0,1),\boldsymbol{e}_y} \equiv \hat{P}_y,
\end{aligned} \tag{5.9}$$

where $\hat{P}_j$, $j = 1, 2, 3$ is the plaquette operator of plaquette j as denoted in Fig. 5.1. Moreover, we defined the string lowering operators $\hat{P}_x \equiv \hat{U}_{(0,0),\boldsymbol{e}_x}\hat{U}_{(1,0),\boldsymbol{e}_x}$ and $\hat{P}_y \equiv \hat{U}_{(0,0),\boldsymbol{e}_y}\hat{U}_{(0,1),\boldsymbol{e}_y}$.

The magnetic Hamiltonian for the periodic plaquette in Fig. 5.1(b),

$$\hat{H}_B = -\frac{1}{2g^2a^2}\left(\hat{P}_1 + \hat{P}_2 + \hat{P}_3 + \hat{P}_4 + h.c.\right), \tag{5.10}$$

is proportional to the sum of four plaquette operators, while there are only three independent rotators. The fourth rotator can be written as a combination of the others, since the effect of lowering (raising) all other rotators, i.e. $\hat{R}_1$, $\hat{R}_2$ and $\hat{R}_3$, amounts to raising (lowering) $\hat{R}_4$. In particular, one can verify using (5.8) that lowering all of the three rotators $\hat{R}_1$, $\hat{R}_2$ and $\hat{R}_3$

is equivalent to raising the electric fields on the links constituting $\hat{R}_4$. As such, the magnetic Hamiltonian becomes

$$\hat{H}_B = -\frac{1}{2g^2a^2}\left(\hat{P}_1 + \hat{P}_2 + \hat{P}_3 + \hat{P}_3^\dagger \hat{P}_2^\dagger \hat{P}_1^\dagger + h.c.\right), \tag{5.11}$$

while, by inserting (5.8) into (5.1), the electric term takes the form:

$$\begin{aligned}\hat{H}_E = g^2\Bigg\{ & 2\left[\hat{R}_1^2 + \hat{R}_2^2 + \hat{R}_3^2 - \hat{R}_2(\hat{R}_1 + \hat{R}_3)\right] + \hat{R}_x^2 + \hat{R}_y^2 + (\hat{R}_1 + \hat{R}_2 - \hat{R}_3)\hat{R}_x \\ & - (\hat{R}_1 - \hat{R}_2 - \hat{R}_3)\hat{R}_y - \Big[\hat{q}_{(1,0)}(\hat{R}_1 + \hat{R}_x) + \hat{q}_{(0,1)}(\hat{R}_2 - \hat{R}_1 + \hat{R}_y) \\ & + \hat{q}_{(1,1)}(2\hat{R}_1 - \hat{R}_2 + \hat{R}_x)\Big] + \frac{\hat{q}_{(1,0)}^2 + \hat{q}_{(0,1)}^2 + 2\hat{q}_{(1,1)}(\hat{q}_{(1,0)} + \hat{q}_{(1,1)})}{2}\Bigg\}. \end{aligned} \tag{5.12}$$

Next, we consider the matter Hamiltonian $\hat{H}_{\text{matter}} = \hat{H}_M + \hat{H}_K$. While the mass term in (5.5) is independent of the gauge fields, the kinetic contribution has to be modified. The kinetic contribution in (5.6) corresponds to the creation or annihilation of a particle-antiparticle pair on neighbouring lattice sites and the simultaneous adjustment of the electric field on the link in between. The green lines in Fig. 5.1(b) mark the fields $\hat{E}_{(0,0),\boldsymbol{e}_x}$, $\hat{E}_{(0,0),\boldsymbol{e}_y}$ and $\hat{E}_{(1,0),\boldsymbol{e}_y}$ which are automatically adjusted when charges are created. This fact follows from our choice of enforcing the three Gauss' law constraints on exactly those links. For any other link, we require combinations of raising and lowering operators $\hat{P}_j$ and $\hat{P}_\mu$ ($j = 1, 2, 3$ and $\mu = x, y$) such that the specific link is adjusted, while all others remain unchanged. As an example, let us consider the generation of a particle in position $(1, 1)$ and an antiparticle in $(1, 0)$. This choice implies either that the electric field $\hat{E}_{(1,0),\boldsymbol{e}_y}$ has to decrease , or that the electric field $\hat{E}_{(1,1),\boldsymbol{e}_y}$ has to increase and hence the rotator $\hat{R}_3$ has to decrease. However, this action changes the electric fields $\hat{E}_{(1,1),\boldsymbol{e}_x}$, $\hat{E}_{(0,1),\boldsymbol{e}_y}$ and $\hat{E}_{(1,0),\boldsymbol{e}_x}$ as well. To remedy that, we lower the rotator $\hat{R}_2$, adjusting $\hat{E}_{(1,1),\boldsymbol{e}_x}$ and $\hat{E}_{(1,0),\boldsymbol{e}_x}$, and raise the string $\hat{R}_y$ to compensate for the change in $\hat{E}_{(0,1),\boldsymbol{e}_y}$. Following the same procedure, the rules for translating the kinetic Hamiltonian of (5.6) into the language of rotators and strings

read

$$
\begin{aligned}
&\hat{\Psi}^\dagger_{(0,0)}\hat{U}^\dagger_{(0,0),\boldsymbol{e}_x}\hat{\Psi}_{(1,0)} \to \hat{\Psi}^\dagger_{(0,0)}\hat{\Psi}_{(1,0)},\\
&\hat{\Psi}^\dagger_{(1,0)}\hat{U}^\dagger_{(1,0),\boldsymbol{e}_x}\hat{\Psi}_{(0,0)} \to \hat{\Psi}^\dagger_{(1,0)}\hat{P}^\dagger_x\hat{\Psi}_{(0,0)},\\
&\hat{\Psi}^\dagger_{(1,0)}\hat{U}^\dagger_{(1,0),\boldsymbol{e}_y}\hat{\Psi}_{(1,1)} \to \hat{\Psi}^\dagger_{(1,0)}\hat{\Psi}_{(1,1)},\\
&\hat{\Psi}^\dagger_{(1,1)}\hat{U}^\dagger_{(1,1),\boldsymbol{e}_y}\hat{\Psi}_{(1,0)} \to \hat{\Psi}^\dagger_{(1,1)}\hat{P}^\dagger_y\hat{P}_2\hat{P}_3\hat{\Psi}_{(1,0)},\\
&\hat{\Psi}^\dagger_{(0,1)}\hat{U}^\dagger_{(0,1),\boldsymbol{e}_x}\hat{\Psi}_{(1,1)} \to \hat{\Psi}^\dagger_{(0,1)}\hat{P}_1\hat{\Psi}_{(1,1)},\\
&\hat{\Psi}^\dagger_{(1,1)}\hat{U}^\dagger_{(1,1),\boldsymbol{e}_x}\hat{\Psi}_{(0,1)} \to \hat{\Psi}^\dagger_{(1,1)}\hat{P}^\dagger_x\hat{P}_2\hat{\Psi}_{(0,1)},\\
&\hat{\Psi}^\dagger_{(0,0)}\hat{U}^\dagger_{(0,0),\boldsymbol{e}_y}\hat{\Psi}_{(0,1)} \to \hat{\Psi}^\dagger_{(0,0)}\hat{\Psi}_{(0,1)},\\
&\hat{\Psi}^\dagger_{(0,1)}\hat{U}^\dagger_{(0,1),\boldsymbol{e}_y}\hat{\Psi}_{(0,0)} \to \hat{\Psi}^\dagger_{(0,1)}\hat{P}^\dagger_y\hat{\Psi}_{(0,0)}.
\end{aligned}
\tag{5.13}
$$

Inserting these into (5.6), we obtain the kinetic contribution to the total Hamiltonian as

$$
\begin{aligned}
\hat{H}_K \;=\; \kappa\Big[&\hat{\Psi}^\dagger_{(0,0)}(\mathbb{1}+\hat{P}_x)\hat{\Psi}_{(1,0)} + \hat{\Psi}^\dagger_{(0,1)}(\hat{P}_1+\hat{P}_2^\dagger\hat{P}_x)\hat{\Psi}_{(1,1)}\\
&+\hat{\Psi}^\dagger_{(0,0)}(\mathbb{1}+\hat{P}_y)\hat{\Psi}_{(0,1)} + \hat{\Psi}^\dagger_{(1,0)}(\mathbb{1}+\hat{P}_2^\dagger\hat{P}_3^\dagger\hat{P}_y)\hat{\Psi}_{(1,1)} + h.c.\Big].
\end{aligned}
\tag{5.14}
$$

The effective Hamiltonian we derive here for a periodic plaquette can be extended to a torus of arbitrary size [see Sec. 5.4.2]. We will use the just derived Hamiltonian to compute the expectation value of the plaquette operator

$$
\langle\Box\rangle = -\frac{g^2a^2}{V}\langle\Psi_0|\,\hat{H}_B\,|\Psi_0\rangle\,,
\tag{5.15}
$$

where $|\Psi_0\rangle$ is the ground state, and V the number of plaquettes in the lattice, $V=4$ in this case. The expectation value of the operator $\Box$ is defined as a dimensionless number, which is bounded by ±1 and proportional to the magnetic energy.

5.2 Transformation into the magnetic representation

In the following, we describe a transformation between the so-called electric representation, where $\hat{H}_E$ is diagonal, to the magnetic one, where $\hat{H}_B$ is diagonal. We demonstrate it for the minimal periodic system introduced in Sec. 5.1.2 and consider its generalisations in Sec. 5.4.

We consider the pure gauge Hamiltonian, which is the sum of (5.11,5.12), where all charges $\hat{q}_{\boldsymbol{n}}$ in (5.12) are set to zero. Furthermore, we observe that the lowering (raising) operators $\hat{P}_x^{(\dagger)}$

and $\hat{P}_y^{(\dagger)}$ acting on the strings are solely contained in the now absent kinetic Hamiltonian in (5.14). Therefore, the considered Hamiltonian commutes with $\hat{R}_x$ and $\hat{R}_y$, i.e. $[\hat{H}_{\text{gauge}}, \hat{R}_x] = [\hat{H}_{\text{gauge}}, \hat{R}_y] = 0$, and thus, the strings are constants of motion. The dynamics induced by the pure gauge Hamiltonian are then restricted to different subspaces defined by $\hat{R}_\mu |r_\mu\rangle = r_\mu |r_\mu\rangle$, for $\mu = x, y$. In Sec. 5.3, we will be interested in a ground state property, and thus, we restrict ourselves to the subspace where both strings are confined to the vacuum, i.e, $r_\mu = 0$. The effective Hamiltonian of this subspace can be readily obtained by setting $\hat{R}_x = \hat{R}_y = 0$ in (5.11,5.12), which yields

$$\begin{aligned}
\hat{H}^{(\text{e})} &= \hat{H}_E^{(\text{e})} + \hat{H}_B^{(\text{e})}, \\
\hat{H}_E^{(\text{e})} &= 2g^2 \left[\hat{R}_1^2 + \hat{R}_2^2 + \hat{R}_3^2 - \hat{R}_2(\hat{R}_1 + \hat{R}_3)\right], \\
\hat{H}_B^{(\text{e})} &= -\frac{1}{2g^2a^2}\left[\hat{P}_1 + \hat{P}_2 + \hat{P}_3 + \hat{P}_1\hat{P}_2\hat{P}_3 + h.c.\right],
\end{aligned} \tag{5.16}$$

where we introduced the superscript (e) to denote the *electric* representation.

Since the three rotators possess discrete but infinite spectra, any numerical approach for simulating the Hamiltonian in (5.16) requires a truncation of the Hilbert space. In the following, l denotes the cut-off value which is identified by

$$\hat{R}_j |r_j\rangle = r_j |r_j\rangle \;\; \forall\, r_j = -l, -l+1, \ldots, l. \tag{5.17}$$

Thus, the action of the truncated lowering operators is given as

$$\hat{P}_j |r_j\rangle = \begin{cases} |r_j - 1\rangle, & \text{if } r_j > -l \\ 0, & \text{if } r_j = -l. \end{cases} \tag{5.18}$$

Note that the total dimension of the Hilbert space is reduced to $(2l+1)^3$. The challenge remains that calculations in the weak coupling regime typically require large values of l, leading to a large memory requirement, and until now, no practical methods to solve this issue have been available.

Let us now introduce a formulation that allows for an efficient representation of the Hamiltonian's eigenstates in the weak coupling regime, where $g \ll 1$. It is based on the exchange of the continuous U(1) group with the discrete group $\mathbb{Z}_{2L+1}$, which provides a discrete basis for the vector potential operators $\hat{A}_{\boldsymbol{n},\boldsymbol{e}_\mu}$ and enables a direct transformation into this dual basis via a Fourier transform. The approach is motivated by the key observation that, in the electric representation, the Hamiltonians of the continuous U(1) group and the discrete $\mathbb{Z}_{2L+1}$ group after truncation ($l < L$) are equivalent. The group $\mathbb{Z}_{2L+1}$ consists of $2L+1$ elements, thus the parameter L indicates the size of the Hilbert space. In particular, the rotators $\hat{R}_j$ and lowering (raising)

operators $\hat{P}_j^{(\dagger)}$ $(j = 1, 2, 3)$ take the form

$$\begin{aligned} \hat{R}_j |r_j\rangle &= r_j |r_j\rangle \ \forall\, r_j = -L, \ldots, L \\ \hat{P}_j |r_j\rangle &= \begin{cases} |r_j - 1\rangle\,, & \text{if}\, r_j > -L \\ |L\rangle\,, & \text{if}\, r_j = -L. \end{cases} \end{aligned} \tag{5.19}$$

The only difference between the truncated U(1) group and untruncated $\mathbb{Z}_{2L+1}$ group is the cyclic property of the lowering (raising) operator, which maps $|L\rangle$ to $|-L\rangle$ (and vice versa). However, after a truncation of $\mathbb{Z}_{2L+1}$ with $l < L$, this property is lost, meaning that (5.18,5.19) correspond to each other and the two truncated groups become equivalent.

We begin by considering the Hamiltonian which employs the complete $\mathbb{Z}_{2L+1}$ group. Importantly, the relations in (5.19) resort to a compact description of the electric field since the spectra of the rotators and strings are constrained to the compact interval $[-L, L]$. We now introduce the following replacement rules for these operators,

$$\begin{aligned} \hat{R} &\mapsto \sum_{\nu=1}^{2L} f_\nu^s \sin\left(\frac{2\pi\nu}{2L+1}\hat{R}\right), \\ \hat{R}^2 &\mapsto \sum_{\nu=1}^{2L} f_\nu^c \cos\left(\frac{2\pi\nu}{2L+1}\hat{R}\right) + \frac{L(L+1)}{3}\mathbb{1}, \end{aligned} \tag{5.20}$$

which reassemble Fourier series expansions. Crucially, this replacement is exact, i.e. there is no truncation of the Fourier series. Using the fact that the spectrum of $\hat{R}$ is discrete and integer-valued, the periodicity of the trigonometric functions can be exploited, which allows one to perform a summation over all coefficients where the sine (cosine) is equivalent. Hence, a finite number of $2L$ coefficients remain, which take the form

$$f_\nu^s = \frac{(-1)^{\nu+1}}{2\pi}\left[\psi_0\left(\frac{2L+1+\nu}{2(2L+1)}\right) - \psi_0\left(\frac{\nu}{2(2L+1)}\right)\right] \tag{5.21}$$

$$f_\nu^c = \frac{(-1)^{\nu}}{4\pi^2}\left[\psi_1\left(\frac{\nu}{2(2L+1)}\right) - \psi_1\left(\frac{2L+1+\nu}{2(2L+1)}\right)\right]. \tag{5.22}$$

Here, $\psi_k(\cdot)$ is the k-th polygamma function. Let us further remark that these rules can be extended to higher powers in the variables $\hat{R}$ than considered in (5.20).

This replacement turns out to be convenient for the basis transformation explained below. Introducing the convention $|\boldsymbol{r}\rangle = |r_1\rangle\,|r_2\rangle\,|r_3\rangle$ and recalling (5.19), the electric contribution from

(5.16) reads

$$\hat{H}_E^{(\mathrm{e})} = 2g^2 \sum_{\boldsymbol{r}=-\boldsymbol{L}}^{\boldsymbol{L}} \sum_{\nu=1}^{2L} \left\{ f_\nu^c \sum_{j=1}^{3} \cos\left(\frac{2\pi\nu}{2L+1} r_j\right) - f_\nu^s \sin\left(\frac{2\pi\nu}{2L+1} r_2\right) \sum_{\mu=1}^{2L} f_\mu^s \Big[\sin\left(\frac{2\pi\mu}{2L+1} r_1\right) + \sin\left(\frac{2\pi\mu}{2L+1} r_3\right) \Big] \right\} |\boldsymbol{r}\rangle\langle\boldsymbol{r}| \,. \tag{5.23}$$

Note that we use the notation $\sum_{\boldsymbol{r}=-\boldsymbol{L}}^{\boldsymbol{L}}$ to indicate that the sum collects all combinations of r_j, where $r_j \in [-L, L]$, $j = 1, 2, 3$ and we neglected the constant energy shifts introduced by (5.20). The $\mathbb{Z}_{2L+1}$ magnetic Hamiltonian $\hat{H}_B^{(\mathrm{e})}$ can be obtained by substituting the cyclic $\hat{P}_j$ of (5.19) into (5.16).

We can now perform the transformation to the dual basis. It can be straightforwardly verified that

$$\hat{\mathcal{F}}_{2L+1} \hat{P}^\gamma \hat{\mathcal{F}}_{2L+1}^\dagger = \sum_{r=-L}^{L} \exp^{-i\frac{2\pi}{2L+1}\gamma r} |r\rangle\langle r| \,, \tag{5.24}$$

where $\gamma \in \mathbb{Z}$ [1]. Moreover, for any $N - 1 \geq J \in \mathbb{N}$, we have that

$$\hat{\mathcal{F}}_{2L+1}^{\otimes J} \left[\bigotimes_{j=1}^{J} \hat{P}_j^\gamma \right] (\hat{\mathcal{F}}_{2L+1}^\dagger)^{\otimes J} = \sum_{\boldsymbol{r}=-\boldsymbol{L}}^{\boldsymbol{L}} \exp^{-i\frac{2\pi}{2L+1}\boldsymbol{\gamma}\boldsymbol{r}} |\boldsymbol{r}\rangle\langle\boldsymbol{r}| \,, \tag{5.25}$$

where $\boldsymbol{r} = (r_1, r_2, \ldots, r_J)^{\mathrm{T}}$, $\boldsymbol{\gamma} = (\gamma_1, \gamma_2, \ldots, \gamma_J)^{\mathrm{T}}$, and the tensor product of the Fourier transforms act on the separate $N - 1$ spaces. Note that, in particular $(\hat{P}^\gamma)^\dagger = \hat{P}^{-\gamma}$ and therefore:

$$(\hat{\mathcal{F}}_{2L+1})^{\otimes J} \left[\bigotimes_{j=1}^{J} \hat{P}_j^\gamma \pm \bigotimes_{j=1}^{J} \hat{P}_j^{-\gamma} \right] (\hat{\mathcal{F}}_{2L+1}^\dagger)^{\otimes J} = 2 \sum_{\boldsymbol{r}=-\boldsymbol{L}}^{\boldsymbol{L}} \begin{cases} \cos\left(\frac{2\pi\boldsymbol{r}\boldsymbol{\gamma}}{2L+1}\right) |\boldsymbol{r}\rangle\langle\boldsymbol{r}| & \text{for } + \\ -i \sin\left(\frac{2\pi\boldsymbol{r}\boldsymbol{\gamma}}{2L+1}\right) |\boldsymbol{r}\rangle\langle\boldsymbol{r}| & \text{for } - \end{cases} . \tag{5.26}$$

[1] This relation is quite clear from the perspective of quantum arithmetic. Note that operationally, $\hat{P}^\gamma$ performs a modulo-$(2L+1)$ addition of a classical number on a quantum state, i.e., $|a\rangle \to |a + \gamma\rangle$. As pointed out in in [164], modular addition can be implemented efficiently as bit-wise phase gates on $|a\rangle$ in the Fourier basis.

Hence, by applying the discrete Fourier transform to the pure gauge Hamiltonian we diagonalise the magnetic contributions, while sacrificing the diagonal structure in the electric part, i.e.

$$\hat{H}_E^{(\mathrm{b})} = g^2 \sum_{\nu=1}^{2L} \left\{ f_\nu^c \sum_{j=1}^{3} \hat{P}_j^\nu + \frac{f_\nu^s}{2} \left[\hat{P}_2^\nu - (\hat{P}_2^\dagger)^\nu \right] \sum_{\mu=1}^{2L} f_\mu^s \left[\hat{P}_1^\mu + \hat{P}_3^\mu \right] \right\} + h.c., \tag{5.27}$$

and

$$\hat{H}_B^{(\mathrm{b})} = \frac{-1}{g^2 a^2} \sum_{\boldsymbol{r}=-\boldsymbol{L}}^{\boldsymbol{L}} \left[\cos\left(\frac{2\pi(r_1+r_2+r_3)}{2L+1} \right) + \sum_{i=1}^{3} \cos\left(\frac{2\pi r_i}{2L+1} \right) \right] |\boldsymbol{r}\rangle\langle\boldsymbol{r}| \,, \tag{5.28}$$

where the superscript (b) refers to the *magnetic* representation of the Hamiltonian. Using this representation, computations in the weak coupling regime $g \ll 1$ can be performed efficiently, as a truncation l now dictates the cut-off for the magnetic field energy. We emphasize that although we employed the rotator formulation of the Hamiltonian, the just presented procedure is likewise valid for the link formulation utilizing the electric field operators. Indeed, the replacement rules in (5.20) are then formulated in terms of $\hat{E}$ instead of $\hat{R}$ and inserted into the Hamiltonian in (5.1). The corresponding magnetic representation is analogously obtained via an application of the Fourier transform.

The parameter L now affects the accuracy of the simulation. In fact, while L is completely irrelevant in the electric representation (truncated U(1) and truncated $\mathbb{Z}_{2L+1}$ are equivalent), it strongly influences the results derived in the magnetic representation. The relationship between L and l is examined in more detail in Sec. 5.3. In the following, we qualitatively discuss our procedure to simulate the U(1) group with the two representations of $\mathbb{Z}_{2L+1}$. In the electric representation, for any g, we can always formulate a sequence of approximating representations for any quantum state of the system in the computational basis defined by $|\boldsymbol{r}\rangle$, i.e.,

$$|\psi^{(\mathrm{e})}(g)\rangle = \sum_{\boldsymbol{r}=-\boldsymbol{\infty}}^{\boldsymbol{\infty}} p_{U(1)}(g,\boldsymbol{r}) \, |\boldsymbol{r}\rangle \approx \sum_{\boldsymbol{r}=-\boldsymbol{L}}^{\boldsymbol{L}} p_{\mathbb{Z}_{2L+1}}(g,\boldsymbol{r}) \, |\boldsymbol{r}\rangle \approx \sum_{\boldsymbol{r}=-\boldsymbol{l}}^{\boldsymbol{l}} p^{(\mathrm{e})}(g,\boldsymbol{r}) \, |\boldsymbol{r}\rangle \,. \tag{5.29}$$

Here, $p^{(\mathrm{e})}$ denotes the expansion coefficients in the electric representation, with the subscript indicating the group to which they are referring to (no subscript stands for the truncated $\mathbb{Z}_{2L+1}$). The first approximation in (5.29) is due to the approximation from U(1) to the $\mathbb{Z}_{2L+1}$ group, while the second approximation represents the *truncation* from $(2L+1)^3$ down to $(2l+1)^3$ states.

The same scheme exists for the magnetic representation, where the weights $p^{(\mathrm{b})}(g,\boldsymbol{r},L)$ are used for the state $\left|\psi^{(\mathrm{b})}(g,L)\right\rangle$. In this case, however, the choice of L is important. While the truncated electric representation directly corresponds to the truncated and compact U(1) formulation, the magnetic representation is crucially affected by the level of discretisation L. This relation is examined further in Sec. 5.3.1, where we study the convergence of the two representations to U(1) for intermediate values of the coupling g.

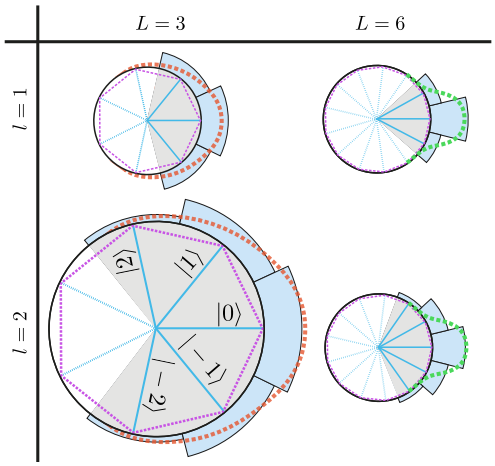

Figure 5.2: **Discrete approximation of a continuous distribution of states in the magnetic representation.** The ability to approximate a state is related to the quotient l/L. For a given l, L controls the resolution of the approximation, which is always centred around the vacuum $|\mathbf{0}\rangle$. Black circles represent the U(1) group, the violet $2L+1$ edged polygon the $\mathbb{Z}_{2L+1}$ group. Blue lines (solid and dashed) mark the $2L+1$ states of $\mathbb{Z}_{2L+1}$, while only the $2l+1$ states indicated with the solid lines are kept after truncating. Red and green markers are pictorial representations of states in U(1) while the light blue areas correspond to their binned approximation.

The interplay of the parameters L and l can be intuitively understood by employing a geometrical illustration. In Fig. 5.2, the black circles represent the continuous U(1) group, which is approximated by $2L+1$ possible states (blue lines) of the $\mathbb{Z}_{2L+1}$ group. For $l = L$, we faithfully describe the untruncated $\mathbb{Z}_{2L+1}$ group, and use both the solid and the dashed blue lines in the figure. By choosing $l < L$, we select the states marked with solid blue lines that lie symmetrically around $|\boldsymbol{r} = \mathbf{0}\rangle$ and achieve a binned approximation of any continuous $p_{U(1)}$ lying in the grey area. Furthermore, for any fixed l, the parameter L controls the spread of the available basis states (or bins) around $|\mathbf{0}\rangle$. Since we are interested in the convergence of the truncated $\mathbb{Z}_{2L+1}$ to U(1) which occurs for $L \to \infty$, we only consider the $2l+1$ states that are important for the dynamics. In particular, we disregard cyclic effects from the lowering operator $\hat{P}$ that are a distinctive feature of $\mathbb{Z}_{2L+1}$ with respect to U(1) [see (5.19)].

As an example of this relationship between l and L, consider the two distributions drawn from U(1), represented by the red and green dashed lines in Fig. 5.2. Clearly, the combination $L = 3$, $l = 1$ is insufficient to approximate the broad red distribution. Hence, we increase l to completely cover the target distribution within the grey shaded area. By increasing L to 6, our binned approximation has a higher resolution around the zero state. However, depending on the target distribution, one may also need a higher l. For instance, for $L = 6$, $l = 2$ approximates

the green state better than $l = 1$. To summarise, L is determined by the spread of the target distribution, while l determines the number of bins stored in the simulation. In practice, l will be limited by the amount of memory of a classical or quantum computer.

5.3 Performance and application of the new approach

In the previous section we outlined the transformation from the electric to the magnetic representation, suited to describe the strong and the weak coupling limits, respectively. Here, we develop a protocol which allows for assessing convergence of the truncated representations.

Hereafter, we set the lattice spacing $a = 1$, but emphasise that the following results hold for other values of a.

5.3.1 Fidelity and convergence of the two representations

This section is devoted to a convergence analysis, which examines the agreement between the two representations. Although we have developed a scheme that allows one to represent, discretise and truncate the Hamiltonian in the weak coupling regime, the optimal choice of the parameter L is not clear a priori. Clearly, l should usually be chosen according to the availability of the computational resources, which then determines the most suitable L depending on the bare coupling. Furthermore, it is unclear which representation to choose if one is not explicitly considering one of the extremal regimes, $g \gg 1$ and $g \ll 1$.

We first develop a criteria to estimate the agreement of the two representations. Therefore, we employ their relation via a unitary transformation and define the *Fourier fidelity* F_{f} with respect to the same state derived in both representations, e.g. an eigenstates belonging to the same eigenvalue of some observable, such as the ground state derived in both (truncated) representations for a fixed value of g. We write F_{f} as

$$F_{\mathrm{f}}(l) = \max_{L>l} \left| \left\langle \psi^{(\mathrm{b})}(L,l) \right| \hat{\mathcal{F}}(L,l) \left| \psi^{(\mathrm{e})}(l) \right\rangle \right|^2 , \tag{5.30}$$

where the Fourier transform

$$\hat{\mathcal{F}}(L,l) = \left(\frac{1}{\sqrt{2L+1}} \sum_{k,j=-l}^{l} \mathrm{e}^{i\frac{2\pi}{2L+1}jk} \, |j\rangle\langle k| \right)^{\otimes 3} \tag{5.31}$$

is truncated, i.e. the indices of the sums are limited by $\pm l$ instead of $\pm L$[2]. Due to the truncation, the features captured in both states are not necessarily equivalent which results in low values

[2]Note that this is a consequence of the truncated Hilbert space. However, the operator in (5.31) not being unitary is no limitation, since the states in (5.30) could be embedded in the Hilbert space required by the full Fourier transform. Here, the coefficients for each basis element c_n with $n > l$ are set to zero in both representations.

of the Fourier fidelity. Vice versa, high values indicate that – for the considered state – the representations are equivalent and yield the same result. Note that this further suggests that the result is close to the hypothetical one derived within the untruncated theory, since the unification of both representations nearly covers the total Hilbert space[3].

A low Fourier fidelity, however, is not the only decisive criteria whether a derived result is robust against changes in l or L, especially in the extremal regimes of the bare coupling where the truncation effects of the unsuitable representation are severe. We thus employ the so called *sequence Fidelity* F_s, which measures the overlap of the same state (in the chosen representation) derived within successive values of truncations $l-1$ and l,

$$F_\mathrm{s}^{(\mu)}(l,L) = \sum_{\boldsymbol{r}=-\boldsymbol{l}+\boldsymbol{1}}^{\boldsymbol{l}-\boldsymbol{1}} \left\langle \psi^{(\mu)}(l-1,L)\middle|\boldsymbol{r}\right\rangle \left\langle \boldsymbol{r}\middle|\psi^{(\mu)}(l,L)\right\rangle . \tag{5.32}$$

Here, $\mu = e, b$ indicates considered representation while L is only present in the magnetic case (in the electric representation we can use the truncated U(1) model). Since the truncated models converge to the untruncated U(1) model in the limit $l \to \infty$, high values of F_s indicate, under a suitable assumption, that the chosen truncation l is able to capture the whole distribution of the wave vector (as for the case $l = 2$, $L = 3$ in Fig. 5.2). Such a conclusion cannot be drawn in the case where the distribution is multimodal with disjoint fractions that lay outside the covered space. Then, the sequence fidelity yields high values for subsequent values of l but would not for larger differences of the considered truncation. Nevertheless, this represents a common issue present in all approaches employing truncation techniques that lack the exact true solution.

Let us now return to the ground state of the pure gauge model. Due to their diagonal forms, the electric (magnetic) representation yields more accurate results in the strong (weak) coupling regime. In the intermediate regime $g \approx 1$, we use the Fourier fidelity as an indicator as to whether the chosen representation and truncation is enough to capture the properties of the ground state. Fig. 5.3(a) illustrates the Fourier infidelity $1 - F_\mathrm{f}(l)$ of the ground state for different values of g^{-2}. The global minimum of the Fourier infidelity implies that the truncation l and resolution L are big enough to both contain and resolve the details of the state's distribution. For example, in Fig. 5.2, it becomes clear that an increase in resolution L reduces the available domain to accommodate a distribution with too high spread if l is not increased accordingly.

In the remainder of this section, we will focus on the strong and weak coupling regime where the Fourier fidelity is not meaningful due to the inability of both representations to express the state within a truncated basis. For the electric representation, the sequence Fidelity has a simple interpretation (L is absent here) as it quantifies the overlap between the ground state obtained with different truncations. Since the energy spectrum is fixed and does not depend upon L, a unit

[3]Recall that under the Fourier transform, local features are transformed into global ones and vice versa, e.g. a Gaussian is transformed into a Gaussian with inverse width.

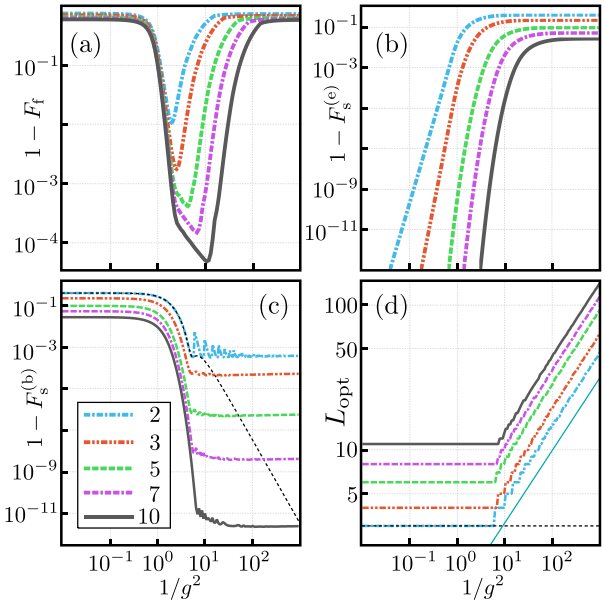

Figure 5.3: **Convergence analysis of the basis representations.** In (a), the Fourier infidelity in the intermediate region is decreasing with l as the whole wave function can be captured by the truncation. The sequence infidelities in (b) and (c) illustrate convergence to the U(1) theory and the freezing effect respectively. The values of L optimizing the sequence fidelities of (c) are displayed in (d). Here, freezing is detected by curves similar to the black dashed lines.

value of $F_\mathrm{s}^{(\mathrm{e})}(l)$ implies that the considered state is unaffected by an increase in l. This suggests that higher truncations do not improve the result and that the model converged to the untruncated U(1) ground state, which can be further motivated by examining the behaviour of $1-F_\mathrm{s}^{(\mathrm{e})}(l)$ in Fig. 5.3(b). As expected, in the strong coupling regime the sequence Fidelity approaches unity, indicating convergence to the untruncated model, where it is helpful to recall that the ground state in this limit is given by a single basis state, $|\mathbf{0}\rangle$. Approaching the intermediate regime $g \approx 1$, $F_\mathrm{s}^{(\mathrm{e})}(l)$ reduces to a l-dependent constant value, which indicates that the truncation is insufficient to describe all features of the ground state appropriately.

In the magnetic representation, the situation is substantially more complicated, since the approximation of the continuous U(1) group with the discrete $\mathbb{Z}_{2L+1}$ group introduces the intricate interplay of l and L. As mentioned above, higher values of L allow for a better local approximation of the state which comes at the expense of the tails, which are cut off if l is too small (see Fig. 5.2). In terms of the sequence fidelity $F_\mathrm{s}^{(\mathrm{b})}(l, L)$, this implies that for each value of l there exists a unique optimal value L_opt of L. Let us stress that this is only true for the ground state of the pure gauge theory considered here. In a more general setting, possibly including matter and higher excited

states, $F_{\mathrm{s}}^{(\mathrm{b})}(l, L)$ might have multiple optimal values of L.

Another complication is given by the fact that L_{opt} does not necessarily corresponds to the global maximum of the sequence fidelity. In particular, a *freezing* effect can occur for highly localised distributions, where the resolution L is insufficient to capture any of its features. Consequently $\left|\psi^{(\mathrm{b})}(l, L)\right\rangle$ and $\left|\psi^{(\mathrm{b})}(l+1, L)\right\rangle$ are practically the same state and thus yield high values of the sequence fidelity in (5.32). In the scenario examined here, the freezing mechanism can be observed in the weak coupling regime, where the ground state is highly localised around $|\mathbf{0}\rangle$. If L is too small, i.e. the bin belonging to the latter state is to wide, all population is accumulated there and the state does not change if g is decreased while L is kept constant. However, it is possible to identify the freezing effect by an educated interpretation of $F_{\mathrm{s}}^{(\mathrm{b})}$.

Fig. 5.3(c) illustrates that the sequence infidelity $1-F_{\mathrm{s}}^{(\mathrm{b})}(l, L_{\mathrm{opt}})$ in both regimes saturates at a l-dependent value. Analogous to the electric representation, it saturates in the strong coupling regime ($g \gg 1$), however the saturation for weak coupling stems from the limited ability to approximate a continuous approximation with a fixed number of discrete levels. To be more precise, for every l the optimal L_{opt} is chosen as the best compromise of resolution around $|\mathbf{0}\rangle$ and a proper representation of the tails of the distribution. In Fig. 5.3(d), We demonstrate numerically that L_{opt} increases as g is decreased (see App. F in [3] for more details). Moreover, the black dashed line in Fig. 5.3(c) corresponds to the global maximum of $F_{\mathrm{s}}^{(\mathrm{b})}(l=1, L)$ for all g^{-2}. It does not saturate and vanishes in the limit $g^{-2} \to \infty$. Comparison with the black dashed line in Fig. 5.3(d), which indicates that $L_{\mathrm{opt}} \equiv l+1$, reveals this as a characteristic of the mentioned freezing effect.

In conclusion, both the Fourier and the sequence fidelities in (5.30,5.32) can be used to assess the convergence of and agreement between the two representations. While the sequence fidelity must be applied in the extremal regimes, the Fourier fidelity yields a valuable quantification of the combined capabilities of the two representations for intermediate values of the bare coupling.

5.3.2 Estimation of $\langle \square \rangle$

We now apply the tools developed in Sec. 5.3.1 to calculate the expectation value $\langle \square \rangle$ as defined in (5.15). The value of $\langle \square \rangle$ with respect to the system's ground state is an important quantity in LGTs, as it can be related to the running of the coupling (see [1] and Sec. 3.3.3).

In the absence of dynamical matter, the total Hamiltonian solely consists of the two gauge field contributions. Therefore, we may determine a value g_{m} separating the regimes where either of the respective representations is advantageous. Let g_{m} be the value of g for which the Fourier fidelity in (5.30) is maximal with respect to the ground state, i.e.

$$F_{g_{\mathrm{m}}}(l) = \max_{\substack{L>l \\ g}} \left| \left\langle \mathrm{GS}^{(\mathrm{b})}(L, l, g) \right| \hat{\mathcal{F}}(L, l) \left| \mathrm{GS}^{(\mathrm{e})}(l, g) \right\rangle \right| . \tag{5.33}$$

Since the electric (magnetic) representation shows exceeding performance in the strong (weak) coupling regime, we can assume that for a given truncation l, the best approximation is achieved by considering the electric representation in the range $g \in [g_{\mathrm{m}}, \infty)$ and the magnetic one for $g \in [0, g_{\mathrm{m}}]$ (compare also Sec. 5.3.1 and Fig. 5.3).

Fig. 5.4 shows $\langle \square \rangle$ for various truncations, derived both in the electric [panel (a)] and magnetic [panel (b)] representation. In the latter, we obtained the L_{opt} values via the sequence fidelity as described above. From here, the true curve as it would be obtained from the untruncated U(1) theory can be estimated via the asymptotic values of the different representations when the truncation l is increased, since in the limit $l \to \infty$ both representations converge to the full theory. We exemplify such an estimation with the inset in Fig. 5.4(a), that contains the results for different l at $g^{-2} = 10$. The convergence can be clearly observed, and both representations yield the same result up to the fourth decimal at $l = 10$ ($\langle \square \rangle = 0.9572 \pm 0.0001$). Note that this convergence is not necessarily monotonic. However, in the extremal regimes, we observe that the expectation value of $\square$ increases with the truncation l when employing the electric representation, while it decreases with the magnetic one. (An in-depth analytical analysis is given in App. D of [3])

To summarize this section, we recall that a naive approximation of U(1) with $\mathbb{Z}_{2L+1}$ (with L fixed) leads to dramatically increasing computational costs when working on a wide range of g-values. As explained intuitively in Sec. 5.2, the problem originates from the fact that $\mathbb{Z}_{2L+1}$ converges pointwise to U(1). For fixed resolution L and fixed computational resources l, there is always a coupling g small enough such that the $\mathbb{Z}_{2L+1}$ description displays freezing and hence cannot approximate the U(1) continuum physics accurately. This can be understood by noting that the magnetic field Hamiltonian is gapless in both the continuum theory and in the U(1)-lattice description, but gapped in the $\mathbb{Z}_{2L+1}$-formulation. If the energy in the system becomes comparable to the gap, the difference between $\mathbb{Z}_{2L+1}$ and the true gauge group U(1) becomes noticeable, which leads to the freezing effect (see Fig. 5.3). Crucially, working with a value of L suitable for the regime $g \ll 1$ will lead to exploding computational costs, i.e. will require very large values of l, in the intermediate coupling regime $g \approx 1$ to capture the relevant physics there. Our solution to this problem is the dynamical adjustment of the parameter L with the coupling g, that allows us to approximate U(1) well for a wide range of couplings while including only a minimal number of states in our simulation (see Fig. 5.2).

5.4 Generalisations: Dynamical matter and arbitrary torus

In the following, we extend the results presented in Sec. 5.3 by including staggered fermions in the numerical simulations. In particular, we show that fermionic matter does not introduce any fundamental complication for the formulation introduced in Sec. 5.1. Moreover, to pave the way for further developments in the field, we derive the Hamiltonian for an arbitrary number of

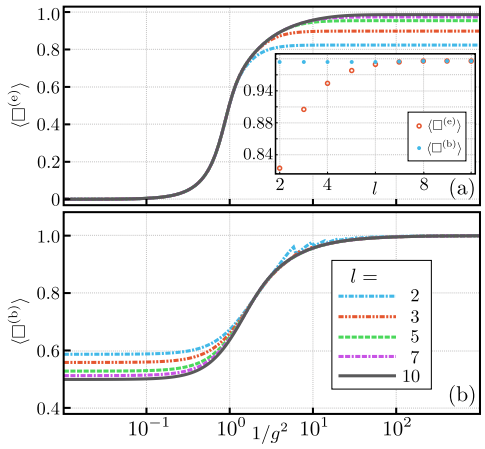

Figure 5.4: **Estimation the plaquette operator.** Panel (a) displays the obtained curves in the electric representation, where the line styles correspond to different values of the truncation l. For the magnetic representation in panel (b), each point has been obtained via the optimisation of the sequence fidelity over L. We stress the considerably higher resource requirements (l) of the electric representation for calculations in the regime $g^{-2} > 1$. The inset in (a) shows the values for the different representations for all values of l shown here when $g^{-2} = 10$.

plaquettes on a torus with matter and periodic boundary conditions, and explain how to include static charges.

5.4.1 Including dynamical charges

Since the completely compact formulation only affects the gauge fields, the inclusion of matter is straightforward. Recall first the electric Hamiltonian in (5.12) and the substitution rules in (5.20). By using the relations for the Fourier transform derived in (5.26), the magnetic representation of the electric term in (5.12) is found to be

$$\begin{aligned}\hat{H}_E^{(\mathrm{b})} \quad &= g^2 \sum_{\nu=1}^{2L} \Bigg\{ f_\nu^c \left[\hat{\mathcal{K}}_1^\nu + \hat{\mathcal{K}}_2^\nu + \hat{\mathcal{K}}_3^\nu + \frac{\hat{\mathcal{K}}_x^\nu + \hat{\mathcal{K}}_y^\nu}{2} \right] + f_\nu^s \Bigg[\sum_{\mu=1}^{2L} f_\mu^s \Bigg\{ \frac{1}{2} \hat{\mathcal{L}}_2^\mu \left(\hat{\mathcal{L}}_1^\nu + \hat{\mathcal{L}}_3^\nu \right) \\ &\quad - \frac{1}{4} \hat{\mathcal{L}}_x^\mu \left(\hat{\mathcal{L}}_1^\nu + \hat{\mathcal{L}}_2^\nu - \hat{\mathcal{L}}_3^\nu \right) + \frac{1}{4} \hat{\mathcal{L}}_y^\mu \left(\hat{\mathcal{L}}_1^\nu - \hat{\mathcal{L}}_2^\nu - \hat{\mathcal{L}}_3^\nu \right) \Bigg\} \quad + i \frac{\hat{q}_{(1,0)}}{2} \left(\hat{\mathcal{L}}_1^\nu + \hat{\mathcal{L}}_x^\nu \right) \\ &\quad + i \frac{\hat{q}_{(0,1)}}{2} \left(\hat{\mathcal{L}}_2^\nu - \hat{\mathcal{L}}_1^\nu + \hat{\mathcal{L}}_y^\nu \right) \quad + i \frac{\hat{q}_{(1,1)}}{2} \left(2\hat{\mathcal{L}}_1^\nu - \hat{\mathcal{L}}_2^\nu - \hat{\mathcal{L}}_x^\nu \right) \Bigg] \Bigg\} \\ &\quad + g^2 \frac{\hat{q}_{(1,0)}^2 + \hat{q}_{(0,1)}^2 + 2\hat{q}_{(1,1)} [\hat{q}_{(1,0)} + \hat{q}_{(1,1)}]}{2}. \end{aligned} \tag{5.34}$$

For the sake of clarity, we defined the shorthand notations

$$\hat{\mathcal{K}}_j^\nu = \hat{P}_j^\nu + (\hat{P}_j^\dagger)^\nu \text{ and } \hat{\mathcal{L}}_j^\nu = \hat{P}_j^\nu - (\hat{P}_j^\dagger)^\nu. \tag{5.35}$$

The magnetic field Hamiltonian $\hat{H}_B^{(\mathrm{b})}$ remains the same as in (5.28), since it does not involve fermionic terms. However, the kinetic Hamiltonian in (5.14) is modified in the presence of matter, yielding

$$\begin{aligned}\hat{H}_K^{(\mathrm{b})} = \kappa \sum_{\boldsymbol{r}=-\boldsymbol{L}}^{\boldsymbol{L}} \Big[&\hat{\Psi}_{(0,0)}^\dagger \left(1 + \mathrm{e}^{-i\frac{2\pi}{2L+1}r_x}\right) \hat{\Psi}_{(1,0)} + \hat{\Psi}_{(0,1)}^\dagger \left(\mathrm{e}^{-i\frac{2\pi}{2L+1}r_1} + \mathrm{e}^{i\frac{2\pi}{2L+1}(r_2-r_x)}\right) \hat{\Psi}_{(1,1)} + \\ &\hat{\Psi}_{(0,0)}^\dagger \left(1 + \mathrm{e}^{-i\frac{2\pi}{2L+1}r_y}\right) \hat{\Psi}_{(0,1)} + \hat{\Psi}_{(1,0)}^\dagger \left(1 + \mathrm{e}^{i\frac{2\pi}{2L+1}(r_2+r_3-r_y)}\right) \hat{\Psi}_{(1,1)} + h.c.\Big] |\boldsymbol{r}\rangle\langle\boldsymbol{r}| \,. \end{aligned} \tag{5.36}$$

In order to simulate fermionic matter, we recall the Jordan-Wigner transformation [124]

$$\hat{\Psi}_{\boldsymbol{n}}^\dagger \mapsto \prod_{\boldsymbol{l}<\boldsymbol{n}} (i\hat{\sigma}_z^{\boldsymbol{l}}) \hat{\sigma}_-^n, \tag{5.37}$$

where the vectorial relation $\boldsymbol{l} < \boldsymbol{n}$ is defined by $(0,0) < (0,1) < (1,1) < (1,0)$ to satisfy the fermionic commutation relations. While we do not insert these equations into (5.36), we remark that the mass Hamiltonian in (5.5) is simplified to

$$\hat{H}_M = \frac{m}{2} \left(\hat{\sigma}_z^1 - \hat{\sigma}_z^2 + \hat{\sigma}_z^3 - \hat{\sigma}_z^4\right), \tag{5.38}$$

which is independent of the chosen representation.

Since these simulations are costly, i.e. the dimension of the truncated Hilbert space is given by $2^4(2l+1)^5$ (four charges, three rotators and two strings), we estimate the plaquette expectation value employing a harsh truncation of $l = 2$, while fixing L to the optimal values L_{opt} found in Sec. 5.3.1 for the pure gauge case. We further introduce the mass and kinetic energy parameters as $m = \kappa = 10$. In Fig. 5.5, we display the ground state expectation value $\langle\square\rangle$ as a function of g^{-2}, together with the Fourier infidelity $1 - F_{\mathrm{f}}(l)$. In the asymptotic regimes $g \ll 1$ and $g \gg 1$, there is no qualitative difference in comparison to the pure gauge case. However, in the intermediate regime, there are novel features in both the electric and magnetic representations, such as the appearance of a negative dip. Nevertheless, we stress that conclusions drawn from this plot have to be taken with care, as the employed truncation limits the Fourier fidelity below 90%. While we have demonstrated that our method is suitable to tackle simulations with matter, a detailed analysis of novel effects and an accompanying study of the convergence is beyond the scope of this manuscript and left for future works.

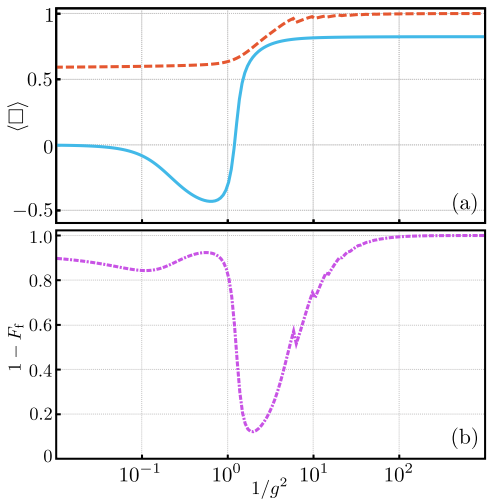

Figure 5.5: **Plaquette expectation value in the presence of dynamical charges.** Panel (a) displays the expectation value for $l = 2$ and (b) the Fourier fidelity derived in this case. The red dashed line in (a) corresponds to results derived in the magnetic representation, while the solid line is a result of the electric representation. For all curves we set $m = \kappa = 10$.

5.4.2 Hamiltonian for an arbitrary torus and charges

Here, we generalise the Hamiltonian of the minimal system considered in Sec. 5.1.2 to any two-dimensional lattice with periodic boundary conditions. As shown in Fig. 5.6, we extend the strategy used above to a torus of size (N_x, N_y). By removing redundant degrees of freedom, we obtain the effective Hamiltonian in terms of two strings and $N_xN_y - 1$ rotators. As before, we indicate each plaquette with its bottom-left site $\boldsymbol{n} = (n_x, n_y)$, where $n_x(n_y) = 0, \ldots, N_x - 1\,(N_y - 1)$. In addition, the rotator associated with the plaquette $\boldsymbol{n}$ is denoted by $\hat{R}_{\boldsymbol{n}}$, and the two strings by $\hat{R}_x$ and $\hat{R}_y$ (see Fig. 5.6). This leads to N_xN_y pairwise expressions for the electric fields,

$$\begin{aligned} \hat{E}_{\boldsymbol{n},\boldsymbol{e}_x} &= \delta_{n_y,0}\hat{R}_x + \hat{R}_{\boldsymbol{n}} - \hat{R}_{\boldsymbol{n}-\boldsymbol{e}_y} + \hat{q}_{\boldsymbol{n},x}, \\ \hat{E}_{\boldsymbol{n},\boldsymbol{e}_y} &= \delta_{n_x,0}\hat{R}_y + \hat{R}_{\boldsymbol{n}-\boldsymbol{e}_x} - \hat{R}_{\boldsymbol{n}} + \hat{q}_{\boldsymbol{n},y}, \end{aligned} \tag{5.39}$$

where $\delta_{n,m} = 1$ for $n = m$, and zero otherwise. Moreover, $\hat{q}_{\boldsymbol{n},x}$ and $\hat{q}_{\boldsymbol{n},y}$ are the electric field's corrections due to the presence of dynamical charges, in accordance with Gauss' law. Since there are multiple ways to implement Gauss' law, a possible choice for $\hat{q}_{\boldsymbol{n},x}$ and $\hat{q}_{\boldsymbol{n},y}$ is (see the green

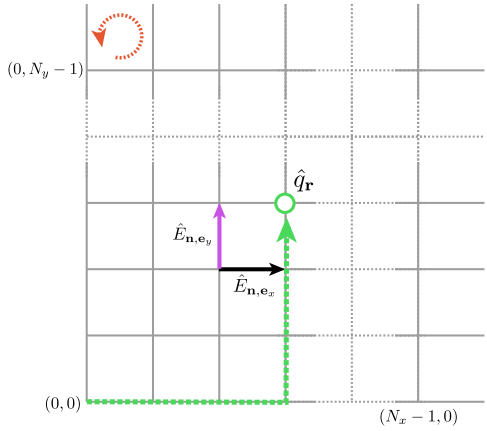

Figure 5.6: **Periodic torus with charges.** We extend the construction of the periodic plaquette to a generic torus. We fix the rotator at $(0, N_y - 1)$ to zero and choose the links' corrections to the electric field introduced by charges in accordance with the green dotted line. In particular, for any charge $\hat{q}_{\boldsymbol{r}}$, we connect the origin to the site $\boldsymbol{r}$ by moving first horizontally and then vertically.

lines in Fig. 5.6)

$$\begin{aligned} \hat{q}_{\boldsymbol{n},x} &= -\sum_{r_x=n_x+1}^{N_x-1} \sum_{r_y=0}^{N_y-1} \delta_{n_y,0} \hat{q}_{\boldsymbol{r}}, \\ \hat{q}_{\boldsymbol{n},y} &= -\sum_{r_x=0}^{N_x-1} \sum_{r_y=n_y+1}^{N_y-1} \delta_{r_x,n_x} \hat{q}_{\boldsymbol{r}}, \end{aligned} \tag{5.40}$$

where $\hat{q}_{\boldsymbol{n}}$ is the charge operator as defined in (5.7). Note that also in this general case it is convenient to explicitly fix one of the rotators to zero, for instance $\hat{R}_{(0,N_y-1)} = 0$.

Moving to the kinetic term, we employ the string convention presented in (5.40), which yields the replacement rules (for details, see App. B.3 in [3])

$$\begin{aligned} \hat{\Psi}^\dagger_{\boldsymbol{n}} \hat{U}^\dagger_{\boldsymbol{n},\boldsymbol{e}_x} \hat{\Psi}_{\boldsymbol{n}+\boldsymbol{e}_x} &\mapsto \hat{\Psi}^\dagger_{\boldsymbol{n}} \left(\hat{P}_x^{-\delta_{n_x,N_x-1}} \prod_{r_y=0}^{n_y-1} \hat{P}_{(n_x,r_y)} \right) \hat{\Psi}_{\boldsymbol{n}+\boldsymbol{e}_x}, \\ \hat{\Psi}^\dagger_{\boldsymbol{n}} \hat{U}^\dagger_{\boldsymbol{n},\boldsymbol{e}_y} \hat{\Psi}_{\boldsymbol{n}+\boldsymbol{e}_y} &\mapsto \hat{\Psi}^\dagger_{\boldsymbol{n}} \left(\hat{P}_y^\dagger \prod_{r_x=n_x}^{N_x-1} \prod_{r_y=0}^{N_y-1} \hat{P}_{(r_x,r_y)} \right)^{\delta_{n_y,N_y-1}} \hat{\Psi}_{\boldsymbol{n}+\boldsymbol{e}_y}. \end{aligned} \tag{5.41}$$

From the above equations and from (5.39), we can calculate the components of the gauged Hamiltonian in the rotator and string basis as

$$\begin{aligned}
\hat{H}_E &= \frac{g^2}{2}\sum_{\boldsymbol{n}} \hat{E}^2_{\boldsymbol{n},\boldsymbol{e}_x} + \hat{E}^2_{\boldsymbol{n},\boldsymbol{e}_y}, \\
\hat{H}_B &= -\frac{1}{2g^2a^2}\left(\prod_{\boldsymbol{n}\neq(0,N_y-1)} \hat{P}_{\boldsymbol{n}} + \sum_{\boldsymbol{n}\neq(0,N_y-1)} \hat{P}_{\boldsymbol{n}}\right) + \text{h.c.}, \\
\hat{H}_K &= \kappa\sum_{\boldsymbol{n}} \hat{\Psi}^\dagger_{\boldsymbol{n}}\left[\hat{\Psi}_{\boldsymbol{n}+\boldsymbol{e}_x}\hat{P}_x^{-\delta_{n_x,N_x-1}}\prod_{r_y=0}^{n_y-1}\hat{P}_{(n_x,r_y)} + \hat{\Psi}_{\boldsymbol{n}+\boldsymbol{e}_y}\left(\hat{P}_y^\dagger\prod_{r_x=n_x}^{N_x-1}\prod_{r_y=0}^{N_y-1}\hat{P}_{(r_x,r_y)}\right)^{\delta_{n_y,N_y-1}}\right] \\
&+ \text{h.c.}, \\
\hat{H}_M &= m\sum_{\boldsymbol{n}}(-1)^{n_x+n_y}\hat{\Psi}^\dagger_{\boldsymbol{n}}\hat{\Psi}_{\boldsymbol{n}}.
\end{aligned} \tag{5.42}$$

We note that the kinetic term contains string terms that depend on the choice of the background strings (see Fig. 5.6). Importantly, employing the relations derived in (5.26), one can transform between the electric and magnetic representations.

5.5 Conclusion

We developed a new strategy for studying gauge theories. Our method is suited for quantum and classical simulations of fundamental particle interactions in all coupling regimes in a resource-efficient manner. As a testbed, we applied our method to the Hamiltonian formulation of lattice QED in $(2+1)$ dimensions.

The key insight is the approximation of the continuous U(1) gauge group with finite truncations of the $\mathbb{Z}_{2L+1}$ group, where $L \in \mathbb{N}$ can be arbitrarily large and is scaled with the value of the bare coupling g. This strategy allows us to work with fewer computational resources than just employing a truncated U(1) group. At weak couplings we truncate the gauge fields in the magnetic representation of $\mathbb{Z}_{2L+1}$, while the truncation is performed in the electric representation for strong coupling. We benchmarked this novel regularisation scheme by computing the expectation value of the plaquette operator on a small periodic lattice, with and without dynamical matter, and estimated the accuracy of the computation. Since our methods allows us to work at all values of g and therefore at arbitrarily small values of the lattice spacing a, it provides the perspective to access, in principle, non-perturbative physics close to the continuum limit.

Chapter 6

A (3+1)D Topological θ–term in the Hamiltonian formulation of Lattice Gauge Theories

Lattice gauge theories (LGTs) with topological θ-terms are an important class of sign-problem afflicted problems [19, 165] due to their relevance to the strong CP problem [35]. Briefly, this problem describes the mystery in QCD: while the θ-term, which violates the combined charge conjugation and parity (CP) symmetry, could contribute to the observed matter-anti-matter asymmetry, there is minimal experimental evidence for CP violation in QCD. Indeed, measurements of the neutron electric dipole moment [166, 167] constrain the parameter of the θ-term to be smaller than $\sim 10^{-10}$, which results in a fine-tuning problem. LGTs with θ-terms are largely inaccessible to Markov chain Monte Carlo (MCMC) simulations but can be simulated using tensor networks (TNs) and quantum simulations performed on classical and quantum computers, respectively. Indeed, (1+1)D LGTs with topological θ-terms have been simulated using TNs [168, 169, 170, 171] and a digital quantum computer [60]. Both approaches can in principle be extended to higher dimensions. TNs have successfully simulated U(1) LGTs in (2+1)D [172] and (3+1)D [173]. Recently, efficient quantum algorithms for simulating Abelian and non-Abelian LGTs in any dimensions on universal quantum computers have been developed [2, 107]. Given the rapid developments of sign-problem-free algorithms for LGTs in higher dimensions, it is therefore of timely importance to explore lattice θ-terms beyond (1+1)D. Unlike conventional MCMC LGT simulations, quantum simulations and many TN methods rely on the Hamiltonian formulation. Here, we fill a gap in the literature and present the first derivation of the Hamiltonian 3+1D θ-term for Abelian and non-Abelian lattice gauge theories, using the transfer matrix method [153].

In Sec. 6.1, we review the transfer matrix derivation of the Kogut-Susskind Hamiltonian

from Wilson's lattice action. In Sec. 6.2, from the Lagrangian definition in [174], we derive the topological θ-term for generic (3+1)D (non-)Abelian lattice gauge theories in the Hamiltonian formulation, using the transfer matrix method. In Sec. 6.4, we focus on a particular example and perform numerical calculations for a (3+1)D compact U(1) lattice gauge theory in the Hamiltonian formulation using exact diagonalization for a single cube. Our numerical results indicate a phase transition at constant values of θ. In Sec. 6.4, we summarize and compare our results to relevant analytical and numerical studies. In Sec. 6.5, we discuss our findings in light of recent developments in tensor network and quantum simulations.

Throughout this chapter, we disregard the Einstein notation and explicitly display all sums. In order to distinguish the variables in the Lagrangian formulation and operators in the Hamiltonian formulation, we express the latter with a hat ($\hat{}$) symbol.

6.1 Lattice formulation: from Lagrangian to Hamiltonian

In this section, for the convenience of readers who are unfamiliar with lattice gauge theories, we review two standard approaches to lattice gauge theory, namely Wilson's Lagrangian approach [14] and Kogut-Susskind's Hamiltonian approach [105]. Moreover, we review the derivation of the Kogut-Susskind Hamiltonian from Wilson's lattice action using the transfer matrix method [153], since it will also be used for the derivation of the topological θ-term.

In the Lagrangian formulation, the standard approach introduced by Wilson [14] defines gauge theories on a hypercubic lattice with spacing a in Euclidean spacetime. The sites are labelled by a four-vector $\boldsymbol{n} \equiv \sum_{\mu=0}^{3} n_\mu \hat{\mu}$, where n_0 denotes the temporal component, n_i with $i \in \{1,2,3\}$ are the spatial components, and $\hat{\mu}$ is a unit vector in the direction μ. In the Hamiltonian formulation, time is continuous, and thus, gauge theories are defined on a cubic lattice. The links are denoted by their originating sites $\boldsymbol{n}$ and directions μ. On the lattice, the vector potential, which starts from site $\boldsymbol{n}$ and points to direction μ, is represented by $A_{\boldsymbol{n},\mu} = \sum_b A^b_{\boldsymbol{n},\mu}\lambda^b$, where $A^b_{\boldsymbol{n},\mu}$ are real-valued vector fields that correspond to the generators λ^b of the gauge group [161]. Then, the discretized field strength tensor is defined as

$$F^b_{\boldsymbol{n},\mu\nu} \equiv \frac{1}{a}\left(A^b_{\boldsymbol{n}+\hat{\mu},\nu} - A^b_{\boldsymbol{n},\nu} - A^b_{\boldsymbol{n}+\hat{\nu},\mu} + A^b_{\boldsymbol{n},\mu}\right). \tag{6.1}$$

Using these degrees of freedom, one defines a link variable

$$U_{\boldsymbol{n},\mu} \equiv e^{iga\sum_b A^b_{\boldsymbol{n},\mu}\lambda^b}. \tag{6.2}$$

In terms of the link variable, we construct a gauge-invariant plaquette variable

$$U_{\boldsymbol{n},\mu\nu} \equiv U_{\boldsymbol{n},\mu}U_{\boldsymbol{n}+\hat{\mu},\nu}U^\dagger_{\boldsymbol{n}+\hat{\nu},\mu}U^\dagger_{\boldsymbol{n},\nu} = e^{iga^2\sum_b F^b_{\boldsymbol{n},\mu\nu}\lambda^b}, \tag{6.3}$$

which is a product of link variables around a closed loop on the lattice (see the right panel of Fig. 6.1 for an illustration). Using the fact that $F^b_{\boldsymbol{n},\mu\nu} = -F^b_{\boldsymbol{n},\nu\mu}$, one can show that $U^\dagger_{\boldsymbol{n},\mu\nu} = U_{\boldsymbol{n},\nu\mu}$. In terms of the plaquette variables, the gauge-invariant Wilson's gauge-field action on the lattice reads [14]

$$S_W = -\frac{1}{2g^2}\sum_{\boldsymbol{n}}\sum_{\mu,\nu;\nu>\mu}\mathrm{Tr}\left[U_{\boldsymbol{n},\mu\nu} + U^\dagger_{\boldsymbol{n},\mu\nu}\right]. \tag{6.4}$$

For small a, we can expand the plaquette variables as an exponential function of a, as defined in (6.3), and obtain

$$\begin{aligned} S_W &= -\frac{1}{2g^2}\sum_{\boldsymbol{n}}\sum_{\mu,\nu}\mathrm{Tr}\left[U_{\boldsymbol{n},\mu\nu}\right] \\ &\xrightarrow[a\approx 0]{} \frac{a^4}{4}\sum_{\boldsymbol{n},\mu,\nu,b} F^b_{\boldsymbol{n},\mu\nu}F^b_{\boldsymbol{n},\mu\nu} \\ &\xrightarrow[a\to 0]{} \frac{1}{4}\int d^4x \sum_{\mu,\nu,b} F^b_{\mu\nu}(x)F^b_{\mu\nu}(x), \end{aligned} \tag{6.5}$$

where in the first line, we have used the fact that $U^\dagger_{\boldsymbol{n},\mu\nu} = U_{\boldsymbol{n},\nu\mu}$, and in the second line, the linear term vanishes in the expansion due to $F^b_{\boldsymbol{n},\mu\nu} = -F^b_{\boldsymbol{n},\nu\mu}$. Thus, only the quadratic term in the action survives. In the continuum limit, where $a \to 0$, the sum becomes an integral and therefore yields the correct continuum expression.

In the following, we reproduce the derivation of the Kogut-Susskind Hamiltonian using the transfer matrix method [153]. The action and the Hamiltonian are related by the partition function, which is defined as

$$Z = \int DU e^{-S} = \mathrm{Tr}\left[\left(e^{-a_0\hat{H}}\right)^N\right], \tag{6.6}$$

where $\int DU$ is an integral over the gauge group [161], a_0 is the temporal lattice spacing, and N is the number of time steps. Since, in the Hamiltonian formulation, time and space are not treated isotropically, we hereafter denote the temporal and spatial lattice spacing as a_0 and a, respectively. The transfer matrix is defined as

$$\hat{T} \equiv e^{-a_0\hat{H}}. \tag{6.7}$$

The Hamiltonian is defined through the transfer matrix in the temporal continuum limit, where $N \to \infty$ and $a_0 \to 0$ with $t = Na_0$ fixed. The transfer matrix can be expressed in a complete and orthonormal product basis

$$\{|U\rangle = \prod_{\boldsymbol{n},i}|U_{\boldsymbol{n},i}\rangle\}, \tag{6.8}$$

where $|U_{\boldsymbol{n},i}\rangle$ is an element of the gauge group on the link $(\boldsymbol{n}, i)$. The inner product and the completeness relation in this basis are given by

$$\langle U'|U\rangle = \prod_{\boldsymbol{n},i} \delta(U'_{\boldsymbol{n},i}, U_{\boldsymbol{n},i}), \quad \int DU\, |U\rangle\langle U| = 1. \tag{6.9}$$

In this basis, we prove the relation in (6.6)

$$\begin{aligned} Z &= \int DU e^{-S} \\ &= \int DU \langle U_t| \hat{T} |U_{t-2a_0}\rangle \langle U_{t-a_0}| \hat{T} |U_{t-a_0}\rangle ... \langle U_{a_0}| \hat{T} |U_0\rangle \\ &= \int DU \langle U| \hat{T}^N |U\rangle = \mathrm{Tr}[\hat{T}^N], \end{aligned} \tag{6.10}$$

where in the second equality, we split the Euclidean path integral e^{-S} into N infinitesimal Euclidean evolution operators, i.e., the transfer matrix, and in the last two equalities, we have used the completeness relation and imposed periodic boundary conditions in the temporal direction such that $|U_t\rangle = |U_0\rangle$.

Working in the temporal gauge $\hat{U}_{\boldsymbol{n},0} = 1$, the elements of the transfer matrix, which satisfy (6.10), are

$$\langle U'| \hat{T} |U\rangle = e^{\frac{a}{2g^2 a_0} \sum_{\boldsymbol{n},i} \mathrm{Tr}\left[U'_{\boldsymbol{n},i} U^\dagger_{\boldsymbol{n},i} + U^{\dagger\prime}_{\boldsymbol{n},i} U_{\boldsymbol{n},i}\right]} e^{\frac{a_0}{2g^2 a} \sum_{\boldsymbol{n},j,k} \mathrm{Tr}\left[U_{\boldsymbol{n},jk} + U^\dagger_{\boldsymbol{n},jk}\right]}, \tag{6.11}$$

where $U'_{\boldsymbol{n},i}$ and $U_{\boldsymbol{n},i}$ are link variables from consecutive time slices. Then, we express the transfer matrix in terms of the matrix operators

$$\hat{U}_{\boldsymbol{n},i} |U\rangle = U_{\boldsymbol{n},i} |U\rangle, \tag{6.12}$$

which are diagonal in the product basis $|U\rangle$, and the unitary operators

$$\hat{R}_{\boldsymbol{n},i}(g) |U\rangle = |U'\rangle, \tag{6.13}$$

where only $|U_{\boldsymbol{n},i}\rangle$ is changed in $|U\rangle$, i.e.,

$$|U'_{\boldsymbol{n},i}\rangle = |g_{\boldsymbol{n},i} U_{\boldsymbol{n},i}\rangle. \tag{6.14}$$

Here, $g_{\boldsymbol{n},i}$ is an element in our unitary group, which is parametrized as

$$g_{\boldsymbol{n},i} = e^{i \sum_b x^b_{\boldsymbol{n},i} \lambda^b}, \tag{6.15}$$

where $x^b_{\boldsymbol{n},i} \in \mathbb{R}$ are the group parameters, and the group generators for the fundamental representation are normalized such that

$$\mathrm{Tr}[\lambda^a \lambda^b] = \delta_{ab}. \tag{6.16}$$

Now, the unitary operators can be parametrized as

$$\hat{R}_{\boldsymbol{n},i}(g_{\boldsymbol{n},i}) \equiv e^{i \sum_b x^b_{\boldsymbol{n},i} \hat{E}^b_{\boldsymbol{n},i}}, \tag{6.17}$$

where we have introduced the electric field operators $\hat{E}^b_{\boldsymbol{n},i}$ that act on the links (see right panel of Fig. 6.1 for an illustration) and are conjugate to the link operators $\hat{U}_{\boldsymbol{n},i}$. They satisfy the commutation relations

$$\left[\hat{E}^a_{\boldsymbol{n},i}, \hat{E}^b_{\boldsymbol{n},i}\right] = i \sum_c f^{abc} \hat{E}^c_{\boldsymbol{n},i}, \tag{6.18}$$

$$\left[\hat{E}^a_{\boldsymbol{n},i}, \hat{U}_{\boldsymbol{n},i}\right] = -\lambda^a \hat{U}_{\boldsymbol{n},i}, \tag{6.19}$$

where f^{abc} are the structure constants of the gauge group. In a U(1) theory, there is only one generator $\lambda^a = 1$ for the fundamental representation and one operator $\hat{E}^a_{\boldsymbol{n},i} = \hat{E}_{\boldsymbol{n},i}$, and the structure constants vanish. Thus, (6.18) becomes trivial, and (6.19) can be simplified. In terms of these operators, we can write the transfer operator as

$$\begin{aligned}\hat{T} &= \prod_{\boldsymbol{n},i} \int_{g\in G} dg_{\boldsymbol{n},i} \hat{R}_{\boldsymbol{n},i}(g_{\boldsymbol{n},i}) e^{\frac{a}{2g^2 a_0}\mathrm{Tr}\left[g_{\boldsymbol{n},i} + g^\dagger_{\boldsymbol{n},i}\right]} e^{\frac{a_0}{2g^2 a}\sum_{\boldsymbol{n},j,k}\mathrm{Tr}\left[\hat{U}_{\boldsymbol{n},jk} + \hat{U}^\dagger_{\boldsymbol{n},jk}\right]} \\ &= \prod_{\boldsymbol{n},i} \int \left(\prod_b dx^b_{\boldsymbol{n},i}\right) e^{i\sum_b x^b_{\boldsymbol{n},i}\hat{E}^b_{\boldsymbol{n},i}} e^{\frac{a}{2g^2 a_0}\mathrm{Tr}\left[2\cos\left(\sum_b x^b_{\boldsymbol{n},i}\lambda^b\right)\right]} e^{\frac{a_0}{2g^2 a}\sum_{\boldsymbol{n},j,k}\mathrm{Tr}\left[\hat{U}_{\boldsymbol{n},jk} + \hat{U}^\dagger_{\boldsymbol{n},jk}\right]}.\end{aligned} \tag{6.20}$$

In the continuum limit, as $a_0 \to 0$, the integral is dominated by the maximum of $\mathrm{Tr}\left[2\cos\left(\sum_b \lambda^b x^b_{\boldsymbol{n},i}\right)\right]$. Expanding around $x^b_{\boldsymbol{n},i} = 0$, where the maximum is located, we have

$$\mathrm{Tr}\left[2\cos\left(\sum_b \lambda^b x^b_{\boldsymbol{n},i}\right)\right] \approx 2D - \sum_b x^b_{\boldsymbol{n},i} x^b_{\boldsymbol{n},i}, \tag{6.21}$$

where D is the dimension of the group generators. Inserting the expansion into the integral, we obtain a Gaussian integral, which evaluates to

$$\hat{T} \propto e^{-a_0\left(\frac{g^2}{2a}\sum_{\boldsymbol{n},i,b}\hat{E}^b_{\boldsymbol{n},i}\hat{E}^b_{\boldsymbol{n},i} - \frac{1}{2g^2 a}\sum_{\boldsymbol{n},j,k}\mathrm{Tr}\left[\hat{U}_{\boldsymbol{n},jk} + \hat{U}^\dagger_{\boldsymbol{n},jk}\right]\right)}. \tag{6.22}$$

From this, we can directly read off the Kogut-Susskind pure gauge Hamiltonian [105]

$$\hat{H}_{KS} = \frac{g^2}{2a}\sum_{\boldsymbol{n},i,b}\hat{E}^b_{\boldsymbol{n},i}\hat{E}^b_{\boldsymbol{n},i} - \frac{1}{2g^2 a}\sum_{\boldsymbol{n},j,k}\mathrm{Tr}\left[\hat{U}_{\boldsymbol{n},jk} + \hat{U}^\dagger_{\boldsymbol{n},jk}\right]. \tag{6.23}$$

6.2 (3+1)D topological terms in the Hamiltonian formulation

In this section, we derive a lattice definition of the (3+1)D topological θ-term in the Hamiltonian formulation, using the transfer matrix method [153]. This novel derivation complements the well-known lattice definitions of the (3+1)D θ-term in the Lagrangian formulation (see [175] for a review).

In terms of the field strength tensor, the continuum topological θ-term in the Lagrangian formulation reads

$$\begin{aligned}
\theta Q(x) &= \frac{\theta g^2}{16\pi^2} \sum_{\mu,\nu} F_{\mu\nu}(x) \tilde{F}_{\mu\nu}(x) \\
&= \frac{\theta g^2}{32\pi^2} \sum_{\mu,\nu,\rho,\sigma} \varepsilon_{\mu\nu\rho\sigma} F_{\mu\nu}(x) F_{\rho\sigma}(x) \\
&= \frac{\theta g^2}{8\pi^2} \sum_{i,j,k} \varepsilon_{ijk} F_{0i}(x) F_{jk}(x) \\
&= \frac{\theta g^2}{8\pi^2} \sum_{i,j,k,b} \varepsilon_{ijk} \mathrm{Tr} \left[F^b_{0i}(x) F^b_{jk}(x) \right] ,
\end{aligned} \tag{6.24}$$

where $Q(x)$ is the topological charge, $\varepsilon_{\mu\nu\rho\sigma}$ is the 4D Levi-Civita symbol, $F_{\mu\nu}(x) = \sum_b F^b_{\mu\nu}(x) \lambda^b$ is the field strength tensor, $\tilde{F}_{\mu\nu}(x) = \frac{1}{2} \sum_{\rho,\sigma} \varepsilon_{\mu\nu\rho\sigma} F_{\rho\sigma}(x)$ is the Hodge dual of $F_{\mu\nu}(x)$, and θ is an angular variable that can be shifted by $\theta \to \theta + n2\pi$, $n \in \mathbb{Z}$, keeping the Lagrangian invariant. In the third equality, we used the fact that both the Levi-Civita symbol and the field strength tensor gain minus signs when exchanging two of their indices, which cancel out.

In order to derive the generic structure of the θ-term on the lattice in the Hamiltonian formulation, we start with Peskin's original lattice definition of the topological charge in the Lagrangian formulation [176, 174],

$$Q_{\boldsymbol{n}} = -\frac{1}{32\pi^2} \sum_{\mu,\nu,\rho,\sigma} \varepsilon_{\mu\nu\rho\sigma} \, \mathrm{Tr} \left[U_{\boldsymbol{n},\mu\nu} U_{\boldsymbol{n},\rho\sigma} \right] , \tag{6.25}$$

and perform an expansion of the first plaquette variable,

$$\begin{aligned} Q_{\boldsymbol{n}} &= -\frac{1}{32\pi^2}\sum_{\mu,\nu,\rho,\sigma,b}\varepsilon_{\mu\nu\rho\sigma}\mathrm{Tr}\left[\left(1+iga_\mu a_\nu F^b_{\boldsymbol{n},\mu\nu}\lambda^b+\ldots\right)U_{\boldsymbol{n},\rho\sigma}\right] \\ &= -\frac{1}{16\pi^2}\sum_{i,j,k,b}\varepsilon_{ijk}\mathrm{Tr}\left[\left(1+igaa_0\left(F^b_{\boldsymbol{n},0i}-F^b_{\boldsymbol{n},i0}\right)\lambda^b+\ldots\right)U_{\boldsymbol{n},jk}\right] \\ &= -\frac{1}{8\pi^2}\sum_{i,j,k,b}\varepsilon_{ijk}\,\mathrm{Tr}\left[\left(1+igaa_0E^b_{\boldsymbol{n},i}\lambda^b+\ldots\right)U_{\boldsymbol{n},jk}\right] \\ &= -\frac{igaa_0}{8\pi^2}\sum_{i\perp j\perp k,b}\mathrm{Tr}\left[E^b_{\boldsymbol{n},i}\lambda^b\left(U_{\boldsymbol{n},jk}-U^\dagger_{\boldsymbol{n},jk}\right)+\ldots\right], \end{aligned} \tag{6.26}$$

where $a_\mu = a_0$ for $\mu = 0$, and $a_\mu = a$ otherwise. At first sight, it seems as if this naive expansion does not yield the correct prefactor for the θ-term in the Hamiltonian formulation. Similarly, it seems as if a naive expansion of Wilson's lattice action in (6.4) does not yield the correct prefactors for the electric and magnetic terms of the Kogut-Susskind Hamiltonian in (6.23). From the transfer matrix derivation in Sec. 6.1 we know that the magnetic term in the Hamiltonian formulation has the same $1/g^2$ prefactor as in the Lagrangian formulation, but the electric term acquires a g^2 prefactor through the Gaussian integration in (6.22). This apparent deviation can be explained by the fact that the electric fields in the Hamiltonian and Lagrangian formulations are defined differently. In particular, these two electric fields are related via $\hat{E}^b_{\boldsymbol{n},i} = (a^2/g)E^b_{\boldsymbol{n},i}$ [159]. In order to demonstrate that this is indeed the case [see (6.34)], we will derive the topological θ-term using the transfer matrix method in the following.

The Euclidean lattice action, including the topological charge in (6.25) with a vacuum angle θ, is [177]

$$S = S_W + i\theta\sum_{\boldsymbol{n}} Q_{\boldsymbol{n}}, \tag{6.27}$$

where the topological charge picks up a factor of i when going from Minkowski to Euclidean spacetime [178].

Just as in the second line of (6.26), we isolate the temporal components of $Q_{\boldsymbol{n}}$ in the action,

$$\begin{aligned} &\mathrm{Tr}\left[U_{\boldsymbol{n},0i}U_{\boldsymbol{n},jk}-U_{\boldsymbol{n},i0}U_{\boldsymbol{n},jk}\right] \\ =&\,\mathrm{Tr}\left[U_{\boldsymbol{n},0i}U_{\boldsymbol{n},jk}-U^\dagger_{\boldsymbol{n},0i}U_{\boldsymbol{n},jk}\right] \\ =&\,\mathrm{Tr}\left[(U_{\boldsymbol{n},0i}-U^\dagger_{\boldsymbol{n},0i})U_{\boldsymbol{n},jk}\right], \end{aligned} \tag{6.28}$$

such that we can write the action as

$$S = S_W - \frac{i\theta}{16\pi^2}\sum_{\boldsymbol{n},i,j,k}\varepsilon_{ijk}\mathrm{Tr}\left[\left(U_{\boldsymbol{n},0i}-U^\dagger_{\boldsymbol{n},0i}\right)U_{\boldsymbol{n},jk}\right]. \tag{6.29}$$

Working in the temporal gauge, we write the transfer matrix elements, which satisfy (6.10), as

$$\begin{aligned}\left\langle U'\right|\hat{T}\left|U\right\rangle = e^{\frac{a}{2g^2a_0}\sum_{\boldsymbol{n},i}\mathrm{Tr}\left[U'_{\boldsymbol{n},i}U^\dagger_{\boldsymbol{n},i}+U^{\dagger'}_{\boldsymbol{n},i}U_{\boldsymbol{n},i}\right]}e^{\frac{i\theta}{16\pi^2}\sum_{\boldsymbol{n},i,j,k}\varepsilon_{ijk}\mathrm{Tr}\left[\left(U'_{\boldsymbol{n},i}U^\dagger_{\boldsymbol{n},i}-U^{\dagger'}_{\boldsymbol{n},i}U_{\boldsymbol{n},i}\right)U_{\boldsymbol{n},jk}\right]} \\ \times e^{\frac{a_0}{2g^2a}\sum_{\boldsymbol{n},j,k}\mathrm{Tr}\left[U_{\boldsymbol{n},jk}+U^\dagger_{\boldsymbol{n},jk}\right]}.\end{aligned} \tag{6.30}$$

In terms of the operators defined in (6.12) and (6.17), we write the transfer matrix as

$$\begin{aligned}\hat{T} &= \prod_{\boldsymbol{n},i}\int_{g\in G}dg_{\boldsymbol{n},i}\hat{R}_{\boldsymbol{n},i}(g_{\boldsymbol{n},i})e^{\frac{a}{2g^2a_0}\mathrm{Tr}\left[g_{\boldsymbol{n},i}+g^\dagger_{\boldsymbol{n},i}\right]}e^{\frac{i\theta}{16\pi^2}\sum_{j,k}\varepsilon_{ijk}\mathrm{Tr}\left[\left(g_{\boldsymbol{n},i}-g^\dagger_{\boldsymbol{n},i}\right)\hat{U}_{\boldsymbol{n},jk}\right]} \\ &\quad\times e^{\frac{a_0}{2g^2a}\sum_{\boldsymbol{n},j,k}\mathrm{Tr}\left[\hat{U}_{\boldsymbol{n},jk}+\hat{U}^\dagger_{\boldsymbol{n},jk}\right]} \\ &= \prod_{\boldsymbol{n},i}\int\left(\prod_b dx^b_{\boldsymbol{n},i}\right)e^{i\sum_b x^b_{\boldsymbol{n},i}\hat{E}^b_{\boldsymbol{n},i}}e^{\frac{a}{2g^2a_0}\mathrm{Tr}\left[2\cos\left(\sum_b x^b_{\boldsymbol{n},i}\lambda^b\right)\right]} \\ &\quad\times e^{\frac{i\theta}{16\pi^2}\sum_{j,k}\varepsilon_{ijk}\mathrm{Tr}\left[2i\sin\left(\sum_b x^b_{\boldsymbol{n},i}\lambda^b\right)\hat{U}_{\boldsymbol{n},jk}\right]}e^{\frac{a_0}{2g^2a}\sum_{\boldsymbol{n},j,k}\mathrm{Tr}\left[\hat{U}_{\boldsymbol{n},jk}+\hat{U}^\dagger_{\boldsymbol{n},jk}\right]}.\end{aligned} \tag{6.31}$$

In the continuum limit, as $a_0\to 0$, the integral is dominated by the maximum of the cosine term. Expanding the cosine and sine terms around $x^b_{\boldsymbol{n},i}=0$, we obtain

$$\begin{aligned}\hat{T} \approx \prod_{\boldsymbol{n},i}\int\left(\prod_b dx^b_{\boldsymbol{n},i}\right)e^{i\sum_b x^b_{\boldsymbol{n},i}\hat{E}^b_{\boldsymbol{n},i}-\frac{a}{2g^2a_0}\sum_b x^b_{\boldsymbol{n},i}x^b_{\boldsymbol{n},i}}e^{\frac{-\theta}{8\pi^2}\sum_{j,k,b}\varepsilon_{ijk}x^b_{\boldsymbol{n},i}\mathrm{Tr}\left[\lambda^b\hat{U}_{\boldsymbol{n},jk}\right]} \\ \times e^{\frac{a_0}{2g^2a}\sum_{\boldsymbol{n},j,k}\mathrm{Tr}\left[\hat{U}_{\boldsymbol{n},jk}+\hat{U}^\dagger_{\boldsymbol{n},jk}\right]}.\end{aligned} \tag{6.32}$$

This Gaussian integral evaluates to

$$\hat{T}\propto e^{-a_0\{\hat{H}_{KS}-\frac{ig^2\theta}{8\pi^2a}\sum_{\boldsymbol{n},i,j,k,b}\varepsilon_{ijk}\mathrm{Tr}\left[\hat{E}^b_{\boldsymbol{n},i}\lambda^b\hat{U}_{\boldsymbol{n},jk}\right]\}}. \tag{6.33}$$

We note that at first sight, it seems as if the Gaussian integration yields an $O(\theta^2)$ term, which comes from squaring the exponent in the second line of (6.32). However, this term is proportional to $\sum_{\boldsymbol{n},i,j,k,l,m}\varepsilon_{ijk}\varepsilon_{ilm}\mathrm{Tr}[\lambda^b\hat{U}_{\boldsymbol{n},jk}]\mathrm{Tr}[\lambda^b\hat{U}_{\boldsymbol{n},lm}]$, where i is an index of the integral variable. This term cancels exactly due to $\sum_i\varepsilon_{ijk}\varepsilon_{ilm}=\delta_{jl}\delta_{km}-\delta_{jm}\delta_{kl}$. Thus, we obtain the topological θ-term in the Hamiltonian formulation,[1]

$$\begin{aligned}\theta\hat{Q} &= -\frac{ig^2\theta}{8\pi^2a}\sum_{\boldsymbol{n},i,j,k,b}\varepsilon_{ijk}\mathrm{Tr}\left[\hat{E}^b_{\boldsymbol{n},i}\lambda^b\hat{U}_{\boldsymbol{n},jk}\right] \\ &= -\frac{ig^2\theta}{4\pi^2a}\sum_{\boldsymbol{n},b}\sum_{(i,j,k)\in\mathrm{even}}\mathrm{Tr}\left[\hat{E}^b_{\boldsymbol{n},i}\lambda^b\left(\hat{U}_{\boldsymbol{n},jk}-\hat{U}^\dagger_{\boldsymbol{n},jk}\right)\right].\end{aligned} \tag{6.34}$$

[1] While our numerical calculations were already running, we became aware of a recent arXiv paper [100] that independently derived a result similar to (6.34) in a different context. We added a comparison between our derivation and the one in [100] to App. A in [4].

In the last line, (i,j,k) is summed over the set of even permutations, and we have used $\hat{U}_{\boldsymbol{n},jk} = \hat{U}^{\dagger}_{\boldsymbol{n},kj}$.

To improve the definition in (6.34), for each site $\boldsymbol{n}$, we replace the outgoing electric field $\hat{E}^b_{\boldsymbol{n},i}$ with an average of the incoming and outgoing electric fields, which better approximates the field at each site, and obtain

$$\theta\hat{Q} = -\frac{ig^2\theta}{8\pi^2 a}\sum_{\boldsymbol{n},b}\sum_{(i,j,k)\in\text{even}} \text{Tr}\left[\left(\hat{E}^b_{\boldsymbol{n}-\hat{i},i} + \hat{E}^b_{\boldsymbol{n},i}\right)\lambda^b\left(\hat{U}_{\boldsymbol{n},jk} - \hat{U}^{\dagger}_{\boldsymbol{n},jk}\right)\right]. \tag{6.35}$$

Note that the θ-term is not invariant under the CP transformation $\hat{U}_{\boldsymbol{n},i} \to \hat{U}^{\dagger}_{\boldsymbol{n},i}$, since the topological charge changes its sign. This is due to the totally antisymmetric ε_{ijk} symbol in (6.34), which changes its sign when reversing two indices, corresponding to a parity transformation. This CP violation manifests in the pseudovector nature of the magnetic field, $B_i = -\frac{1}{2}\varepsilon_{ijk}F_{jk}$, which appears in the θ-term, $\theta Q \propto \varepsilon_{\mu\nu\rho\sigma}F_{\mu\nu}F_{\rho\sigma} \propto \mathbf{E}\cdot\mathbf{B}$. As explained in the introduction, the CP violating nature of the θ-term is the origin of the strong CP problem, which is the problem that QCD does not seem to distinguish matter from antimatter [35].

Since continuous gauge groups lead to infinite-dimensional Hilbert spaces, in order to simulate the Hamiltonian on a finite-sized classical or quantum computer, it is necessary to truncate these to render the problem finite-dimensional. For any finite or compact Lie group, this can be accomplished by expanding the electric field and link operators in the group representation basis, and truncating the irreducible representation labels. This method is detailed in [106]. In this work, we choose to focus on the simplest non-trivial truncation of the U(1) gauge group.

6.3 Model and methods

As a particular example for the generic expression derived in (6.35), we now numerically investigate a (3+1)D U(1) lattice gauge theory. We use a single cube with periodic boundary conditions (see Fig. 6.1) and explore the theory in the Hamiltonian formulation at non-vanishing θ using exact diagonalization. In our computations, we set the lattice spacing $a = 1$ and consider the

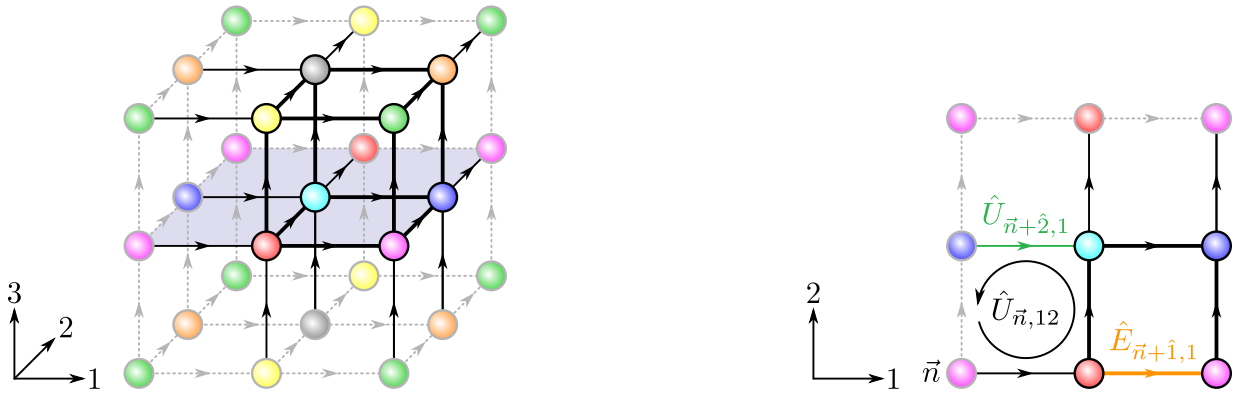

Figure 6.1: Left: Sketch of the 3D cube with periodic boundary conditions. The upper right corner shows the cube with bold black lines, where the colored circles with black outlines correspond to the 8 different vertices at the corners. To illustrate the periodic boundary conditions, the original 8 vertices are mirrored in every direction with mirrored vertices indicated by the same color as the original ones but with grey outlines. The 24 links are indicated as solid black lines with the arrows indicating the orientation of the links. The dashed grey lines correspond to mirrored links due to the periodic boundary conditions. Right: Illustration of a cut through the middle layer of the cube along the 1-2 plane, which is highlighted in light blue in the left panel. For illustration purposes, we show a link operator (green), an electric field operator (orange), and a plaquette operator (black) corresponding to the product of the link operators around the plaquette as indicated by the circular arrow.

Hamiltonian

$$\hat{H} = \hat{H}_E + \hat{H}_B + \tilde{\theta}\hat{Q}, \tag{6.36}$$

$$\hat{H}_E = \frac{1}{2\beta}\sum_{\boldsymbol{n}}\sum_{j=1}^{3}\hat{E}^2_{\boldsymbol{n},j}, \tag{6.37}$$

$$\hat{H}_B = -\frac{\beta}{2}\sum_{\boldsymbol{n}}\sum_{j,k=1;k>j}^{3}(\hat{U}_{\boldsymbol{n},jk} + \hat{U}^\dagger_{\boldsymbol{n},jk}), \tag{6.38}$$

$$\tilde{\theta}\hat{Q} = -i\frac{\tilde{\theta}}{\beta}\sum_{\boldsymbol{n}}\sum_{(i,j,k)\in\text{even}}(\hat{E}_{\boldsymbol{n}-\hat{i},i} + \hat{E}_{\boldsymbol{n},i})(\hat{U}_{\boldsymbol{n},jk} - \hat{U}^\dagger_{\boldsymbol{n},jk}), \tag{6.39}$$

where $\tilde{\theta} = \theta/8\pi^2$, $\beta = 1/g^2$, (i,j,k) is summed over the set of even permutations, and the link operators satisfy the commutation relation

$$[\hat{E}_{\boldsymbol{n},j}, \hat{U}_{\boldsymbol{n}',j'}] = \delta_{\boldsymbol{n},\boldsymbol{n}'}\delta_{j,j'}\hat{U}_{\boldsymbol{n},j}. \tag{6.40}$$

The eigenstates of the electric field operators

$$\hat{E}_{\boldsymbol{n},j}\,|E_{\boldsymbol{n},j}\rangle = E_{\boldsymbol{n},j}\,|E_{\boldsymbol{n},j}\rangle\,,\; E_{\boldsymbol{n},j} \in \mathbb{Z} \tag{6.41}$$

form a basis for the Hilbert space of the gauge fields. In this basis, the gauge field operators can be represented as

$$\hat{E}_{\boldsymbol{n},j} = \sum_{E_{\boldsymbol{n},j}\in\mathbb{Z}} E_{\boldsymbol{n},j}\,|E_{\boldsymbol{n},j}\rangle\langle E_{\boldsymbol{n},j}|\,, \tag{6.42}$$

$$\hat{U}_{\boldsymbol{n},j} = \sum_{E_{\boldsymbol{n},j}\in\mathbb{Z}} |E_{\boldsymbol{n},j}-1\rangle\langle E_{\boldsymbol{n},j}|\,. \tag{6.43}$$

It can be checked straightforwardly that these operators satisfy the commutation relation in (6.40). In order to represent the infinite-dimensional gauge-field operators on a finite-size computer, their Hilbert space must be truncated at a cutoff, s. Thus, the gauge field operators become

$$\hat{E}_{\boldsymbol{n},j} = \sum_{E_{\boldsymbol{n},j}=-s}^{s} E_{\boldsymbol{n},j}\,|E_{\boldsymbol{n},j}\rangle\langle E_{\boldsymbol{n},j}|\,, \tag{6.44}$$

$$\hat{U}_{\boldsymbol{n},j} = \sum_{E_{\boldsymbol{n},j}=-s+1}^{s} |E_{\boldsymbol{n},j}-1\rangle\langle E_{\boldsymbol{n},j}|\,. \tag{6.45}$$

Throughout this work, we choose the simplest nontrivial symmetric truncation corresponding to $s = 1$.

Furthermore, the Hamiltonian is gauge invariant because it commutes with the Gauss' law operators

$$\hat{G}_{\boldsymbol{n}} = \sum_{i=1}^{3}(\hat{E}_{\boldsymbol{n},i} - \hat{E}_{\boldsymbol{n}-\hat{i},i}),\; \forall \boldsymbol{n}. \tag{6.46}$$

The gauge-invariant physical states $|\Psi\rangle$ are constrained by the Gauss' law operators via the relation

$$\hat{G}_{\boldsymbol{n}}\,|\Psi\rangle = 0,\; \forall \boldsymbol{n}. \tag{6.47}$$

However, the Hamiltonian acts on a Hilbert space that contains many unphysical states, which violate the gauge-invariance condition in (6.47). Therefore, the spectrum of the Hamiltonian, without enforcing Gauss' law, will be contaminated by unphysical states. A possible way to suppress the unphysical states is to diagonalize $\hat{H} + r\sum_{\boldsymbol{n}}\hat{G}^2_{\boldsymbol{n}}$ with $r \gg 1$, where the squared Gauss' law operators are included as a penalty term [66, 162]. Since the physical states lie in the kernel of the Gauss' law operators, they will be unaffected by the penalty. We choose to use

an alternative and more resource-efficient way to incorporate Gauss' law into our Hamiltonian, following [3]. In particular, we treat (6.47) as a set of constraints on the electric operators

$$\sum_{i=1}^{3}(\hat{E}_{\boldsymbol{n},i} - \hat{E}_{\boldsymbol{n}-\hat{i},i}) = 0, \ \forall \boldsymbol{n}, \tag{6.48}$$

and solve this as a system of equations over the electric operators. Since the sum of all the Gauss' law constraints evaluates to zero, $\sum_{\boldsymbol{n}=1}^{N} \hat{G}_{\boldsymbol{n}} = 0$, there are only $N-1$ independent constraints on a lattice with N sites. Hence, we can eliminate $N-1$ arbitrary electric field operators by expressing them in terms of the remaining ones [3]. Since the eliminated electric field operators no longer contribute directly to the dynamics, their corresponding link operators become identities. In one dimension with open boundary conditions, this method allows one to completely eliminate the gauge fields, leaving only matter degrees of freedom [112, 179, 180]. This method can be applied to higher dimensions, as discussed in [181, 159, 182], and has recently been demonstrated on a (2+1)D lattice gauge theory [3]. For a 3D cubic lattice with periodic boundary conditions, where $N = L^3$, $L^3 - 1$ out of $3L^3$ link degrees of freedom are eliminated, and thus, the Hamiltonian can be expressed solely in terms of the gauge field operators acting on the remaining $2L^3 - 1$ links. Here, L denotes the number of sites along each direction. Compared to the penalty method, where the dimensions of the Hamiltonian remain unchanged, this method reduces the number of basis states from $(2s+1)^{3L^3}$ to $(2s+1)^{2L^3-1}$.

6.4 Results

Here, we report our numerical findings in [4]. We use exact diagonalization to compute the low-lying spectrum of the Hamiltonian in (6.39) on a single periodic cube. We focus on the θ-dependence of the energy spectrum and of the ground-state expectation value of various observables. In particular, we study the plaquette expectation value

$$\langle \mathcal{P} \rangle = -\frac{1}{V\beta}\langle \Psi_0 | \hat{H}_B | \Psi_0 \rangle, \tag{6.49}$$

where V is the number of plaquettes in the lattice and $|\Psi_0\rangle$ is the ground state, the bare topological charge density

$$\langle \mathcal{Q} \rangle = -\frac{\beta}{V}\langle \Psi_0 | \hat{Q} | \Psi_0 \rangle, \tag{6.50}$$

and the bare electric energy density

$$\langle \mathcal{E}^2 \rangle = \frac{\beta}{V}\langle \Psi_0 | \hat{H}_E | \Psi_0 \rangle. \tag{6.51}$$

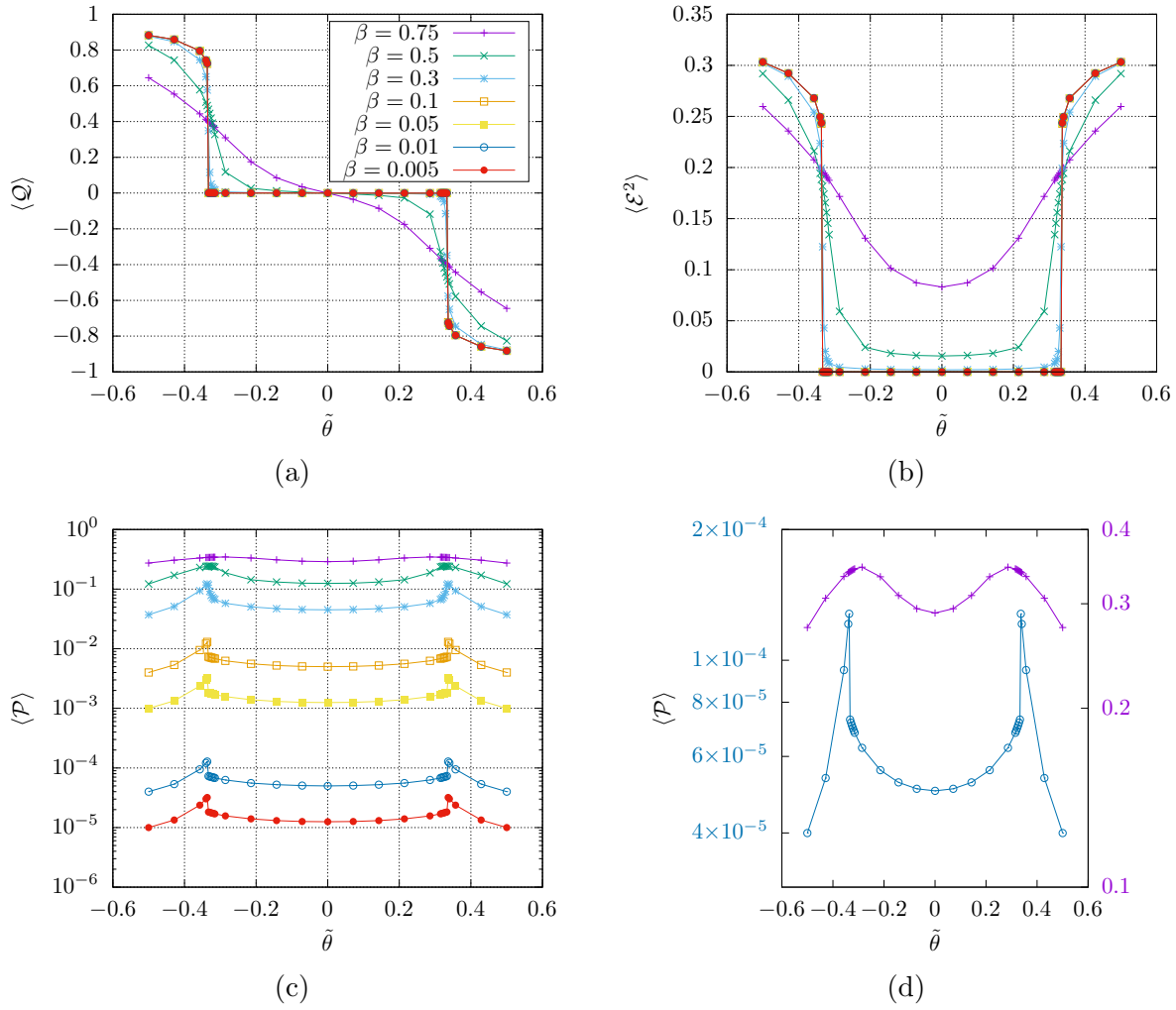

Figure 6.2: (a) Bare topological charge density, (b) bare electric energy density, and (c) plaquette expectation value as a function of $\tilde{\theta}$ for $\beta \leq 0.75$. (d) The plaquette expectation values for $\beta = 0.01$ (left y-axis) and 0.75 (right y-axis) are shown in greater detail to highlight the change in the behavior as β increases. Note that in panels (a) and (b) the lines for $\beta = 0.1, 0.05, 0.01$ are covered by the red line.

We summarize our results for the topological charge density, the electric energy density, and the plaquette expectation value in Fig. 6.2. We simulated a wide range of couplings $\beta \in [0.005, 0.75]$, and for each value of β, a range of values $\tilde{\theta} \in [-0.5, 0.5]$. Both the topological charge density and the electric energy density exhibit discontinuities at $|\tilde{\theta}| \approx 0.333$ when $\beta \leq 0.3$, as shown in Figs. 6.2(a) and 6.2(b). The plaquette expectation value displays spikes at these points, as depicted in Figs. 6.2(c) and 6.2(d). These abrupt changes point towards a phase transition occurring at $|\tilde{\theta}| \approx 0.333$. Also shown in Fig. 6.2, these distinct features vanish as β increases beyond 0.3, suggesting the disappearance of the phase transition in this regime.

Our observed phase transition most likely corresponds to the theoretically predicted phase transition at $\theta = \pi$ [183, 184]. The main reason is that this transition, to our knowledge, is the only analytically predicted constant-θ transition in a compact U(1) gauge theory. Furthermore, in agreement with our observed transition, the analytical studies [183, 184] predict the occurrence of this transition for small β, which vanishes at large β as one approaches the Coulomb phase. However, since we only simulate a single cube, which is the minimal volume in 3+1D, harsh finite-volume effects are expected. In particular, we attribute the shift in our observed transition point from $\theta = \pi$ and the lack of the predicted 2π-periodicity in θ [183, 184] to finite-volume effects. For evidences, we turn to related numerical studies of 1+1D U(1) models with a θ-term [185, 168, 169, 170], since, to our knowledge, similar studies to ours in 3+1D do not exist. A lack of periodicity in θ and noticeable shifts of the $\theta = \pi$ transition point to larger θ-values were reported for simulations of lattices with only a few sites, i.e., $\lesssim 10$ [185, 170]. In [169], a discontinuity in the topological charge density emerged only when the lattice size reached 64 sites, and was not observed in lattices with ≤ 32 sites. Only in simulations of larger lattices with $\gtrsim 100$ sites are both the 2π-periodicity and the $\theta = \pi$ transition point fully restored [185, 168, 169, 170]. As such, in 3+1D, we expect to recover both the periodicity and the correct transition point in larger lattices as well. In the future, this could be verified by including our θ-term in the TN simulations for 3+1D U(1) LGTs [173], as well as eventual quantum simulations of LGTs. We note in passing that the truncation of electric fields could have plausibly played a role in the lack of periodicity and the shift in transition point. However, such truncation effects were shown to be neglibigle in [4]. Additionally, we note that in our simulations, the observables obey the following symmetries: $\langle \mathcal{P}(\theta) \rangle = \langle \mathcal{P}(-\theta) \rangle$, $\langle \mathcal{E}^2(\theta) \rangle = \langle \mathcal{E}^2(-\theta) \rangle$, and $\langle \mathcal{Q}(\theta) \rangle = -\langle \mathcal{Q}(-\theta) \rangle$. Similar symmetries were observed in [185, 168, 169]. We remark that these symmetries can be directly inferred from the fact that the CP transformation $U_{\boldsymbol{n},i} \to U^{\dagger}_{\boldsymbol{n},i}$ flips the sign of the topological charge but not that of the plaquette expectation and electric energy density.

Next, we investigate the order of the quantum phase transition, which is unknown from analytical predictions [186, 183]. We focus on the low-lying energy spectrum of the Hamiltonian at $\beta = 0.3$ and near the transition point $\tilde{\theta} \approx 0.333$. Our results for the first four energy levels, shown in Fig. 6.3, reveal an avoided level-crossing between the ground state and the first excited state at the transition point. These findings rule out a first-order transition, where one would expect a level crossing. Instead, the spectrum suggests that a second or higher-order phase

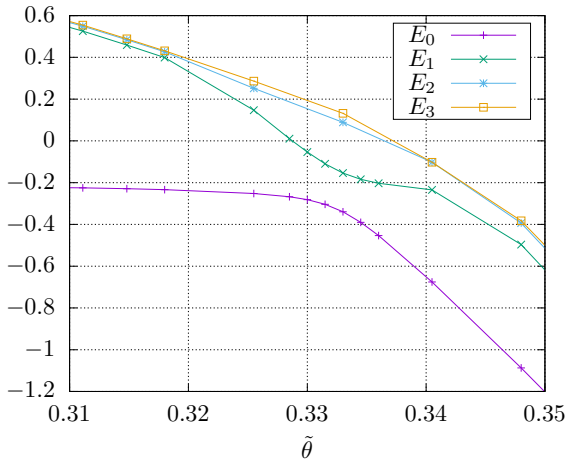

Figure 6.3: Low-lying spectrum as a function of $\tilde{\theta}$ for $\beta = 0.3$. The ground state and the first excited state show an avoided level-crossing at $\tilde{\theta} \approx 0.333$.

transition is causing the sudden changes in the observables in Fig. 6.2.

6.5 Outlook

Using the TN methods developed for 3+1D LGTs in [173], our numerical results can be readily cross-checked and extended to larger lattices. Furthermore, in the light of the recently developed quantum algorithms for LGTs [2, 107], we envision future fault-tolerant quantum simulations of 3+1D LGTs including our θ-term. To build towards this vision, one can create efficient quantum circuits to simulate our θ-term following [2]. One begins by expanding the electric field and link operators in the group representation basis [6, 106], as we have done in this work for the U(1) case. The electric field operators in this basis for the SU(2) and SU(3) cases were shown in [151] and [187], respectively. The SU(2) and SU(3) link operators in the fundamental representation in this basis can be found in [6]. As such, the circuit synthesis techniques in [2] can be applied to construct gate-by-gate quantum circuits to simulate our θ-term.

Chapter 7

Conclusion and future directions

In this thesis, we contributed to three aspects of quantum simulation of LGTs, namely, algorithms, resource estimation and model-building.

In chapter 2, we introduced the Kogut-Susskind Hamiltonian formulation of LGTs, the variational quantum eigensolver and the product-formula approach to simulate quantum dynamics, and provided a general framework for fault-tolerant resource estimation of product-formula quantum simulation.

In chapter 3, we considered the simulation of quantum electrodynamics on a two-dimensional lattice using the variational quantum eigensolver. We found small variational quantum circuits that are able to obtain the ground states of quantum electrodynamics on the smallest two-dimensional lattices, namely a plaquette with open boundary conditions and periodic boundary conditions. While the results were obtained via classical simulations of the circuits, we showed that quantum electrodynamics beyond one spatial dimension can be potentially solved on a near-term quantum device.

In chapter 4, we constructed explicit gate-by-gate quantum algorithms, based on second-order product formula, to simulate lattice quantum electrodynamics and chromodynamics, which are described by the Kogut-Susskind Hamiltonians for U(1), SU(2), and SU(3) LGTs. These algorithms are efficient in the simulation time, lattice size, desired precision, and the truncation of the bosonic gauge fields. Furthermore, we evaluated commutator bounds for product formulas, and provided concrete estimations of T-gate and qubit counts for simulations of LGTs in any spatial dimension and lattice size.

In chapter 5, we developed a memory-efficient basis to simulate lattice quantum electrodynamics. In this basis, the U(1) Kogut-Susskind Hamiltonian is compressed into a smaller effective Hamiltonian. We numerically showed that this approach enabled accurate simulations with much

less memory. Furthermore, this approach made possible the small variational quantum circuits used in chapter 3.

In chapter 6, we derived for the first time a $(3+1)$D topological θ-term, directly relevant to the strong CP problem in particle physics, in the Hamiltonian formulation. Furthermore, we numerically showed a phase transition induced by the θ-term in a U(1) LGT. Lattice gauge theories with a θ-term are an important class of problems that are difficult to simulate classically using Monte Carlo methods due to the infamous sign problem. We provided a concrete starting point for Hamiltonian-based sign-problem-free simulations, such as classical tensor network simulation and quantum simulation, of LGTs with a θ-term.

7.1 Looking forward

In this section, we present our perspectives on the challenges ahead in quantum simulation of LGTs.

While VQEs are a potentially useful application of current noisy quantum devices, all the realized or proposed VQEs that we are aware of were cross-checked against classical circuit simulators and/or exact diagonalization (ED) results. In order to achieve any practical quantum advantage via VQEs, this reliance on classical results must somehow be weaned off. Otherwise, once the size of the simulated system grows beyond the reach of classical circuit simulators or ED, which can be easily done, the results obtained from VQEs can no longer be trusted. Moreover, the intended value of VQEs as a computational tool is lost. However, there may be useful insights that can be drawn from VQEs, even if such reliance remains. For instance, perhaps the designs for VQE ansatzes may provide hints for constructing good initial state preparation oracles, the access to which is typically assumed, in fault-tolerant ground-state preparation algorithms.

While analog quantum simulation is not the focus of this thesis, its potential applications should not be overlooked, particularly in light of analog simulators' success in simulating condensed matter systems [188, 189, 190, 191] and Abelian LGTs [43, 44, 45, 46]. In analog simulations, the dynamics (Hamiltonian) of the native hardware are engineered to closely mimic that of the simulated model. Analog simulations of LGTs are typically more sophisticated and require more engineering than those of condensed matter systems. This is because the hardware Hamiltonians resemble condensed matter systems more than LGTs. For instance, two-qubit Ising interactions are commonplace in spin systems and various hardware platforms, such as trapped-ion and Rydberg quantum devices. However, many-body interactions that arise in the kinetic and magnetic parts of LGTs are not native to any hardware, and thus require more engineering. On the one hand, it is encouraging to see that LGT interactions can in theory be engineered on analog simulators. See section 1.3 for references to experimental and theoretical papers on analog quantum simulations of LGTs. On the other hand, since analog simulators are not error-corrected,

and given the experimental complexities of analog LGT simulations, it seems appropriate to raise the following questions: Under the influence of decoherence and errors, how long can a LGT simulation last before we can no longer reliably and accurately extract useful physical insights from it? What are the appropriate measures of accuracy and reliability for analog simulators? Within the reliable simulation time, is it possible to perform a simulation and extract information, which would be otherwise intractable via classical simulations?

Looking forward to the future, we will offer some ideas on how to alleviate the enormous resource overhead for fault-tolerant LGT simulations in light of the results presented in chapter 4. One way is to improve the error analyses in chapter 4. Recently shown in [107], the Trotter error bounds for simulating certain bosonic systems, including U(1) and SU(2) LGTs, can in principle be tightened by reasonably assuming knowledge of the initial state. Another way is to come up with simulation algorithms with better gate complexities, as further shown in [107]. However, when applied to finite-size problems, the resource required for an algorithm with a better asymptotic complexity may not be lower. The constant overhead of for instance circuit synthesis has to be taken into account. Indeed, product formula algorithms can incur a lower gate count than quantum signal processing for simulating spin chains [26]. Therefore, it is important to construct more efficient circuit implementation of various simulation algorithms. Compared to simulations of systems with binary local degrees of freedom, i.e., fermions and spin-1/2 particles, simulations of systems with larger local degrees of freedom like bosons are far less studied. Therefore, it is likely that the algorithms for bosonic simulations and their implementations are far from optimal, and have ample room for improvements.

It is also interesting to wonder what kind of a hardware will be running these LGT simulations in the future. Assuming the algorithms in the future, similar to ours, will heavily rely on arithmetic operations, the hardware will have to be able to execute quantum arithmetic circuits accurately and at a similar rate to modern classical computers, in order to execute fast and reliable LGT simulations. While we cannot think of any physical laws forbidding that, that is an unwieldy task from where we stand currently in quantum computing. More specifically, as a result of the large spatial and temporal overhead of implementing fault-tolerance and error correction based on the current state of the art, the clock-speed, which roughly translates to time per logical operation, of quantum computers are far slower than that of classical computers. Therefore, in order to meet this requirement, reaching fault-tolerance is only the first step. Eventually, we will need to figure out how to significantly streamline the implementation of fault-tolerance.

References

[1] D. Paulson et al. Simulating 2D Effects in Lattice Gauge Theories on a Quantum Computer. *PRX Quantum*, 2:030334, 2021.

[2] A. Kan and Y. Nam. Lattice Quantum Chromodynamics and Electrodynamics on a Universal Quantum Computer. *arXiv preprint arXiv:2107.12769*, 2021.

[3] J. F. Haase, L. Dellantonio, A. Celi, D. Paulson, A. Kan, K. Jansen, and C. A. Muschik. A resource efficient approach for quantum and classical simulations of gauge theories in particle physics. *Quantum*, 5:393, 2021.

[4] A. Kan, L. Funcke, S. Kühn, L. Dellantonio, J. Zhang, J. F. Haase, C. A. Muschik, and K. Jansen. Investigating a $(3+1)$D topological θ-term in the Hamiltonian formulation of lattice gauge theories for quantum and classical simulations. *Phys. Rev. D*, 104:034504, 2021.

[5] A. Kan, L. Funcke, S. Kühn, L. Dellantonio, J. Zhang, J. F. Haase, C. A. Muschik, and K. Jansen. 3+1D θ-Term on the Lattice from the Hamiltonian Perspective. *arXiv preprint arXiv:2111.02238*, 2021.

[6] T. Byrnes and Y. Yamamoto. Simulating lattice gauge theories on a quantum computer. *Physical Review A*, 73(2):022328, 2006.

[7] A. F. Shaw, P. Lougovski, J. R. Stryker, and N. Wiebe. Quantum Algorithms for Simulating the Lattice Schwinger Model. *Quantum*, 4:306, 2020.

[8] L. C. Biedenharn and J. D. Louck. A pattern calculus for tensor operators in the unitary groups. *Communications in Mathematical Physics*, 8(2):89–131, 1968.

[9] J. D. Louck. Recent progress toward a theory of tensor operators in the unitary groups. *American Journal of Physics*, 38(1):3–42, 1970.

[10] R. P. Feynman. Simulating physics with computers. *Int. J. Theor. Phys*, 21(6/7), 1982.

[11] Yuri Alexeev et al. Quantum computer systems for scientific discovery. *PRX Quantum*, 2:017001, 2021.

[12] J. Preskill. Simulating quantum field theory with a quantum computer. In *The 36th Annual International Symposium on Lattice Field Theory. 22-28 July*, page 24, 2018.

[13] A. Bazavov, F. Karsch, S. Mukherjee, and P. Petreczky. Hot-dense lattice QCD. *The European Physical Journal A*, 55(11):194, 2019.

[14] K. G. Wilson. Confinement of quarks. *Phys. Rev. D*, 10:2445–2459, 1974.

[15] S. Dürr et al. Ab initio determination of light hadron masses. *Science*, 322(5905):1224–1227, 2008.

[16] S. Aoki et al. FLAG review 2019: Flavour Lattice Averaging Group (FLAG). *The European Physical Journal C*, 80(2):1–268, 2020.

[17] Z. Davoudi, W. Detmold, P. Shanahan, K. Orginos, A. Parreño, M. J. Savage, and M. L. Wagman. Nuclear matrix elements from lattice qcd for electroweak and beyond–standard-model processes. *Physics Reports*, 2020.

[18] Michael Creutz, Laurence Jacobs, and Claudio Rebbi. Monte carlo computations in lattice gauge theories. *Physics Reports*, 95(4):201–282, 1983.

[19] M. Troyer and U.-J. Wiese. Computational complexity and fundamental limitations to fermionic quantum monte carlo simulations. *Physical Review letters*, 94(17):170201, 2005.

[20] S. Lloyd. Universal quantum simulators. *Science*, pages 1073–1078, 1996.

[21] E. A. Martinez et al. Real-time dynamics of lattice gauge theories with a few-qubit quantum computer. *Nature*, 534(7608):516–519, 2016.

[22] M. Suzuki. General theory of fractal path integrals with applications to many-body theories and statistical physics. *Journal of Mathematical Physics*, 32(2):400–407, 1991.

[23] A. M. Childs, Y. Su, M. C. Tran, N. Wiebe, and S. Zhu. Theory of Trotter error with commutator scaling. *Phys. Rev. X*, 11:011020, 2021.

[24] D. W. Berry, A. M. Childs, R. Cleve, R. Kothari, and R. D. Somma. Simulating hamiltonian dynamics with a truncated taylor series. *Physical Review letters*, 114(9):090502, 2015.

[25] G. H. Low and I. L. Chuang. Optimal hamiltonian simulation by quantum signal processing. *Physical Review letters*, 118(1):010501, 2017.

[26] A. M. Childs, D. Maslov, Y. Nam, N. J. Ross, and Y. Su. Toward the first quantum simulation with quantum speedup. *Proceedings of the National Academy of Sciences*, 115(38):9456–9461, 2018.

[27] J. Preskill. Quantum Computing in the NISQ era and beyond. *Quantum*, 2:79, 2018.

[28] J. R. McClean, J. Romero, R. Babbush, and A. Aspuru-Guzik. The theory of variational hybrid quantum-classical algorithms. *New J. Phys.*, 18(2):023023, 2016.

[29] M. Cerezo et al. Variational quantum algorithms. *Nature Reviews Physics*, pages 1–20, 2021.

[30] J. R. McClean, S. Boixo, V. N. Smelyanskiy, R. Babbush, and H. Neven. Barren plateaus in quantum neural network training landscapes. *Nature communications*, 9(1):1–6, 2018.

[31] M. Cerezo, A. Sone, T. Volkoff, L. Cincio, and P. J. Coles. Cost function dependent barren plateaus in shallow parametrized quantum circuits. *Nature communications*, 12(1):1–12, 2021.

[32] L. Bittel and M. Kliesch. Training variational quantum algorithms is np-hard. *Phys. Rev. Lett.*, 127:120502, 2021.

[33] A. Peruzzo et al. A variational eigenvalue solver on a photonic quantum processor. *Nat. Commun.*, 5:4213, 2014.

[34] C. Kokail et al. Self-verifying variational quantum simulation of lattice models. *Nature*, 569(7756):355–360, 2019.

[35] A. Hook. TASI lectures on the strong CP problem and axions. *arXiv preprint arXiv:1812.02669*, 2018.

[36] Hartmut Neven. Day 1 opening keynote by Hartmut Neven (quantum summer symposium 2020). https://www.youtube.com/watch?v=TJ6vBNEQReU&ab_channel=TensorFlow/, Sep 2020.

[37] Get to know Honeywell's latest quantum computer system model H1. https://www.honeywell.com/us/en/news/2020/10/get-to-know-honeywell-s-latest-quantum-computer-system-model-h1/, 2020.

[38] IBM's roadmap for scaling quantum technology. https://www.ibm.com/blogs/research/2020/09/ibm-quantum-roadmap/, 2020.

[39] IBM's roadmap for building an open quantum software ecosystem. https://www.ibm.com/blogs/research/2021/02/quantum-development-roadmap/, 2021.

[40] Scaling IonQ's quantum computers: The roadmap. https://ionq.com/posts/december-09-2020-scaling-quantum-computer-roadmap/, 2020.

[41] M.-C. Banuls et al. Simulating lattice gauge theories within quantum technologies. *The European physical journal D*, 74(8):1–42, 2020.

[42] N. Klco, A. Roggero, and M. J. Savage. Standard model physics and the digital quantum revolution: Thoughts about the interface. *arXiv preprint arXiv:2107.04769*, 2021.

[43] F. Görg, K. Sandholzer, J. Minguzzi, R. Desbuquois, M. Messer, and T. Esslinger. Realization of density-dependent Peierls phases to engineer quantized gauge fields coupled to ultracold matter. *Nature Physics*, 15(11):1161–1167, 2019.

[44] C. Schweizer et al. Floquet approach to Z2 lattice gauge theories with ultracold atoms in optical lattices. *Nature Physics*, 15(11):1168–1173, 2019.

[45] A. Mil et al. A scalable realization of local U(1) gauge invariance in cold atomic mixtures. *Science*, 367(6482):1128–1130, 2020.

[46] B. Yang et al. Observation of gauge invariance in a 71-site Bose-Hubbard quantum simulator. *Nature*, 587(7834):392–396, 2020.

[47] N. Klco et al. Quantum-classical computation of schwinger model dynamics using quantum computers. *Physical Review A*, 98(3):032331, 2018.

[48] E. F. Dumitrescu et al. Cloud quantum computing of an atomic nucleus. *Phys. Rev. Lett.*, 120(21):210501, 2018.

[49] O. Shehab et al. Toward convergence of effective-field-theory simulations on digital quantum computers. *Physical Review A*, 100(6):062319, 2019.

[50] C. W. Bauer, M. Freytsis, and B. Nachman. Simulating collider physics on quantum computers using effective field theories. *arXiv preprint arXiv:2102.05044*, 2021.

[51] E. Gustafson, Y. Zhu, P. Dreher, N. M. Linke, and Y. Meurice. Real-time quantum calculations of phase shifts using wave packet time delays. *arXiv preprint arXiv:2103.06848*, 2021.

[52] M. Kreshchuk, S. Jia, W. M. Kirby, G. Goldstein, J. P. Vary, and P. J. Love. Light-front field theory on current quantum computers. *Entropy*, 23(5):597, 2021.

[53] Y. Atas, J. Zhang, R. Lewis, A. Jahanpour, J. F. Haase, and C. A. Muschik. SU(2) hadrons on a quantum computer. *arXiv preprint arXiv:2102.08920*, 2021.

[54] B. Nachman, D. Provasoli, W. A. de Jong, and C. W. Bauer. Quantum algorithm for high energy physics simulations. *Physical Review Letters*, 126(6):062001, 2021.

[55] M. Kreshchuk, S. Jia, W. M. Kirby, G. Goldstein, J. P. Vary, and P. J. Love. Simulating hadronic physics on noisy intermediate-scale quantum devices using basis light-front quantization. *Phys. Rev. A*, 103:062601, 2021.

[56] H.-H. Lu et al. Simulations of subatomic many-body physics on a quantum frequency processor. *Physical Review A*, 100(1):012320, 2019.

[57] S. A. Rahman, R. Lewis, E. Mendicelli, and S. Powell. Su(2) lattice gauge theory on a quantum annealer. *Phys. Rev. D*, 104:034501, 2021.

[58] N. Klco, M. J. Savage, and J. R. Stryker. SU (2) non-Abelian gauge field theory in one dimension on digital quantum computers. *Physical Review D*, 101(7):074512, 2020.

[59] A. Roggero, A. C. Y. Li, J. Carlson, R. Gupta, and G. N. Perdue. Quantum computing for neutrino-nucleus scattering. *Physical Review D*, 101(7):074038, 2020.

[60] D. E. Kharzeev and Y. Kikuchi. Real-time chiral dynamics from a digital quantum simulation. *Physical Review Research*, 2(2):023342, 2020.

[61] A. Ciavarella, N. Klco, and M. J. Savage. Trailhead for quantum simulation of SU (3) Yang-Mills lattice gauge theory in the local multiplet basis. *Physical Review D*, 103(9):094501, 2021.

[62] N. H. Nguyen, M. C. Tran, Y. Zhu, A. M. Green, C. H. Alderete, Z. Davoudi, and N. M. Linke. Digital quantum simulation of the schwinger model and symmetry protection with trapped ions. *arXiv preprint arXiv:2112.14262*, 2021.

[63] S. P. Jordan, K. S. M. Lee, and J. Preskill. Quantum algorithms for quantum field theories. *Science*, 336(6085):1130–1133, 2012.

[64] D. Banerjee, M. Dalmonte, M. Müller, E. Rico, P. Stebler, U.-J. Wiese, and P. Zoller. Atomic quantum simulation of dynamical gauge fields coupled to fermionic matter: From string breaking to evolution after a quench. *Phys. Rev. Lett.*, 109:175302, 2012.

[65] E. Zohar, J. I. Cirac, and B. Reznik. Simulating compact quantum electrodynamics with ultracold atoms: Probing confinement and nonperturbative effects. *Physical review letters*, 109(12):125302, 2012.

[66] P. Hauke, D. Marcos, M. Dalmonte, and P. Zoller. Quantum simulation of a lattice Schwinger model in a chain of trapped ions. *Phys. Rev. X*, 3:041018, 2013.

[67] K. Kasamatsu, I. Ichinose, and T. Matsui. Atomic quantum simulation of the lattice gauge-higgs model: Higgs couplings and emergence of exact local gauge symmetry. *Phys. Rev. Lett.*, 111:115303, 2013.

[68] L. Tagliacozzo, A. Celi, P. Orland, M. W. Mitchell, and M. Lewenstein. Simulation of non-Abelian gauge theories with optical lattices. *Nature communications*, 4(1):1–8, 2013.

[69] U.-J. Wiese. Ultracold quantum gases and lattice systems: quantum simulation of lattice gauge theories. *Ann. Phys.*, 525(10-11):777–796, 2013.

[70] E. Zohar, J. I. Cirac, and B. Reznik. Cold-atom quantum simulator for su(2) yang-mills lattice gauge theory. *Phys. Rev. Lett.*, 110:125304, 2013.

[71] E. Zohar, J. I. Cirac, and B. Reznik. Quantum simulations of gauge theories with ultracold atoms: Local gauge invariance from angular-momentum conservation. *Phys. Rev. A*, 88:023617, 2013.

[72] S. P. Jordan, K. S. M. Lee, and J. Preskill. Quantum algorithms for fermionic quantum field theories. *arXiv preprint arXiv:1404.7115*, 2014.

[73] S. P. Jordan, K. S.M. Lee, and J. Preskill. Quantum computation of scattering in scalar quantum field theories. *Quantum Information & Computation*, 14(11-12):1014–1080, 2014.

[74] D. Marcos, P. Widmer, E. Rico, M. Hafezi, P. Rabl, U.-J. Wiese, and P. Zoller. Two-dimensional lattice gauge theories with superconducting quantum circuits. *Ann. Phys.*, 351:634–654, 2014.

[75] Y. Kuno, K. Kasamatsu, Y. Takahashi, I. Ichinose, and T. Matsui. Real-time dynamics and proposal for feasible experiments of lattice gauge-higgs model simulated by cold atoms. *New Journal of Physics*, 17(6):063005, 2015.

[76] A. Mezzacapo, E. Rico, C. Sabín, I. L. Egusquiza, L. Lamata, and E. Solano. Non-abelian su(2) lattice gauge theories in superconducting circuits. *Phys. Rev. Lett.*, 115:240502, 2015.

[77] V. Kasper, F. Hebenstreit, M. K. Oberthaler, and J. Berges. Schwinger pair production with ultracold atoms. *Phys. Lett. B*, 760:742–746, 2016.

[78] Y. Kuno, S. Sakane, K. Kasamatsu, I. Ichinose, and T. Matsui. Atomic quantum simulation of a three-dimensional u(1) gauge-higgs model. *Phys. Rev. A*, 94:063641, 2016.

[79] D. González-Cuadra, E. Zohar, and J. I. Cirac. Quantum simulation of the Abelian-Higgs lattice gauge theory with ultracold atoms. *New Journal of Physics*, 19(6):063038, 2017.

[80] Y. Kuno, S. Sakane, K. Kasamatsu, I. Ichinose, and T. Matsui. Quantum simulation of $(1+1)$-dimensional u(1) gauge-higgs model on a lattice by cold bose gases. *Phys. Rev. D*, 95:094507, 2017.

[81] C. Muschik et al. U(1) Wilson lattice gauge theories in digital quantum simulators. *New Journal of Physics*, 19(10):103020, 2017.

[82] E. Zohar, A. Farace, B. Reznik, and J. I. Cirac. Digital quantum simulation of z 2 lattice gauge theories with dynamical fermionic matter. *Physical review letters*, 118(7):070501, 2017.

[83] E. Rico, M. Dalmonte, P. Zoller, D. Banerjee, M. Bögli, P. Stebler, and U.-J. Wiese. So(3) "nuclear physics" with ultracold gases. *Ann. Phys.*, 393:466–483, 2018.

[84] A. H. Moosavian and S. Jordan. Faster quantum algorithm to simulate fermionic quantum field theory. *Physical Review A*, 98(1):012332, 2018.

[85] T. V. Zache, F. Hebenstreit, F. Jendrzejewski, M. K. Oberthaler, J. Berges, and P. Hauke. Quantum simulation of lattice gauge theories using Wilson fermions. *Quantum science and technology*, 3(3):034010, 2018.

[86] J. Bender, E. Zohar, A. Farace, and J. I. Cirac. Digital quantum simulation of lattice gauge theories in three spatial dimensions. *New Journal of Physics*, 20(9):093001, 2018.

[87] N. Klco and M. J. Savage. Digitization of scalar fields for quantum computing. *Physical Review A*, 99(5):052335, 2019.

[88] H. Lamm, S. Lawrence, and Y. Yamauchi. General methods for digital quantum simulation of gauge theories. *Physical Review D*, 100(3):034518, 2019.

[89] A. Alexandru et al. Gluon field digitization for quantum computers. *Physical Review D*, 100(11):114501, 2019.

[90] A. Celi, B. Vermersch, O. Viyuela, H. Pichler, M. D. Lukin, and P. Zoller. Emerging two-dimensional gauge theories in rydberg configurable arrays. *Physical Review X*, 10(2):021057, 2020.

[91] N. Klco and M. J. Savage. Minimally entangled state preparation of localized wave functions on quantum computers. *Physical Review A*, 102(1):012612, 2020.

[92] N. Klco and M. J. Savage. Fixed-point quantum circuits for quantum field theories. *Physical Review A*, 102(5):052422, 2020.

[93] A. J. Buser, T. Bhattacharya, L. Cincio, and R. Gupta. State preparation and measurement in a quantum simulation of the O(3) sigma model. *Physical Review D*, 102(11):114514, 2020.

[94] Z. Davoudi et al. Towards analog quantum simulations of lattice gauge theories with trapped ions. *Physical Review Research*, 2(2):023015, 2020.

[95] N. Klco and M. J. Savage. Systematically localizable operators for quantum simulations of quantum field theories. *Physical Review A*, 102(1):012619, 2020.

[96] H. Lamm, S. Lawrence, and Y. Yamauchi. Parton physics on a quantum computer. *Physical Review Research*, 2(1):013272, 2020.

[97] N. Mueller, A. Tarasov, and R. Venugopalan. Deeply inelastic scattering structure functions on a hybrid quantum computer. *Physical Review D*, 102(1):016007, 2020.

[98] M. Kreshchuk, W. M. Kirby, G. Goldstein, H. Beauchemin, and P. J. Love. Quantum simulation of quantum field theory in the light-front formulation. *arXiv preprint arXiv:2002.04016*, 2020.

[99] Y. Ji, H. Lamm, and S. Zhu. Gluon field digitization via group space decimation for quantum computers. *Phys. Rev. D*, 102:114513, 2020.

[100] T. D. Cohen, H. Lamm, S. Lawrence, and Y. Yamauchi. Quantum algorithms for transport coefficients in gauge theories. *Phys. Rev. D*, 104:094514, Nov 2021.

[101] Z. Davoudi, N. M. Linke, and G. Pagano. Toward simulating quantum field theories with controlled phonon-ion dynamics: A hybrid analog-digital approach. *arXiv preprint arXiv:2104.09346*, 2021.

[102] B. Chakraborty, M. Honda, T. Izubuchi, Y. Kikuchi, and A. Tomiya. Digital quantum simulation of the Schwinger model with topological term via adiabatic state preparation. *arXiv preprint arXiv:2001.00485*, 2021.

[103] R. R. Ferguson, L. Dellantonio, A. Al Balushi, K. Jansen, W. Dür, and C. A. Muschik. Measurement-based variational quantum eigensolver. *Phys. Rev. Lett.*, 126:220501, 2021.

[104] J. R. Stryker. Shearing approach to gauge invariant trotterization. *arXiv preprint arXiv:2105.11548*, 2021.

[105] J. Kogut and L. Susskind. Hamiltonian formulation of Wilson's lattice gauge theories. *Phys. Rev. D*, 11(2):395, 1975.

[106] E. Zohar and M. Burrello. Formulation of lattice gauge theories for quantum simulations. *Phys. Rev. D*, 91(5):054506, 2015.

[107] Y. Tong, V. V. Albert, J. R. McClean, J. Preskill, and Y. Su. Provably accurate simulation of gauge theories and bosonic systems. *arXiv preprint arXiv:2110.06942*, 2021.

[108] J. Smit. *Introduction to quantum fields on a lattice.* Cambridge University Press, 2002.

[109] M. A. Nielsen and I. L. Chuang. *Quantum Computation and Quantum Information.* Cambridge University Press, 2010.

[110] S. Bravyi and A. Kitaev. Universal quantum computation with ideal clifford gates and noisy ancillas. *Phys. Rev. A*, 71:022316, 2005.

[111] C. J. Hamer, J. Kogut, D. P. Crewther, and M. M. Mazzolini. The massive schwinger model on a lattice: Background field, chiral symmetry and the string tension. *Nucl. Phys. B*, 208(3):413–438, 1982.

[112] C. J. Hamer, W. Zheng, and J. Oitmaa. Series expansions for the massive Schwinger model in Hamiltonian lattice theory. *Phys. Rev. D*, 56:55–67, 1997.

[113] C. Alexandrou, V. Drach, K. Jansen, C. Kallidonis, and G. Koutsou. Baryon spectrum with $N_f = 2 + 1 + 1$ twisted mass fermions. *Phys. Rev. D*, 90:074501, 2014.

[114] R. A. Briceño, H.-W. Lin, and D. R. Bolton. Charmed-baryon spectroscopy from lattice qcd with N_f=2+1+1 flavors. *Phys. Rev. D*, 86:094504, 2012.

[115] L. Liu, H.-W. Lin, K. Orginos, and A. Walker-Loud. Singly and doubly charmed $j = 1/2$ baryon spectrum from lattice qcd. *Phys. Rev. D*, 81:094505, 2010.

[116] J. Stokes, J. Izaac, N. Killoran, and G. Carleo. Quantum natural gradient. *Quantum*, 4:269, 2020.

[117] M. Schuld, V. Bergholm, C. Gogolin, J. Izaac, and N. Killoran. Evaluating analytic gradients on quantum hardware. *Phys. Rev. A*, 99(3):032331, 2019.

[118] R. Hooke and T. A. Jeeves. "direct search"solution of numerical and statistical problems. *Journal of the ACM (JACM)*, 8(2):212–229, 1961.

[119] D. R. Jones, C. D. Perttunen, and B. E. Stuckman. Lipschitzian optimization without the lipschitz constant. *J. Optimiz. Theory App.*, 79(1):157–181, 1993.

[120] D. E. Finkel and C. T. Kelley. Convergence analysis of the direct algorithm. *Optimization Online*, 14(2):1–10, 2004.

[121] P. E. Nicholas. A dividing rectangles algorithm for stochastic simulation optimization. *Proc. INFORMS Comput. Soc. Conf.*, 14:47–61, 2014.

[122] H. Liu, S. Xu, X. Wang, J. Wu, and Y. Song. A global optimization algorithm for simulation-based problems via the extended direct scheme. *Eng. Optimiz.*, 47(11):1441–1458, 2015.

[123] P. I. Frazier. A tutorial on bayesian optimization. *arXiv preprint arXiv:1807.02811*, 2018.

[124] P. Jordan and E. Wigner. Über das paulische äquivalenzverbot. *Zeitschrift für Physik*, 47(9):631–651, 1928.

[125] F. Verstraete, V. Murg, and J. I. Cirac. Matrix product states, projected entangled pair states, and variational renormalization group methods for quantum spin systems. *Adv. Phys.*, 57(2):143–224, 2008.

[126] A. Uvarov, J. D. Biamonte, and D. Yudin. Variational quantum eigensolver for frustrated quantum systems. *Physical Review B*, 102(7), 2020.

[127] Andrew Jena, Scott Genin, and Michele Mosca. Pauli partitioning with respect to gate sets. *arXiv preprint arXiv:1907.07859*, 2019.

[128] A. Salam and J. C. Ward. Weak and electromagnetic interactions. *Il Nuovo Cimento*, 11(4):568–577, 1959.

[129] S. L. Glashow. The renormalizability of vector meson interactions. *Nuclear Physics*, 10:107–117, 1959.

[130] S. Weinberg. A model of leptons. *Physical Review letters*, 19(21):1264, 1967.

[131] Y. Ne'eman. Derivation of strong interactions from a gauge invariance. *Nuclear physics*, 26(2):222–229, 1961.

[132] M. Gell-Mann. Symmetries of baryons and mesons. *Physical Review*, 125(3):1067, 1962.

[133] M. Gell-Mann. A schematic model of baryons and mesons. *Physics Letters*, 8(3):214–215, 1964.

[134] Richard P Feynman. The qualitative behavior of yang-mills theory in 2+1 dimensions. *Nuclear Physics B*, 188(3):479–512, 1981.

[135] A. Bocharov, M. Roetteler, and K. M. Svore. Efficient synthesis of universal repeat-until-success quantum circuits. *Physical Review letters*, 114(8):080502, 2015.

[136] M. K. Bhaskar, S. Hadfield, A. Papageorgiou, and I. Petras. Quantum algorithms and circuits for scientific computing. *Quantum Information & Computation*, 16(3-4):197–236, 2016.

[137] C. Gidney. Halving the cost of quantum addition. *Quantum*, 2:74, 2018.

[138] Y. Nam and D. Maslov. Low-cost quantum circuits for classically intractable instances of the hamiltonian dynamics simulation problem. *npj Quantum Information*, 5(1):1–8, 2019.

[139] M. G. Alford, A. Schmitt, K. Rajagopal, and T. Schäfer. Color superconductivity in dense quark matter. *Review Modern Physics*, 80:1455–1515, Nov 2008.

[140] J. E. Kim and G. Carosi. Axions and the strong CP problem. *Reviews of Modern Physics*, 82(1):557, 2010.

[141] G. Ortiz, J. E. Gubernatis, E. Knill, and R. Laflamme. Quantum algorithms for fermionic simulations. *Physical Review A*, 64(2):022319, 2001.

[142] E. Wigner and P. Jordan. Über das paulische äquivalenzverbot. *Z. Phys*, 47:631, 1928.

[143] A. Y. Kitaev, A. Shen, M. N. Vyalyi, and M. N. Vyalyi. *Classical and quantum computation*. American Mathematical Soc., 2002.

[144] Q. Wang, M. Li, C. Monroe, and Y. Nam. Resource-Optimized Fermionic Local-Hamiltonian Simulation on a Quantum Computer for Quantum Chemistry. *Quantum*, 5:509, 2021.

[145] D. Maslov. Advantages of using relative-phase toffoli gates with an application to multiple control toffoli optimization. *Physical Review A*, 93(2):022311, 2016.

[146] C. Jones. Low-overhead constructions for the fault-tolerant toffoli gate. *Physical Review A*, 87(2):022328, 2013.

[147] Y. Nam, Y. Su, and D. Maslov. Approximate quantum fourier transform with O(nlog(n)) T gates. *npj Quantum Information*, 6(1):1–6, 2020.

[148] T. G. Draper, S. A. Kutin, E. M. Rains, and K. M. Svore. A logarithmic-depth quantum carry-lookahead adder. *Quantum Information & Computation*, 6(4):351–369, 2006.

[149] A. M. Childs and N. Wiebe. Hamiltonian simulation using linear combinations of unitary operations. *Quantum Information & Computation*, 12(11-12):901–924, 2012.

[150] H. M. Georgi. *Lie algebras in particle physics: from isospin to unified theories*. Benjamin-Cummings, 1982.

[151] D. Robson and D. M. Webber. Gauge covariance in lattice field theories. *Zeitschrift für Physik C Particles and Fields*, 15(3):199–226, 1982.

[152] V. Giovannetti, S. Lloyd, and L. Maccone. Quantum random access memory. *Physical Review letters*, 100(16):160501, 2008.

[153] M. Creutz. Gauge fixing, the transfer matrix, and confinement on a lattice. *Phys. Rev. D*, 15(4):1128, 1977.

[154] J. J. De Swart. The octet model and its Clebsch-Gordan coefficients. *Reviews of Modern Physics*, 35(4):916, 1963.

[155] S. Gasiorowicz. *Elementary particle physics*. Wiley New York, 1966.

[156] P. A. Carruthers. *Introduction to unitary symmetry*. Interscience, 1966.

[157] J. Kogut, D. K. Sinclair, and L. Susskind. A quantitative approach to low-energy quantum chromodynamics. *Nuclear Physics B*, 114(2):199–236, 1976.

[158] T. A. Kaeding. Tables of SU(3) isoscalar factors. *Atomic Data and Nuclear Data Tables*, 61(2):233–288, 1995.

[159] David B. Kaplan and Jesse R. Stryker. Gauss's law, duality, and the hamiltonian formulation of u(1) lattice gauge theory. *Phys. Rev. D*, 102:094515, 2020.

[160] M. Creutz. Monte carlo study of quantized su (2) gauge theory. *Physical Review D*, 21(8):2308, 1980.

[161] H. J. Rothe. *Lattice Gauge Theories: An Introduction Third Edition*, volume 74. World Scientific Publishing Company, 2005.

[162] S. Kühn, J. I. Cirac, and M.-C. Bañuls. Quantum simulation of the Schwinger model: A study of feasibility. *Phys. Rev. A*, 90:042305, 2014.

[163] J. C. Halimeh, H. Lang, J. Mildenberger, Z. Jiang, and P. Hauke. Gauge-symmetry protection using single-body terms. *arXiv preprint arXiv:2007.00668*, 2020.

[164] T. G. Draper. Addition on a quantum computer. *arXiv preprint quant-ph/0008033*, 2000.

[165] C. Gattringer and K. Langfeld. Approaches to the sign problem in lattice field theory. *Int. J. Mod. Phys. A*, 31(22):1643007, 2016.

[166] R. J. Crewther, P. Di Vecchia, G. Veneziano, and E. Witten. Chiral estimate of the electric dipole moment of the neutron in quantum chromodynamics. *Phys. Lett. B*, 88(1):123, 1979.

[167] C. Abel et al. Measurement of the permanent electric dipole moment of the neutron. *Phys. Rev. Lett.*, 124(8):081803, 2020.

[168] L. Funcke, K. Jansen, and S. Kühn. Topological vacuum structure of the Schwinger model with matrix product states. *Phys. Rev. D*, 101:054507, 2020.

[169] Y. Kuramashi and Y. Yoshimura. Tensor renormalization group study of two-dimensional U(1) lattice gauge theory with a θ term. *Journal of High Energy Physics*, 2020(4):1–11, 2020.

[170] J. Zhang, R. Ferguson, S. Kühn, J. F. Haase, C. M. Wilson, K. Jansen, and C. A. Muschik. Simulating gauge theories with variational quantum eigensolvers in superconducting microwave cavities. *arXiv preprint arXiv:2108.08248*, 2021.

[171] Lena Funcke, Karl Jansen, and Stefan Kühn. CP-violating Dashen phase transition in the two-flavor Schwinger model: a study with matrix product states. *arXiv preprint arXiv:2110.15642*, 2021.

[172] T. Felser, P. Silvi, M. Collura, and S. Montangero. Two-dimensional quantum-link lattice quantum electrodynamics at finite density. *Phys. Rev. X*, 10:041040, 2020.

[173] G. Magnifico, T. Felser, P. Silvi, and S. Montangero. Lattice Quantum Electrodynamics in (3+1)-dimensions at finite density with Tensor Networks. *arXiv preprint arXiv:2011.10658*, 2020.

[174] P. Di Vecchia, K. Fabricius, G. C. Rossi, and G. Veneziano. Preliminary Evidence for $U_A(1)$ Breaking in QCD from Lattice Calculations. *Nucl. Phys. B*, 192:392, 981.

[175] C. Alexandrou, A. Athenodorou, K. Cichy, A. Dromard, E. Garcia-Ramos, K. Jansen, U. Wenger, and F. Zimmermann. Comparison of topological charge definitions in Lattice QCD. *Eur. Phys. J. C*, 80(5):424, 2020.

[176] M. Peskin. Cornell University preprint CLNS 395, Thesis, 1978.

[177] G. Bhanot, E. Rabinovici, N. Seiberg, and P. Woit. Lattice θ vacua. *Nucl. Phys. B*, 230(3):291, 1984.

[178] A. Bilal. Lectures on anomalies. *arXiv preprint arXiv:0802.0634*, 2008.

[179] M.-C. Bañuls, K. Cichy, K. Jansen, and J. I. Cirac. The mass spectrum of the Schwinger model with matrix product states. *J. High Energy Phys.*, 2013(11):158, 2013.

[180] M.-C. Bañuls, K. Cichy, J. I. Cirac, K. Jansen, and S. Kühn. Density induced phase transitions in the Schwinger model: A study with matrix product states. *Phys. Rev. Lett.*, 118:071601, 2017.

[181] Yannick Meurice. Discrete aspects of continuous symmetries in the tensorial formulation of abelian gauge theories. *Phys. Rev. D*, 102:014506, 2020.

[182] Judah F. Unmuth-Yockey. Gauge-invariant rotor hamiltonian from dual variables of 3d $u(1)$ gauge theory. *Phys. Rev. D*, 99:074502, 2019.

[183] J. L. Cardy. Duality and the θ parameter in abelian lattice models. *Nucl. Phys. B*, 205(1):17, 1982.

[184] M. Honda and Y. Tanizaki. Topological aspects of 4d abelian lattice gauge theories with the θ parameter. *J. High Energy Phys.*, 2020(12):1, 2020.

[185] C. Gattringer, T. Kloiber, and M. Müller-Preussker. Dual simulation of the two-dimensional lattice U(1) gauge-Higgs model with a topological term. *Phys. Rev. D*, 92:114508, 2015.

[186] J. L. Cardy and E. Rabinovici. Phase Structure of Z(p) Models in the Presence of a Theta Parameter. *Nucl. Phys. B*, 205:1, 1982.

[187] N. Mukunda and L. K. Pandit. Tensor Methods and a Unified Representation Theory of SU3. *Journal of Mathematical Physics*, 6(5):746–765, 1965.

[188] J. Zhang et al. Observation of a many-body dynamical phase transition with a 53-qubit quantum simulator. *Nature*, 551(7682):601–604, 2017.

[189] M. Schreiber et al. Observation of many-body localization of interacting fermions in a quasirandom optical lattice. *Science*, 349(6250):842–845, 2015.

[190] H. Bernien et al. Probing many-body dynamics on a 51-atom quantum simulator. *Nature*, 551(7682):579–584, 2017.

[191] G. Semeghini et al. Probing topological spin liquids on a programmable quantum simulator. *Science*, 374(6572):1242–1247, 2021.